

Coherent Lattice and Molecular Dynamics

in

Ultrafast Single-Shot Spectroscopy

by

Peter Roland Poulin

B.Sc. Chemistry, University of Western Ontario, 1996

M.Sc. Chemistry, University of Toronto, 1999

Submitted to the Department of Chemistry
in partial fulfillment of the requirements for the degree of

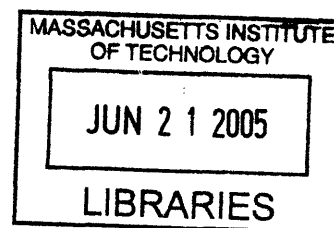
Doctor of Philosophy

at the

MASSACHUSETTS INSTITUTE OF TECHNOLOGY

June 2005

© Massachusetts Institute of Technology, MMV
All rights reserved



Author _____

Department of Chemistry
April 1, 2005

Certified by _____

Keith A. Nelson
Thesis Supervisor

Accepted by _____

Robert W. Field
Chairman, Departmental Committee on Graduate Students

ARCHIVES

This doctoral thesis has been examined by a committee of the Department of Chemistry as follows:

Professor Andrei Tokmakoff



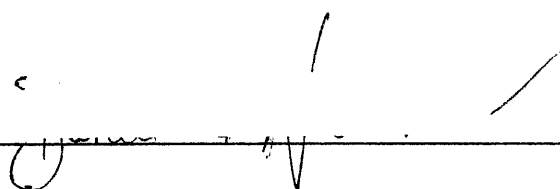
Chairman

Professor Keith A. Nelson



Thesis Supervisor

Professor Daniel G. Nocera



Coherent Lattice and Molecular Dynamics

in

Ultrafast Single-Shot Spectroscopy

by

Peter Roland Poulin

Submitted to the Department of Chemistry on April 1, 2005
in partial fulfillment of the requirements for the degree of
Doctor of Philosophy at the Massachusetts Institute of Technology

Abstract

This thesis focuses on the development, refinement, and application of dual-echelon single-shot ultrafast spectroscopy to the study of coherent nuclear motion in condensed phase systems. The general principles of the single-shot method are described, and particular emphasis is given to the general applicability and shortcomings of this technique and the extraction of data from raw laboratory images. Coupled to the single-shot system is a synchronously pumped dual-beam noncollinear optical parametric amplifier which was developed to provide independently tunable pump and probe beams in the visible and UV regions of the electromagnetic spectrum.

The second part of the thesis concerns the application of this technique to the study of atomic motions in liquids and solids. Single-shot nonresonant impulsive stimulated Raman scattering (ISRS) measurements in *m*-iodoanisole and bismuth germanate reveal the existence of transient coherent behavior. High-field resonant excitation of the semimetals bismuth, antimony and tellurium, as well as the semiconductor germanium telluride, reveals dramatic lattice anharmonicity as a function of pump fluence. Finally, ultrafast photodissociation of the triiodide ion both in solution and in the solid state gives considerable insight regarding the role of the local environment in mediating chemical reaction dynamics.

Thesis Supervisor: Keith A. Nelson
Title: Professor of Chemistry

Acknowledgements

It is with great pleasure that I acknowledge, first and foremost, my supervisor Keith Nelson for his enthusiasm, insight, vision and patience, without which the single-shot project would remain little more than a dream. In my time at MIT, he has been a source of guidance and inspiration without whom the work reported in this thesis simply could not have been completed. I don't think it's possible to come away from a conversation about science with Keith in a state other than "fired up", and it's his infectious enthusiasm which keeps all of us going.

I also wish to thank my committee members, Andrei Tokmakoff and Dan Nocera, for their guidance and support during the course of my graduate career. Andrei is a superb spectroscopist, and Dan can scarcely go an hour without coming up with a great new idea, and the combination is potent indeed.

I have had the distinct pleasure of working with and around so many wonderful individuals in the Nelson group, and the loss of this daily contact is one of the most difficult aspects of leaving MIT. Greg Wakeham introduced me to the lab and to the single-shot experiment, and I owe a large debt of gratitude to him. Tim Crimmins, Richard Koehl and Rebecca Slayton also welcomed me warmly when I joined the group, and for that I am most grateful.

The cast of characters who constituted "my generation" in the lab are a diverse bunch indeed. Nikolay Stoyanov, the dancing phenom, left an impression on us all which defies description. Jaime Choi (*nee* Beers), my sushi-eating pal, is a sweetheart through-and-through. David "Dubya" Ward has a presence unlike any other. Josh Vaughan is a good friend, a great scientist, and a man of boundless curiosity. Ben Paxton is a man after my own heart, and I value tremendously the times we've shared playing baseball and talking sports and life (go Red Sox!) Darius Torchinsky and I have spent many hours discussing politics and grad school, and I respect his thoughtfulness and perseverance. Eric Statz, to whom the torch is now passed with our recent graduations – how I'll miss the lunch time round table in the office! And finally, Thomas Feurer, a constant source of fresh ideas and insight, and one of the best scientists I have ever met.

So many others have come and gone in the Nelson group during my time, and made it such an enjoyable place to work, that I would be remiss if I failed to acknowledge them: Christ, Thomas, Efren, Kenji, Masashi, Cindy, Kathy, Ka-Lo, Emmanuel, Christoph, Gagan, Tina and Taeho – thank you all.

Outside the lab, I feel truly privileged to count among my good friends Jenny Yang (go Red Sox again!), Dave Lahr, Sean Hopkins, Steve Soares, Lynne Woodroffe, Oded Rabin and Scott Witonsky. Your friendship and support have added to my life in ways which I cannot adequately express.

I wish to acknowledge also the unfailing support of my mother, brother and sister-in-law, who have always taken an interest in my work at MIT, and whose strength and love have made this journey so much more bearable.

Finally, I wish to thank Sandra, who I love dearly and who is closer to me than any other. This thesis, I dedicate to you...

*Do not follow where the path may lead.
Go instead where there is no path and leave a trail.*

Ralph Waldo Emerson

Life's a journey, not a destination.

Steven Tyler

Table of Contents

Abstract.....	3
Acknowledgements.....	5
1. Introduction	31
2. Dual Echelon Single-Shot Ultrafast Spectroscopy	41
2.1 Amplified Titanium-Sapphire Laser System	41
2.2 The Dual Echelon Single-Shot Technique.....	47
2.3 Analysis of Single-Shot Images.....	57
2.4 Sources of Error in Single-Shot Measurements.....	72
2.4.1 Fabrication and Construction Imperfections.....	72
2.4.2 Sensitivity Limitations	74
2.4.3 Temporal Dispersion of Probe Pulses.....	79
2.4.4 Wavevector Mismatch	85
2.4.5 Diffraction by Optical Elements	87
3. Generation of Tunable Ultrashort Pulses	103
3.1 Wavelength Tuning by Parametric Amplification.....	103
3.2 Noncollinear Broadband Phase-Matching in an OPA	107
3.3 Experimental Setup for a Noncollinear OPA.....	116
3.4 Results.....	125
3.5 Dual Beam Phase-Locked Single-Shot NOPA.....	137
3.6 Conclusion	144
4. Time-resolved Nonresonant Raman Scattering in Liquids and Solids	147
4.1 Classical Theory of Stimulated Raman Scattering	147
4.2 ISRS Measurements in Bismuth Germanate.....	158
4.3 Stimulated Raman Scattering in 3-Iodoanisole.....	169
4.4 Conclusion	180
5. Impulsive Absorption in Semimetals and Semiconductors	185
5.1 Introduction to Ultrafast Photoexcitation of Semimetals.....	186
5.2 Apparatus for Time-Resolved Reflectivity Experiments.....	192
5.3 Single-Shot Coherent Phonon Dynamics in Bi, Sb and Te	195

5.4	Coherent Control of Semimetal Phonon Evolution	212
5.5	Long-Time Lattice Dynamics at High Pump Intensities	223
5.6	Ultrafast Phase Transition in Germanium Telluride	243
5.7	Theory of Impulsive Absorption in Semimetals and Semiconductors.....	257
5.7.1	Classical Theory of Reflectivity	260
5.7.2	Microscopic Theory of Coherent Phonon Oscillations.....	268
5.7.3	Variation of Coherent Phonon Frequency	274
5.7.4	Intensity-Dependent Reflectivity and Carrier Relaxation.....	279
5.7.5	Ultrafast Phase Transitions	282
5.8	Conclusion	286
6.	Ultrafast Triiodide Photochemistry in Solution	293
6.1	Introduction to the Triiodide System	293
6.2	Transient Absorption Experimental Setup.....	300
6.3	Transient Absorption of Triiodide and Diiodide in Ethanol.....	301
6.4	Solvent-Dependent Reaction Dynamics	311
6.5	Viscosity-Dependent Reaction Dynamics	319
6.6	Triiodide in a Glass-Forming Liquid	325
6.7	Analysis of Vibrational Energy	337
6.8	Conclusion	355
7.	Solid State Triiodide Photochemistry	361
7.1	Synthesis of Single Crystal Triiodide Samples.....	363
7.1.1	Tetra- <i>n</i> -butylammonium Triiodide	365
7.1.2	Tetraphenylphosphonium Triiodide.....	367
7.1.3	Tetraethylammonium Triiodide	369
7.2	Transient Absorption of Solid-State Triiodides.....	371
7.3	Molecular Dynamics Simulation of I ₃ ⁻ Photodissociation	380
7.4	Discussion of Results.....	397
7.5	Conclusion	405
8.	Conclusions and Future Work	409

List of Figures

2-1	The top panel illustrates spectral measurement of pulses from the Kerr-lens modelocked oscillator. The FWHM bandwidth is about 40 nm. The bottom panel shows the measurement of the intensity autocorrelation for the same pulses. Assuming a Gaussian envelope shape yields a FWHM duration of 72 fs.	43
2-2	The top panel illustrates the spectral bandwidth of the amplified 10 Hz pulse train. Each pulse has a FWHM bandwidth of roughly 30 nm. In the bottom panel, the intensity autocorrelation trace for the amplified pulses has a FWHM duration of 85 fs, corresponding to a 55 fs pulse duration.	46
2-3	Schematic diagram of a transmissive echelon.	51
2-4	Crossed-echelon method for generating a time-structured probe pulse where temporal delay is mapped onto the spatial profile of the pulse. Only 25 independent delay steps are shown in the figure, but the actual echelons generate 400 individual steps.	52
2-5	Schematic illustration of the dual echelon single-shot experiment.	53
2-6	CCD image showing sample (left) and reference (right) beams. Both beams contain an image of the crossed echelons, but only the sample beam has passed through the material under investigation. The earliest time delay points are located in the top left corner of the sample image and the bottom right corner of the reference image. Traversing row-by-row down any column, successive delay increments are 25 fs. From column-to-column across any row, the delay increment is 500 fs. The total time window for the 20×20 2-D array of 400 delay points is 10 ps. The darkened area on the sample image corresponds to a reduction of transmitted light intensity due to the material response. Here, a 400 nm pump pulse induces a fast “electronic” time-dependent response. The modulation of 800 nm probe light over a time window of about 350 fs is due to hot-electron generation at the surface of the fused silica sample.	56

2-7	Schematic of algorithm used to extract single-shot data from raw CCD images. Four processed echelon images are needed to reconstruct and correct the response function data: the sample image, the reference image, and the corresponding background images.....	59
2-8	Illustration of the procedure used to isolate the sample image from the raw CCD image data. Raster-scanning in all four directions indicated along the vertical and horizontal scan lines locates the first non-zero-valued pixel on each edge of the image. The global maximum and minimum are taken to define the pixel area occupied by the sample image. The heavy white box in the figure represents the retrieved boundaries. Note that the thick white line in the center of the raw image is only a guide for the eye – there is no such division on the actual images. This procedure works in similar fashion for the reference image, which is then inverted.	60
2-9	Numerical procedure for locating the divisions between echelon time points. In this most accurate method, each row and column of the image is raster-scanned to find the locations where the absolute intensity falls below a zero-threshold, and the spatial derivative of the intensity changes sign. In most cases, these conditions are sufficient to define the division points.....	62
2-10	Application of window function to individual echelon time squares. In the left panel, the echelon divisions are located by raster-scanning individual rows and columns of the image, creating a 2-D grid pattern defining the spatial divisions between time points. In the right panel, the number of usable pixels in each square is further reduced via application of a window function which preferentially selects a certain fraction of the centermost pixels, typically 75%. The window boundaries for each square are indicated by the rectangles drawn within each.	64
2-11	Horizontal scan through row 500 of an echelon image. The usable fraction of pixels is determined for each square by applying a window function centered on the midpoint of the intensity distribution for that square.	65
2-12	(Left) Image of echelon square (1,9). Note the higher intensity in the top left corner, due to edge diffraction. (Right) Image of square (1,3). Here, an edge imperfection results in the inclusion of many zero-valued pixels in the mean intensity summation. These effects can be removed either by iteratively adjusting the window function, which is computationally expensive, or by utilizing a smoothing function on selected troublesome echelon locations.....	67

2-13	Recovered mean signal intensities from the sample image of the data scan. No corrections to the single-shot data have been applied. Note that the strong $t = 0$ feature is clearly visible, but the prior and subsequent baseline is very noisy. The baseline noise contains an oscillatory component with period 500 fs, which matches the periodicity of the thin echelon. This feature is introduced systematically into the data by discontinuities in the mean signal intensities when moving from the bottom row of one echelon column to the top row of the next.	69
2-14	Instrument response function for a single-shot experiment derived from the reference image of the data scan. This response function contains sharp features due to anomalously large or small pixel intensities at particular spatial locations on the echelon image. These anomalous values introduce systematic error into the measurement; the instrument response function is used to correct the recovered data for such errors.	70
2-15	Single-shot data after the instrument response function is applied to remove baseline systematic noise. The data correction procedure is effective for low pump pulse intensities but becomes increasingly less effective at higher intensities.	71
2-16	Defect regions in the cross-section view of the echelon matrix. Edge imperfections are indicated by arrows and internal scattering centers are circled. Such noise sources are very difficult to compensate on account of the unpredictable nature of the transverse distribution of scattered probe light they produce.	73
2-17	Continuum generation in 1 mm crystal quartz. Pump pulses of 10 μ J and 50 fs at 800 nm are focused to a 150 μ m diameter spot on the front surface of the crystal. The resulting self-phase modulation due to the high pump intensity modifies the spectral properties of the pump pulse, generating frequency components over a very broad bandwidth.	76
2-18	Temporal dispersion of probe pulses as a function of echelon delay. The linear dispersion of the echelon glass broadens the temporal profile of the ultrashort probe pulses. The initial probe pulse has a FWHM duration of 31.5 fs, but is stretched to a duration of 49.6 fs at $t = 9000$ fs on the spatial echelon grid.	82
2-19	Temporal broadening of probe pulses at wavelengths of 500 nm (top) and 650 nm (bottom). The echelon glass exhibits normal dispersion, so pulse broadening is more severe at shorter wavelengths. The furthest delayed probe pulses at 500 nm may no longer satisfy the conditions for impulsive excitation.	84

2-20	Probe pulse phase delay induced by wavevector mismatch. The wavevector of most spatial regions of the probe beam (which correspond to probe delay times) deviates from the ideal forward-scattering direction. The effect of this mismatch is to introduce a phase delay contribution to the nominal arrival time at the focal plane for each spatial region.	86
2-21	Echelon image aberration introduced by passage through the sample. Here the sample is a 200 μm thick solution-grown molecular triiodide crystal. The left hand sample image results from a complex series of scattering events within the bulk crystal. In spite of the distortion, individual echelon time points remain defined with enough contrast such that extraction of numerical data is possible.	88
2-22	Schematic illustration of diffraction calculation for the single-shot setup. The initial beam profile is a square wave due to the 1" diameter aperture in the optical layout. The beam traverses four separate stages, each of which constitutes a propagation calculation: passage through the echelons, free-space evolution, lens passage, and free-space evolution to the sample.	93
2-23	Probe beam intensity profiles at the sample position for a series of wavelengths. The intensity distribution depends critically on the phase delay acquired via passage through the echelon. When the delay is an integer multiple of the wavelength, all interference is constructive and only a central peak is observed. However, when this condition is not satisfied, multiple diffraction peaks result, with positions and intensities dependent upon the relative sign of the phase shift.	95
2-24	Calculation of probe beam spatial profile after scattering in the sample and reconstruction by a collimating lens. The top panel shows the placement of the scattering defect. Lower panels show the calculation of the probe profile as a function of the displacement of the defect from the focal point.	98
3-1	Group velocity matching in a collinear optical parametric amplifier. On the left hand side, signal and idler pulses are time-coincident when they begin to interact. In a normally dispersive medium, the group velocity of the idler pulses is greater than the group velocity of the signal pulses, so that the two separate as they propagate through the material. On the right hand side, the pulses continue to interact but because of their separation, new idler photons are added to the trailing edge of the idler field, whereas new signal photons are added to the leading edge of the signal field. The result is temporal broadening of both pulses.	108

3-2	Phase-matching geometry for noncollinear three-wave mixing in BBO. Pump, signal and idler beams propagate in the x - z plane of the crystal. The thick arrows represent the wavevectors of the three beams and the thin vectors represent their group velocities.	109
3-3	Phase-matching curves for type-I three-wave mixing in BBO. The phase-matched signal wavelength is plotted as the ordinate against the polar angle θ , for a series of noncollinear angles α . The shape of the curves changes from a reflexive “U” with an inflection to a monotonically-decreasing function of the polar angle as α increases. At a noncollinear angle of 3.7° , the curve is nearly vertical from 500-750 nm, suggesting the possibility of very broadband phase-matching with this geometry.	110
3-4	Group velocity matching in a noncollinear optical parametric amplifier. The group velocities of signal and idler pulses are different, but the projection of the idler group velocity along the direction of the signal field is equal to the group velocity of the signal. As a result, the signal and idler pulses propagate together through the nonlinear medium. No pulse broadening results from temporal walkoff as in the case of collinear phase-matching. However, since the idler velocity contains a nonzero component normal to the signal propagation direction, the pulses walk off laterally from one another. As this occurs, new photons are added to both fields on the interior edges of each pulse. Both pulses emerge spatially wider, but unchanged temporally except for dispersion due to the medium. ...	115
3-5	Schematic view of the single-shot noncollinear optical parametric amplifier. Single pulses gated out of the Ti:sapphire amplifier are divided and used to generate both pump and seed pulses for the parametric interaction. The center wavelength is controlled by adjusting the seed pulse delay line. Following amplification, OPA pulses are recompressed in a double-pass prism compressor with a deformable mirror retroreflector, providing fine control over the spectral phase.	117
3-6	Parametric superfluorescence from a 1 mm BBO crystal pumped with individual 400 nm, 70 μ J pulses from a Ti:sapphire laser. The bright spot in the center is pump light exiting through the back surface of the crystal. The superfluorescence is emitted along a right-angled cone at an angle of 3.7° and corresponds to signal wavelengths in the range 500-750 nm. Another ring of larger circumference is also present but invisible in the figure; it corresponds to emission at idler wavelengths which all fall beyond the detection range of the camera. The above pattern is generated in a single-shot OPA.	119

3-7	Continuum generation in sapphire. Focusing weak 0.5 μ J, 800 nm pulses in a 1.2 mm thick sapphire plate generates a broadband continuum. Self-focusing in the crystal leads to nonlinear self-phase modulation, which in turn modulates the optical phase of the driving field, generating new frequency components. The highly-structured shape of the spectrum is characteristic of this process.	120
3-8a	Spectra of pulses generated in a single-shot OPA. Wavelengths are tuned to 480 nm, 515 nm and 555 nm respectively.	126
3-8b	Spectra of pulses generated in a single-shot OPA. Wavelengths are tuned to 630 nm, 670 nm and 710 nm respectively.	127
3-9a	Interferometric autocorrelation traces of NOPA pulses at wavelengths 480 nm, 515 nm and 555 nm.	131
3-9b	Interferometric autocorrelation traces of NOPA pulses at wavelengths 630 nm, 670 nm and 710 nm.	132
3-10a	Interferometric autocorrelation of compressed NOPA pulses at wavelengths of 480 nm, 515 nm and 555 nm.	135
3-10b	Interferometric autocorrelation of compressed NOPA pulses at wavelengths of 630 nm, 670 nm and 710 nm.	136
3-11	Schematic illustration of the dual beam phase-locked single-shot NOPA. Two continuum generation stages are used to seed the OPA on both sides of the pump beam, producing two independently tunable ultrafast outputs. Since both beams traverse the same optical elements, the accumulated dispersion in each case is the same.	138
3-12	(Top) NOPA operating with a single seed input. The bright center spot is the pump beam, and the beam on the left is the amplified signal beam. Note that it is located on the circumference of the superfluorescence ring. (Bottom) NOPA operating with two seed pulses, located on either side of the pump beam. The right-hand pulse is tuned to 550 nm and the pulse on the left has 720 nm center wavelength.	141
3-13	Fringe patterns which result from interference between the two NOPA output beams. The large wavelength range over which this occurs implies phase-coherent output which spans the entire tuning range of the amplifier.	143

4-1	Crystal structure of BGO reproduced from reference 17. Individual GeO_4 tetrahedra are indicated by solid lines. Each Bi^{3+} is loosely coordinated to three nearest-neighbor and three next-nearest-neighbor oxygen atoms.	159
4-2	HH and HV Raman spectra for BGO, reproduced from reference 41. Note that the HV spectrum is enhanced by a factor of 11 for visibility. A particularly intense Raman mode is located at 90 cm^{-1} in the HH spectrum....	160
4-3	Raw data scan recorded on the CCD camera for a $100 \mu\text{m}$ thick sample of BGO pumped by an 820 nm , 50 fs single pulse and probed at 410 nm . A very strong initial response lasting about 225 fs is visible, but no further modulation of transmitted light intensity is apparent.	162
4-4a	Single-shot nonresonant Raman scattering measurements in BGO. A strong vibrational signature appears after the initial modulation of transmitted light intensity near $t = 0$ and continues throughout the experimental time window. Two separate single-shot measurement results are shown.	164
4-4b	Single-shot nonresonant Raman scattering measurements in BGO. A strong vibrational signature appears after the initial modulation of transmitted light intensity near $t = 0$ and continues throughout the experimental time window. Two separate single-shot measurement results, distinct from those on the previous page, are shown.....	165
4-5	(Top) Comparison of stimulated Raman scattering in BGO at three different laser fluences. Larger amplitude vibrations result from more intense pump pulses. (Bottom) Maximum oscillation amplitude (proportional to signal amplitude) as a function of pump pulse intensity. The scaling is approximately linear, in accordance with the classical model of ISRS.....	166
4-6	Power spectrum of the time-resolved response of BGO. The 90 cm^{-1} mode is easily recovered, although none of the weaker modes are visible.	167
4-7	(Top) Schematic illustration of probe spectrum filtering in order to detect modulations in transmitted intensity resulting from coherent oscillations in the sample. (Bottom) Spectral filtering on opposite sides of the probe pulse central wavelength produces oppositely-phased oscillatory signals.	168
4-8	Chemical structure of 3-iodoanisole.	170
4-9	Excitation of 3-iodoanisole at 800 nm by a single pump pulse at varying intensities. Clockwise from top left: $6 \mu\text{J}/\text{cm}^2$, $12 \mu\text{J}/\text{cm}^2$, $25 \mu\text{J}/\text{cm}^2$, $35 \mu\text{J}/\text{cm}^2$	171

4-10	Single-shot response of 3-iodoanisole at an excitation intensity of 15 mJ/cm ² . Oscillation amplitude is a maximum at roughly 400 fs and then rapidly decays away in 1.5 ps. The oscillatory signal returns again at later times and reaches a second local maximum at 2.3 ps.....	173
4-11	Power spectrum of the time-resolved response of 3-iodoanisole. There are two closely spaced modes apparent at 248 cm ⁻¹ and 264 cm ⁻¹ . The inset shows the CW Raman spectrum of both iodobenzene and 3-iodoanisole for comparison.	174
5-1	Crystal structure of bismuth. Bismuth belongs to monoclinic space group C2/m with two of three unit cell angles equal to 90°. The solid lines in the figure are provided as a guide to the eye.	186
5-2	Crystal structure of antimony. The lattice structure is trigonal, with space group R3-mh. As before, the solid lines are included as a guide to visualize the symmetry of the lattice.	188
5-3	Crystal structure of tellurium viewed along the z-axis. Tellurium atoms of the same shading lie in the same plane. The dark atoms lie below the plane of the paper and the white atoms lie above the paper plane. The lattice constant <i>a</i> characterizes the interhelical spacing, <i>u</i> represents the helix spacing, and the parameters <i>r</i> and <i>R</i> correspond to the nearest neighbor and next-nearest neighbor distances. The figure is adapted from reference 10.....	189
5-4	Single-shot experimental apparatus for performing experiments in reflectivity mode. Instead of imaging the echelon grid through the sample, the polished sample surface acts as a mirror. The reflected echelon image is collimated by a curved mirror and 20 cm f.l. lens combination and then reduced in size by a factor of four prior to being imaged onto the surface of a CCD camera. The reference arm of the apparatus remains unchanged from the transmission version of the experiment.....	193
5-5	Generation of a multiple-pulse pump train. A single input pulse is split by a series of beamsplitters with R/T ratios of 1:3, 1:2 and 1:1 into four independently delayed replicas. A variable filter (VF) in each beam path permits amplitude attenuation of each beam. The four beams are recombined such that they traverse a common optical path to the sample, permitting multiple-pulse excitation of coherent responses.	195

5-6a	Time-dependent single-shot reflectivity of single crystal bismuth at 800 nm at a range of pump pulse intensities. Both the amplitude of the observed oscillations and the electronic background signal due to newly generated conduction band electrons increase with increasing pump fluence (indicated on each data trace). The data sweeps shown here all correspond to below-damage-threshold excitation.	196
5-6b	Time-dependent single-shot reflectivity of single crystal bismuth at 800 nm at a range of pump pulse intensities. Both the amplitude of the observed oscillations and the electronic background signal due to newly generated conduction band electrons increase with increasing pump fluence (indicated on each data trace). The 25.0 mJ/cm ² trace represents excitation at the bismuth single-shot damage threshold, although multi-shot structural damage may occur at lower fluences.	197
5-7	Illustration of the origin of the cosine-like phase dependence of oscillations in bulk reflectivity due to impulsive absorption in bismuth. Absorption at the pump wavelength promotes valence electrons to the conduction band and effectively shifts the equilibrium lattice potential (grey curve, minimum r_0) to a new, larger separation (black curve, minimum r_p) on account of the reduced nuclear charge screening. Bismuth atoms experience increased mutual repulsion and motion is directed along coordinates which correspond to “breathing modes” of A ₁ symmetry. A vibrational wave packet is created via this process, initially located at the inner turning point of the lattice potential. The packet evolves according to the specific shape of the black curve; however, since the initial position is one of maximum displacement from the equilibrium position, the oscillations have cosine-like phase character.....	199
5-8	Comparison of oscillations in bismuth reflectivity at four different pump pulse fluences. Near $t = 0$, the reflectivity oscillations are all in phase. On account of differing A _{1g} phonon frequencies, the phase relationship changes as a function of time. After seven oscillation cycles, the responses at 2.0 mJ/cm ² and 4.0 mJ/cm ² are 180° out of phase, whereas the response for 9.0 mJ/cm ² excitation is 180° out of phase with the 2.0 mJ/cm ² response after only three cycles.	202
5-9a	Variation of phonon frequency (top) and phonon amplitude (bottom) with excitation intensity in single crystal bismuth. In both cases, the response scales almost linearly with pump intensity to roughly 6.0 mJ/cm ² , and then a distinct plateau region occurs. The responses at very high intensities also follow a qualitative trend, but it is difficult to extract reliable parameters since there are few oscillations in the data.	203

5-9b	Variation of phonon dephasing time with excitation intensity in single crystal bismuth. As before, the response scales almost linearly with pump intensity to roughly 6.0 mJ/cm^2 , and then a distinct plateau region occurs. The high intensity points are determined semiquantitatively due to the small number of cycles in the experimental data.....	204
5-10a	Time-resolved reflectivity of single crystal antimony measured in one laser shot. The induced reflectivity change is positive for antimony, and results from impulsive absorption at the pump wavelength of 800 nm. The amplitude of the coherent oscillations increases with increasing pump intensity, and the phonon frequency shifts noticeably lower. The oscillation dephasing rate also appears to increase for more intense pump pulses.....	206
5-10b	Time-resolved reflectivity of single crystal antimony measured in one laser shot. The induced reflectivity change is positive for antimony, and results from impulsive absorption at the pump wavelength of 800 nm. The amplitude of the coherent oscillations increases with increasing pump intensity, and the phonon frequency shifts noticeably lower. The oscillation dephasing rate also appears to increase for more intense pump pulses. The dephasing rate changes dramatically for the last three scans which are in the region of antimony's single-shot damage threshold.	207
5-11a	Coherent phonon frequency and amplitude as a function of pump pulse intensity for single crystal antimony. In each case, the response scales linearly with intensity up to about 10.0 mJ/cm^2 , and then saturates.....	209
5-11b	Coherent phonon dephasing time as a function of pump pulse intensity for single crystal antimony. The response scales linearly with intensity up to about 10.0 mJ/cm^2 , and then saturates.	210
5-12	Oscillatory component of the time-dependent reflectivity of antimony. The top panels show windowed Fourier transforms (normalized real part only) of the reflectivity signal for several pump intensities. At low intensity, the phonon peak is sharp. As the intensity increases, the phonon peak amplitude decreases and the peak width increases. The presence of only a few cycles at the highest fluences yields a nondescript spectrum. In the bottom panel, the early-time oscillations are compared as a function of laser intensity. A strongly intensity-dependent phonon frequency causes the measured responses to propagate in and out of phase with one another.....	211
5-13a	Time-resolved single-shot reflectivity of single crystal tellurium. The reflectivity increases on account of the excitation pulse. The oscillation frequency, amplitude and dephasing rate all scale with the pump pulse intensity, and dephasing is rapid in all cases.	213

5-13b	Time-resolved single-shot reflectivity of single crystal tellurium. The reflectivity increases on account of the excitation pulse. The oscillation frequency, amplitude and dephasing time all scale with the pump pulse intensity, and dephasing is rapid in all cases. The scan at 30.0 mJ/cm ² is above the single-shot damage threshold for Te, and the oscillatory component of the signal disappears in under two cycles.....	214
5-14a	Variation of the coherent phonon frequency (top) and amplitude (bottom) in tellurium. In each case, the response scales linearly with intensity up to 8.0 mJ/cm ² and then reaches a plateau.....	215
5-14b	Variation of the coherent phonon dephasing time in tellurium. The dephasing time scales linearly with intensity up to 8.0 mJ/cm ² and then reaches a plateau.	216
5-15	Single-shot data showing two-pulse excitation sequences in bismuth, with the second pulse arriving between the second and third (top) or fifth and sixth (bottom) vibrational cycles. When the second pulse arrives in phase, the oscillation amplitude is enhanced. Cancellation of the oscillations can be achieved when the arrival time of the second pulse is exactly one-half cycle out of phase, although intensity adjustment is necessary. Intermediate cases result in both amplitude and phase shifts.	218
5-16	Single-shot measurements showing two-pulse excitation of single crystal bismuth. Excitation pulses are 9.00 mJ/cm ² and the second pulse arrives either during the third or the sixth vibrational cycle. In-phase arrival times produce amplification as before, but clear saturation of the phonon amplitude is observed. At arrival times which are 180° out of phase, nearly complete cancellation of the coherent response is still possible with intensity adjustment of the second pulse. As before, at intermediate times, both the amplitude and phase of the coherence are modified.	220
5-17	Single-shot data showing coherent two-pulse excitation of tellurium. Pump pulse intensities are 3.00 mJ/cm ² (top) and 7.00 mJ/cm ² (bottom). The maximum tellurium reflectivity change is roughly 1.6% so saturation effects are not as obvious. Amplification and cancellation of the coherent response are possible with suitably chosen pulse pairs.	222
5-18a	Two-pulse excitation of bismuth. The intensity of the first pulse is 9.0 mJ/cm ² (top) or 13.0 mJ/cm ² (bottom). The second interrogating pulse intensity is 6.0 mJ/cm ² in both instances, and arrives at a fixed delay, relative to the first pump pulse, of 3.0, 4.0, 5.0, 6.0 or 7.0 ps.	225

- 5-18b** Two-pulse excitation of bismuth. The intensity of the first pulse is 17.0 mJ/cm² (top) or 21.0 mJ/cm² (bottom). The second interrogating pulse intensity is 6.0 mJ/cm² in both instances, and arrives at a fixed delay, relative to the first pump pulse, of 3.0, 4.0, 5.0, 6.0 or 7.0 ps.226
- 5-18c** Two-pulse excitation of bismuth. The intensity of the first pulse is 28.0 mJ/cm². The second interrogating pulse intensity is 6.0 mJ/cm², and it arrives at a fixed delay, relative to the first pump pulse, of 3.0, 4.0, 5.0, 6.0 or 7.0 ps.....227
- 5-19a** Single-shot data showing the results of double-pulse excitation of bismuth at very high intensities. The intensity of the second pump pulse is 3.0 mJ/cm² in each case in order to ensure that the material response is not perturbed too strongly. The initial pump pulse intensities are 26.0 mJ/cm² (top) and 30.0 mJ/cm² (bottom) and the second pulse arrives after 3.0 ps (bottom scan in each panel) or 7.0 ps (top scan in each panel).229
- 5-19b** Single-shot data showing the results of double-pulse excitation of bismuth at very high intensities. The intensity of the second pump pulse is 3.0 mJ/cm² in each case in order to ensure that the material response is not perturbed too strongly. The initial pump pulse intensities are 34.0 mJ/cm² (top) and 50.0 mJ/cm² (bottom) and the second pulse arrives after 3.0 ps (bottom scan in each panel) or 7.0 ps (top scan in each panel).230
- 5-20a** Single-shot data showing long-time evolution probed by induced lattice coherences in bismuth. The initial pump pulse intensity is 26.0 mJ/cm² (top) and 30.0 mJ/cm² (bottom), while the second pulse is maintained at 3.0 mJ/cm². The delay times between the pump pulses are indicated on the right hand side of the data sweeps. Since the two pump pulses are separated by a delay greater than the total 10 ps window of the experiment, only the response due to the second pump can be captured in a single laser shot.....232
- 5-20b** Single-shot data showing long-time evolution probed by induced lattice coherences in bismuth. The initial pump pulse intensity is 34.0 mJ/cm² (top) and 40.0 mJ/cm² (bottom), while the second pulse is maintained at 3.0 mJ/cm². The delay times between the pump pulses are indicated on the right hand side of the data sweeps. Since the two pump pulses are separated by a delay greater than the total window of the experiment, only the response due to the second pump can be captured in a single laser shot....233

5-20c	Single-shot data showing long-time evolution probed by induced lattice coherences in bismuth. The initial pump pulse intensity is 50.0 mJ/cm ² and the second pulse is maintained at 3.0 mJ/cm ² . The delay times between the pump pulses are indicated on the right hand side of the data sweeps. Since the two pump pulses are separated by a delay greater than the total window of the experiment, only the response due to the second pump can be captured in a single laser shot.....	234
5-21a	Single-shot impulsive absorption of tellurium with two excitation pulses. The intensity of the first pump pulse is 9.0 mJ/cm ² (top) or 11.0 mJ/cm ² (bottom) and the second is 6.0 mJ/cm ² . Relative delay times between the pulses are indicated to the right of each data sweep.	236
5-21b	Single-shot impulsive absorption of tellurium with two excitation pulses. The intensity of the first pump pulse is 15.0 mJ/cm ² (top) or 19.0 mJ/cm ² (bottom) and the second is 6.0 mJ/cm ² . Relative delay times between the pulses are indicated to the right of each data sweep.	237
5-21c	Single-shot impulsive absorption of tellurium with two excitation pulses. The intensity of the first pump pulse is 23.0 mJ/cm ² (top) or 27.0 mJ/cm ² (bottom) and the second is 6.0 mJ/cm ² . Relative delay times between the pulses are indicated to the right of each data sweep.	238
5-22a	Single-shot data showing double-pulse excitation of tellurium for very long inter-pulse delays (indicated at the right of each sweep). Excitation intensities are 19.0 mJ/cm ² (top) and 22.0 mJ/cm ² (bottom).	240
5-22b	Single-shot data showing double-pulse excitation of tellurium for very long inter-pulse delays (indicated at the right of each sweep). Excitation intensities are 28.0 mJ/cm ² (top scan) and 34.0 mJ/cm ² (bottom scan).	241
5-22c	Single-shot data showing double-pulse excitation of tellurium for very long inter-pulse delays (indicated at the right of each sweep). Excitation intensities are 40.0 mJ/cm ² (top scan) and 50.0 mJ/cm ² (bottom scan).	242
5-23	Schematic illustration of solid-solid phase transition in germanium telluride. The light spheres are Ge atoms, and the dark spheres are Te atoms. The low temperature structure has rhombohedral symmetry. At a critical temperature of 625 K, a lattice rearrangement occurs which corresponds closely to motion along the A _{1g} optic phonon, resulting in the high temperature cubic phase of GeTe.	245
5-24a	Time-dependent reflectivity of GeTe measured in a single laser shot. Pump pulse intensity is indicated on the right hand side of each data scan.....	246

5-24b	Expanded view of time-resolved reflectivity measurements for germanium telluride at various excitation intensities. As the pump pulse fluence increases from 8.0 mJ/cm ² to 11.0 mJ/cm ² , the frequency of the A _{1g} phonon decreases and the dephasing rate increases. At 20.0 and 24.0 mJ/cm ² , the reflectivity falls very rapidly after the initial electronic contribution to the signal, and ΔR even changes sign for up to 3.5 ps.	247
5-25	Variation of phonon frequency with excitation pulse intensity for germanium telluride. At low fluences, the frequency appears to scale almost linearly with intensity, but no plateau region is observed as for the semimetals.....	248
5-26a	Two-pulse excitation of the A _{1g} lattice mode in germanium telluride. Amplification of the coherent response is achieved by adjusting the delays of pump pulses such that vibrational motion is driven in-phase. The damping rate increases strongly and the phonon frequency shifts lower as the pump intensity increases.	251
5-26b	Three-pulse excitation of the A _{1g} lattice mode in germanium telluride. Amplification of the coherent response is achieved by adjusting the delays of pump pulses such that vibrational motion is driven in-phase. The damping rate increases strongly and the phonon frequency shifts lower as the pump intensity increases.	252
5-26c	Four-pulse excitation of the A _{1g} lattice mode in germanium telluride. Amplification of the coherent response is achieved by adjusting the delays of pump pulses such that vibrational motion is driven in-phase. The damping rate increases strongly and the phonon frequency shifts lower as the pump intensity increases.	253
5-27a	Excitation of germanium telluride with three intense pump pulses and a variably delayed weak fourth pump pulse. In the top panel, three pulses of intensity 4.0 mJ/cm ² are used and in the bottom panel, three 8.0 mJ/cm ² pulses are employed. The fourth pulse is maintained at 5.0 mJ/cm ² in all cases. The delay time (relative to $t = 0$) of the fourth pulse is indicated to the right of each data sweep.....	255
5-27b	Excitation of germanium telluride with three intense pump pulses of 12.0 mJ/cm ² and a variably delayed weak fourth pump pulse of intensity 5.0 mJ/cm ² . The delay time (relative to $t = 0$) of the fourth pulse is indicated to the right of each data sweep.....	256

5-28a	Long-time evolution of the coherent response in germanium telluride. A single excitation pulse of intensity 12.0 mJ/cm^2 (top) or 20.0 mJ/cm^2 (bottom) arrives at time zero. A second much weaker interrogating pulse (5.0 mJ/cm^2) arrives after a delay indicated to the right of each trace. The probe window is adjusted such that the second pump pulse dynamics are captured.....	258
5-28b	Long-time evolution of the coherent response in germanium telluride. Three excitation pulses of intensity 8.0 mJ/cm^2 (top) or 12.0 mJ/cm^2 (bottom) arrive in-phase to drive the A_1 phonon mode. A second much weaker interrogating pulse (5.0 mJ/cm^2) arrives after a delay indicated to the right of each trace. The probe window is adjusted such that the second pump pulse dynamics are captured.	259
5-28c	Long-time evolution of the coherent response in germanium telluride. Three excitation pulses of intensity 16.0 mJ/cm^2 arrive in-phase to drive the A_1 phonon mode. A second much weaker interrogating pulse (5.0 mJ/cm^2) arrives after a delay indicated to the right of each trace. The probe window is adjusted such that the second pump pulse dynamics are captured.....	260
5-29	Variation of phonon frequency with carrier density for single- and double-pump excitation of bismuth.	277
6-1	Absorption spectrum of triiodide ion in ethanol. Inset: Diiodide absorption spectrum in ethanol from reference 65.	296
6-2	Gas-phase energy levels of triiodide, diiodide and iodine relevant to our experiments. Absorption from the ground state of triiodide into the high energy excited state band leads to photodissociation, yielding diiodide and atomic iodine in one of two spin states. Absorption by the nascent diiodide ion leads to further dissociation, giving iodide ion and an iodine atom.....	298
6-3a	Single-shot transient absorption scans for triiodide in ethanol solution. The probe pulse wavelength is indicated on the right hand side of each trace. The wavelengths represented here probe the blue edge of the ground state diiodide absorption band, which is centered at 740 nm.	302
6-3b	Single-shot transient absorption scans for triiodide in ethanol solution. The probe pulse wavelength is indicated on the right hand side of each trace. The wavelengths represented here probe the red edge of the ground state diiodide absorption band, which is centered at 740 nm.	303

6-3c	Transient absorption scan for triiodide in ethanol solution. The photolysis and probe pulses are both 300 nm, so the observed transient absorption dynamics are due to residual ground state triiodide ions.	304
6-4	Wavepacket dynamics of triiodide and diiodide following interaction with a photolysis pulse at 300 nm. Wavelength-dependent probing in the visible and near-IR interrogates I_2^- at particular locations along the molecular coordinate. Due to the coherent nature of diiodide oscillations, opposite-phase behavior is observed on opposite sides of the absorption maximum.	306
6-5	Comparison of the oscillatory component of transient absorption signals at 660 nm and 780 nm. The oscillations show opposite phases, reflecting the average location of the molecular wavepacket along the I-I vibrational coordinate.	308
6-6	Diiodide absorption band narrowing in ethanol. Gaussian fits to transient absorption data at multiple wavelengths are shown at intervals of 1500, 3000, 5000 and 7000 fs following the initial photolysis pulse. The reduced width of the 740 nm absorption line at later times is clearly evident.	310
6-7a	Transient absorption scans of photolyzed triiodide ion in a series of solvents (indicated at right). Probe wavelengths are 660 nm (top) and 700 nm (bottom).	312
6-7b	Transient absorption scans of photolyzed triiodide ion in a series of solvents (indicated at right). Probe wavelengths are 780 nm (top) and 820 nm (bottom).	313
6-7c	Expanded view of transient absorption of photolyzed triiodide ion at a probe wavelength of 660 nm. The solvent is indicated to the right of each data sweep.	314
6-8a	Temperature dependence of the viscosity of ethylene glycol.	319
6-8b	Dielectric spectra of ethylene glycol at various temperatures reproduced from data in references 92 and 93.	320
6-9	Temperature-dependent transient absorption measurements for triiodide in ethylene glycol. Probe wavelengths are 700 nm (top) and 800 nm (bottom).	322
6-10	Structure of cresolphthalein dimethylether, a glass-forming liquid used as a solvent in the photodissociation reaction of triiodide ions.	325

6-11	Position of the triiodide absorption maximum as a function of temperature....	326
6-12a	Single-shot transient absorption of diiodide ion at 660 nm in a solution of cresolphthalein dimethylether as a function of temperature (indicated to the right of each scan). Data sweeps which are shown in grey (310 K, 307 K and 303 K) correspond to solutions at or below the glass transition temperature for CDE.....	327
6-12b	Single-shot transient absorption of diiodide ion at 700 nm in a solution of cresolphthalein dimethylether as a function of temperature (indicated to the right of each scan). Data sweeps which are shown in grey (310 K, 307 K and 303 K) correspond to solutions at or below the glass transition temperature for CDE.....	328
6-12c	Single-shot transient absorption of triiodide ion at 300 nm in a solution of cresolphthalein dimethylether as a function of temperature (indicated to the right of each scan). Data sweeps which are shown in grey (310 K, 307 K and 303 K) correspond to solutions at or below the glass transition temperature for CDE.....	329
6-13	Fitting examples for transient absorption of triiodide and diiodide ions in CDE solution at 310 K.....	334
6-14a	Time-dependent I_2^- absorption profiles at 363 K and 318 K in CDE solution.....	339
6-14b	Time-dependent I_2^- absorption profiles at 310 K in CDE solution.....	340
6-15a	Calculated absorption profiles and vibrational distributions at four different time delays for I_2^- in CDE solution at 363 K.	342
6-15b	Calculated absorption profiles and vibrational distributions at four different time delays for I_2^- in CDE solution at 318 K.	343
6-15c	Calculated absorption profiles and vibrational distributions at four different time delays for I_2^- in CDE solution at 310 K.	344
6-16a	Diiodide excess vibrational energy as a function of time, calculated from instantaneous absorption spectra as demonstrated previously. Data are shown for 363 K and 318 K. In each case, the dissipation of excess energy follows single-exponential kinetics, with time constants of 3.6 ps and 4.1 ps, respectively.....	350

6-16b	Diiodide excess vibrational energy as a function of time, calculated from instantaneous absorption spectra as demonstrated previously. Data are shown for 310 K. The dissipation of excess energy follows single-exponential kinetics, with a time constant of 4.4 ps.	351
6-17	Single exponential fit of the fast decay component of I_3^- absorption in ethanol. The data corresponds to temperature 310 K (top), 318 K (middle) and 363 K (bottom).	353
7-1	Crystal structure of tetra- <i>n</i> -butyl ammonium triiodide viewed along the a axis. The large, darkly shaded spheres are iodine atoms (as triiodide ions) arranged in two crystallographically independent, nearly linear chains. The smaller white spheres are the carbon and nitrogen atoms comprising the tetra- <i>n</i> -butylammonium counterions. The counterions are arranged in a network-like geometry, separating the triiodide chains.	366
7-2	Expanded view of tetra- <i>n</i> -butylammonium cation and the triiodide ion, indicating the relative orientation of each within the triclinic crystal structure.	367
7-3	Unit cell for tetraphenylphosphonium triiodide. There are two triiodide ions per cell and each sits in a “pocket” formed by seven neighboring tetraphenylphosphonium cations. The overall structure is monoclinic.	368
7-4	Enlarged view of tetraphenylphosphonium and triiodide ions within the crystal structure.	369
7-5	View of tetraethylammonium triiodide along the b axis, adapted from reference 3. Triiodide ions are located at the corners of the orthorhombic unit cell. Open circles are iodine atoms, with the heavy circles in the plane of the page and the lighter circles behind the plane. The triiodide ions form stacked arrays with columns of tetraethylammonium cations acting as spacers.	370
7-6	Single-shot transient absorption of photogenerated diiodide ions in the photodissociation of tetra- <i>n</i> -butylammonium triiodide. The photolysis wavelength is 300 nm and the probe wavelength, indicated to the right of each data sweep, is adjusted to monitor wave packet dynamics of the diiodide ions in various geometries. Single-shot damage in the crystal is observed by visual inspection, so each scan is recorded after translating an optimizing the orientation of the sample under very low illumination intensity.	372

7-7	Comparison of single-shot transient absorption signals for photogenerated diiodide ion in tetra- <i>n</i> -butylammonium triiodide single crystals. Sweeps at 600 and 880 nm each display contributions from coherent motion of the I ₂ ⁻ fragment, although these are almost exactly out of phase since the two wavelengths probe opposite sides of the diiodide ground state potential energy surface. The oscillation frequency is roughly 105 cm ⁻¹ which corresponds well with the gas phase value for diiodide ion.	374
7-8	Single-shot transient absorption of diiodide ions following photolysis at 300 nm of tetraphenylphosphonium triiodide single crystals. The probe wavelength is indicated to the right of each data sweep. Coherent contributions to the TA signal are observed when probing near the edges of the diiodide absorption band, and reflect time-dependent motion of the diiodide wave packet.....	376
7-9	Short-time evolution of transient absorption signals at probe wavelengths of 600 and 880 nm for photogenerated diiodide ions in tetraphenylphosphonium triiodide. Coherent oscillations due to diiodide vibrational motion are clearly observed and are anti-phased when measured on opposite sides of the absorption band center.	377
7-10	Single-shot transient absorption of diiodide ions generated in the photolysis of tetraethylammonium triiodide single crystals. The probe wavelength is indicated to the right of each data sweep. As in the TA profiles for the other crystals employed in these experiments, an oscillatory contribution to the absorption signal is visible at wavelengths near the diiodide absorption band edge.	379
7-11	Simulated transient absorption spectrogram for the diiodide ions in the photodissociation of crystalline tetra- <i>n</i> -butylammonium triiodide. The signal shows oscillatory behavior as the diiodide wave packet propagates along its ground state electronic surface.	391
7-12	Nine randomly selected classical diiodide trajectories from the photodissociation simulation for tetra- <i>n</i> -butylammonium triiodide, illustrating varied contributions to the overall transient absorption signal which result from different initial states.	392
7-13	Simulated transient absorption spectrogram for crystalline tetraphenylphosphonium triiodide. Several coherent oscillation cycles are visible after the diiodide ions are born between 300-350 fs, and these gradually dephase, accompanied by incoherent relaxation of excess vibrational energy which produces the absorption band narrowing at later times.	393

7-14	Simulated transient absorption spectrogram for the dissociation of crystalline tetraethylammonium triiodide. The initial signal is similar to the results for other solid-state triiodides, with coherent wave packet motion observed for about three cycles. The absorption signal decays rapidly starting at about 1400 fs.....	395
7-15	Fifteen randomly-selected trajectories from the Gaussian swarm used to simulate the tetraethylammonium triiodide transient absorption spectrogram.....	396
7-16a	Measured (black) and calculated (grey) transient absorption profiles for diiodide ions generated in the photodissociation of crystalline tetra- <i>n</i> -butylammonium triiodide. Probe wavelengths are 600 nm (top) and 740 nm (bottom).	398
7-16b	Measured (black) and calculated (grey) transient absorption profiles for diiodide ions generated in the photodissociation of crystalline tetra- <i>n</i> -butylammonium triiodide. The probe wavelength is 880 nm.	399
7-17a	Simulated (grey) and measured (black) transient absorption profiles at a probe wavelengths of 600 nm and 740 nm for the photodissociation of crystalline tetraphenylphosphonium triiodide.....	401
7-17b	Simulated (grey) and measured (black) transient absorption profiles at a probe wavelength of 880 nm for the photodissociation of crystalline tetraphenylphosphonium triiodide.	402
7-18a	Calculated (grey) and measured (black) transient absorption profiles for diiodide ion generated in the photodissociation of crystalline tetraethylammonium triiodide. The probe wavelengths are 660 nm and 740 nm.	403
7-18b	Calculated (grey) and measured (black) transient absorption profiles for diiodide ion generated in the photodissociation of crystalline tetraethylammonium triiodide. The probe wavelength is 820 nm.	404

List of Tables

3-1	Spectral bandwidths for pulses generated in the single-shot OPA.	128
3-2	Pre-compression duration and time-bandwidth product for NOPA pulses.	133
3-3	Temporal duration and time-bandwidth product for compressed NOPA pulses.....	137
4-1	Modes in HH polarized Raman spectrum of BGO, reproduced from reference 41. Symbols used are: vvw = very, very weak; m = medium; w = weak; vvs = very, very strong.....	161
5-1	Material properties from analysis of impulsive absorption measurements.	267
6-1	Fitting parameters for temperature-dependent transient absorption of diiodide ion in fluid and glassy CDE solution at 660 nm.	335
6-2	Fitting parameters for temperature-dependent transient absorption of triiodide ion in fluid and glassy CDE solution at 300 nm.....	337

Chapter 1

Introduction

The microscopic world is “alive” with motion – in the form of individual atoms, and groups of atoms, which move in random fashion. Substances which are chemically inert under a given set of conditions are comprised of atoms whose kinetic energy is insufficient to overcome the strong forces which bind the atoms and as such, remain chemically unchanged under normal circumstances. The motions which occur for atoms in stable chemical environments, in the absence of a strong perturbation, consist of small displacements about an equilibrium multidimensional configuration which represents a local energy minimum, balancing the Coulombic repulsions among electrons and among nuclei, and the attractions between electrons and nuclei.

However, it is evident that the “business” of chemical and/or physical change involves the rearrangement of atoms into a new minimum local energy configuration, usually in response to the application of a driving force which supplants a barrier in the complex energetic landscape and thereby facilitates the change. This is where the excitement lies, because the driving force is often under the control of the experimentalist. By judicious manipulation of this force, which can be chemical (reagents, catalysts) or physical (temperature, pressure, radiation, etc.), both the structural identity of the product(s) and the kinetics of the change can often be manipulated.

In this thesis, we will be concerned with the nature and dynamics of structural rearrangements in liquids and solids. The driving force for these rearrangements is a high-amplitude transient electric field due to one or more laser pulses, which couples very strongly to valence electrons. Atomic nuclei move in response to the large perturbations induced in the local distribution of electrons. The unique aspect of inducing structural change in this manner is that atomic motions occur *collectively* – that is, atoms move in unison to their new equilibrium positions. Such motions typically occur on the timescale of bond vibration frequencies, from a few tens to a few hundreds of femtoseconds ($1 \text{ fs} = 1 \times 10^{-15} \text{ s}$).

Given the rapidity with which physical and chemical change occurs, it is evident that in order to properly capture the dynamical evolution of atomic motion it is necessary to perform measurements with extremely high temporal fidelity. This effectively implies that the kind of collective change investigated herein is best captured by analyzing the interactions between the material in question and a series of well-characterized ultrashort pulses of light. The suitability of optical pulses derives from the fact that it is now possible to routinely generate, by means of solid-state lasers, pulses with durations less than 10 fs. Because the theory of light-matter interactions is well established, we can extract from optical measurements the microscopic details of chemical and physical change.

Most time-resolved spectroscopy involves more-or-less exotic variations of the pump-probe technique. In such experiments, one or more “pump” pulses are used to induce a material response by any one of a number of possible physical mechanisms, and then a much weaker “probe” pulse is used to interrogate the induced response. In the

simplest variant of the technique, a single pump pulse is employed, followed by a single probe pulse separated in time from the pump by a well-characterized interval. The measured perturbation of the electric field of the probe pulse is due to time-evolving sample response to the pump. One measurement of this type characterizes the sample at a particular point in time (relative to the pump-defined zero of time). Generally, such experiments are repeated in sequence, each time changing the delay between pump and probe to interrogate the sample at a different relative interval, and ensuring that the sample returns to equilibrium before another pump-probe pulse pair is applied.

The pump-probe method is robust and has enjoyed remarkably widespread application to the study of a great variety of materials, and in a great number of increasingly sophisticated incarnations. However, on account of the need for the sample to return to its original equilibrium state between pump-probe sequences, it is imperative that no permanent change in structure occur or that the irradiated sample be replenished in between repetitions of the measurement. Practically, this limits the use of pump-probe techniques to the study of reversible responses in most solids. In order to induce and measure truly irreversible chemical and physical change, it is necessary to manipulate the sample between pump-probe sequence shots. For solids, this is usually accomplished by translating the sample in a plane perpendicular to the direction of pulse propagation. For liquid samples, which are almost exclusively homogeneous, flow cells are most commonly employed to refresh the volume of material being investigated between shots. Either of these approaches works well if the materials under consideration are available as large samples of good optical quality. Unfortunately, many interesting and highly reactive species, which would otherwise be quite worthy of study, are difficult to obtain

either in quantity or in good quality. The solution to this problem is to develop a new ultrafast pump-probe technique which allows us to capture all of the time-dependent dynamical information in a single laser shot. In this way, only a single spot of good quality on a single sample is necessary in order to conduct the experiment.

The first part of this thesis will focus on the introduction of a dual echelon single-shot pump-probe technique which was designed to circumvent the difficulties outlined above. As the details of the technique have been previously described [1,2], the discussion will center upon the general applicability of the technique and its inherent limitations and systematic errors. Further, more detailed attention will be given to the development of numerical techniques to extract information from the raw image data which the experiment generates, since standard pump-probe data are captured in an entirely different fashion.

As mentioned, collective irreversible structural change is the very nature of chemistry, and there are a large number of candidate systems for investigation which are important for both fundamental and practical reasons. We have chosen materials for study on the basis of their varied responses to optical excitation, and indeed for the increasingly dramatic structural modifications which result. For solid-state irreversible chemical reactions, we have sought a family of crystalline solids in which the elementary chemistry is similar but the local and collective structural constraints are varied, so that the effects of such constraints on reaction dynamics and results may be studied. For solid-state structural change, we have examined systems in which high-intensity electronic excitation may yield either new solid or liquid phases, and examined the responses to differing excitation intensities and waveforms.

The investigation of nonequilibrium lattice dynamics in dielectric materials has been a hallmark of research in our laboratory for some years. The generation of coherent lattice vibrations via nonresonant impulsive stimulated Raman scattering, and the characterization of these responses, has provided valuable insights into the nature of phonon and phonon-polariton dynamics in ionic crystals and the fundamental coupling between ion motions and optical fields [3-9]. All such experiments to-date have involved the repetitive pump-probe sequences outlined above, ultimately limiting the intensity of the applied driving field in order to avoid material damage. Dual echelon single-shot spectroscopy introduces the possibility of exploring a new regime of high-field physics in such samples.

While most ionic crystals are optically transparent in the visible region of the spectrum, and contain very strong bonds, other classes of materials exhibit much different bonding characteristics. Substances which are classified as semimetals, owing to partially occupied conduction band energy levels, naturally possess markedly different physical properties. Crystalline bonding forces tend to be smaller than those in ionic substances and consequently, it is often possible to induce much larger lattice perturbations. For these reasons, carefully chosen semimetal species are particularly well suited for study by the dual echelon single-shot technique.

Finally, we observe that the most extreme of induced structural changes involves the breaking of chemical bonds, a truly irreversible process in many instances, and the original motivation for the development of single-shot methods of study. Development of a detailed, time-resolved microscopic picture of this process gives us the experimental tools we require in order to ultimately control its outcome. Along the way, all of the

various factors at play can be investigated: the effect of laser pulse duration, wavelength, chirp, timing, etc. An equally important aspect of condensed phase photochemistry is the role of the environment in mediating reactivity. Solvent effects have been explored in great detail in liquid environments, but the complicated and irregular local structure makes these systems difficult to model theoretically. Considerably more insight might be derived by exploring photochemical reactions in molecular crystals where the detailed structure of the environment can be specified. Unfortunately, little work to-date has been performed in this area as the experimental tools for such investigations await development. In addition, coherent control experiments in which the selection of molecular products and states depends sensitively upon the characteristics of the optical waveform might be performed and modeled much more incisively in ordered crystalline environments. All of these applications, however, require effective methods for the real-time observation of solid-state chemistry.

This thesis presents the results of time-resolved experiments designed to generate condensed-phase atomic motions of increasing amplitude and chemical or physical consequence. Chapter 2 outlines the dual echelon single-shot pump-probe technique, discusses its limitations, and highlights the differences between this approach and standard pump-probe spectroscopy.

Chapter 3 describes the development of a two-beam noncollinear optical parametric amplifier (NOPA) which is synchronized with the single-shot detection system. Experiments in photochemistry involve electronic absorption at selected optical frequencies, and it is therefore imperative that the single-shot system possess wavelength tunability. The NOPA provides a means by which tunable pulses spanning the entire

visible region of the electromagnetic spectrum may be generated. Owing to the unique phase-matching characteristics of the amplifier, pulses with enormous spectral bandwidths may be generated and compressed to durations of less than 20 fs. Also, the design of the pulse compressor permits programmable temporal shaping of the output field for more sophisticated pump-probe experiments.

In chapter 4, the very first successful single-shot nonresonant Raman scattering experiments are presented in both liquids and solids. The particular liquid chosen, *m*-iodoanisole, exhibits complex time-dependent evolution of the initially created ground state vibrational wavepacket. The material response of crystalline bismuth germanate is observed to scale with pump intensity in a manner consistent with a stimulated Raman excitation mechanism, providing encouraging evidence of the single-shot technique's sensitivity.

Chapter 5 presents the results of impulsive absorption experiments on the semimetals bismuth, antimony and tellurium. We are able to excite these materials above the single-pulse damage threshold and still observe the evolution of lattice dynamics. Dramatic softening of the A_1 mode is observed in the time-resolved data. Multiple pulse sequences are employed to drive these systems even further from equilibrium, resulting in dephasing rates which closely correspond to a single vibrational period. This suggests the possibility of an induced phase change in the material. The semiconductor germanium telluride is also investigated under high-fluence excitation with multiple pulse sequences, and strong evidence for a reversible phase change involving a bulk coherent lattice deformation is observed.

In chapter 6, the time-resolved photodissociation of triiodide ions in solution is investigated. The results of transient absorption experiments at multiple wavelengths are interpreted in the context of a wavepacket picture of dynamic absorption and the evolution of absorbing species on multiple energy surfaces. The nature of the solvent is also observed to exert a dramatic influence upon the detailed photodissociation mechanism.

Chapter 7 concerns the results of photodissociation experiments in crystalline triiodides. Here, the absorption band shape of the diiodide photoproduct is heavily depended upon the crystalline environment. Molecular dynamics simulations are employed in an effort to understand the complicated nature of the observed interactions.

Finally, in chapter 8, the results of the preceding experiments are summarized in the context of the overarching theme of collective structural change, and future directions for work in this field are suggested.

References

- [1] Wakeham, G.P., *Dual-Echelon Single-Shot Femtosecond Spectroscopy*, Ph.D. Thesis, Massachusetts Institute of Technology, 2001.
- [2] Wakeham, G.P. and Nelson, K.A., *Opt. Lett.* **25**, 505 (2000).
- [3] Koehl, R.M., Adachi, S. and Nelson, K.A., *J. Chem. Phys.* **110**, 1317 (1999).
- [4] Crimmins, T.F., Stoyanov, N.S. and Nelson, K.A., *J. Chem. Phys.* **117**, 2882 (2002).
- [5] Dougherty, T.P. *et al.*, *Science* **258**, 770 (1992).
- [6] Dougherty, T.P. *et al.*, *Phys. Rev. B* **50**, 8996 (1994).
- [7] Dougherty, T.P., Wiederrecht, G.P. and Nelson, K.A., *Ferroelectrics* **164**, 253 (1995).
- [8] Romero-Rochin, V. *et al.*, *J. Chem. Phys.* **111**, 3559 (1999).
- [9] Stoyanov, N.S., *Phonon-Polaritons in Bulk and Patterned Materials*, Ph.D. Thesis, Massachusetts Institute of Technology, 2003.

Chapter 2

Dual Echelon Single-Shot Ultrafast Spectroscopy

This chapter describes the optical layout and software which together constitute the single-shot experimental apparatus. The laser system which provides the optical pulses for our laboratory work has been previously described in detail [1] and thus, only an overview is provided here. The performance and fidelity of the single-shot measurement technique are examined in detail.

2.1 Amplified Titanium-Sapphire Laser System

Ultrashort optical pulses are generated in the laboratory via a custom-built amplified titanium-sapphire (Ti:S) laser. The master oscillator generates timing signals to enable the synchronization of all electronic components within the system. In order to generate the oscillator's stable pulse train, the 532 nm, 4.5 W continuous-wave (CW) output from a Coherent Verdi Nd:YVO₄ intracavity frequency-doubled laser is focused using a 12 cm focal length (f.l.) objective into a 4% doped, 3 mm thick, Brewster-cut titanium-sapphire crystal. Two dielectric 10 cm f.l. mirrors, a flat dielectric high-reflector, and a 10% output coupler together constitute the asymmetric cavity. Intracavity dispersion compensation to third order is achieved with two 1 cm fused silica prisms, separated by roughly 80 cm, in a minimum-deviation configuration. The master oscillator operates as a stable CW laser, with center-frequency tunable from roughly 775-

835 nm by adjustment of the prism configuration. The average output power for this mode of operation is 300-350 mW.

Introduction of a transient noise source in the cavity initiates self modelocking via the Kerr lensing mechanism. In this case, proper adjustment of cavity mirrors and prisms is needed in order to realize maximum gain bandwidth. Typically, the modelocked pulse train consists of 5-7 nJ individual pulses at a repetition rate of 82 MHz. Measurement in a dual-grating spectrometer reveals a full-width half-maximum (FWHM) spectral bandwidth of 40-45 nm at a central wavelength of 815 nm. As in the CW mode of operation, the center wavelength can be shifted by appropriate tuning of the intracavity prisms. Autocorrelation measurements via second-harmonic generation in a 50 μm thick β -barium borate (BBO) crystal yield a correlation signal of 72 fs FWHM. Clearly, the oscillator pulses are not bandwidth-limited, but this is of little consequence since they are subsequently chirped prior to entering the amplifier, and recompressed following amplification. Figure 2-1 (top) illustrates the results of spectral measurement of the oscillator pulses, while the bottom of the figure demonstrates the second-order intensity autocorrelation and subsequent fit to a Gaussian pulse shape.

Oscillator pulses are directed into the input aperture of a pulse selector, consisting of a calcite polarizer, a KD*P Pockels' cell, another polarizer, and then a half-wave plate. The function of the initial polarizer is to ensure clean linear horizontal polarization of the oscillator train. With no voltage across the electro-optic KD*P crystal, the pulses pass through it unchanged, and are extinguished at the second polarizer, which is aligned to permit only vertically polarized pulses to pass through. The function of the pulse selector is to reduce the 82 MHz pulse train to a 10 Hz pulse train for amplification, and in order

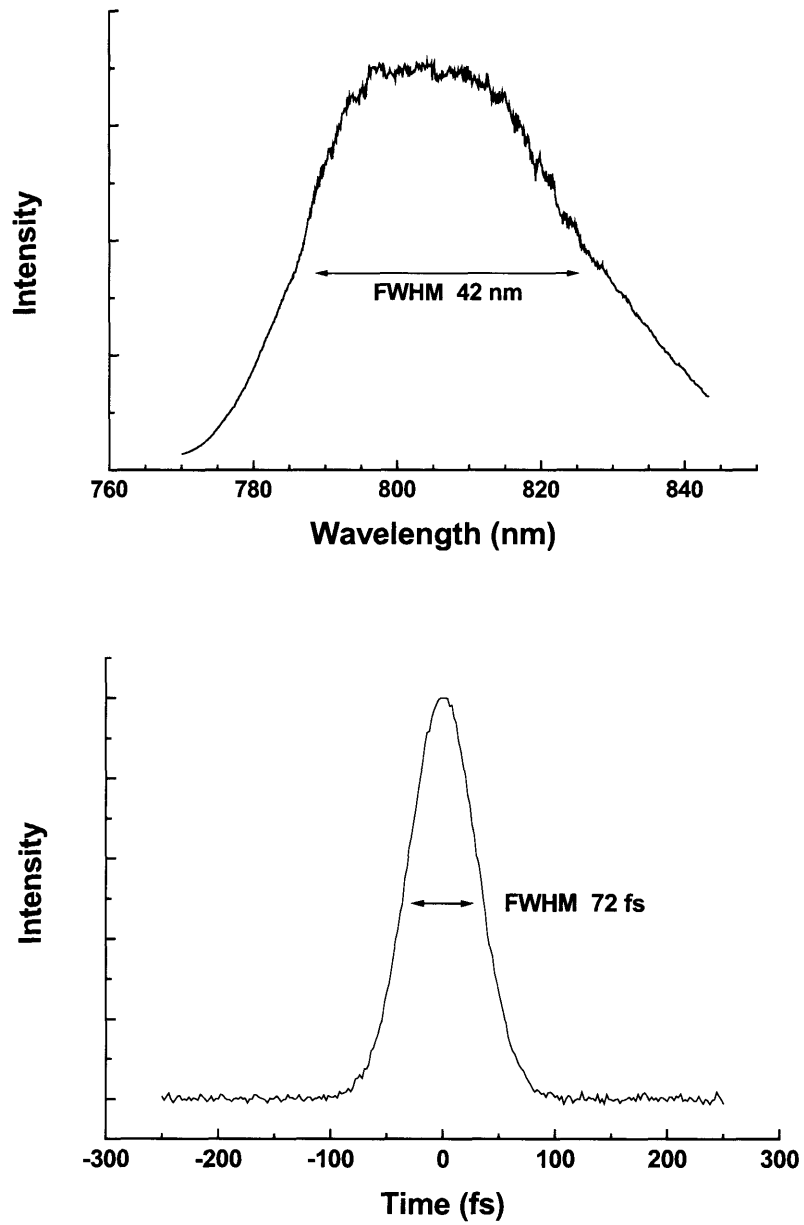


Figure 2-1. The top panel illustrates spectral measurement of pulses from the Kerr-lens modelocked oscillator. The FWHM bandwidth is about 40 nm. The bottom panel shows the measurement of the intensity autocorrelation for the same pulses. Assuming a Gaussian envelope shape yields a FWHM duration of 72 fs.

to accomplish this, a photodiode (Thorlabs DET210) samples the 82 MHz train in the oscillator and relays the resulting signal to a series of timing electronics. A frequency down-counter (Optima Technologies) uses the diode signal as an input to a divider circuit which produces a 10 Hz, synchronized output clock. The clock signal is coupled into a delay generator (Stanford Instruments DG-535) which creates three synchronized outputs. Two of these are passed to high-voltage power supplies which drive the Pockels' cell, and the third is further passed to a control computer via a data acquisition card (National Instruments). In this way, the Pockels' cell is time-synchronized to the input pulse train from the master oscillator. When a high-amplitude electric field is applied across the KD*P crystal, the field modifies the crystal's static dielectric tensor and thereby modulates the bulk refractive index. Pulses entering from the oscillator during this time encounter differing ordinary and extraordinary refractive indices, and the polarization of each pulse is thus rotated (but remains linear) such that pulses exiting are vertically polarized. These pulses pass through the second polarizer and enter the amplifier. Since the KD*P crystal is itself pulsed every 100 ms, the net effect of the pulse selector is to extract one out of every 8.2 million oscillator pulses.

The amplifier is a multi-pass, two-stage design which takes advantage of the chirped pulse amplification technique [2]. Accordingly, seed pulses transmitted through the Pockels' cell are first stretched temporally to roughly 50 ps duration in a double-pass reflective grating stretcher [3,4]. The stretched pulses enter a three-mirror multipass ring cavity [5], making eight round trips through the cavity. On each round trip, the seed pulses are focused with a 50 cm f.l. spherical mirror into an 8 mm, 4% doped, Brewster-cut Ti:sapphire crystal. The crystal is pumped from the opposite side with 12-13 mJ, 8 ns

pulses from a 10 Hz, externally frequency-doubled Nd:YAG laser (Continuum Surelite I) which is Q-switched in synchronization with the seed pulse train. As a result, and owing to the relatively long excited state lifetime of Ti:sapphire, the 5 nJ oscillator pulses are amplified to energies of 1.3-1.5 mJ. On each trip around the cavity, the seed beam path is displaced laterally and after 8 passes, the beam is intercepted and extracted.

The high energy pulses are spatially filtered using a 100 μm aperture, collimated, and coupled into a second-stage amplifier. The second stage is aligned such that the seed pulses make four passes, in a “bow-tie” configuration, through a second Brewster-cut Ti:sapphire crystal with the same specifications as the first. The seed pulses pass through the crystal unfocused in this stage and have a beam waist of roughly 5 mm. The Ti:sapphire crystal is pumped with 85 mJ pulses from the same Nd:YAG source which pumps the first stage amplifier, thereby ensuring temporal synchronization. Following this second amplification, pulse energies are typically 3-5 mJ. A convex cylindrical mirror with very long effective focal length (~ 10 m) is used to compensate the astigmatism in the output beam’s intensity profile which results from the horizontally-displaced beam paths (and hence, astigmatic cross-sectional gain profile) inherent in the first stage of the amplifier.

The pulses, which remain temporally stretched, are then recompressed in a double-pass, reflective grating compressor of the type first introduced by Treacy [6-9]. The amplification process reduces the overall bandwidth of each pulse; this is due to the gain process occurring most efficiently at the spectral maximum, where the pulse intensity is highest. Thus, in Figure 2-2 (top), spectral measurement reveals an amplified pulse bandwidth of about 30 nm. In the bottom panel of Figure 2-2, the intensity

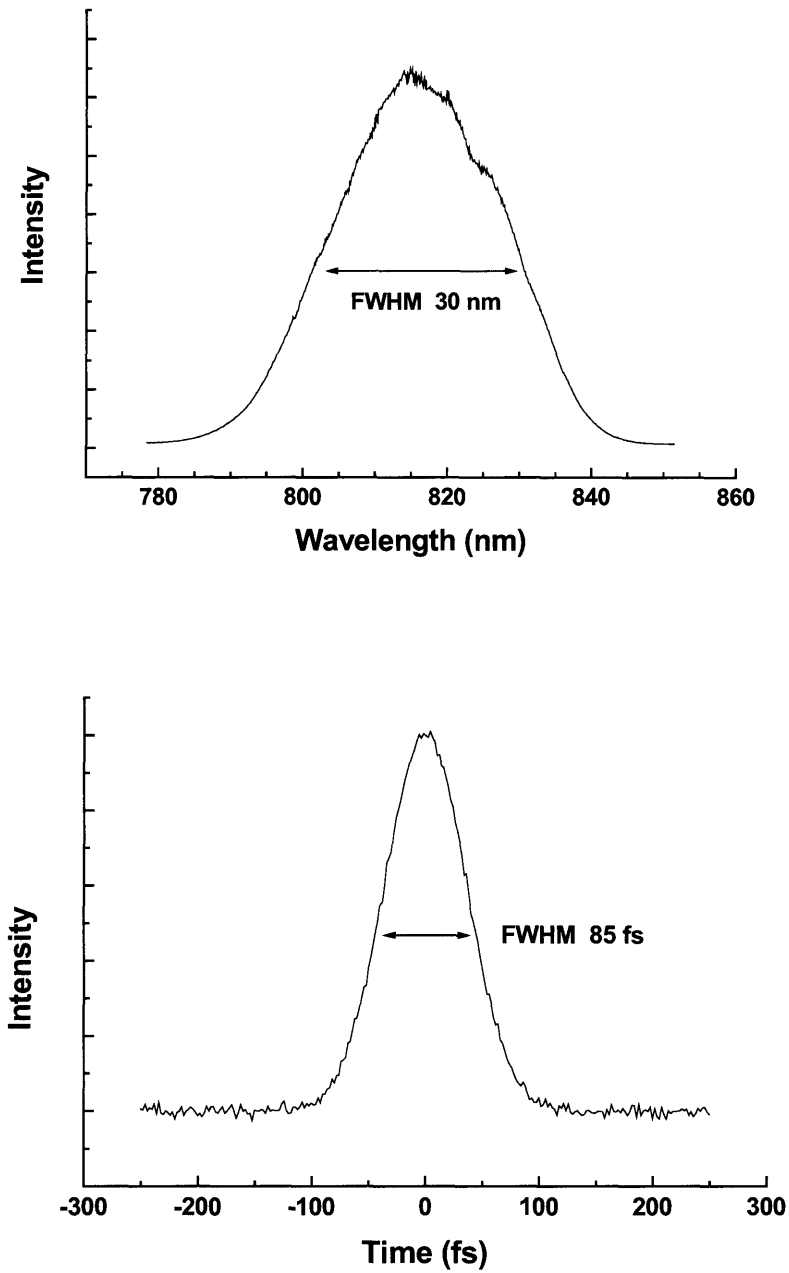


Figure 2-2. The top panel illustrates the spectral bandwidth of the amplified 10 Hz pulse train. Each pulse has a FWHM bandwidth of roughly 30 nm. In the bottom panel, the intensity autocorrelation trace for the amplified pulses has a FWHM duration of 85 fs, corresponding to a 55 fs pulse duration.

autocorrelation trace is fitted to a Gaussian envelope function and the resulting FWHM duration is 85 fs. This corresponds [10] to an amplified pulse duration of 55 fs. The pulses are not transform-limited due to higher-order spectral phase terms which cannot be fully compensated in a grating compressor of this design. In terms of the experiments we wish to conduct with this laser system, however, 55 fs pulses are quite suitable. At this stage, introduction of additional negative dispersion can help to compensate for dispersive optical elements placed further down in the beam path (frequency-doubling crystals, polarization optics, experimental samples, etc.)

2.2 The Dual Echelon Single-Shot Technique

Most ultrafast time-resolved spectroscopy experiments reported in the literature utilize a variation of the pump-probe technique, wherein one or more “pump” pulses are used to initiate a material response, followed by a much weaker “probe” pulse which interrogates the induced response without initiating a second large perturbation in the sample. The delay between pump and probe pulses is well characterized, and by repeating the pump-probe sequence with adjustment of this delay, a complete time-dependent material response function is obtained. The important contingency is that the material under consideration returns to its initial state after each pump-probe event.

It is clear, however, that for many interesting types of materials, including those that undergo photodissociation, photo-induced phase transformations, and high-optical-field damage, the contingency upon which the success of standard pump-probe techniques depends cannot be satisfied. In order to investigate irreversible processes in materials displaced far from their equilibrium states, new methods of pump-probe

spectroscopy are required. Specifically, an optimal technique would realize high time resolution by utilizing femtosecond optical pulses, but in a configuration which would allow complete measurement of a material's time-dependent response in a single laser shot. This is indeed a challenging task, and serves as the motivation for the development of the technique described herein.

Other researchers have recognized the need for single-shot methods, and a number of approaches to this problem have been attempted. These include time-to-space mapping of probe light [11], single-shot spectral interferometry [12-14], time-to-wavelength mapping with a chirped probe pulse [24], and fairly exotic versions of correlation spectroscopy [15]. There are significant disadvantages to each of these, however. Time-to-space mapping of probe light, at least performed in the manner of Dhar *et al.*, is extremely sensitive to the alignment of optical components in the experiment. In addition, due to wavelength-dependent indices of refraction in both the optical elements of the experiment and the sample itself, achieving good temporal resolution involves careful recalibration of the instrument each time the probe wavelength is changed. Finally, due to the angular nature of the experimental geometry, different temporal slices of the probe pulse sample different spatial volumes of excited material. For very large excitation volumes this may not be important, but it is evident that at moderate intensities and in materials where the response is confined primarily to a small focal region of optical excitation, inhomogeneous spatial sampling errors become important.

Spectral interferometry is a very sensitive technique owing to the nature of the measurement, wherein the probe electric field is detected directly. The experiment involves two measurements of the sample, the first occurring without a preceding pump

pulse, and the second as part of a pump-probe sequence. Comparison of the probe fields with and without the pump permits the determination of the material response's effect upon the probe and hence, the dynamics of that response. For this method to yield good results, the reference field (probe without pump) must be known to a very high degree of accuracy. In addition, the requirements for good sample quality and uniformity are stringent, as is the need for the probe to sample a spatially homogenous excitation volume. Additional problems can occur with high excitation intensities, which may induce wavelength-dependent features in the measured interferograms.

Time-to-wavelength mapping schemes utilize a probe pulse with well-characterized frequency chirp to investigate time-dependent material dynamics. A single chirped probe pulse interacts with the sample and is then analyzed in a spectrometer. With knowledge of the instantaneous frequency, the wavelength-dependent response captured by the spectrometer is converted to a temporal response function. This method is effective under certain circumstances, but suffers from several potentially critical limitations. First, there are practical limitations regarding the magnitude of frequency chirp which must be observed. Since the chirp rate effectively establishes the probe temporal window, a large rate is typically desired. However, many experiments demand that the probe pulse duration remain temporally impulsive in relation to the material dynamics. This imposes severe limitations on the magnitude of the chirp, and thus on the accessible temporal response range. Second, the probe pulse chirp must be extremely well characterized. Given the dispersive optical elements preceding and following the sample, this procedure can be time-consuming and subject to errors from even small adjustments in experimental alignment. Also, nonlinear effects within the sample can

induce additional probe pulse chirp, and these must be carefully determined for each sample in order to deconvolve the additional phase structure from the pulse. Third, the method is very difficult to employ with samples which undergo absorption processes. While such effects can be measured and compensated by post-processing of the single-shot spectrum, it is clearly much easier to utilize this technique when it can be assumed that the material response is spectrally flat (i.e. for non-resonant, non-absorbing samples).

The approach described in this thesis to the problem of single-shot ultrafast measurement of material dynamics is an extension of an old technique designed for picosecond experiments. Topp *et al.* introduced the concept of an “echelon” as a means to divide the cross-sectional profile of the probe beam into variably delayed spatial “pieces” [16-18]. Each piece of the probe beam is focused into the sample in the same manner as in an ordinary pump-probe experiment. Ultimately, it is necessary to spatially resolve the measurement of the probe beam in order to obtain temporal information.

Originally, the echelon technique was developed to circumvent shot-to-shot instability of the laser in pump-probe measurements. Modern lasers do not suffer from these problems, and the advent of electronic streak cameras with 1 ps resolution has rendered the echelon approach less useful for picosecond spectroscopy. In addition, the original implementation of this approach required very thick glass structures to achieve picosecond delay times, and was markedly less useful on account of the relative dearth of CCD cameras or other multi-element detectors with high spatial resolution. However, the all-optical methods required for signal detection in the femtosecond regime suggest a new application of echelon spectroscopy. The method described herein is an extension of the echelon technique to two spatial dimensions and femtosecond time resolution.

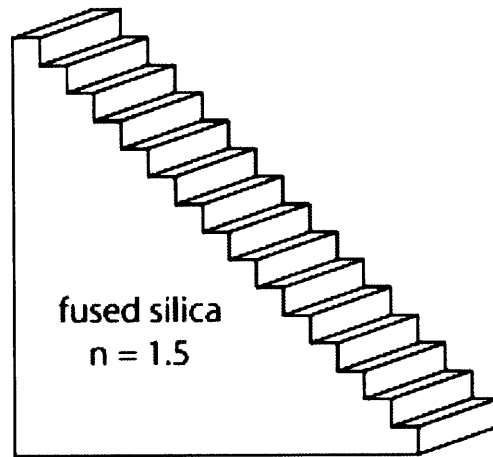


Figure 2-3. Schematic diagram of a transmissive echelon.

Figure 2-3 illustrates schematically the structure of a transmissive echelon. The optic is constructed by coating the hypotenuse of a right-angled prism with an index-matched polymer, and then carefully machining a stair-step structure in the polymer. Echelons are sometimes referred to as “grating-prisms” or just “grisms” in the literature, for obvious reasons. The simple physics underlying the function of the optic is intuitive. When a beam of light passes through an optically dense material (i.e. $n > 1$), the speed of light is reduced. The echelons utilized in our experiments are fabricated from fused silica substrates, for which $n \sim 1.5$. As a result, cross-sectional areas of the beam which pass through larger thicknesses of glass are delayed by larger amounts, relative to the minimum-delay section of the beam, and when focused by subsequent lenses, arrive at the focal plane at later times. The approach employed here extends the method of Topp by employing two crossed echelons with differing step thicknesses to create a transmissive grid pattern overlaying the beam cross-section. The layout of the echelon optics is illustrated schematically in Figure 2-4. The input probe pulse first passes

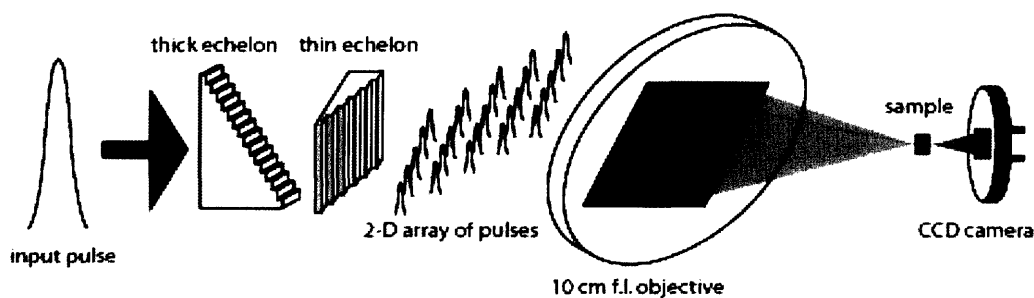


Figure 2-4. Crossed-echelon method for generating a time-structured probe pulse where temporal delay is mapped onto the spatial profile of the pulse. Only 25 independent delay steps are shown in the figure, but the actual echelons generate 400 individual steps.

through a thick echelon, where the 20 steps are each of thickness $300\ \mu\text{m}$. This maps a series of delays onto the spatial profile of the beam; each step contributes another 500 fs of delay. The temporally sectioned beam then passes through a second echelon oriented at right angles to the first. This thin echelon, which is fabricated with 20 steps of $15\ \mu\text{m}$ thickness, imparts relative delays within each of the spatial-delay sections from the thick echelon. The thin steps each introduce an additional 25 fs delay. Within each delay stripe from the thick echelon, there are 20 divisions separated by increasing 25 fs increments for a total delay window of 500 fs. There are 20 thick 500 fs strips, for a total time window of 10 ps. The combined effect of both echelons is to overlay a time-to-space mapped grid over the probe beam profile containing 400 distinct time points, in increasing 25 fs relative delays, providing a 10 ps experimental probe window. It is possible to increase or decrease both the overall window and the relative time step by utilizing alternately cut echelons, but the temporal properties we have chosen are suitable for a wide range of applications. The probe beam is focused into the sample by a 10 cm f.l. objective and, in the transmission version of the experiment, re-imaged by a second 10 cm f.l. lens on the other side of the sample. Ultimately, the probe beam cross-

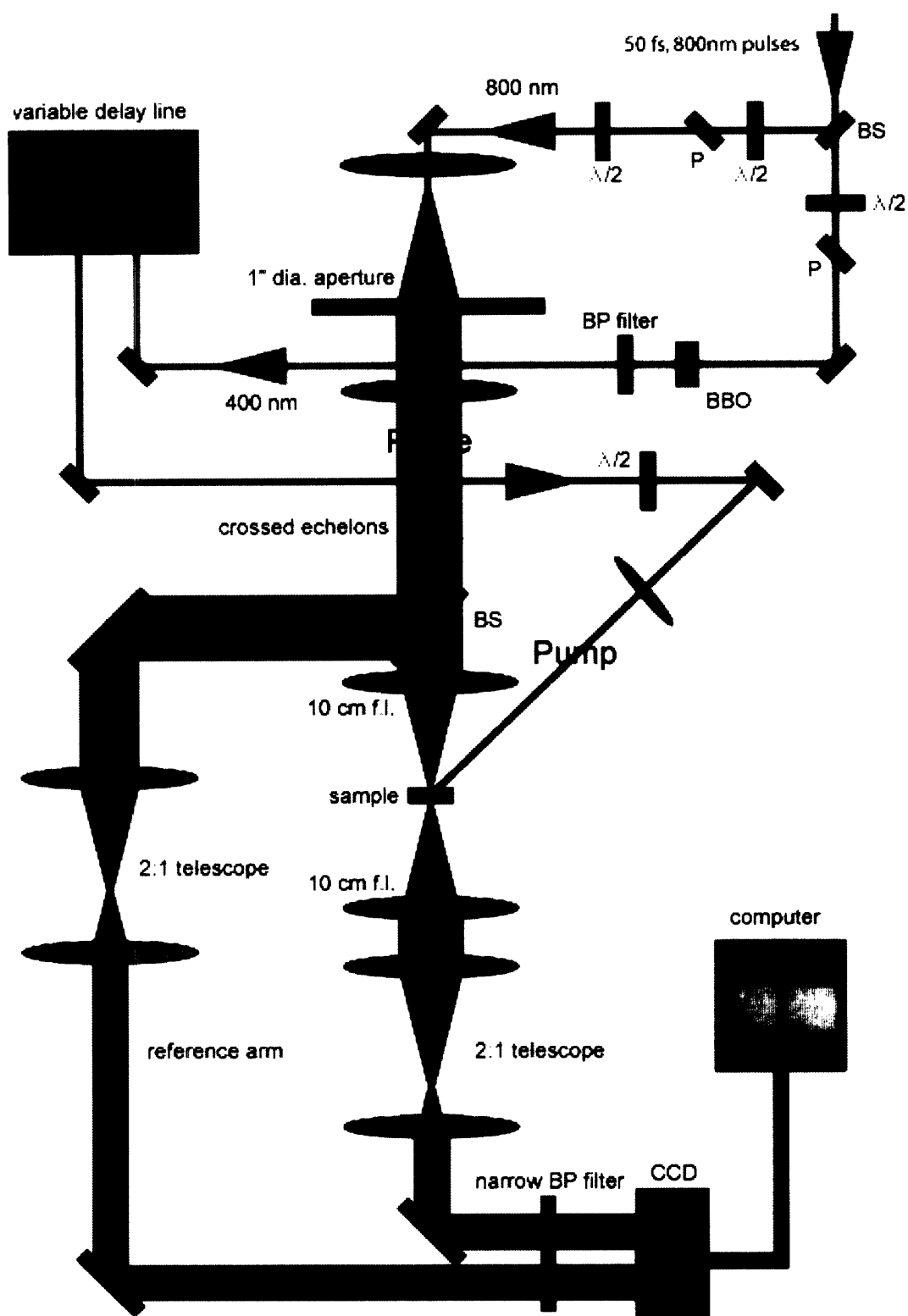


Figure 2-5. Schematic illustration of the dual echelon single-shot experiment.

sectional profile is captured on the surface of a CCD and analyzed to extract the material response. A schematic view of the entire experiment is shown in Figure 2-5. The illustration characterizes the simplest configuration typically used in the laboratory for the measurement of nonresonant forward impulsive stimulated Raman scattering (ISRS). Amplified 50 fs, 800 nm pulses enter the measurement system from the laser. A 10% reflecting beamsplitter divides the input pulses into pump (90%) and probe. The pump arm passes through a half-wave plate ($\lambda/2$) and polarizer (P) combination to provide a means for variable attenuation. In the version of the experiment shown in the figure, 400 nm pump pulses are obtained by frequency-doubling in a 100 μm thick BBO crystal. A bandpass filter removes remaining 800 nm light and the pump pulses traverse a long delay line. For ISRS measurements, time-dependent spectral shifts in the probe light are measured by means of a narrow-bandpass (BP) filter before the CCD camera. Ultimately, the pump pulses pass through a second half-wave plate, which ensures control over their polarization, and are focused onto the surface of the sample by a 25 cm f.l. singlet lens.

The probe pulses also pass through a half-waveplate and polarizer combination for variable attenuation, then through another half-waveplate to fix the polarization. The beam is focused by a 3 cm f.l. singlet lens and spatially filtered at the focus if necessary. On the other side of the focal plane, the beam diameter expands rapidly and the beam is projected down the laser table until its waist is larger than 15 cm. A 1" diameter spatial aperture then selects only the center portion of the beam profile, converting the approximately Gaussian intensity profile of the original beam into a "top-hat" shape. The beam is recollimated on the other side of the aperture by a 250 cm f.l. lens, and then

passed through the crossed echelons. The echelon orientation determines the spatial locations of the earliest and subsequent time-delayed regions. In our experiments the echelons are generally oriented such that the smallest steps are located on the left (thick echelon) and top (thin echelon), forming a two-dimensional matrix where the earliest time point is located in the top left corner of the beam profile, and later times run row-to-row down each column, all relative to the CCD camera's point of view.

The temporally sectioned probe pulse is focused onto the surface of the sample with a 10 cm f.l. objective. In the transmission version of the experiment depicted above, the diverging beam is recollimated on the other side of the sample by a corresponding 10 cm f.l. lens. The beam diameter is reduced by a factor of two in a standard Keplerian telescope and then imaged onto a CCD camera.

An achromatic beamsplitter (chromium-coated fused silica) is inserted in the beam path prior to the focusing lens in front of the sample. The beamsplitter generates a second pulse, the "reference", which is reduced in diameter by a factor of two and also imaged onto the surface of the CCD. Note that this pulse does not pass through the sample, but does traverse the echelons. It is used to correct the measured image data for echelon imperfections (damage spots, chips, step aberrations) and imaging errors, diffraction effects in particular.

In Figure 2-5, both the sample and reference beams pass through a super-Gaussian narrow bandpass (3 nm) filter prior to impinging upon the CCD. Wavelength-shifting is the principal means of detection for coherent lattice vibrations in our setup; the signal arises from small, time-dependent shifts in the probe pulse spectral distribution induced by oscillating ions or dipoles in the sample crystal lattice [25]. Such tiny shifts

are only observable if a small window of the entire probe spectrum is examined. Much of the probe light is discarded in this type of detection scheme, effectively limiting sensitivity to a certain extent. Dynamic wavelength shifting will be discussed in more detail in connection with ISRS measurements in Chapter 4.

A raw CCD image showing both the sample and reference pulses is shown in Figure 2-6. The “sample” pulse – which passes through the material under investigation – is on the left, and the reference is on the right. Note that, as indicated by the arrows, the relative time delay from step to step increases in 25 fs increments down each row (the thin echelon is oriented horizontally) and the step-delay increment from column to

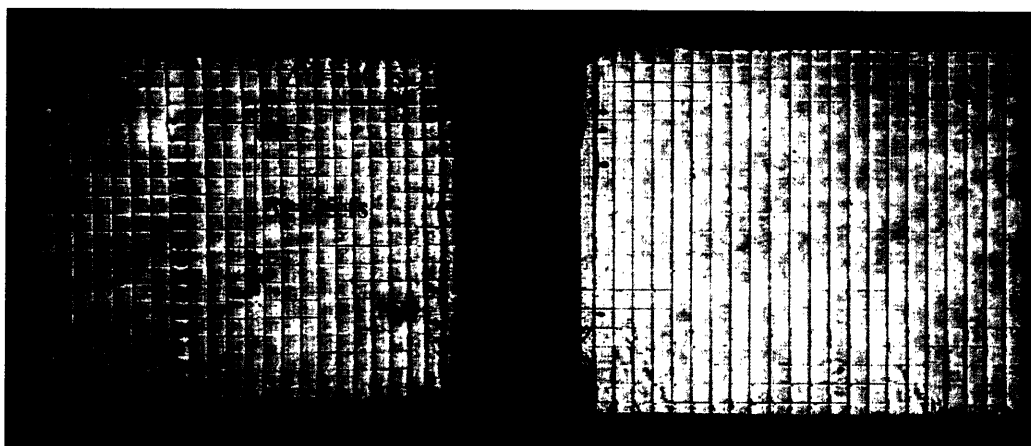


Figure 2-6. CCD image showing sample (left) and reference (right) beams. Both beams contain an image of the crossed echelons, but only the sample beam has passed through the material under investigation. The earliest time delay points are located in the top left corner of the sample image and the bottom right corner of the reference image. Traversing row-by-row down any column, successive delay increments are 25 fs. From column-to-column across any row, the delay increment is 500 fs. The total time window for the 20×20 2-D array of 400 delay points is 10 ps. The darkened area on the sample image corresponds to a reduction of transmitted light intensity due to the material response. Here, a 400 nm pump pulse induces a fast “electronic” time-dependent response. The modulation of 800 nm probe light over a time window of about 350 fs is due to hot-electron generation at the surface of the fused silica sample.

column is 500 fs (thick echelon oriented vertically). Note also that the thick echelon has more than 20 steps; we make use of this extra window to attempt to eliminate edge effects which arise from fabrication imperfections and handling. Utilizing matrix coordinates to refer to specific squares, the earliest time point on the sample image is located at (1,1), the upper left corner. This corresponds to position (20,20) on the reference image. The sample image traverses two telescopes, a 1:1 telescope through the sample itself which inverts the image, and a 2:1 telescope which re-inverts it. Since the reference passes through only a single reducing telescope, its image is inverted on the CCD. The sample in Figure 2-6 is a 100 μm thick piece of fused silica. The pump pulse is a 400 nm, 50 fs pulse focused onto the surface of the fused silica to generate an excitation density of 6.5 TW/cm². The 800 nm probe pulse is roughly a factor of 100 times less intense than the pump. The dark region in the middle of the left-hand echelon image is the fused silica's single-shot response. The pump pulse creates a distribution of hot conduction band electrons via multiphoton absorption [19-21]. The hot electrons exhibit very broad bandwidth absorption throughout the visible and near infrared region of the spectrum. The dark region on the echelons corresponds to probe pulse absorption, negatively modulating the transmitted light intensity when it occurs. This type of experiment is useful for the investigation of the short-time response of transparent dielectric materials to very large excitation fields.

2.3 Analysis of Single-Shot Images

Considerable effort has been expended in automating the recovery of numerical data from echelon images captured on the CCD camera, and a combination of

mathematical techniques is employed. Collection of the images is relatively straightforward. First, with the pump beam blocked and the probe path open such that the echelon images are viewable in real-time using the CCD camera and its control computer, the position and angle of the sample under study is adjusted using a home-built 3-axis, 2-angle mount. Particularly when dealing with laboratory-grown molecular crystals, it can be difficult to locate regions of sufficient optical quality for even a few shots. Whereas typical pump-probe experiments require only that the probe beam scatter due to the sample be sufficiently small that a photodiode mounted on the transmission side can measure any signal, the single-shot experiment necessarily involves *imaging* the echelons through the sample. As a result, bulk scattering events and surface diffraction/refraction, even for thin samples, can seriously degrade the captured images, and therefore introduce significant systematic noise into the recovered numerical data. Compensating these effects on a single shot basis is very difficult.

Once the sample is properly aligned, and assuming the pump and probe beams are already overlapped spatially and temporally at the sample position, the amplifier shutter is closed to block all pulses from reaching the single-shot instrument. A beam-block is placed to intercept the path of the pump beam. Then, a computer control program written in the LabVIEW language initiates the data collection by setting camera parameters, synchronizing its internal timebase to a 10 Hz clock signal from the laser amplifier driving electronics, and opening the amplifier shutter for 10 ms to allow exactly one pulse to escape. The pulse traces the optical path shown in Figure 2-5 except for the blocked pump pulse. The probe pulse image (sample and reference) without a pump

pulse is captured on the CCD camera. This is referred to henceforth as the background scan.

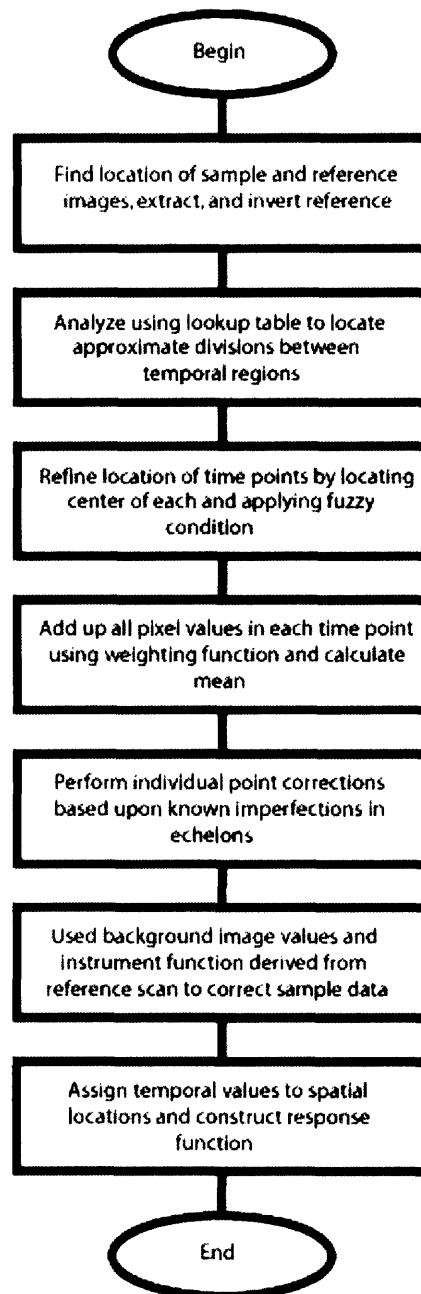


Figure 2-7. Schematic of algorithm used to extract single-shot data from raw CCD images. Four processed echelon images are needed to reconstruct and correct the response function data: the sample image, the reference image, and the corresponding background images.

With the beam block removed, the scan is repeated, capturing a sample image perturbed by the presence of the pump. In the following discussion, this is referred to as the data scan. Both images are then stored for further processing. In total, the acquisition of an entire 10 ps data sweep requires about 3 seconds (most of this is synchronization and image transfer time).

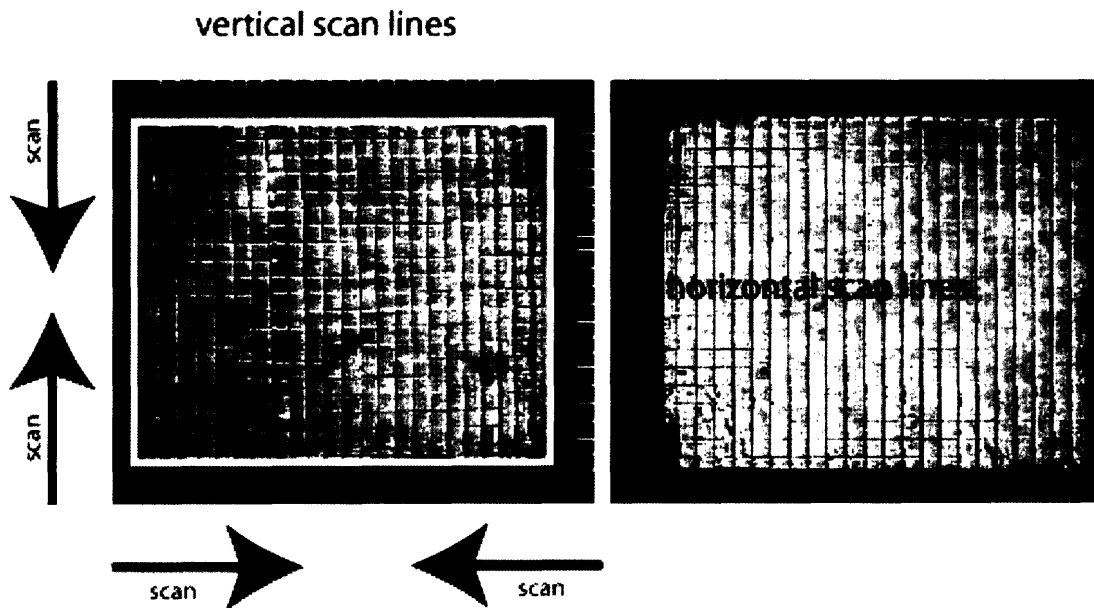


Figure 2-8. Illustration of the procedure used to isolate the sample image from the raw CCD image data. Raster-scanning in all four directions indicated along the vertical and horizontal scan lines locates the first non-zero-valued pixel on each edge of the image. The global maximum and minimum are taken to define the pixel area occupied by the sample image. The heavy white box in the figure represents the retrieved boundaries. Note that the thick white line in the center of the raw image is only a guide for the eye – there is no such division on the actual images. This procedure works in similar fashion for the reference image, which is then inverted.

Analysis of the raw CCD images is a conceptually straightforward but numerically intensive task due to the size of each scan (1344×1200 pixels \times 12 bits per pixel). Figure 2-7 illustrates graphically the entire automated procedure, which generally

requires 3 minutes. First, the boundaries of the sample and reference echelon images are identified by scanning horizontally and vertically along individual slices through the CCD image. Typically, roughly 50 horizontal slices and 50 vertical slices are used for each of the sample and reference. The procedure is illustrated in Figure 2-8 for the sample image (on the left). Fifty horizontal slices are taken from the leftmost edge of the raw CCD image to its midpoint and analyzed for the first non-zero values from: (a) the left edge moving to the right; (b) the midpoint moving left. The global minimum values (furthest left and right zeros) are fixed as the horizontal starting points for the sample image. In similar fashion, 50 slices vertically from top to bottom are examined for the first nonzero values moving downward and upward, respectively, toward the center of the image. The global minimum first nonzero values (i.e. the closest to the top and bottom) are selected as the vertical edges of the sample echelon image. A similar procedure is carried out on the reference image, and then the two are numerically extracted from the overall image. The reference image is inverted about its center so that its spatial orientation corresponds to the sample image.

The next operation undertaken is to roughly establish the boundaries between echelon time points (squares). The spatial positions of the echelon images can change from shot to shot due to beam pointing fluctuations and aberrations introduced by the irregular nature of the sample itself, but the image size (i.e. magnification) does not change very much. Taking this into account, two approaches to this aspect of the problem are possible. The most accurate method is to raster-scan along each horizontal and vertical line of the echelon image, identifying the divisions between echelon squares as the locations where: (a) the intensity falls below a certain threshold; (b) the sign of the

derivative of the intensity changes. Mathematically, we have the following

$$I(x_0) < \sigma, \quad \left. \frac{dI}{dx} \right|_{x \rightarrow x_0^-} < 0, \quad \left. \frac{dI}{dx} \right|_{x \rightarrow x_0^+} > 0 \quad (2.1)$$

where I is the light intensity, σ is the threshold value for zero detection, and x_0 is the location of the potential division. This method is most accurate because it allows for non-rectangular echelon squares, thereby providing a means to numerically compensate for imaging imperfections in the instrument.

Figure 2-9 illustrates the process of raster-scanning through each horizontal and vertical line of the echelon image to locate the divisions between squares. Note that

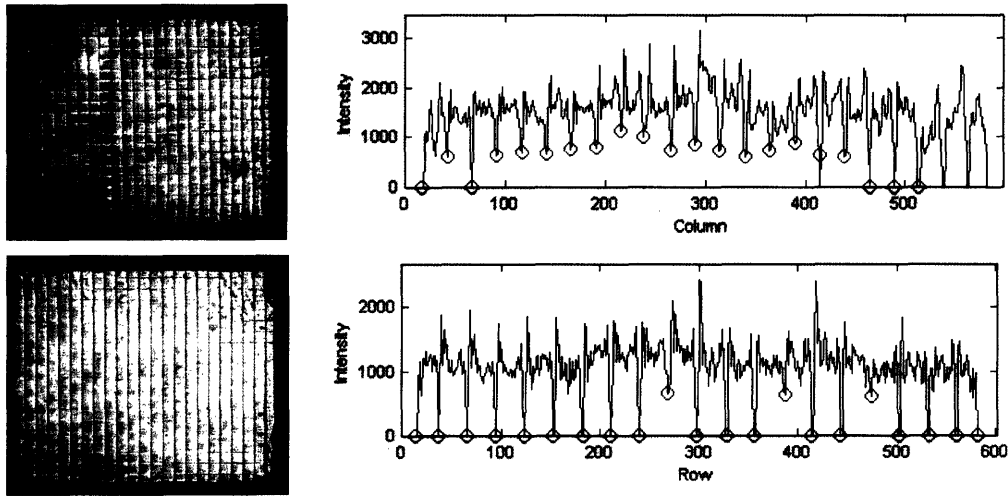


Figure 2-9. Numerical procedure for locating the divisions between echelon time points. In this most accurate method, each row and column of the image is raster-scanned to find the locations where the absolute intensity falls below a zero-threshold, and the spatial derivative of the intensity changes sign. In most cases, these conditions are sufficient to define the division points.

when the relay imaging optics (the two telescopes) are properly aligned, it is fairly straightforward to perform this procedure numerically. As a practical matter, perfect imaging of the echelons to any plane, including the plane of the CCD detector, is impossible owing to the thickness of the 500 fs echelon. There is always some

“fuzziness” to the images on account of the fact that one must choose which planar slice of the echelons along the beam propagation axis is imaged perfectly. In Figure 2-9, the retrieved positions of the echelon divisions are indicated with circles. The contrast is better in the bottom raster scan, which occurs over a row (and thus samples the thick echelon, for which diffraction effects are larger). In the top scan – down a column of the image – a relatively poorer contrast is obtained owing to the relatively small diffractive effect of the thin echelon. Ironically, the higher the fidelity of the imaging system, the poorer the contrast between steps for the numerical algorithm. However, if the fidelity is too low, systemic noise creeps into the system due to defocusing. Thus, there is a subtle interplay which must be balanced in order to achieve optimum results. Note that, in cases where significant noise is present in an echelon image, an average step width is employed to aid the search algorithm in separating true divisions from noise. For example, in the top raster scan of the image of Figure 2-9, between the first and second retrieved minima there is a large negative spike in intensity. Such imperfections are filtered out by locating the first minimum point, and then only searching for the second within a narrowly specified spatial window. As mentioned previously, since the magnification factor of the setup is very nearly constant from one shot to the next, this approach is robust.

The second method for locating echelon divisions involves careful prior calibration of an echelon image to establish a grid pattern of rectangular divisions. Since the magnification factor of the single-shot setup changes very little from shot to shot, this calibrated grid can then be overlaid on any echelon image using only three location points: the first establishes the location of a reference point on the grid relative to the real image, and the other two are used to calculate the (very nearly unit) stretching factors.

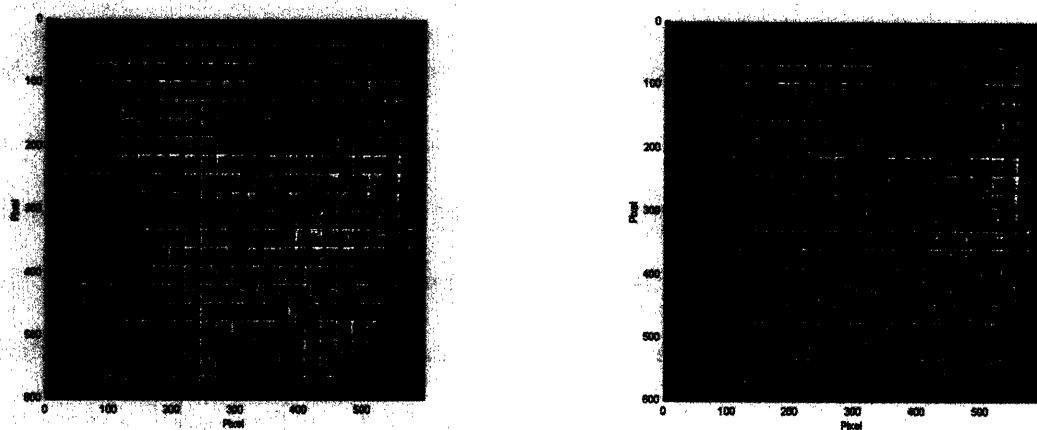


Figure 2-10. Application of window function to individual echelon time squares. In the left panel, the echelon divisions are located by raster-scanning individual rows and columns of the image, creating a 2-D grid pattern defining the spatial divisions between time points. In the right panel, the number of usable pixels in each square is further reduced via application of a window function which preferentially selects a certain fraction of the centermost pixels, typically 75%. The window boundaries for each square are indicated by the rectangles drawn within each.

The next step in the extraction is to identify the usable fraction of pixels within each echelon step. In most cases, diffraction effects from the echelon step edges are manifest as sharp positive- or negative-going features in the spatial intensity distribution. The two raster scans of Figure 2-9 illustrate this. Scanning from left to right, the divisions are sharp downward spikes, which are almost always followed by sharply peaked positive spikes. Clearly, this rapid spatial intensity variation is a function of the instrument's imperfections (diffractive light scattering) and needs to be excluded from the recovered numerical data. This is achieved by first locating the center of the pixel distribution for a given echelon time point, and then applying a windowing or "fuzzy" function to select only a particular central fraction of points. Typically, the centermost

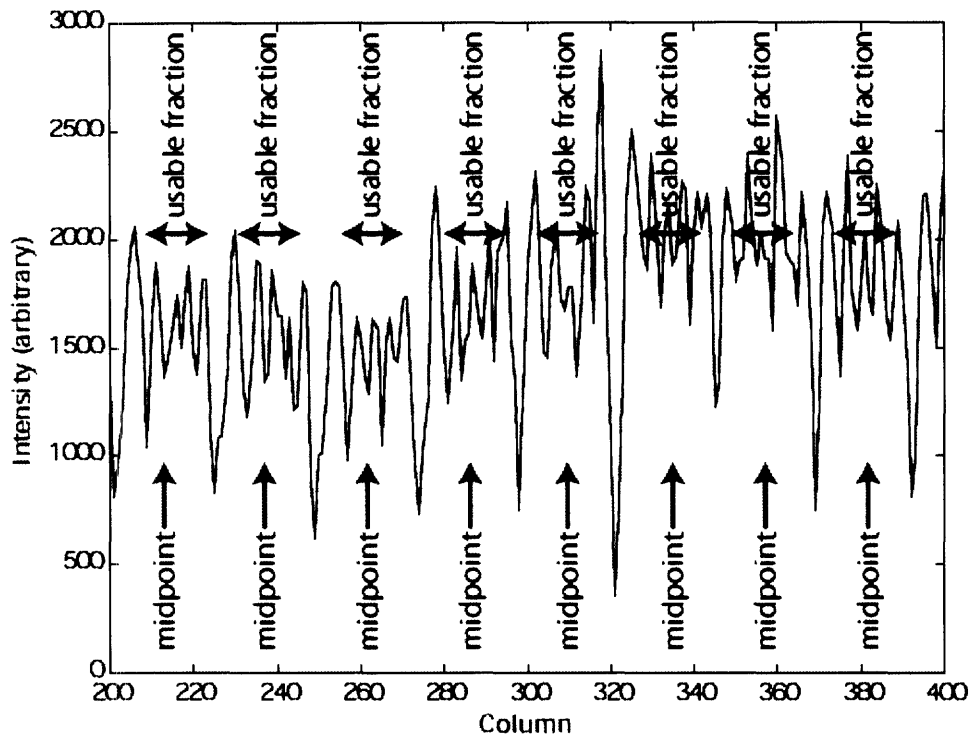


Figure 2-11. Horizontal scan through row 500 of an echelon image. The usable fraction of pixels is determined for each square by applying a window function centered on the midpoint of the intensity distribution for that square.

75% of the pixels in any given echelon square are employed in further calculations. This process is illustrated in Figure 2-10. Since the echelon squares are, on average, roughly 30 pixels by 30 pixels, applying the 75% condition results in averaging over nearly 500 pixels per time point, sufficient to ensure reasonable signal-to-noise levels. The center of the pixel distribution for each echelon square is located by taking the mean of the midpoints of each of the rows and columns of pixels which constitute that square. Figure 2-11 illustrates the windowing process in greater detail for a horizontal scan along row 500 of the left image in Figure 2-10 above.

Next, the signal intensity as a function of time is calculated for each echelon square by simply adding up the individual pixel intensity values, multiplying each by a Gaussian weighting function centered at the midpoint of the square, and calculating the mean of the distribution. The inclusion of a weighting function is phenomenological and accounts only for the assumption that pixel intensities nearer the center of the echelon squares are less likely to suffer from systematic error due to light scattering from edges, fabrication errors, etc., and are therefore more accurately representative of the true transmitted light intensity as a function of time. The mean intensity $S(i,j)$ at a given time point is calculated as

$$S(i, j) = \frac{\sum_{n_x^l} \sum_{n_y^l} I(x, y) G(x_0, y_0; x, y)}{\sum_{n_x^l} \sum_{n_y^l} G(x_0, y_0; x, y)} \quad (2.2)$$

where $I(x,y)$ is the pixel intensity at position (x,y) of the image and the sum runs over all n_x columns and n_y rows of pixels corresponding to time point (i,j) . The Gaussian weighting function G is defined as

$$G(x_0, y_0; x, y) = e^{-\left(\frac{(x-x_0)^2 + (y-y_0)^2}{2\eta^2}\right)} \quad (2.3)$$

where (x_0, y_0) is the center of time point (i,j) and the FWHM of the weighting function is given by

$$\eta = 2\sqrt{\ln 2} \cdot FWHM \quad (2.4)$$

The FWHM is treated as an adjustable parameter in the algorithm and is typically adjusted to match the half-width of the echelon square.

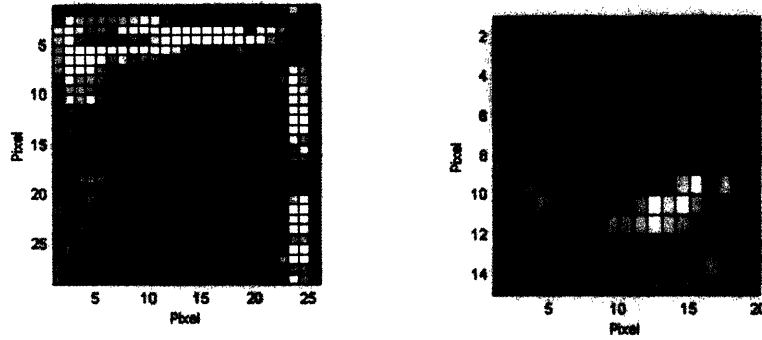


Figure 2-12. (Left) Image of echelon square (1,9). Note the higher intensity in the top left corner, due to edge diffraction. (Right) Image of square (1,3). Here, an edge imperfection results in the inclusion of many zero-valued pixels in the mean intensity summation. These effects can be removed either by iteratively adjusting the window function, which is computationally expensive, or by utilizing a smoothing function on selected troublesome echelon locations.

The numerical procedure has thus yielded a spatial intensity map which is a 20×20 mean-valued array. At this stage a smoothing algorithm is applied to edge-located time points to ensure continuity. Ordinarily, discontinuities in the mean signal intensity are not observed for time points which fall within the central regions of the echelon images. However, these types of anomalous signal are observed in the mean signal intensities derived from edge-bound time points. On the edge squares, chips, fabrication errors and diffraction produce anomalous light and dark pixel regions which, when included in the sum in Equation (2.2), skew the mean signal intensity either higher or lower than it should be. Examples of these effects are illustrated in Figure 2-12 for two echelon squares located along the top row of the crossed-echelon image. On the left, the echelon square depicted is at position (1,9) of the array. An intensity spike due to edge diffraction is located in the top left corner of the image, and in spite of the Gaussian filter function applied when summing the pixel contributions to the mean intensity, the true

mean value is inappropriately skewed higher by inclusion of the bright pixels. On the right, the image is of echelon square (1,3) which is oddly shaped due to an edge imperfection. Summing over all pixel values within this square will include dark regions where the pixel intensity is zero on account of the defect. This operation skews the mean intensity too low.

There are two solutions to this problem. The first is to iteratively shrink the window function by a small amount, say 5%, until the mean intensity does not substantially change. This severely limits the number of pixels included within the summation, however, and can itself skew the data inappropriately. In addition, such operations are very expensive computationally, since they involve tedious raster-scanning through individual squares. A more expedient approach is to utilize a lookup table of troublesome echelon locations and, for each entry in the table, apply a smoothing function to interpolate between the mean intensities in the previous and subsequent temporal locations. This is the approach we employ in the recovery of our data.

The procedure described so far is undertaken on the sample and reference images from the scan taken with a pump pulse (the data scan), and also on the sample and reference images taken without a pump pulse (the background scan). This yields four separate 20×20 spatial arrays of mean intensity values. The reference image mean intensity values from the data scan are used to correct those from the sample image of the data scan by dividing the two, in order to normalize the measured intensity distribution of the probe pulse. Although care has been taken to ensure that the probe intensity profile is very nearly a square function, the intensity does diminish slightly toward the edges of the echelons and if a correction scheme is not employed, time-dependent features with

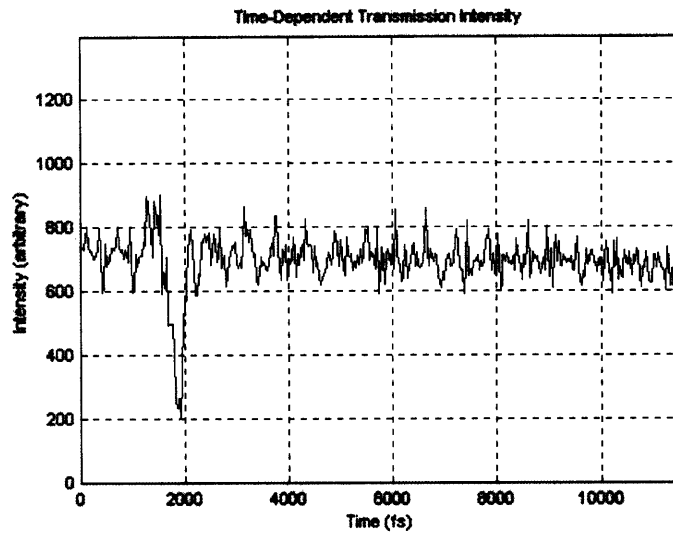


Figure 2-13. Recovered mean signal intensities from the sample image of the data scan. No corrections to the single-shot data have been applied. Note that the strong $t = 0$ feature is clearly visible, but the prior and subsequent baseline is very noisy. The baseline noise contains an oscillatory component with period 500 fs, which matches the periodicity of the thin echelon. This feature is introduced systematically into the data by discontinuities in the mean signal intensities when moving from the bottom row of one echelon column to the top row of the next.

periodicity 500 fs (the thin echelon total time window) are observed in the recovered data points. In addition, small deviations from an initial (prior to the 1" aperture) ideal Gaussian intensity distribution are significant here given that the probe beam waist has been magnified by a factor of 25. Similarly, the sample image from the background scan is adjusted by dividing its values with those of the reference image from the background scan. Figure 2-13 illustrates the uncorrected sample image mean intensities extracted from the data scan. The strong modulation feature at $t = 0$ is clearly visible, but the baseline response both prior to and subsequent to $t = 0$ is very noisy. The oscillatory component of baseline noise (with period 500 fs) is clearly visible. Figure 2-14

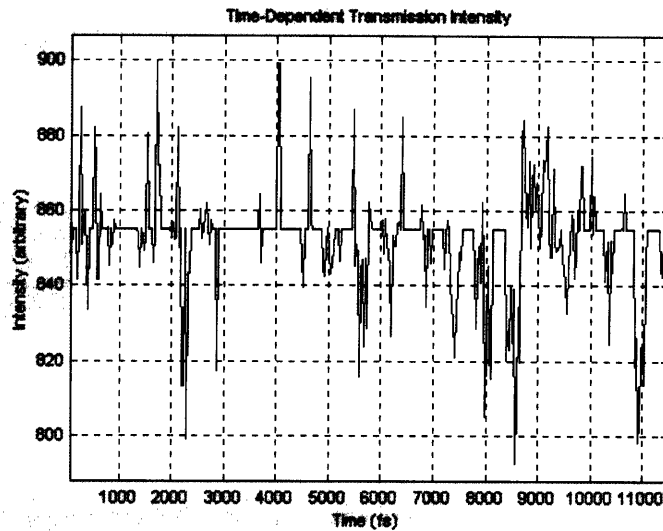


Figure 2-14. Instrument response function for a single-shot experiment derived from the reference image of the data scan. This response function contains sharp features due to anomalously large or small pixel intensities at particular spatial locations on the echelon image. These anomalous values introduce systematic error into the measurement; the instrument response function is used to correct the recovered data for such errors.

illustrates the normalized intensity profile of the reference image on the data scan. The resulting distribution is effectively an instrument response function for a particular scan of the single-shot experiment, describing primarily those temporal regions of the echelon array where anomalously large or small pixel intensities occur due to systematic errors in the measurement itself.

Finally, the adjusted mean intensities from the sample image of the data scan are corrected with the adjusted mean intensities from the sample image of the background scan. The effect of this correction is to counter imaging defects and inhomogeneities introduced by the material under investigation. Such defects can include diffraction from surface features (front or back) and scattering from impurities or defects within the bulk. The background sample image adjusted mean intensities are typically subtracted from the

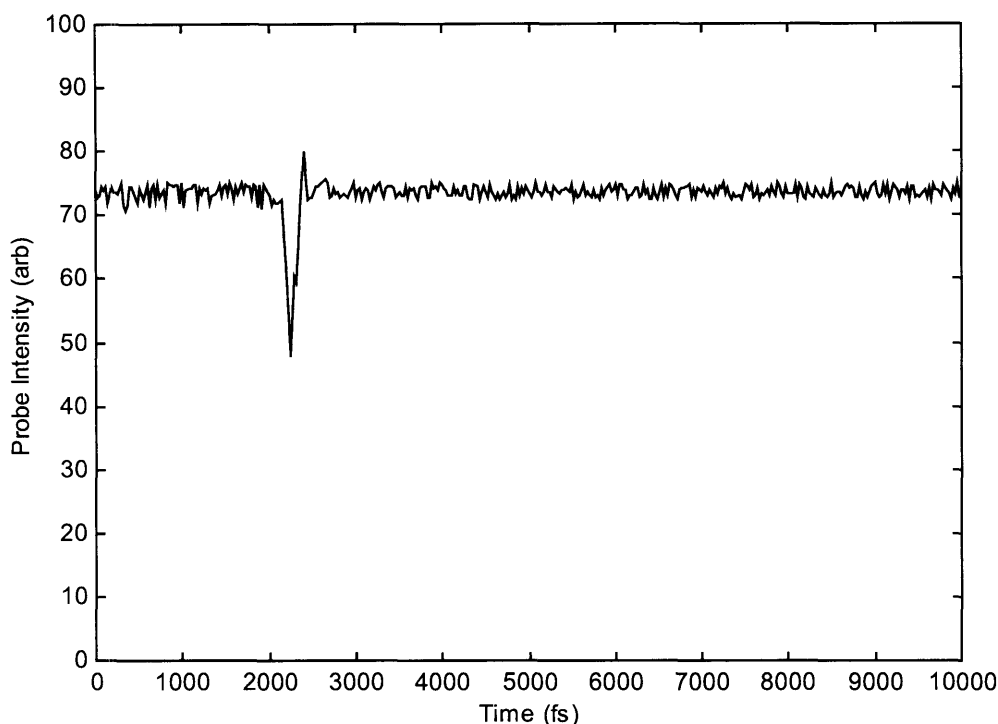


Figure 2-15. Single-shot data after the instrument response function is applied to remove baseline systematic noise. The data correction procedure is effective for low pump pulse intensities but becomes increasingly less effective at higher intensities.

data sample image adjusted mean intensities, and the result is then divided by the background sample image adjusted mean intensities in order to effect the normalization. The resulting modified data sample image intensities are effectively percent changes in transmitted light intensity.

The final step in the process is to translate the spatial intensities to a time-dependent response function by carefully calibrating each individual echelon step for the precise relative delay it represents. In practice, the relative step increment is 25 ± 3 fs, so this uncertainty can be overlooked without serious consequence. Figure 2-15 illustrates the final time-dependent transmitted light intensity for the original data of Figure 2-13. Note the influence of the instrument response function, which has drastically reduced the

anomalous baseline signal. The overall procedure is naturally less effective with poorer quality samples, greater shot-to-shot fluctuations in laser intensity, and very high intensity pump pulses which cause nonlinear effects in the sample (Kerr-lens-induced refraction, continuum generation) which are very difficult to compensate. The described algorithm includes the only means of data correction employed in our use of the single-shot experimental technique. All subsequent data shown in this thesis are acquired in a single laser shot and recovered using the method just described.

2.4 Sources of Error in Single-Shot Measurements

This section will discuss sources of error inherent in the single-shot experiments undertaken with our apparatus. We use this term to refer collectively to those issues which ultimately affect both the resolution and accuracy of the measurements, and note that all of these effects are not fully compensated in the subsequently reported data.

2.4.1 Fabrication and Construction Imperfections

This designation refers to difficulties which arise from the fabrication of the transmission echelons used in the single-shot experiment. While difficult to quantify, such effects ultimately limit the sensitivity of the measurement by introducing spurious background noise into the single-shot data. In certain cases, such sources of noise might be effectively random and therefore are mitigated in multi-shot pump-probe experiments. However, utilizing the echelons also introduces noise from a number of factors which might be termed *semi-random*; that is, occurring at repeatable times, but at varying intensity levels, making robust correction of such effects difficult. Echelon aberrations, particularly near the edge steps, fall chiefly into this category. Figure 2-12 (right)

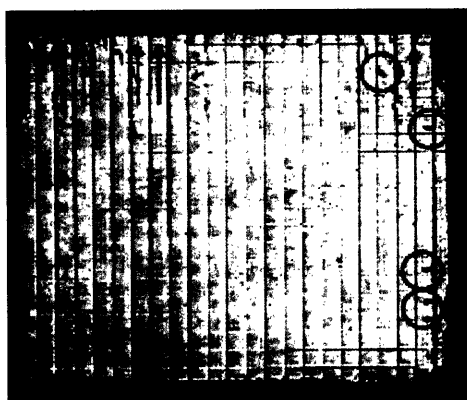


Figure 2-16. Defect regions in the cross-section view of the echelon matrix. Edge imperfections are indicated by arrows and internal scattering centers are circled. Such noise sources are very difficult to compensate on account of the unpredictable nature of the transverse distribution of scattered probe light they produce.

illustrates an edge defect (a chip) which, although identified and explicitly treated, is difficult to fully work around. The left image in Figure 2-12 illustrates an optical aberration (diffraction from a step edge) which, although not a manufacturing defect, can also introduce abnormally high signal levels. These defects were both introduced while describing the data correction mechanisms employed in the single-shot algorithm, but it is important to recognize that no algorithm, with only one working set of data, can fully compensate such effects, since the algorithm has no sense of how the data *should* appear. Optical damage spots in the interior regions of the echelons are rarer, but have the same effect upon the measured data. Figure 2-16 highlights some of the most severe defect regions of the echelon set currently employed. Edge defects are highlighted by arrows and interior defects are circled. The difficulty in correcting for such errors lies in the fact that light scattering by the probe pulse from such regions is unpredictable, as it depends on many factors including the probe pulse spatial intensity distribution, wavelength, geometrical alignment (i.e. variation in beam-pointing), etc. Thus, the distribution of

scattered light effectively changes from one shot to the next, making the development of a universal correction scheme a very difficult task.

2.4.2 Sensitivity Limitations

While limitations to the overall sensitivity of the experiment are not strictly sources of error, the task of separating genuine signal from spurious noise is rendered more difficult on account of these factors, and hence they are included in the present discussion. The most serious limitation the single-shot experiment suffers from is the absence of any sort of signal averaging mechanism. Of course, this is by design – however, it remains that the sensitivity of the more commonly used pump-probe techniques is due in large part to the ability to average over many thousands of pump-probe events at a given delay time, thereby mitigating random sources of noise. Typically, material responses induced by the pump pulse, especially if they arise from nonlinear interactions, are weak and difficult to detect. For instance, in stimulated Raman scattering experiments, the maximum change in probe pulse intensity is about 1%. Thus, our all-optical detection scheme must be able to detect changes in signal which are of the order of 0.1% in order to capture the response of the sample.

Fortunately, the coherent signal is heterodyned with the probe itself, so we must attempt to detect *changes* in a strong probe signal, rather than a weak signal rising above background noise. Nonetheless, separating this weak coherence signature from the inherent noise background in single-shot experiments can prove to be daunting. If one considers that the CCD array used for signal detection assigns 12 bits per pixel, then the probe intensity can vary over 4096 intensity levels. Assuming we maintain the probe intensity at 3200 counts or lower to avoid saturation effects, a 1% change in probe

intensity corresponds, at best, to a change in measured signal intensity of 32 counts. All sources of background noise, taken together, must therefore contribute less than 32 noise counts per time point in order for the signal to be measurable. In practice, the situation becomes even more problematic, as one would ideally prefer to have signal-to-noise ratios of at least 2:1 in order to confidently extract the data from the optical images. Further, as the material response becomes weaker over time, the induced change in probe intensity falls as well – in the event that it is possible to detect signal at all, the signal may only exist for a short time before its amplitude decays sufficiently that it is lost in the noise background.

In principle, one could increase signal strength simply by employing higher average power pump pulses. Unfortunately, for most molecular and inorganic crystals, undesirable nonlinear effects in the sample arise for pump power densities greater than about 10 TW/cm^2 . The most severe of these is self-phase modulation, which leads to continuum generation in the sample. For many materials, the white light spectrum generated is extremely broad, covering wavelengths from near-UV, throughout the visible region, and into the near IR. Figure 2-17 illustrates the measured spectrum from continuum generation via $10 \text{ }\mu\text{J}$, 50 fs pulses at 800 nm , focused to a $150 \text{ }\mu\text{m}$ diameter spot in a 1 mm thick sample of crystal quartz. The spectrum covers the entire visible region and in particular, contains frequency components at both 800 nm and 400 nm . Ordinarily, when using an 800 nm pump and 400 nm probe for the single-shot experiment, the narrow bandpass filter employed in the detection scheme is fixed either a little to the blue or red side of the maximum intensity wavelength in the probe spectrum – in this case, at about 397 nm or 403 nm . This effectively ensures that none of the light

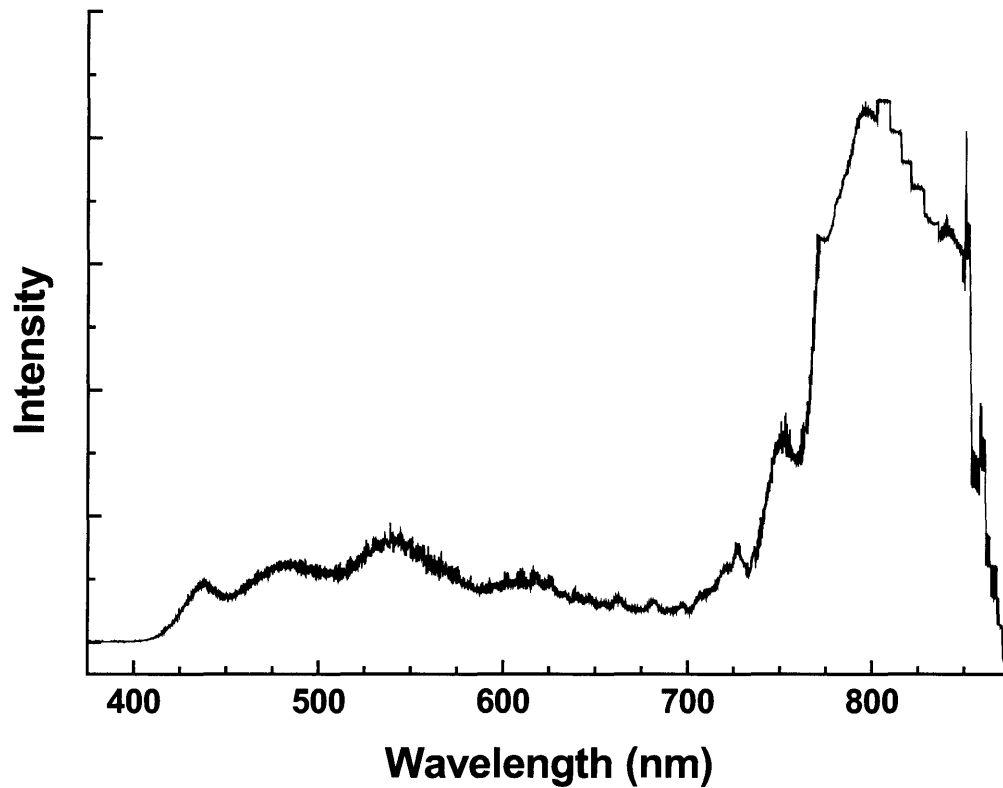


Figure 2-17. Continuum generation in 1 mm crystal quartz. Pump pulses of 10 μJ and 50 fs at 800 nm are focused to a 150 μm diameter spot on the front surface of the crystal. The resulting self-phase modulation due to the high pump intensity modifies the spectral properties of the pump pulse, generating frequency components over a very broad bandwidth.

from the pump pulse is scattered into the probe path and detected by the CCD. However, continuum generation in the sample at high pump intensities scatters light at many frequencies into a forward cone, parts of which will overlap with the paths of parts of the probe light reaching the CCD. The cone angle is particularly wide if the process occurs via multiple filaments. In either case, the result is that light at the frequency of the bandpass filter is scattered with a widely varying spatial distribution and detected at some

regions of the CCD. There is no algorithmic solution to removing the effects of this noise source in the measured data.

An additional limitation to sensitivity results from the inherent design of the single-shot experiment. The distance along the probe beam's propagation axis from the front of the thick echelon to the rear of the thin echelon, including the space between the two in a typical mounting configuration, is about 2 cm. The imaging setup in the sample arm of the experiment is designed to transfer the cross-sectional profile of the echelons, which is superimposed upon the probe beam profile, onto the surface of the CCD camera. The difficulty lies in defining the object plane for the transfer optics. In fact, any plane which falls within the 2 cm window can be effectively transferred to the CCD image plane. However, all other points which are displaced along the propagation axis will not be focused at the image plane. Thus, for example, it is possible to correctly image, with minimal distortion, all of the steps on the thin echelon at the CCD surface; we need only choose the central step as the object plane (by translation along the z -axis) and then the other steps are displaced no more than 150 μm from the object plane. The defocusing at the image plane is minimal under these conditions. However, if we choose the central step of the thick echelon as the object plane, then steps at either extreme are 3 mm from the object plane, and cannot be focused properly to the image plane. Similarly, *all* of the steps of the thin echelon in such an arrangement would be badly defocused at the image plane. The solution in such a scenario is to interpolate between these cases and fix the object plane in the air gap between the echelons, effecting a compromise.

There is a subtle interplay at work in the above scenario. Some defocusing at the image plane is needed in order to provide enough image contrast to correctly identify the

divisions between echelon steps – the algorithm we use for data extraction depends upon this. However, too much defocusing results in high noise levels and, as a result, an inability to resolve weak signals. Balancing these competing requirements has a direct and substantial effect on the overall performance of the instrument. The effects of defocusing at the image plane, and the contrast it produces, can be observed in the depth of modulation of the minima defining the divisions between echelon squares in Figure 2-9. The top scan on the right side is down a column (i.e. through the thin echelon) and the bottom scan is across a row (thick echelon). The depth of modulation in the bottom scan is significantly greater than in the top scan, due to the fact that the thicker echelon steps cannot be collectively imaged as successfully to the plane of the CCD camera as the thin steps.

Finally, it must be noted that a fundamental difference exists between the single-shot technique and a standard pump-probe approach. In a standard approach, we have one pump event and then one probe event, at a fixed delay. The intensity of the probe is generally much weaker than that of the pump, for obvious reasons: the object is to interrogate the evolving state of the material, perturbing it as little as possible with the probe pulse in the process.

Within the single-shot regime, one seeks to maintain a similar relationship between pump and probe intensities. However, typically we find that because single-shot signals are so weak, it is often necessary to employ slightly more intense probe pulses in order to make measurements. The single-shot scheme also differs in another important respect: we utilize a single pump pulse, followed by 400 individual probe pulses. While a single weak probe pulse might have little effect upon an evolving response in the

material, the total effect of 400 pulses might well be severe enough to warrant consideration. The nature of the induced response and its dependence on light intensity, wavelength, and other parameters must be assessed in order to minimize adverse effects of the probe light. We will revisit this issue subsequently in the context of specific measurements and their constraints.

2.4.3 Temporal Dispersion of Probe Pulses

In the idealized description of the single-shot apparatus, a single probe pulse of a few tens of femtoseconds duration passes through the crossed echelons and is spatially subdivided into a sequence of 400 probe pulses, each one of the same duration and delayed by an additional 25 fs relative to its predecessor. This description omits the important consideration of temporal broadening which occurs for ultrashort pulses traversing a dispersive medium. In order to assess the importance of temporal dispersion, we follow closely the treatment of Yariv [22]. An ultrashort pulse can effectively be described as an oscillating electric field underneath a smoothly-varying continuous envelope. If we assume a Gaussian shape for the envelope function, and assume propagation along the z -axis only, then we can ignore the vector properties of the field, and write simply

$$E(t) = \text{Re} \left[E_0 e^{-\frac{t^2}{\tau^2}} e^{i\omega_0 t} \right] \quad (2.5)$$

where E_0 is the maximum field amplitude, τ is related to the FWHM duration of the pulse, and ω_0 is the optical carrier frequency. For this simple description, the spectral content of the pulse is determined from the Fourier transform of Equation (2.5), which gives

$$E(\omega) = A_0 e^{-\frac{(\omega-\omega_0)^2 \tau^2}{4}} \quad (2.6)$$

The amplitude factor A_0 is not important for the purposes of this discussion. The pulse defined in Equations (2.5) and (2.6) is said to be transform-limited, because the temporal profile can be reconstructed from the inverse Fourier transform of the power spectrum, $I(\omega) = |E(\omega)|^2$. The power spectrum contains no phase information, implying that a transform-limited pulse also contains no additional spectral or temporal phase terms. Temporally dispersed pulses acquire both temporal and spectral phase terms which, among other consequences, can change the envelope function of an ultrashort pulse and also affect the instantaneous frequency distribution. The additional phase is most often introduced as a frequency-dependent term in Equation (2.6):

$$E(\omega) = A_0 e^{-\frac{(\omega-\omega_0)^2 \tau^2}{4} + i\varphi(\omega)} \quad (2.7)$$

Since the phase term $\varphi(\omega)$ typically results from the complicated interaction between an ultrashort pulse and a dispersive medium, the phase is commonly expanded in a Taylor series about the carrier frequency:

$$\varphi(\omega) = \varphi(\omega_0) + \left(\frac{d\varphi}{d\omega}\right)_{\omega_0} (\omega - \omega_0) + \frac{1}{2!} \left(\frac{d^2\varphi}{d\omega^2}\right)_{\omega_0} (\omega - \omega_0)^2 + \dots \quad (2.8)$$

The first two terms correspond to a constant phase shift and group delay, respectively, and do not affect the overall pulse shape or duration. The first important term is the third, which depends quadratically on the frequency detuning. It is commonly referred to as the group velocity dispersion (GVD), or second-order chirp. Higher-order terms can also become important, especially for very broad bandwidth pulses compressed near the transform limit. These are referred to according to the order of their dependence on the

frequency (i.e. third-order chirp, fourth-order chirp, etc.) Including the second-order chirp in Equation (2.8) and then performing an inverse Fourier transform to the time domain, we find

$$E(t) = E_0 e^{\left(\frac{-t^2}{\tau^2 - 2i \left(\frac{d^2 \varphi}{d\omega^2} \right)_{\omega_0}} \right)} e^{i\omega_0 t} \quad (2.9)$$

Comparing this result to Equation (2.5), it is evident that any non-zero value of the GVD results in a temporally broadened pulse. Higher-order dispersion terms can be included in the same fashion, although analytic expressions for the inverse Fourier transforms become increasingly complicated, and it is usually more facile to perform the calculation numerically.

When an ultrashort pulse travels through a linear dispersive medium of length L , it acquires a frequency-dependent phase shift which may be described as

$$\varphi(\omega) = -\frac{\omega n(\omega)L}{c} \quad (2.10)$$

where $n(\omega)$ is the material's frequency-dependent refractive index. The empirical Sellmeier's formula can be used to describe the variation of refractive index with wavelength for a wide variety of materials:

$$n^2 - 1 = \lambda^2 \left[\frac{B_1}{\lambda^2 - C_1} + \frac{B_2}{\lambda^2 - C_2} + \frac{B_3}{\lambda^2 - C_3} \right] \quad (2.11)$$

The B_i and C_i coefficients have been measured for a large number of glasses and crystalline materials, and are widely available in the literature. By calculating $n(\lambda)$ for a particular material of interest, conversion to $n(\omega)$ is straightforward, as is the subsequent calculation of $\varphi(\omega)$. The second- and higher-order chirp terms are easily calculated by approximating the derivatives of the phase with finite differences. With the chirp terms

determined, the electric field in the frequency domain can be constructed according to Equation (2.7), and the inverse Fourier transform taken to find the temporal evolution of the field.

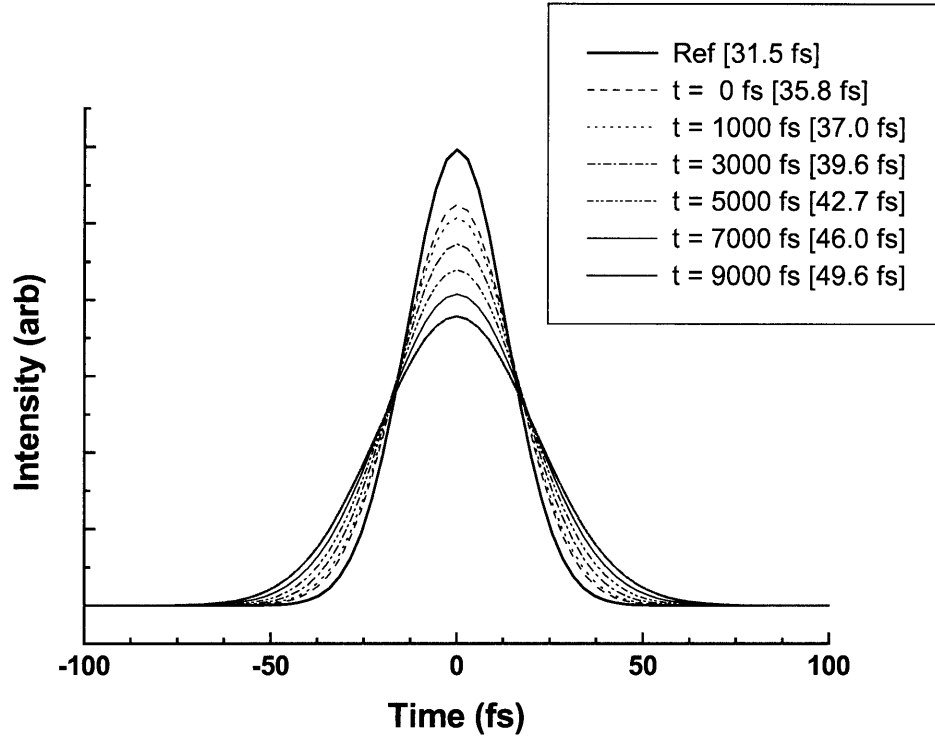


Figure 2-18. Temporal dispersion of probe pulses as a function of echelon delay. The linear dispersion of the echelon glass broadens the temporal profile of the ultrashort probe pulses. The initial probe pulse has a FWHM duration of 31.5 fs, but is stretched to a duration of 49.6 fs at $t = 9000$ fs on the spatial echelon grid.

In Figure 2-18 we illustrate the dispersive effect of the echelons on the temporal duration of the probe pulse. The pulse intensity is shown as a function of time to emphasize the effect of dispersion on the overall envelope. An 800 nm unchirped pulse with 30 nm of bandwidth, the idealized model probe pulse, is shown for reference. Other

pulse shapes shown correspond to varying thicknesses of echelon glass through which the probe pulse passes. Note that even the spatial region of the probe which corresponds to the earliest time point passes through several millimeters of glass. The prisms on which the echelons are inscribed are fabricated such that the hypotenuse sits atop a square prism base which is about 2 mm thick. Thus, every region of the probe beam passes through 4 mm of glass, at minimum. The earliest time region of the probe beam also passes through the thinnest step on each of the echelons, which contributes an extra 315 μm of glass. The total thickness of glass for the first time point is therefore 4.315 mm. Chirped pulses at other time points are also plotted; the obvious trend is the increasing pulse duration at later probe times. For the other times shown, the corresponding glass thicknesses are 4.915 mm, 6.115 mm, 7.315 mm, 8.515 mm and 9.715 mm respectively. Note that the FWHM pulse duration increases from 35.8 fs at the $t = 0$ fs region of the echelon to 49.6 fs for the $t = 9000$ fs region. This is significant, as the temporal intensity profile in the interaction region of the sample and the time resolution with which the sample response is probed therefore varies substantially during the course of the experiment.

We have used 800 nm pulses for the calculation above, since the design of the experiment (and specifically, the dispersion of the optics) was optimized for this wavelength. Recent developments (see Chapter 3 for details) have added multiple-wavelength capability to the single-shot experiment, such that both pump and probe pulses are tunable throughout the visible region of the spectrum (480-720 nm). However, as with most materials, the wavelength-dependent dispersion of the echelon glass is more severe at shorter wavelengths. In Figure 2-19, the calculation of Figure 2-18 is repeated

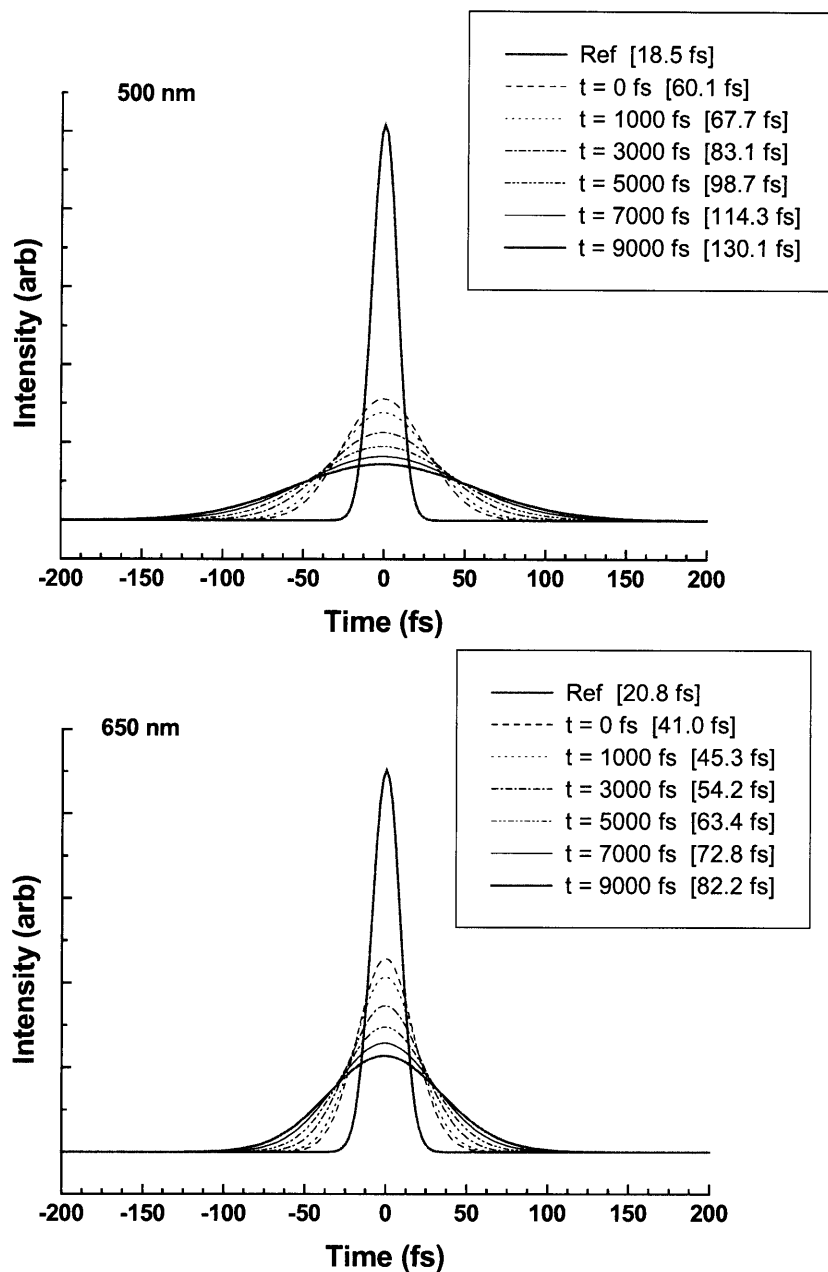


Figure 2-19. Temporal broadening of probe pulses at wavelengths of 500 nm (top) and 650 nm (bottom). The echelon glass exhibits normal dispersion, so pulse broadening is more severe at shorter wavelengths. The furthest delayed probe pulses at 500 nm may no longer satisfy the conditions for impulsive excitation.

for pulses at 650 nm and 500 nm, with 30 nm and 20 nm of bandwidth respectively. As expected, the temporal broadening is even more severe and in fact raises the possibility that perhaps the probe pulses, particularly at later delays, no longer provide sufficient time resolution for observation of features such as coherent lattice or molecular vibrations with frequencies above, say, 200 cm^{-1} . This frequency corresponds to a vibrational period of 167 fs, which is close to the pulse duration at 9000 fs for a 500 nm probe wavelength.

2.4.4 Wavevector Mismatch

Wavevector mismatch is a consequence of the off-axis spatial location of most of the distinct temporal regions of the probe. The obvious deviation of the probe, at most times, from the geometrically-ideal forward scattering direction is difficult to analyze because of the complex interaction between probe wavevector components and the sample. Rather than pursue a frequency-domain argument, it is perhaps easier to consider an alternative picture in which wavevector mismatch contributes an additional phase term to the description of the probe electric field, the effect of which is to introduce a time delay between the ideal arrival time of the probe and the actual arrival time. A simple picture of the disruption in probe pulse arrival times at the sample surface is obtained by calculating the additional geometrical distance that each spatial region of the probe must travel to reach the focal point, relative to the center delay point (10,10) on the echelon grid. In Figure 2-20, the additional time delay due to wavevector mismatch is plotted as a function of echelon probe delay. The time delay function oscillates with two frequencies, the faster envelope due to scanning delays vertically along the thin echelon, and the slower envelope due to scanning horizontally across the thick echelon. For this calculation, a probe pulse focusing distance of 5 cm is used. In our actual experiment,

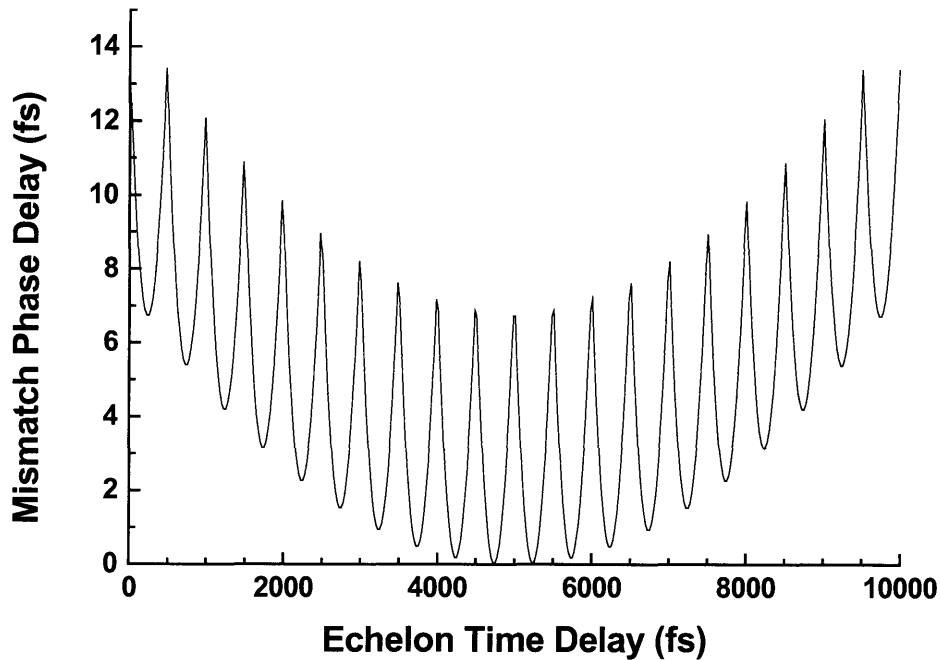


Figure 2-20. Probe pulse phase delay induced by wavevector mismatch. The wavevector of most spatial regions of the probe beam (which correspond to probe delay times) deviates from the ideal forward-scattering direction. The effect of this mismatch is to introduce a phase delay contribution to the nominal arrival time at the focal plane for each spatial region.

the probe focal length is 10 cm. It is worthwhile noting that focusing the probe beam closer to the echelons increases the problem of wavevector mismatch.

In essence, wavevector mismatch introduces a kind of temporal smearing on account of uneven probe sampling of the material response. Unfortunately, the effect is strongly wavelength dependent and is also influenced heavily by the day-to-day alignment of optics; numerical correction is virtually impossible. However, the total effect can be mitigated substantially with careful experimental design.

2.4.5 Diffraction by Optical Elements

The final major source of error inherent in the single-shot experimental setup is diffraction by the various optical elements involved. Most severe among these are diffraction due to the echelons, and diffraction by the sample.

Light scattering and diffraction in the sample, particularly for materials which are laboratory grown crystals, can be the major factor limiting the usefulness of the single shot apparatus. Because the echelon spatio-temporal grid is *imaged* through the sample, any material imperfections – scattering centers, defects, growth planes, stepped surfaces – will disperse or reflect light, often strongly. Since material defects occur in more or less random fashion, it is perhaps not so useful to attempt to model their effects. We note however that numerical correction is possible if scattering is not too severe, via the reference image and background scans. An example of the effect of scattering by the sample is illustrated in Figure 2-21 for a solution-grown molecular crystal of 200 μm thickness. The distortion of the echelon image on the left is clearly evident when comparing to the right side reference image. In spite of the complex optical aberrations introduced by the sample, the numerical correction algorithm we employ is capable of extracting single-shot data from such an image.

In order to evaluate the effects of diffraction by the echelons, it is necessary to introduce some elements of diffraction theory. We will follow closely the treatment of Haus [23]. Consider an electric field in free space, which must at all times satisfy Maxwell's equations and in particular, must be divergence-free. The vector potential \mathbf{A} also obeys the wave equation, but its divergence need not be zero.

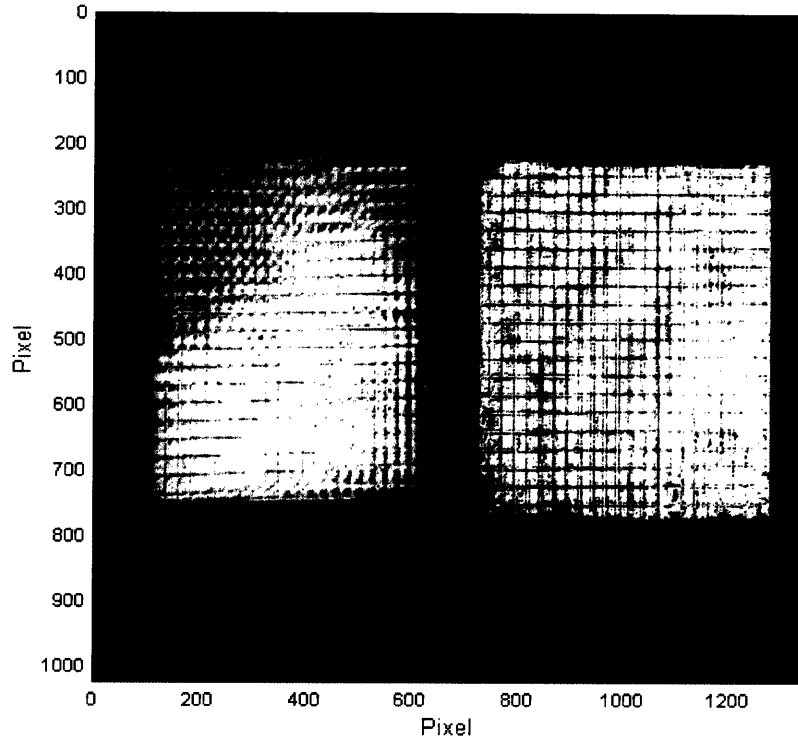


Figure 2-21. Echelon image aberration introduced by passage through the sample. Here the sample is a 200 μm thick solution-grown molecular triiodide crystal. The left hand sample image results from a complex series of scattering events within the bulk crystal. In spite of the distortion, individual echelon time points remain defined with enough contrast such that extraction of numerical data is possible.

If we assume for the functional dependence of \mathbf{A} the following

$$\mathbf{A}(r, t) = \mathbf{n} \psi(x, y, z) e^{i\omega t} \quad (2.12)$$

then substitution into the wave equation

$$\nabla^2 \mathbf{A} - \mu_0 \epsilon \frac{\partial^2 \mathbf{A}}{\partial t^2} = 0 \quad (2.13)$$

yields the following result:

$$\nabla^2 \psi + k^2 \psi = 0 \quad (2.14)$$

The vector potential amplitude function $\psi(x,y,z)$ obeys the scalar wave equation, with no further constraints. In Cartesian coordinates, a general plane-wave solution of Equation (2.14) will take the form

$$e^{-ik_x x} e^{-ik_y y} e^{-ik_z z} \quad (2.15)$$

where the wavevector k is defined via the relationship

$$k_x^2 + k_y^2 + k_z^2 = k^2 = \frac{\omega^2}{c^2} \quad (2.16)$$

If the propagation direction defined by \mathbf{k} deviates only slightly from the z -axis, then the wave vector may be described within the paraxial approximation as

$$k_z = \sqrt{k^2 - k_x^2 - k_y^2} \sim k - \frac{k_x^2 + k_y^2}{2k} \quad (2.17)$$

For convenience in the following discussion, the phase term $\exp(-ikz)$ will be omitted by defining

$$\psi(x, y, z) = u(x, y, z) e^{-ikz} \quad (2.18)$$

The function $u(x,y,z)$ will be used as the amplitude distribution for calculations; the phase factor can easily be restored if a complete field solution is necessary.

The amplitude distribution $u(x,y,z)$ can be constructed through a superposition of plane waves in wavevector-space:

$$u(x, y, z) = \int_{-\infty}^{\infty} dk_x \int_{-\infty}^{\infty} dk_y U_0(k_x, k_y) e^{-i(k_x x + k_y y)} e^{i \left[\frac{k_x^2 + k_y^2}{2k} \right] z} \quad (2.19)$$

The function U_0 is the amplitude of the plane wave (in wavevector space) with components k_x and k_y of the wavevector \mathbf{k} . Substituting $z = 0$ in Equation (2.19) to examine the limiting behavior, we find that

$$u_0(x, y) = \int_{-\infty}^{\infty} dk_x \int_{-\infty}^{\infty} dk_y U_0(k_x, k_y) e^{-i(k_x x + k_y y)} \quad (2.20)$$

and it is evident that U_0 is the spatial Fourier transform of u_0 , the amplitude distribution at $z = 0$. Taking the inverse Fourier transform

$$U_0(k_x, k_y) = \left(\frac{1}{2\pi} \right)^2 \int_{-\infty}^{\infty} dx_0 \int_{-\infty}^{\infty} dy_0 u_0(x_0, y_0) e^{i(k_x x_0 + k_y y_0)} \quad (2.21)$$

Providing the field propagation direction is along, or nearly along, the z -axis, the field can be expressed as a superposition of plane waves with paraxial wave vectors. Further, Equations (2.19) and (2.21) suggest that the spatial amplitude of the field $u(x, y, z)$ at any point z can be determined if the initial amplitude u_0 at $z = 0$ is known. Combining Equations (2.19) and (2.21) we find

$$u(x, y, z) = \int_{-\infty}^{\infty} dx_0 \int_{-\infty}^{\infty} dy_0 u_0(x_0, y_0) \left(\frac{1}{2\pi} \right)^2 \int_{-\infty}^{\infty} dk_x \int_{-\infty}^{\infty} dk_y \times \left\{ e^{-i[k_x(x-x_0) + k_y(y-y_0)]} e^{i \left[\frac{k_x^2 + k_y^2}{2k} \right] z} \right\} \quad (2.22)$$

The inner integral over wavevector space is commonly referred to as the *Fresnel diffraction kernel* $h(x, y, z)$:

$$h(x, y, z) = \left(\frac{1}{2\pi} \right)^2 \int_{-\infty}^{\infty} dk_x \int_{-\infty}^{\infty} dk_y e^{-i(k_x x + k_y y)} e^{i \left[\frac{k_x^2 + k_y^2}{2k} \right] z} \quad (2.23)$$

The integration in Equation (2.23) can be carried out analytically to yield the following expression for the kernel:

$$h(x, y, z) = \frac{i}{\lambda z} e^{-ik \left[\frac{x^2 + y^2}{2z} \right]} \quad (2.24)$$

This provides a compact and convenient means of writing an analytical expression describing the field profile at any point, $u(x,y,z)$. By inserting Equation (2.23) into (2.22), we can express $u(x,y,z)$ as the convolution between the initial profile $u_0(x_0,y_0)$ and the Fresnel kernel:

$$\begin{aligned} u(x,y,z) &= \frac{i}{\lambda z} \int_{-\infty}^{\infty} dx_0 \int_{-\infty}^{\infty} dy_0 u_0(x_0,y_0) e^{-i\left(\frac{k}{2z}\right)[(x-x_0)^2+(y-y_0)^2]} \\ &= h(x-x_0, y-y_0) \otimes u_0(x_0,y_0) \end{aligned} \quad (2.25)$$

Equation (2.25) provides the means by which it is possible to calculate the effects of diffractive elements in the beam path. In the following discussion, an initial profile u_0 will be assumed and then propagated through the optical elements of the single-shot experimental setup.

The only other remaining consideration is the effect of a standard focusing lens upon the field amplitude profile. For a thin lens, the magnitude of the amplitude profile is unchanged. The lens instead introduces a spatial phase delay $\varphi(x,y)$ which can be expressed compactly as

$$\varphi(x,y) = \varphi_0 - \frac{k}{2f}(x^2 + y^2) \quad (2.26)$$

where the first term is the delay at the center of the lens (and may be omitted since it is the same at all spatial positions) and f is the focal length. Since the field profile acquires only phase terms, the new amplitude function can be expressed as

$$\begin{aligned}
u'(x, y) &= u(x, y) e^{-i\phi(x, y)} \\
&= u(x, y) e^{i\left(\frac{k}{2f}\right)(x^2 + y^2)} \\
&= u(x, y) l(x, y)
\end{aligned} \tag{2.27}$$

The action of the lens is contained in the function $l(x, y)$ which multiplies the old spatial profile to generate the post-lens profile $u'(x, y)$.

Consider again the single-shot experimental setup of Figure 2-5. After passing through the 1" diameter aperture and being collimated, the beam profile is approximately "top-hat" in shape (i.e. spatially uniform within the spot size and abruptly zero outside), in either the x - or y -dimension (i.e. transverse to the propagation axis). Since the beam possesses radial symmetry in the x - y plane, we will restrict ourselves to one dimension only in the discussion of diffraction effects. Therefore, we choose an initial top-hat beam profile along the x -dimension and propagating along the z -axis. In addition, we fix $z = 0$ at the front surface of the first echelon. The calculation of the beam profile after propagation through the echelons, traversing a region of free space between the echelons and the focusing lens, through the thin focusing lens, and finally to the focal plane (location of sample) is illustrated graphically in Figure 2-22. Since the calculation is performed in one dimension only, we include only one of the echelons – the thin echelon, with 15 μm steps. This is justified since the steps of the thicker echelon produce sufficient time delay between different spatial regions of the probe beam that interference effects between field components that pass through different regions are substantially smaller.

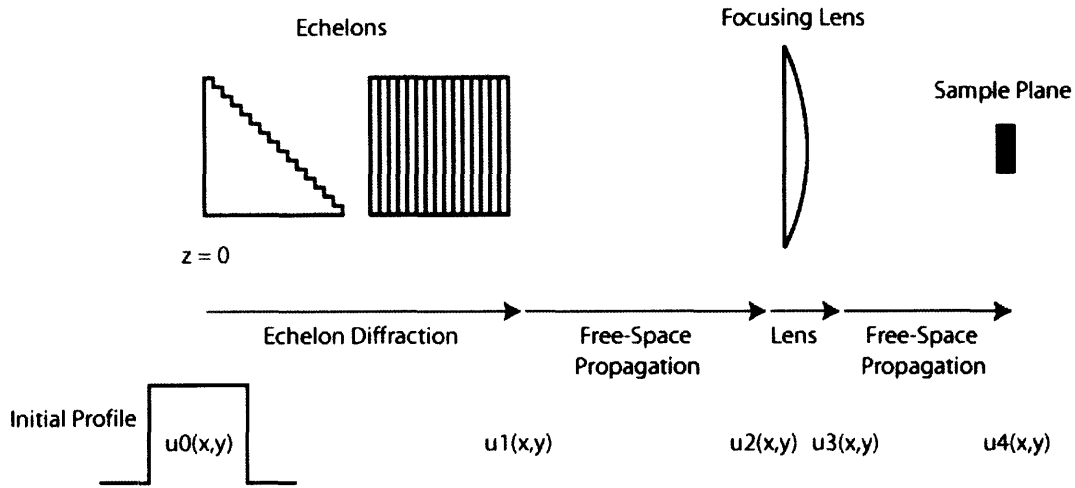


Figure 2-22. Schematic illustration of diffraction calculation for the single-shot setup. The initial beam profile is a square wave due to the 1" diameter aperture in the optical layout. The beam traverses four separate stages, each of which constitutes a propagation calculation: passage through the echelons, free-space evolution, lens passage, and free-space evolution to the sample.

The calculation is summarized as follows. The initial beam profile $u_0(x)$ traverses the echelon, which contributes a spatially dependent phase $e(x)$. The beam profile $u_1(x)$ after passing through the echelon is given simply by

$$u_1(x_1) = u_0(x_0) e(x_0) \quad (2.28)$$

in analogy with Equation (2.27). Free-space propagation of the beam from the rear surface of the echelon to the front surface of the focusing lens is described by

$$u_2(x_2) = h(x_2 - x_1) \otimes u_1(x_1). \quad (2.29)$$

Passage of u_2 through the lens generates the beam profile u_3 which is calculated as

$$u_3(x_3) = u_2(x_2) l(x_2) \quad (2.30)$$

Finally, free space propagation from the lens to the plane of the sample occurs according to another convolution with the Fresnel kernel:

$$u_4(x_4) = h(x_4 - x_3) \otimes u_3(x_3) \quad (2.31)$$

Note that the subscripts on the variable x are only used to indicate specific locations along the propagation axis where the beam profile is evaluated; all x_i 's refer to the same spatial variable. Substituting Equations (2.28), (2.29) and (2.30) into (2.31) we find that the final spatial profile of the beam in the sample plane is given by

$$u_4(x_4) = h(x_4 - x_3) \otimes \left[l(x_2) \left[h(x_2 - x_1) \otimes [u_0(x_0) e(x_0)] \right] \right] \quad (2.32)$$

In practice, however, the calculation is performed in four separate stages to verify the accuracy following each.

The thin echelon, with steps oriented perpendicular to the x -axis, contributes a step-wise phase as a function of x which is expressed as a time delay t_e :

$$t_e = \left\{ \begin{array}{ll} t_c & x > 10d \\ t_c + \frac{\left[10 + \text{fix} \left(\frac{x}{d} \right) \right] l_s}{\left(\frac{c}{n} \right)} & 0 < x \leq 10d \\ t_c + \frac{\left[10 - \text{fix} \left(\frac{x}{d} \right) \right] l_s}{\left(\frac{c}{n} \right)} & -10d \leq x < 0 \\ t_c & x < -10d \end{array} \right\} \quad (2.33)$$

where t_c is a constant delay due to the thickness of the echelon base, d is the transverse echelon step width, l_s is the echelon step thickness (15 μm) and n is the index of refraction of the echelon glass ($n = 1.5$). The spatial phase delay function $e(x)$ is then given by

$$e(x) = e^{-i\omega t_e(x)} \quad (2.34)$$

The results of the calculation are shown in Figure 2-23. The scattering is wavelength-dependent, as evidenced by Equation (2.24), and so the transverse beam

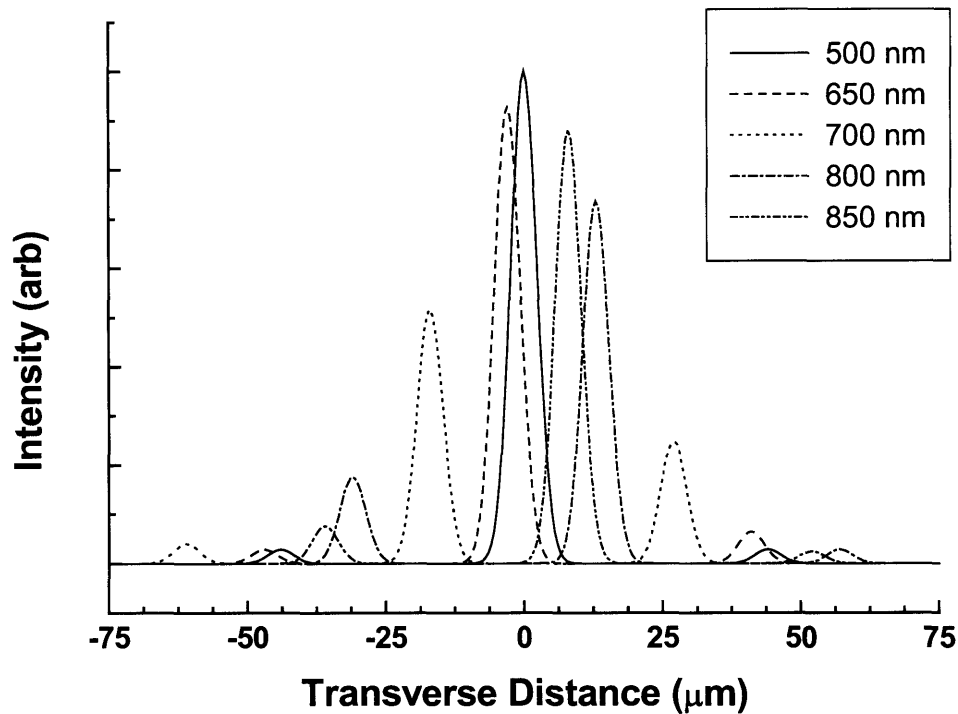


Figure 2-23. Probe beam intensity profiles at the sample position for a series of wavelengths. The intensity distribution depends critically on the phase delay acquired via passage through the echelon. When the delay is an integer multiple of the wavelength, all interference is constructive and only a central peak is observed. However, when this condition is not satisfied, multiple diffraction peaks result, with positions and intensities dependent upon the relative sign of the phase shift.

profiles are shown as a function of probe wavelength. Fields radiated from different spatial regions of the echelons interfere at the focal plane, producing the observed intensity distributions. At wavelengths for which the step phase of the echelon is an integral multiple, the interference is completely constructive and the result is a single central peak at the focal point. This is the case for the probe beam at 500 nm, 600 nm and 750 nm. At other wavelengths, the phase delay introduced by the echelons creates multiple spots in the focal plane due to interference. The distribution of peaks is sensitive

to the sign of the phase shift as well as the magnitude. Probe beams at wavelengths of 650 nm and 700 nm experience phase shifts of one sign and the central peaks of these diffraction patterns appear to the left of the zero-order peak in Figure 2-23, whereas beams at 800 nm and 850 nm acquire phases of the opposite sign (the determination of the sign itself is arbitrary) and thus appear to the right of the zero-order peak. In addition, the distribution of satellite peak intensities changes with the sign of the phase shift.

The importance of the diffractive effects of the echelons with regard to the single-shot experiment lies in the fact that in order to achieve good signal-to-noise ratio, it is extremely important that the probe beam effectively sample only the volume of material subjected to the pump pulse. Aligning the pump and probe can be difficult, however, as the probe position is highly dependent upon echelon diffraction. This is particularly true when performing multiple wavelength experiments. In addition, diffraction reduces the intensity of the central peak in the probe amplitude profile, resulting in weaker interaction with the evolving response in the sample.

As a final exploration of scattering effects in the experiment, we introduce a small defect (in effect, a negative aperture) along the transverse axis of the beam profile at the focal plane. The defect is meant to represent a scattering center within the sample, any type of bulk or surface defect which will scatter probe light. Any probe beam intensity at the position of the defect is blocked, while light on either side of the defect is transmitted. The initial sample profile is $u_4(x_4, y_4)$ from the previous calculation, and this profile is propagated in three steps. The first is to multiply u_4 by a mask function $s(x)$ which represents sample scatter, generating u_5 . The second step is free-space propagation from the sample to a collimating lens of focal length $f = 10$ cm (the same as the focusing lens),

located 10 cm behind the focal plane. This is accomplished, as before, by convolving u_5 with the Fresnel kernel to generate u_6 . Finally, the third step is to pass the beam through the collimating lens $l(x,y)$, in the process acquiring a spatially-dependent phase as in Equation (2.27). The effect of the focusing lens is to perform a spatial Fourier transform of the beam profile at the focal plane, and the collimating lens performs the inverse Fourier transform to reconstruct the amplitude function in real space. The resulting spatial profile, $u_7(x_7,y_7)$, represents the amplitude profile of the probe after it emerges from the interaction region with the sample and just before it enters the 2:1 reducing telescope of the single-shot setup.

The results of this calculation are shown in Figure 2-24. The top panel illustrates schematically the placement of the scattering center in relation to the probe amplitude function in the focal plane. We have used the minimum-diffraction probe profile from Figure 2-23 as the initial amplitude. The scattering center is 3 μm wide and located at a distance d from the nominal focal point. Final probe beam profiles are calculated for several values of d , and the results are shown in the lower panels of Figure 2-24. The effects of scattering by the sample are most catastrophic when $d = 0$; that is, when the scattering center is located at the apex of the probe beam in the focal plane. The probe profile is badly distorted, making proper imaging of the echelons impossible. Light is effectively scattered in every direction and the probe profile bears no resemblance to the initial top-hat shape. As the scattering center moves progressively further from the focal point, the reconstructed probe beam begins to bear increasing likeness to the ideal square-wave shape.

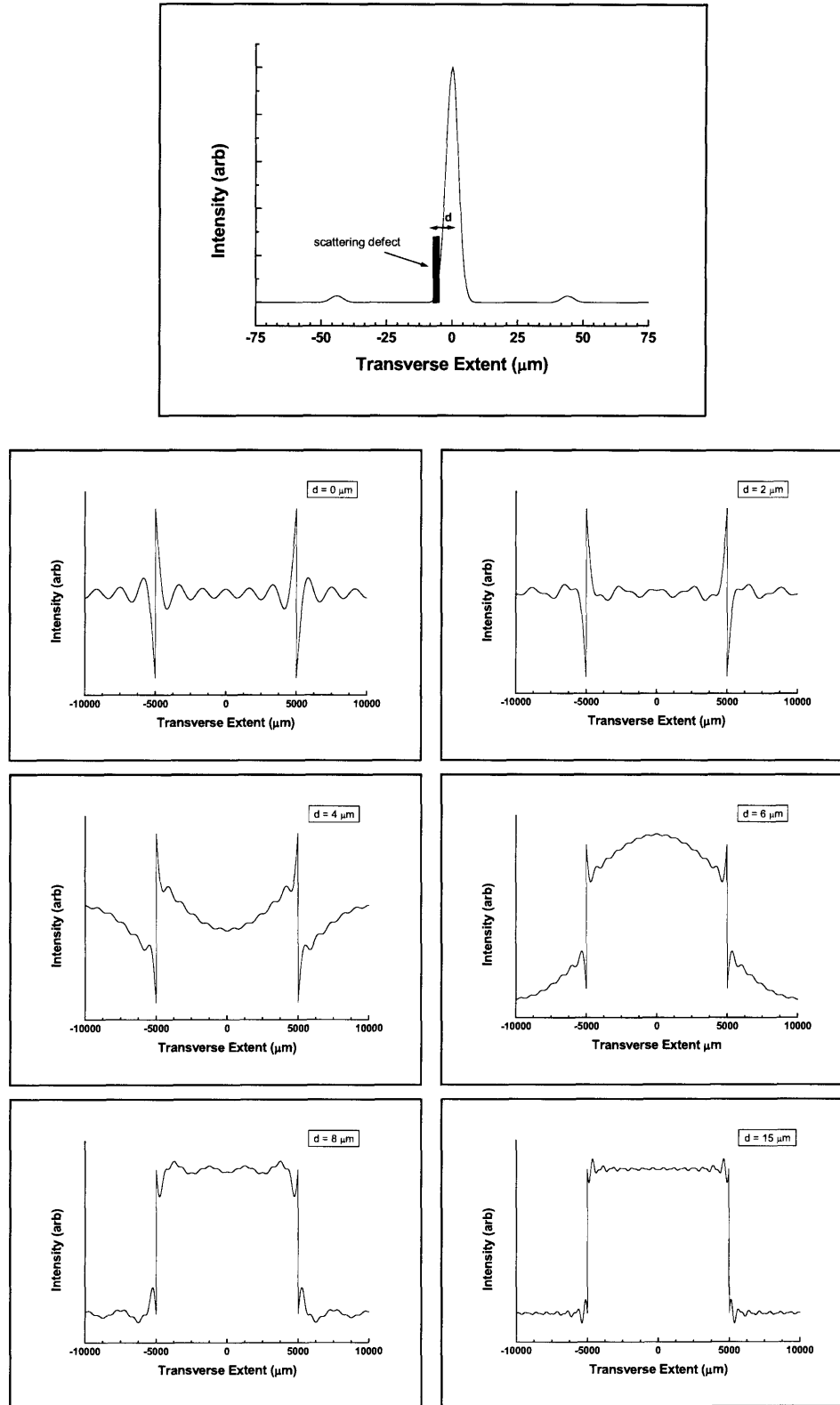


Figure 2-24. Calculation of probe beam spatial profile after scattering in sample and reconstruction by collimating lens. The top panel shows the placement of the scattering defect. Lower panels show the calculation of the probe profile as a function of the displacement of the defect from the focal point.

This simple calculation, while not nearly detailed enough to reproduce the sort of complex scattering events which produce images such as that of Figure 2-21, gives an approximate idea of the great importance of light scattering by the sample. More than any other, this aspect of the single-shot experiment determines how sensitively and how accurately the instrument can measure and recover sample responses. The requirements for good sample optical quality and careful attention to the construction of an aberration-free imaging system ultimately play the greatest role in determining the utility of the single-shot technique.

If the scattering is as severe as shown in Figure 2-24 for $d = 0 \text{ }\mu\text{m}$ or $d = 2 \text{ }\mu\text{m}$, there is little chance of successfully recovering good single-shot data from CCD images. However, as the scattering center moves outward from the center of the probe spot, the recovered beam profile improves markedly. Under these conditions, by numerically selecting only the center fraction of pixels in each echelon step for analysis, and by compensating the data scan's signal image with the reference image and the background scan, time-resolved material dynamics can be recovered. It is clear that the sample orientation must be adjusted carefully with regard to the probe focal location. Fortunately, for the samples used in this thesis, relatively aberration-free single-shot probe locations were found in all cases.

References

- [1] Wakeham, G.P., *Dual-Echelon Single-Shot Femtosecond Spectroscopy*, Ph.D. Thesis, Massachusetts Institute of Technology, 2001.
- [2] Strickland, D., and Mourou, G., *Opt. Commun.* **56**, 219 (1985).
- [3] Zhou, J. *et al.*, *Opt. Lett.* **19**, 126 (1993).
- [4] Zhou, J. *et al.*, *Opt. Lett.* **20**, 64 (1995).
- [5] Backus, S. *et al.*, *Opt. Lett.* **20**, 2000 (1995).
- [6] Treacy, E.B., *IEEE J. Quant. Electron.* **QE-5**, 454 (1969).
- [7] Christov, I. and Tomov, I., *Opt. Commun.* **58**, 338 (1986).
- [8] Martinez, O., *J. Opt. Soc. Am. B*, **3**, 929 (1986).
- [9] Fork, R. *et al.*, *Opt. Lett.* **12**, 483 (1987).
- [10] Ippen, E.P. and Shank, C.V., "Techniques For Measurement", *Topics in Applied Physics Vol. 18*, 83-122 (Springer-Verlag, New York, 1976).
- [11] Dhar, L., Fourkas, J.T. and Nelson, K.A., *Opt. Lett.* **19**, 643 (1994).
- [12] Jiang, Z.P. and Zhang, X.C., *Appl. Phys. Lett.* **72**, 1945 (1998).
- [13] Geindre, J.-P. *et al.*, *Opt. Lett.* **26**, 1612 (2001).
- [14] Scherer, N. *et al.*, *J. Chem. Phys.* **95**, 1487 (1991).
- [15] Zhang, J.-Y. *et al.*, *Opt. Expr.* **12**, 574 (2004).
- [16] Topp, M.R., Rentzepis, P.M. and Jones, R.P., *Chem. Phys. Lett.* **9**, 1 (1971).
- [17] Topp, M.R. and Orner, G., *Chem. Phys. Lett.* **3**, 407 (1975).
- [18] Topp, M.R., *Opt. Commun.* **14**, 126 (1975).
- [19] Du, D. *et al.*, *Appl. Phys. Lett.* **64**, 3071 (1994).
- [20] Tien, A.-C. *et al.*, *Phys. Rev. Lett.* **82**, 3883 (1999).
- [21] Lenzner, M. *et al.*, *Phys. Rev. Lett.* **80**, 4076 (1998).
- [22] Yariv, A., *Quantum Electronics* (John Wiley & Sons, New York, 1989).

- [23] Haus, H.A., *Waves and Fields in Optoelectronics* (Prentice Hall, Englewood Cliffs, NJ, 1984).
- [24] Lang, T. and Motzkus, M., *J. Opt. Soc. Am. B* **19**, 340 (2002).
- [25] Yan, Y.-X., Gamble, E.B. and Nelson, K.A., *J. Chem. Phys.* **83**, 5391 (1985).

Chapter 3

Generation of Tunable Ultrashort Pulses

It is desirable for a variety of reasons to have the ability to adjust the wavelengths of pump and probe pulses utilized in ultrafast spectroscopic experiments. The present chapter contains a discussion of a recently developed method for achieving wavelength tunability across the entire visible region of the spectrum without sacrificing temporal duration, in a compact table-top system.

3.1 Wavelength Tuning by Parametric Amplification

In terms of optical wavelengths, the single-shot experimental setup as described in Chapter 2 affords only the possibility of operating at 800 nm, the Ti:sapphire fundamental wavelength, and its second and third harmonics. Considerable utility may be derived from the setup despite these limitations; in particular, nonresonant Raman scattering experiments are insensitive to the optical frequency, and the signal strength in such a measurement is dependent to a much larger extent upon the temporal duration of pump and probe pulses, the spatial quality of the beam, and the stability of the laser source.

However, it was recognized that for a great many systems where one wishes to investigate the dynamic evolution of electronically-resonant processes, some mechanism for changing the operating wavelength of the experiment had to be developed. Such

processes include resonance-enhanced Raman scattering, transient electronic absorption, and femtosecond photochemistry. In addition, the signal-to-noise ratio can sometimes be improved even in frequency-insensitive experiments by choosing pump and probe wavelengths which are well-separated spectrally from one another. For example, pump-probe experiments in non-centrosymmetric materials yield appreciable amounts of both fundamental and second-harmonic light as a matter of course, and adjusting the probe wavelength to fall in a window region of the spectrum solves the problem of trying to separate spurious signal and probe light when both lie within a narrow frequency band.

Reliable generation of femtosecond pulses was first achieved by Shank and coworkers [1,2] who utilized a colliding-pulse modelocked laser with a dye gain medium at modest energies. Variable wavelengths were obtained by continuum generation and seeding of a second dye amplifier stage. In order to reach the sub-10 fs regime, further spectral broadening in single-mode fiber, followed by pulse compression with a series of prisms and gratings, was employed [3]. The limitations of these early attempts to provide wavelength tunability are evident: the limited bandwidth amenable to amplification via available laser dyes, and the technical demands associated with the operation of these systems.

The development of Ti:sapphire hosts and subsequent observation of the enormous gain bandwidth of the material suggested the possibility of wavelength-tunable laser cavities, but a couple of Ti:sapphire shortcomings quickly became apparent: first, the center wavelength is 800 nm, and so roughly half the tuning range lies in the infrared region of the spectrum, which is unsuitable for most electronic spectroscopy; second, Ti:sapphire suffers from extreme bandwidth-narrowing during amplification. Methods to

circumvent this limitation have since been developed, but it remains difficult to shift the center of the Ti:sapphire emission band by more than ± 35 nm. Efficient nonlinear conversion materials have also been developed for generating the 400 nm and 267 nm harmonics of Ti:sapphire, providing some modest coverage of the ultraviolet region.

The most efficient means to wavelength tunability lies with optical parametric conversion, a third-order nonlinear effect. Optical parametric generation with the second harmonic of Ti:sapphire, and subsequent amplification to microjoule energies, was first employed as a means to generate pulses in the visible region directly [4-8]. Unfortunately, pulses derived in this fashion were of fairly long duration. Seeding the optical parametric amplifier (OPA) with a phase-locked continuum source [9,10] provides substantially more bandwidth and, with appropriate compression optics, much shorter pulses.

The typical phase-matching geometry employed in OPA systems involves collinear propagation of pump, signal and idler within the mixing crystal. Such an arrangement is easy to align and maintain. Its greatest shortcoming lies in the fact that group velocity mismatch between the three wavelengths limits the size of the interaction region along the propagation axis. In effect, this limits the pulse duration of such systems because no matter how broad a continuum enters the crystal as the seed or idler, only a portion of the bandwidth can be effectively mixed with the pump pulses due to the spectral acceptance of the mixing crystal at a given angle. At best, pulses of 50 fs duration can be achieved in such collinearly phase-matched OPAs.

Gale and coworkers were first to report an amazing property of the nonlinear crystal β -barium borate (BBO) in 1995 [11]. In typical collinear OPA arrangements, the

desired wavelength is obtained by angle-tuning the mixing crystal for a particular phase-matched wavelength. A broad range of wavelengths can be generated in such fashion, and indeed it is straightforward to calculate the appropriate angle for any particular wavelength, but the total phase-matched bandwidth at any particular central wavelength is relatively small. Gale *et al.* pointed out that by utilizing a *noncollinear* geometry in BBO, it was possible to simultaneously phase-match wavelengths over an enormously broad bandwidth covering a significant portion of the visible region of the spectrum. They were able to exploit this favorable property in the construction of a synchronously pumped optical parametric oscillator (OPO) in order to generate widely tunable pulses [12]. By virtue of the need for synchronization with a pump laser, and also due to the reflectivity of the cavity mirrors, the bandwidth of OPOs is limited when compared with the phase-matching capabilities of BBO. Optical parametric amplifiers are not subject to these stability criteria, and it was soon recognized by a number of researchers that parametric amplification in BBO suggested the possibility of extremely short visible-wavelength pulses.

Considerable work in this field has been reported in the past eight years. De Silvestri and co-workers investigated the influence of continuum chirp on the phase-matching efficiency in white-light seeded OPAs and suggested the possibility of utilizing broadband chirped mirrors for continuum precompression [13-15]. Kobayashi and co-workers have built a noncollinear OPA which generates pulses with 2000 cm^{-1} of bandwidth and compressible to 4.7 fs by employing a pulse-front tilting scheme to maximize the three-wave interaction volume [16-19], an idea based upon the earlier work of Danielius, Piskarskas *et al.* [20]. The research group of E. Riedle has successfully

demonstrated wavelength tunability of the signal output throughout the visible region from a noncollinear OPA, and has also seeded the OPA along the idler phase-matching direction to generate tunable pulses from 1-7 μm , suitable for high-resolution vibrational spectroscopy [21,22]. Several other groups have explored various phase-matching schemes (i.e. type-II vs. type-I), frequency down- and up-conversion techniques, seeding options, compression methods and nonlinear materials within the broad context of noncollinear optical parametric oscillators [23-30] and amplifiers [31-33].

3.2 Noncollinear Broadband Phase-Matching in an OPA

In the following section, we will restrict ourselves to a discussion of phase-matching in a blue-pumped (400 nm) optical parametric amplifier with BBO as the nonlinear mixing crystal. The short-wavelength photons of the blue pump are split into signal (visible) and idler (infrared) photons, both of wavelength greater than the pump photons. In order for the interaction to occur efficiently, two separate conditions must be satisfied. The energy conservation condition

$$\omega_p = \omega_s + \omega_i \quad (3.1)$$

derives directly from the photon energies of the pump (p), signal (s) and idler (i) beams respectively, and constitutes a scalar restriction on the phase-matching process. The momentum conservation condition

$$\mathbf{k}_p = \mathbf{k}_s + \mathbf{k}_i \quad (3.2)$$

imposes an additional vector restriction on phase-matching which can only be satisfied with a suitable choice of nonlinear crystal (BBO) and orientation of said crystal. The phase-matching condition for maximum three-wave interaction is usually expressed as

$$\Delta \mathbf{k} = \mathbf{k}_p - \mathbf{k}_s - \mathbf{k}_i = 0 \quad (3.3)$$

Phase-matching does not, however, simultaneously assure group velocity matching. Typically, three waves of different frequencies propagate at different speeds within a nonlinear crystal so that the volume of spatial and temporal overlap is relatively small. For collinearly propagating pump, signal and idler, this places a fundamental restriction upon the ultimate temporal duration of signal and idler pulses generated in this fashion,

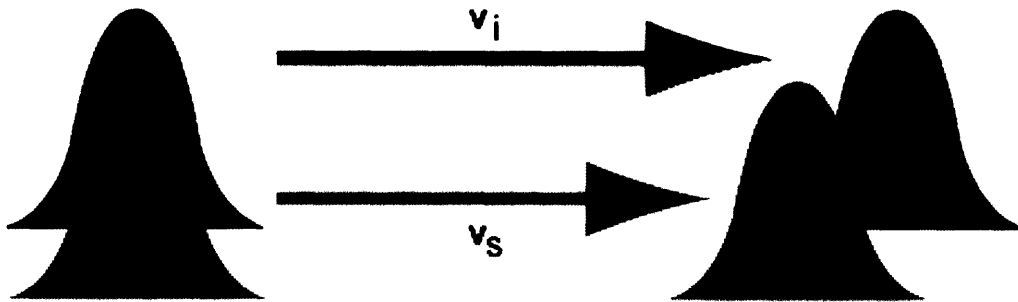


Figure 3-1. Group velocity matching in a collinear optical parametric amplifier. On the left hand side, signal and idler pulses are time-coincident when they begin to interact. In a normally dispersive medium, the group velocity of the idler pulses is greater than the group velocity of the signal pulses, so that the two separate as they propagate through the material. On the right hand side, the pulses continue to interact but because of their separation, new idler photons are added to the trailing edge of the idler field, whereas new signal photons are added to the leading edge of the signal field. The result is temporal broadening of both pulses.

as noted in Section 3.1. The situation is illustrated graphically in Figure 3-1. Signal and idler pulses are initially temporally and spatially overlapped on the left hand side. Their relative group velocities are shown by the arrows. Since most nonlinear materials are normally dispersive, the group velocity of the idler is greater than that of the signal. As a result, after the pulses have propagated through some thickness of the material, the idler pulse leads the signal pulse in time by an amount equal to the length of material traversed divided by the difference in group velocities. The pulses continue to interact as long as

parts of the envelopes overlap, but it is evident that as they begin to separate, new signal photons are added on to the leading edge of the signal field and new idler photons are added to the trailing edge of the idler field. This unavoidably produces lengthened pulses in each case.

The work of Gale and coworkers [11,12] was originally directed towards achieving much higher amplification bandwidths than was traditionally possible with collinear OPA arrangements. They constructed an optical parametric oscillator (OPO) based upon a noncollinear phase-matching scheme in BBO. Figure 3-2 illustrates the

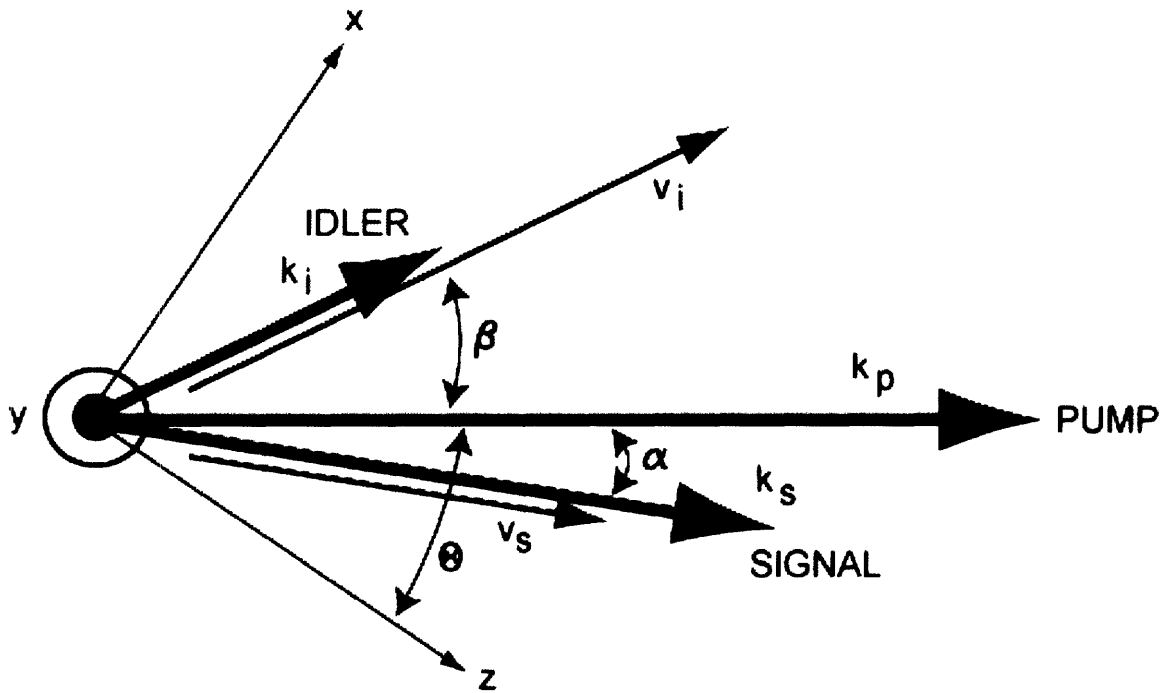


Figure 3-2. Phase-matching geometry for noncollinear three-wave mixing in BBO. Pump, signal and idler beams propagate in the x - z plane of the crystal. The thick arrows represent the wavevectors of the three beams and the thin vectors represent their group velocities.

geometry of the three-wave interaction and defines the relevant parameters. We consider interactions only within the x - z plane of the BBO crystal. The blue pump field

propagates through the crystal at angle θ to the BBO z-axis. Note that the wavevectors of the three fields are indicated with heavy arrows in the figure, while the group velocities are shown with thin arrows. The angle between the pump and signal beams is α , the noncollinear angle. In a conventional OPA, $\alpha = 0$, but here we relax this restriction in order to enhance the phase-matched bandwidth. The pump-idler angle is β .

If we calculate the phase-matching curve for three-wave mixing in BBO as a function of α , a remarkable property is evident. Figure 3-3 shows the results of this

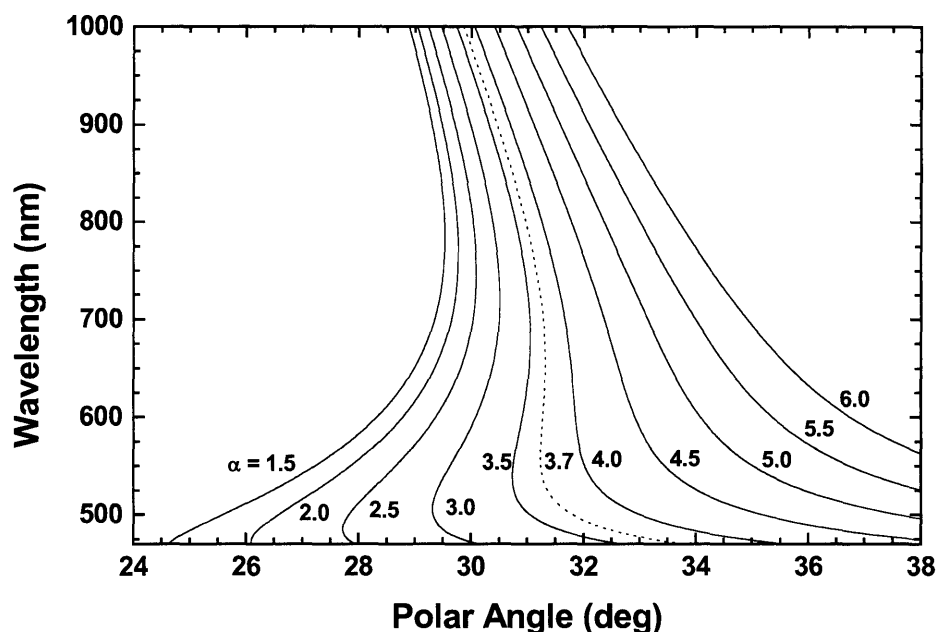


Figure 3-3. Phase-matching curves for type-I three-wave mixing in BBO. The phase-matched signal wavelength is plotted as the ordinate against the polar angle θ , for a series of noncollinear angles α . The shape of the curves changes from a reflexive “U” with an inflection to a monotonically-decreasing function of the polar angle as α increases. At a noncollinear angle of 3.7° , the curve is nearly vertical from 500-750 nm, suggesting the possibility of very broadband phase-matching with this geometry.

calculation for several different values of the noncollinear angle. As α increases, the shape of the curve changes from a reflexive “U” shape with a distinct inflection point to a

monotonically decreasing function of θ . The shape of the curve is very sensitive to the value of the noncollinear angle; note that the total variation in α across Figure 3-3 is only 4.5° .

At a noncollinear angle of 3.7° , the shape of the phase-matching curve is particularly noteworthy. For signal wavelengths between about 500 nm and 750 nm, the curve is nearly vertical – in other words, all of these wavelengths can be successfully phase-matched at the same polar angle $\theta = 31.5^\circ$. This suggests the possibility of employing this geometry in an OPA to generate signal pulses with enormous bandwidth, capable of being compressed to extremely short durations.

As noted previously, the phase-matching condition does not guarantee group velocity matching among pump, signal and idler. However, in a variety of nonlinear processes appropriate group velocity (GV) matching conditions can be found through suitable orientation of the birefringent nonlinear medium. It remains to be seen whether GV matching can be achieved under the geometry suggested by $\alpha = 3.7^\circ$ in Figure 3-3.

We will follow the treatment of Riedle and co-workers [34] in analyzing phase mismatch. In order to achieve broadband phase-matching, it is necessary that the wavevector mismatch $\Delta\mathbf{k}$ does not change with the wavelength of the seed (i.e. signal) pulse. The wavevector mismatch can be expanded in powers of the seed wavelength detuning $\Delta\lambda_s$ for a constant pump wavelength λ_p :

$$\Delta\mathbf{k} = \Delta\mathbf{k}_0 + \frac{\partial\Delta\mathbf{k}}{\partial\lambda_s}\Delta\lambda_s + \frac{1}{2!}\frac{\partial^2\Delta\mathbf{k}}{\partial\lambda_s^2}\Delta\lambda_s^2 + \dots \quad (3.4)$$

Applying the broadband phase-matching criterion in addition to the usual phase-matching requirement implies

$$\Delta \mathbf{k}_0 = 0 \quad (3.5)$$

$$\frac{\partial \Delta \mathbf{k}}{\partial \lambda_s} = 0$$

In order to relate the phase mismatch to group velocities, we first begin with the energy conservation condition given by Equation (3.1) expressed in terms of wavelengths:

$$\frac{1}{\lambda_p} = \frac{1}{\lambda_s} + \frac{1}{\lambda_i} \quad (3.6)$$

From Equation (3.6), with λ_p assumed constant, we find by differentiation that

$$\frac{\partial \lambda_i}{\partial \lambda_s} = -\frac{\lambda_i^2}{\lambda_s^2} \quad (3.7)$$

Differentiating the magnitude of the signal wavevector with respect to the signal wavelength yields the following relation:

$$\frac{\partial k_s}{\partial \lambda_s} = \frac{\partial}{\partial \lambda_s} \left(\frac{2\pi n_s}{\lambda_s} \right) = 2\pi n_s \left(-\frac{1}{\lambda_s^2} \right) = -\frac{2\pi c}{\lambda_s^2 v_g^s} \quad (3.8)$$

In Equation (3.8), we have made use of the following identity:

$$v_g = \frac{c}{n} \quad (3.9)$$

The quantity v_g is referred to as the group velocity. A similar procedure is carried out for the magnitude of the idler wavevector, and inserting the result from Equation (3.7) at the appropriate point, we find

$$\frac{\partial k_i}{\partial \lambda_s} = \frac{\partial}{\partial \lambda_s} \left(\frac{2\pi n_i}{\lambda_i} \right) = 2\pi n_i \left(-\frac{1}{\lambda_i^2} \right) \left(\frac{\partial \lambda_i}{\partial \lambda_s} \right) = \frac{2\pi c}{\lambda_s^2 v_g^i} \quad (3.10)$$

Referring to Figure 3-2, the phase mismatch vector $\Delta \mathbf{k}$ can be written in terms of components parallel and perpendicular to the signal wavevector \mathbf{k}_s . The results are:

$$\Delta k_{\parallel} = k_s + k_i \cos(\alpha + \beta) - k_p \cos \alpha \quad (3.11)$$

$$\Delta k_{\perp} = k_i \sin(\alpha + \beta) - k_p \sin \alpha$$

Differentiation of Equations (3.11) with respect to the signal wavelength λ_s leads to the following expressions:

$$\frac{\partial}{\partial \lambda_s} \Delta k_{\parallel} = \frac{\partial k_s}{\partial \lambda_s} + \frac{\partial k_i}{\partial \lambda_s} \cos(\alpha + \beta) - k_i \sin(\alpha + \beta) \frac{\partial \beta}{\partial \lambda_s} \quad (3.12)$$

$$\frac{\partial}{\partial \lambda_s} \Delta k_{\perp} = k_i \cos(\alpha + \beta) \frac{\partial \beta}{\partial \lambda_s} + \frac{\partial k_i}{\partial \lambda_s} \sin(\alpha + \beta) \quad (3.13)$$

In the above, the pump wavevector \mathbf{k}_p and the pump-signal angle α are assumed to be constant. In order to achieve broadband phase-matching, both parallel and perpendicular components of the phase mismatch must vanish. We can therefore set Equations (3.12) and (3.13) equal to zero. Further, multiplying (3.12) by $\cos(\alpha + \beta)$ and (3.13) by $\sin(\alpha + \beta)$ and adding the resulting equations gives

$$\frac{\partial k_s}{\partial \lambda_s} \cos(\alpha + \beta) + \frac{\partial k_i}{\partial \lambda_s} = 0 \quad (3.14)$$

Substituting Equations (3.8) and (3.10) in Equation (3.14) and simplifying gives the final result:

$$v_g^i \cos(\alpha + \beta) = v_g^s \quad (3.15)$$

Equation (3.15) has been derived under the assumption that this process of three-wave mixing is perfectly phase-matched. For these conditions, the projection of the group velocity of the idler in the direction of the signal is equal to the group velocity of the signal field. For type-I phase-matching in a blue-pumped OPA – our starting consideration – the idler group velocity is always larger than the signal group velocity.

As a result, with α fixed, it is always possible to find a suitable angle β to satisfy Equation (3.15). The broader implication of the above consideration is that for the conditions of broadband phase-matching in BBO, a suitable geometry can be chosen which also *guarantees group velocity matching*. This is critically important, for it ensures that parametric conversion is efficient and pulse broadening effects are minimized. Riedle has given an approximate condition for the specific situation considered here. The pump-signal angle, which can be adjusted experimentally, is related to the signal-idler angle ($\alpha+\beta$) according to

$$\alpha \approx \frac{\alpha + \beta}{\left(1 + \frac{\lambda_i}{\lambda_s}\right)} \quad (3.16)$$

Rearranging Equation (3.16) to isolate β we find

$$\beta \approx \frac{\lambda_i}{\lambda_s} \alpha \quad (3.17)$$

The error in this approximation is less than 4%. The derivation is based upon the fact that the indices of refraction of the *o*-polarized signal and idler, and the *e*-polarized pump, are all very nearly equal. As is clearly evident from Figure 3-3, between 500 nm and about 750 nm, the value of α is between 3° and 4°.

The effect of group velocity matching in the noncollinear geometry is illustrated schematically in Figure 3-4. The projection of the idler group velocity in the direction of the signal field is equal to the signal group velocity. As the two fields propagate through the nonlinear crystal, they exchange energy, adding photons to both. Because they propagate at the same velocity in the direction of the signal field, there is no temporal broadening due to the parametric conversion process (although there is always some

dispersion introduced by the medium itself). However, because the idler group velocity vector contains a component normal to the signal group velocity, both beams emerge

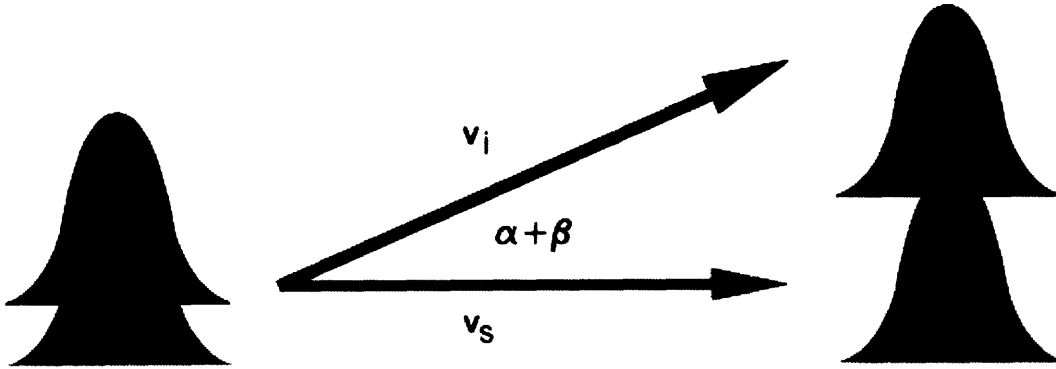


Figure 3-4. Group velocity matching in a noncollinear optical parametric amplifier. The group velocities of signal and idler pulses are different, but the projection of the idler group velocity along the direction of the signal field is equal to the group velocity of the signal. As a result, the signal and idler pulses propagate together through the nonlinear medium. No pulse broadening results from temporal walkoff as in the case of collinear phase-matching. However, since the idler velocity contains a nonzero component normal to the signal propagation direction, the pulses walk off laterally from one another. As this occurs, new photons are added to both fields on the interior edges of each pulse. Both pulses emerge spatially wider, but unchanged temporally except for dispersion due to the medium.

spatially broadened. As the two walk off spatially from one another, photons are preferentially added to the interior wings of each pulse, an effect analogous to the temporal walkoff discussed previously.

With the phase-matching and group velocity matching conditions satisfied for the optical parametric amplification process, it remains only to construct a device which incorporates the noncollinear geometry and to determine its performance. The balance of this chapter is devoted to this goal. Before we continue, however, let us make note once more of the remarkable property of BBO which permits phase-matching over such an enormous band of frequencies. Even further, by extremely fortuitous circumstance, the same conditions which permit such a broad range of frequencies also *simultaneously*

guarantee group velocity matching for all components within that band. It is only on account of BBO's very unique set of properties that we can considerably extend the utility of ultrafast spectroscopy within the visible region of the spectrum in this fashion.

3.3 Experimental Setup for a Noncollinear OPA

The goal of investigating noncollinear optical parametric amplification in our laboratory was to extend the capabilities of the single-shot experiment by providing tunable ultrashort pulses in the visible region of the spectrum for use in a number of investigations. In a single-shot experiment, pulse timings are crucial, as is synchronization of the electronics and computers which control data acquisition, pulse gating, etc. It was imperative that any OPA be synchronized with the rest of the experiment, and of course be capable of operating under single-shot constraints. The first of these conditions implied that the pump source for the OPA be the same as the source for the rest of the experiment: the amplified 10 Hz laser system described in Chapter 2. The second condition remained an unknown since there are no reports in the literature of single-shot operation of noncollinear OPA devices, either in spectroscopic experiments or elsewhere. As we shall see, owing to the absence of energy storage in the nonlinear medium (unlike, say, a Ti:sapphire laser), the OPA functions quite stably even in single-shot mode.

A schematic diagram of the OPA is shown in Figure 3-5. Single pulses are gated out from the amplified 10 Hz Ti:sapphire laser system and typically are of 50 fs duration, centered at 800 nm. After passing through two alignment apertures, the pulses are split by a 90:10 R/T beamsplitter. The reflected photons pass through a half-waveplate and

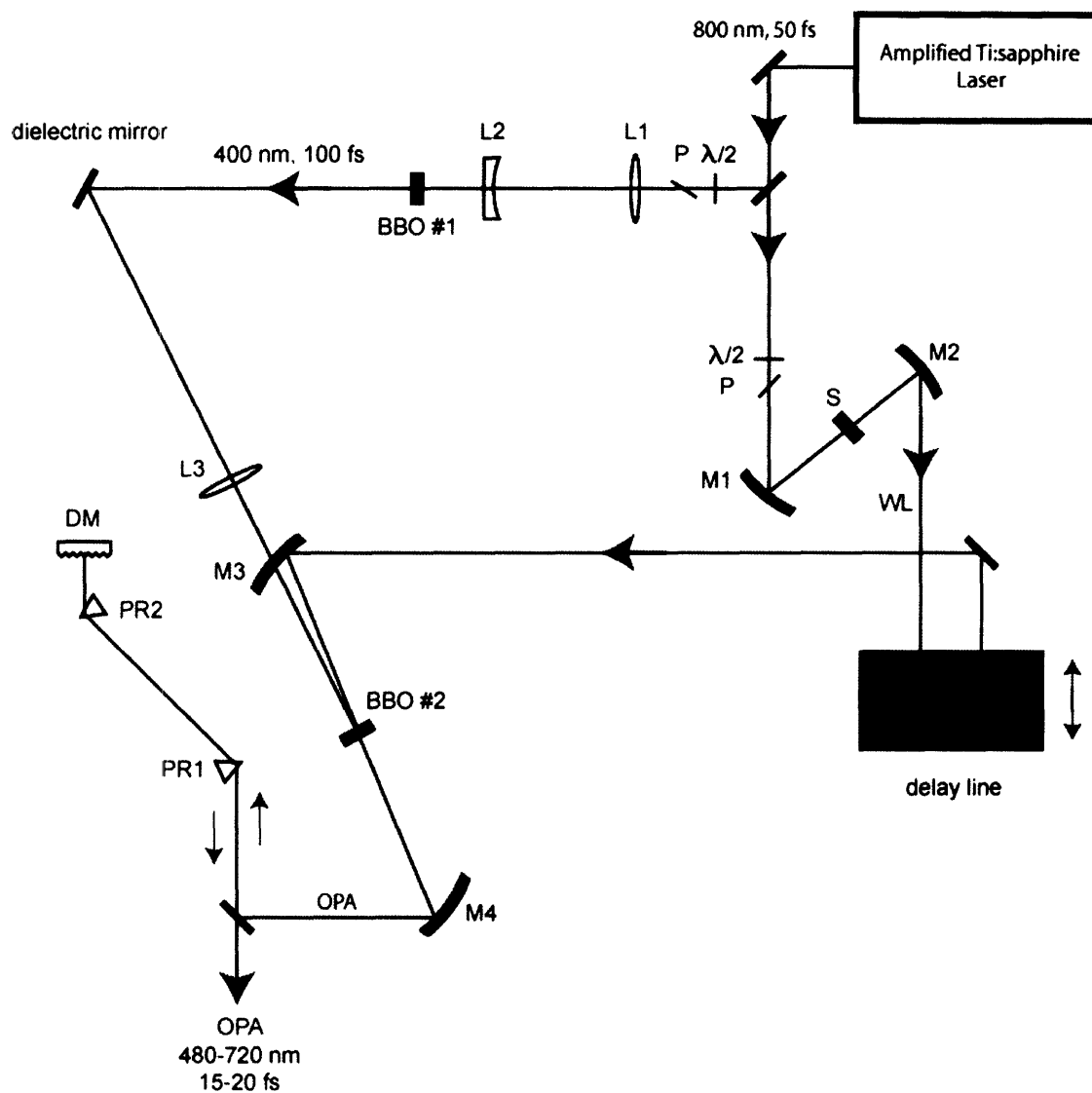


Figure 3-5. Schematic view of the single-shot noncollinear optical parametric amplifier. Single pulses gated out of the Ti:sapphire amplifier are divided and used to generate both pump and seed pulses for the parametric interaction. The center wavelength is controlled by adjusting the seed pulse delay line. Following amplification, OPA pulses are recompressed in a double-pass prism compressor with a deformable mirror retroreflector, providing fine control over the spectral phase.

polarizer combination which permits intensity attenuation. The beam then passes through a two-lens Galilean telescope (lenses L1 and L2) which reduces the diameter from 8 mm to roughly 500 μm . The object of the telescope is to increase the spatial energy density in the beam in order to improve the efficiency of the conversion to its second harmonic without the need to focus directly into the nonlinear crystal.

The beam is converted to the second harmonic with about 40% efficiency via type-I phase-matching in a 1.5 mm BBO crystal (BBO #1). After this process, the pulses are of roughly 100 fs duration and about 70 μJ energy. These are the pump pulses for the OPA. They are used without further compression; in fact, it is advantageous for the pump pulses to have some chirp. If they are too short temporally, nonlinear frequency mixing with wavelength components of the seed cannot occur for the entire bandwidth, since the seed pulses are chirped following generation and remain uncompensated. This limits considerably the attainable bandwidth for the amplified signal pulses. There is a limit, however, to the desired amount of chirp; if the pump pulses are stretched sufficiently such that the peak intensity is dramatically lowered, the efficiency of the parametric interaction (which scales linearly with the pump intensity) is much reduced. Like many other situations, then, adjustment of the pump chirp is a tradeoff between competing effects.

The pump pulses are focused by lens L3 to a point just in front of the surface of a 1 mm BBO crystal (BBO #2) cut at 31.5° to the z -axis. Experimentally, it is found that focusing into the crystal itself leads to the formation of multiple filaments and the instability inherent in this process. This is easy to avoid by locating the focus just in front of the crystal.

Under these conditions, the pump pulses generate a rainbow-like, many-colored ring pattern which emerges from the rear of the crystal and can easily be observed with the naked eye. This phenomenon is referred to as *parametric superfluorescence*. Figure 3-6 shows a photograph of single-shot superfluorescence projected onto a white screen

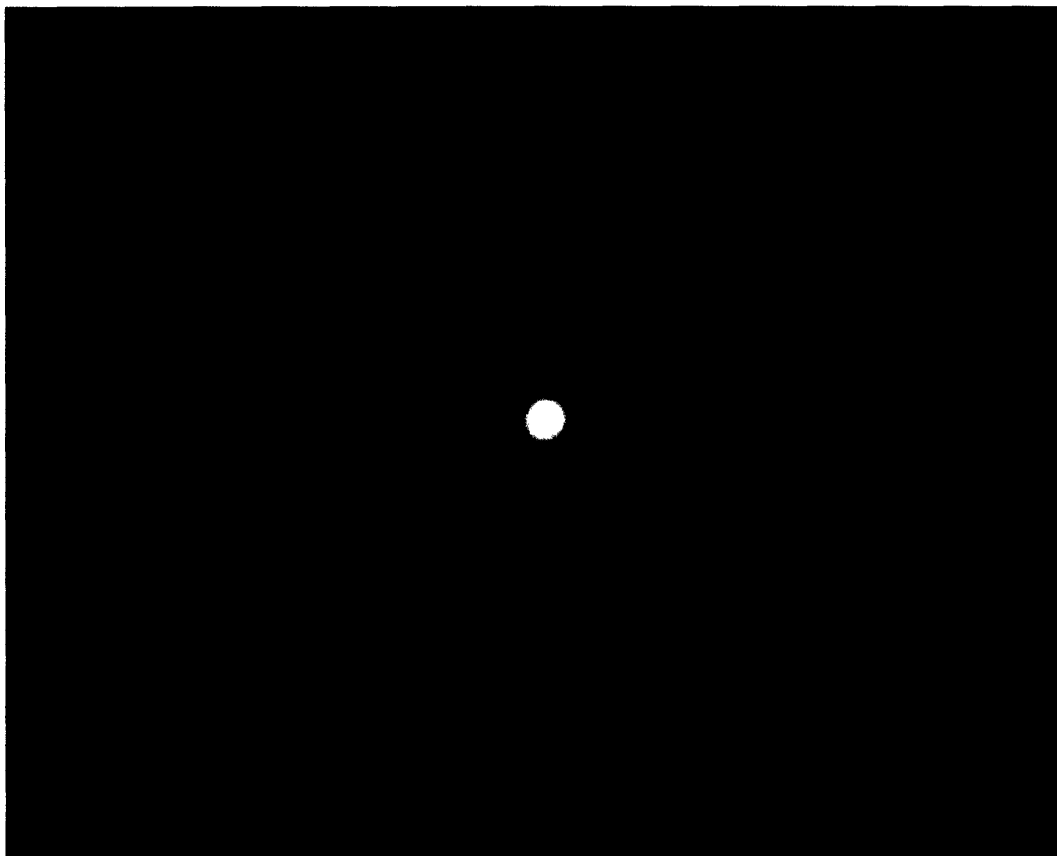


Figure 3-6. Parametric superfluorescence from a 1 mm BBO crystal pumped with individual 400 nm, 70 μ J pulses from a Ti:sapphire laser. The bright spot in the center is pump light exiting through the back surface of the crystal. The superfluorescence is emitted along a right-angled cone at an angle of 3.7° and corresponds to signal wavelengths in the range 500-750 nm. Another ring of larger circumference is also present but invisible in the figure; it corresponds to emission at idler wavelengths which all fall beyond the detection range of the camera. The above pattern is generated in a single-shot OPA.

located on the opposite side of the crystal from the pump beam. The ring-like pattern is clearly visible. The bright region in the center is pump light that emerges from the rear of the crystal.

The observation of superfluorescence actually makes the OPA very easy to align. The broad bandwidth of the superfluorescence results from parametric conversion of pump photons to signal and idler photons. The frequencies in the fluorescence ring all

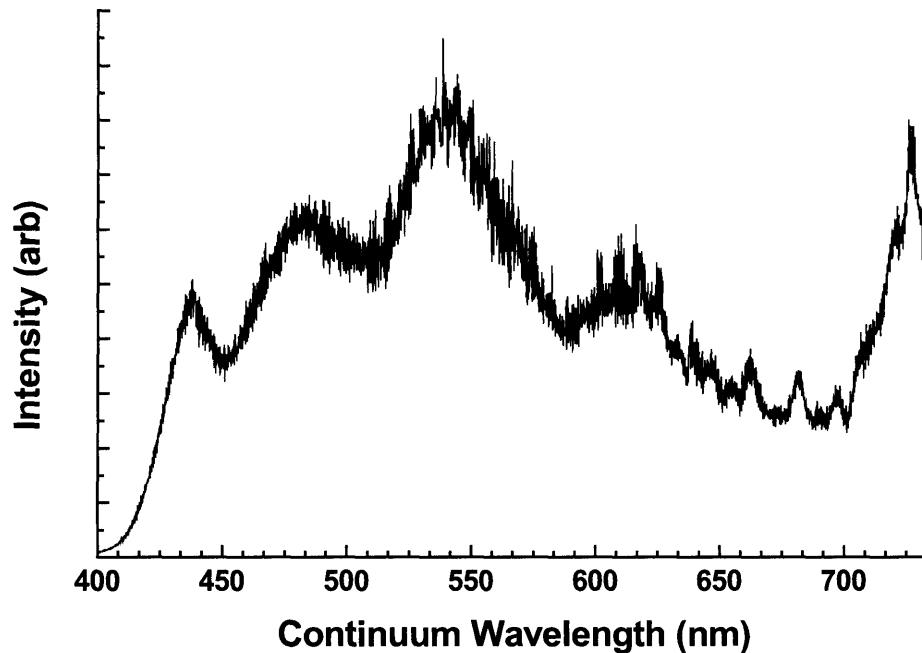


Figure 3-7. Continuum generation in sapphire. Focusing weak $0.5 \mu\text{J}$, 800 nm pulses in a 1.2 mm thick sapphire plate generates a broadband continuum. Self-focusing in the crystal leads to nonlinear self-phase modulation, which in turn modulates the optical phase of the driving field, generating new frequency components. The highly-structured shape of the spectrum is characteristic of this process.

fall within the visible region of the spectrum, and correspond to signal photons generated by the pump beam. There is a second, larger ring that is visible with an infrared camera;

this corresponds to the idler beam. The seed for the parametric conversion process in each case may be thought of as quantum noise in the crystal itself.

Both signal and idler photons are emitted in a cone geometry which appears as a ring in transverse cross-section. In fact, pump photons are scattered in many directions within the BBO crystal; however, it is only that particular direction which corresponds to the superfluorescence cone where the photons can interact coherently and therefore build up a field large enough to observe. The angle of the visible cone is 3.7° , which corresponds to the broadband phase-matching condition of Figure 3-3, as expected. Thus, one obtains visual guidance for the alignment of the device. It is clear that for a given pump-generated superfluorescence pattern, the amplifier must be arranged such that the seed pulses pass through the pump spot at the front surface of the crystal, and travel along the direction of the superfluorescence cone. This will guarantee that the parametric conversion process is properly phase-matched over a broad band of frequencies.

The remaining 10% of the original Ti:sapphire pump photons pass through a separate waveplate-polarizer combination to provide adjustable attenuation. This pulse is used to generate the broadband seed employed in the parametric conversion process. It is critically important that the seed chirp be minimized and so subsequent optics in the seed beam path are all reflective, where possible. The weak 800 nm pulses are focused by a curved spherical mirror of 10 cm f.l. into a 1.2 mm sapphire window in order to generate a broadband continuum of frequencies. The input pulse energy threshold for single-filament continuum generation in sapphire is about $0.5 \mu\text{J}$, and the beam emerges from the back of the crystal in a nearly white, circular profile.

The importance of maintaining a single-filament continuum cannot be overstated. Seeding the BBO crystal with white light from multiple filaments greatly reduces the efficiency of the overall parametric conversion, since the light from each filament will interact coherently with the pump pulse, but there is no coherence relationship between multiple filaments and so there is no larger buildup of photon density in the emergent field. Multiple-filament sources tend to generate unusual interference patterns in the far field which can often prove to be difficult to overcome in imaging experiments. The absence of a well-defined coherence relationship among multiple filaments is due to the same self-phase modulation which is responsible for continuum generation.

The white light emerges along a cone with an angle that is generally a little larger than that of the original 800 nm light. The beam is collimated with a second curved mirror of 10 cm f.l. and sent through an adjustable delay line. Ultimately, the beam is focused through the pump spot on the second BBO crystal, along the direction defined by the superfluorescence cone. A single-shot spectrum of the sapphire-generated continuum is shown in Figure 3-7. The spectrum has been artificially terminated beyond 750 nm since it is strongly peaked near 800 nm, the wavelength of the original pulse. The spectrum is highly structured – typical of a continuum generated in this fashion – although the structure rides atop a plateau region from 440-625 nm. In sapphire, wavelengths in this region have previously been attributed to the multiphoton excitation of electrons to the conduction band and the subsequent spectral superbroadening caused by such free electrons, but analytic theory of the process is not well developed.

Focusing of the white light pulses through the mixing crystal is achieved by a spherical mirror of focal length 25 cm (M3). When temporal and spatial overlap with the

pump pulses is good and the seed wavevector follows the phase-matching direction, efficient single-pass amplification of the continuum – up to 13% – is achievable. Wavelength tuning occurs by adjusting the relative delay between pump and seed, and thereby varying the wavelength within the continuum which overlaps temporally with the maximum in the pump pulse (and hence, is most efficiently amplified). Wavelength adjustment is reproducible enough to afford the opportunity to automate the process via computer. Once calibrated, the system can be instructed to “dial” any wavelength by setting the appropriate delay.

Following the parametric interaction within the crystal, the OPA pulses are positively chirped due to material dispersion and need to be recompressed. Negative group velocity dispersion is introduced via a double pass prism compressor. The SF10 prism spacing is dependent upon the center wavelength of the pulses and is also automatically adjustable. The prisms themselves are different sizes to account for the broad spectral content of the amplified pulses. Spherical mirror M4 collimates the amplified output to a beam diameter of about 1 mm. The prism PR1 has face lengths of about 1 cm since the spot size is relatively small at this location. However, prism PR2, which lies in the spectral plane of the compressor, requires 2.5 cm face lengths to accommodate the spatial extent of the pulse spectrum.

The retroreflector in the prism compressor is a 19-element deformable mirror (OKO Technologies) which is controlled by a genetic algorithm. Although not strictly necessary for pulse compression, the deformable mirror (DM) permits fine-grained control over spectral chirp in the spectral domain. More importantly, the mirror permits adaptive pulse shaping of the OPA pulses for specific spectroscopic applications. In

similar fashion, the genetic algorithm-based logic controller is not strictly necessary for pulse compression alone. In fact, the individual mirror settings can be adjusted manually to achieve optimum compression, and since the dispersion of the instrument remains constant over time, the mirror settings rarely need to be changed after the initial calibration. Instead, the algorithm finds its greatest use in generating waveforms of arbitrary shape, where manual adjustment would simply be too tedious.

Starting from a random distribution of mirror settings, the genetic algorithm requires approximately 15 minutes to achieve optimum compression of the OPA pulses. The feedback signal is pulse intensity measured by a two-photon Si photodiode, which represents the intensity maximum in an autocorrelation measurement. Clearly, as the amplified pulse duration becomes shorter, the maximum in the autocorrelation function is higher, and so it is easy to specify the quality criterion for the genetic algorithm. If the algorithm is seeded with the previously determined optimum as one of its candidate solutions, convergence typically requires 1-2 minutes, as the new “best solution” is expected to represent only a small deviation.

In this way, efficient compression of OPA pulses can be achieved to high order, making the generation of short pulses relatively straightforward. It should be noted, however, that the goal of the OPA is to provide a single-shot source of wavelength-tunable pulses, not to achieve the shortest possible durations. Indeed, when performing experiments such as transient absorption, the important criterion is the center wavelength of the pulse (i.e. is it electronically resonant?) and not the bandwidth. In such situations, extra bandwidth can even be disadvantageous if the specific experimental signatures of interest are not well separated spectrally. Since extremely short pulses have such broad

frequency content, absorption literally occurs at all wavelengths simultaneously. This often creates more problems than it solves.

As such, we have elected to design our system around the ability to operate in single-shot fashion, and the ability to easily tune the center wavelength of the output pulses. In terms of pulse duration restrictions, providing the pulses are compressible to roughly 30 fs, they are suitable for our purposes. In order to achieve sub-10 fs pulses, additional elements would need to be introduced into the system. Precompensation of the seed continuum using chirped mirrors, and a suitable pulse-front matching scheme in order to maximize interaction length between seed and pump would need to be employed. Also, a double-pass configuration could be used, splitting the gain profile in two halves and amplifying each separately. However, these techniques introduce substantial additional complexity into the system and as such, we have chosen to sacrifice some temporal resolution for ease of daily use.

3.4 Results

Figure 3-8 illustrates spectral measurements for six different pulse wavelengths from the single-shot noncollinear optical parametric amplifier. At the two edges of the OPA tuning range (480 nm and 710 nm) the pulse bandwidth is reduced. Throughout the visible region from 500-700 nm however, very broad bandwidth pulses are routinely generated.

The spectra are all roughly Gaussian in shape, suggesting a smooth temporal profile. The noise level is slightly higher than is typical for spectral measurements on account of the fact that these are single-shot spectra, where no averaging is employed.

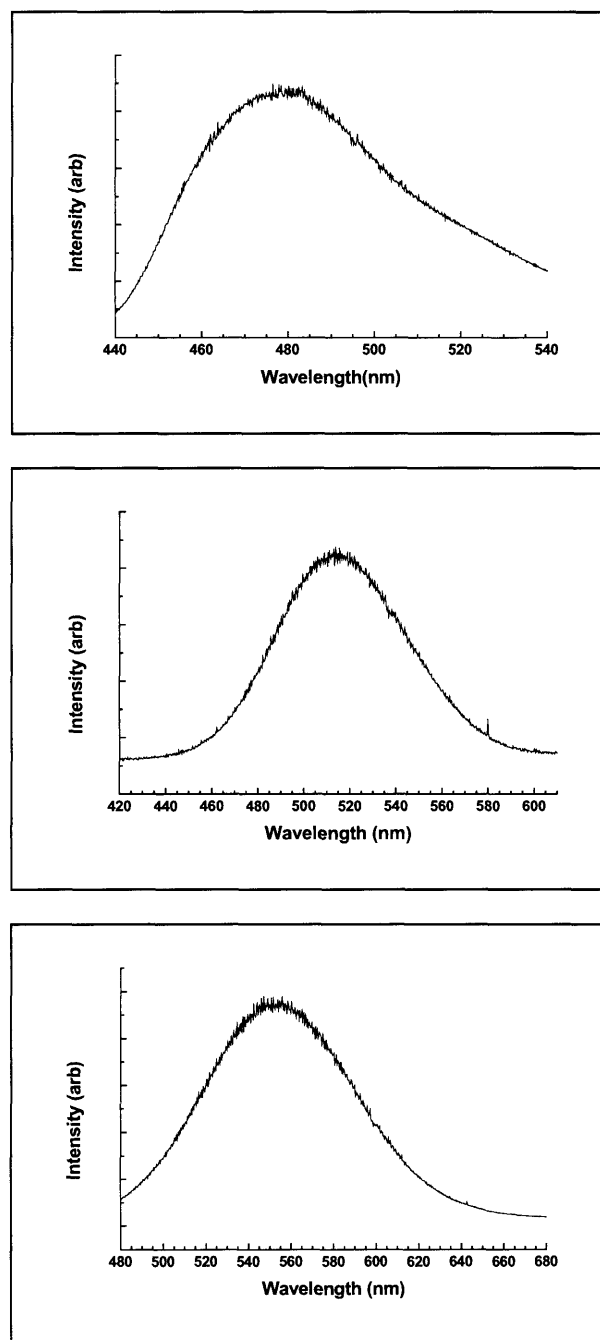


Figure 3-8. Spectra of pulses generated in a single-shot OPA. Wavelengths are tuned to 480 nm, 515 nm and 555 nm respectively.

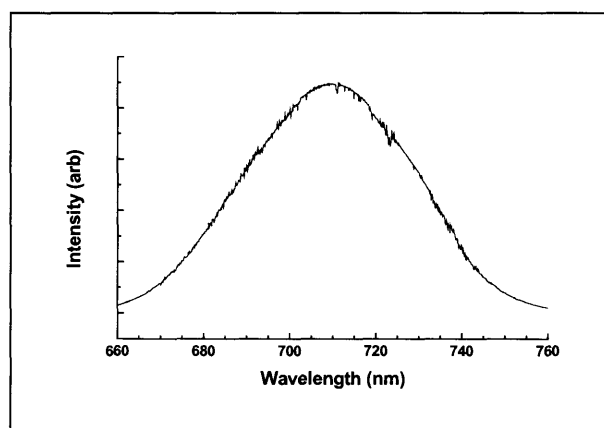
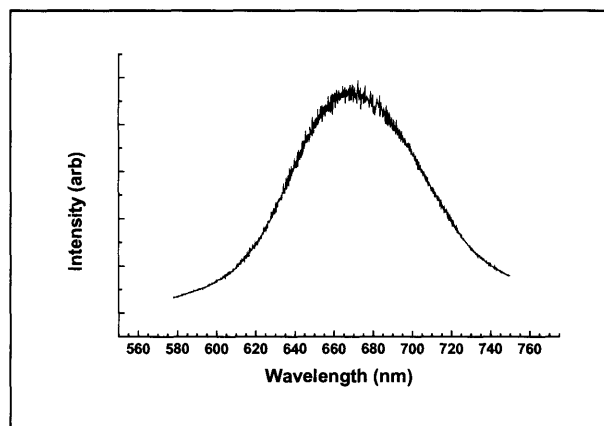
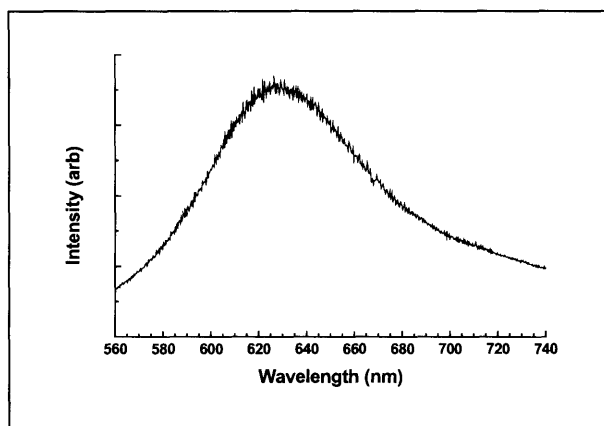


Figure 3-8 (cont'd). Spectra of pulses generated in a single-shot OPA. Wavelengths are tuned to 630 nm, 670 nm and 710 nm respectively.

The pre-compression bandwidths (Gaussian) are compiled in Table 3-1. Pulses at each wavelength are sufficiently broad spectrally to achieve sub-25 fs compression.

Table 3-1. Spectral bandwidths for pulses generated in the single-shot OPA.

Center Wavelength (nm)	Spectral Bandwidth (nm)
480	46
515	56
555	69
630	61
670	67
710	42

For each of the six wavelengths in Figure 3-8, the genetic algorithm was permitted to optimize the NOPA compressor to achieve the minimum-duration output. The deformable mirror has 19 actuators, each of which consists of a metal electrode bonded to the reverse side of the membrane mirror and a mating electrode on a solid support. The electrodes attached to the mirror itself are maintained at a large positive potential. The mating electrodes are also maintained at a positive potential. The resulting electrostatic repulsion between pairs of electrodes attached to the membrane and the support produces deformation in the membrane. Because the membrane is continuous, even though there are only 19 actuators, there are no pixellation effects or dead space, unlike the situation with a programmable liquid crystal modulator [37,38].

The limitation of only 19 actuators restricts the complexity of the deformed mirror surface. However, for the application described here, exotic mirror profiles are not required – in fact, it is much more important that the adjustable element be continuous.

Each support electrode can be assigned one of 256 unique voltage values to control the magnitude of deformation at a particular lateral location on the mirror surface. Thus, there are 256^{19} possible mirror configurations. The genetic algorithm efficiently explores a large search space such as this. We define the root-mean-square optimization error for one run as

$$E_{rms} = \sqrt{\sum_{i=1}^{19} (V_{i,eq} - V_i)^2} \quad (3.18)$$

where $V_{i,eq}$ is the optimized voltage setting for actuator i determined from an initial optimization run. For each of the wavelengths 480 nm, 515 nm, 555 nm, 630 nm, 670 nm and 710 nm, five optimizations were undertaken following the initial determination of ideal settings. In each wavelength instance, the maximum RMS error for any one run was less than 2%; the algorithm converged reproducibly under a fairly wide range of conditions. In practice, the ideal settings for a given wavelength were stored and immediately recalled when NOPA output at that frequency was desired.

This greatly simplifies operation of the device. When a new wavelength is desired, the continuum seed delay line is automatically adjusted to produce the correct temporal overlap in the parametric mixing process. The BBO crystal is not adjusted (although to achieve maximum single-pass gain, it would have to be). Then, the compressor prism spacing and deformable mirror profile are adjusted automatically to compensate the pulse's temporal dispersion at the new wavelength. Since the wavelength-dependent dispersion of the instrument remains very nearly constant from

one day to the next, these settings are quite reproducible and the need for recalibration is infrequent.

Single-shot operation of the NOPA yields tunable pulses from 470-720 nm at pulse energies up to 10 μ J. The single-pass efficiency in our device is typically about 9-10% of the pump pulse energy. In order to measure pulse durations, we employ interferometric autocorrelation in a Michaelson interferometer arrangement. The second harmonic crystal is a 20 μ m thick BBO which is angle-tuned for the appropriate measurement wavelength. The crystal is thin enough that its dispersive contribution to pulse broadening is not too severe. The only other element in the autocorrelator which is transmissive, and which therefore has a dispersive effect on pulse duration, is the beamsplitter. In order to minimize its effect, the beamsplitter has been custom-manufactured and consists of a 50 μ m thick CaF_2 window upon which a thin coating of chromium has been deposited by electron-beam sputtering. The thickness of the coating is adjusted to ensure a 50:50 R/T splitting. No other coating is applied to the beamsplitter and as such, it must be stored under vacuum when not in use to prevent oxidation. The beamsplitter undoubtedly has some effect upon the measured pulse duration (especially post-compression), but its effects cannot easily be circumvented.

Figure 3-9 illustrates the results of autocorrelation measurements on uncompressed pulses at the six wavelengths of Figure 3-8. Pulse durations are estimated by fitting the autocorrelation trace to a Gaussian envelope shape. Using this approach, we discover that wavelengths toward the blue end of the NOPA tuning range emerge with the largest chirp, a finding which is not unexpected. By contrast, pulses near the red edge of the tuning range – especially near 700 nm – are not badly chirped at all, and could

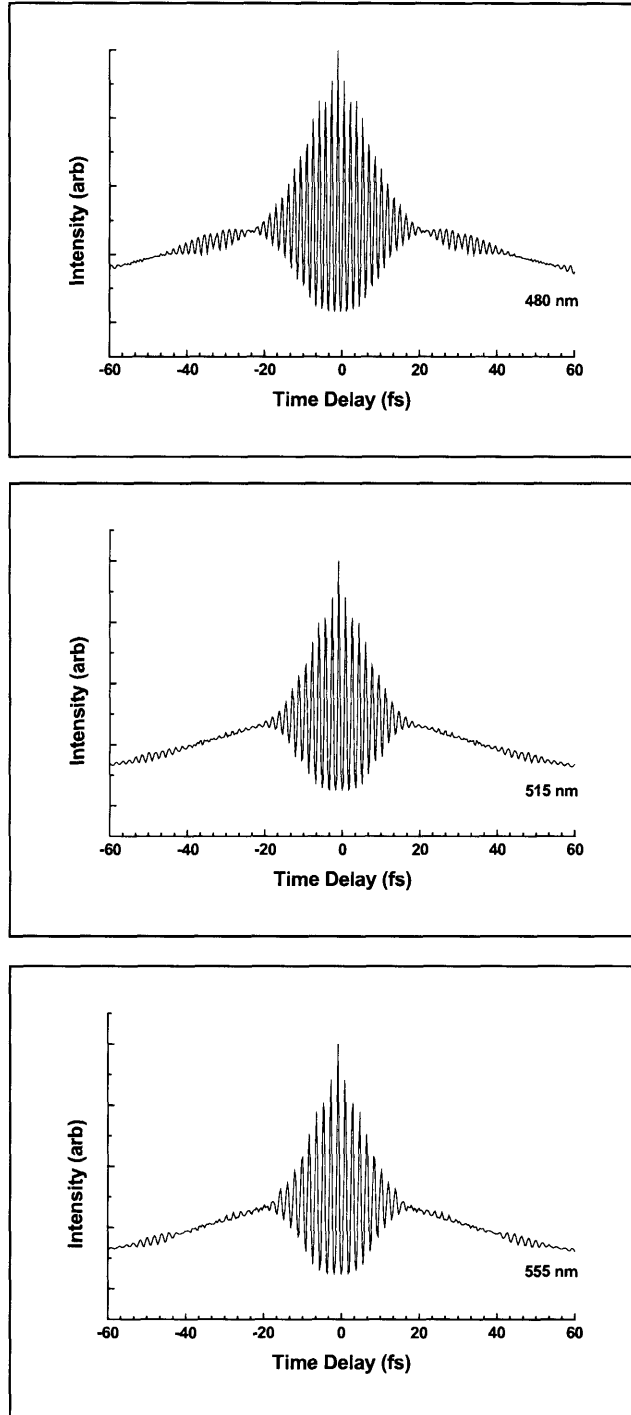


Figure 3-9. Interferometric autocorrelation traces of NOPA pulses at wavelengths 480 nm, 515 nm and 555 nm.

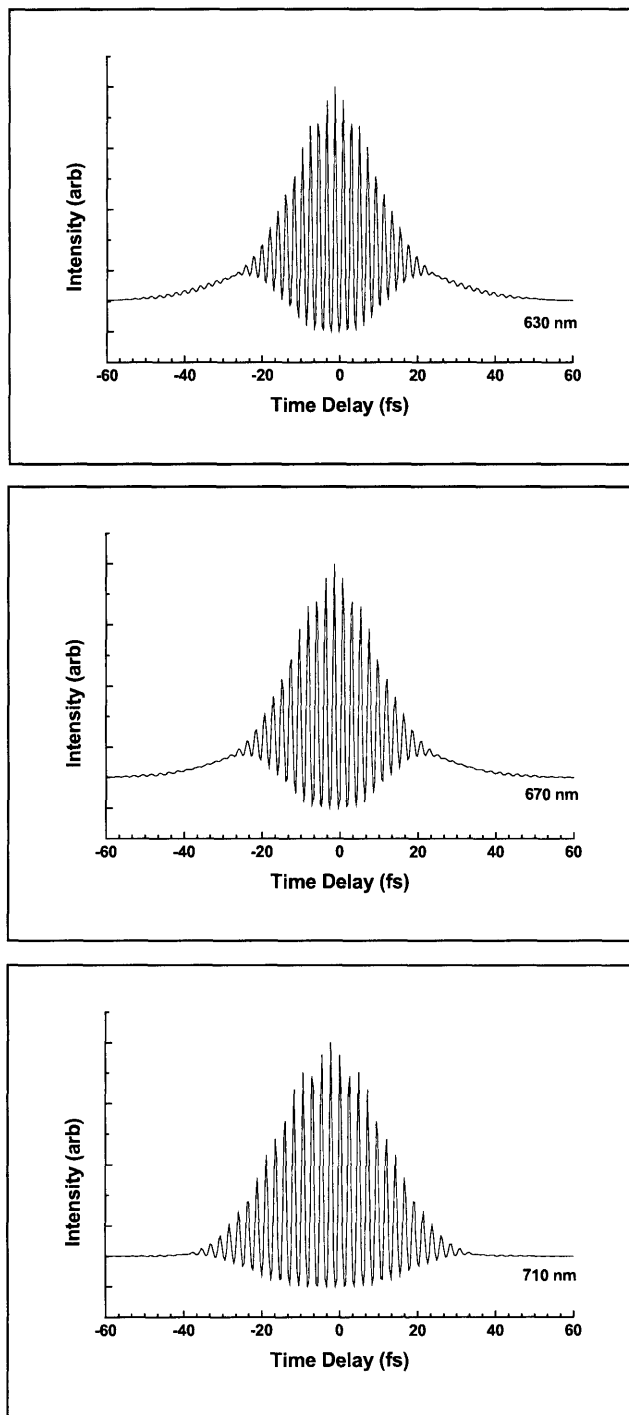


Figure 3-9 (cont'd). Interferometric autocorrelation traces of NOPA pulses at wavelengths 630 nm, 670 nm and 710 nm.

easily be employed directly in experiments. In fact, over the entire tuning range, the longest-duration pulses which emerge are about 60 fs, which is more than suitable for use in the single-shot experiment and in most cases where the complex phase structure does not play an important role. The results of the analysis are displayed in Table 3-2 for the purposes of comparison.

From the measured pulse durations, it is clear that improvement can be realized by optimizing the NOPA compressor. In Figure 3-10, the results of this optimization are

Table 3-2. Pre-compression duration and time-bandwidth product for NOPA pulses.

Wavelength (nm)	Bandwidth (nm)	Duration (fs)	T-B Product
480	46	63.3	3.78
515	56	52.4	3.31
555	69	50.3	3.37
630	61	32.8	1.51
670	67	30.6	1.37
710	42	23.5	0.62

presented for pulses at the six frequencies of Figure 3-9 in the form of the measured interferometric autocorrelation traces. In each case, except for 710 nm, the compression is significant. Once again, we employ a Gaussian fitting routine to try and estimate the

pulse duration from the trace data. We have been able to compress the single-shot output of the NOPA to less than 25 fs at all wavelengths within the tuning range.

The chief source of error in the pulse duration measurements, especially following compression, is the dispersion introduced by the BBO crystal and the beamsplitter in the autocorrelator. In fact, the true pulse durations may be even shorter than measured. In any event, pulses of duration 25 fs or less are perfectly suitable for use in the single-shot experiment. The original design of the NOPA was optimized with regard to repeatability, ease of day-to-day use, a wide tuning range, and high quality beam profiles. All of these attributes have been realized. For certain applications, the bandwidth of these pulses may actually need to be reduced with notch filters in order to isolate features in congested molecular spectra. A summary of the properties of the compressed NOPA pulses is given in Table 3-3.

In order to generate even shorter pulses, greater effort must be expended with regard to dispersion management. The shortest NOPA pulse durations recorded to-date have been 4.7 fs. In order to achieve this remarkable result, Kobayashi and coworkers employed a number of additional sources of negative GVD [16-19,35] in order to minimize seed chirp. Following continuum generation in sapphire, the white light seed was compressed by custom-designed ultrabroadband chirped mirrors. Performing this precompression prior to parametric generation ensures that the full continuum bandwidth is amplified under the envelope of the pump pulse. In addition, Kobayashi *et al.* employed a prism and telescope system to introduce pulse front tilt. Since the pump and signal beams do not propagate collinearly, their wave fronts intersect at the same angle α formed by their wavevectors. This angular dispersion imposes a small spatial restriction

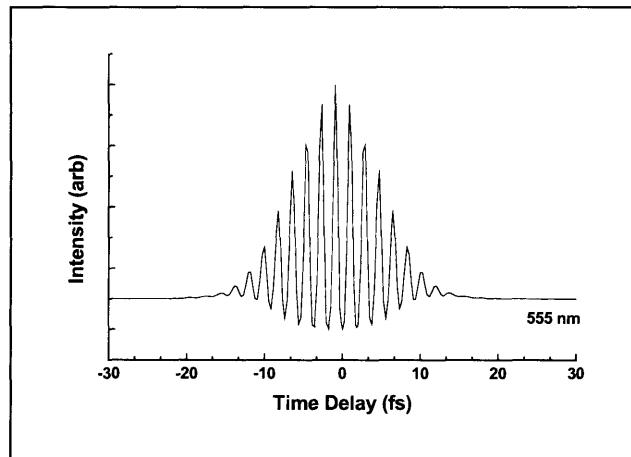
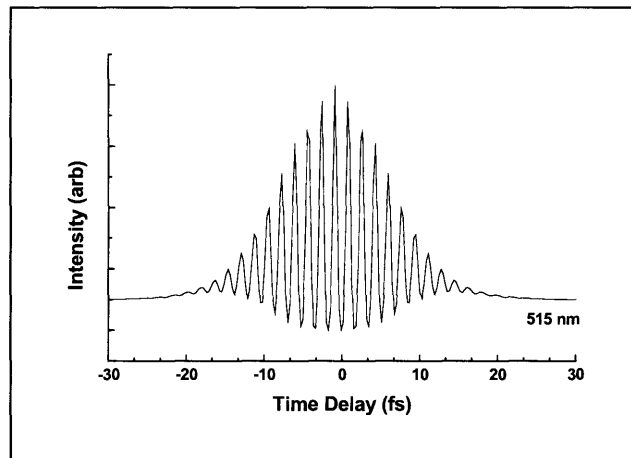
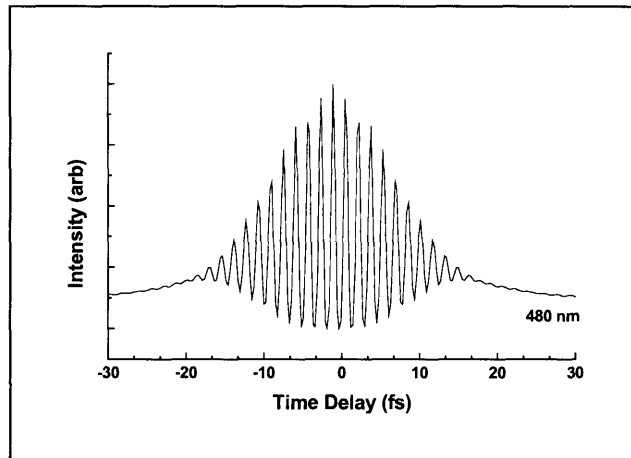


Figure 3-10. Interferometric autocorrelation of compressed NOPA pulses at wavelengths of 480 nm, 515 nm and 555 nm.

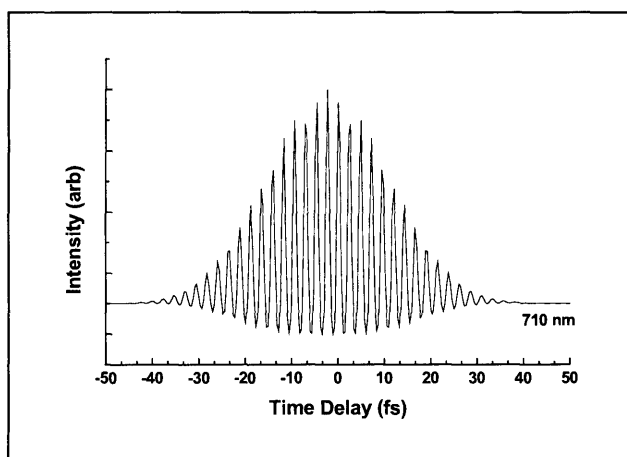
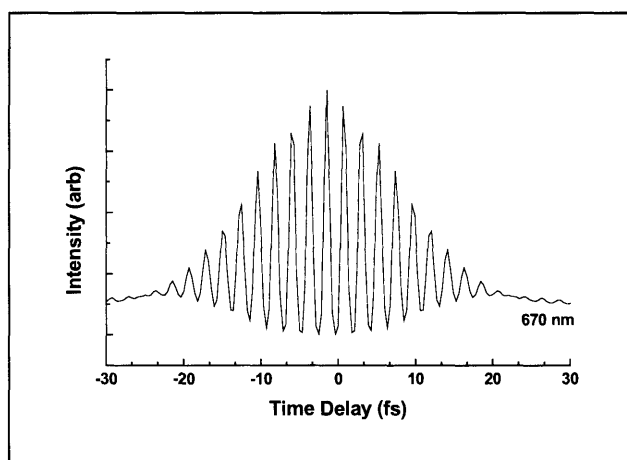
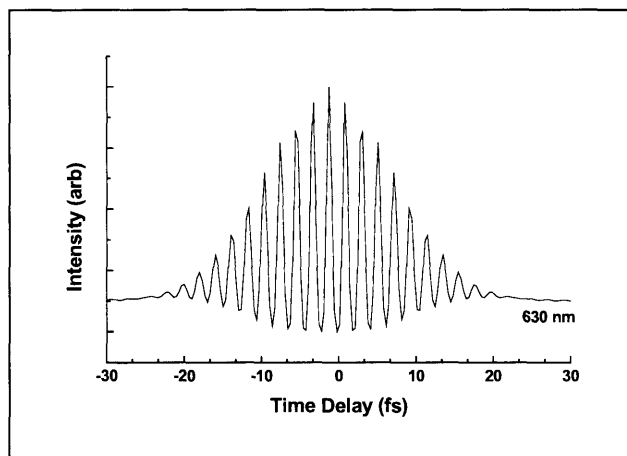


Figure 3-10 (cont'd). Interferometric autocorrelation of compressed NOPA pulses at wavelengths of 630 nm, 670 nm and 710 nm.

Table 3-3. Temporal duration and time-bandwidth product for compressed NOPA pulses.

Wavelength (nm)	Bandwidth (nm)	Duration (fs)	T-B Product
480	46	19.5	1.16
515	56	14.8	0.93
555	69	10.6	0.71
630	61	16.4	0.75
670	67	19.8	0.89
710	42	22.8	0.57

on the size of the interaction volume. By tilting either the pump or signal wavefronts, this restriction is removed, improving both the phase-matched bandwidth and efficiency of the parametric process.

3.5 Dual Beam Phase-Locked Single-Shot NOPA

Recent work by Bellini and Hansch [36] on interferometry with CaF_2 -generated continuum pulses suggested an extension of the current NOPA design. Bellini and Hansch were able to show that two continuum pulses independently generated by photons from the same ultrafast Ti:sapphire laser remained phase-coherent and produced smooth interference fringes when combined in a Michaelson setup.

Examination of the phase-matching conditions for parametric amplification in BBO of the type described herein reveals that the only condition which must be satisfied

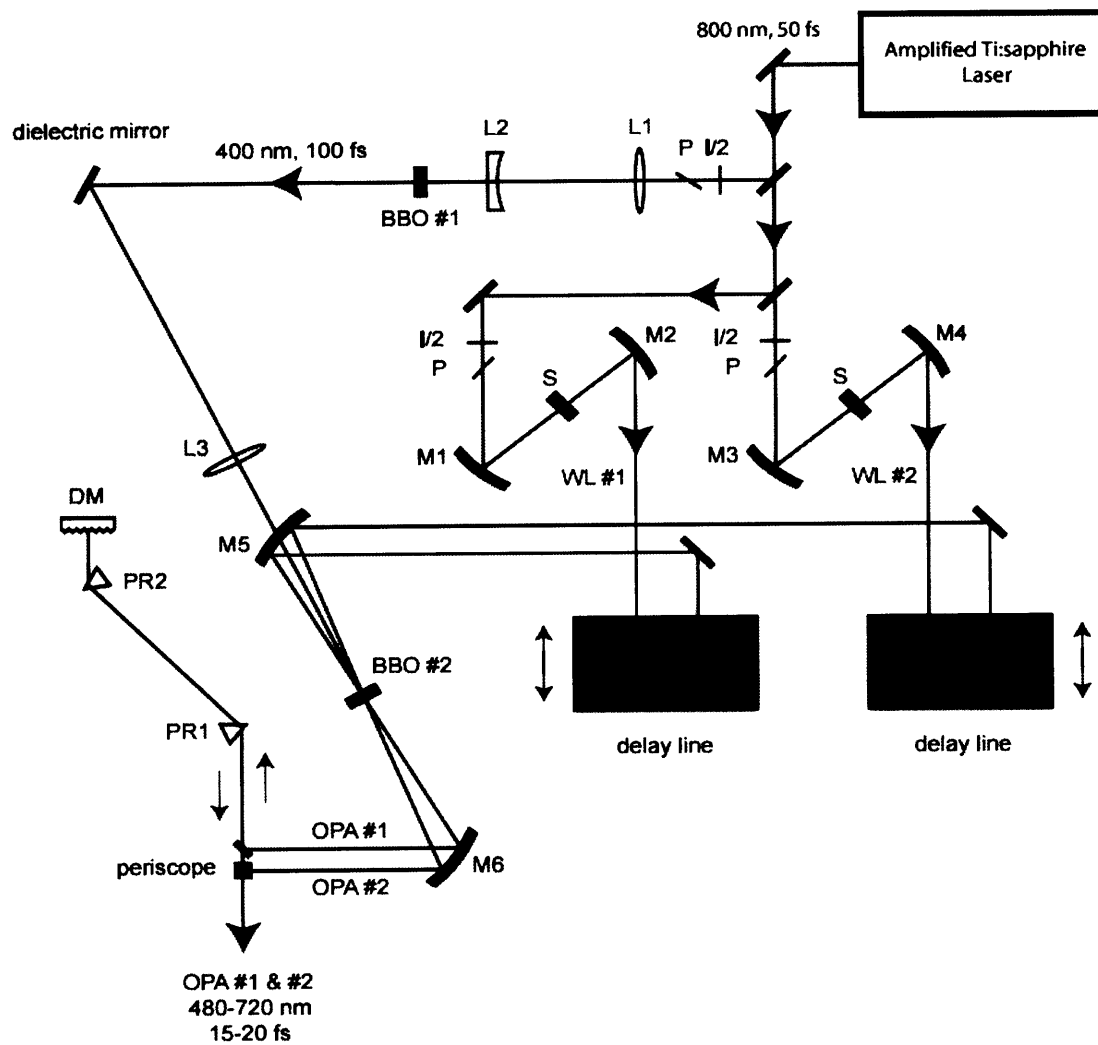


Figure 3-11. Schematic illustration of the dual beam phase-locked single-shot NOPA. Two continuum generation stages are used to seed the OPA on both sides of the pump beam, producing two independently tunable ultrafast outputs. Since both beams traverse the same optical elements, the accumulated dispersion in each case is the same.

in all cases is the pump-signal angle $\alpha = 3.7^\circ$. If the pump beam wavevector is normal to the crystal surface, then there exists a set of signal wavevectors which maintain the appropriate pump-signal angle; these collectively form a cone. Seeding the OPA anywhere along this cone results in parametric amplification. This is verified visually by the superfluorescence emission which occurs along exactly this solution cone.

With the knowledge that two independent but phase-coherent continuum seed pulses could be generated from the same Ti:sapphire laser pulse, the possibility of adding a second tunable signal beam to the NOPA was raised. Another continuum generation step was added to the existing NOPA layout by dividing the photons from the beam transmitted through the first beamsplitter. A schematic diagram of the dual beam layout is shown in Figure 3-11. The white light generation stages (WL #1 and WL #2) are identical in construction. Each has an independent delay line. The pulses are ultimately focused into the parametric mixing crystal by the same curved mirror M5. However, one seed beam enters the BBO crystal at an angle of 3.7° to the left of the pump beam in the x - z plane, while the other enters at 3.7° to the right in the x - z plane. The signal beams both appear on the circumference of the superfluorescence ring, but on opposite sides.

Adjustment of either delay line shifts the center wavelength of the corresponding amplified beam, without changing the other beam. Since the single-pass gain in the parametric process is only about 15% at maximum, there is more than enough pump energy to amplify both beams. The combined process is slightly parasitic – when a second beam is introduced, the intensity of the first decreases slightly – but the effect is not large, and straightforward generation of two independently tunable outputs with pulse

energies approaching 10 μJ each is facile. The pulses are both collimated by mirror M6 and sent into the NOPA compressor. Since the pulses pass through the same dispersive elements, the accumulated material dispersion in each case is similar. Thus, it is possible to use a common set of compensation optics to compress each pulse. This has the added benefit that even in the presence of vibrations of the table and optics, the relative phases of the two pulses remain the same. One of the OPA beams is displaced vertically relative to the other in a periscope, and then the two pass in tandem through both prisms, reflect from the deformable mirror, and travel the same path in reverse through the prisms and out of the system. At the exit port emerge the independent beams. If both beams are set for the same center wavelength, then both can be compressed to near the transform limit by a unique setting of the prism spacing and deformable mirror. If the beams are of different wavelengths, this is of course not possible. In such a situation, either one beam can be compressed and the other left unmodified by bypassing the compressor, or both beams can be partially compressed or left uncompensated. The second OPA beam possesses the same temporal attributes as the first, and compresses to near transform-limited duration, just as the original beam does. Uncompressed pulses from either OPA output range from 25-50 fs in duration, which is sufficient for our experiments. Thus, utilizing two different wavelengths simultaneously does not restrict the utility of the NOPA even though one or both outputs may be uncompressed. An alternative would be to employ two compressors in tandem, at the risk of introducing phase error between the pulses. Figure 3-12 shows the spatial location of the amplified signal beam(s) in both the

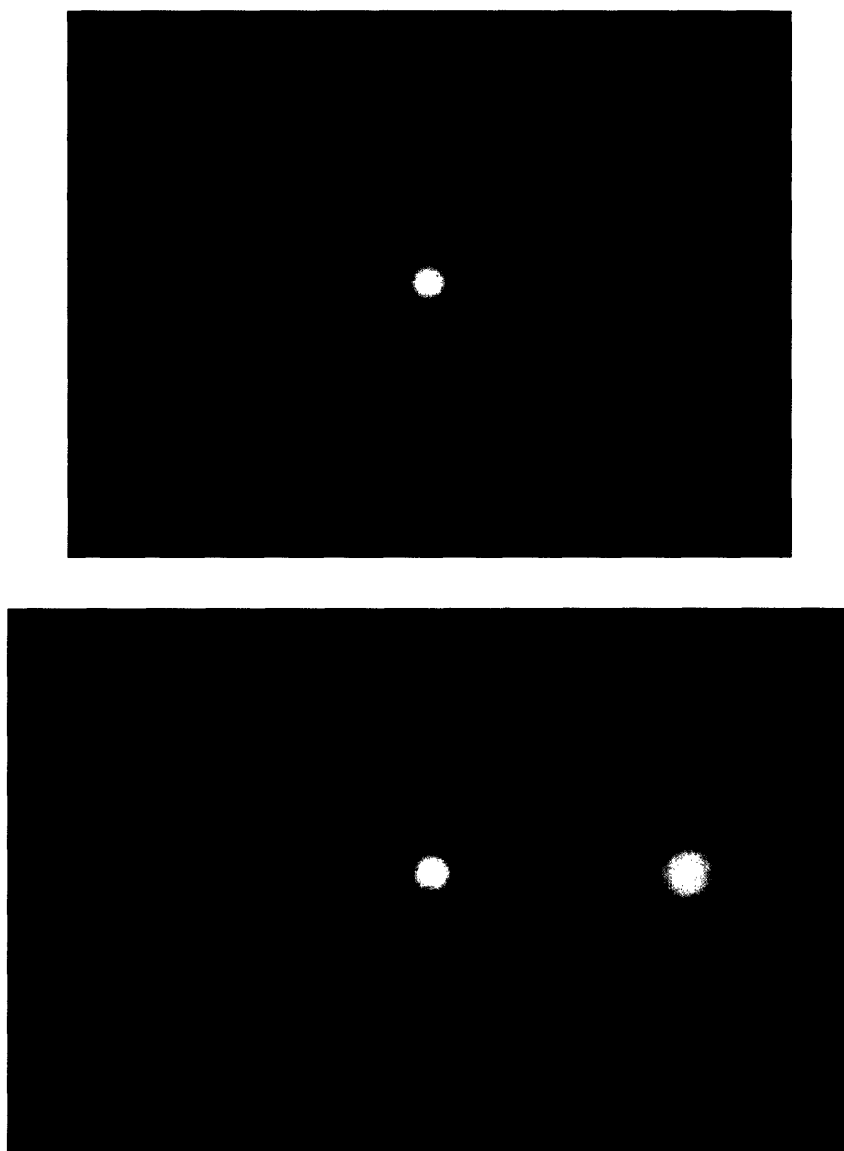


Figure 3-12. (Top) NOPA operating with a single seed input. The bright center spot is the pump beam, and the beam on the left is the amplified signal beam. Note that it is located on the circumference of the superfluorescence ring. (Bottom) NOPA operating with two seed pulses, located on either side of the pump beam. The right-hand pulse is tuned to 550 nm and the pulse on the left has 720 nm center wavelength.

single-seed and dual-seed versions of the NOPA. In the top half of the figure, the single amplified signal beam is located on the circumference of the faint superfluorescence ring. In the bottom half of the figure, both amplified NOPA outputs are visible (the left-hand beam is tuned to 720 nm – the edge of the NOPA wavelength range – and so is weaker than the 550 nm beam on the right).

In an effort to measure phase coherence, an interferometer was constructed with one of the NOPA output beams in each arm. One of the arms had an adjustable delay line to control temporal overlap of the two pulses. A CCD camera was placed at the location of spatial overlap between the beams to record interference patterns. For these measurements, the center wavelengths of the two pulses were equalized in order to employ the compressor, and also to ensure that fringes would be readily visible. The results for several different wavelengths are shown in Figure 3-13. Interference fringes are clearly visible at all wavelengths, indicating phase coherence between the dual NOPA outputs over a very broad tuning range. The fringe spacing, which changes as a function of wavelength, is due principally to the alignment of the interferometer. As the wavelength of the NOPA beams changes, the spatial location of the beams changes in concert due to the inherent spatial chirp of the beams which results from signal-idler walkoff within the BBO crystal. The shifting spatial location of the beams affects their paths through the interferometer and is manifest as a variable fringe spacing.

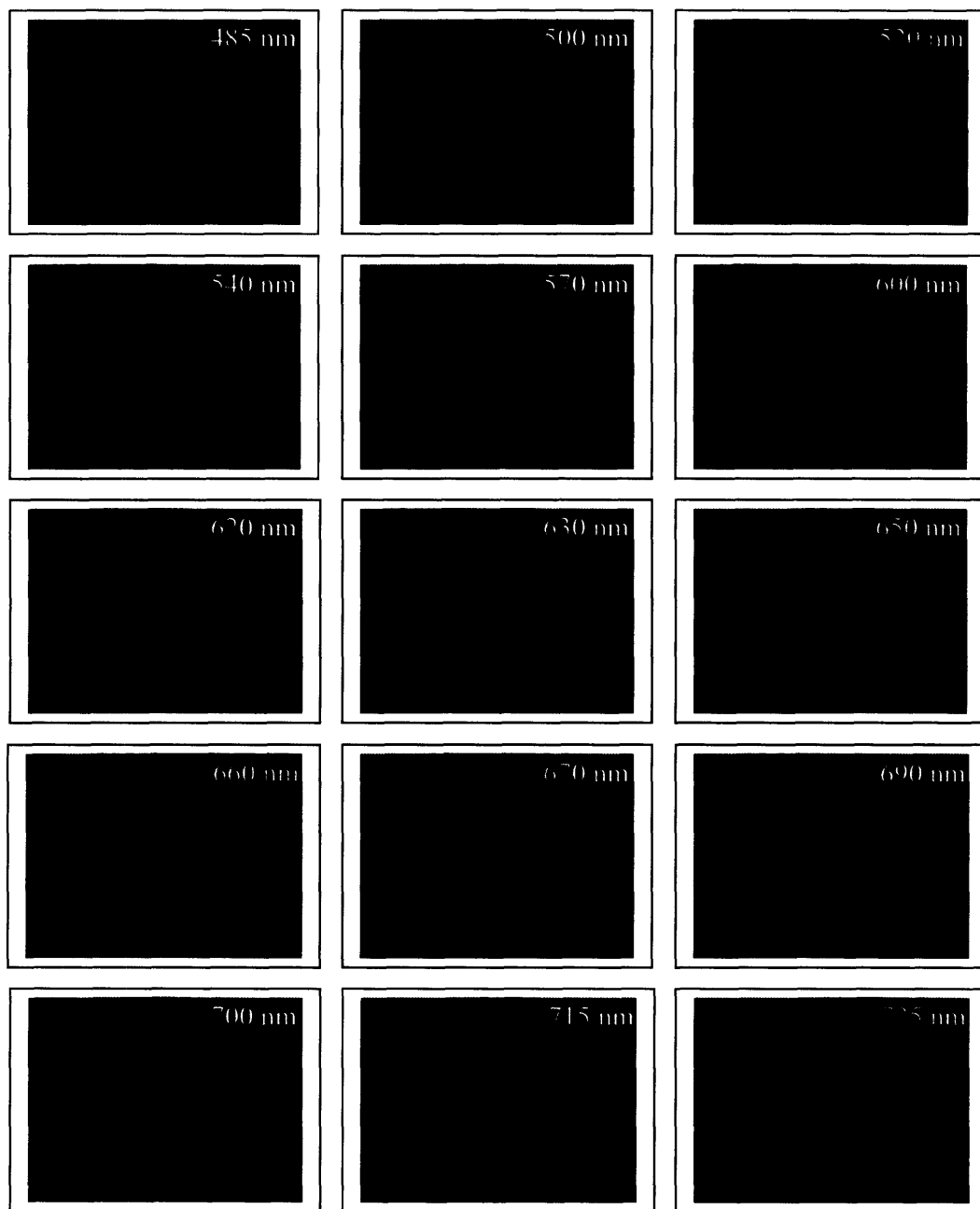


Figure 3-13. Fringe patterns which result from interference between the two NOPA output beams. The large wavelength range over which this occurs implies phase-coherent output which spans the entire tuning range of the amplifier.

3.6 Conclusion

A single-shot dual beam phase-locked noncollinear optical parametric amplifier has been constructed. The device provides tunable pump and probe pulses to the rest of the single-shot experimental apparatus, enabling the application of single-shot measurement techniques to a wide variety of condensed-phase systems. In particular, ultrafast photoinitiated events such as transient absorption and photodissociation which require pump pulse frequencies to match electronic transitions are now accessible by the general single-shot technique. The pulses generated by the NOPA are tunable between 500 nm and 720 nm and compressible to 25 fs or less, depending upon wavelength. Single-pass gain of 10-15% results in pulse energies of up to 10 μ J – more than suitable for pump-probe applications. In addition, NOPA wavelength tuning and pulse compression can be fully automated if desired, making the day-to-day operation of the device straightforward and reproducible. Finally, frequency-doubling of the NOPA output(s) is possible to extend the range of tunable wavelengths into the ultraviolet range, a feature that will be exploited subsequently.

References

- [1] Fork, R.L., Greene, B.I. and Shank, C.V., *Appl. Phys. Lett.* **38**, 671 (1981).
- [2] Schoenlein, R.W. *et al.*, *Appl. Phys. Lett.* **58**, 801 (1991).
- [3] Fork, R.L. *et al.*, *Opt. Lett.* **12**, 483 (1987).
- [4] Petrov, V., Seifert, F., and Noack, F., *Appl. Opt.* **33**, 6988 (1994).
- [5] Petrov, V. *et al.*, *J. Appl. Phys.* **76**, 7704 (1994).
- [6] Greenfield, S.R. and Wasielewski, M.R., *Appl. Opt.* **34**, 2688 (1995).
- [7] Di Trapani, P. *et al.*, *Opt. Commun.* **119**, 327 (1995).
- [8] Di Trapani, P. *et al.*, *J. Opt. Soc. Am. B* **14**, 1245 (1997).
- [9] Reed, M.K., Steiner-Shepard, M.K. and Negus, D.K., *Opt. Lett.* **19**, 1855 (1994).
- [10] Reed, M.K. *et al.*, *J. Opt. Soc. Am. B* **12**, 2229 (1995).
- [11] Gale, G.M. *et al.*, *Opt. Lett.* **20**, 1562 (1995).
- [12] Gale, G.M., Cavallari, F. and Hache, F., *J. Opt. Soc. Am. B* **15**, 702 (1998).
- [13] Cerullo, G., Nisoli, M. and De Silvestri, S., *Appl. Phys. Lett.* **71**, 3616 (1997).
- [14] Cerullo, G. *et al.*, *Opt. Lett.* **23**, 1283 (1998).
- [15] Cerullo, G. *et al.*, *Opt. Lett.* **24**, 1529 (1999).
- [16] Shirakawa, A. and Kobayashi, T., *Appl. Phys. Lett.* **72**, 147 (1998).
- [17] Shirakawa, A., Sakane, I. and Kobayashi, T., *Opt. Lett.* **23**, 1292 (1998).
- [18] Shirakawa, A. *et al.*, *Appl. Phys. Lett.* **74**, 2268 (1999).
- [19] Shirakawa, A. and Kobayashi, T., *J. Lumin.* **119-120**, 87 (2000).
- [20] Danielius, R. *et al.*, *Opt. Lett.* **21**, 973 (1996).
- [21] Wilhelm, T., Piel, J. and Riedle, E., *Opt. Lett.* **22**, 1494 (1997).
- [22] Piel, J., Beutter, M. and Riedle, E., *Opt. Lett.* **25**, 180 (2000).
- [23] Reid, D.T. *et al.*, *IEEE J. Quant. Electron.* **33**, 1 (1997).

- [24] Wang, J., Dunn, M.H. and Rae, C.F., *Opt. Lett.* **22**, 763 (1997).
- [25] Oien, A.L. *et al.*, *Opt. Lett.* **22**, 859 (1997).
- [26] Lee, S.-W. *et al.*, *Opt. Commun.* **144**, 241 (1997).
- [27] Huang, S.-D. *et al.*, *J. Opt. Soc. Am. B* **15**, 1375 (1998).
- [28] Urschel, R. *et al.*, *J. Opt. Soc. Am. B* **16**, 565 (1999).
- [29] Sirutkaitis, V. *et al.*, *J. Opt. B: Quantum Semiclass. Opt.* **1**, 139 (1999).
- [30] Smilgevicius, V. *et al.*, *Opt. Commun.* **173**, 365 (2000).
- [31] Krylov, V. *et al.*, *Opt. Lett.* **23**, 100 (1998).
- [32] Rotermund, F., Petrov, V. and Noack, F., *Opt. Commun.* **169**, 183 (1999).
- [33] Kummrow, A. *et al.*, *Appl. Phys. B* **71**, 885 (2000).
- [34] Riedle, E. *et al.*, *Appl. Phys. B* **71**, 457 (2000).
- [35] Kobayashi, T. and Shirakawa, A., *Appl. Phys. B* **70**, S239 (2000).
- [36] Bellini, M. and Hansch, T.W., *Opt. Lett.* **25**, 1049 (2000).
- [37] Wefers, M.M. and Nelson, K.A., *J. Opt. Soc. Am. B* **12**, 1343 (1995).
- [38] Wefers, M.M. and Nelson, K.A., *IEEE J. Quant. Electron.* **32**, 161 (1996).

Chapter 4

Time-resolved Nonresonant Raman Scattering in Liquids and Solids

In this chapter the first reported single-shot measurements of nonresonant stimulated Raman scattering in crystalline solids and molecular liquids are presented along with a classical description of the excitation and probing processes. All data in this chapter are obtained with the single-shot experimental setup described in the preceding two chapters. No data averaging or correction beyond the numerical extraction techniques described thus far has been employed – the results presented represent truly single-shot material responses unless specified otherwise.

4.1 Classical Theory of Stimulated Raman Scattering

Many of the essential attributes of the ultrafast stimulated Raman scattering process can be understood within the context of a relatively straightforward classical theory. We will consider a single optic phonon mode of a scattering medium, and label the (scalar) normal coordinate of that mode Q . The equation of motion of Q , following Shen and Bloembergen [1], is

$$\frac{\partial^2 Q}{\partial t^2} + 2\gamma \frac{\partial Q}{\partial t} + \omega_0^2 Q = \Omega \quad (4.1)$$

where γ is the natural damping rate of Q and ω_0 is the natural oscillation frequency. In the subsequent analysis, we will closely follow the treatment of Yan and Nelson [2-5]. The quantity \mathcal{Q} represents the driving force upon Q . In the present case, the driving force is exerted by a single ultrashort pulse propagating in the forward direction, and can be expressed as the change in the electrostatic stored energy density W with respect to the normal coordinate Q :

$$\Omega = \frac{\partial W}{\partial Q} \quad (4.2)$$

The stored energy W is expressed in terms of the electric field \mathbf{E} according to

$$W = \frac{1}{2} \varepsilon \mathbf{E}^* \mathbf{E} \quad (4.3)$$

The dielectric permittivity ε is related to both the number density of oscillators N and the polarizability of the medium α through the relation $\varepsilon = \varepsilon_0(1+N\alpha)$. It is evident that the stored energy density, and hence the driving term Ω , are modulated by Q through the influence of the polarizability. Using the well-known Placzek approximation [6] we can expand α in terms of Q which gives

$$\alpha = \alpha_0 + \left(\frac{\partial \alpha}{\partial Q} \right)_0 Q + \dots \quad (4.4)$$

and truncating the expansion after the second term we find that the permittivity is given approximately by

$$\varepsilon \approx \left(\varepsilon_0 + N\alpha_0\varepsilon_0 + \varepsilon_0 N \left(\frac{\partial \alpha}{\partial Q} \right)_0 Q \right) \quad (4.5)$$

Substituting this result into Equation (4.3) and taking the derivative with respect to Q according to Equation (4.2) yields the driving term Ω :

$$\Omega = \frac{1}{2} \varepsilon_0 N \left(\frac{\partial \alpha}{\partial Q} \right)_0 \mathbf{E}^* \mathbf{E} \quad (4.6)$$

Substitution of Equation (4.6) into Equation (4.1) gives a modified equation of motion for the normal coordinate Q :

$$\frac{\partial^2 Q}{\partial t^2} + 2\gamma \frac{\partial Q}{\partial t} + \omega_0^2 Q = \frac{1}{2} \varepsilon_0 N \left(\frac{\partial \alpha}{\partial Q} \right)_0 \mathbf{E}^* \mathbf{E} \quad (4.7)$$

The quantity in brackets on the right-hand side of Equation (4.7) is referred to as the differential polarizability. For many materials the numerical value of the differential polarizability is not known, but can be estimated from tabulated values of the Raman scattering cross-section for mode Q .

The electric field \mathbf{E} of an ultrafast pulse can be described as the product of a Gaussian field envelope function and a term which oscillates at the laser carrier frequency ω_L :

$$\mathbf{E} = \mathbf{E}_0 e^{-\frac{\left(t - \frac{zn}{c}\right)^2}{2\tau_L^2}} \cos \left[\omega_L \left(t - \frac{zn}{c} \right) \right] \quad (4.8)$$

In the above equation, n is the material index of refraction at frequency ω_L , c is the vacuum speed of light, \mathbf{E}_0 is the maximum field amplitude and τ_L is the temporal width of the pulse. The pulse is propagating along the z -axis only, which allows us to consider only scalar aspects of the field – the transverse spatial profile is neglected. In addition, the zero of time occurs when the maximum point of the excitation pulse enters the front surface of the sample, which is located at $z = 0$; hence, the field expression is written in terms of the retarded time.

Computing the product $\mathbf{E}^* \mathbf{E}$ from Equation (4.8) yields

$$\mathbf{E}^* \mathbf{E} = E^2 = E_0^2 e^{-\frac{\left(t - \frac{zn}{c}\right)^2}{\tau_L^2}} \cos^2 \left[\omega_L \left(t - \frac{zn}{c} \right) \right] \approx \frac{1}{2} E_0^2 e^{-\frac{\left(t - \frac{zn}{c}\right)^2}{\tau_L^2}} \quad (4.9)$$

where a higher-frequency term which oscillates at $2\omega_L$ has been dropped since it does not effectively couple to Q . Substituting Equation (4.9) into (4.7) yields

$$\frac{\partial^2 Q}{\partial t^2} + 2\gamma \frac{\partial Q}{\partial t} + \omega_0^2 Q = \frac{1}{4} \varepsilon_0 N \left(\frac{\partial \alpha}{\partial Q} \right)_0 E_0^2 e^{-\frac{\left(t - \frac{zn}{c}\right)^2}{\tau_L^2}} \quad (4.10)$$

The above equation assumes that the depletion of the incident field due to Raman scattering is negligible. For small γ , Equation (4.10) can be solved using a Green's function method, giving

$$Q(z, t) = \frac{\sqrt{\pi} \varepsilon_0 N \left(\frac{\partial \alpha}{\partial Q} \right)_0 E_0^2 \tau_L}{4\omega_0} e^{-\frac{\tau_L^2 \omega_0^2}{4}} e^{-\gamma \left(t - \frac{zn}{c} \right)} \sin \left[\omega_0 \left(t - \frac{zn}{c} \right) \right] \quad (4.11)$$

It is clear from the product in the first exponent of Equation (4.11) that an ultrafast pulse with duration less than the vibrational period can directly excite material motion along the normal mode coordinate Q .

The relationship between the instantaneous intensity $I(t)$ and the electric field $E(t)$ is given by

$$I(t) = nc\varepsilon_0 |E(t)|^2 \quad (4.12)$$

Integrating Equation (4.9) for the total laser fluence results in

$$I_L = \frac{1}{2} \sqrt{\pi} nc\varepsilon_0 \tau_L E_0^2 \quad (4.13)$$

Substituting this result back into Equation (4.11) for $Q(z, t)$ yields

$$Q(z,t) = \frac{N\left(\frac{\partial\alpha}{\partial Q}\right)_0 I_L}{2nc\omega_0} e^{-\frac{\tau_L^2\omega_0^2}{4}} e^{-\gamma\left(t-\frac{zn}{c}\right)} \sin\left[\omega_0\left(t-\frac{zn}{c}\right)\right] \quad (4.14)$$

The maximum amplitude of the normal mode from Equation (4.14) is

$$Q_0 = \frac{N\left(\frac{\partial\alpha}{\partial Q}\right)_0 I_L}{2nc\omega_0} e^{-\frac{\tau_L^2\omega_0^2}{4}} \quad (4.15)$$

It is worthwhile to note that the amplitude of normal mode excitation never reaches Q_0 since, for $t = 0$, the sine function is zero, and for $t > 0$, the maximum value of the sine function is 1 but the value of the exponent preceding it is less than 1.

In order to relate the normal mode displacement to a displacement from equilibrium, we will consider a scenario in which mode Q is composed at the microscopic level of a collection of oscillators, each consisting of equal masses m vibrating about their common center of mass. The normal coordinate Q can be related to R , the displacement from the oscillator's equilibrium separation, by

$$Q = \sqrt{\frac{mN}{2}} R \quad (4.16)$$

Combining Equation (4.16) with Equation (4.14) gives the equilibrium displacement as a function of time, $R(t)$:

$$R(t,z) = \frac{\left(\frac{\partial\alpha}{\partial R}\right)_0 I_L}{nc\omega_0 m} e^{-\frac{\tau_L^2\omega_0^2}{4}} e^{-\gamma\left(t-\frac{zn}{c}\right)} \sin\left[\omega_0\left(t-\frac{zn}{c}\right)\right] \quad (4.17)$$

The maximum displacement R_0 is defined in a similar fashion to Equation (4.15):

$$R_0 = \frac{\left(\frac{\partial\alpha}{\partial R}\right)_0 I_L}{nc\omega_0 m} e^{-\frac{\tau_L^2\omega_0^2}{4}} \quad (4.18)$$

The above equations illustrate that a single ultrashort pulse produces oscillatory vibrational motion in the sample at its characteristic mode frequency, with a well-defined phase relationship relative to the timing of the exciting pulse. The inclusion of z -dependence in the expression for $R(t,z)$ reflects the fact that the front of the sample encounters the driving field before the back of the sample; hence, oscillations induced at the front surface will be out of phase with respect to those at the rear surface. In a crossed-pulse excitation scheme, phonons in the sample are excited at the difference wavevector defined by the excitation pulses' wavevectors. In a single-pulse scheme as outlined here, photons within the laser bandwidth are scattered into lower frequency photons – still within the pulse bandwidth – and the difference in energy corresponds to the phonon wavevector. The process can be thought of as mixing among Fourier components within the same excitation pulse. The distance that is traveled by the excitation pulse inside the sample during a single vibrational period defines the vibrational wavelength, and the corresponding wavevector that is collinear with the excitation pulse wavevector. Since the temporal phase of the induced material response is well characterized, time-resolved probing of the oscillations is possible.

Consider a second, weaker probe pulse at time delay t_D relative to the pump pulse, which excites the sample in a fashion similar to the pump. The combined normal mode excitation will be

$$\begin{aligned}
 Q(t,z) &= Q_{pump} + Q_{probe} \\
 &= Q_\Sigma e^{-\gamma\left(t-\frac{zn}{c}\right)} \sin\left[\omega_0\left(t-\frac{zn}{c}\right) + \varphi\right]
 \end{aligned}
 \tag{4.19}$$

where we have defined

$$Q_{\Sigma} = \sqrt{Q_0^2 e^{-2\gamma t_D} + 2Q_0 Q_1 e^{-\gamma t_D} \cos(\omega_0 t_D) + Q_1^2} \quad (4.20)$$

In the above expressions, in order to emphasize our interest in the probe beam (which provides the measurement signal), the time axis has been shifted such that the intensity maximum of the probe pulse enters the front surface of the sample at $t = 0$; the pump pulse precedes the probe at $t = -t_D$. The individual pump and probe vibrational responses in Equation (4.19) are given by

$$\begin{aligned} Q_{pump} &= Q_0 e^{-\gamma t_D} e^{-\gamma \left(t - \frac{zn}{c}\right)} \sin \left[\omega_0 \left(t + t_D - \frac{zn}{c} \right) \right] \\ Q_{probe} &= Q_1 e^{-\gamma \left(t - \frac{zn}{c}\right)} \sin \left[\omega_0 \left(t - \frac{zn}{c} \right) \right] \end{aligned} \quad (4.21)$$

In a typical pump-probe experiment, the probe pulse energy is much weaker than the pump, and so it is assumed that $Q_1 \ll Q_0$. Equation (4.20) illustrates the dependence of the vibrational amplitude on the relative time delay between pump and probe. For probe pulses which are in phase with the vibrational motion induced by the pump ($t_D = 0, T, 2T$, etc.) the cosine function takes value +1 and the amplitude increases. For out-of-phase probe pulses ($t_D = T/2, 3T/2$, etc.) the cosine function takes value -1 and the overall vibrational amplitude decreases. The period is $T = \omega_0^{-1}$.

In consideration of the effect of the probe pulse on the already-oscillating sample after the pump has passed through, any subsequent increase or decrease in vibrational amplitude must result from a transfer of energy from or to the probe field. The change in probe field energy is therefore simply the negative of the sample's change in vibrational energy at any point in time, which is calculated by taking the difference between the vibrational energy of the sample before and after the probe pulse:

$$\begin{aligned}
\Delta E_{vib}^{sample} &= \frac{1}{2} \omega_0^2 (Q_\Sigma^2 - Q_0^2 e^{-2\gamma t_D}) \\
&= \frac{1}{2} \omega_0^2 [Q_1^2 + 2Q_0 Q_1 e^{-\gamma t_D} \cos(\omega_0 t_D)]
\end{aligned} \tag{4.22}$$

For a sample of length l , the overall change in probe pulse energy is given by

$$\begin{aligned}
\frac{\Delta I_{probe}}{I_{probe}} &= - \frac{\Delta E_{vib}^{sample} l}{I_{probe}} \\
&= - \frac{N^2 \left(\frac{\partial \alpha}{\partial Q} \right)_0^2 I_L e^{-\gamma t_D} \cos(\omega_0 t_D) l}{4n^2 c^2}
\end{aligned} \tag{4.23}$$

where the result of Equation (4.15) is used in conjunction with Equation (4.22).

The energy loss or gain by the probe field due to Raman scattering is manifest as a dynamic red- or blue-shifting of the probe pulse spectrum. It is this effect which is ultimately used to measure sample vibrational motion in the single-shot experiment, and so we will discuss the manner in which such spectral shifting occurs. The magnitude of the polarization induced in the sample of interest by an electric field E can be expressed, with the result of Equation (4.4), as

$$P = \epsilon_0 N \alpha E = \epsilon_0 N \left[\alpha_0 + \left(\frac{\partial \alpha}{\partial Q} \right)_0 Q \right] E \tag{4.24}$$

The Raman effect occurs through the second term in Equation (4.24) which expresses a change in the bulk polarizability. Maxwell's equations for the general coupling between E and Q give

$$\frac{\partial^2 E}{\partial z^2} - \frac{n^2}{c^2} \frac{\partial^2 E}{\partial t^2} = \frac{1}{\epsilon_0 c^2} \frac{\partial^2}{\partial t^2} \left[\epsilon_0 N \left(\frac{\partial \alpha}{\partial Q} \right)_0 Q E \right] \tag{4.25}$$

The probe pulse is assumed weak relative to the pump, and so the total normal mode excitation can be approximated as the motion arising from the pump only; $Q \approx Q_{pump}$. In addition, stimulated Raman scattering is a relatively weak third order nonlinear effect, and we can assume that the laser pulse is not significantly depleted via the interaction. Thus, the pulse shape remains unchanged on passage through the medium. However, in order to distinguish between the laser field and the induced nonlinear polarization in the material, the laser field of Equation (4.8) is renamed E_{laser} . After replacing t with $t' = t - zn/c$ to reflect the phase difference across the thickness of the material, Equation (4.25) is rewritten as

$$\frac{\partial^2 E}{\partial z^2} - \frac{2n}{c} \frac{\partial^2 E}{\partial z \partial t'} = \frac{1}{\epsilon_0 c^2} \frac{\partial^2}{\partial t'^2} \left[\epsilon_0 N \left(\frac{\partial \alpha}{\partial Q} \right)_0 Q(t') E_{laser}(t') \right] \quad (4.26)$$

A general solution of Equation (4.26) is then

$$E(z, t') = E_{laser}(t') - \frac{N \left(\frac{\partial \alpha}{\partial Q} \right)_0 z}{2cn} \frac{\partial}{\partial t'} [Q(t') E_{laser}(t')] \quad (4.27)$$

We are particularly concerned with the spectral content of the field, and so we consider the Fourier transform of Equation (4.27):

$$\begin{aligned} E(l, \omega) &= e^{\frac{i n \omega l}{c}} E_{laser}(\omega) \\ &+ \frac{N \left(\frac{\partial \alpha}{\partial Q} \right)_0 Q_0 e^{-\gamma l_D} e^{\frac{i n \omega l}{c}} l \omega}{4cn} \left[e^{i \omega_0 t_D} E_{laser}(\omega + \omega_0) - e^{-i \omega_0 t_D} E_{laser}(\omega - \omega_0) \right] \end{aligned} \quad (4.28)$$

The quantity $E_{laser}(\omega)$ is the Fourier transform of $E_{laser}(t')$ at $z = 0$. We detect only the spectral intensity in our experiments, not the field directly, but $I(\omega)$ is easily calculated from Equation (4.28):

$$\begin{aligned}
I(\omega) = & \frac{nc\varepsilon_0\tau_L^2 E_0^2}{4} e^{-(\omega-\omega_L)^2 \tau_L^2} \\
& + \frac{1}{8} \varepsilon_0 N \left(\frac{\partial \alpha}{\partial Q} \right)_0 Q_0 e^{-\gamma t_D} l \omega \tau_L^2 E_0^2 e^{-\frac{\omega_0^2 \tau_L^2}{4}} \cos(\omega_0 t_D) \\
& \times \left[e^{-\left[\omega - \left(\omega_L - \frac{\omega_0}{2}\right)\right]^2 \tau_L^2} - e^{-\left[\omega - \left(\omega_L + \frac{\omega_0}{2}\right)\right]^2 \tau_L^2} \right] \\
& + \frac{\varepsilon_0 \left[N \left(\frac{\partial \alpha}{\partial Q} \right)_0 \tau_L E_0 Q_0 e^{-\gamma t_D} \omega l \right]^2}{64nc} \\
& \times \left[e^{-[\omega - \omega_L + \omega_0]^2 \tau_L^2} + e^{-[\omega - \omega_L - \omega_0]^2 \tau_L^2} - 2 \cos(2\omega_0 t_D) e^{-\frac{\omega_0^2 \tau_L^2}{4}} e^{-(\omega - \omega_L)^2 \tau_L^2} \right] \quad (4.29)
\end{aligned}$$

Equation (4.29) contains six terms. The first represents most of the probe pulse intensity which is unchanged on passing through the sample. The last three terms are small in magnitude for ultrashort pulses and can be neglected. It is the second and third terms which illustrate the frequency shifting of the ultrashort probe pulse's spectrum. As an example, consider that for probe pulses which arrive in phase with the vibrational oscillations ($t_D = 0, T, 2T$, etc.) the cosine function takes on a value of +1 and the pulse emerges with more light at frequencies in the vicinity of $\omega_L - \omega_0/2$ and less at frequencies around $\omega_L + \omega_0/2$. When the probe pulse arrives out-of-phase, the cosine function takes a value of -1 and the situation is exactly reversed.

Typical vibrational displacements can be estimated for Raman active materials by inserting appropriate values for the parameters in Equation (4.17). Yan and Nelson report that maximum vibrational displacements in the vicinity of 2×10^{-3} Å are to be expected for nonresonant scattering in transparent materials with pulse intensities of

roughly 50 mJ/cm^2 . In their calculations, they report that the second and third terms of Equation (4.29) account for up to 40% of the probe light emerging red- or blue-shifted. For materials with larger Raman scattering cross-sections (especially where the laser pump frequency is resonant with an electronic transition), much larger induced vibrational amplitudes are possible.

There have been numerous reports in the literature in the past few years of time-domain measurements of impulsive stimulated Raman scattering in a number of systems, including gases [7,8], molecular liquids [9-11] and crystalline solids [12-16]. In all cases, the experiments are conducted using the standard pump-probe method – a multi-shot technique. For off-resonant samples, the amplitude of material vibrational motion is very small, and high quality data are obtained only after averaging over many scans.

Our goal in constructing the single-shot apparatus was to open an experimental window into those systems where multi-shot probing is not possible – where the sample is changed structurally after a single pump pulse and so the response must be measured all at once. Impulsive stimulated Raman scattering measurements can be performed even on molecules or crystals undergoing irreversible structural change in order to provide a real-time picture of bond-breaking events. Unfortunately, the single-shot system's most stringent limitation is the signal detection threshold; if the material response is weak and lost in the instrument's baseline noise level, nothing worthwhile can be recovered.

In spite of our best efforts, the single-shot technique demands a somewhat judicious choice of sample. The optical quality of the specimen must be sufficiently high such that the probe beam is left relatively undistorted on its passage through the material. But most importantly, the Raman signal must be strong enough to detect in a single laser

shot. We have attempted single-shot measurements on a large variety of materials without success, in spite of the fact that multi-shot pump-probe techniques are able to resolve time-dependent oscillatory behavior. The remainder of this chapter describes the first-ever *successful* single-shot impulsive stimulated Raman scattering measurements in two different types of systems: a crystalline solid and a molecular liquid.

4.2 ISRS Measurements in Bismuth Germanate

Bismuth germanate is a colorless, transparent crystalline solid which occurs in two forms: $\text{Bi}_4\text{Ge}_3\text{O}_{12}$ and $\text{Bi}_{12}\text{GeO}_{20}$. Both forms are well characterized [17-22] in the literature and available commercially. The first form (which we shall henceforth refer to as BGO) in particular is of interest on account of a number of unusual properties it possesses. BGO undergoes multiphoton absorption at high pump intensities and then exhibits broadband (“white light”) luminescence [23-34] which is easily visible to the naked eye. The material has therefore been widely adopted as a photon-detector, particularly for x-rays and other difficult-to-measure pulse sources. Also, BGO is either uniaxial or biaxial, depending upon the crystal orientation, and exhibits a strong electro-optic effect; the use of BGO as an optical modulator and waveguide material has been investigated [35-40]. The BGO crystal structure, reprinted from [17], is shown in Figure 4-1. The cubic unit cell consists of GeO_4 tetrahedra surrounded by Bi^{3+} ions. The bismuth ions are loosely coordinated in an octahedral geometry to three nearest-neighbor and three next-nearest-neighbor oxygen (O^{2-}) atoms. The resonance Raman spectrum of BGO has also been studied by a number of groups [41-44]. In Figure 4-2, the measured

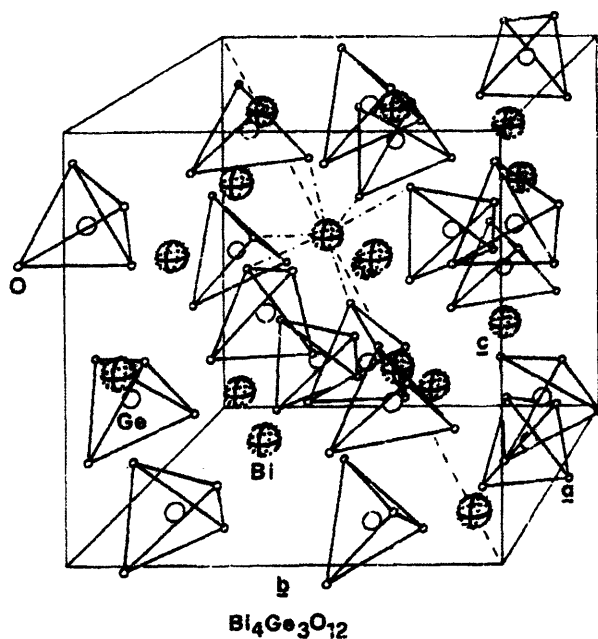


Figure 4-1. Crystal structure of BGO reproduced from reference 17. Individual GeO_4 tetrahedra are indicated by solid lines. Each Bi^{3+} is loosely coordinated to three nearest-neighbor and three next-nearest-neighbor oxygen atoms.

HH and HV Raman spectra are reproduced from reference 41. The HV spectrum is enhanced by a factor of 11 relative to the HH spectrum, and for our purposes is unsuitable for study on account of the relatively weak Raman response. However, the HH polarized spectrum contains a number of peaks and in particular, a very sharp and intense transition near 90 cm^{-1} . In fact, this particular mode has one of the largest reported scattering cross-sections in the literature [42] and as such, represents an attractive candidate for single-shot time-domain Raman scattering measurements. A summary of the HH polarized Raman spectrum from reference 41 is given in Table 4-1. As noted in the table, the 90 cm^{-1} mode corresponds to a complicated Bi-Ge low frequency vibrational motion.

Experiments are conducted using the single-shot apparatus in the configuration outlined in Chapter 2. Horizontally polarized, 50 fs pump pulses at 820 nm are focused

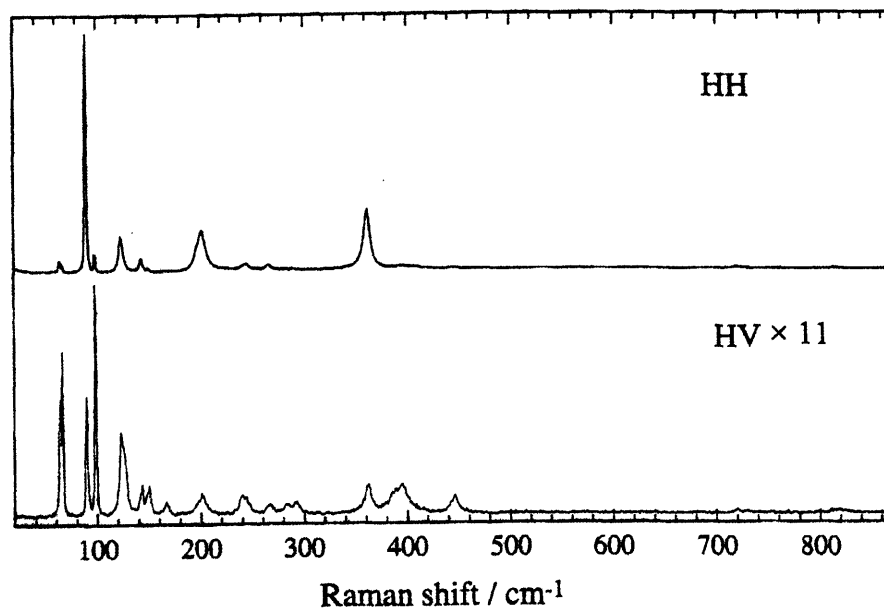


Figure 4-2. HH and HV Raman spectra for BGO, reproduced from reference 41. Note that the HV spectrum is enhanced by a factor of 11 for visibility. A particularly intense Raman mode is located at 90 cm^{-1} in the HH spectrum.

to a spot size of $100\text{ }\mu\text{m}$ by a 25 cm f.l. lens. The probe is generated by frequency-doubling in BBO which yields 80 fs, 410 nm pulses. In performing the experiment, a single pulse is electronically gated out of the laser amplifier and used to produce both pump and probe. The optical image of the probe is captured in a single frame by a CCD camera. The camera examines a narrow slice of the probe spectrum which is selected using a bandpass filter placed just in front of the CCD surface. Data are extracted from individual images by a semi-autonomous algorithm following calibration for the sample

optical properties, alignment, and the optical wavelengths of the pump and probe. An example of a raw data scan for BGO is shown in Figure 4-3. As before, the first time

Table 4-1. Modes in HH polarized Raman spectrum of BGO, reproduced from reference 41. Symbols used are: vvw = very, very weak; m = medium; w = weak; vvs = very, very strong.

Frequency (cm ⁻¹)	Symmetry	Vibration Type
818 vvw	A	Ge-O stretch
720 vvw	E	O-Ge-O bend
409 vvw	E	O-Ge-O bend
406 vvw	E	O-Ge-O bend
362 m	A	Bi-O stretch
267 w	E	Bi-O-Bi, O-Bi-O bend
244 w	E	Bi-O-Bi, O-Bi-O bend
201 m	A	Ge-O rocking
142 w	E	Bi-O-Bi bend
123 m	E	Bi-O-Ge bend
90 vvs	A	Bi ... Ge vibration

point is located in the top left-hand corner, and time runs forward in 25 fs increments from row-to-row down each column. A very strong negative modulation of the

transmitted optical intensity is visible on the image. This is a general feature of high field excitation of most samples and results from high-order nonlinear processes involving bound electrons located near the material surface. Following the initial strong response,

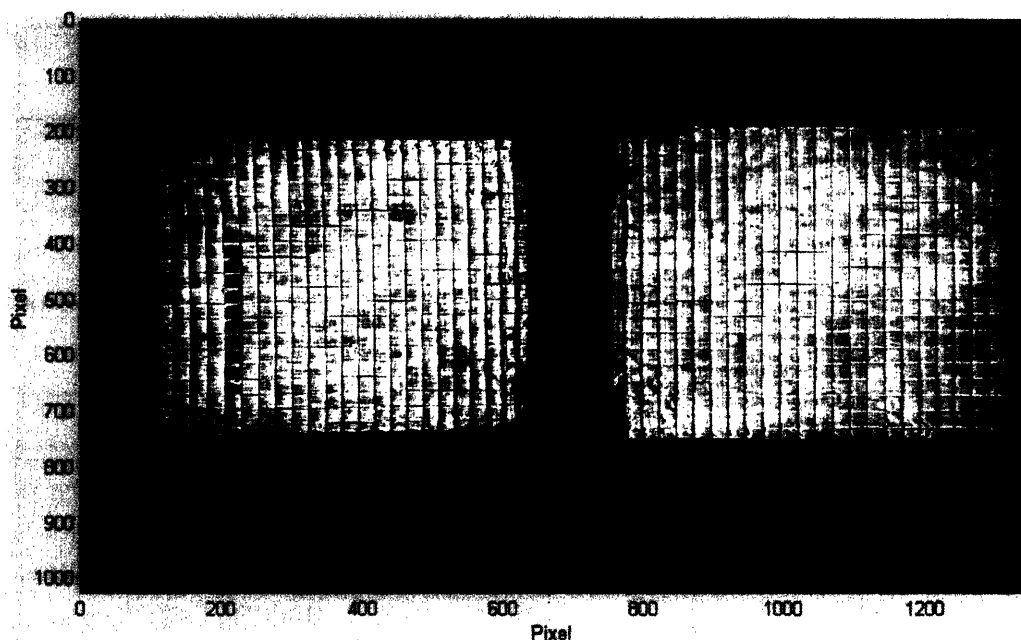


Figure 4-3. Raw data scan recorded on the CCD camera for a 100 μm thick sample of BGO pumped by an 820 nm, 50 fs single pulse and probed at 410 nm. A very strong initial response lasting about 225 fs is visible, but no further modulation of transmitted light intensity is apparent.

no further modulation of transmitted probe intensity is visible, although it is clear that if oscillatory behavior has been induced in the BGO sample, it should result in periodic modulations superimposed upon the echelon image.

The sample utilized in these experiments is a 100 μm thick BGO single crystal in the [001] orientation. Treatment of the raw image with the single-shot algorithm results

in the data extraction shown in Figure 4-4. After the strong initial modulation feature, the transmitted light intensity returns to the initial baseline intensity, with clear periodic modulations superimposed thereon. Four separate scans are shown in Figure 4-4, each corresponding to one single-shot experimental run, in order to demonstrate the repeatability of the results. With the exception of relatively small noise contributions to the signal, the recovered BGO response is consistent from scan to scan.

The data in Figure 4-4 correspond to an excitation fluence of 30 mJ/cm^2 . In order to assess the dependence of the observed scattering signal on the pump pulse intensity, a number of scans at different fluences were recorded. The top panel of Figure 4-5 illustrates three such scans. Clearly, the amplitude of the Raman signal decreases as weaker pump pulses are used. In the bottom panel of Figure 4-5, the maximum oscillation amplitude is plotted as a function of laser fluence. The relationship between the two is roughly linear, as one would expect from Equation (4.23).

The weakest observable signals occur with a pump fluence of 15 mJ/cm^2 . Below this threshold, oscillatory signal cannot be reliably extracted from the single-shot data. Above roughly 32 mJ/cm^2 , the BGO sample undergoes multiphoton absorption and emits a bright white luminescence which cannot be filtered out and which effectively fixes an upper limit on the intensity region which can be probed. The single-shot damage threshold for BGO (ascertained from visual inspection) appears to be roughly 40 mJ/cm^2 . At this intensity, a single excitation pulse produces permanent damage in the sample at the focal plane. Unfortunately, we are not able to recover high quality data at damaging fluences.

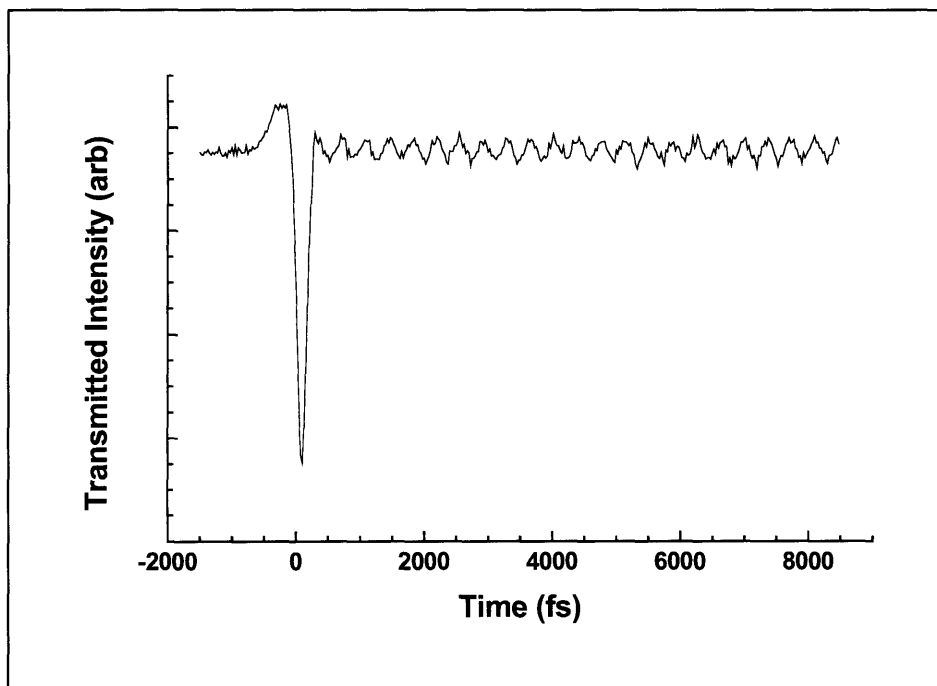
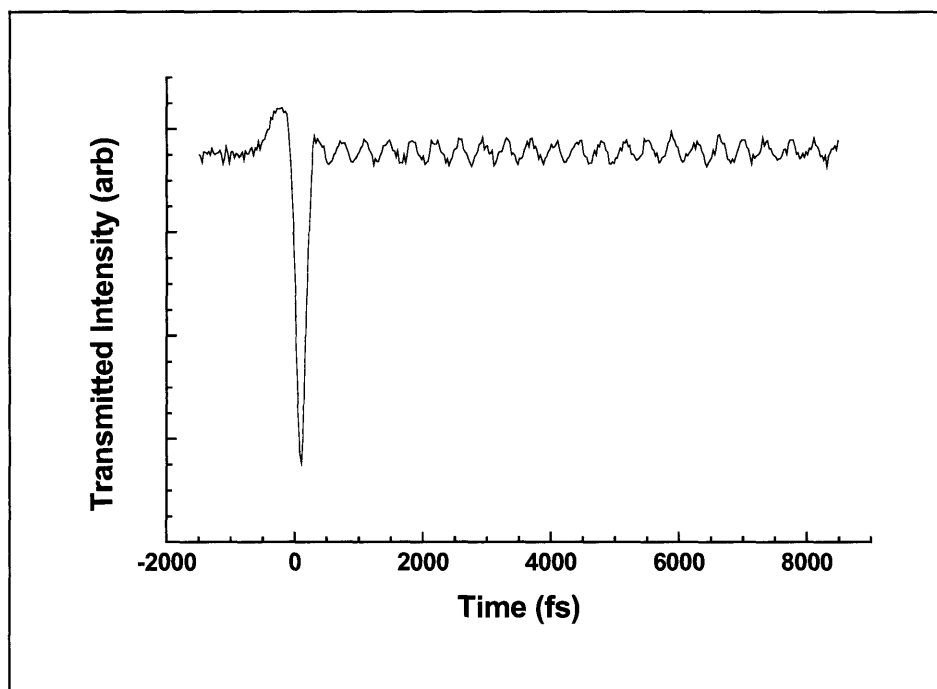


Figure 4-4. Single-shot nonresonant Raman scattering measurements in BGO. A strong vibrational signature appears after the initial modulation of transmitted light intensity near $t = 0$ and continues throughout the experimental time window. Two separate single-shot measurement results are shown.

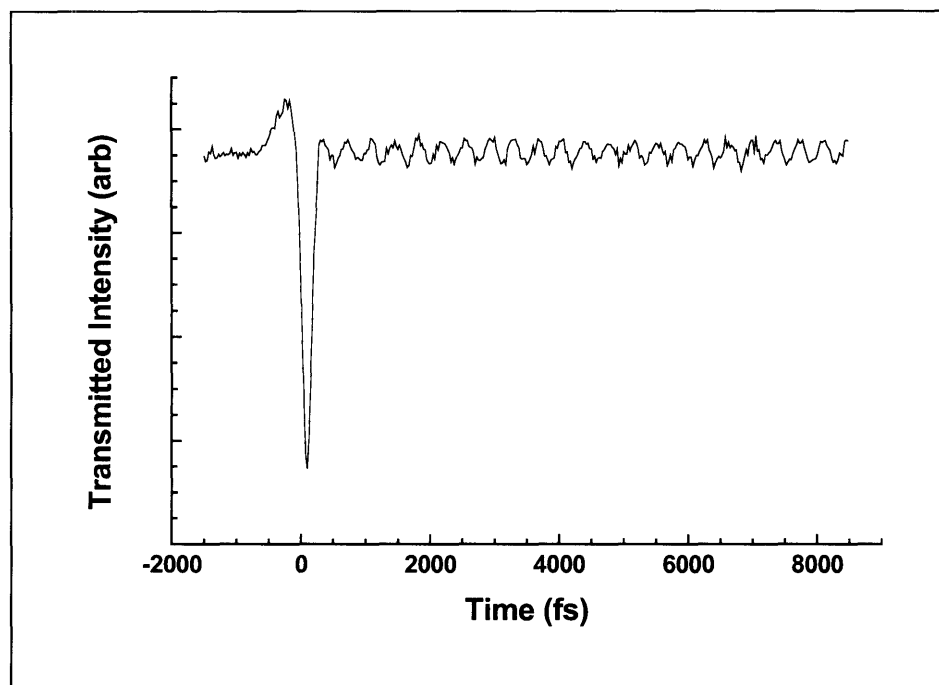
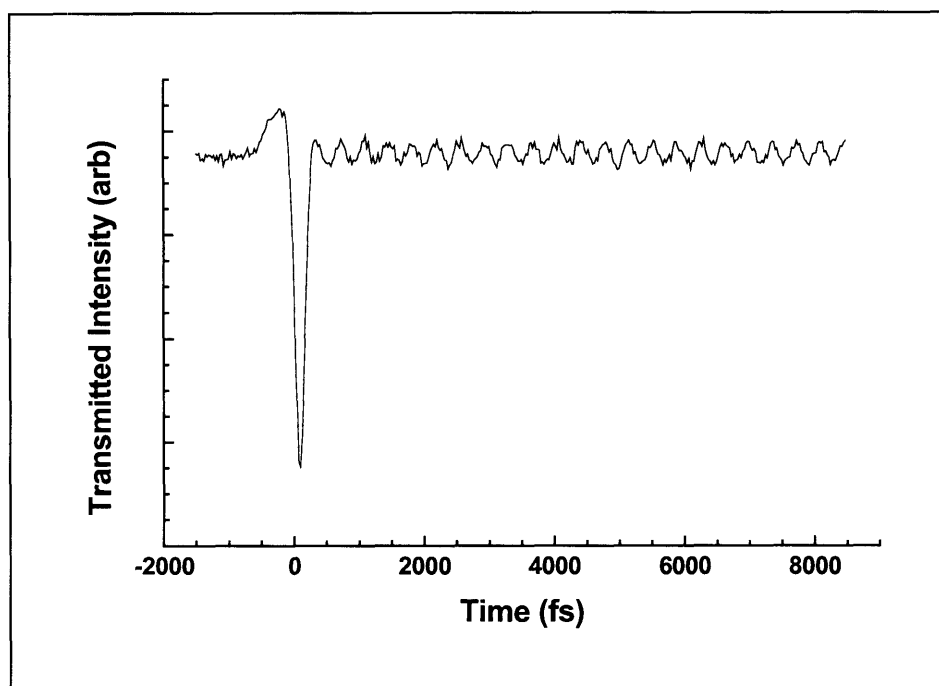


Figure 4-4 (cont'd). Single-shot nonresonant Raman scattering measurements in BGO. A strong vibrational signature appears after the initial modulation of transmitted light intensity near $t = 0$ and continues throughout the experimental time window. Two separate single-shot measurement results, distinct from those on the previous page, are shown.

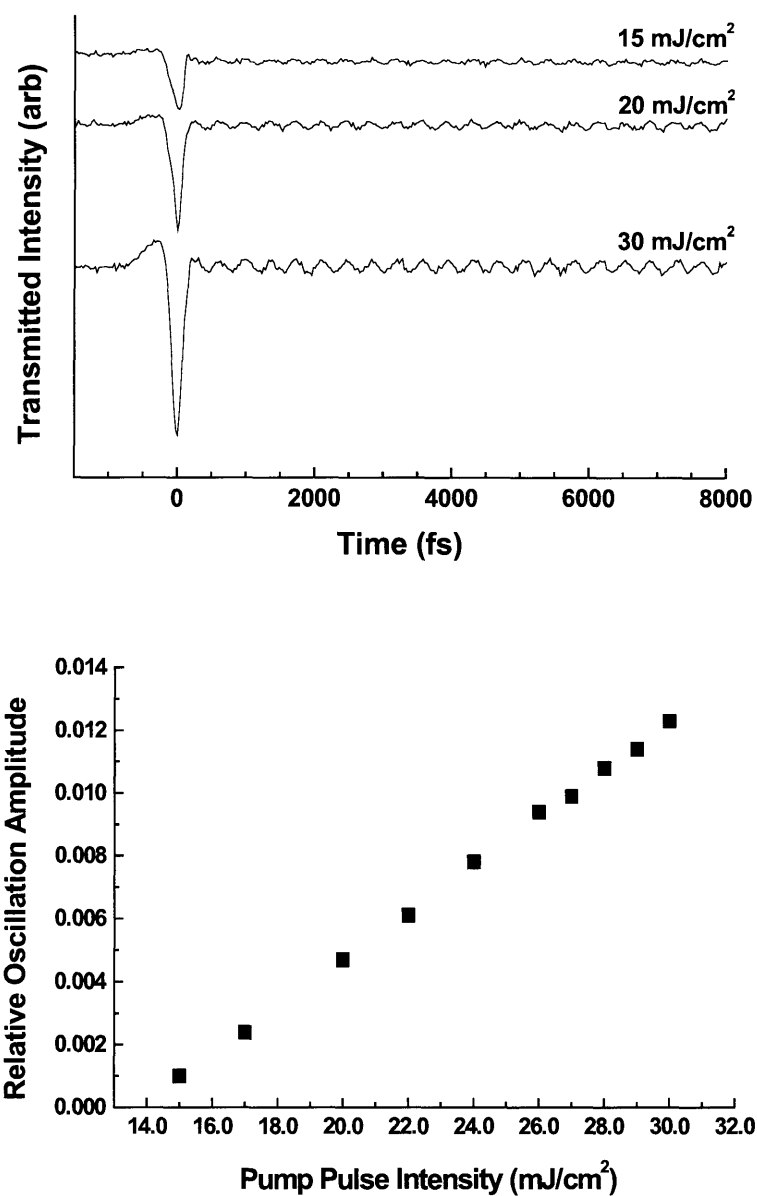


Figure 4-5. (Top) Comparison of stimulated Raman scattering in BGO at three different laser fluences. Larger amplitude vibrations result from more intense pump pulses. (Bottom) Maximum oscillation amplitude (proportional to signal amplitude) as a function of pump pulse intensity. The scaling is approximately linear, in accordance with the classical model of ISRS.

Figure 4-6 presents the power spectrum of the high-intensity excitation data in Figure 4-4. The spectrum shown is for a single data scan only. The signal-to-noise level is relatively high, suggesting that the single-shot method is sensitive enough to extract vibrational information even if the sample response is not as strong as it is for BGO. The 90 cm^{-1} mode which has been observed in frequency domain Raman measurements is easily recovered, but none of the other BGO modes are visible.

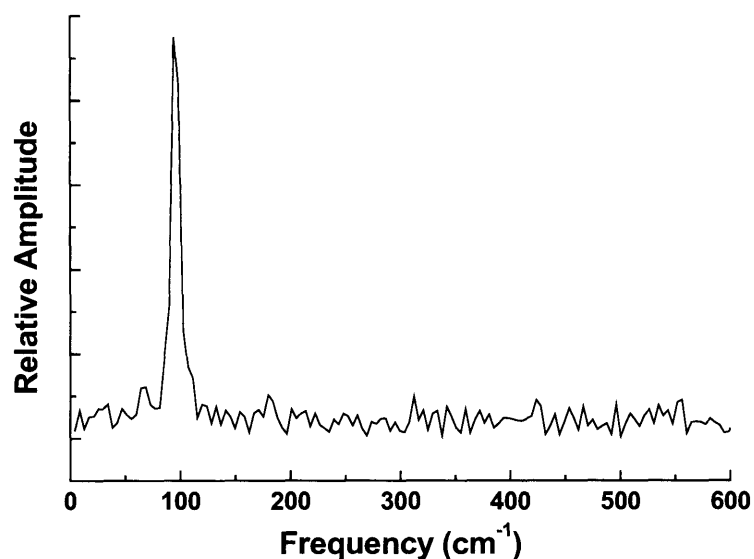


Figure 4-6. Power spectrum of the time-resolved response of BGO. The 90 cm^{-1} mode is easily recovered, although none of the weaker modes are visible.

As noted, the detection scheme used to record all of the data shown took advantage of dynamic shifting of the probe pulse spectrum in order to recover a modulated signal. A narrow-bandpass interference filter was used to select a small subset of the probe pulse bandwidth. As the probe spectrum shifted, the integrated intensity within the selected band either increased or decreased according to the direction of the shift. This suggests that by filtering on either side of the center wavelength of the probe,

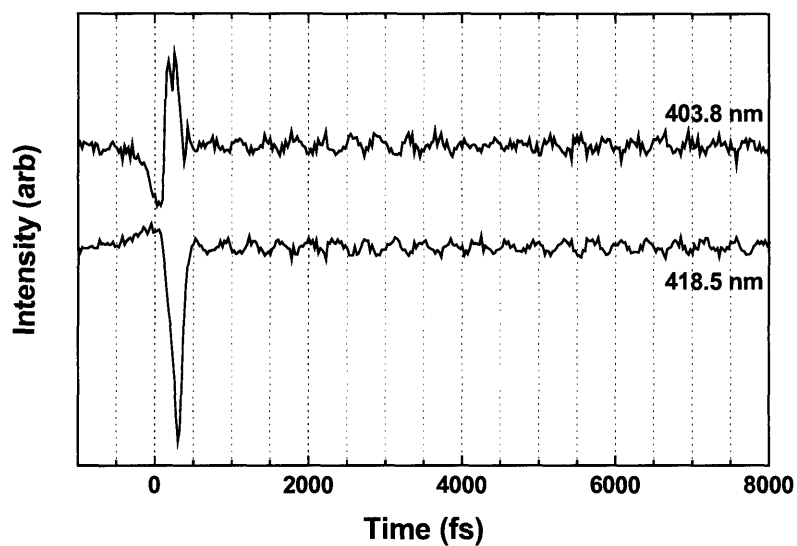
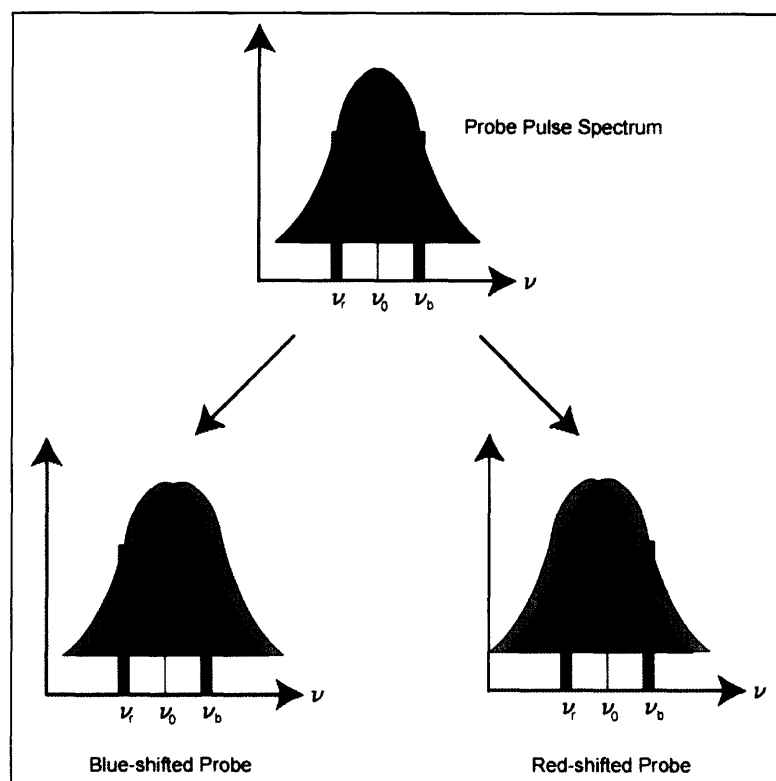


Figure 4-7. (Top) Schematic illustration of probe spectrum filtering in order to detect modulations in transmitted intensity resulting from coherent oscillations in the sample. **(Bottom)** Spectral filtering on opposite sides of the probe pulse central wavelength produces oppositely-phased oscillatory signals.

oppositely-phased material oscillations should be observable. The filtering scheme is illustrated in the top half of Figure 4-7. The probe pulse spectral distribution is centered at frequency ν_0 . The spectrum can be examined on either side of the maximum, at ν_b on the high-frequency side or ν_r on the low-frequency side. It is evident from the figure that when the probe spectrum shifts in the high-frequency direction, the intensity at ν_b increases and the intensity at ν_r falls. The opposite scenario occurs when the probe spectrum shifts toward lower frequencies. Thus, for the same material vibrational excitation, the phase of the measured response depends upon the spectral location of the detection filter. This is verified experimentally in the lower half of Figure 4-7, where two data scans taken on either side of the 410 nm probe spectral maximum show equal amplitude oscillations offset by half a vibrational period.

It is evident from the preceding data that single-shot detection of impulsive stimulated Raman scattering in crystalline solids is now possible using our present laboratory instrument, provided that the sample optical quality is sufficiently good and the material response is reasonably strong. Intense Raman peaks are more likely in solids where the number density of oscillators is relatively high. It remains to be seen, however, whether Raman responses from pure liquids or molecules dissolved in solution can be measured in single-shot fashion. The remainder of the chapter is devoted to the discussion of nonresonant Raman scattering in liquid samples.

4.3 Stimulated Raman Scattering in 3-Iodoanisole

Coherent vibrations can be excited in a wide variety of condensed phase systems. In addition to crystalline lattice phonons, intramolecular vibrational motion can be

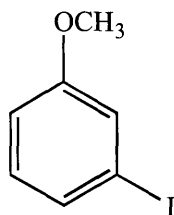


Figure 4-8. Chemical structure of 3-iodoanisole.

induced and detected providing the frequency of the motion is not too high – in other words, on the condition that, given the temporal resolution of the instrument, the conditions of impulsive excitation and probing are satisfied. In practical terms, the reduced mass of an oscillator in such a system must be rather large for the scheme to be successful. Compounds containing iodine atoms, with their low frequency bending and stretching modes, are ideal candidates for investigation. We selected as a target 3-iodoanisole, the structure of which is shown in Figure 4-8. The compound is obtained in pure form (Aldrich) as a clear yellow liquid with a pungent odor. Single-shot stimulated Raman scattering experiments are performed as described previously; the only difference is the fixing of 800 nm as both pump and probe wavelength. The reasons for this are twofold: to ensure that the shortest possible pulses are used, and to avoid any possible electronic absorption at the second harmonic of Ti:sapphire. Pure 3-iodoanisole is placed in a quartz cuvette of path length 1 mm and the system is aligned in the same manner as for crystalline samples. The cuvette is not translated laterally between every shot, but after every 10 shots. No permanent buildup of any “reaction products” is observed after excitation of the sample, but the sample is translated from time to time anyway.

Performing single-shot stimulated Raman scattering measurements on molecular liquids differs in a several ways from solid-state experiments. Most importantly, the

number density of interacting species (oscillators here, but also absorbers, scatterers, etc.) in the liquid is considerably less, and so Raman signals are typically weaker. Given the lower liquid density, much more of the pump light “leaks” further into the material, resulting in a broader effective probe signal, since the pump and probe pulses are not collinear, but oriented at an angle of 5-10° with respect to one another. Due to the angle

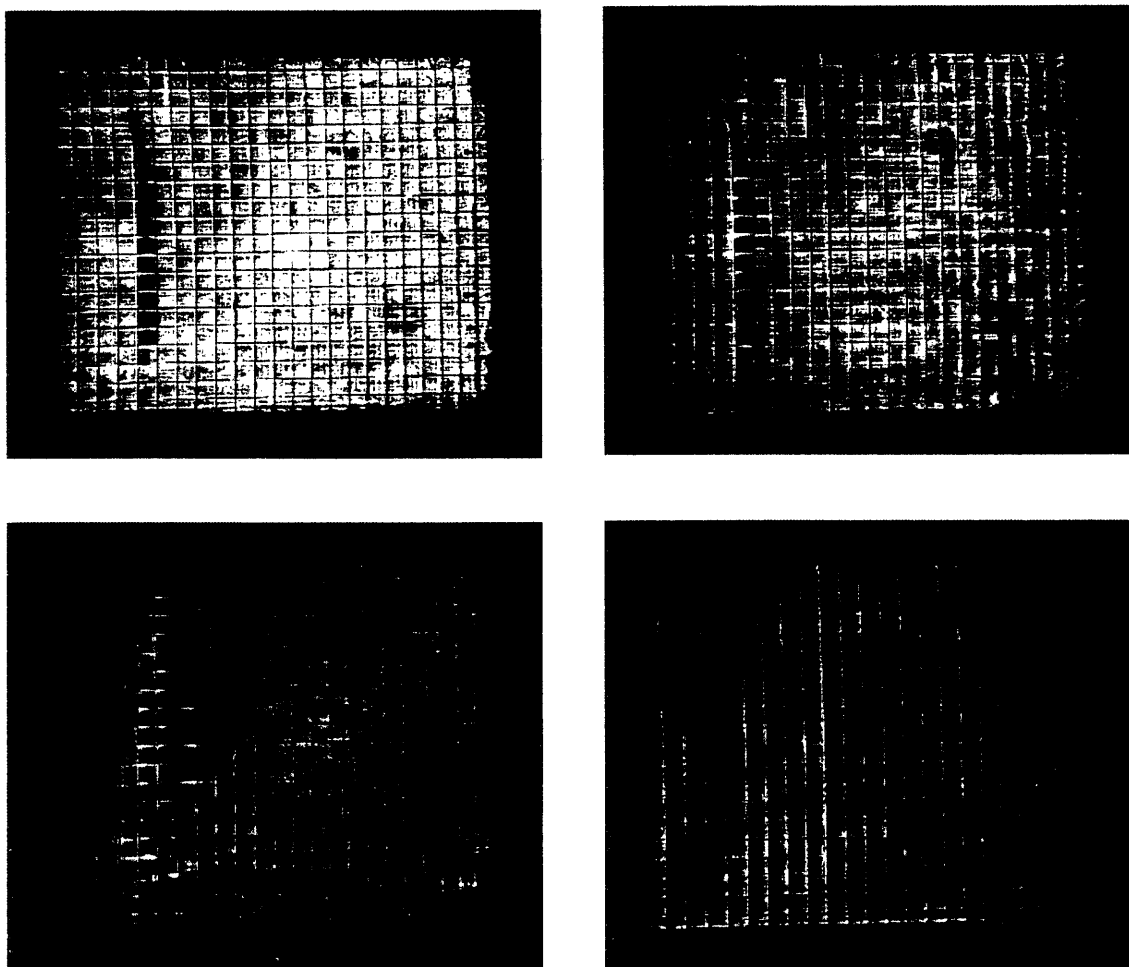


Figure 4-9. Excitation of 3-iodoanisole at 800 nm by a single pump pulse at varying intensities. Clockwise from top left: $6 \mu\text{J}/\text{cm}^2$, $12 \mu\text{J}/\text{cm}^2$, $25 \mu\text{J}/\text{cm}^2$, $35 \mu\text{J}/\text{cm}^2$.

of the pump beam (the probe is oriented normal to the plane of the sample), the volume of excited sample is larger in cross-section. The material response is mapped spatially onto the profile of the probe beam, resulting in an apparently “broadened” electronic response which can persist for picoseconds. Figure 4-9 illustrates this phenomenon for 800 nm excitation of 3-iodoanisole at different pump pulse intensities. Note how the initial strongly-modulated response lasts for roughly 300 fs at the lowest excitation intensity and appears to persist for nearly 1.5 ps at the highest intensity. This effect is due to a larger volume of excited sample, and can be eliminated with a collinear pump-probe geometry.

It should also be noted that the threshold for continuum generation in liquids is typically lower than for solids, which can limit the useful operating range of the single-shot instrument. In practice, it would be preferable to perform standard pump-probe experiments on liquids using a flow cell rather than to pursue single-shot methods, so this is not a significant limitation. However, with photochemically active liquids in cryostats, high-pressure cells, or other non-flowing apparatus, the need for measurements with single or limited numbers of shots could arise.

Single-shot time-resolved Raman scattering data are shown for 3-iodoanisole in Figure 4-10. As before, there is a strong initial modulation of the probe pulse intensity which corresponds to nonresonant interaction with bound valence electrons, and which lasts for about 375 fs. Following this, clear oscillations in the transmitted probe intensity are observed and persist for a few picoseconds. The detection method utilized for all data shown was spectral shifting, with the bandpass filter fixed at 825.4 nm. The oscillations are much more strongly damped than in the case of BGO. For BGO, the oscillatory

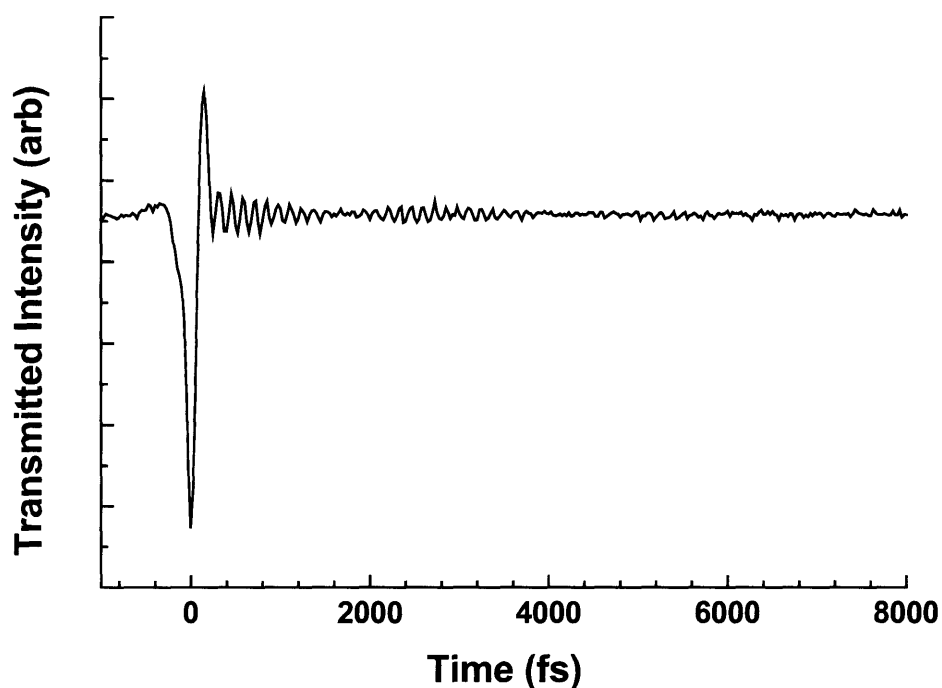


Figure 4-10. Single-shot response of 3-iodoanisole at an excitation intensity of 15 mJ/cm². Oscillation amplitude is a maximum at roughly 400 fs and then rapidly decays away in 1.5 ps. The oscillatory signal returns again at later times and reaches a second local maximum at 2.3 ps.

response was due to excitation of lattice phonons – waves propagating in a well-ordered system of oscillators. In 3-iodoanisole, oscillators are initially synchronized due to the strong laser field but rapidly lose coherence on account of their interactions with neighboring molecules.

Further examination of the data shows that the oscillation amplitude reaches a maximum shortly after the rapid electronic response peak, at about 400 fs, and appears to subsequently dephase such that there is almost no oscillation at 1.9 ps. The signal then begins to grow in amplitude and reaches a local maximum at 2.3 ps, before again decaying away. There appears to be some further very weak oscillatory behavior

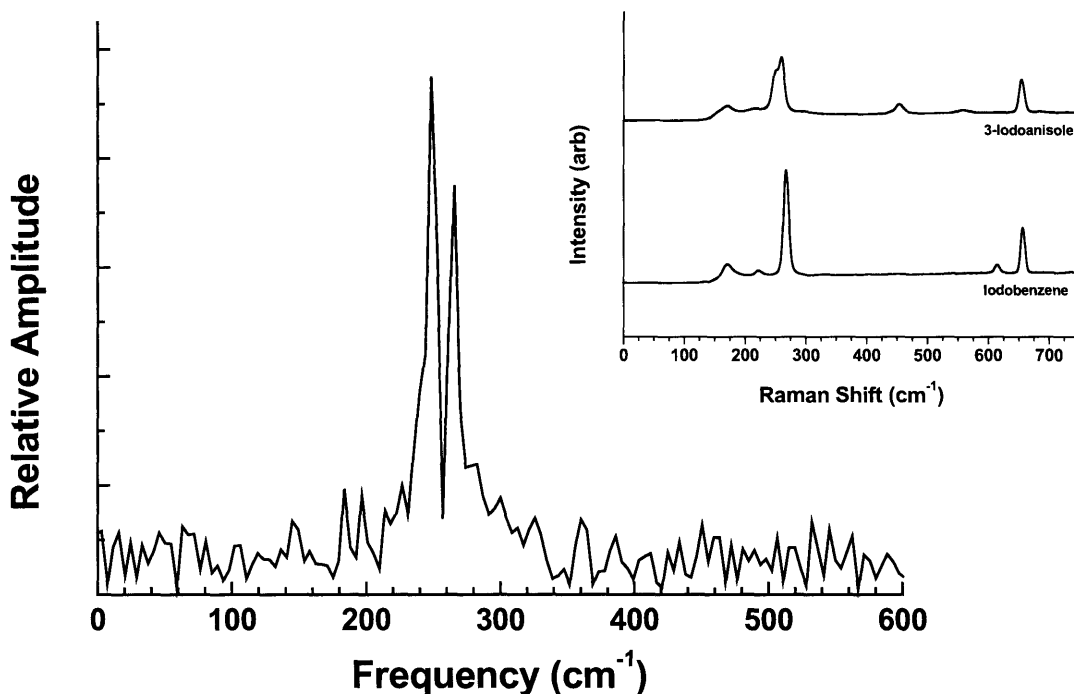


Figure 4-11. Power spectrum of the time-resolved response of 3-iodoanisole. There are two closely spaced modes apparent at 248 cm^{-1} and 264 cm^{-1} . The inset shows the CW Raman spectrum of both iodobenzene and 3-iodoanisole for comparison.

following the second minimum, although the experimental noise level is such that the signal is mostly obscured.

The Raman spectrum of iodobenzene contains a single vibrational frequency corresponding to a carbon-iodine stretching mode at 262 cm^{-1} [45]. The lineshape is relatively broad at room temperature. The power spectrum of the time-resolved response of 3-iodoanisole is shown in Figure 4-11. There are two modes visible, of approximately equal intensity, at 248 cm^{-1} and 264 cm^{-1} . The figure inset shows CW Raman spectra for both iodobenzene and 3-iodoanisole. Although the spectrometer resolution was insufficient to completely resolve the band for 3-iodoanisole at 260 cm^{-1} , the observed lineshape suggests the presence of two closely-spaced modes.

The peculiar behavior of the time-resolved signal can be understood in terms of the excitation of a molecular vibrational wave packet. The broadening of the wave packet is due to both the differing character of propagation in different vibrational modes and/or overtones, and to dephasing from interaction with surrounding bath modes. The latter leads to irreversible wave packet dispersion, but the former is completely reversible. The effect has been observed for ISRS experiments [47,48] as well as for a wide range of time-domain measurements ranging from FT-NMR to femtosecond transient absorption [46].

In order to acquire some insight into the time-dependent oscillatory signal observed for 3-iodoanisole, we first consider that unlike the situation in crystalline solids where vibrational excitation involves collective phonon modes, molecular Raman scattering – especially where the anharmonicity of the ground state electronic potential is sampled – typically involves excitation into a superposition of vibrational eigenstates. The oscillator density in each eigenstate evolves according to that state's energy and vibrational period. Thus, the wave packet superposition state typically starts out with a particular width in both momentum and position space, and the distribution broadens as the coherence evolves.

Reversible dephasing and rephasing of a vibrational superposition state is generally described in terms of wave packet “revivals”. A number of authors have investigated the phenomenon of revivals since the wave packet formalism is ubiquitous in atomic and molecular physics [49-52]. A brief discussion of the origin of the observed time-resolved response of 3-iodoanisole in the context of wave packet revivals will be given by adhering closely to the approach developed by Averbukh and Perelman [53].

As noted previously, in molecular systems, impulsive stimulated Raman scattering excites a superposition of vibrational eigenstates within the ground electronic state manifold of a given oscillator. In certain cases, vibrational level spacings are such that the principal contribution to this superposition is in fact the *only* significant contribution. In general, however, we can write the state of an oscillator as a superposition. Assuming a harmonic manifold, the expression for the wave packet is of the form

$$\psi(x,t) = \sum_{n=1}^{\infty} c_n u_n(x) \exp\left(-\frac{i}{\hbar} E_n t\right) \quad (4.30)$$

where $u_n(x)$ is the (stationary) wavefunction which corresponds to vibrational quantum number n and energy E_n , and the c_n 's are arbitrary constants. The dependence of c_n on the value of n determines the localization of the wave packet in energy space. A coherent state of the harmonic oscillator can be created [54] by setting

$$c_n = \exp\left(-\frac{1}{2}|a|^2\right) \frac{a^n}{\sqrt{(n!)}} \quad (4.31)$$

For the initial condition $t = 0$ and real value of a , the summation in Equation (4.30) can be performed explicitly to give

$$\psi(x,0) = \left(\frac{1}{\pi\sigma^2}\right)^{1/4} \exp\left[-\frac{1}{2\sigma^2}\left(x - \sqrt{2}a\sigma\right)^2\right] \quad (4.32)$$

where the harmonic oscillator expression for E_n

$$E_n = \hbar\omega\left(n + \frac{1}{2}\right) \quad (4.33)$$

has been used. In addition, the parameter σ is given by

$$\sigma = \sqrt{\frac{\hbar}{M\omega}} \quad (4.34)$$

where M is the mass of the oscillator. The wave function $\psi(x,0)$ is the ground state eigenfunction displaced from the equilibrium point to position $x_m = 2^{1/2} a\sigma$. The wave packet is unchanged in shape at x_m and has dispersion which is of the order of the zero-point oscillatory fluctuations. The evolution of the wave packet is governed by the time propagator in the form of a Green's function:

$$\psi(x,t) = \int dx' G(x,t;x',0) \psi(x',0) \quad (4.35)$$

The Green's function for a harmonic oscillator is calculated as [55]:

$$G(x,t;x',0) = \sqrt{\frac{M\omega}{2\pi i\hbar \sin \omega t}} \exp \left[\frac{iM\omega}{2\hbar \sin \omega t} \left[(x^2 + x'^2) \cos \omega t - 2xx' \right] \right] \quad (4.36)$$

Using Equations (4.35) and (4.36), the probability distribution for the oscillator's vibrational wavefunction can be evaluated:

$$|\psi(x,t)|^2 = \sqrt{\frac{1}{\pi\sigma^2}} \exp \left[-\frac{1}{\sigma^2} (x - \bar{x}(t))^2 \right] \quad (4.37)$$

The overbar indicates the mean value in Equation (4.37), and the average is calculated for the oscillator displacement in standard fashion:

$$\bar{x}(t) = \int dx \psi^*(x,t) x \psi(x,t) = x_m \cos \omega t \quad (4.38)$$

The average displacement of the oscillator shifts between $-x_m$ and $+x_m$ at frequency ω , where the classical oscillation period for the wavepacket is defined as $T_{cl} = 2\pi/\omega$. Generally, the oscillations in any potential well become quasi-classical for large displacements from equilibrium, since the average value of n becomes large.

For the harmonic oscillator, the uncertainties in position and momentum are independent of time and are given by

$$\Delta x = \frac{\sigma}{\sqrt{2}} \quad (4.39)$$

$$\Delta p = \frac{\hbar}{\sqrt{2}\sigma}$$

such that their product is a minimum. The implication is that the wave packet evolves without spreading over an arbitrarily long time (except, of course, for dispersion due to interaction of the coherent state with bath modes of the environment, which is not treated here).

In molecular systems, potentials are not harmonic, even for moderate n values, and a superposition state which samples this anharmonicity will evolve in a slightly different manner. Consider that the frequency spacing $\omega_{n+1,n}$ between levels $(n+1)$ and n is nearly equidistant (but not exactly so), such that the following relationship holds:

$$\omega_{n+1,n} \approx \frac{1}{\hbar}(E_{n+1} - E_n) \approx \omega_{cl}(E) = \frac{2\pi}{T_{cl}(E)} \quad (4.40)$$

The subscript cl indicates the classical frequency or period. The difference between adjacent energy gaps is a function, to first order, of the potential's anharmonicity according to

$$\omega_{n+1,n} - \omega_{n,n-1} \approx \hbar \omega_{cl} \frac{\partial \omega_{cl}}{\partial E} \quad (4.41)$$

Alternatively, the energy E can be expanded about the mean value for the wave packet in the form of

$$E \approx E_n + 2\pi\hbar \frac{(n-\bar{n})}{T_{cl}} \pm 2\pi\hbar \frac{(n-\bar{n})^2}{T_{rev}} + \dots \quad (4.42)$$

where the \pm refers to the sign of the derivative in Equation (4.41) and once again, the overbar indicates the mean value – in this case, the mean value of the vibrational

quantum number n of the states which constitute the wave packet. In Equation (4.42), in addition to the classical period T_{cl} , another period emerges which is purely quantum-mechanical in nature. It is referred to as the revival period, and is expressed as

$$T_{rev} = 2T_{cl} \left(\hbar \left| \frac{\partial \omega_{cl}}{\partial E} \right| \right)^{-1} \quad (4.43)$$

It is clear from Equation (4.43) that the revival period $T_{rev} \gg T_{cl}$. Nonetheless, it plays an important role in the evolution of the wave packet. Taking only the first three terms in Equation (4.42) and substituting for E in Equation (4.30), we find that

$$\psi(x, t) = \sum_m c_m u_m(x) \exp \left[-2\pi i \left(\frac{mt}{T_{cl}} + \frac{m^2 t}{T_{rev}} \right) \right] \quad (4.44)$$

$$m = n - \bar{n}$$

The sum in Equation (4.44) is carried out over all states which contribute to the wave packet. At early times such that $t \ll T_{rev}$ (but t can be larger or smaller than T_{cl}), the phase terms proportional to m^2 in Equation (4.44) are insignificant and the wave packet evolves in classical fashion. After undergoing motion for a single classical period, the packet returns to its original position unchanged. If an experiment is conducted which monitors the evolution of the wave packet, modulation will be observed which corresponds to this classical period. For much longer times, the additional phase terms in Equation (4.44) begin to become important, and cause additional dephasing. However, when $t = jT_{rev}$, where j is any positive integer, the phase contribution from the m^2 terms in Equation (4.44) is an integral multiple of 2π , and contributes no additional broadening to the packet.

Thus, there is a second, purely quantum-mechanical dephasing time T_{rev} which also contributes to the dephasing and rephasing of the overall wave packet. Experimentally, if T_{rev} is not too large, the wave packet revivals should be manifest as a periodic “restoration” of classical oscillations. This is the source of the low-frequency envelope observed in the time-resolved Raman scattering data for 3-iodoanisole. There is no evidence of the revival frequency in the power spectrum because the low-frequency peak is removed by the algorithm which subtracts the DC component of the Fourier transform. It is clear that the evolution of the vibrational oscillations in 3-iodoanisole is fundamentally quantum-mechanical in nature, and distinctly different from what might be described as the quasi-classical lattice vibrations of bismuth germanate.

4.4 Conclusion

In this chapter, the very first (to our knowledge) single-shot impulsive stimulated Raman scattering measurements have been presented for two very different systems. The results show that the single-shot technique is sensitive enough to uncover surprising detail regarding the evolution of even weak sample responses. However, the data shown so far only demonstrate the capabilities of the instrument, without motivating its application. In the next three chapters, we will apply the single-shot technique to examine classes of materials which are perturbed well beyond equilibrium conditions to the point of irreversible structural change. Interrogation of such systems is the primary goal underlying the development of the single-shot method – it enables the investigation of previously unexplored regimes of physics and chemistry.

References

- [1] Shen, Y.R. and Bloembergen, N., *Phys. Rev. A* **137**, 1787 (1965).
- [2] Yan, Y.-X., Gamble, E.B. and Nelson, K.A., *J. Chem. Phys.* **83**, 5391 (1985).
- [3] Yan, Y.-X. and Nelson, K.A., *J. Chem. Phys.* **87**, 6240 (1987).
- [4] Yan, Y.-X. and Nelson, K.A., *J. Chem. Phys.* **87**, 6257 (1987).
- [5] Yan, Y.-X., Cheng, L.-T. and Nelson, K.A., "Impulsive Stimulated Light Scattering", *Advances in Non-linear Spectroscopy* (John Wiley & Sons, 1987).
- [6] Placzek, G., in *Marx Handbuch der Radiologie*, Volume 6, Part II, pp. 205-374 (Akademische Verlagsgesellschaft, Leipzig, 1934).
- [7] Korn, G., Duhr, O. and Nazarkin, A., *Phys. Rev. Lett.* **81**, 1215 (1998).
- [8] Nazarkin, A. *et al.*, *Phys. Rev. Lett.* **83**, 2560 (1999).
- [9] Ruhman, S. *et al.*, *IEEE J. Quant. Electron.* **24**, 460 (1988).
- [10] Ruhman, S. *et al.*, *IEEE J. Quant. Electron.* **24**, 470 (1988).
- [11] Ruhman, S. *et al.*, *Chem. Phys. Lett.* **141**, 16 (1987).
- [12] Weiner, A.M. *et al.*, *J. Opt. Soc. Am. B* **8**, 1264 (1991).
- [13] Dougherty, T.P., Wiederrecht, G.P. and Nelson, K.A., *Ferroelectrics* **120**, 79 (1991).
- [14] Dougherty, T.P. *et al.*, *Ferroelectrics* **135**, 197 (1992).
- [15] Dougherty, T.P., Wiederrecht, G.P. and Nelson, K.A., *J. Opt. Soc. Am. B* **9**, 2179 (1992).
- [16] Grabtchikov, A.S., *Opt. Lett.* **28**, 926 (2003).
- [17] Fischer, P. and Waldner, F., *Solid State Commun.* **44**, 657 (1982).
- [18] Pizzini, S. and Allegretti, F., *Nucl. Instr. Meth. in Phys. Res. A* **279**, 402 (1989).
- [19] Smet, F. *et al.*, *J. Cryst. Growth* **97**, 430 (1989).
- [20] Tarasova, L.S., Kosov, A.V. and Skorikov, V.M., *Izvestiya Akad. Nauk SSSR* **14**, 702 (1978).
- [21] Junod, A. and Roulet, C., *J. Cryst. Growth* **69**, 138 (1984).
- [22] Baglikov, V.B. *et al.*, *Izvestiya Akad. Nauk SSSR* **21**, 830 (1985).

- [23] Kovacs, L. *et al.*, *Appl. Phys. A* **52**, 307 (1991).
- [24] Koepke, Cz. and Lempicki, A., *J. Lumin.* **47**, 227 (1991).
- [25] Koepke, Cz. and Lempicki, A., *Chem. Phys. Lett.* **172**, 224 (1990).
- [26] Koepke, Cz. and Lempicki, A., *Chem. Phys. Lett.* **172**, 227 (1990).
- [27] Pustovarov, V.A. *et al.*, *Nucl. Inst. Meth. in Phys. Res. A* **282**, 595 (1989).
- [28] Casalboni, M. *et al.*, *Phys. Stat. Sol. B* **151**, 347 (1989).
- [29] Kalent'ev, V.A. *et al.*, *Izvestiya Akad. Nauk SSSR* **23**, 521 (1987).
- [30] Yi-fan, G. *et al.*, *Chinese Phys.* **4**, 373 (1984).
- [31] Groom, D.E., *Nucl. Inst. Meth. in Phys. Res.* **219**, 141 (1984).
- [32] Casalboni, M. *et al.*, *J. Lumin.* **31**, 93 (1984).
- [33] Zaldo, C. and Moya, E., *J. Phys. Condens. Matter* **5**, 4935 (1993).
- [34] Zeinally, A.K. *et al.*, *Indian J. Pure Appl. Phys.* **17**, 661 (1979).
- [35] Antonangeli, F., Zema, N. and Piacentini, M., *Phys. Rev. B* **37**, 9036 (1988).
- [36] Medrano, C., Meseguer, F. and Contreras, L., *Phys. Rev. B* **34**, 1308 (1986).
- [37] Chmyrev, V.I. and Skorikov, V.M., *Izvestiya Akad. Nauk SSSR* **19**, 259 (1983).
- [38] Mahdavi, S.M., Lifante, G. and Townsend, P.D., *Nucl. Instr. Meth. in Phys. Res. B* **65**, 251 (1992).
- [39] Jazmati, A.K. and Townsend, P.D., *Nucl. Instr. Meth. in Phys. Res. B* **148**, 698 (1999).
- [40] Link, J., Fontanella, J. and Andeen, C.G., *J. Appl. Phys.* **51**, 4352 (1980).
- [41] Mihailova, B. *et al.*, *Solid State Commun.* **112**, 11 (1999).
- [42] Beneventi, P., Bersani, D. and Lottici, P.P., *Solid State Commun.* **93**, 143 (1995).
- [43] Imaino, W., Ramdas, A.K. and Rodriguez, S., *Phys. Rev. B* **22**, 5679 (1980).
- [44] Venugopalan, S. and Ramdas, A.K., *Phys. Rev. B* **5**, 4065 (1972).
- [45] O'Brien, D. *et al.*, *J. Chem. Phys.* **96**, 62 (1992).
- [46] Gruebele, M. *et al.*, *Chem. Phys. Lett.* **166**, 459 (1990).
- [47] De Silvestri, S. *et al.*, *Chem. Phys. Lett.* **116**, 146 (1985).
- [48] Nelson, K.A. and Ippen, E.P., *Adv. Chem. Phys.* **75**, 1 (1989).
- [49] Eberly, J.H., Narozhny, N.B. and Sanchez-Mondragon, J.J., *Phys. Rev. Lett.* **44**, 1323, 1980.

- [50] Parker, J. and Stroud, C.R., *Phys. Rev. Lett.* **56**, 716 (1986).
- [51] Averbukh, I. Sh. *et al.*, *Phys. Rev. Lett.* **77**, 3518 (1996).
- [52] Averbukh, I. Sh. and Perelman, N.F., *Phys. Lett. A* **139**, 449 (1989).
- [53] Averbukh, I. Sh. and Perelman, N.R., *Sov. Phys. Usp.* **34**, 572 (1991).
- [54] Messiah, A., *Quantum Mechanics* (North-Holland, 1991).
- [55] Feynman, R. and Hibbs, A., *Quantum Mechanics and Path Integrals* (McGraw-Hill, New York, 1965).

Chapter 5

Impulsive Absorption in Semimetals and Semiconductors

Modulation of the bulk reflectivity of semimetals under intense femtosecond irradiation has been studied by several groups over the past 15 years. A number of remarkable features of the measured response are common to all samples under study. Coherent oscillations in reflectivity due to impulsive phonon excitation are frequently observed. Phonon amplitudes, frequencies and dephasing rates scale roughly linearly with pump pulse intensity over a significant intensity range, suggesting that a common mechanism underlies the coupling between strong pump absorption and subsequent material oscillations. Typically, semimetal samples are probed within the aforementioned linear regime, since the observed response tends to plateau just prior to the threshold intensity for permanent sample damage. Little or no attention has been focused on the material dynamics above this threshold – in other words, on the material response *as it undergoes irreversible structural change*. This chapter presents the results of measurements on three different semimetals: bismuth, antimony and tellurium. We examine in particular the phonon “frequencies” of rapidly damped vibrations, the intensity-dependent dephasing rates, and the saturation behavior of phonon amplitudes. In doing so, an extension of the single-shot method to opaque samples is demonstrated successfully.

5.1 Introduction to Ultrafast Photoexcitation of Semimetals

In this section, we will introduce the semimetals that represent the focus of the present investigation, and briefly summarize the existing literature which concerns the optical response of these materials to intense femtosecond pulses.

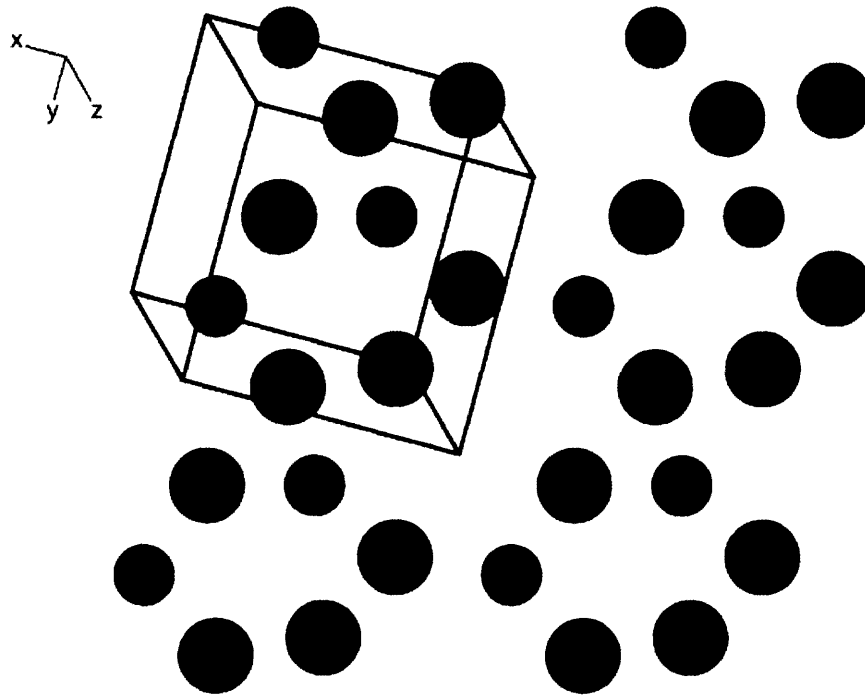


Figure 5-1. Crystal structure of bismuth. Bismuth belongs to monoclinic space group C2/m with two of three unit cell angles equal to 90°. The solid lines in the figure are provided as a guide to the eye.

Bismuth is a group V(A) semimetal which crystallizes in a monoclinic unit cell of space group C2/m. The cell parameters determined for the equilibrium phase of bismuth [1,2] under standard conditions are: $a = 6.674 \text{ \AA}$, $b = 6.117 \text{ \AA}$, $c = 3.304 \text{ \AA}$, $\alpha = 90.00^\circ$, $\beta = 110.33^\circ$, $\gamma = 90.00^\circ$. An illustration of the bismuth crystal structure is shown in Figure 5-1. The solid lines are provided as a guide to visualize the symmetry arrangement of the Bi atoms. The A7 lattice structure, viewed along the y -axis, consists

of alternating triads of bismuth atoms rotated with respect to one another from layer to layer. The overall geometry is effectively a trigonally distorted cubic structure with two atoms per primitive cell.

At $q = 0$, there are three optical phonon modes available for this lattice: a totally symmetric A_{1g} singlet and a doubly degenerate E_g mode [3]. All modes are Raman active but IR inactive, with the following first-order Raman tensors [4]:

$$A_{1g} = \begin{pmatrix} a & 0 & 0 \\ 0 & a & 0 \\ 0 & 0 & b \end{pmatrix} \quad (5.1)$$

$$E_g = \begin{pmatrix} c & 0 & 0 \\ 0 & -c & d \\ 0 & d & 0 \end{pmatrix}, \quad \begin{pmatrix} 0 & -c & -d \\ -c & 0 & 0 \\ -d & 0 & 0 \end{pmatrix}$$

The frequencies of these modes have been determined experimentally [5] via CW Raman scattering and are 98 cm^{-1} for the A_{1g} mode and 74 cm^{-1} for the E_g modes. The scattering cross-sections for both symmetry classes have also been measured experimentally [3], and it has been found that the A_{1g} mode cross-section is a factor of 5 larger than the cross-section for the E_g modes. Accordingly, the A_{1g} mode represents the most likely candidate for photoexcitation in our single-shot experiments.

The crystal structure of antimony is shown in Figure 5-2. Antimony crystallizes in an $R\bar{3}m$ space group. The lattice is trigonal with $\alpha = \beta = 90^\circ$, $\gamma = 120^\circ$ and unit cell dimensions $a = b = 4.307 \text{ \AA}$, $c = 11.273 \text{ \AA}$ [6]. The similarity to the bismuth lattice is apparent in the figure; for antimony, the three-atom triads are of slightly higher symmetry, leading to an overall lattice of a higher symmetry class. Analysis of the structure of antimony [3] reveals that it supports Raman active vibrations of exactly the

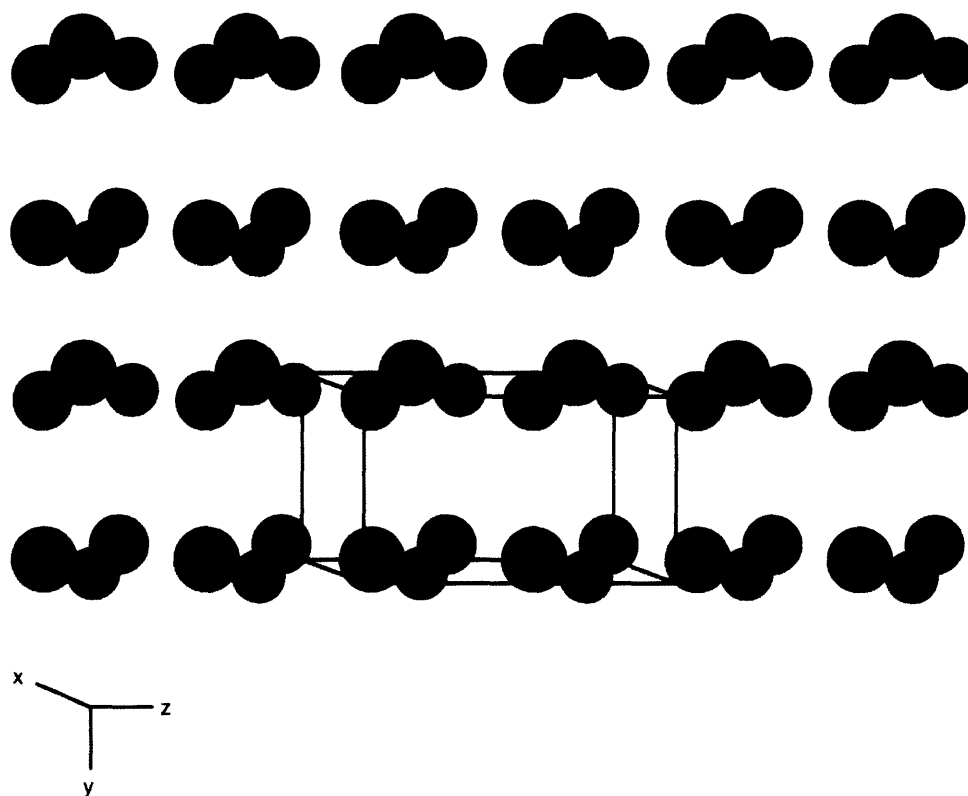


Figure 5-2. Crystal structure of antimony. The lattice structure is trigonal, with space group R3-mh. As before, the solid lines are included as a guide to visualize the symmetry of the lattice.

same symmetry as bismuth: one A_{1g} mode and a doubly degenerate E_g mode, with Raman tensors as in Equation (5.1). The relevant A_{1g} mode frequency in antimony has also been determined experimentally as 152 cm^{-1} [7].

Finally, structure of tellurium is shown in Figure 5-3. Like antimony, tellurium crystallizes in a trigonal lattice, in this case with space group $P3_121$. The primitive cell consists of three atoms located at $(u, 0, 1/3)$, $(0, u, 2/3)$ and $(-u, -u, 0)$. The structure in Figure 5-3 is viewed along the z -axis and essentially consists of helices of Te atoms (three per turn) arranged in a hexagonal array. Equilibrium lattice constants are found experimentally to be $a = 4.456 \text{ \AA}$ and $c = 5.927 \text{ \AA}$, the ratio of the helical radius to the interhelical spacing is $u = 0.2633$, and the vertical atom spacing is $c/3$ [1]. Nearest

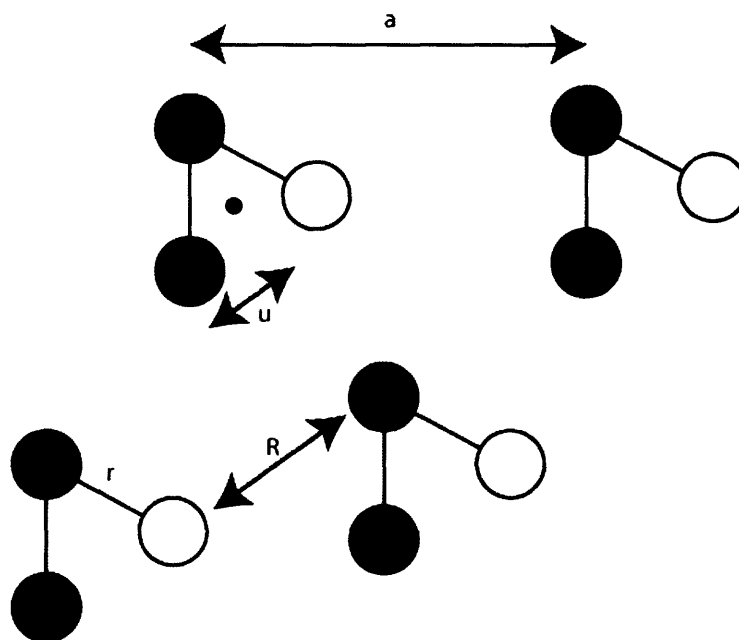


Figure 5-3. Crystal structure of tellurium viewed along the z -axis. Tellurium atoms of the same shading lie in the same plane. The dark atoms lie below the plane of the paper and the white atoms lie above the paper plane. The lattice constant a characterizes the interhelical spacing, u represents the helix spacing, and the parameters r and R correspond to the nearest neighbor and next-nearest neighbor distances. The figure is adapted from reference 10.

neighbor bond lengths, from the same reference, are found to be $r = 2.834 \text{ \AA}$, and next-nearest neighbor bond lengths are $R = 3.494 \text{ \AA}$. Tellurium exhibits six unique optical phonon modes [8,9], all of which have been detected experimentally. As in the case of bismuth and antimony, the mode of largest scattering cross-section is of A_{1g} symmetry – the so-called “breathing mode” for which the helical radius u changes with a and c constant. Also in concert with bismuth and antimony, tellurium is optically anisotropic according to the polarization of the laser pulse relative to the z -axis.

A considerable amount of experimental work directed toward the measurement and control of optical responses in bismuth, antimony and tellurium via intense femtosecond irradiation has already been undertaken by several research groups. Cheng, Dresselhaus and co-workers were first to report the observation of large modulations in

the bulk reflectivity of bismuth, antimony and tellurium following single-pulse excitation at the Ti:sapphire fundamental frequency [11-15]. Strong modulation of the reflectivity of samples of Ti_2O_3 undergoing a semiconductor-semimetal transition was also observed. Results were interpreted within the framework of a phenomenological first-principles model referred to as “displacive excitation of coherent phonons” (DECP) which postulates that promotion of electrons from the valence band to the conduction band due to strong absorption at the pump wavelength alters the effective lattice potential by reducing electronic screening of individual nuclear positive charges. As a result, the net repulsive force between nuclei increases, leading to rapid lattice expansion (in the impulsive limit) along symmetric coordinates, which accounts for the observation that typically, only modes of A_1 or A_{1g} symmetry are observed in the time-resolved reflectivity data. Modulation of the bulk reflectivity in the semimetals can be very large – up to 1.5% at the excitation intensities employed.

DeCamp and co-workers [15] have extended the results for bismuth to a regime where measured reflectivity changes no longer scale linearly with excitation fluence, and the laser intensity approaches the single-shot damage threshold for the material. They have also explored the possibility of manipulating the material dynamics by variably-delayed two-pulse excitation sequences.

Hase and colleagues, in a series of publications, have also investigated the impulsive excitation of A_{1g} phonons in single-crystal and thin film bismuth samples using single pulses and multiple pulse sequences [16-21]. In addition to demonstrating the capability of controlling vibrational amplitudes in the sample, their sensitive

measurements have successfully identified an oscillatory component of reflectivity which is due to coherent excitation of the degenerate E_g modes of bismuth.

Finally, Misochko and co-workers, through careful room temperature measurements [22,23], have identified the presence of a squeezed phonon state [24-26] in crystalline bismuth through its phase-dependent noise signature. At 10 K, phonon autoechoes are observed in bismuth, though anomalous dephasing is too rapid at room temperature to observe the phenomenon.

The examination of coherent phonons in antimony has encompassed similar themes. Two studies in particular highlight important aspects of the coherence excitation process and nonequilibrium character of the material state. In the first, Garrett and co-workers [27] have examined the phase of reflectivity oscillations as a function of the angle between pump and probe polarizations, and have observed that evolving coherences with phase character intermediate between the limiting cases of DECP and ISRS can be generated. This has led the authors to construct a microscopic, quantum mechanical interpretation for the general case of semimetal impulsive absorption which renders DECP as a special case of a more general coherent Raman scattering mechanism.

Misochko and colleagues have examined the noise properties of antimony phonons [28] and, based upon the phase dependence of the measured variance, have inferred the presence of squeezed phonon states in analogous fashion to their work on bismuth phonons.

Phonon dynamics on an impulsive time scale in tellurium have been examined by Kurz and co-workers, who have noted a continuous red shift of the phonon frequency with increasing excitation laser fluence [29-31]. Two-pulse experiments by this group

are also used to demonstrate that the shift is predominantly electronic in character. Tangney and Fahy have provided perhaps the most comprehensive theoretical treatment of DECP via density functional plane-wave pseudopotential calculation of the time-dependent reflectivity oscillations, accounting for carrier diffusion and recombination, optical absorption and A_1 phonon anharmonicity [32-33]. Their results imply that carrier recombination rates are relatively slow – from a few tens to hundreds of picoseconds – at moderate excitation densities. Further, for low fluences (i.e. the “linear scaling” region of tellurium), the intensity dependent change in the phonon frequency is calculated as -0.085 THz per mJ/cm^2 which agrees reasonably well with measured data.

A number of other semiconductor systems have also been explored with regard to their time-dependent reflectivity [34-37], in analogous fashion to bismuth, antimony and tellurium. Of particular note are systems based upon GaAs where it is proposed that temporal waveguide structures can be induced due to large changes in the bulk index of refraction which is responsible for time-dependent reflectivity oscillations.

5.2 Apparatus for Time-Resolved Reflectivity Experiments

Our desire to investigate samples of bismuth, antimony and tellurium at high excitation fluences (including above the threshold fluence for permanent material damage) naturally suggests the use of single-shot methods already developed and outlined in this thesis. However, all of the samples we have employed so far have been transparent and of good optical quality in order to ensure recovery of the material response with an acceptably low contribution from systematic instrument and

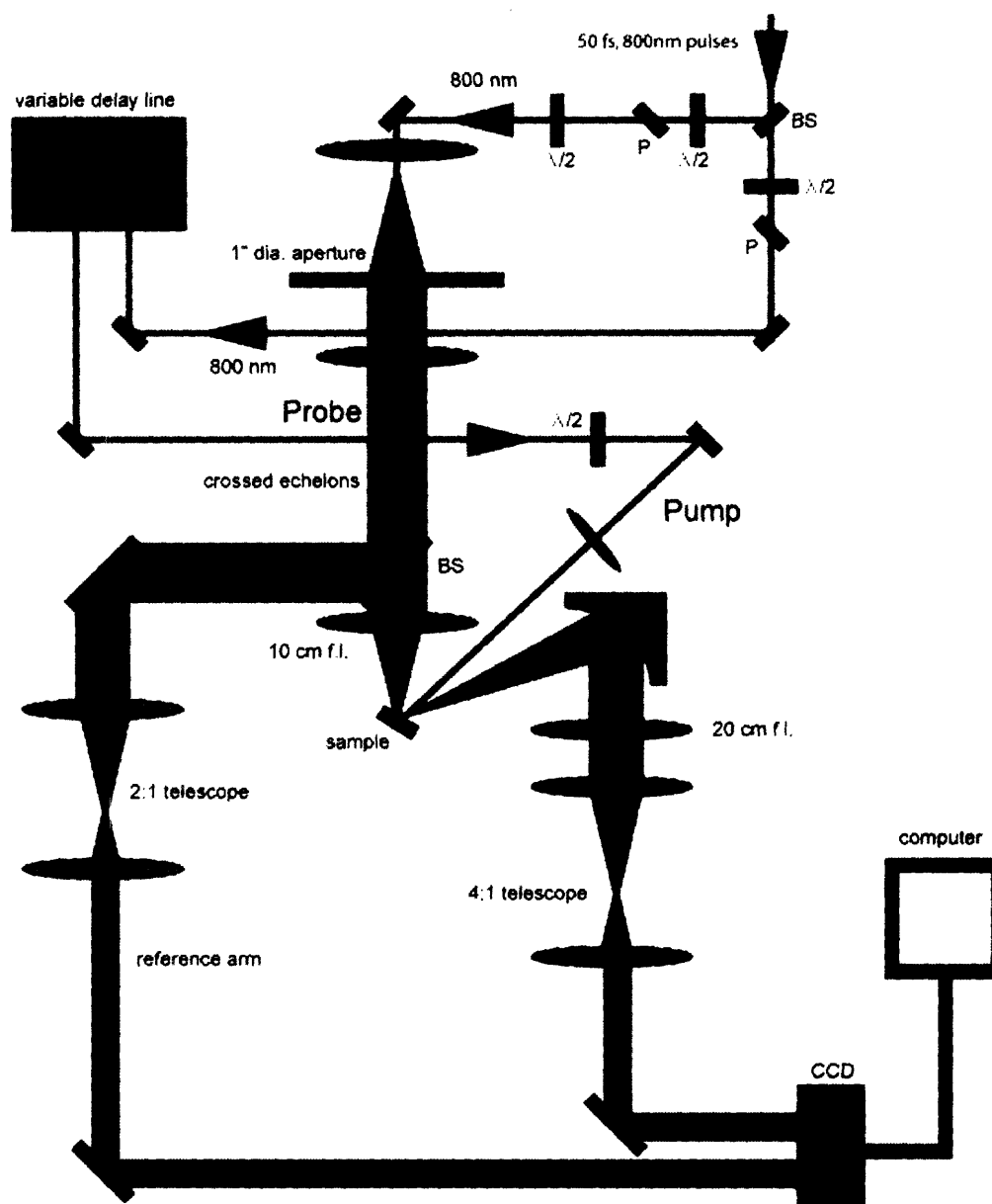


Figure 5-4. Single-shot experimental apparatus for performing experiments in reflectivity mode. Instead of imaging the echelon grid through the sample, the polished sample surface acts as a mirror. The reflected echelon image is collimated by a curved mirror and 20 cm f.l. lens combination and then reduced in size by a factor of four prior to being imaged onto the surface of a CCD camera. The reference arm of the apparatus remains unchanged from the transmission version of the experiment.

measurement noise. Since the three semimetals of interest are opaque, the single-shot experiment must be conducted in reflection mode, using the surface of the sample as a mirror. Single crystal ingots of Bi, Sb and Te were obtained from commercial sources and polished using a fine-grit, water-based rotary polisher to achieve high surface reflectivity. The samples were subsequently inserted into a modified single-shot apparatus, as shown in Figure 5-4. The echelon image projected onto the probe beam reflects from the surface of the sample and is re-collimated by a curved mirror with a radius of 200 cm and a 20 cm f.l. lens. Due to the increased propagation distance after the sample relative to the transmission version of the experiment, the collimated echelon image must be reduced by a factor of four prior to being re-imaged at the surface of the CCD camera. The reference arm in the experiment remains unchanged from the previous configuration. In addition, the pump beam alignment requires no modification other than small adjustments of the relative delay time.

Single-shot experiments are conducted using 800 nm, vertically polarized pulses gated out from the amplifier, as described previously. The spatial isolation of pump and probe enables the use of common wavelengths. Narrow bandpass filtering is not employed in these experiments, as the signal arises from time-dependent changes in the sample reflectivity, an effect which naturally induces modulation in reflected light intensity.

In some experiments, it is desirable to generate up to four separate pump pulses, where the relative delay of each can be independently controlled. This is accomplished with a series of beamsplitters and delay lines as shown in Figure 5-5. Three successive beamsplitters with R/T ratios of 1:3, 1:2 and 1:1 are used to split an initial input pulse

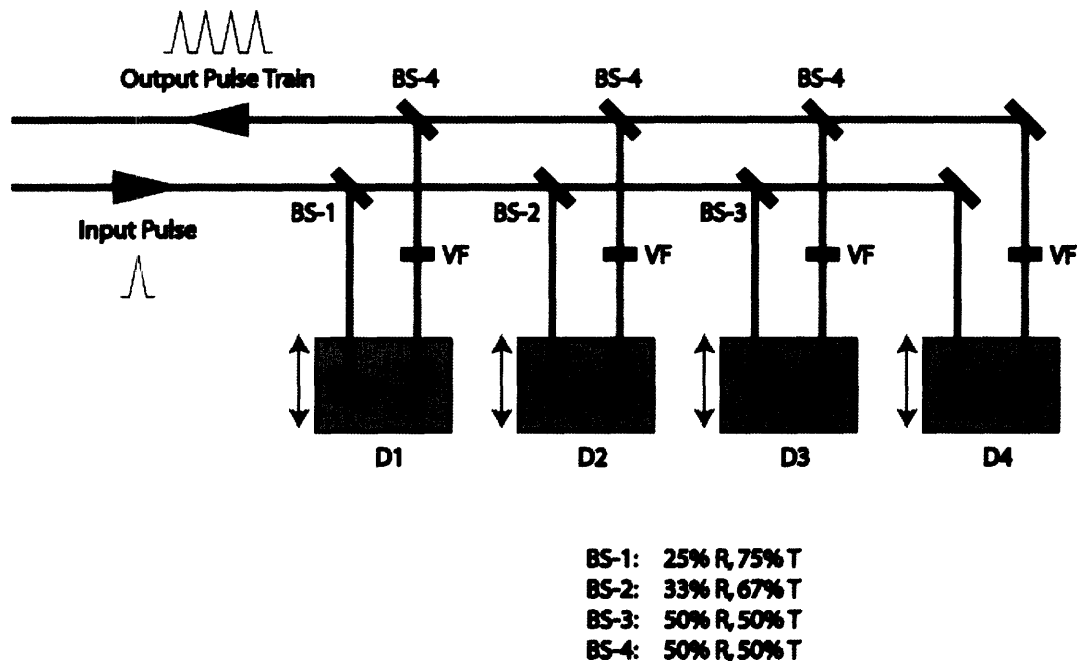


Figure 5-5. Generation of a multiple-pulse pump train. A single input pulse is split by a series of beamsplitters with R/T ratios of 1:3, 1:2 and 1:1 into four independently delayed replicas. A variable filter (VF) in each beam path permits amplitude attenuation of each beam. The four beams are recombined such that they traverse a common optical path to the sample, permitting multiple-pulse excitation of coherent responses.

into four replicas. Adjustment of the intensity of each pulse is achieved by a variable filter (VF) following the delay line. The four beams are recombined such that they travel along a common optical path, and each is focused by the same subsequent optical elements onto the surface of the sample. In this way, multiple-pulse excitation of coherent responses in the semimetal samples is possible.

5.3 Single-Shot Coherent Phonon Dynamics in Bi, Sb and Te

The following figures illustrate the results of single-pump experiments on the three semimetals of interest. The change in reflectivity (where the intensity units are

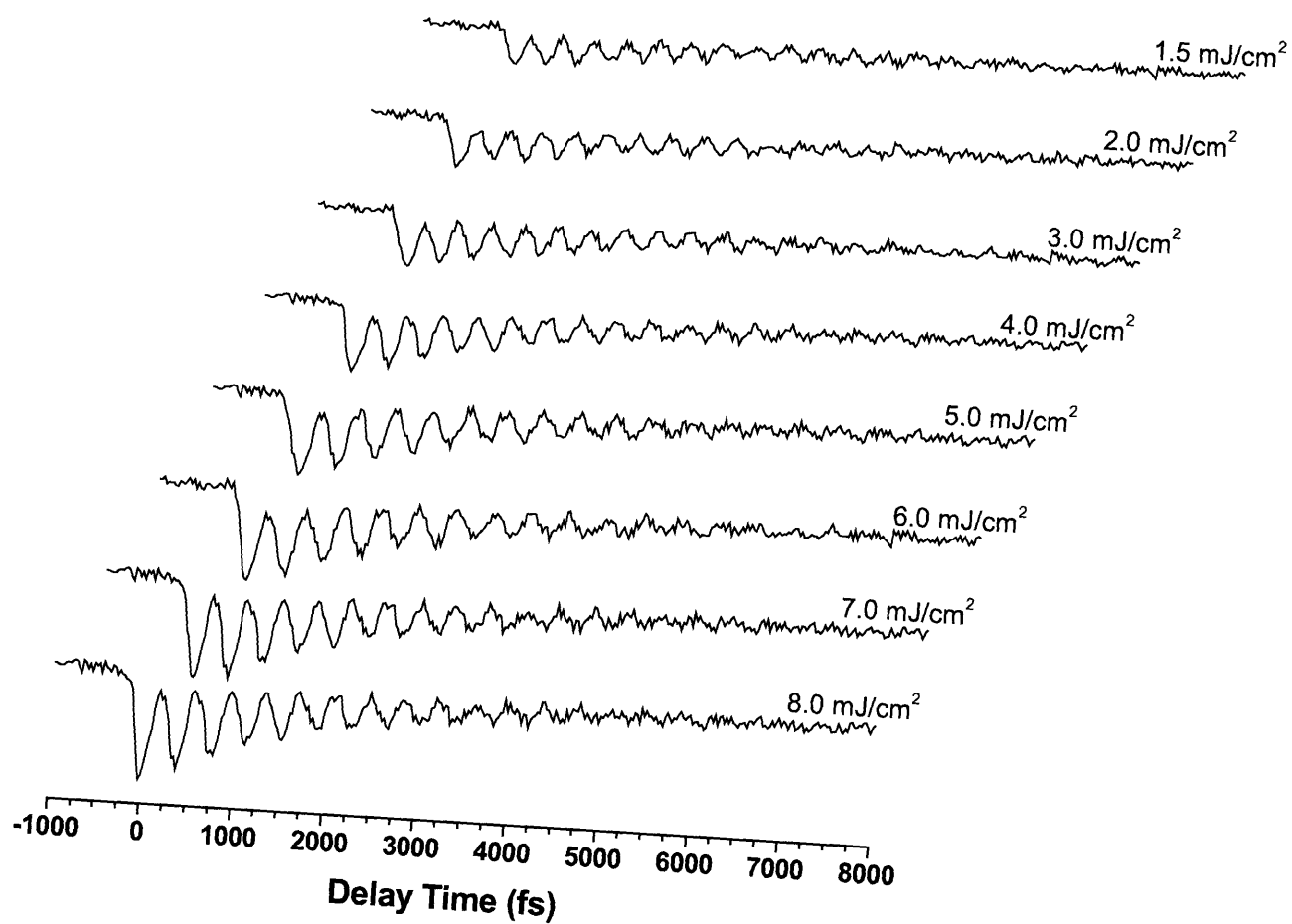


Figure 5-6. Time-dependent single-shot reflectivity of single crystal bismuth at 800 nm at a range of pump pulse intensities. Both the amplitude of the observed oscillations and the electronic background signal due to newly generated conduction band electrons increase with increasing pump fluence (indicated on each data trace). The data sweeps shown here all correspond to below-damage-threshold excitation.

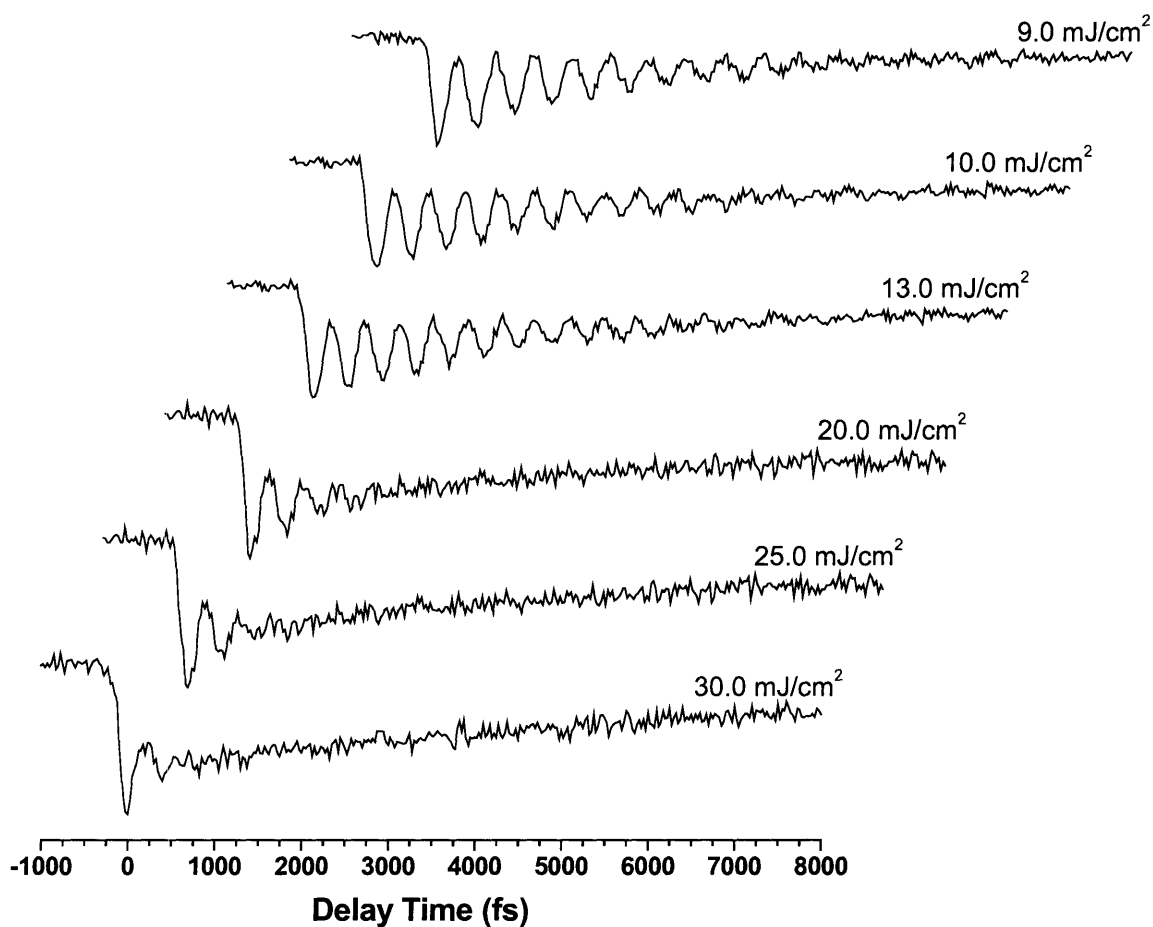


Figure 5-6 (cont'd). Time-dependent single-shot reflectivity of single crystal bismuth at 800 nm at a range of pump pulse intensities. Both the amplitude of the observed oscillations and the electronic background signal due to newly generated conduction band electrons increase with increasing pump fluence (indicated on each data trace). The 25.0 mJ/cm² trace represents excitation at the bismuth single-shot damage threshold, although multi-shot structural damage may occur at lower fluences.

arbitrary) is plotted as the ordinate against probe temporal delay. Multiple scans are shown on each plot for comparative purposes. Figure 5-6 illustrates the response of single crystal bismuth samples at a range of pump pulse fluences. For excitation intensities lower than 1.0 mJ/cm^2 it is difficult to reliably measure the sample response owing to noise contributions to the data. For fluences from 1.5 mJ/cm^2 and greater, large oscillations of the sample reflectivity are observed, superimposed on a monotonically decaying background signal. The responses are qualitatively similar at all intensities, but a number of trends are apparent. The magnitude of the background signal and its decay rate increase with increasing pump fluence. The oscillatory contribution to the signal also increases strongly with intensity, as does the corresponding dephasing rate associated with the oscillations. As the damage threshold (25.0 mJ/cm^2) is approached, the apparent oscillation dephasing time decreases dramatically. For 20.0 mJ/cm^2 excitation, only about 3 oscillation cycles are observed prior to the complete loss of coherence in the sample. At 25.0 mJ/cm^2 , roughly two cycles are observed. Rapid dephasing occurs at this intensity within a couple of vibrational periods. At even higher 30.0 mJ/cm^2 fluence, the loss of coherence occurs in fewer than two cycles.

Optic phonons are a very sensitive probe of lattice geometry in materials such as bismuth, and the loss of coherence suggests the possibility that at very high pulse intensities, rapid changes in the structure of the bulk crystal are induced. The apparent time scale for structural modification is important since it is suggestive of possible physical mechanisms. Thermal excitation of lattice modes and eventual melting is a process which occurs within nanoseconds; however, the possible structural changes in

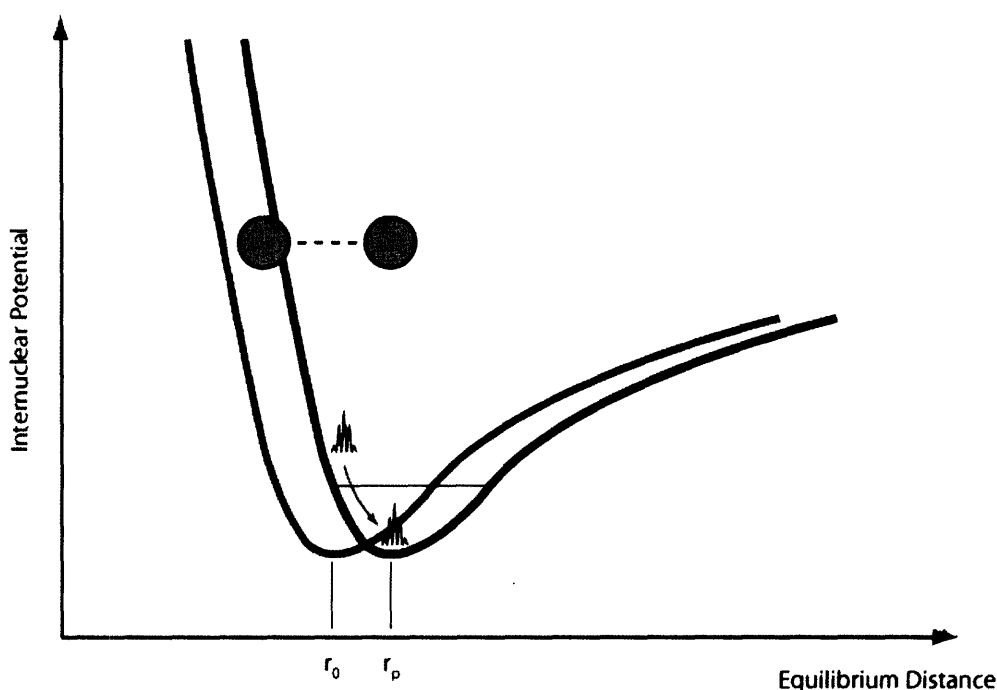


Figure 5-7. Illustration of the origin of the cosine-like phase dependence of oscillations in bulk reflectivity due to impulsive absorption in bismuth. Absorption at the pump wavelength promotes valence electrons to the conduction band and effectively shifts the equilibrium lattice potential (grey curve, minimum r_0) to a new, larger separation (black curve, minimum r_p) on account of the reduced nuclear charge screening. Bismuth atoms experience increased mutual repulsion and motion is directed along coordinates which correspond to “breathing modes” of A_1 symmetry. A vibrational wave packet is created via this process, initially located at the inner turning point of the lattice potential. The packet evolves according to the specific shape of the black curve; however, since the initial position is one of maximum displacement from the equilibrium position, the oscillations have cosine-like phase character.

our experiments suggest a significantly faster process. Interaction with the pump field begins with strong absorption, promoting valence band electrons to the conduction band. The newly generated electron and hole carriers can diffuse and recombine, which commonly occurs on a time scale of tens of picoseconds [16-19]. The rapid change in the distribution of valence band electrons occurs within a time window of a few femtoseconds – essentially instantaneous when compared with the duration of the pump

pulse (50 fs). The effect of this *impulsive* absorption is therefore to change the equilibrium lattice potential by reducing the effective screening of positive nuclear charges. Atoms of the lattice therefore begin to adjust to the new potential. Since the potential is more repulsive than previously, atoms move along directions which lead them away from nearest neighbors. Normal modes which have a “breathing”-like motion correspond to this type of displacement, where the entire lattice expands locally. For this reason, the modes of A_1 or A_{1g} symmetry are strongly favored for excitation.

It is also notable that by introducing a modified lattice potential in quasi-instantaneous fashion, the lattice atoms are initially in their maximum displacement configuration along the inner wall of the potential. The effect of the impulsive absorption is to create a superposition state of relatively narrow width which then evolves according to the specific shape of the new potential. The situation is illustrated graphically in Figure 5-7. In terms of a classical picture, the motion of the wave packet oscillates back and forth between inner and outer turning points, passing through the zero-displacement minimum. The importance of the initial position of the wave packet is reflected in the phase of the observed oscillations. Since the lattice atoms are *initially* at maximum inner displacement, the amplitude of the oscillatory contribution to the signal is also a maximum at $t = 0$. Thus, the oscillations follow a cosine-like phase dependence. This is fundamentally different from the ISRS mechanism introduced in Chapter 4, for which the oscillatory contribution shows a sine-like phase dependence.

The time-resolved reflectivity data are understood within the context of the impulsive absorption picture by considering the individual contributions to the overall reflectivity. Following initial absorption at $t = 0$, a rapid decrease in reflectivity can be

attributed to the generation of conduction band free electrons. The sign of the change in reflectivity varies from one material to another. For bismuth, the reflectivity falls, whereas for antimony and tellurium, it increases. The physical mechanisms underlying this are complex and are not considered herein. Oscillation of the reflectivity change is immediately apparent, with the cosine-like character alluded to earlier. The oscillations dephase and the “electronic” background contribution also decays in time, with a rate which varies according to excitation fluence.

An expanded view of the data for several excitation intensities is shown in Figure 5-8. The oscillation frequency at 1.5 mJ/cm^2 in Figure 5-6, obtained by linear-prediction singular value decomposition (LP-SVD), is 2.9 THz, which agrees very well with CW Raman measurements [5]. The data in Figure 5-8 show, however, a strong dependence of the oscillation frequency on the pump intensity. Near $t = 0$, the phases of the oscillations at each of the pump intensities shown are the same. The differing frequencies are reflected in the time-dependent change of this relative phase relationship. For instance, the responses at 2.0 mJ/cm^2 and 4.0 mJ/cm^2 show frequencies which are relatively close to one another. It is only after roughly seven vibrational periods that the signals are exactly out of phase. However, the vibrational frequency at 2.0 mJ/cm^2 is markedly higher than the frequency at 9.0 mJ/cm^2 and the oscillations in reflectivity are out of phase after only three vibrational cycles. Such dramatic frequency shifts for the A_{1g} normal mode can only be achieved if the lattice potential of Figure 5-7 shifts dramatically. The results of Figure 5-8 imply that the induced shift is essentially a continuous function of the fraction of valence band electrons which can be successfully transferred to the conduction band.

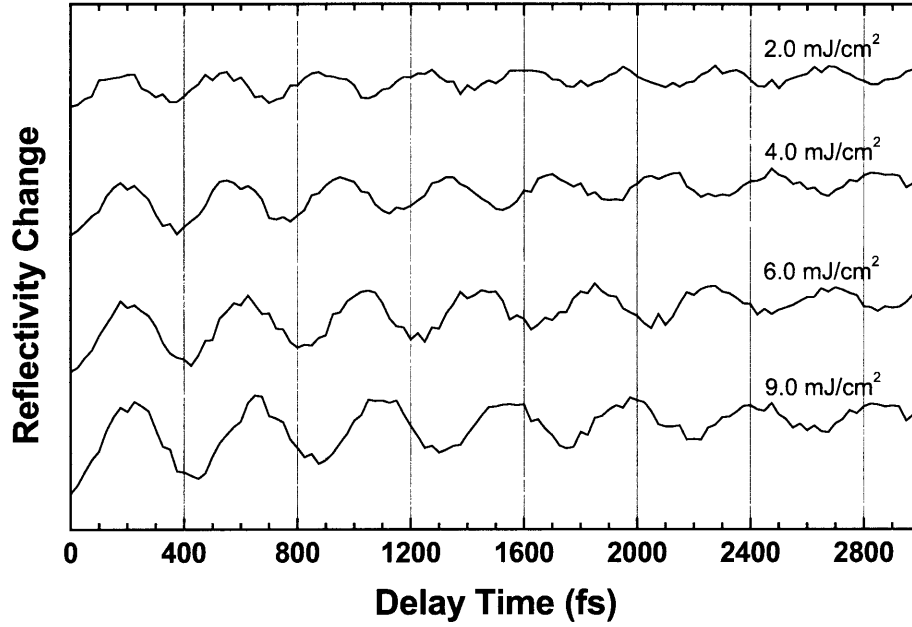


Figure 5-8. Comparison of oscillations in bismuth reflectivity at four different pump pulse fluences. Near $t = 0$, the reflectivity oscillations are all in phase. On account of differing A_{1g} phonon frequencies, the phase relationship changes as a function of time. After seven oscillation cycles, the responses at 2.0 mJ/cm^2 and 4.0 mJ/cm^2 are 180° out of phase, whereas the response for 9.0 mJ/cm^2 excitation is 180° out of phase with the 2.0 mJ/cm^2 response after only three cycles.

The responses at each of the excitation fluences can be fitted to a function of the form

$$\frac{\Delta R}{R} = Ae^{-\beta t} + Be^{-\gamma t} \cos \omega_p t + C \quad (5.2)$$

where the first term on the right hand side represents the electronic contribution to the signal and the second term represents the oscillatory contribution. This permits the extraction of parameters which characterize the coherent response: the phonon frequency ω_p , the oscillation dephasing rate γ , and the oscillation amplitude B . The results of this analysis are shown in Figure 5-9. In all cases, the oscillation parameters scale almost

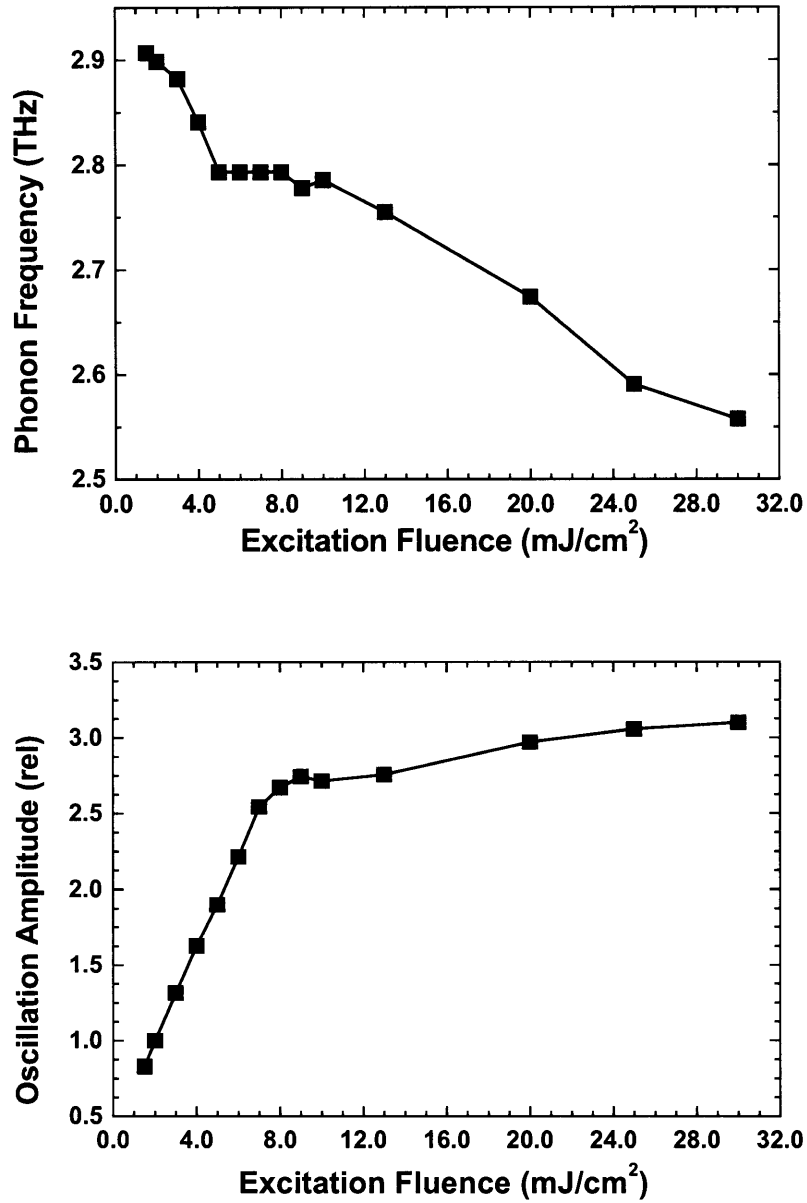


Figure 5-9. Variation of phonon frequency (top) and phonon amplitude (bottom) with excitation intensity in single crystal bismuth. In both cases, the response scales almost linearly with pump intensity to roughly $6.0 \text{ mJ}/\text{cm}^2$, and then a distinct plateau region occurs. The responses at very high intensities also follow a qualitative trend, but it is difficult to extract reliable parameters since there are few oscillations in the data.

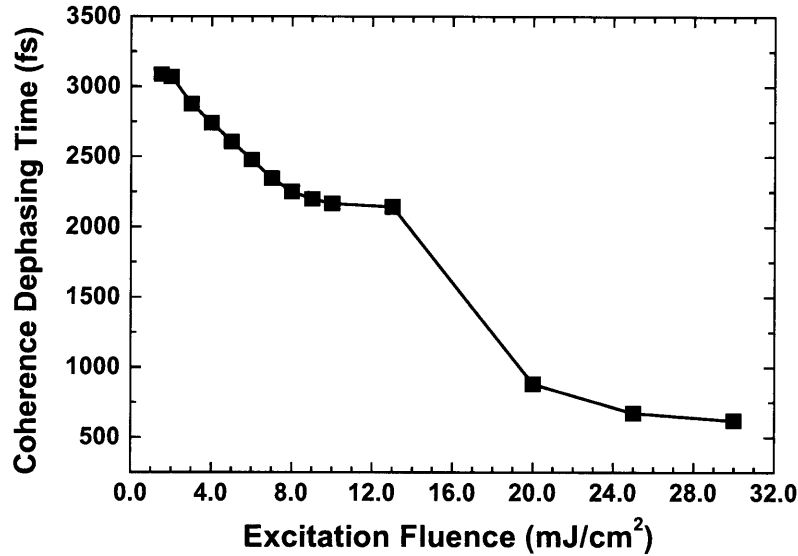


Figure 5-9 (cont'd). Variation of phonon dephasing time with excitation intensity in single crystal bismuth. As before, the response scales almost linearly with pump intensity to roughly 6.0 mJ/cm², and then a distinct plateau region occurs. The high intensity points are determined semiquantitatively due to the small number of cycles in the experimental data.

linearly with pump pulse intensity up to roughly 6.0 mJ/cm², where a distinct plateau in the response is observed. The data points at high intensity follow a qualitatively consistent trend but are not always quantitatively reliable owing to the absence of all but a few cycles in the measured data (and large noise contributions as well). Since the bismuth response arises from the promotion of electrons to the conduction band via absorption, the roughly linear dependence of the oscillation parameters confirms that absorption is a single-photon event. Saturation of the response implies that promotion of additional free carriers to the conduction band does not further increase the modulation of the bulk refractive index. The results shown in Figure 5-9 are consistent with observations of bismuth under similar conditions by other workers [11-15] although to-

date, other groups have only been able to reach fluences above 20 mJ/cm^2 by raster-scanning the sample from one pump-probe pulse pair to the next.

Single-shot excitation of single crystal antimony is undertaken in the same manner as for bismuth, and the results are qualitatively quite similar. Antimony also exhibits strong electronic absorption at 800 nm, and so the impulsive absorption mechanism leads to efficient excitation of the A_1 -symmetry lattice breathing mode. The measured change in reflectivity is shown as a function of probe delay time in Figure 5-10 for a number of different pump pulse intensities. Note that for antimony, the change in reflectivity on photoexcitation is positive.

LP-SVD analysis of the lowest intensity data gives a frequency of 4.5 THz for the phonon mode, in good agreement with other published Sb results [7,11,12]. The data in Figures 5-6 and 5-10 are independently scaled such that direct comparison between the two is not possible. However, it is notable that for bismuth, the maximum change in reflectivity which we were able to induce was 0.35%. By contrast, modulation of the antimony reflectivity is significantly greater, and reflectivity changes of the order of 3% are achieved at the highest fluences shown in Figure 5-10. As for bismuth, the observed phonon amplitude, dephasing rate and frequency all appear to be intensity dependent. The scaling is qualitatively similar to that of bismuth, and in fact the numerical trend (linear dependence, followed by a plateau region) is exactly the same.

The final three data sweeps in Figure 5-10 correspond to pump intensities of 20.0, 25.0 and 30.0 mJ/cm^2 which are near (first) and above (second and third) the antimony single-shot damage threshold. This is the region where the most interesting dynamical

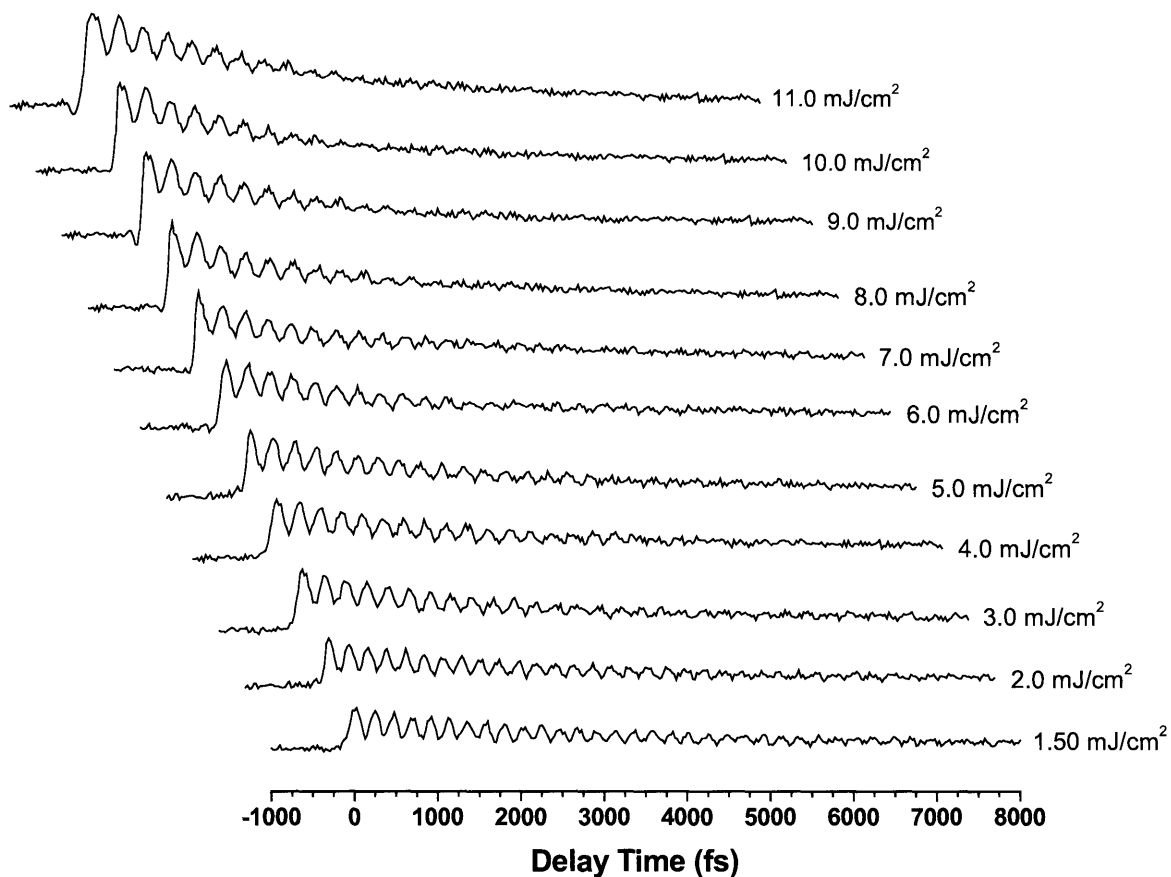


Figure 5-10. Time-resolved reflectivity of single crystal antimony measured in one laser shot. The induced reflectivity change is positive for antimony, and results from impulsive absorption at the pump wavelength of 800 nm. The amplitude of the coherent oscillations increases with increasing pump intensity, and the phonon frequency shifts noticeably lower. The oscillation dephasing rate also appears to increase for more intense pump pulses.

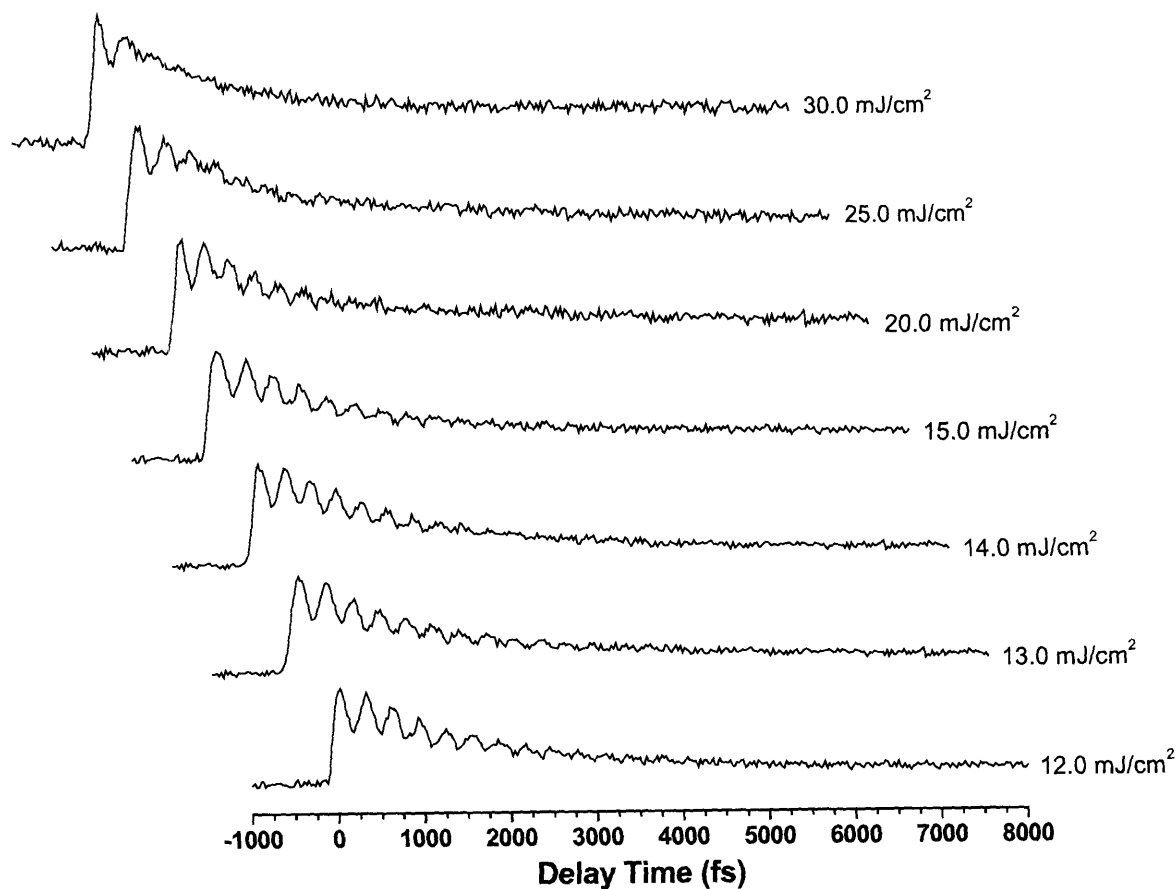


Figure 5-10 (cont'd). Time-resolved reflectivity of single crystal antimony measured in one laser shot. The induced reflectivity change is positive for antimony, and results from impulsive absorption at the pump wavelength of 800 nm. The amplitude of the coherent oscillations increases with increasing pump intensity, and the phonon frequency shifts noticeably lower. The oscillation dephasing rate also appears to increase for more intense pump pulses. The dephasing rate changes dramatically for the last three scans which are in the region of antimony's single-shot damage threshold.

behavior occurs. Oscillation dephasing occurs much more rapidly in direct analogy with the bismuth results. As before, quantitative analysis of the vibrational component of the signal is difficult since there are only a few cycles visible and the noise contribution is higher.

Nonetheless, the antimony response is markedly stronger than the bismuth response and data analysis is more robust. A similar fitting procedure for Equation (5.2) is carried out and the results are shown in Figure 5-11. The linear scaling of the coherent phonon frequency, amplitude and dephasing rate occurs from the lowest intensities up to about 10.0 mJ/cm^2 . The onset of the plateau region is less dramatic for antimony than for bismuth, but is clearly visible. As before, the high intensity parameters are less reliable but appear to be qualitatively correct.

At most fluences, antimony dephasing occurs less rapidly than bismuth dephasing, and given a stronger coherent contribution to the observed signal, Fourier analysis is possible. The power spectrum for several pump intensities is shown in Figure 5-12. At low fluences, the single-peak spectrum is sharp and well-defined. As the intensity increases, the width of the phonon peak increases and the central frequency shifts lower. This observation is similar to the phenomenon of temperature-dependent mode-softening which is common for materials which undergo structural phase transitions. However, in this case the mechanism is considerably different.

In the bottom panel of Figure 5-12, the early-time reflectivity oscillations are shown for several pump intensities. As with bismuth, the intensity-dependent phonon frequency causes the oscillations, which are all initially in phase, to cycle in and out of

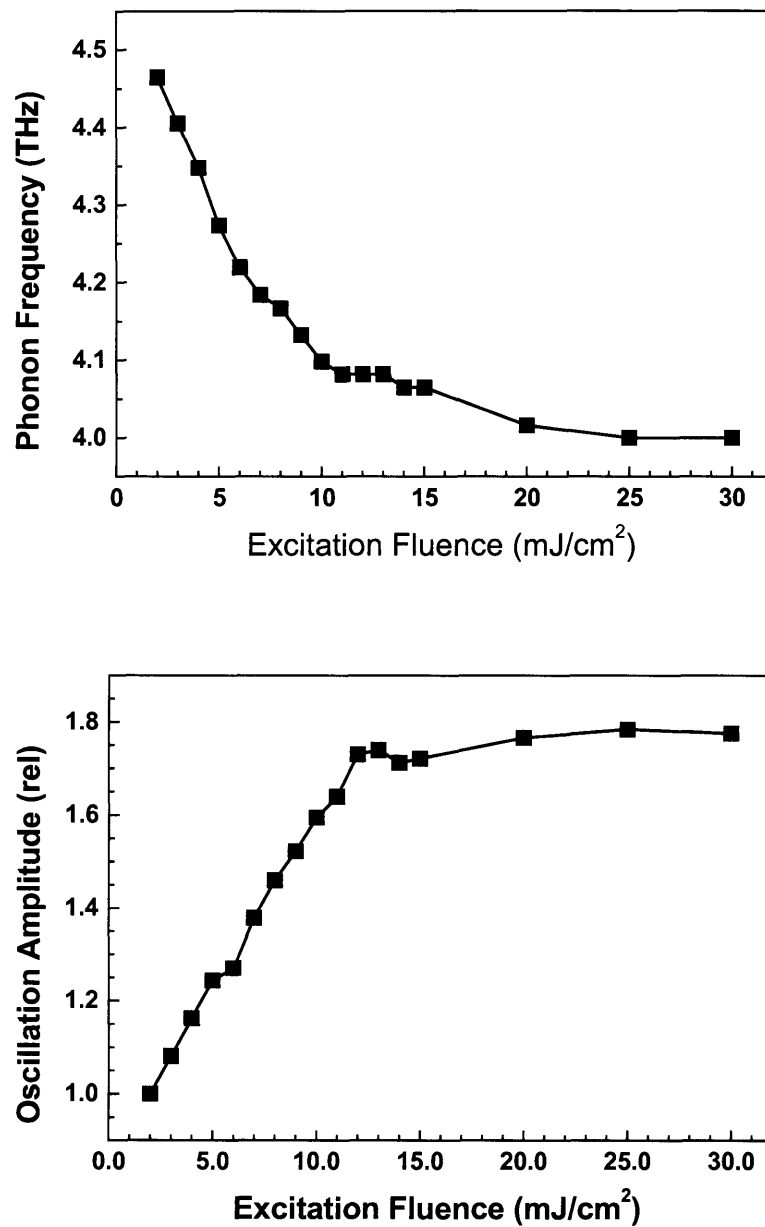


Figure 5-11. Coherent phonon frequency and amplitude as a function of pump pulse intensity for single crystal antimony. In each case, the response scales linearly with intensity up to about $10.0 \text{ mJ}/\text{cm}^2$, and then saturates.

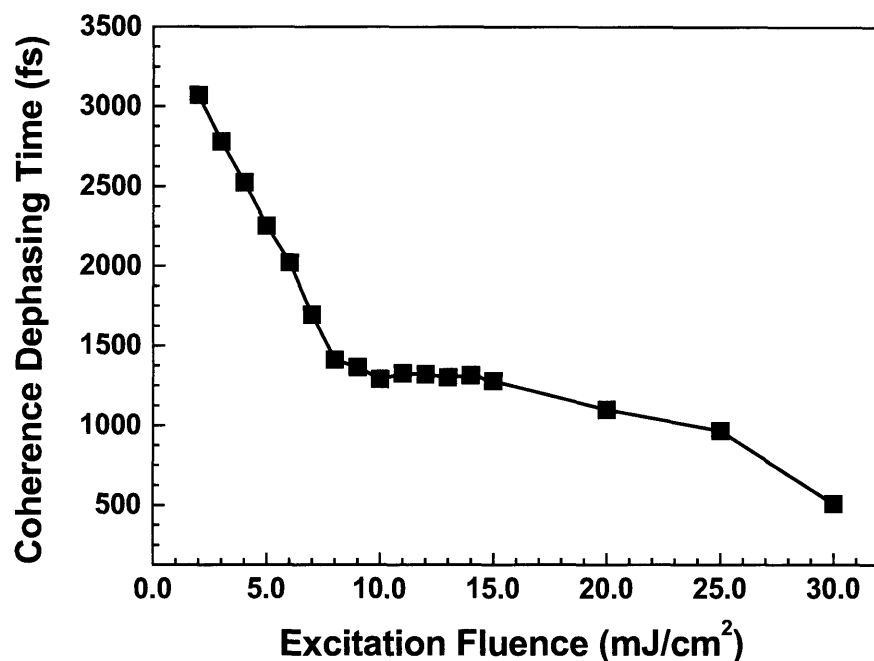


Figure 5-11 (cont'd). Coherent phonon dephasing time as a function of pump pulse intensity for single crystal antimony. The response scales linearly with intensity up to about 10.0 mJ/cm², and then saturates.

phase as a function of probe delay. The oscillatory signals from 2.0 and 4.0 mJ/cm² excitation require six cycles before they are 180° apart. However, the signals corresponding to 2.0 and 10.0 mJ/cm² are exactly out of phase after only a little more than two cycles, or 500 fs, demonstrating dramatic frequency shifting with increasing pump intensity.

Tellurium, the third of the semimetals under investigation, was the subject of similar single-shot experiments. As for bismuth and antimony, the symmetry of the Te lattice and its band structure are such that it should support efficient generation of coherent phonon responses via an impulsive absorption mechanism. The results are shown in Figure 5-13 as a function of the pump pulse intensity. Intensity-dependent

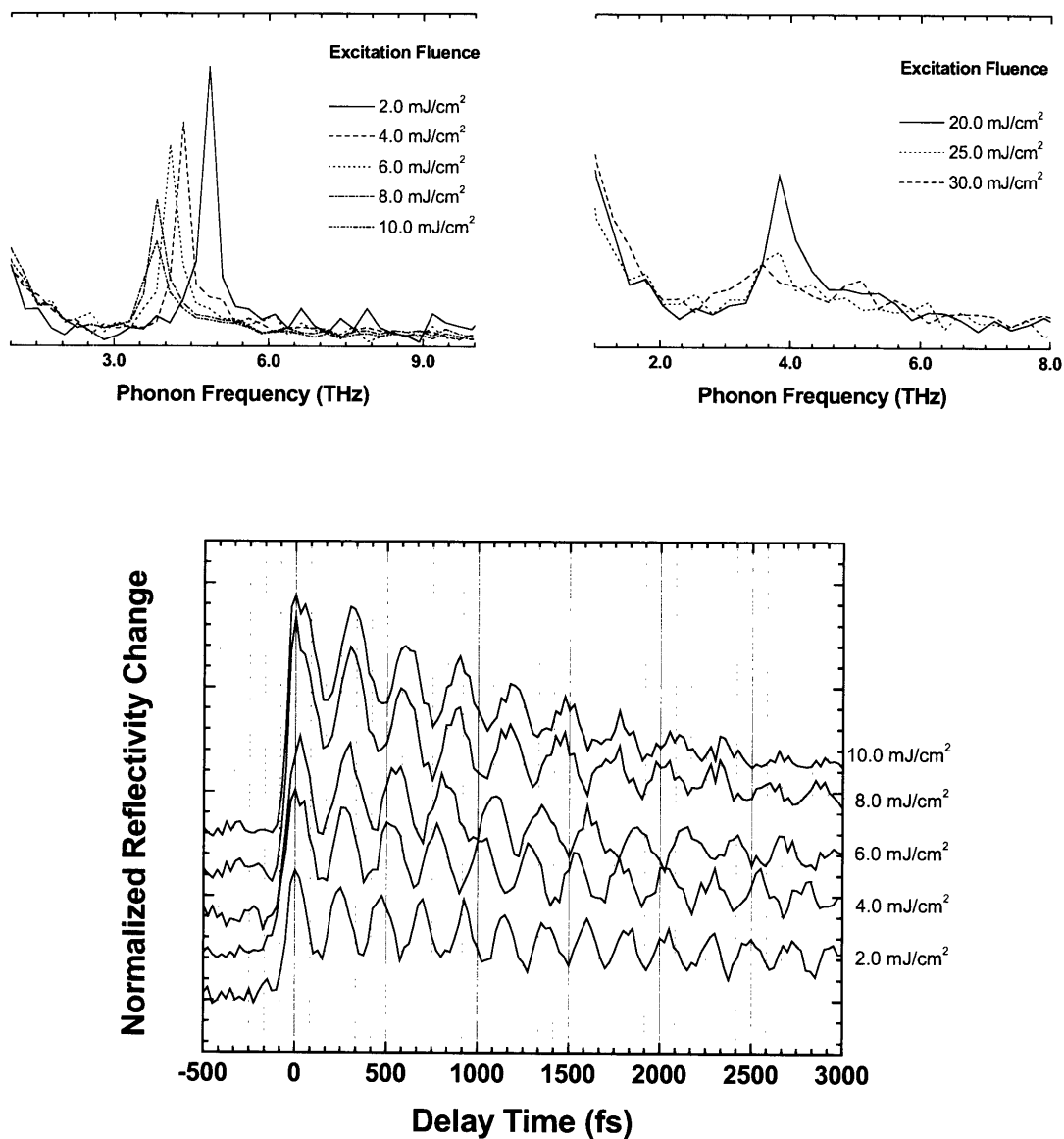


Figure 5-12. Oscillatory component of the time-dependent reflectivity of antimony. The top panels show windowed Fourier transforms (normalized real part only) of the reflectivity signal for several pump intensities. At low intensity, the phonon peak is sharp. As the intensity increases, the phonon peak amplitude decreases and the peak width increases. The presence of only a few cycles at the highest fluences yields a nondescript spectrum. In the bottom panel, the early-time oscillations are compared as a function of laser intensity. A strongly intensity-dependent phonon frequency causes the measured responses to propagate in and out of phase with one another.

scaling of the coherent phonon frequency, amplitude and dephasing rate is apparent. The final scan at 30.0 mJ/cm^2 is above the single-shot damage threshold of 24.0 mJ/cm^2 and demonstrates a rapid loss of coherence in only a couple of vibrational cycles, a result consistent with observations of Bi and Sb. Rapid loss of coherence is also observed just below the damage threshold.

The lowest intensity phonon frequency retrieved by LP-SVD analysis is 3.6 THz, which agrees well with literature data [8,11,12] for the A_1 mode of Te. Analysis of the time-dependent sweeps by fitting to Equation (5.2) is employed and the results are shown in Figure 5-14. The linear scaling region and subsequent plateau are by now familiar features, and the difference relative to Bi and Sb is only the fluence at which the linear region ends, which is roughly 8.0 mJ/cm^2 for Te. The frequency shift for Te is approximately 0.6 THz from the equilibrium value, and the maximum induced change in reflectivity is about 1.6%. The dephasing of the coherence in Te occurs more rapidly than in either Bi or Sb, and at the highest intensity, oscillations disappear within two vibrational cycles.

5.4 Coherent Control of Semimetal Phonon Evolution

In an effort to further investigate the evolution of coherent phonons in the semimetal materials of section 5.3, we constructed a multiple-beam delay line as shown in Figure 5-5 for the purpose of coherent control experiments exploring the dynamical material response. Appropriately timed sequences of two excitation pulses should be

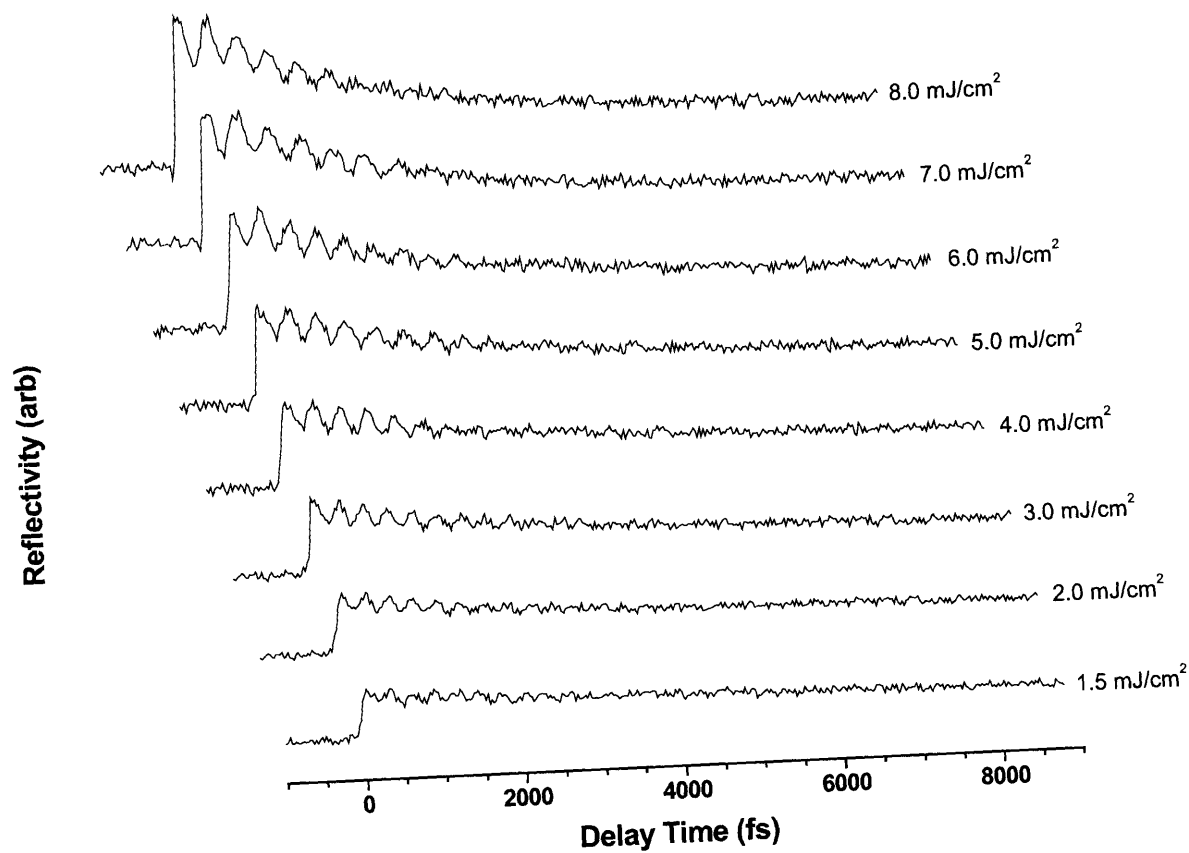


Figure 5-13. Time-resolved single-shot reflectivity of single crystal tellurium. The reflectivity increases on account of the excitation pulse. The oscillation frequency, amplitude and dephasing rate all scale with the pump pulse intensity, and dephasing is rapid in all cases.

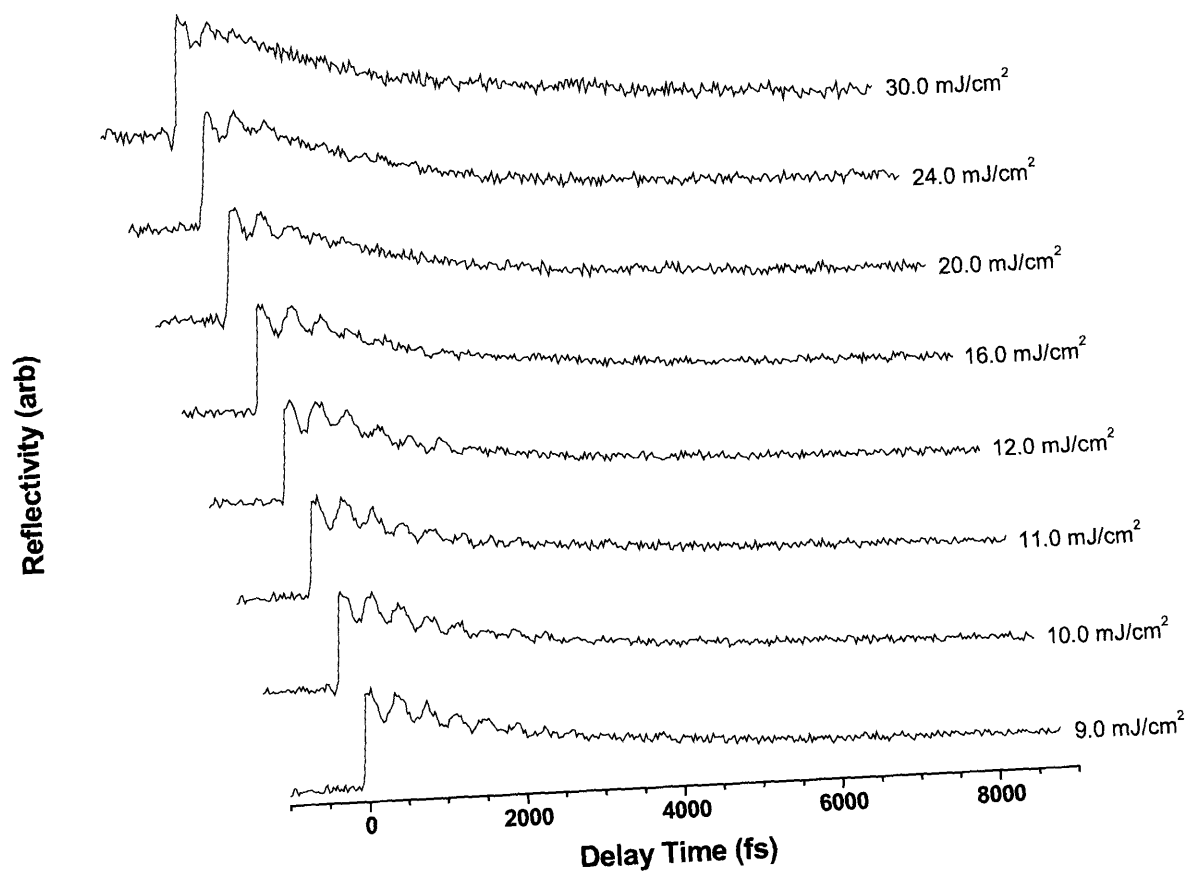


Figure 5-13 (cont'd). Time-resolved single-shot reflectivity of single crystal tellurium. The reflectivity increases on account of the excitation pulse. The oscillation frequency, amplitude and dephasing time all scale with the pump pulse intensity, and dephasing is rapid in all cases. The scan at 30.0 mJ/cm² is above the single-shot damage threshold for Te, and the oscillatory component of the signal disappears in under two cycles.

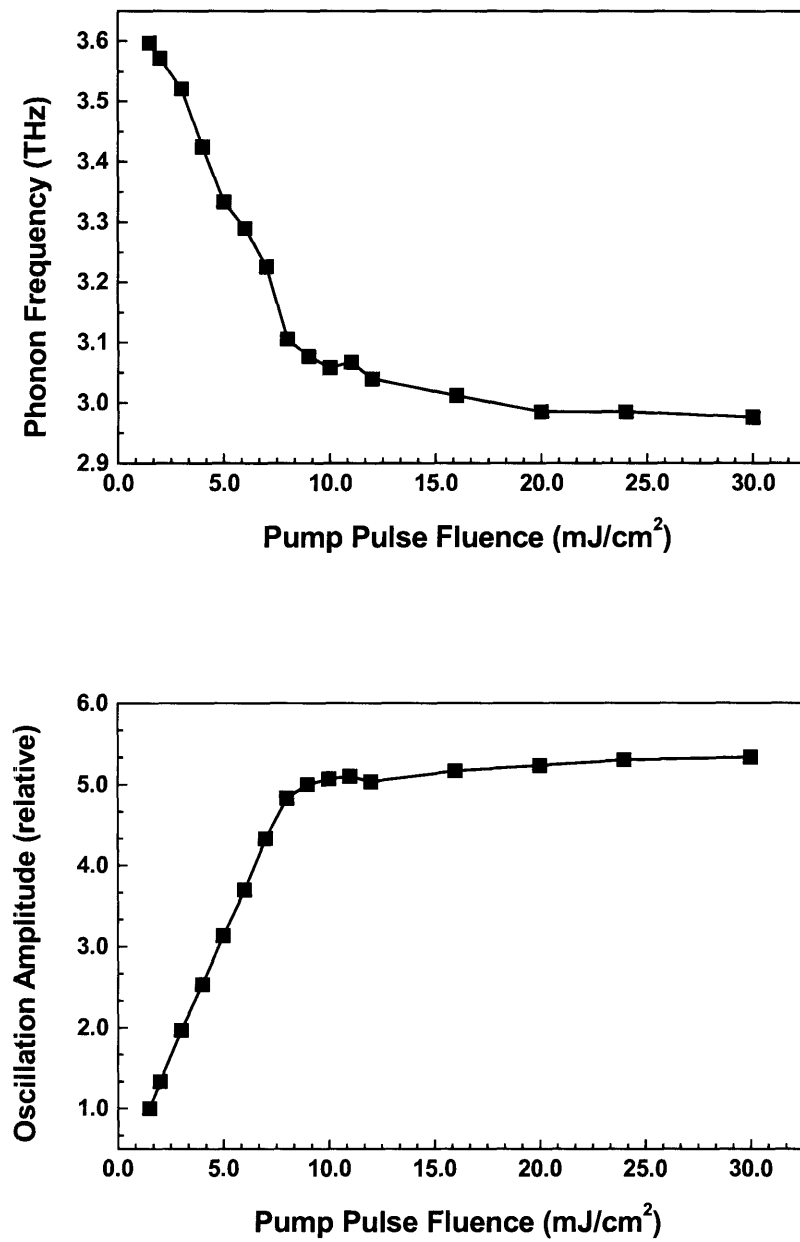


Figure 5-14. Variation of the coherent phonon frequency (top) and amplitude (bottom) in tellurium. In each case, the response scales linearly with intensity up to 8.0 mJ/cm^2 and then reaches a plateau.

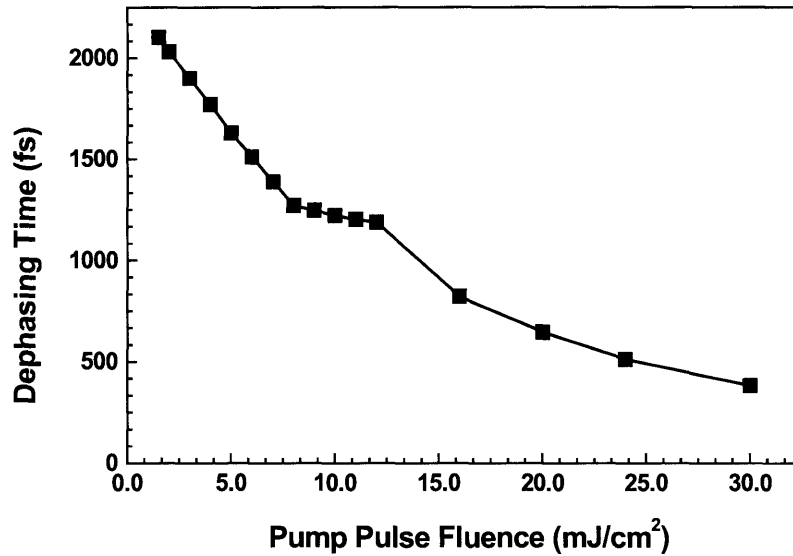


Figure 5-14 (cont'd). Variation of the coherent phonon dephasing time in tellurium. The dephasing time scales linearly with intensity up to 8.0 mJ/cm² and then reaches a plateau.

able to alter both the amplitude and phase of the coherent oscillations in the sample. Accordingly, two of the beam lines in Figure 5-5 were blocked, and the other two were employed in our studies.

An initial excitation pulse of intensity 3.0 mJ/cm² was used to generate an oscillatory response in a single crystal bismuth sample in the same manner as described in the previous section. A second pulse was adjusted to arrive at a later time to perturb the evolving coherence. The intensity of the second pulse was also 3.0 mJ/cm². The results for pulse 2 arrival times between the second and third vibrational period, and between the fifth and sixth vibrational period, are shown in Figure 5-15. The notation used in the figure is as follows: nT refers to the number of vibrational cycles which have

occurred since $t = 0$. For instance, the time point 2.00T refers to the oscillation minimum at roughly 750 fs.

For second excitation pulses which arrive in phase with the already evolving coherent response (2.00T, 3.00T, 5.00 T, 6.00T), the effect is to enhance the coherence by effectively contributing a second in-phase response – the net effect is close to a linear sum. When the second pump pulse arrives on a half-cycle (180° out of phase), the effect is to cancel the original coherence. Cancellation is incomplete, however, due to the fact that the amplitude of the original oscillations has decreased during the interval between pump pulses. The effect is not as pronounced at 2.50T since only two vibrational cycles have occurred; however, at 5.50T, the coherence due to the first pulse is weak and the second pulse, which generates a much larger amplitude response, effectively inverts the sign of the reflectivity change. By appropriate attenuation of the second pump pulse, nearly complete cancellation of the effects of the first pulse can be achieved. At 2.50T, a second pulse of 2.14 mJ/cm^2 accomplishes this. At 5.50T, we find that a 1.68 mJ/cm^2 pulse is sufficient. Note that the electronic contribution to the reflectivity change persists, even when the oscillatory component is removed. The hot conduction band electrons which are responsible eventually dissipate their excess energy via coupling to lattice phonons (of all symmetries), but this process takes tens of picoseconds, and is not fully complete within the 10 ps time window of the single-shot experiment. When the second pulse arrives at intermediate times (2.25T, 2.75T, 5.25T, 5.75T), both the amplitude and phase of the coherence are changed. Neither complete amplitude cancellation or enhancement occurs – the net response is again closer to a linear

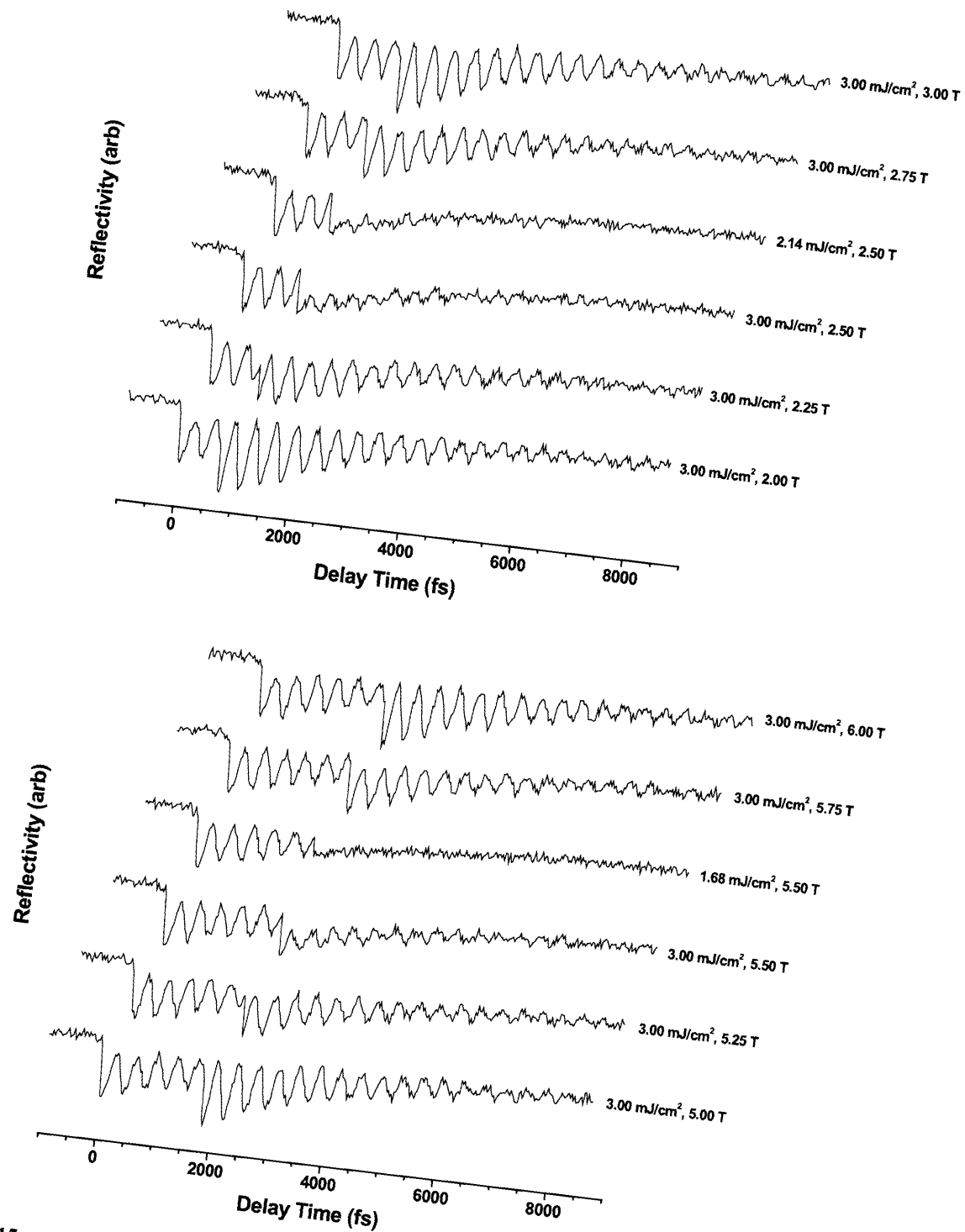


Figure 5-15. Single-shot data showing two-pulse excitation sequences in bismuth, with the second pulse arriving between the second and third (top) or fifth and sixth (bottom) vibrational cycles. When the second pulse arrives in phase, the oscillation amplitude is enhanced. Cancellation of the oscillations can be achieved when the arrival time of the second pulse is exactly one-half cycle out of phase, although intensity adjustment is necessary. Intermediate cases result in both amplitude and phase shifts.

superposition of two individual responses – and the net phase is intermediate between the individual phases.

In order to probe the bismuth response further from equilibrium, the above control experiments were repeated with excitation pulse intensities of 9.0 mJ/cm^2 . The results are shown in Figure 5-16. As above, the second pulse arrives during either the third or sixth vibrational cycle. The data traces at high fluence illustrate behavior which is consistent with the observations of bismuth under high intensity single pulse excitation. As before, adjustment of the second pulse delay such that it arrives in phase with the coherent response generated by the first results in a net amplification of the phonon amplitude. However, no longer is the resulting signal a linear sum of two individual responses. Rather, the oscillation amplitude saturates, just as in Figure 5-9 for single excitation pulses. This is most apparent at times 2.00T and 3.00T, where the response due to pulse 1 is still large and the additional pump pulse produces little in the way of increased amplitude. The same holds true, however, at 5.00T and 6.00T, but since coherence dephasing has occurred for longer, the response induced by pump pulse 2 during the sixth cycle is larger.

When the second pump pulse arrives 180° out of phase with the phonon oscillations, nearly complete cancellation is possible only with adjustment of the second pulse intensity. At 2.50T, a pulse at 6.69 mJ/cm^2 is required and at 5.50T, the required intensity is 3.62 mJ/cm^2 . At intermediate times 2.25T, 2.75T, 5.25T and 5.75T, the second pulse modifies both the amplitude and phase of the oscillations. In particular, on account of fairly rapid dephasing in bismuth, for arrival times which fall during the sixth cycle, the net response is dominated by the effects of the second pump pulse.

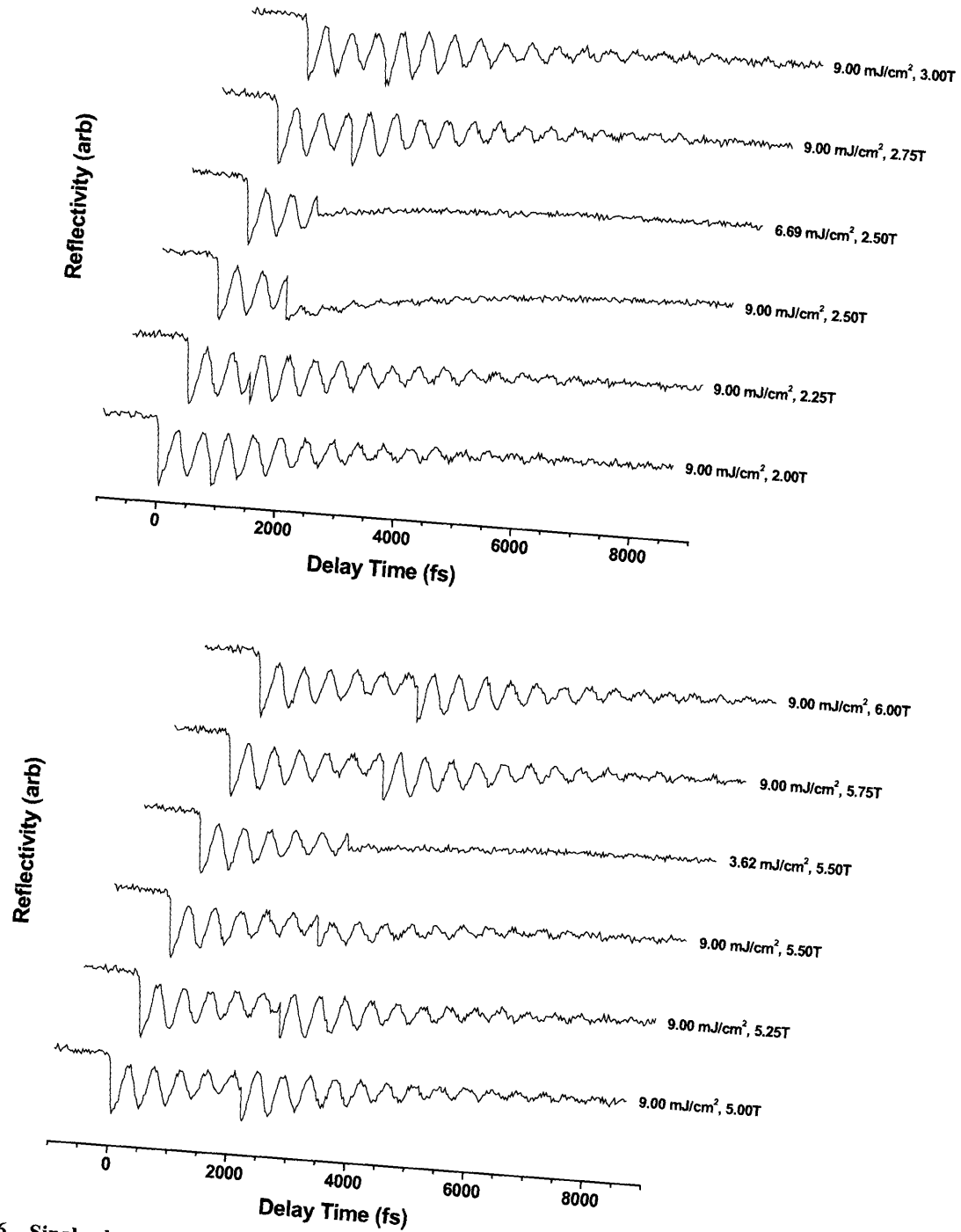


Figure 5-16. Single-shot measurements showing two-pulse excitation of single crystal bismuth. Excitation pulses are 9.00 mJ/cm² and the second pulse arrives either during the third or the sixth vibrational cycle. In-phase arrival times produce amplification as before, but clear saturation of the phonon amplitude is observed. At arrival times which are 180° out of phase, nearly complete cancellation of the coherent response is still possible with intensity adjustment of the second pulse. As before, at intermediate times, both the amplitude and phase of the coherence are modified.

Hase and co-workers have described their double-pulse experiments as simple linear sums of two separate coherent responses [16], and this interpretation is not sufficient in all cases. Not only does the explanation not account for oscillation amplitude saturation at high intensities, but it also does not take into consideration the complex intensity-dependence of the phonon frequency. Even with adjustment of the intensity of the second pump pulse, it is impossible to completely cancel the oscillatory behavior of the reflectivity since the second pulse generates an intensity-dependent coherence which evolves separately from the first and thus ensures that the amplitudes, frequencies and phases of both cannot be matched.

The two-pulse experiments were also performed on single crystal tellurium, where saturation effects are not as prominent at the intensities employed. The change in tellurium reflectivity as a function of probe delay is shown in Figure 5-17 for excitation at 3.00 mJ/cm^2 (top) and 7.00 mJ/cm^2 (bottom). The second excitation pulse arrives during the fourth cycle. Amplification is demonstrated at 3.00T and 4.00T for both fluences, confirming the earlier bismuth results. Also, cancellation of the coherent response is achieved at 3.50T with 1.7 mJ/cm^2 pulses (pulse 1 intensity of 3.00 mJ/cm^2) and 2.4 mJ/cm^2 pulses (pulse 1 intensity of 7.00 mJ/cm^2). The large discrepancy between pulses 1 and 2 in the second case is due to the very rapid vibrational dephasing rate in tellurium.

We have successfully demonstrated control over the short-time dynamics of coherent lattice responses in bismuth and tellurium using excitation pulse pairs, and have maintained our ability to characterize these materials in a single laser shot. Remaining questions regarding the behavior of these semimetals revolve around the effects of high

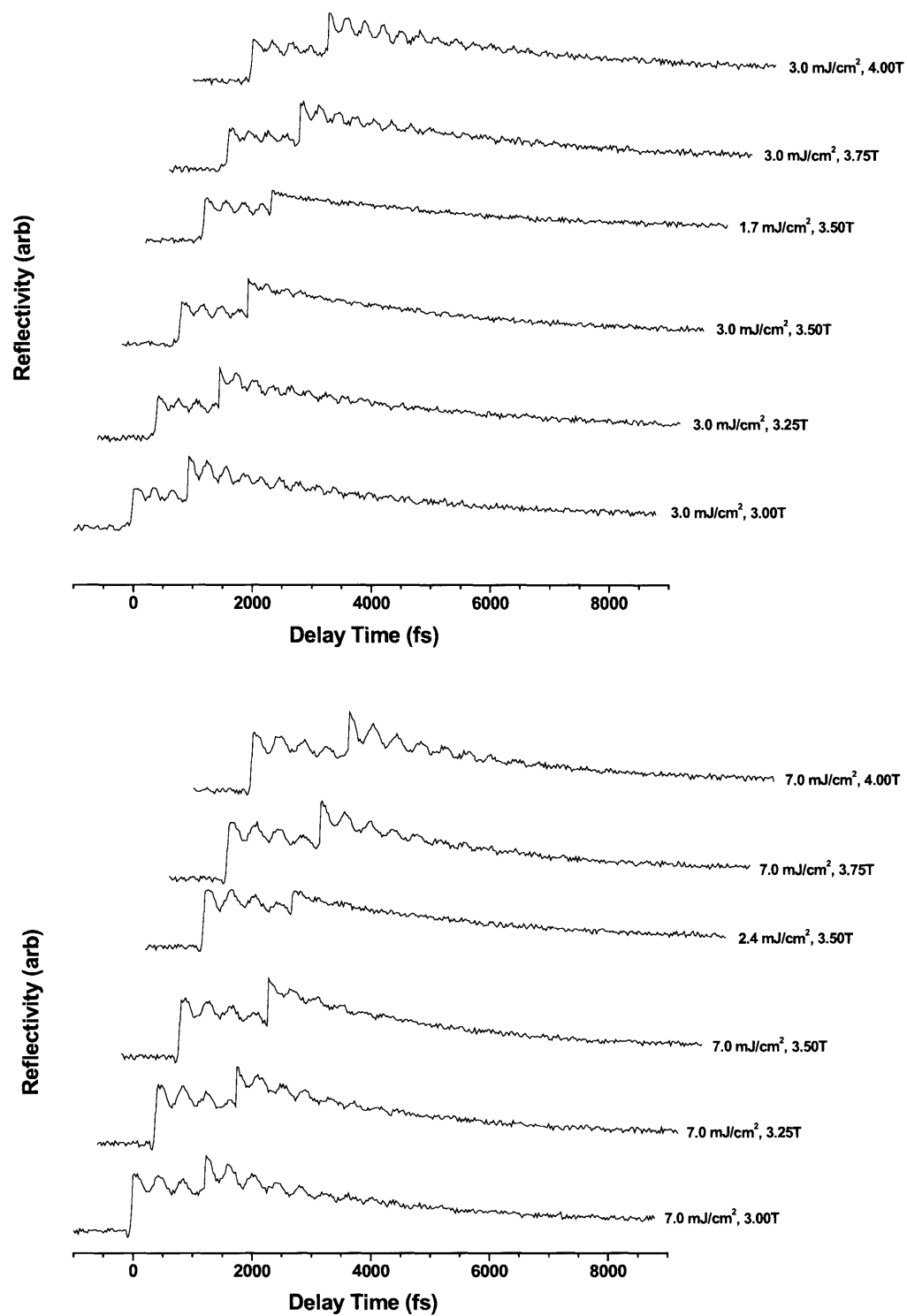


Figure 5-17. Single-shot data showing coherent two-pulse excitation of tellurium. Pump pulse intensities are 3.00 mJ/cm² (top) and 7.00 mJ/cm² (bottom). The maximum tellurium reflectivity change is roughly 1.6% so saturation effects are not as obvious. Amplification and cancellation of the coherent response are possible with suitably chosen pulse pairs.

intensity pulses (near or above the damage threshold) and the evolution of the material response on time scales longer than the 10 ps window covered by our single-shot apparatus. These problems will be addressed in the next section.

5.5 Long-Time Lattice Dynamics at High Pump Intensities

In order to examine the effects of high intensity pulses on these semimetals – that is, in order to understand possible underlying changes in lattice structure, and the timescales on which these occur – we conducted a series of experiments in which an initial pump pulse was focused onto the surface of the sample, exciting lattice phonons as previously described and perhaps, depending upon the pulse intensity, also inducing structural rearrangements which are permanent (damage) or simply long-lived (melting, etc.). A second pump pulse was used, at a well-characterized time delay, to interrogate the integrity of the lattice by attempting to generate further coherent signal via excitation of the symmetric A_1 phonon. Observation of the familiar oscillatory changes in reflectivity can be taken as evidence that the lattice structure, while perturbed, is fundamentally unchanged on the atomic scale. Conversely, the absence of coherent signal can be interpreted as evidence that the local structure of the semimetal lattice within the focal region has been disrupted. Although this method is not nearly as sensitive as other structural methods (such as x-ray crystallography), it provides a *single-shot time-dependent* picture of the evolving structure which is not easily obtained by other means.

The experimental method is identical to that previously described for two-pulse coherent control experiments. The principal difference here is that the second pulse

arrives at later times, usually after the coherence due to the first pulse is lost, and the intensity of the second pulse is adjusted to be less than that of the first. Naturally, there is a trade-off which needs to be balanced: the intensity must be sufficiently low that the second pulse only weakly perturbs the lattice, but must be strong enough that any coherent oscillations – the “signature” of the lattice – are detectable within the constraints of a single-shot experiment.

The results from two-pulse pumping of single crystal bismuth samples are shown in Figure 5-18. The intensities of the first excitation pulse used are 9.0, 13.0, 17.0, 21.0 and 28.0 mJ/cm². The second excitation pulse intensity in all cases is 6.0 mJ/cm² and pulse 2 arrival times are 3.0, 4.0, 5.0, 6.0 and 7.0 ps. In all cases except for the 3.0 ps delay time, the initial coherent oscillations induced by pulse 1 have mostly or fully dephased when the second pulse arrives.

Examination of the data in Figure 5-18 reveals behavior which changes appreciably as a function of the intensity of the first pump pulse. In the first two data sets, where the (first) pump pulse intensity is 9.0 mJ/cm² and 13.0 mJ/cm² respectively, well-defined oscillations in bismuth reflectivity are observed at all interpulse delays, suggesting that the lattice is not altered severely by the initial intense pump pulse. The amplitude of the oscillations after the second pump pulse is reduced at 13.0 mJ/cm² relative to 9.0 mJ/cm². At 17.0 mJ/cm², the amplitude of the oscillations after the second pulse is reduced further. At an intensity of 21.0 mJ/cm², there is only an extremely weak coherent oscillation visible at any delay time and there is no oscillatory contribution at 28.0 mJ/cm². Clearly, the oscillation amplitude and dephasing rate following the second

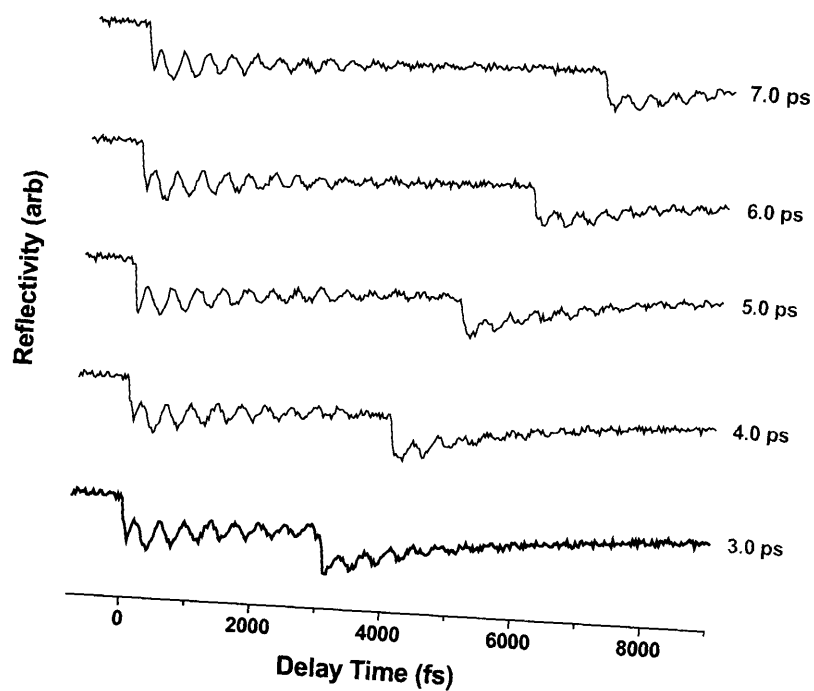
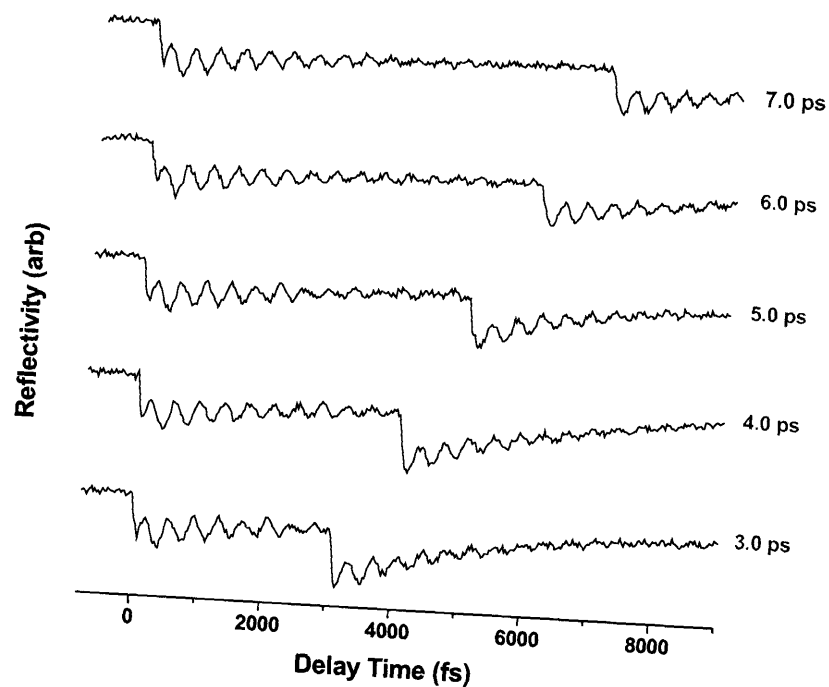


Figure 5-18. Two-pulse excitation of bismuth. The intensity of the first pulse is 9.0 mJ/cm² (top) or 13.0 mJ/cm² (bottom). The second interrogating pulse intensity is 6.0 mJ/cm² in both instances, and arrives at a fixed delay, relative to the first pump pulse, of 3.0, 4.0, 5.0, 6.0 or 7.0 ps.

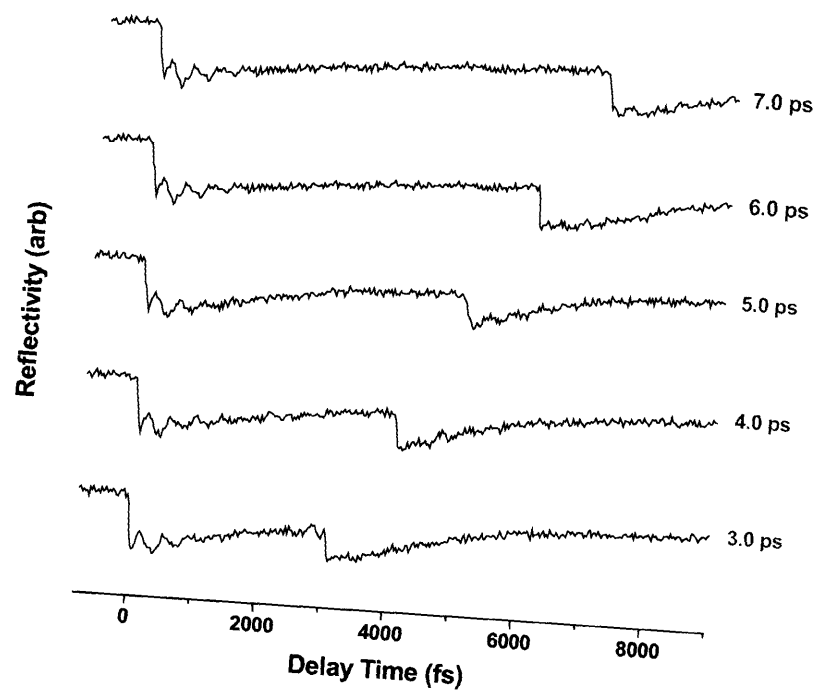
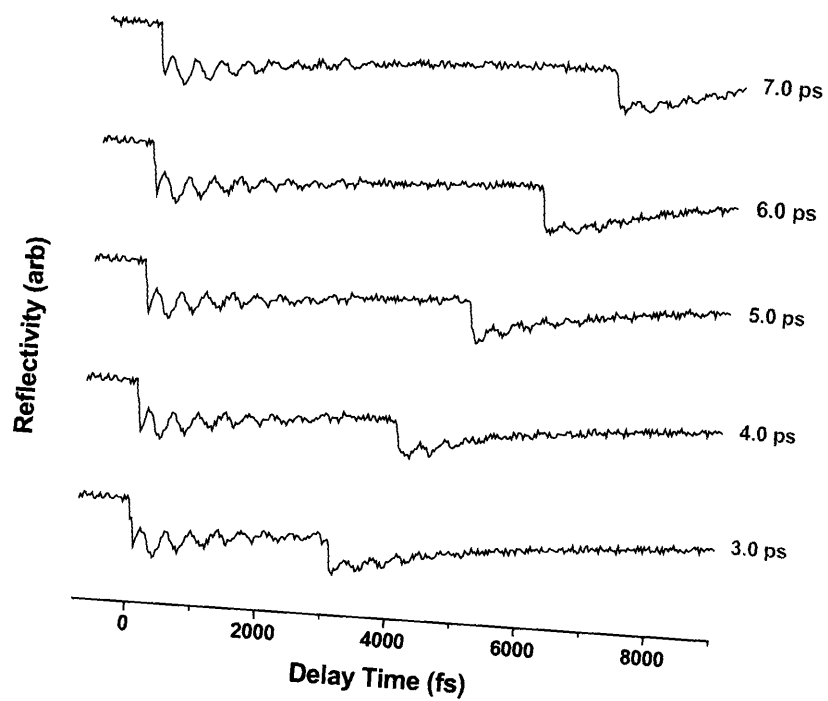


Figure 5-18 (cont'd). Two-pulse excitation of bismuth. The intensity of the first pulse is 17.0 mJ/cm² (top) or 21.0 mJ/cm² (bottom). The second interrogating pulse intensity is 6.0 mJ/cm² in both instances, and arrives at a fixed delay, relative to the first pump pulse, of 3.0, 4.0, 5.0, 6.0 or 7.0 ps.

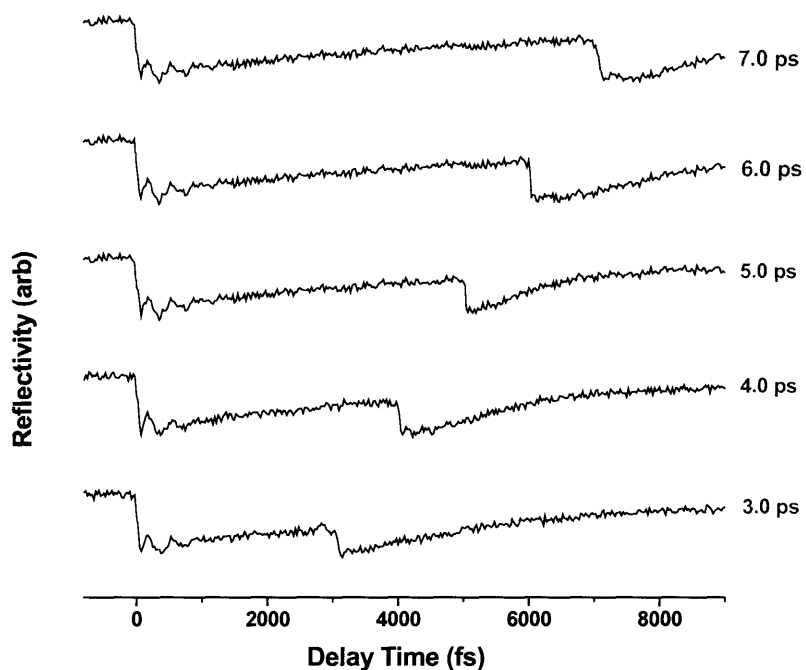


Figure 5-18 (cont'd). Two-pulse excitation of bismuth. The intensity of the first pulse is 28.0 mJ/cm^2 . The second interrogating pulse intensity is 6.0 mJ/cm^2 , and it arrives at a fixed delay, relative to the first pump pulse, of 3.0, 4.0, 5.0, 6.0 or 7.0 ps.

pump pulse are sensitive to the distribution of hot electrons created by the first, in spite of the fact that even for very intense pulses, only $\sim 2\%$ of all valence electrons are promoted to the conduction band [15,29].

Central to these experiments is the notion that the presence of oscillatory behavior in the time-resolved reflectivity implies a structurally intact lattice, and their absence likewise indicates local structural modification. It is plausible that material damage has occurred for a pump fluence of 28.0 mJ/cm^2 , which lies above the damage threshold. However, at lower intensities, the observed absence of oscillations following the second pump pulse, combined with the rapid dephasing of oscillations after the first pump pulse (typically within 2-3 vibrational cycles) suggests the possibility of photoinduced melting

in the sample. If such a phase change is occurring, the time scale is on the order of 500 fs – the time at which coherence is lost after the initial pump pulse.

With the realization that “single-shot damage” might very well be a consequence of local melting, another set of experiments was conducted at even higher pump intensities in order to investigate the nature of photoinduced damage under truly irreversible conditions. A similar experimental two-pulse arrangement was utilized, with initial pump intensities of 26.0, 30.0, 34.0 and 50.0 mJ/cm². The intensity of the second pump was reduced to 3.0 mJ/cm² in order to ensure that the observed effects were not too strongly perturbed by it, and the delay times employed were 3.0 and 7.0 ps. The results are shown in Figure 5-19. The time-resolved reflectivity change at 26.0 mJ/cm² appears to show very weak oscillations following the second pulse, although the data are clearly noisier than previous results at low pump intensities. At 30.0 mJ/cm² an extremely weak coherence can be detected, which disappears at 34.0 and 50.0 mJ/cm². We also observe that the electronic component of the signal produced by the second pump pulse decreases as a function of increasing intensity of the first.

On account of our inability to excite symmetric phonons with the second pump pulse, we find it likely that fundamental modification of the lattice has occurred on a very short time scale after a very intense initial pulse. Questions persist regarding the nature of this modification. Is the mechanism dominated by non-thermal processes which depend only upon the population dynamics of excited electrons [38-42], or is the loss of coherence more highly suggestive of a mechanism involving thermal population of large numbers of phonon modes, inducing lattice instability and possible thermal melting?

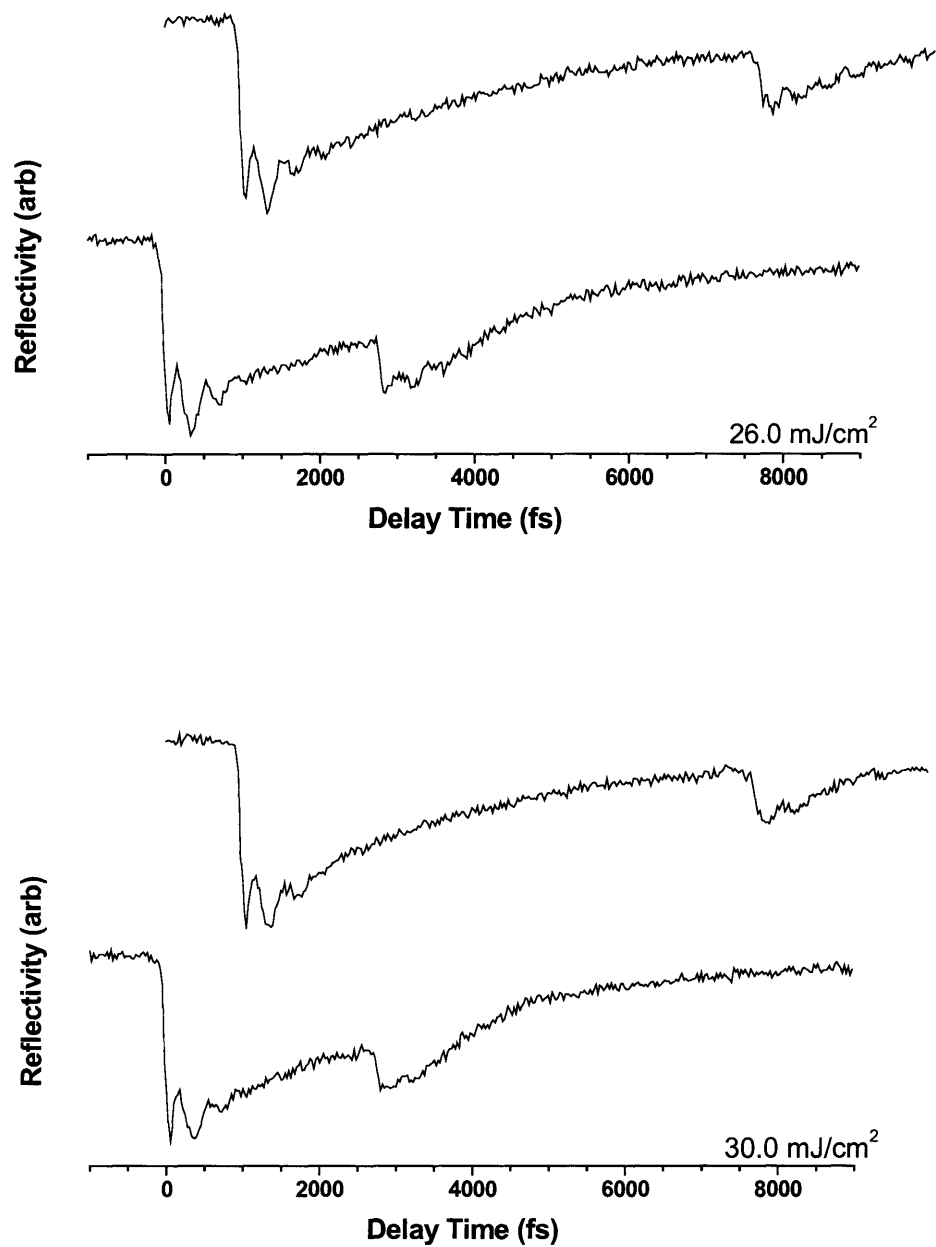


Figure 5-19. Single-shot data showing the results of double-pulse excitation of bismuth at very high intensities. The intensity of the second pump pulse is 3.0 mJ/cm^2 in each case in order to ensure that the material response is not perturbed too strongly. The initial pump pulse intensities are 26.0 mJ/cm^2 (top) and 30.0 mJ/cm^2 (bottom) and the second pulse arrives after 3.0 ps (bottom scan in each panel) or 7.0 ps (top scan in each panel).

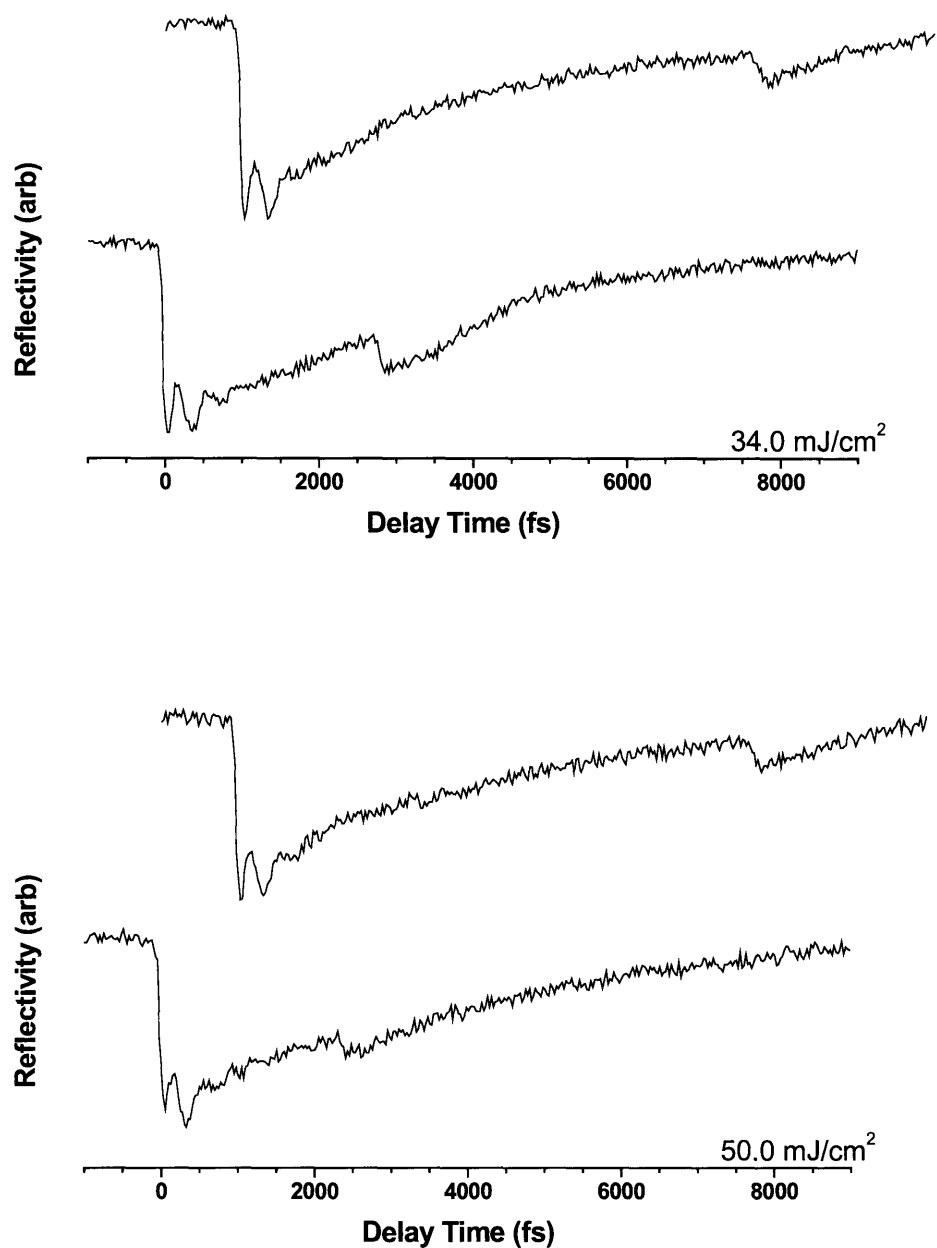


Figure 5-19 (cont'd). Single-shot data showing the results of double-pulse excitation of bismuth at very high intensities. The intensity of the second pump pulse is 3.0 mJ/cm² in each case in order to ensure that the material response is not perturbed too strongly. The initial pump pulse intensities are 34.0 mJ/cm² (top) and 50.0 mJ/cm² (bottom) and the second pulse arrives after 3.0 ps (bottom scan in each panel) or 7.0 ps (top scan in each panel).

Insight into this problem is provided by shifting the time window of the experiment to introduce long delays between the two pump pulses. Pump pulse 2 is adjusted to fall within the 10 ps probe window of the single-shot experiment, whereas pump pulse 1 arrives several tens of picoseconds prior. Investigation of the long-time behavior of the lattice in this manner is designed to determine whether the observed structural modifications are followed by any degree of reversibility on many-picosecond time scales. Pump pulse 1 intensities are 26.0, 30.0, 34.0, 40.0 and 50.0 mJ/cm² while the second pump pulse remains at 3.0 mJ/cm². The data scans are illustrated in Figure 5-20. For 26.0 mJ/cm² initial excitation, only very weak excitation of the A₁ phonon was possible after 7.0 ps (Figure 5-19), but at the longer delays employed in the current experiments, strong oscillations in the bismuth reflectivity are observed at all inter-pump delays, suggesting a well-ordered lattice. At 30.0 mJ/cm², we again observe coherent reflectivity oscillations but strong signal occurs only for inter-pulse delays of 30 ps or greater. At 20 ps, oscillations are resolved but they are of low amplitude. At a pump intensity of 34.0 mJ/cm², coherence is again observed but is much weaker and the oscillation cycles are irregularly defined and noisy. As the initial pump intensity increases, the eventual recovery of the ordered lattice structure appears to occur less readily. At 40.0 mJ/cm² only a very weak oscillatory signal is apparent and at 50.0 mJ/cm², no coherence can be identified in the time-resolved data. In both cases, data sweeps are only shown for delays up to 40 ps – longer delays (up to 100 ps) produced no further change in the recovered reflectivity data.

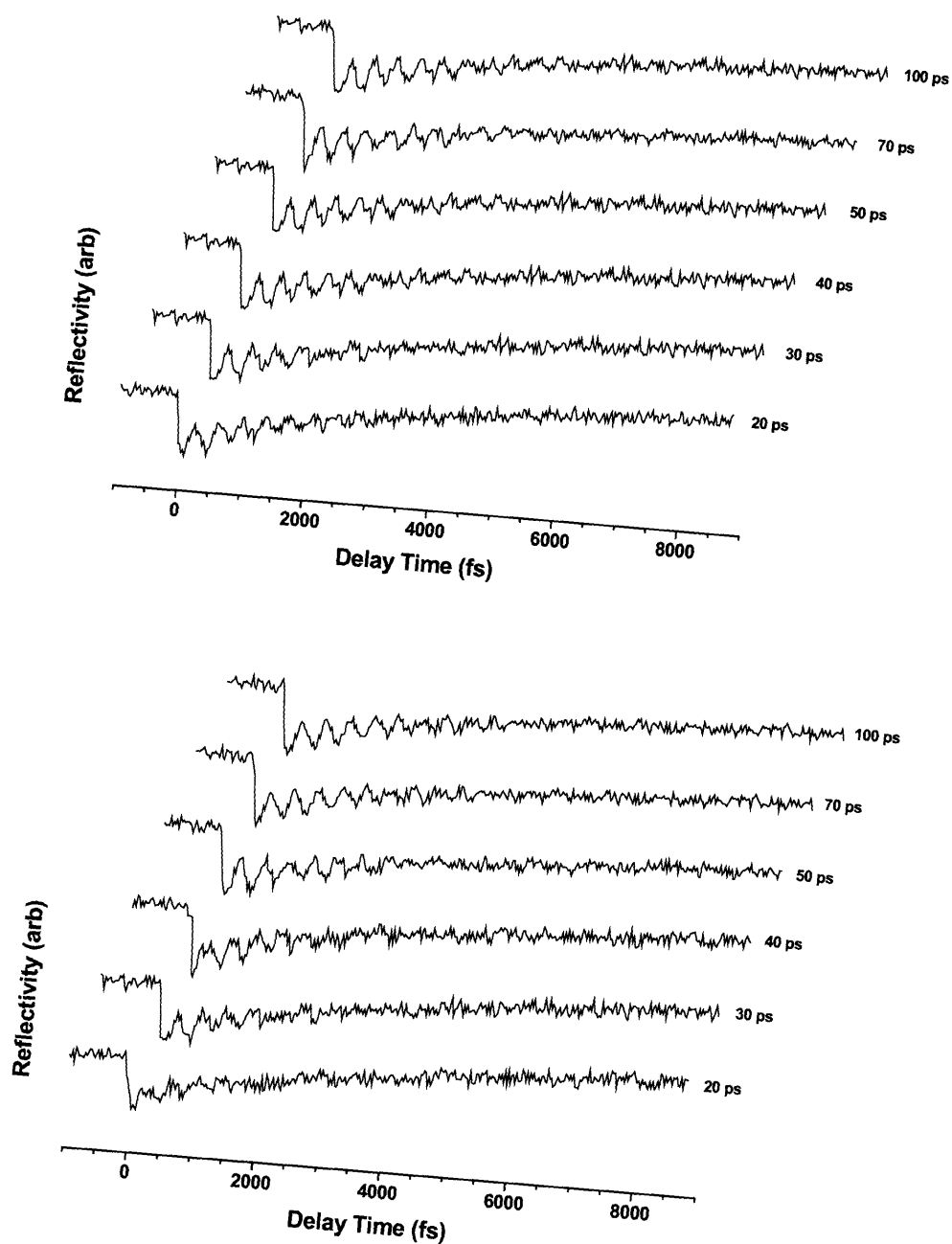


Figure 5-20. Single-shot data showing long-time evolution probed by induced lattice coherences in bismuth. The initial pump pulse intensity is 26.0 mJ/cm² (top) and 30.0 mJ/cm² (bottom), while the second pulse is maintained at 3.0 mJ/cm². The delay times between the pump pulses are indicated on the right hand side of the data sweeps. Since the two pump pulses are separated by a delay greater than the total 10 ps window of the experiment, only the response due to the second pump can be captured in a single laser shot.

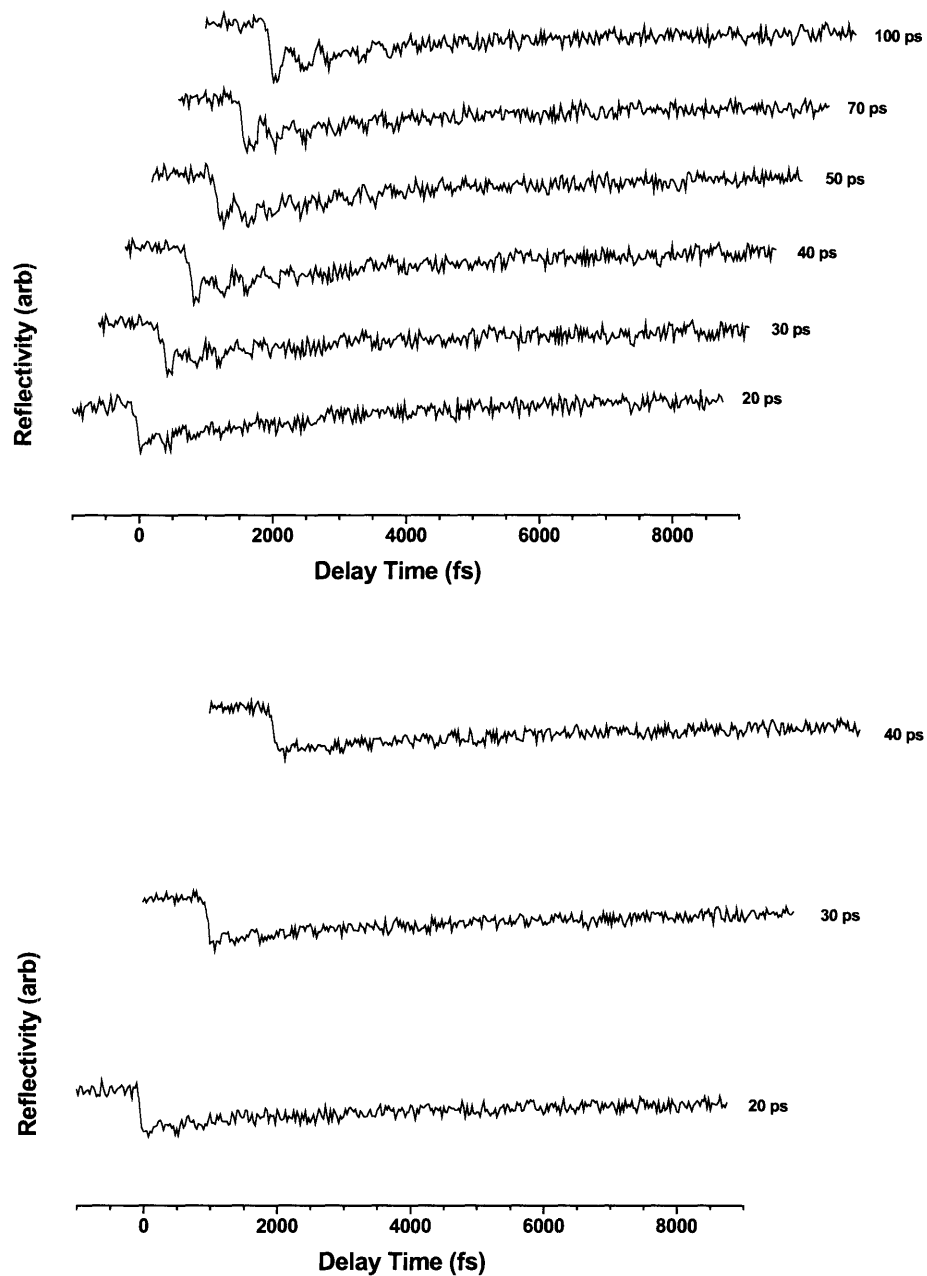


Figure 5-20 (cont'd). Single-shot data showing long-time evolution probed by induced lattice coherences in bismuth. The initial pump pulse intensity is 34.0 mJ/cm^2 (top) and 40.0 mJ/cm^2 (bottom), while the second pulse is maintained at 3.0 mJ/cm^2 . The delay times between the pump pulses are indicated on the right hand side of the data sweeps. Since the two pump pulses are separated by a delay greater than the total window of the experiment, only the response due to the second pump can be captured in a single laser shot.

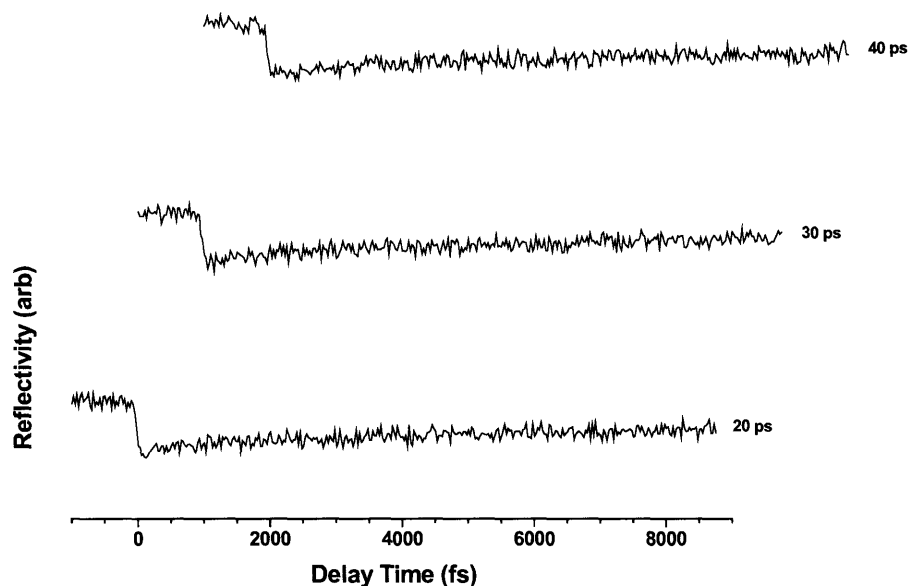


Figure 5-20 (cont'd). Single-shot data showing long-time evolution probed by induced lattice coherences in bismuth. The initial pump pulse intensity is 50.0 mJ/cm^2 and the second pulse is maintained at 3.0 mJ/cm^2 . The delay times between the pump pulses are indicated on the right hand side of the data sweeps. Since the two pump pulses are separated by a delay greater than the total window of the experiment, only the response due to the second pump can be captured in a single laser shot.

The fact that it is possible to excite a coherent lattice response at the lowest pump intensities used in these experiments for delays of 20 ps or more suggests photoinduced melting as the primary source of coherence loss when bismuth is subject to high intensity pump pulses. From the data shown, we conclude that melting must occur on a time scale of a few hundred femtoseconds – two or three vibrational periods – and the reverse phase change can occur as rapidly as 20 ps later. The reflectivity oscillations for even the longest inter-pulse delays are clearly noisier, implying some degree of inhomogeneity remains in the focal region even after the lattice cools. Undoubtedly, a rapidly

thermalizing lattice would reform with defect sites and other irregularities present, so the observation of enhanced background scatter is fundamentally consistent.

At the highest intensities, the second excitation pulse is unable to excite the A_1 phonon, leading to speculation that a larger volume region of the sample has melted, and therefore subsequent “freezing” of the lattice does not occur within the experimental time window. Single-shot damage and reduced sample reflectivity (i.e. after the sample has returned to its equilibrium state) occur at the highest intensities, suggesting that a mechanism which includes strong coupling between hot electrons and lattice atoms plays a role in producing permanent structural change. It is very likely that under these conditions, both melting and vaporization are simultaneously involved in the material dynamics, the former as a reversible modification lasting some hundreds of picoseconds and the latter as an irreversible process.

Observation of complex material dynamics under conditions of irreversibility for these semimetals has not before been undertaken, and so in order to examine the generality of this behavior, we performed similar experiments on single crystal samples of tellurium. As for bismuth, an initial high intensity pump pulse is used to perturb the equilibrium lattice structure and a second weaker pump pulse is used to interrogate the lattice by attempting to coherently excite the symmetric A_1 phonon mode. Initial experiments utilizing high pump pulse intensities of 9.0, 11.0, 15.0, 19.0, 23.0 and 27.0 mJ/cm^2 are shown in Figure 5-21. The second pump pulse intensity is held constant at 6.0 mJ/cm^2 , and arrival times relative to the first pulse are 4.0, 5.0 and 6.0 ps.

For 9.0 mJ/cm^2 excitation, oscillatory behavior is observed in the bulk reflectivity at all delay times. The same holds true at 11.0 mJ/cm^2 , implying a structurally intact, if

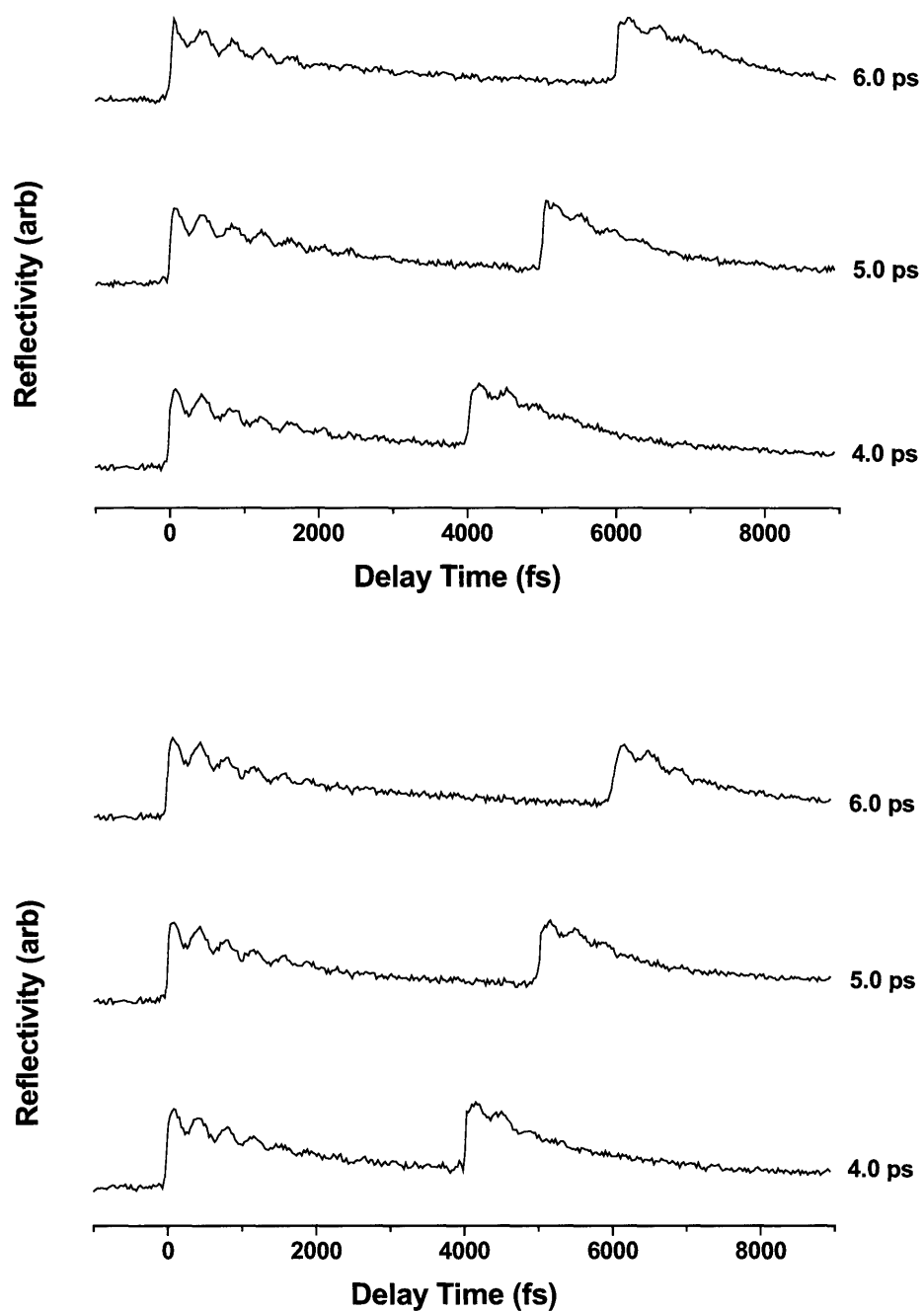


Figure 5-21. Single-shot impulsive absorption of tellurium with two excitation pulses. The intensity of the first pump pulse is 9.0 mJ/cm^2 (top) or 11.0 mJ/cm^2 (bottom) and the second is 6.0 mJ/cm^2 . Relative delay times between the pulses are indicated to the right of each data sweep.

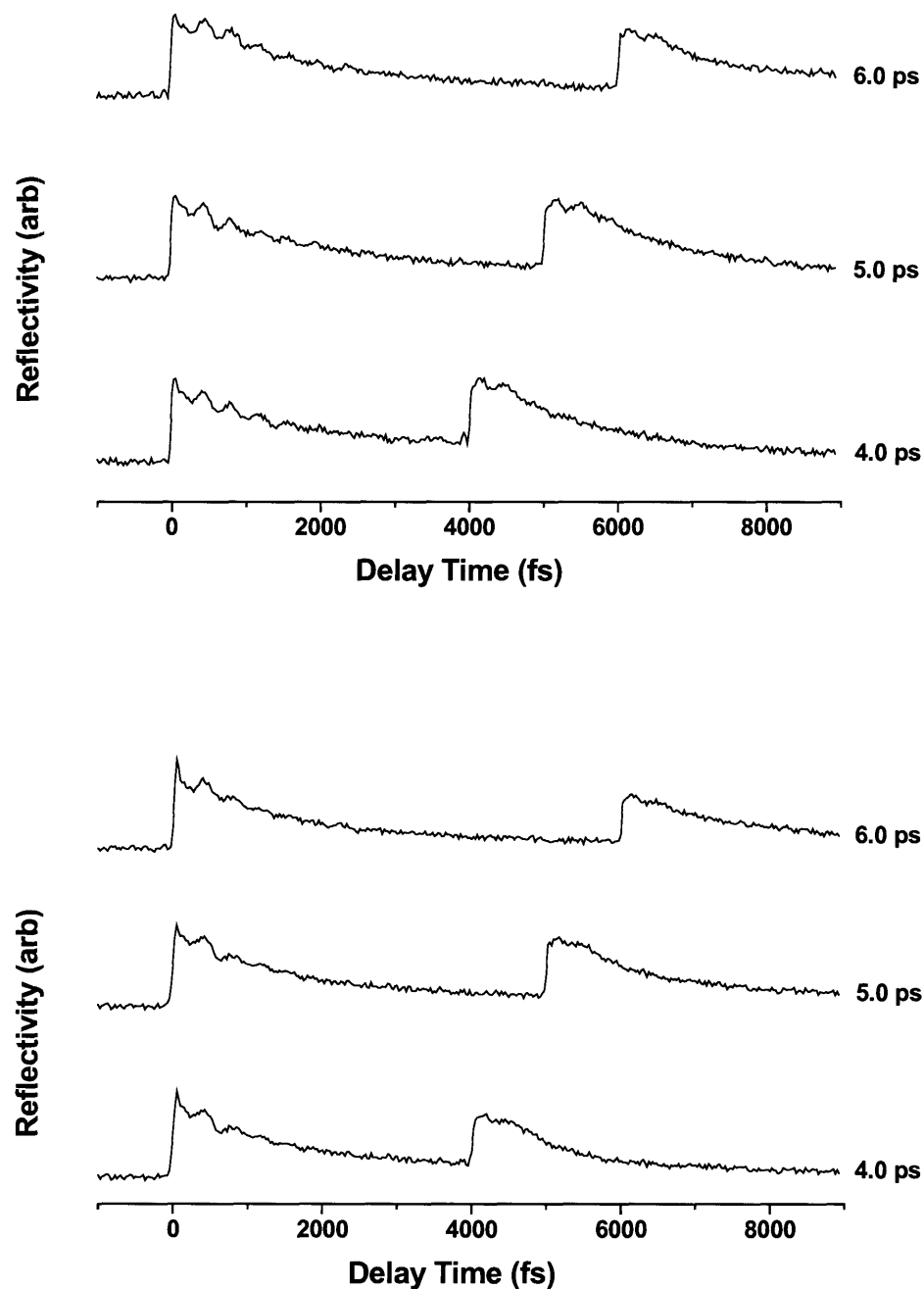


Figure 5-21 (cont'd). Single-shot impulsive absorption of tellurium with two excitation pulses. The intensity of the first pump pulse is 15.0 mJ/cm² (top) or 19.0 mJ/cm² (bottom) and the second is 6.0 mJ/cm². Relative delay times between the pulses are indicated to the right of each data sweep.

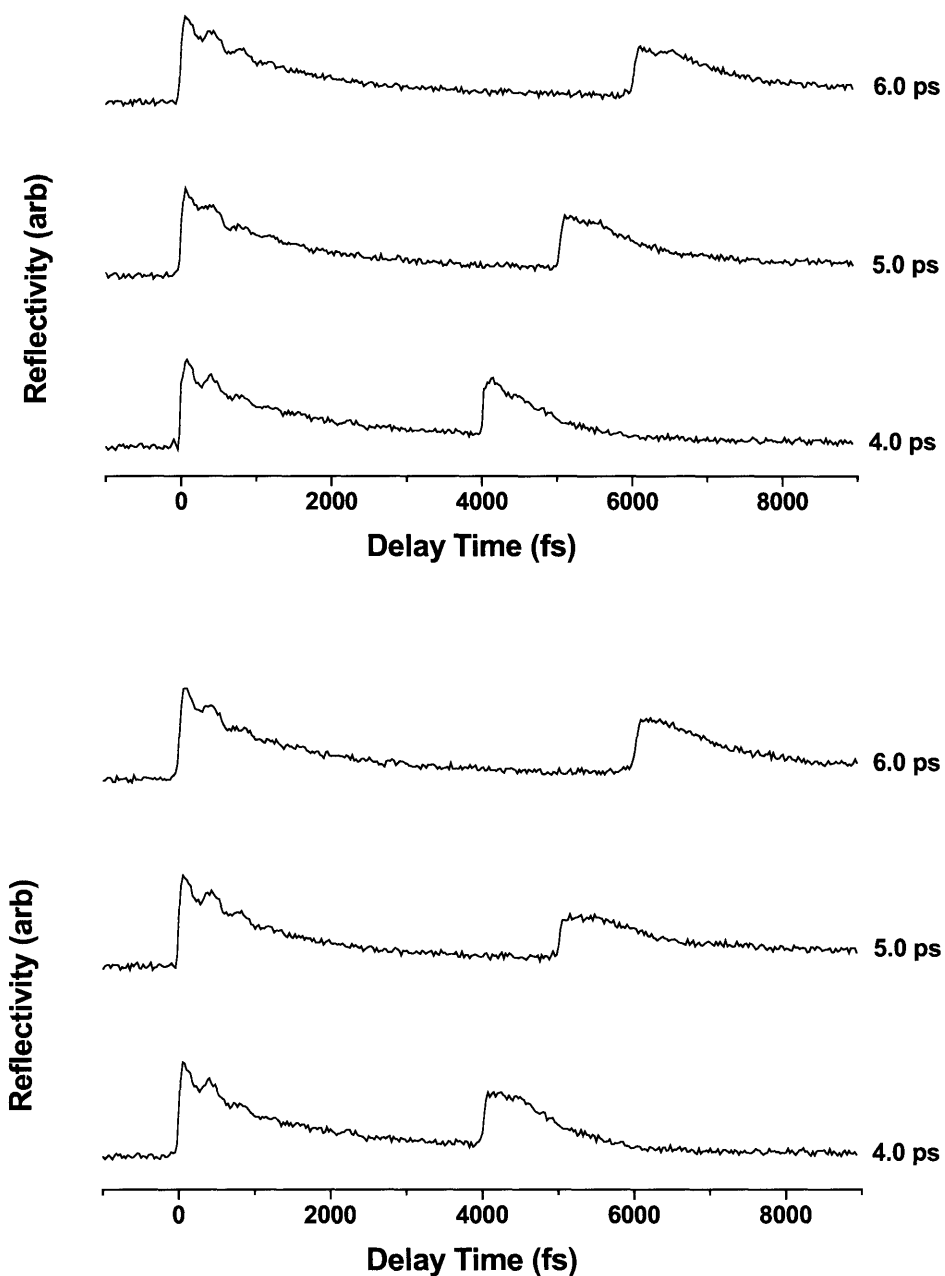


Figure 5-21 (cont'd). Single-shot impulsive absorption of tellurium with two excitation pulses. The intensity of the first pump pulse is 23.0 mJ/cm² (top) or 27.0 mJ/cm² (bottom) and the second is 6.0 mJ/cm². Relative delay times between the pulses are indicated to the right of each data sweep.

thermally excited, lattice is present in the sample. At 15.0 mJ/cm^2 , coherent behavior remains but the oscillation amplitude is much smaller, suggesting possible disordering of the crystalline geometry. Results at intensities of 19.0, 23.0 and 27.0 mJ/cm^2 further confirm this interpretation as phonon excitation is not observed, even for relative delays of 6.0 ps. At these high intensities, coherent oscillations due to the initial pump pulse also dephase very rapidly – within 3-4 vibrational cycles, or about 1.2 ps. As for bismuth, important questions regarding the long-time evolution of the structural character of the lattice are relevant. In order to address these, further experiments were undertaken by introducing very long delays between the first and second pump pulses. In analogy with the results of Figure 5-20, only the effects of the second pulse can be captured during a single-shot experiment. The data are presented in Figure 5-22 as a function of pump pulse 1 intensity. Pulse 2 intensity is maintained at 2.0 mJ/cm^2 throughout. The shortest-delay scan at each intensity is 3.0 ps, and is used to provide a basis of comparison to other results where the effects of the strong initial excitation are not visible.

At 19.0 and 22.0 mJ/cm^2 , well defined coherent phonon excitation is observed following the second pump pulse after inter-pulse delays of 10 and 20 ps, respectively. The recovery of local structural order within the focal region after its initial disappearance once again strongly favors an interpretation based upon a photoinduced phase transition. From the data in Figures 5-21 and 5-22, ultrafast melting in tellurium appears to occur on a time scale of 1.0-1.2 ps. The re-emergence of the A_1 phonon after 10-20 ps suggests a reversal of the transition as lattice order is re-established. Two-pulse excitation data at 28.0, 34.0 and 40.0 mJ/cm^2 support this assertion, as

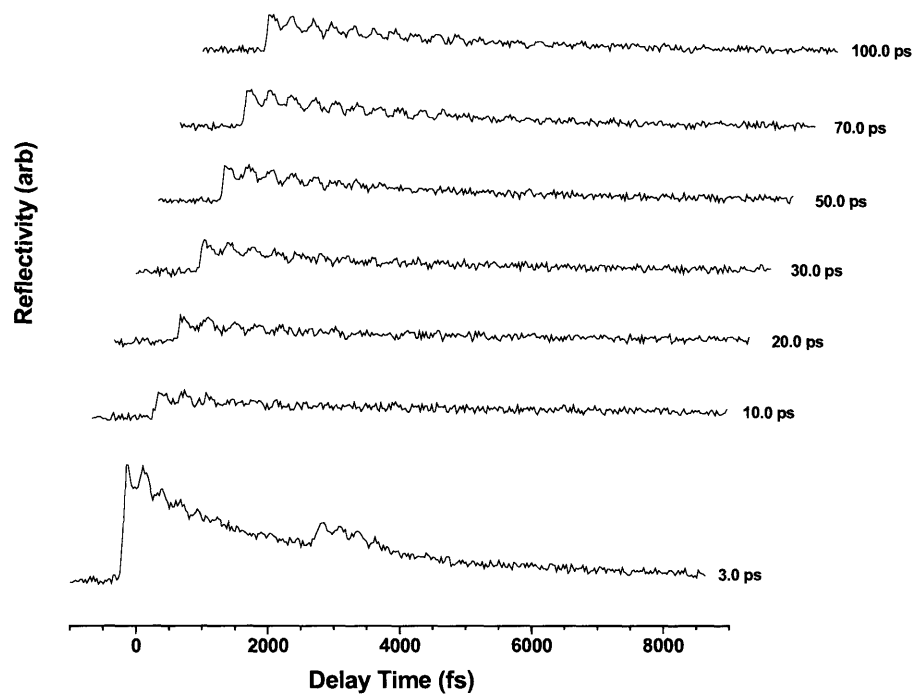
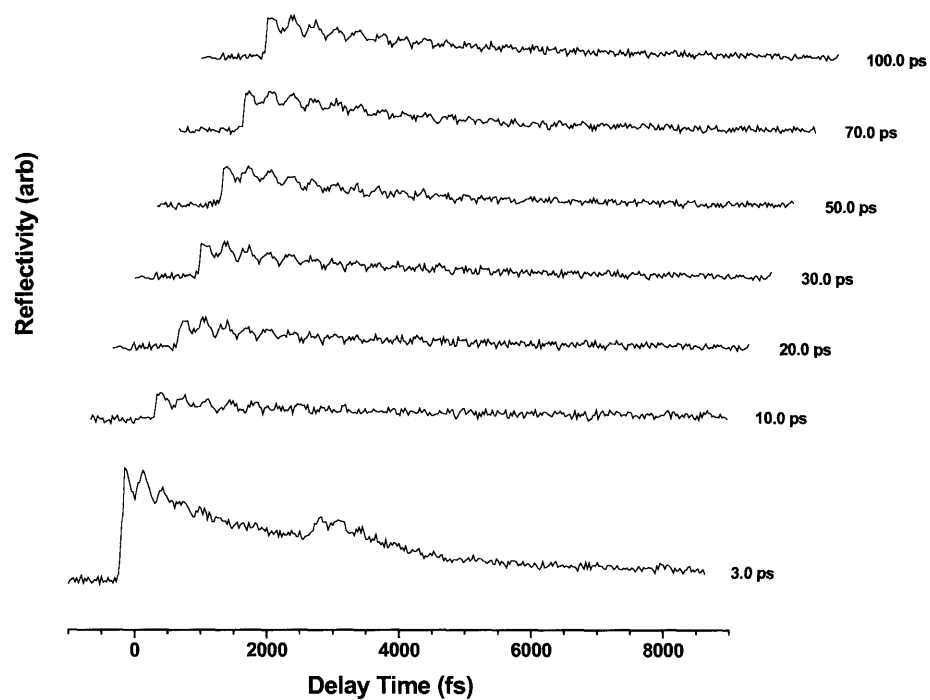


Figure 5-22. Single-shot data showing double-pulse excitation of tellurium for very long inter-pulse delays (indicated at the right of each sweep). Excitation intensities are 19.0 mJ/cm² (top) and 22.0 mJ/cm² (bottom).

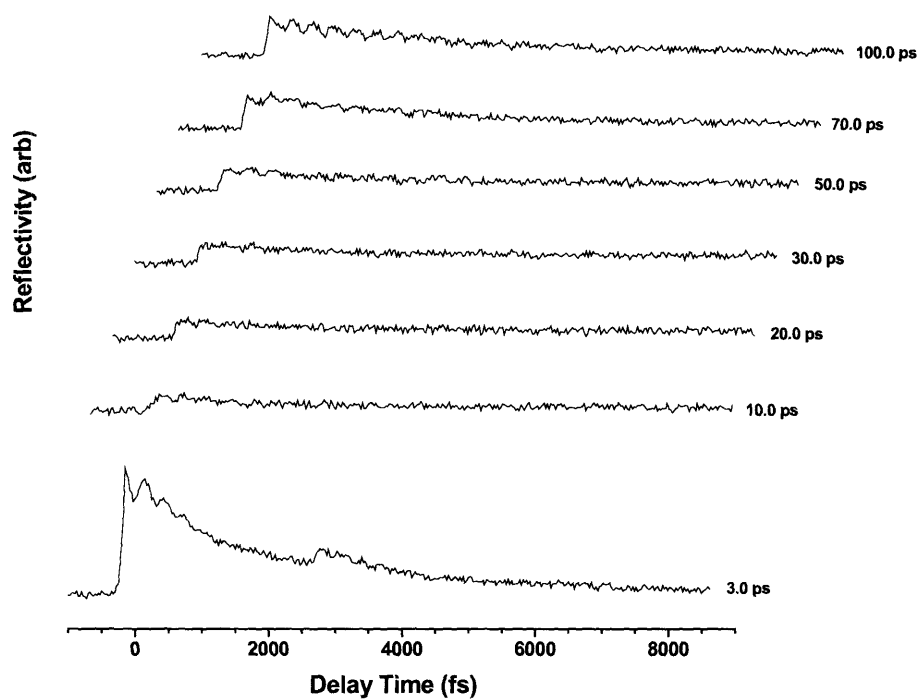
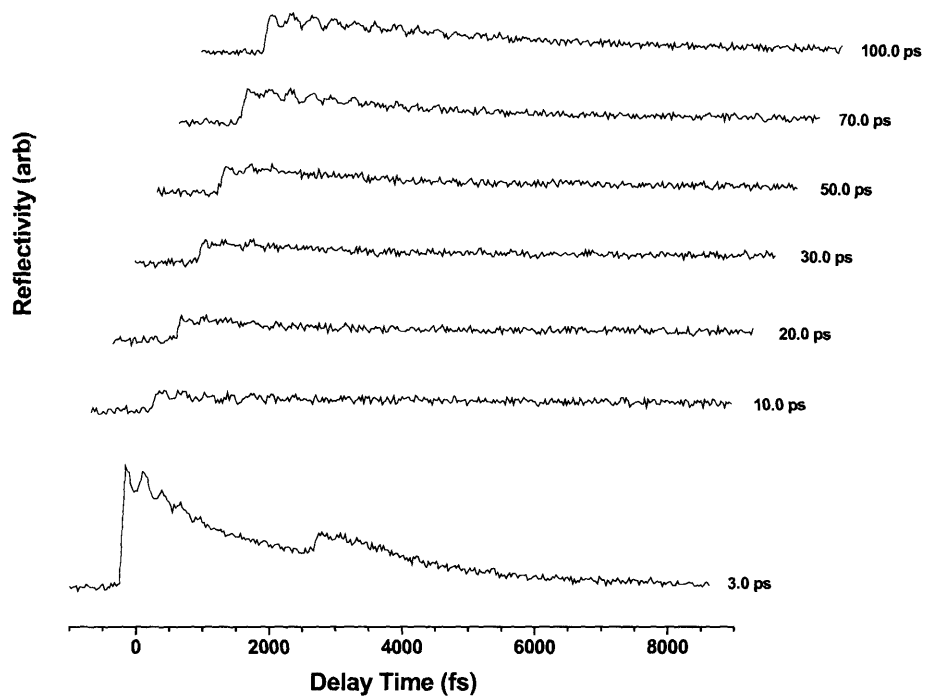


Figure 5-22 (cont'd). Single-shot data showing double-pulse excitation of tellurium for very long inter-pulse delays (indicated at the right of each sweep). Excitation intensities are 28.0 mJ/cm² (top scan) and 34.0 mJ/cm² (bottom scan).

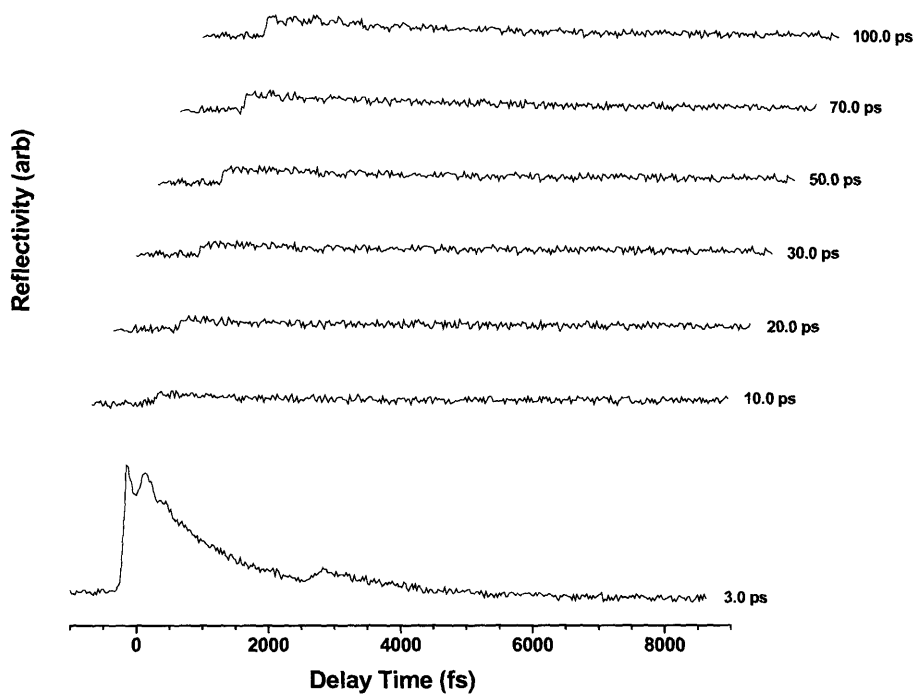
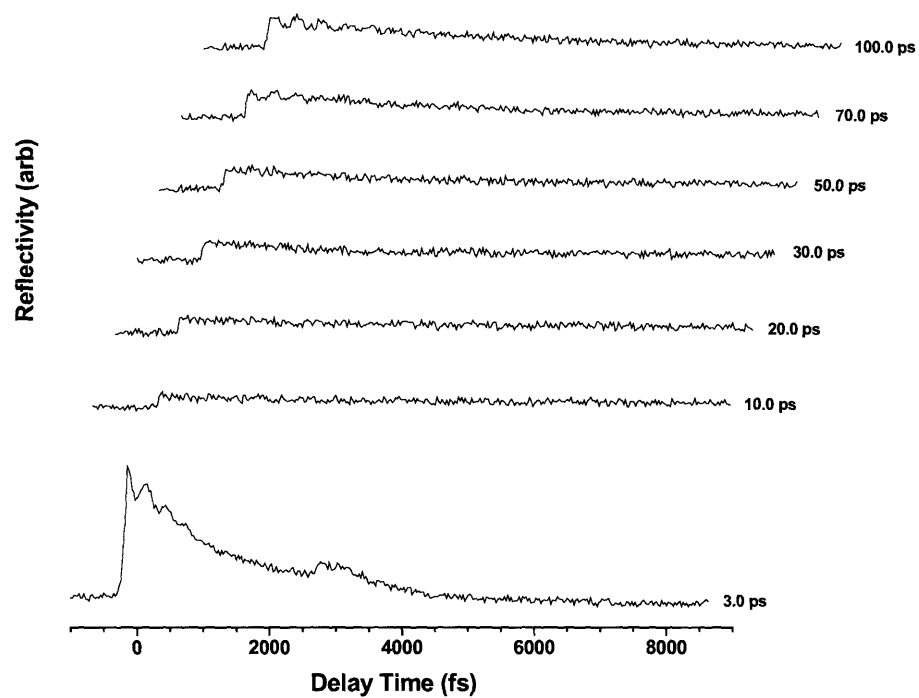


Figure 5-22 (cont'd). Single-shot data showing double-pulse excitation of tellurium for very long inter-pulse delays (indicated at the right of each sweep). Excitation intensities are 40.0 mJ/cm² (top scan) and 50.0 mJ/cm² (bottom scan).

coherent phonon excitation is observed after 70 ps, consistent with the higher fluences producing a larger melted volume. Even at 50.0 mJ/cm^2 , a very weak coherent response appears in the 100 ps data sweep. For tellurium at excitation fluences of 34.0, 40.0 and 50.0 mJ/cm^2 , a permanent reduction of reflectivity is observed, implying strong coupling between hot electrons and lattice ions leading to rapid, irreversible nuclear motion. This is in direct analogy with the results for bismuth, although it appears that in the case of tellurium, the onset of this permanent damage mechanism occurs at higher fluences.

5.6 Ultrafast Phase Transition in Germanium Telluride

The results of the previous section suggest that the combined effects of ultrafast melting and strong electronic coupling to lattice motions are present in the high intensity excitation of the semimetals bismuth and tellurium. No experimental investigation of the responses of these materials in the high intensity regime has previously been undertaken on account of the difficulty of measuring the transient response. Since actual material damage occurs in many cases, standard pump-probe methods are cumbersome. It is only by employing single-shot methods that the rich dynamics of these systems can be explored.

In contrast, germanium telluride is a material which undergoes a well-known thermally driven structural phase transition. At least one research group has attempted to induce the transition optically [43,87] and has observed mode softening along the A_1 direction, but their experiments were not extended to sufficiently high excitation intensity to drive the transition fully. In this section, we describe our efforts to investigate the phase transition in GeTe. Much of the data from GeTe closely resembles the response of

the semimetals Bi, Sb and Te and indeed we observe that similar impulsive absorption mechanisms are responsible for the GeTe phase transition.

Germanium telluride has been the focus of several experimental and computational studies [44-46] on account of its thermally accessible phase transition. The compound itself is one of the limiting cases of a family of substitutional semiconductors $\text{Ge}_j\text{Sb}_k\text{Pb}_l\text{Te}_m$ which have been investigated for possible optical data storage applications [47,48]. Most members of this family of compounds exhibit solid-solid phase transitions, the properties of which can be tuned by manipulating the composition of the material.

The low-temperature phase of the germanium telluride lattice has rhombohedral symmetry. At a transition temperature of 625 K, the lattice rearranges to assume a rocksalt structure of higher symmetry. The respective phases are shown schematically in Figure 5-23. Two independent distortions of the rhombohedral lattice lead to the rocksalt structure. Both distortions occur along the $[1\ 1\ 1]$ lattice direction. The first is described as motion along a $\mathbf{k} = 0$ optic phonon, which constitutes the order parameter of the transition. The second is a shear relaxation along $[1\ 1\ 1]$ and constitutes the secondary order parameter. The GeTe lattice exhibits, among other Raman-active modes, a highly symmetric A_{1g} optic mode which is accessible via impulsive absorption. This lattice “breathing mode” corresponds very closely to the displacive motion along which the GeTe solid-solid phase transition occurs. As a result, excitation and detection of coherent A_{1g} phonon motion should serve as a sensitive probe of lattice dynamics. GeTe is a

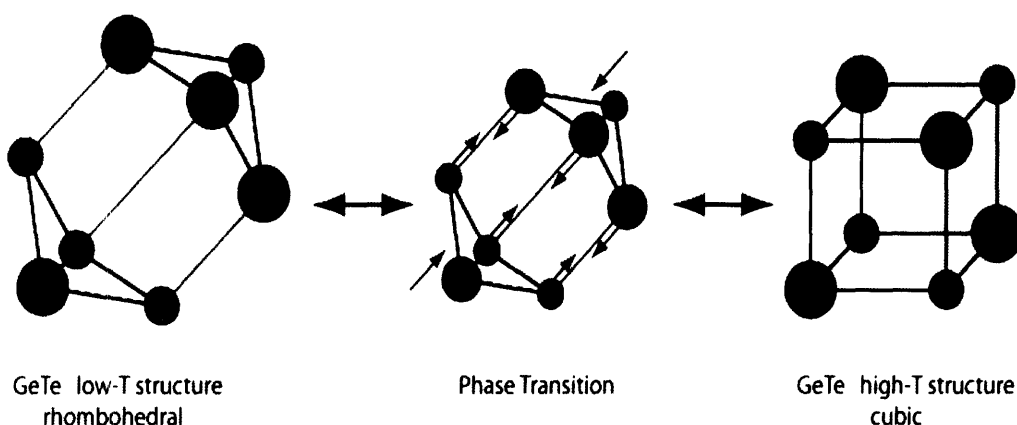


Figure 5-23. Schematic illustration of solid-solid phase transition in germanium telluride. The light spheres are Ge atoms, and the dark spheres are Te atoms. The low temperature structure has rhombohedral symmetry. At a critical temperature of 625 K, a lattice rearrangement occurs which corresponds closely to motion along the A_{1g} optic phonon, resulting in the high temperature cubic phase of GeTe.

IV-VI narrow gap semiconductor, with a strong absorption at the 800 nm fundamental wavelength of Ti:sapphire, making it amenable to study.

Polished samples of [001] GeTe were mounted in the reflection-mode single-shot experimental apparatus. Pump and probe wavelengths were fixed at 815 nm with vertical (+y) polarization. The time-resolved reflectivity of GeTe was measured in the manner described previously for Bi, Sb and Te. Single-pulse excitation results are shown in Figure 5-24. At the lowest pump pulse intensities, impulsive absorption at the laser wavelength generates coherent phonon excitation which is manifest as oscillations in the measured GeTe reflectivity. The observed response corresponds closely to the data for the semimetals Bi, Sb and Te. As the pump intensity increases, substantial red-shifting of the phonon frequency is observed, and the dephasing rate increases rapidly. At 10.0 mJ/cm², coherence is lost after only 3-4 vibrational cycles. For pump intensities of 16.0

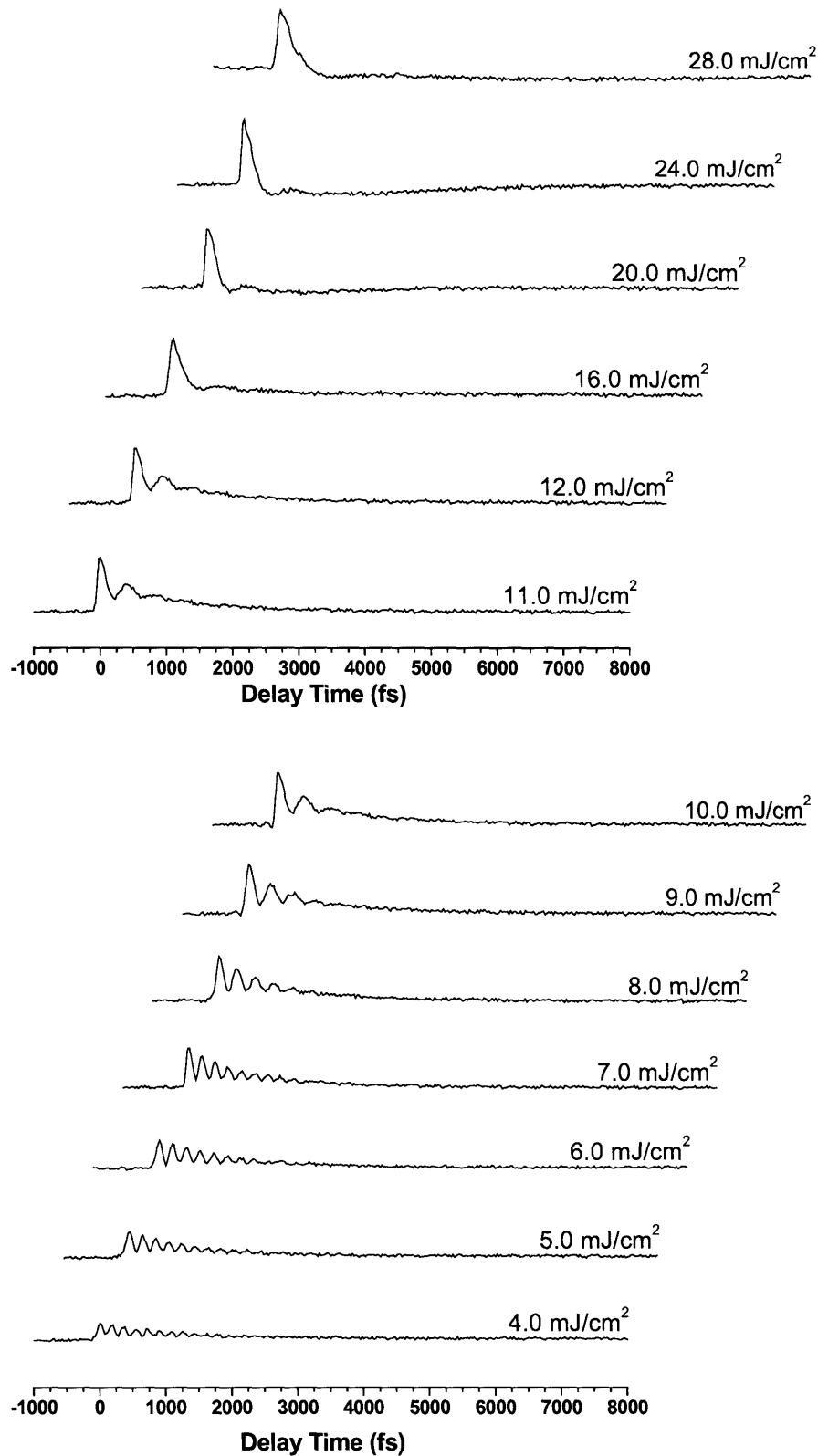


Figure 5-24. Time-dependent reflectivity of GeTe measured in a single laser shot. Pump pulse intensity is indicated on the right hand side of each data scan.

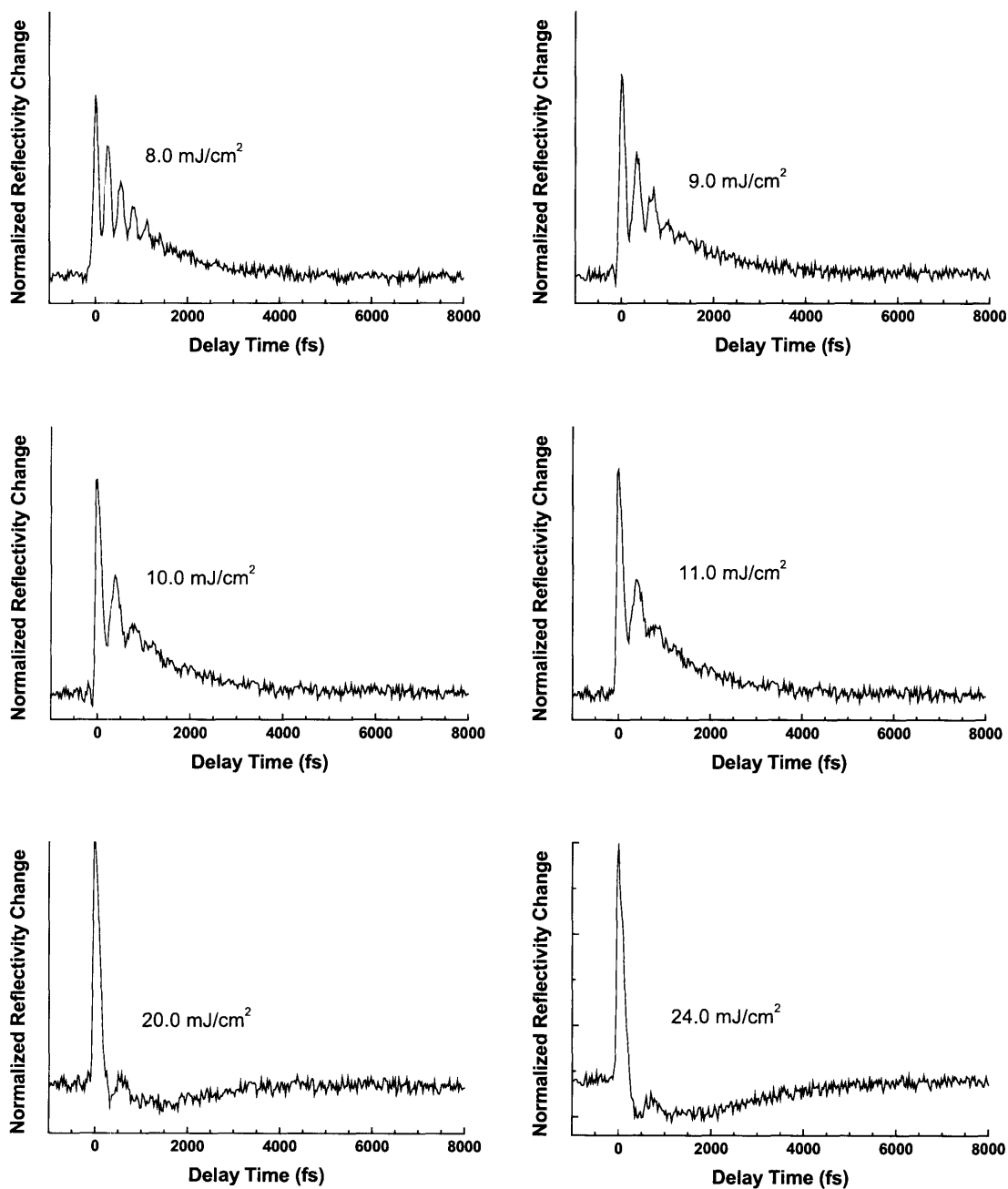


Figure 5-24 (cont'd). Expanded view of time-resolved reflectivity measurements for germanium telluride at various excitation intensities. As the pump pulse fluence increases from 8.0 mJ/cm² to 11.0 mJ/cm², the frequency of the A_{1g} phonon decreases and the dephasing rate increases. At 20.0 and 24.0 mJ/cm², the reflectivity falls very rapidly after the initial electronic contribution to the signal, and ΔR even changes sign for up to 3.5 ps.

mJ/cm^2 , the coherent phonon contribution disappears within 1.5 cycles. Such behavior is consistent with mode-softening which has been observed in other systems such as perovskite single crystals [49,50]. Essentially, as the critical temperature of the phase transition is approached, the bonds between atoms begin to effectively weaken as the atoms have enough thermal energy to sample the anharmonic regions of their potentials. When this occurs, phonon modes which are typically well-described by a harmonic oscillator model change from possessing underdamped to overdamped character on

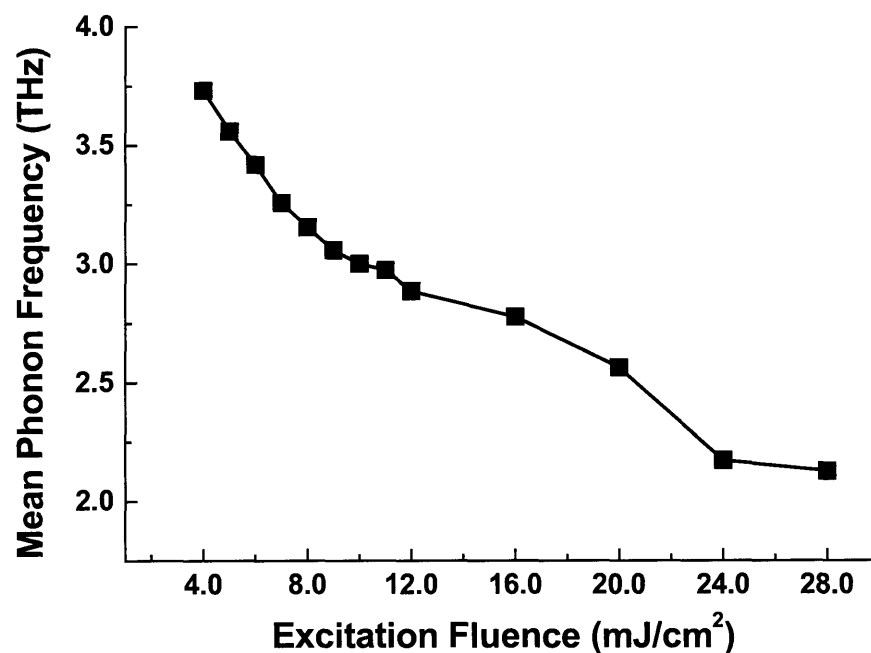


Figure 5-25. Variation of phonon frequency with excitation pulse intensity for germanium telluride. At low fluences, the frequency appears to scale almost linearly with intensity, but no plateau region is observed as for the semimetals.

account of the weaker effective force constants. The lattice no longer supports coherent vibrational motion since the restoring forces are not strong enough to overcome the kinetic energy of the nuclei and confine the atoms in the region of a potential minimum.

At the highest excitation fluences, the change in reflectivity even becomes negative for an interval of up to 3.5 ps. This occurs within about 1-1.5 vibrational cycles (the determination is difficult since the mode is so heavily damped). This is evidence for the occurrence of the solid-solid phase transition in GeTe in which the high temperature phase exhibits lower bulk reflectivity. Rapid cooling of the lattice within the spatial volume defined by the absorption region of the pump pulse leads to recovery of the original reflectivity, implying a reverse transition to the low temperature phase.

Figure 5-25 illustrates the phonon frequency as a function of pump intensity, determined by fitting the data scans of Figure 5-24 to Equation (5.2). At low excitation intensities, the frequency scales almost linearly, in agreement with previous results [87]. However, unlike the semimetal data shown earlier, the characteristic plateau region does not appear for GeTe. Instead, the A_{1g} frequency continues to monotonically red-shift as the pump fluence increases. Note that the total frequency shift is over 1.5 THz! This is plausible in instances where mode-softening via a structural phase transition is occurring. Unfortunately, excitation of the sample at 24.0 and 28.0 mJ/cm² results in surface damage to the sample which is visible under an optical microscope.

In order to drive the sample further from equilibrium while keeping the pulse fluence below damage threshold intensities, we considered the possibility of multiple-pulse excitation of GeTe. Hase and co-workers were able to observe further red-shifting of the A_1 phonon frequency by utilizing appropriately timed pulse pairs for excitation

[87]. To this end, we employed two-, three- and four-pulse trains instead of a single excitation pulse. The timings were adjusted such that each subsequent pulse arrived in-phase with the evolving coherent response in order to effect amplification of the oscillatory lattice motion.

The results of multiple-pulse excitation are shown in Figure 5-26. Double-pulse results exhibit rapid vibrational dephasing as pump intensity increases. For excitation at 10.0 and 12.0 mJ/cm², the change in reflectivity again switches sign shortly after $t = 0$. At 12.0 mJ/cm², the negative ΔR persists for 5.8 ps before the reflectivity is restored to its pre-pump value. Once again, this provides evidence for the existence of an optically-induced structural phase transition in germanium telluride. The trends in the three- and four-pulse excitation data are similar, except that at the highest intensities, the reflectivity change becomes negative and does not recover within the time window of the single-shot experiment.

Clearly, three- and four- pulse sequences are able to strongly drive coherent motion in the GeTe lattice. Based upon the transition from underdamping to overdamping of the A_{1g} mode, the extreme red-shift of the phonon frequency, and the observed sign change in the measured reflectivity signal, we conclude that the GeTe sample has likely undergone an ultrafast phase transition to its high- T structure when pumped at the highest fluences. Further interrogation of the lattice structure following a multipulse sequence is achieved by employing the delayed-pump technique to search for lattice coherences, as outlined for Bi and Te. We utilized all four pump beamlines which provides three intense pulses to drive coherent motion in the lattice and a fourth pump pulse which is used to search for further induced oscillatory behavior in the reflectivity.

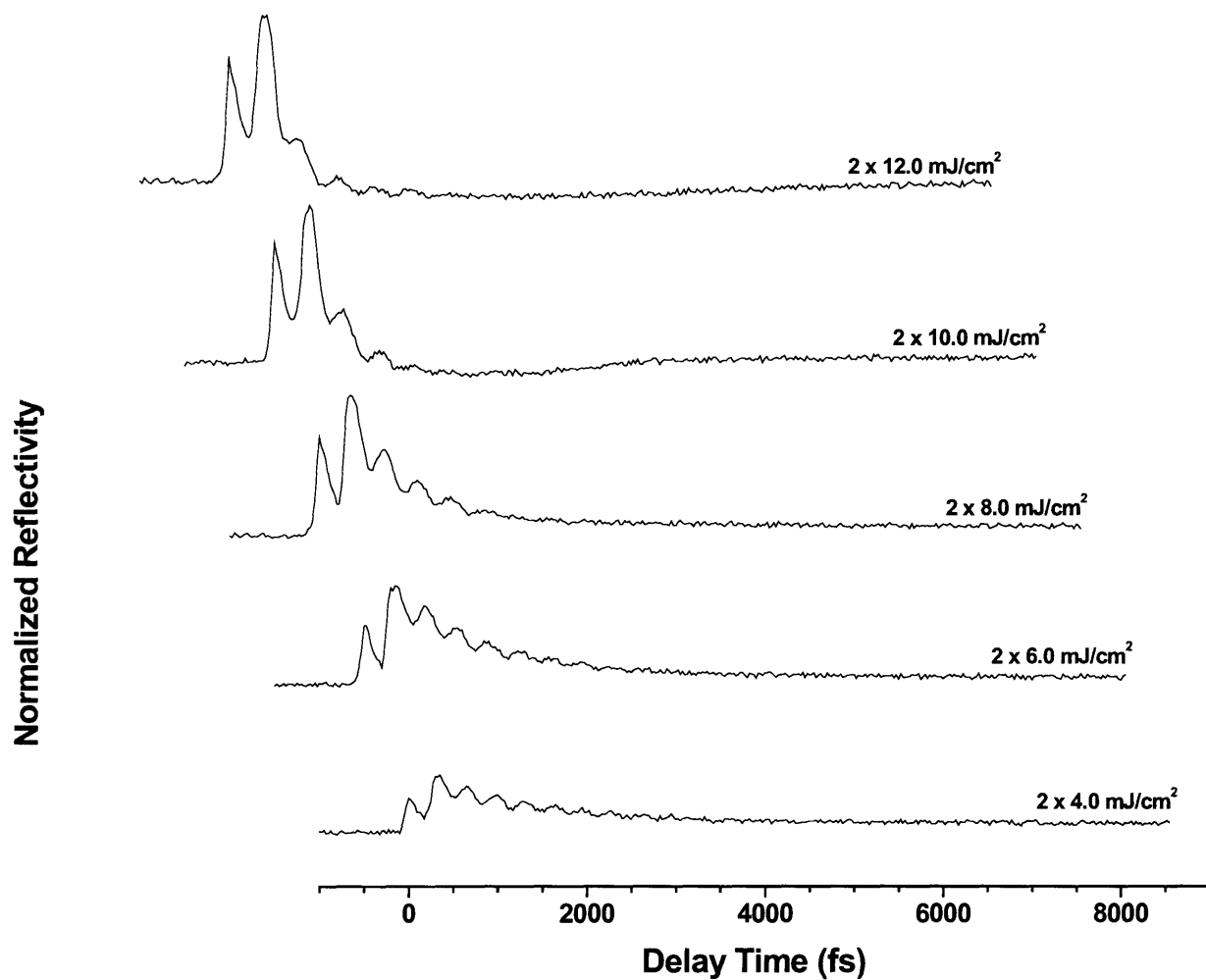


Figure 5-26. Two-pulse excitation of the A_{1g} lattice mode in germanium telluride. Amplification of the coherent response is achieved by adjusting the delays of pump pulses such that vibrational motion is driven in-phase. The damping rate increases strongly and the phonon frequency shifts lower as the pump intensity increases.

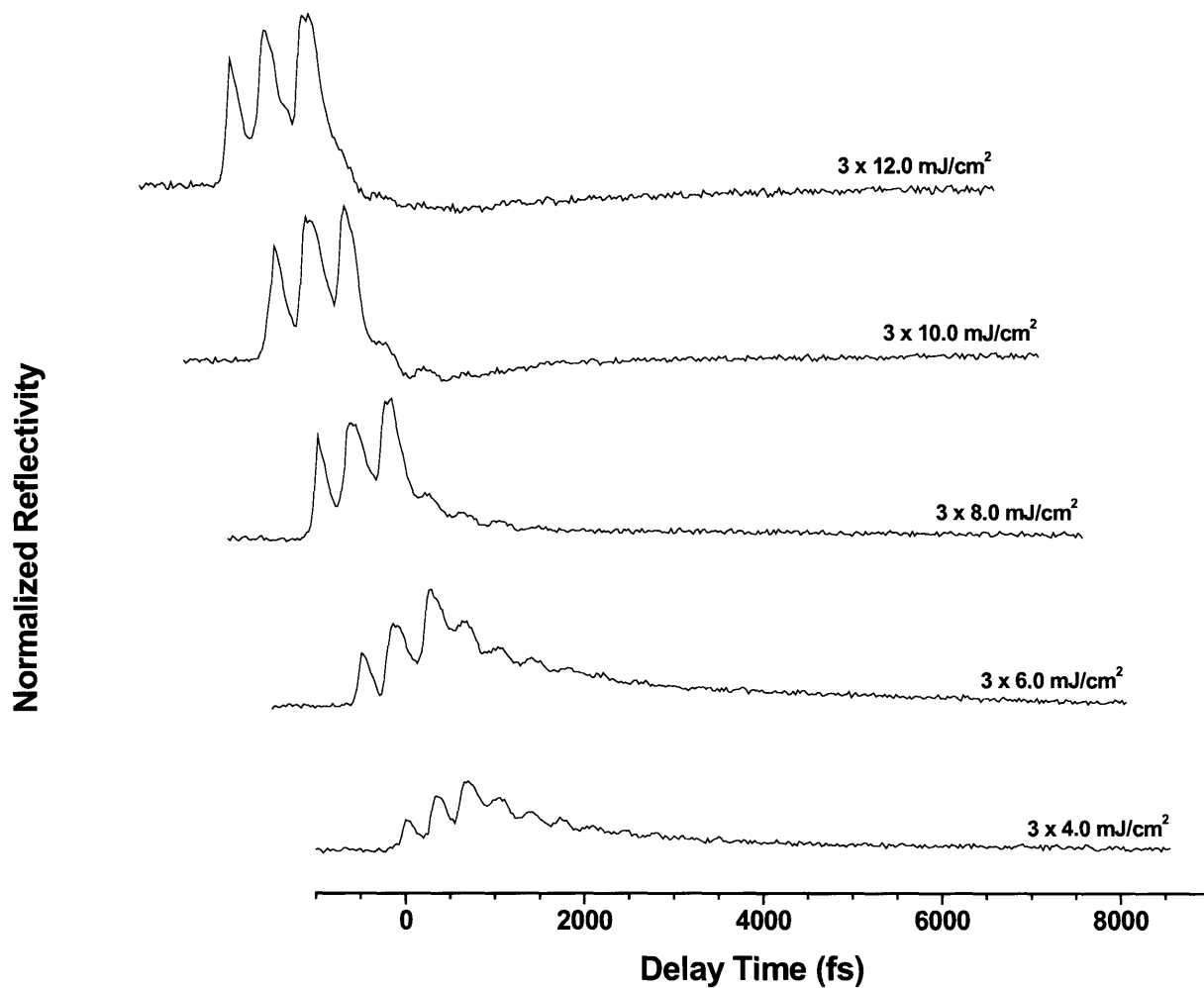


Figure 5-26 (cont'd). Three-pulse excitation of the A_{1g} lattice mode in germanium telluride. Amplification of the coherent response is achieved by adjusting the delays of pump pulses such that vibrational motion is driven in-phase. The damping rate increases strongly and the phonon frequency shifts lower as the pump intensity increases.

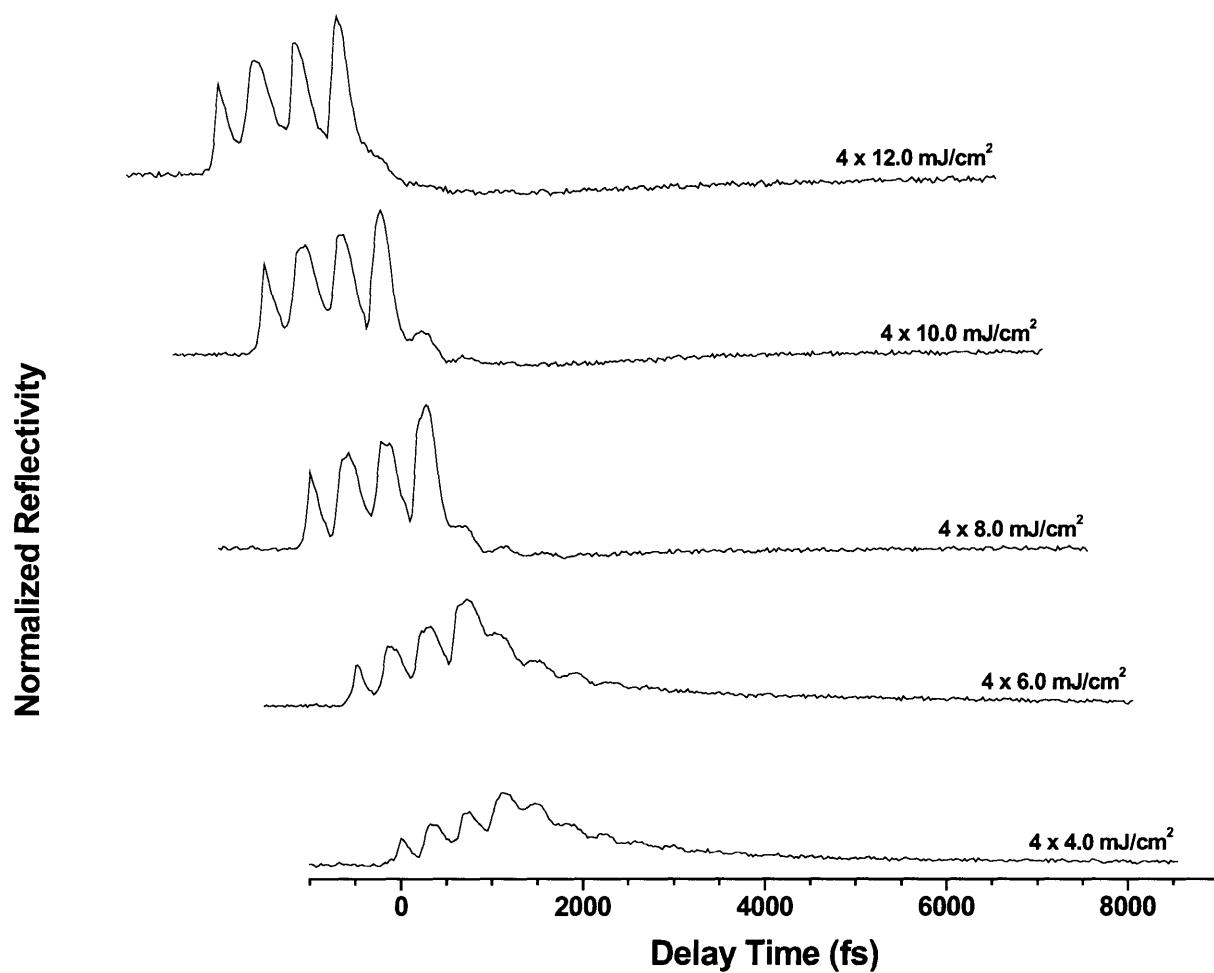


Figure 5-26 (cont'd). Four-pulse excitation of the A_{1g} lattice mode in germanium telluride. Amplification of the coherent response is achieved by adjusting the delays of pump pulses such that vibrational motion is driven in-phase. The damping rate increases strongly and the phonon frequency shifts lower as the pump intensity increases.

Initial results for short delay intervals between the group of three intense pump pulses and the fourth pump pulse are shown in Figure 5-27. Three pump pulses of intensity 4.0, 8.0 or 12.0 mJ/cm² (as indicated in the three panels of the figure) are used. The intensity of pulse 4 is 5.0 mJ/cm² in each case. From the reflectivity data at 4.0 mJ/cm², well defined oscillatory motion is present for each of the 3.0, 5.0 and 7.0 ps delays. The mean phonon frequency is 2.88 THz, a substantial shift from the measured value of 3.75 THz determined for single pulse excitation at 4.0 mJ/cm², and from the value of 3.80 THz extracted from frequency-domain Raman measurements [51]. At excitation intensities of 8.0 mJ/cm², a coherent signature of the lattice is again observed in the reflectivity data, although the depth of modulation in the oscillatory signal is less. The modulation depth increases as a function of delay, however, suggesting time-dependent recovery of the original lattice structure. The dephasing rate of the coherent response also decreases for increasing weak-pump delays, further suggesting vibrational cooling. At 8.0 mJ/cm² the mean phonon frequency is 2.46 THz.

Finally, for three-pulse excitation at 12.0 mJ/cm², no coherent oscillations are observed for any of the three inter-pulse delays. From the figure, the 3.0 ps delay setting corresponds to the region in which the change in reflectivity is negative, the 5.0 ps delay setting falls in the region where ΔR has recovered to approximately zero, and at 7.0 ps, the fourth pump pulse arrives with ΔR weakly positive again. The absence of lattice A₁ mode vibrations in any of these instances implies fundamental changes to the bulk crystal structure.

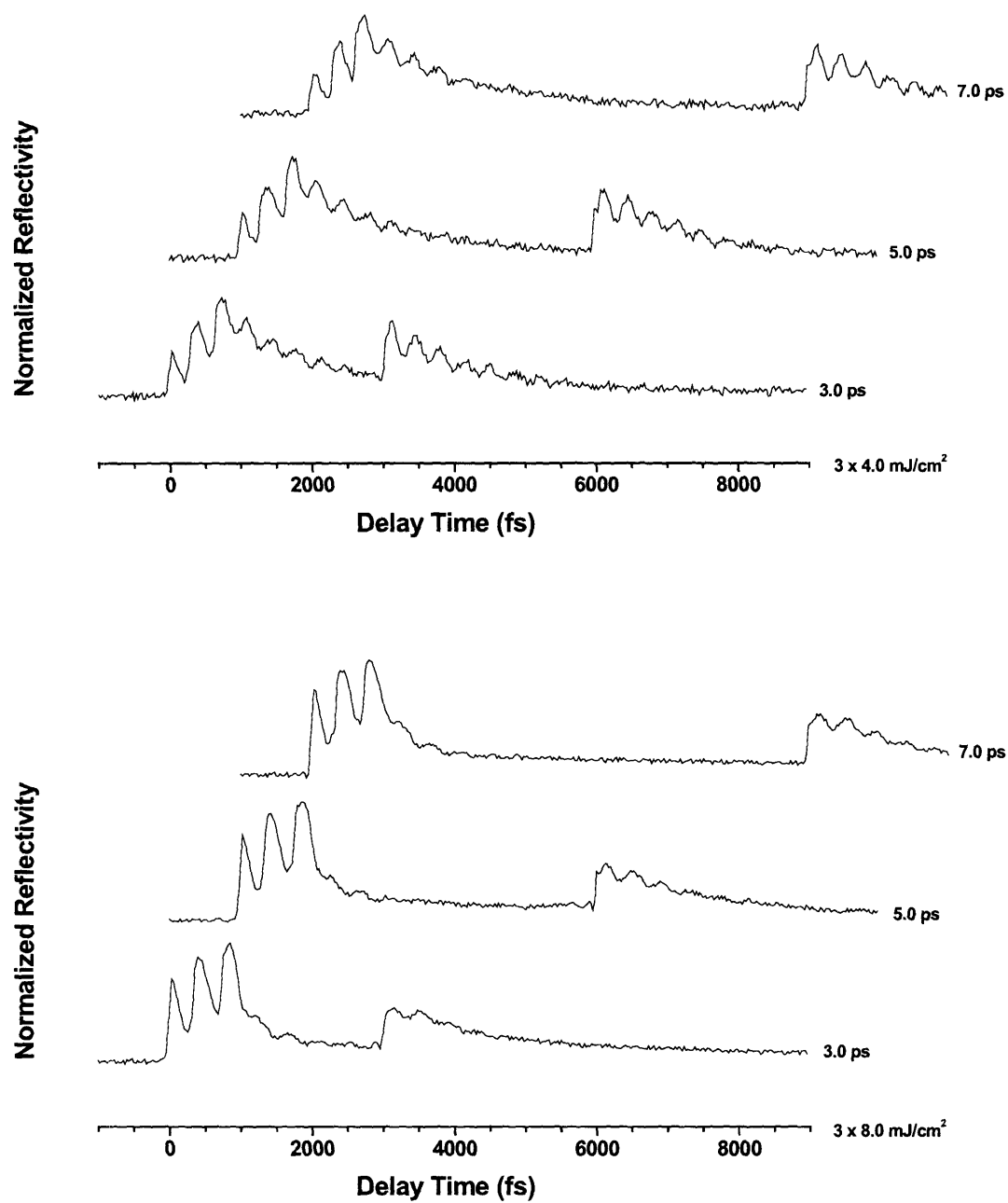


Figure 5-27. Excitation of germanium telluride with three intense pump pulses and a variably delayed weak fourth pump pulse. In the top panel, three pulses of intensity 4.0 mJ/cm^2 are used and in the bottom panel, three 8.0 mJ/cm^2 pulses are employed. The fourth pulse is maintained at 5.0 mJ/cm^2 in all cases. The delay time (relative to $t = 0$) of the fourth pulse is indicated to the right of each data sweep.

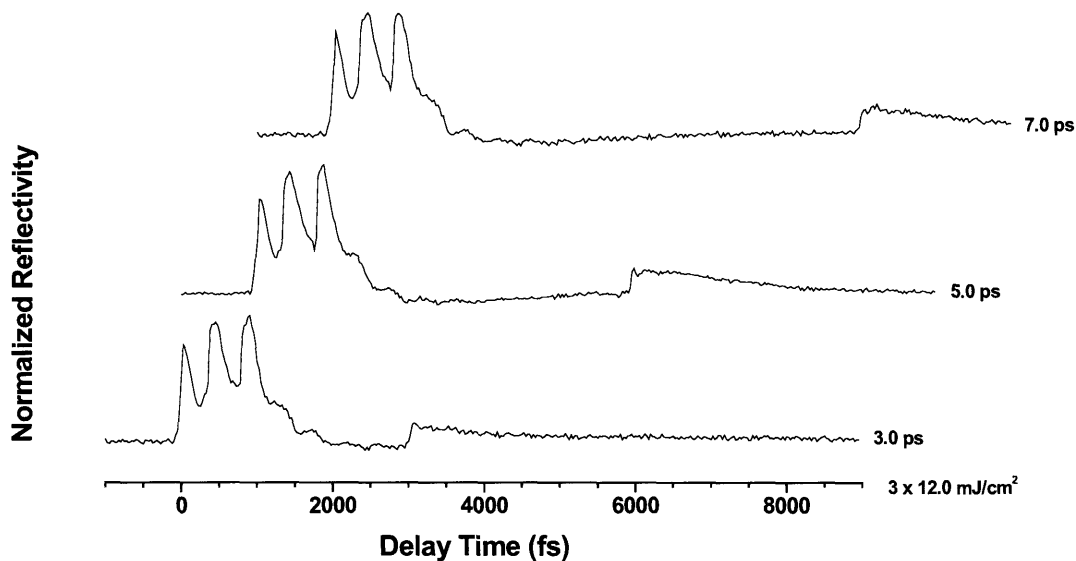


Figure 5-27 (cont'd). Excitation of germanium telluride with three intense pump pulses of 12.0 mJ/cm^2 and a variably delayed weak fourth pump pulse of intensity 5.0 mJ/cm^2 . The delay time (relative to $t = 0$) of the fourth pulse is indicated to the right of each data sweep.

The long-time evolution of lattice structure is investigated, as before, by introducing delays of more than 10 ps for the “interrogating” pump pulse, and shifting the probe window of the single-shot experiment to capture the response of the sample due to the fourth pump. The delays employed are 10, 25, 50, 75 and 100 ps after $t = 0$, for a variety of pump configurations: single pulse excitation at 12.0 and 20.0 mJ/cm^2 , and three-pulse excitation at 8.0 , 12.0 and 16.0 mJ/cm^2 per pulse. The data are illustrated in Figure 5-28. For single-pulse excitation at 12.0 mJ/cm^2 , poorly-resolved, low amplitude coherent oscillations are present after 25 ps, but the reflectivity signal only begins to exhibit well-defined modulations after 75 ps. At 20.0 mJ/cm^2 weaker oscillations are recovered, but only in the 100 ps delay scan. Triple-pulse excitation with 8.0 mJ/cm^2 per

pulse gives a similar result – oscillations in the time-dependent reflectivity are only reasonably well-resolved in the 100 ps sweep. Three-pulse excitation at intensities of 12.0 and 16.0 mJ/cm² yields reflectivities for which no additional coherence due to the weak fourth pump pulse is reliably observed, even after 100 ps. As these fluences are well below the single-pulse damage threshold for GeTe, we conclude that under these conditions, a photoinduced phase transition has taken place and the sample is in its high-temperature phase when the fourth pump pulse arrives.

5.7 Theory of Impulsive Absorption in Semimetals and Semiconductors

In this section, we will develop a straightforward description of the transient reflectivity signal observed for semimetals and semiconductors based upon the bulk properties of the sample. Unfortunately, the microscopic details of reflectivity modulations are extremely complex. The reflection coefficient is ultimately a result of the distribution of excited carriers in the material. However, the exact relationship between the quantum states of the carrier distribution, the topology of the electronic band structure, the carrier dephasing and recombination rates, energy coupling via electron-electron and electron-phonon interactions, and the resultant plasmon broadband absorptive states which characterize the material response is exceedingly difficult to treat theoretically. [84-86] No microscopic (i.e. quantum mechanical) theory exists which successfully incorporates all of these physical processes. Instead, we will focus on readily observable bulk properties and develop a simple picture for changes in reflectivity wherein the observed dynamics are related to a small number of material parameters which obscure deeper complexity.

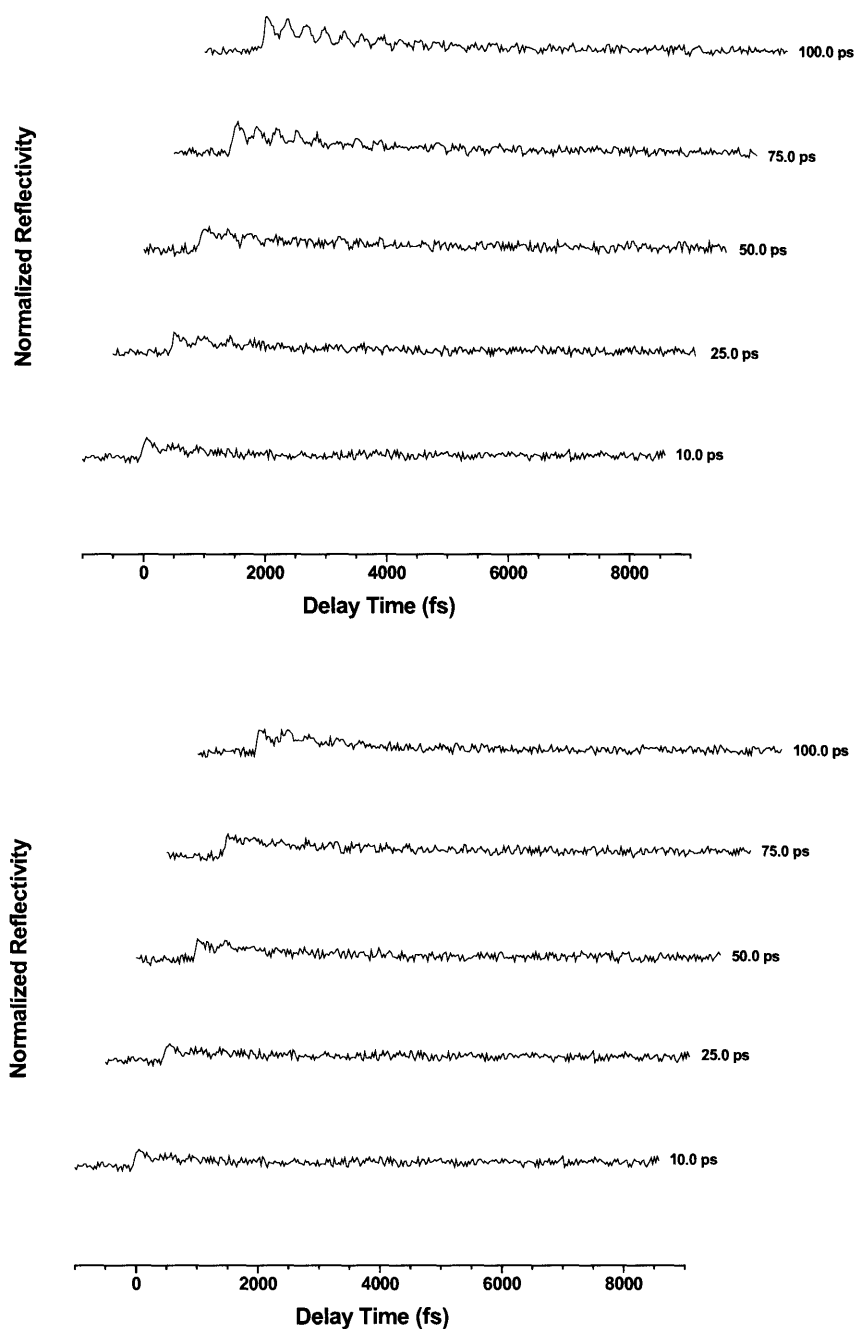


Figure 5-28. Long-time evolution of the coherent response in germanium telluride. A single excitation pulse of intensity 12.0 mJ/cm² (top) or 20.0 mJ/cm² (bottom) arrives at time zero. A second much weaker interrogating pulse (5.0 mJ/cm²) arrives after a delay indicated to the right of each trace. The probe window is adjusted such that the second pump pulse dynamics are captured.

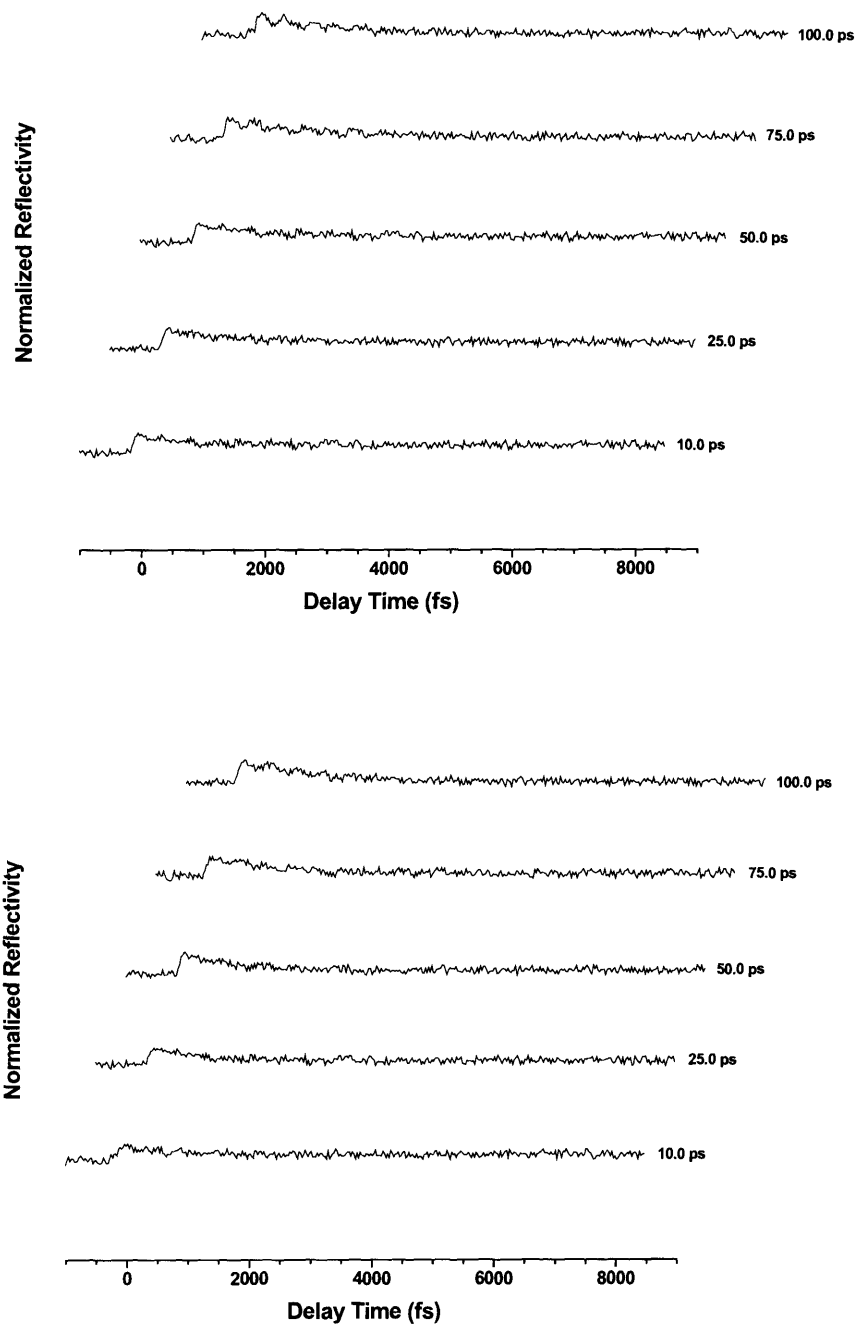


Figure 5-28 (cont'd). Long-time evolution of the coherent response in germanium telluride. Three excitation pulses of intensity 8.0 mJ/cm² (top) or 12.0 mJ/cm² (bottom) arrive in-phase to drive the A₁ phonon mode. A second much weaker interrogating pulse (5.0 mJ/cm²) arrives after a delay indicated to the right of each trace. The probe window is adjusted such that the second pump pulse dynamics are captured.

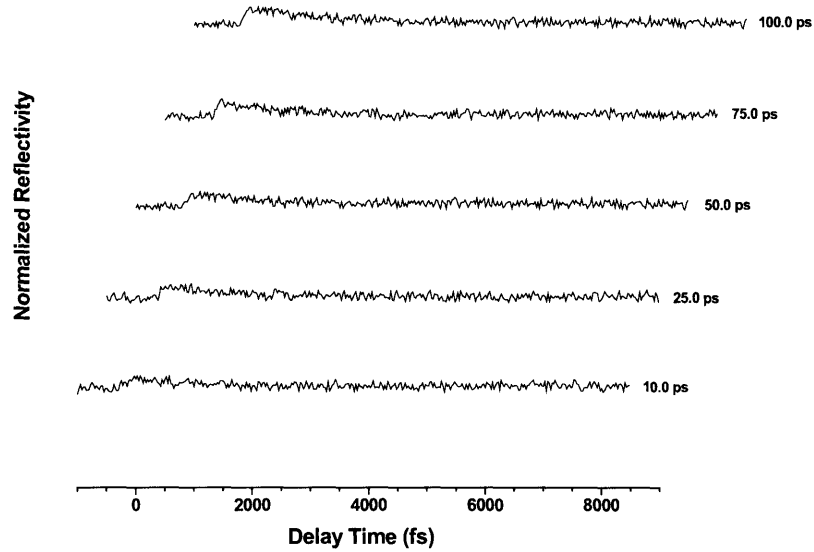


Figure 5-28 (cont'd). Long-time evolution of the coherent response in germanium telluride. Three excitation pulses of intensity 16.0 mJ/cm^2 arrive in-phase to drive the A_1 phonon mode. A second much weaker interrogating pulse (5.0 mJ/cm^2) arrives after a delay indicated to the right of each trace. The probe window is adjusted such that the second pump pulse dynamics are captured.

5.7.1 Classical Theory of Reflectivity

Consider a situation in which an optical pulse of central frequency ω is incident upon a semiconductor or semimetal sample at $t = 0$. The material in question possesses crystalline symmetry such that a Raman-active A_1 phonon mode exists. The effect of the pulse is to produce a change in reflectivity $\Delta R(t)$ which may or may not tend asymptotically to zero at long times. Experiments with pulses of long duration relative to the vibrational period of the A_1 phonon have previously demonstrated reflectivity modulation but no oscillatory behavior [52-54]. In such cases, $\Delta R(t)$ was interpreted as arising from changes in steady-state electron temperature due to pump-pulse excitation of the material. Clearly, this mechanism cannot describe the short-time oscillations we have observed for the materials of this study. Instead, a mechanism based upon impulsive

absorption and subsequent shifting of the equilibrium nuclear coordinate within the lattice structure leads to the observed modulations in reflectivity.

We will follow the development of Zeiger *et al.* in the description of the transient reflectivity signal [14]. If the equilibrium A_1 nuclear coordinate is $Q_0(t)$, where $Q_0 = 0$ before the optical pump pulse arrives, then the effect of the pulse is to shift the equilibrium value of Q_0 to some non-zero quantity. The pulse will also produce a change in the electron temperature at the Fermi level, $\Delta T_e(t)$. Interband absorptive transitions to bands above the Fermi level are possible for all of the investigated materials at the optical frequency employed in our experiments. Such transitions produce a time-dependent population of electrons per unit volume $n(t)$ which are in excited bands. Since the onset of oscillatory behavior in $\Delta R(t)$ coincides with absorption of the pump pulse, it is reasonable to assume that $n(t)$ provides the major contribution to $\Delta R(t)$ within our experimental time window.

Within the thin absorption layer near the surface of the sample, the time rate of change of $n(t)$ is described by

$$\frac{\partial n(t)}{\partial t} = \rho P(t) - \beta n(t) \quad (5.3)$$

The first term on the right hand side of Equation (5.3) is the rate of generation of carriers in excited state bands, assumed proportional to the optical power density $P(t)$. The second term describes the transfer rate of electrons from excited states to the valence band. The A_1 mode is excited due to coupling between the equilibrium coordinate $Q_0(t)$ and the distribution of excited state electrons $n(t)$. In a first order approximation, we can take this coupling to be linear:

$$Q_0(t) = \kappa n(t) \quad (5.4)$$

The equation of motion for the A_1 coordinate is taken to be

$$\frac{\partial^2}{\partial t^2} Q(t) = -\omega_0^2 [Q(t) - Q_0(t)] - 2\gamma \frac{\partial}{\partial t} Q(t) \quad (5.5)$$

where ω_0 is the natural frequency of the A_1 phonon and γ is the (phenomenological) damping rate. For a limited range of $P(t)$, we can assume that ω_0 does not depend too strongly upon $P(t)$ and so the expressions for $n(t)$ and $Q(t)$ can be written in the form

$$n(t) = \rho E_{pump} \int_0^\infty g(t-\tau) e^{-\beta\tau} d\tau \quad (5.6)$$

$$Q(t) = \frac{\omega_0^2 \kappa \rho E_{pump}}{(\omega_0^2 + \beta^2 - 2\gamma\beta)} \int_0^\infty g(t-\tau) \left[e^{-\beta\tau} - e^{-\gamma\tau} \left(\cos(\Omega\tau) - \frac{\beta'}{\Omega} \sin(\Omega\tau) \right) \right] d\tau \quad (5.7)$$

The power density $P(t)$ which correlates with Equations (5.6) and (5.7) is given by

$$P(t) = E_{pump} g(t) \quad (5.8)$$

where E_{pump} is the energy per unit area within the pump pulse and $g(t)$ is a normalized pulse shape function

$$\int_{-\infty}^\infty g(t) dt = 1 \quad (5.9)$$

The frequency Ω is defined as

$$\Omega = \sqrt{\omega_0^2 - \gamma^2} \quad (5.10)$$

and is reduced relative to its equilibrium value. The coupling between the excited state carrier density and phonon mode amplitude is also reduced from the equilibrium value via $\beta' = \beta - \gamma$.

The quantity $R(t)$ represents the reflectivity of the sample prior to the arrival of a pulse. The relative change in reflectivity due to the pulse can be expressed to first order as

$$\frac{\Delta R(t)}{R} = \frac{1}{R} \left[\left(\frac{\partial R}{\partial n} \right) n(t) + \left(\frac{\partial R}{\partial T_e} \right) \Delta T_e(t) + \left(\frac{\partial R}{\partial Q} \right) Q(t) \right] \quad (5.11)$$

In this way, modulation of the sample's reflectivity is expressed in terms of three variables. The first, which corresponds to the first term on the right hand side of Equation (5.11), is the change in reflectivity due to the excited state population of carriers. The second term arises from changes in the electron temperature distribution. The third term is the result of changes in the nuclear coordinates of lattice atoms due to motion along the A_1 coordinate.

For probe pulses of finite duration, the observed reflectivity modulation is effectively a time-average over the pulse width of the form

$$\overline{\frac{\Delta R(t)}{R}} = \frac{1}{R} \left[\left(\frac{\partial R}{\partial n} \right) \overline{n(t)} + \left(\frac{\partial R}{\partial T_e} \right) \overline{\Delta T_e(t)} + \left(\frac{\partial R}{\partial Q} \right) \overline{Q(t)} \right] \quad (5.12)$$

Each of the time-averaged quantities in Equation (5.12) is represented by a convolution over the probe pulse profile according to

$$\overline{\xi(t)} = \int_{-\infty}^{\infty} \xi(t') g(t'-t) dt' \quad (5.13)$$

Implicit in the development of Equations (5.12) and (5.13) is also the assumption that the probe-induced perturbation of the system is negligible.

From Equation (5.6), since there is no pump pulse prior to $t = 0$, we need integrate over only half the domain specified in Equation (5.13). In addition, the expression for $\Delta T_e(t)$ is similar to Equation (5.6) for $n(t)$. As a result, each of the functions $\xi(t)$ can be expressed in the form

$$\xi(t) = \int_0^{\infty} g(t-\tau) \psi(\tau) d\tau \quad (5.14)$$

The time-averaged quantities of Equation (5.13) are then

$$\overline{\xi(t)} = \int_{-\infty}^{\infty} \left(\int_0^{\infty} g(t'-\tau) \psi(\tau) d\tau \right) g(t'-t) dt' \quad (5.15)$$

By introducing $x = t' - t$ and reversing the order of integration in Equation (5.15), we find that

$$\overline{\xi(t)} = \int_0^{\infty} G(t-\tau) \psi(\tau) d\tau \quad (5.16)$$

The pulse autocorrelation function $G(t)$ is defined in Equation (5.16) as

$$G(t) = \int_{-\infty}^{\infty} g(t-\tau) g(\tau) d\tau \quad (5.17)$$

We will proceed under the assumption that the excited state carrier density $n(t)$ constitutes the dominant source term in Equation (5.11). Zeiger *et al.* have shown that if the electron temperature term is dominant, however, a very similar result is obtained [14]. Under these conditions, the expressions for the time-averaged carrier density and phonon coordinate are

$$\overline{n(t)} = \rho E_{pump} \int_0^{\infty} G(t-\tau) e^{-\beta\tau} d\tau \quad (5.18)$$

$$\begin{aligned} \overline{Q(t)} = & \frac{\omega_0^2 \kappa \rho E_{pump}}{(\omega_0^2 + \beta^2 - 2\gamma\beta)} \\ & \times \int_0^{\infty} G(t-\tau) \left[e^{-\beta\tau} - e^{-\gamma\tau} \left(\cos(\Omega\tau) - \frac{\beta'}{\Omega} \sin(\Omega\tau) \right) \right] d\tau \end{aligned} \quad (5.19)$$

The reflectivity R is described in continuum theory as a function of the complex dielectric constant (or index of refraction). Each of the contributions in Equation (5.11) modulates the dielectric constant directly, producing a time-dependent contribution to

$R(t)$. For normal incidence at pump and probe frequency ω , the reflectivity is given by the well-known relation

$$R = \frac{(n_1 - 1)^2 + n_2^2}{(n_1 + 1)^2 + n_2^2} \quad (5.20)$$

$$\varepsilon(\omega) = \varepsilon_1(\omega) + i\varepsilon_2(\omega) = (n_1 + in_2)^2$$

where the index of refraction of the material is given by $n = n_1 + in_2$. Combining the results of Equations (5.11), (5.18) and (5.19), the time-dependent reflectivity is expressed as

$$\begin{aligned} \frac{\overline{\Delta R(t)}}{R} = & A \int_0^\infty G(t-\tau) e^{-\beta\tau} \\ & + B \frac{\omega_0^2}{\omega_0^2 + \beta^2 - 2\gamma\beta} \int_0^\infty G(t-\tau) \left[e^{-\beta\tau} - e^{-\gamma\tau} \left(\cos(\Omega\tau) - \frac{\beta'}{\Omega} \sin(\Omega\tau) \right) \right] d\tau \end{aligned} \quad (5.21)$$

where we have defined the functions A and B as

$$\begin{aligned} A &= \frac{1}{R} \left[\left(\frac{\partial R}{\partial \varepsilon_1} \right) \left(\frac{\partial \varepsilon_1}{\partial n} \right) + \left(\frac{\partial R}{\partial \varepsilon_2} \right) \left(\frac{\partial \varepsilon_2}{\partial n} \right) \right] \rho E_{pump} \\ B &= \frac{1}{R} \left[\left(\frac{\partial R}{\partial \varepsilon_1} \right) \left(\frac{\partial \varepsilon_1}{\partial Q} \right) + \left(\frac{\partial R}{\partial \varepsilon_2} \right) \left(\frac{\partial \varepsilon_2}{\partial Q} \right) \right] \kappa \rho E_{pump} \end{aligned} \quad (5.22)$$

In order to simplify Equation (5.21), we note that for $\beta, \gamma \ll \omega_0$, only the first of the two oscillatory terms is significant. In addition, for the materials under investigation here, both pump and probe pulses are short enough, relative to the vibrational period, that we can approximate $G(t)$ as a δ -function. Under these assumptions, Equation (5.21) now takes the form

$$\begin{aligned}
\frac{\overline{\Delta R(t)}}{R} &= A e^{-\beta t} + B \frac{\omega_0^2}{\omega_0^2 + \beta^2 - 2\gamma\beta} \left[e^{-\beta t} - e^{-\gamma t} \left(\cos(\Omega t) - \frac{\beta'}{\Omega} \sin(\Omega t) \right) \right] \\
&= A e^{-\beta t} + B \frac{\omega_0^2}{\omega_0^2 + \beta^2 - 2\gamma\beta} \left[e^{-\beta t} - e^{-\gamma t} (\cos(\Omega t) + \Phi) \right]
\end{aligned} \tag{5.23}$$

The second oscillatory term effectively contributes an additional phase to the measured signal which is typically less than $\pi/12$ for most semimetals [12-14]. In our experiments, this residual phase is difficult to determine accurately since we sample the evolving material response at discrete 25 fs intervals.

When the rate β at which excited carriers return to the valence band is large, it is evident from Equation (5.23) that the oscillatory component of the reflectivity signal is significantly damped. This situation corresponds to rapid re-establishment of the pre-pump equilibrium nuclear coordinates. With the lattice potential quickly returning to its unperturbed form, there is no driving force for the oscillatory motion. In addition, for large β , the contribution of the second oscillatory term in Equation (5.21) may become non-negligible. In such a case, if the oscillating component of the reflectivity signal is measureable, we expect a phase shift of greater magnitude.

The quantity $(d\varepsilon/dQ)$ which appears in Equation (5.22) is related to the Raman scattering cross-section at the frequency of the pump and probe pulses. As a result, a condition for the detection of A_1 -symmetry oscillations is the presence of a significant Raman cross-section at frequency ω . Within this model, however, only the probing process, and not the excitation process (which arises from $n(t)$), is directly related to the Raman scattering cross section. Through the imaginary part of ε , resonance enhancement of the Raman scattering process can be significant for the semimetals.

Both A and B are proportional to the pump pulse energy, which implies that the measured response depends linearly upon the pulse fluence. These can be thought of as empirically determined parameters which characterize a particular material. In general, the signs of the two parameters appear to be uncorrelated, even for materials other than the semimetals studied here [54]. From Equation (5.22), the magnitude and sign of B depend upon $d\epsilon_1/dQ$ and $d\epsilon_2/dQ$. However, we cannot obtain information about these parameters from spontaneous Raman scattering since the cross-section is proportional to $|d\epsilon/dQ|^2$.

Fitting of the low-intensity data of Figures 5-6, 5-10, 5-13 and 5-24 to Equation (5.23) yields values of the parameters A , B and Φ for the materials Bi, Sb, Te and GeTe respectively. The results are shown in Table 5-1. As noted, the signs of A and B bear no

Table 5-1. Material properties from analysis of impulsive absorption measurements.

Material	A	B	Φ (deg)
Bi	$-4.4 \pm 0.4 \times 10^{-3}$	$+3.3 \pm 0.4 \times 10^{-3}$	-10 ± 5
Sb	$+2.4 \pm 0.1 \times 10^{-3}$	$+2.7 \pm 0.3 \times 10^{-2}$	$+2 \pm 4$
Te	$-6.8 \pm 0.2 \times 10^{-3}$	$+1.5 \pm 0.1 \times 10^{-2}$	$+11 \pm 5$
GeTe	$+1.9 \pm 0.1 \times 10^{-2}$	$+4.3 \pm 0.5 \times 10^{-2}$	-15 ± 4

relationship to one another. Determination of the oscillation phase is subject to errors due to the 25 fs sampling interval, as noted previously. Our results for the semimetals Bi, Sb and Te differ from those of other groups by less than 10% [14]. There are no literature reports of the value of these constants for GeTe.

The simple first-principles model advanced herein captures all of the salient features observed in the reflectivity data. Physically, excitation of electrons from the valence to the conduction band alters the equilibrium positions of lattice atoms along the

A_1 normal mode coordinate. The coherent atomic motion begins from a maximum inner displacement along the new potential. The bulk reflectivity of the sample is modulated both by (coherent) atomic motion along the newly-deformed potential and by the hot-electron distribution created during the absorption process (background). Equation (5.23) captures both of these features. The first two terms are decaying exponential functions, with decay constant β , and correspond to hot-electron population contributions to the reflectivity background. The third term, which oscillates as $\cos(\Omega t)$ with a small phase shift, corresponds to motion along the symmetric phonon coordinate and decays with phenomenological rate γ .

5.7.2 Microscopic Theory of Coherent Phonon Oscillations

In order to achieve some estimation of the lattice displacements involved in our experiments, it is necessary to develop a theory which connects the observed oscillations in reflectivity to the microscopic parameters of the system. In this regard, we will follow the work of Kuznetsov and Stanton [55,56] which was originally developed to examine coherent phonon dynamics in GaAs [57-59]. The theory is closely related to the two-point representation of Scholz, Pfeifer and Kurz [60] which was used to explain coherent responses in Ge, but we will employ a more familiar k -space formalism.

Consider the following Hamiltonian for a material with a two-band electronic structure, and phonon mode q , in the vicinity of an optical transition:

$$\begin{aligned}
 H_{el} = & \sum_{k,\alpha} \varepsilon_{\alpha k} c_{\alpha k}^\dagger c_{\alpha k} + \sum_q \hbar \omega_q b_q^\dagger b_q \\
 & + \sum_{\alpha,k,q} M_{kq} (b_q + b_{-q}^\dagger) c_{\alpha k}^\dagger c_{\alpha k+q}
 \end{aligned} \tag{5.24}$$

In Equation (5.24), c and c^+ are the second-quantization operators of the electron in k -space and $\varepsilon_{\alpha k}$ is the energy dispersion in band $\alpha = \{c, v\}$ (conduction or valence). Lattice vibrational energy is represented by the second summation, which contains terms which depend upon the phonon frequency ω_q and the phonon creation and annihilation operators b_q^+ and b_q for phonon mode q . The third summation describes deformational electron-phonon coupling; that is, the change in the energy of the state $\{\alpha, k\}$ due to lattice displacement. The M_{kq} are coupling constants which characterize the deformation at specific k -points.

The phonon creation and annihilation operators are related to the lattice displacement operator u by the expression [61]

$$u(r) = \sum_q \sqrt{\frac{\hbar}{2\eta V \omega_q}} [b_q e^{iqr} + b_q^\dagger e^{-iqr}] \quad (5.25)$$

The quantity η is the reduced mass density and V is the system volume.

For a nonzero mean lattice displacement which leads to periodic modulation of the properties of the material, the average values of the single-phonon creation and annihilation operators in Equation (5.25) must also be non-zero. In order to connect the real-space motion of lattice atoms to the phonon density, we can define the coherent amplitude of the phonon mode q as

$$D_q = \langle b_q \rangle + \langle b_q^\dagger \rangle = B_q + B_{-q}^* \quad (5.26)$$

such that it is proportional to the Fourier components of the displacement operator given by Equation (5.25):

$$\langle u(r) \rangle = \left\langle \frac{1}{V} \int dr u(r) e^{-iqr} \right\rangle = \sqrt{\frac{\hbar}{2\eta V \omega_q}} D_q \quad (5.27)$$

In Equation (5.26), the mean values of the creation and annihilation operators will be zero if the population in the mode q is a whole number – that is, if the oscillator q is in an eigenstate. In such a case, no average displacement of the lattice exists although statistical fluctuations about the zero-displacement position occur.

However, if the oscillator exists in a coherent superposition of vibrational eigenstates (i.e. a superposition of states with different quanta of phonons), the mean displacement generally does not average to zero. The exact value of the averaged operators in Equation (5.26) depends upon the functional form of the eigenstates of the system. For example, consider a set of states which is frequently used in quantum optics to describe the quantum state of an electromagnetic field:

$$\Psi = |z\rangle = \sum_n \frac{z^n}{\sqrt{n!}} e^{-z^2/2} |n\rangle \quad (5.28)$$

The average for the superposition in Equation (5.28) is given by

$$B_q = \langle z | b_q | z \rangle = z \quad (5.29)$$

In order to establish the equations of motion for the coherent phonon amplitude in the material of interest, we utilize the operator form of the Schrodinger equation. Commuting the Hamiltonian of Equation (5.24) with the phonon annihilation operator, we find the following:

$$\begin{aligned} \frac{\partial B_q}{\partial t} &= i\omega_q B_q + i \sum_{\alpha,k} M_{kq}^{\alpha} n_{k,k+q}^{\alpha} \\ &= i\omega_q B_q + i \sum_{\alpha,k} M_{kq}^{\alpha} \langle c_{\alpha k}^{\dagger} c_{\alpha k+q} \rangle \end{aligned} \quad (5.30)$$

The terms inside the summation of Equation (5.30) consist of the products of coupling constants M with electronic density matrix elements. The spatial charge density of electrons is reflected in the electronic density matrix according to

$$\rho_{el}(r) = \frac{e}{V} \sum_{\alpha, k, q} n_{k, k+q}^{\alpha} e^{iqr} \quad (5.31)$$

From Equation (5.30), it is clear that electron-phonon interactions occur between the coherent phonon amplitude and Fourier components of the electron density at the same wave vector. Taking the time-derivative of Equation (5.30) and adding equations for both B_q and B_{-q}^* from Equation (5.26), the equation of motion for the coherent phonon amplitude D_q is

$$\frac{\partial^2}{\partial t^2} D_q + \omega_q^2 D_q = -2\omega_q \sum_{\alpha, k} M_{kq}^{\alpha} n_{k, k+q}^{\alpha} \quad (5.32)$$

Note that Equation (5.32) closely resembles Equation (5.5) from the phenomenological analysis presented in the previous section. The right hand side of Equation (5.32) constitutes the driving source for the coherent motion, since the electronic density matrix terms are the result of optical excitation. Equation (5.32) is an exact solution within the context of the Hamiltonian specified by (5.24). However, damping of the coherent response due to phonon-phonon interactions is not taken into account. It is expected that such processes are relatively weak compared to the included electronic effects.

An optical pump pulse creates excited state carriers in a state which is macroscopically uniform. As a result, the electronic density matrix is diagonal and appears as

$$n_{k, k'}^{\alpha} = f_k^{\alpha}(t) \delta_{kk'} \quad (5.33)$$

where the quantity f is the carrier distribution function in k -space. As a result, the only mode which can be coherently driven via optical excitation is the $q = 0$ mode. Equation (5.32) contains contributions from the carrier distribution functions in both the valence and conduction bands. Evaluation of such distributions on a femtosecond time scale is a complex process which typically consists of solving the Boltzmann equation while taking into account relevant scattering processes [62]. A simpler approach, however, is to assume that the electron-phonon couplings M are relatively independent of k . In such a case, the sum on the right hand side of Equation (5.32) yields $N(t)$, the total number of electron-hole pairs. The equation of motion for the coherent amplitude becomes

$$\begin{aligned} \frac{\partial^2}{\partial t^2} D_0 + \omega_0^2 D_0 &= 2\omega_0 \sqrt{\frac{\hbar}{2\omega_0 \eta V}} [C^v - C^c] N(t) \\ &= W \times N(t) \end{aligned} \quad (5.34)$$

In Equation (5.34), the subscript “0” has replaced “ q ” since the result is valid for an A_1 mode. C is the deformation potential in either the valence or conduction band.

The electron density is typically assumed to be generated by the optical pump pulse according to the simple relation

$$\frac{dN(t)}{dt} = N_0 I(t) \quad (5.35)$$

where $I(t)$ is the pump intensity. Substituting this result into Equation (5.34), we find that

$$D_0(t) = \frac{W}{\omega_0^2} N_0 [1 - I(\omega_0) \cos \omega_0 t] \quad (5.36)$$

The coherent amplitude of the D_0 phonon contains a constant shift along the phonon coordinate, with oscillations around the new equilibrium displacement. The amplitude of the oscillations is directly related to the amplitude of the Fourier component of the

excitation envelope at ω_0 , the phonon frequency. For excitation pulses much longer than the phonon period, the amplitude is very small. By contrast, for short pulses, the oscillation amplitude is equal to the shift of the equilibrium displacement – the phonon mode behaves as a classical, displaced oscillator released at $t = 0$. The dynamical picture suggested by Equation (5.36) agrees well with the results of the previous section, and also resembles electron-induced acoustic lattice deformation [63]. The principal difference between optical and acoustic deformation is that the $q = 0$ acoustic mode cannot oscillate.

We can now arrive at an estimate of lattice displacements due to coherent oscillations. The real-space amplitude is given by

$$U_0 = \sqrt{\frac{\hbar}{2\omega_0\eta V} \frac{WN_0}{\omega_0^2}} = \frac{C^v - C^c}{\eta\omega_0^2} \frac{N_0}{V} \quad (5.37)$$

Order of magnitude estimates for the quantities in Equation (5.37) are easily obtained. The deformation potential difference is roughly 10^9 eV/cm and the initial excitation density N_0 is roughly 10^{19} cm⁻³ for semimetal systems under our excitation conditions. For an order of magnitude estimate we take the volume to be 1 cm³. For bismuth, with density 9.78 g/cm³ and A₁ mode frequency 2.9 THz, the displacement amplitude is roughly 0.0026 Å. For antimony, with density 6.70 g/cm³ and mode frequency 4.5 THz, the maximum displacement is 0.0012 Å, and for tellurium (density 6.24 g/cm³ and frequency 3.6 THz) the displacement is roughly 0.0020 Å. For germanium telluride at low excitation fluences, the calculated equilibrium displacement is 0.0029 Å. In each of the four cases, these are moderate perturbations of the lattice structure – nearly 0.1% of a typical lattice constant – and they are indicative of a system evolving under non-equilibrium conditions.

In both of the models presented thus far, only the A_1 mode is excited via impulsive absorption on account of the preserved macroscopic symmetry in the non-equilibrium material. In the model of Kuznetsov and Stanton, purely cosinusoidal oscillations result from optical excitation. In the model of Zeiger *et al.*, the observed modulation of the reflectivity shows oscillatory behavior which is *mostly* cosinusoidal, although the residual phase term is observed to be non-zero. The phase term of the Zeiger model (which we will henceforth refer to as the DECP model) is of a sinusoidal functional dependence – the functional form suggests a contribution from ISRS.

The additional phase contribution to the DECP model, as well as the observation by Hase and co-workers of the very weak E_g mode of bismuth in transient reflectivity data [18] implies that the original DECP formalism may be somewhat too restrictive in terms of providing a complete picture of the material dynamics under highly non-equilibrium conditions. To this end, Garrett and co-workers [27] have described the DECP model as a special case of a more general coherent Raman scattering mechanism which includes both impulsive and displacive components. Rather than assuming a diagonal form for the electronic density matrix of Equation (5.32), they expand the summation on the right hand side via second-order perturbation theory. This procedure also imposes no symmetry restrictions on the modes which can be excited, accounting for their own observation of E_g oscillations for antimony.

5.7.3 Variation of Coherent Phonon Frequency

Thus far, the dependence of the oscillation amplitude on excitation pulse intensity has been explained via the dominant contribution of excited state carriers in shifting the equilibrium position of the A_1 lattice mode. The coherence dephasing rate is treated

phenomenologically; in practice, the dephasing time depends in complicated fashion upon incoherent phonon-phonon and electron-phonon scattering processes and the decay rate of photoexcited carriers. In this section, we will briefly discuss possible explanations for the variation of the coherent phonon frequency as a function of excitation fluence.

Hase *et al.* have attributed the frequency dispersion of the A_1 mode in Bi to sampling of the anharmonicity of the lattice potential by ions displaced far from their equilibrium coordinates [18]. They simply construct an expression for the phonon frequency which contains a constant (zero-displacement) term and a term which is quadratic in the displacement. Using this nonlinear equation for ω , they are able to achieve a good numerical fit to experimental data. The quadratic dependence of the oscillator frequency is therefore ascribed to contributions from the anharmonic cubic term of the lattice potential.

In addressing the issue of anharmonicity, we recognize that variation in the phonon frequency due to the anharmonicity of the potential suggests large amplitude oscillatory motion. The overall frequency shift for bismuth is more than 0.3 THz over the range of pump fluences studied. If the ground state potential is essentially harmonic under equilibrium conditions, the range of displacements sampled must be large in order for anharmonicity to shift the phonon frequency by such an amount. Our estimation of the mean oscillation amplitudes in the semimetals do not support this conclusion. In addition, as the anharmonic oscillations decay, one would expect a return to the unperturbed A_1 mode frequency since now, only the harmonic part of the potential is sampled. This is not observed; in Figure 5-6 for instance, the equilibrium phonon frequency in Bi is 2.9 THz. At an excitation fluence of 9.0 mJ/cm^2 , the mean phonon

frequency is 2.77 THz. If we perform a windowed LP-SVD analysis of the signal, the mean frequency of the first two oscillation cycles is 2.75 THz, for cycles 3-5 we find 2.77 THz, and for cycles 6-8 the recovered frequency is 2.78 THz. Clearly, even as the oscillations dephase (presumably near the zero-displacement position on the A_1 coordinate), the phonon frequency does *not* return to the equilibrium value of 2.9 THz. Thus, while anharmonicity may play some role in determining the A_1 mode frequency, the mechanism is unlikely to be as straightforward as arising simply from anharmonic terms describing the potential near the inner and outer turning points of the well. The “new” lattice potential is essentially created instantaneously – relative to the phonon period – via optical excitation, but as excited carriers return to the valence band, the perturbed potential also reverts to its original form. The anharmonicity associated with this process is also just as likely to influence the phonon frequency. In any event, results such as the 9.0 mJ/cm² excitation of Bi described above illustrate a nearly instantaneous shift of the phonon frequency and only a slow return to the equilibrium value, and this behavior is not consistent with the observed changes in frequency being dominated by anharmonicity.

Cheng *et al.* suggest [11-13] that the source of the transient shift in phonon frequency for antimony is due to reduced ionic screening by excited carriers. The promotion of large numbers of valence electrons from bonding to antibonding states naturally reduces the restoring force which stabilizes the lattice. This purely electronic, rather than phonon-dependent, explanation for lattice softening (which increases with increasing number density of carriers) is advanced to account for the shift to lower lattice phonon frequencies.

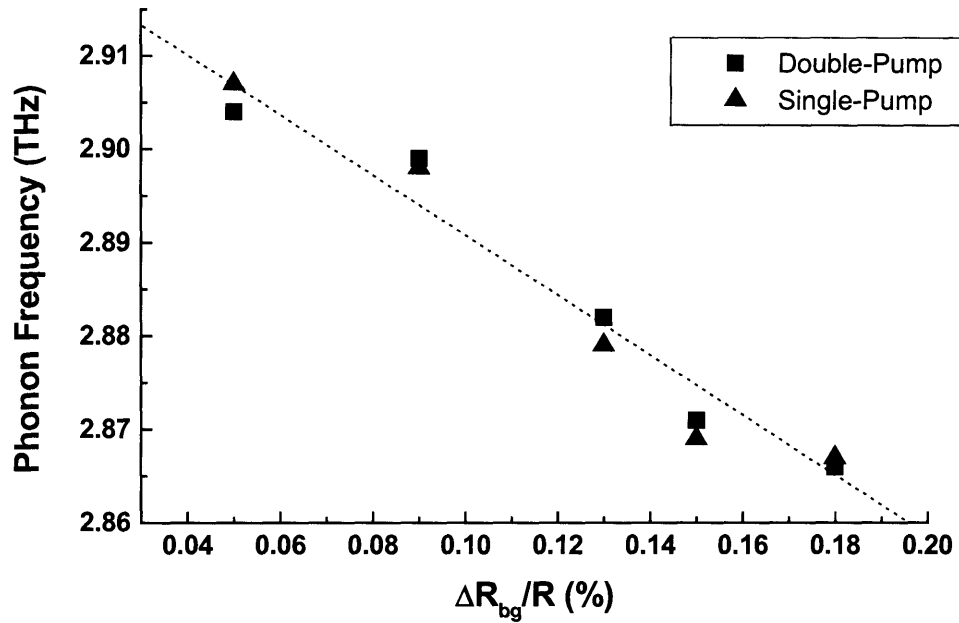


Figure 5-29. Variation of phonon frequency with carrier density for single- and double-pump excitation of bismuth.

This interpretation which attributes phonon frequency shifts to electronic, rather than phonon amplitude-dependent, origins is supported by the two-pulse experimental data for both bismuth and tellurium. Consider for instance the data in Figure 5-18 for double-pulse excitation of Bi. The initial excitation fluence is 9.0 mJ/cm^2 and the second pulse, which arrives at one of a series of delays (3.0, 4.0, 5.0, 6.0, or 7.0 ps) is 6.0 mJ/cm^2 . For each of these cases, the coherence due to the first pulse has largely decayed when the second pulse arrives. However, the electronic background signal, which may be taken as a measure of the density of carriers, has not returned to its equilibrium value. If we plot the phonon frequency following the second excitation pulse as a function of the amplitude of the electronic background signal at the time when the second pulse arrives, a linear relationship is observed, as depicted in Figure 5-29. Also

shown in Figure 5-29 is data from single-pulse excitation of Bi at 6.0 mJ/cm^2 . In this case, a windowed LP-SVD analysis of the oscillatory portion of the signal is performed with the window centered around the response to the second excitation pulse. The phonon frequency thus determined is plotted against the electronic background signal.

The striking feature of these results is the observation that the shift of the phonon frequency is entirely dependent upon the carrier density. The results, within experimental error, are the same for both single- and double-pulse excitation. Similar results are obtained for single crystal samples of tellurium and based upon this data, we conclude that the observed phonon mode softening in the semimetals under consideration is primarily an electronic effect – that is, an effect induced by excited state carriers. Consistent with this is the result that for these excitation intensities, a pulse that is delayed by tens of picoseconds (by which time the excited electrons have returned to the valence band) yields oscillations that match the unperturbed vibrational frequency.

Finally, another mechanism which may contribute to the variation of the phonon frequency is found in the strong inhomogeneity of the initial carrier density. The number density of photoexcited carriers is proportional to the intensity of the initial optical pump pulse. The penetration depth of the pump is not zero, however. Typically, an optical pulse of wavelength 800 nm is absorbed to a depth of about 50 nm. The intensity of the pulse naturally falls as a function of increasing depth, creating a gradient of carrier densities in the propagation direction. Increasing the excitation fluence increases the width of the distribution. Any given carrier density induces a downward shift in the equilibrium phonon frequency and as result, the Fourier spectrum for the A_1 mode will be asymmetrically broadened on the red side of the central frequency. In the time domain,

the result is a net increase in the vibrational period to a value which corresponds to the inverse Fourier transform of the carrier-dependent frequency distribution. Since the decay rate of carriers is proportional to their number density, the phonon frequency will begin to return to its equilibrium value at different rates throughout the excitation volume; the rate will be fastest at the front surface where the carrier density is highest.

5.7.4 Intensity-Dependent Reflectivity and Carrier Relaxation

A number of intensity-dependent effects were observed in the time-resolved reflectivity measurements of Bi, Sb, Te and GeTe. The induced reflectivity change in each of these materials increased with increasing pump pulse intensity, and although the maximum ΔR that we observed varied among them, a common observation was the saturation of ΔR at high fluences, where utilizing increasingly intense excitation produced little or no further increase in the reflectivity modulation. In addition, we also noted that the rate at which the initial increase in reflectivity decayed was intensity-dependent – each of the materials under study exhibited reflectivity decay rates which increased with increasing fluence. Finally, coherence dephasing rates were observed to increase substantially at higher excitation intensities.

Modulation of the bulk reflectivity in semimetals and semiconductors occurs via direct absorption of photons and concomitant promotion of electrons to the conduction band. Saturation of this modulation implies the establishment of a maximum limit upon the density of conduction band electrons. Additional photons impinging on the material continue to be absorbed; however, the relaxation rate of excited carriers must increase in concert, such that as electrons are promoted to the conduction band, similar numbers

return to the valence band. This is the source of the saturation behavior observed for each of these materials.

There are several carrier relaxation mechanisms which operate on different time scales in these systems [88-90]. Carrier-carrier scattering results in thermalization of the hot electron distribution among other carriers on a 10-fs time scale. This process does not reduce the total energy of all carriers, but instead redistributes the energy throughout the conduction band. Inelastic scattering of carriers by lattice phonons is responsible for lattice heating, and the rate at which these processes occur depends substantially upon the topology of the conduction band. However, lattice phonon energies are usually significantly smaller than the excess energy of hot carriers. For instance, a typical LO phonon might correspond to an energy of 30 meV. For semimetal materials, where the band gap is very small (on the order of 0.01-0.05 eV), most of the absorbed pulse energy is kinetic energy of free carriers. For absorption at 800 nm (1.55 eV) and a band gap of 0.05 eV, a free carrier has 1.5 eV of excess energy. Even if the carrier-phonon interaction occurs on a time scale of 100 fs, a total of 50 phonons must be emitted to rid the carrier of its excess energy, and so the relaxation time due to LO phonon emission is about 5 ps.

Radiative and non-radiative recombination of free electrons and holes also reduces the carrier density in the conduction band. Radiative processes, which lower both the total free carrier energy and density, are slow and take place on a time scale of roughly 1 ns. Non-radiative Auger recombination is the inverse of impact ionization. An electron and hole recombine, transferring momentum and energy to a third carrier. This is a three-body process which scales as N^3 , and becomes dominant at high carrier

densities. It is likely that Auger recombination is a primary mechanism responsible for saturation of the reflectivity modulations in semimetals, since this process reduces (and effectively caps) carrier density.

Finally, Mazur has noted that free carrier diffusion, which occurs more readily at elevated electron temperatures, may also play a role in reducing carrier density in the focal region of the laser [88]. Diffusion of free carriers occurs from regions of high carrier density to regions of lower density, but the process is most rapid during the excitation pulse itself. Carrier confinement due to bandgap narrowing in an excited semiconductor acts to countermand this process to some extent [89,90], and it is not clear how much of a role carrier diffusion plays in our observations of semimetal reflectivity.

Thus, we conclude that the observed saturation of reflectivity modulations in our experiments along with the increased decay rates of the initial modulation at high excitation intensities are due to increased rates of relaxation of hot carriers, primarily through rapid Auger recombination. This process is responsible for the fast (sub-1 ps) dynamics we measure. Slower inelastic phonon scattering is the likely mechanism for carrier relaxation on the picosecond time scale, particularly after the very high initial carrier density has been reduced.

The very rapid coherence dephasing which we observed at high fluences is directly attributable to the weakening of lattice bond forces as a result of excited state carrier generation, as described previously. As the hot carrier distribution relaxes rapidly following high intensity excitation, the lattice bond strengths also change rapidly, resulting in the strong dephasing we observe for the highest pump pulse energies. Undoubtedly, lattice heating due to electron-phonon coupling and vibrational energy

redistribution via phonon-phonon scattering also influence the dephasing rate at longer times.

5.7.5 Ultrafast Phase Transitions

Classical melting in crystalline solids results from the propagation of thermal energy throughout the lattice structure. Incoherent population of high energy vibrational eigenstates implies that lattice atoms acquire sufficient thermal energy to overcome the crystal potential, and the ordered lattice collapses to a more disordered liquid state. The entire process is typically a first-order transition which proceeds inhomogeneously by nucleation and growth of the liquid phase along a propagating phase front. The maximum rate of propagation of the phase front is roughly the speed of sound in the material. Van Vechten and co-workers, studying the laser annealing of Si, were the first to suggest the involvement of a photoexcited dense electron-hole plasma in bringing about the transformation of the material [64], in contrast to the established mechanism which was thought to involve thermal melting and epitaxial recrystallization. Experimental and theoretical work on this problem has led to the prevailing view that even for laser pulses as short as a few picoseconds, phase transformations can be described in terms of rapid thermal processes [65,66].

Femtosecond excitation of crystalline solids raises the possibility of driving phase transformations on a much faster time scale. Shank *et al.* were the first to demonstrate a phase transformation in Si from crystalline solid to a metallic liquid state in about 500 fs using pump-probe reflectivity measurements [67]. Measurement of the second harmonic anisotropy which is characteristic of the crystalline phase revealed a transformation

occurring on a time scale comparable to the optic phonon vibrational period of the lattice [68,69].

Since then, a number of other groups have investigated the rapid “non-thermal” melting of solids under intense femtosecond irradiation. Von der Linde and co-workers have examined GaAs [70,71] and Si [72] under highly nonlinear conditions. Stampfli and Bennemann have investigated Si, GaAs, Ge and C and in each case, have been able to destabilize the crystal lattice via optical excitation of a dense electron-hole plasma [73-75]. Mazur and co-workers have measured the dielectric function of GaAs under conditions of intense laser excitation [76] in order to ascertain the underlying electron dynamics. Calculations by Fahy and Merlin [77] and Silvestrelli and co-workers [78] have also demonstrated that non-thermal melting can occur on the time scale of a single vibrational period [79].

The use of excitation pulse pairs with large inter-pulse delays in our experiments has provided evidence for non-thermal melting. The disappearance of the coherent signal contribution after a few hundred femtoseconds and its subsequent recovery after a few tens of picoseconds is conveniently explained by processes which are akin to laser-induced melting and recrystallization of the semimetals Bi, Sb and Te.

Unfortunately, without a direct structural probe such as x-rays, it is nearly impossible to conclusively identify the presence of a liquid phase and to therefore confirm the photoinduced phase transition. We can only state that all of our data currently support this interpretation. Other means of confirmation might include the detection of second harmonic signal from the surface of the sample, since the loss of symmetry on melting will modulate the second harmonic intensity. Dielectric

measurements which recover both the real and imaginary components of ϵ would also be able to provide such conclusive evidence. None of these methods is particularly amenable to single-shot implementation, however.

The mechanism by which non-thermal melting occurs is a natural consequence of the very rapid photogeneration of excited state carriers in an absorbing material. The loss of valence band electrons reduces the crystal lattice bonding potential. With weaker internuclear restoring forces, transverse acoustic phonon modes are destabilized and the crystal will no longer resist shearing stresses – it becomes fluid [80]. The fluidity, however, is distinctly different in origin from that of a thermally-driven first-order phase transition. In the case of ultrafast optical excitation, the energy is retained in the excited carrier distribution. As this distribution decays due to carrier diffusion and loss of energy to incoherent population of phonon modes, covalent bonding within the crystalline phase is re-established and the ordered lattice is recovered, provided that the total absorbed energy does not result, after thermalization, in a lattice temperature above the melting point. This process corresponds to the long-delay reflectivity scans which were shown earlier for Bi and Te.

A different type of phase transition occurs in the case of GeTe. Here, a solid-solid transition from the low-temperature rhombohedral to the high-temperature cubic structure occurs. At very high excitation fluences, the oscillations reach critical damping with a decay rate of 1.96 ps^{-1} , which suggests mode softening along the A_1 phonon coordinate. Previous work on GeTe confirms that the thermally-induced structural transition proceeds by means of a nucleation model [81-83]. However, under femtosecond irradiation, impulsive absorption promotes carriers to the conduction band,

weakening lattice forces sufficiently to permit the displacive phase transition to the high-temperature cubic form of GeTe. As the excited state carriers relax, recovery of oscillations in the long-delay experiments implies re-establishment of the low-temperature GeTe phase.

The data shown supports, but does not conclusively demonstrate, the onset of the structural transformation in GeTe. Further experiments which are sensitive to *both* structural phases are needed to demonstrate interconversion. However, the results obtained to date are consistent with an electronically-driven rearrangement, and the time scale for recovery of the low-temperature phase correlates with carrier dissipation dynamics. The pump intensity dependence can be interpreted as arising from the excited carrier population density as well.

The A_1 optic phonon mode serves as a very sensitive probe of lattice structure since it is strongly Raman-active for the low-temperature phase of GeTe. Steigmeier and Harbeke have made light scattering measurements of GeTe from 82-480 K and have noted the almost complete disappearance of the Raman band corresponding to this mode at elevated temperature [51]. This accounts for the absence of any coherent response due to the cubic phase of GeTe in our data. The remaining question is whether the effect of excitation is to drive a structural phase transition or to simply melt the sample. Crystalline germanium telluride melts at 998 K; it is unlikely that our experiments induce lattice temperatures this high. Even if this did happen, however, it is likely that the process would first proceed through the solid-solid phase transition. We observe large changes in bulk reflectivity on a time scale of a few hundred femtoseconds. A thermally-driven melting mechanism would require at minimum a few picoseconds for electron-

phonon coupling to heat the lattice sufficiently. Thus, if melting does occur, the driving force is certainly electronic in character (i.e. weakened lattice bonds due to impulsive absorption) just like the mechanism for the solid-solid transformation.

The softening of the A_1 mode in GeTe occurs as a consequence of the structural phase transition. Though we are able to observe coherent motion in this mode, the amplitude of such motion is not nearly sufficient to *initiate* the transition. We are currently exploring the application of intense out-of-phase excitation pulse pairs. These should effectively cancel the coherent lattice response but still promote large numbers of carriers to the conduction band. Since the origin of the transition is electronic, we expect similar responses to a weak third pulse as those we already observed for in-phase measurements – the transition to a cubic phase and absence of A_1 phonon oscillations.

5.8 Conclusion

In this chapter, we investigated the semimetals Bi, Sb and Te and the semiconductor GeTe under highly non-equilibrium conditions. The coherent phonon dynamics are strongly influenced by the excitation pulse fluence, which implies that most of the observed effects are of electronic origin – dependent upon the hot carriers generated via impulsive absorption.

For the semimetals Bi, Sb and Te, the material response to excitation is as follows: at low fluences, generation of small numbers of carriers in the conduction band proceeds through direct absorption of a pump pulse. In response to reduced screening of nuclear charges, the lattice atoms move in such a way as to increase their distances from all nearest neighbors. This coherent, symmetric motion occurs along modes of A_1

symmetry, and is responsible for the oscillations in the bulk reflectivity of the material. As the pump pulse intensity increases, the excited state carrier density increases to a point where transverse acoustic phonon modes are no longer stabilized. The crystal will no longer support shear stresses and “melts” non-thermally. The time scale for this process can be as rapid as a single vibrational period. Since the origin of crystal bond weakening is electronic, as the excited carriers relax, lattice bond forces tend towards their equilibrium values and the lattice re-solidifies. From our measurements with longer inter-pump delays, the latter occurs over several tens of picoseconds.

The low intensity response of GeTe is similar to that of the semimetals. As the carrier density increases, lattice forces weaken, enabling (thermal) motion along the A_1 coordinate. The result is a structural phase transition from the low temperature rhombohedral to the high temperature cubic form. This is manifest as the absence of coherent reflectivity oscillations which act as a signature of the low- T phase. At the highest pump fluences, the conversion appears to be complete and we detect no signature of the low temperature phase, even after 100 ps. At slightly lower intensities, small amplitude coherent signatures of the rhombohedral form after 50-75 ps are indicative of a more rapid return to carrier densities which support the low- T phase, a reversible phase transformation, and perhaps a smaller phase-change region.

References

- [1] Donohue, J., *The Structures of the Elements* (John Wiley & Sons, New York, 1974).
- [2] Brugger, R.M., Bennion, R.B. and Worlton, T.G., *Phys. Lett. A* **24A**, 714 (1967).
- [3] Renucci, J.B. *et al.*, *Phys. Stat. Solidi B* **60**, 299 (1973).
- [4] Loudon, R., *Adv. Phys.* **13**, 423 (1964).
- [5] Zitter, R.N., *The Physics of Semimetals and Narrow Gap Semiconductors* (Pergamon Press, New York, 1971).
- [6] Schiferl, R., *Rev. Sci. Instrum.* **48**, 24 (1977).
- [7] Sharp, R.I. and Warming, E., *J. Phys. F* **1**, 570 (1971).
- [8] Grosse, P., “Die Festkorpereigenschaften von Tellur”, *Springer Tracts in Modern Physics*, Vol. 48 (Springer-Verlag, Berlin, 1969).
- [9] Cherin, P. and Unger, P., *Acta Cryst.* **23**, 670 (1967).
- [10] Roeser, C.A.D., *Ultrafast Dynamics and Optical Control of Coherent Phonons in Tellurium*, Ph.D. Thesis, Harvard University, 2003.
- [11] Cheng, T.K., *The Excitation and Dynamics of Coherent Lattice Vibrations in Semimetals and Narrow-gap Semiconductors*, Ph.D. Thesis, Massachusetts Institute of Technology, 1994.
- [12] Cheng, T.K. *et al.*, *Appl. Phys. Lett.* **57**, 1004 (1990).
- [13] Cheng, T.K. *et al.*, *Appl. Phys. Lett.* **59**, 1923 (1991).
- [14] Zeiger, H.J. *et al.*, *Phys. Rev. B* **45**, 768 (1992).
- [15] DeCamp, M.F. *et al.*, *Phys. Rev. B* **64**, 092301 (2001).
- [16] Hase, M. *et al.*, *Appl. Phys. Lett.* **69**, 2474 (1996).
- [17] Hase, M. *et al.*, *Appl. Phys. Lett.* **76**, 1258 (2000).
- [18] Hase, M. *et al.*, *Phys. Rev. Lett.* **88**, 067401 (2002).
- [19] Hase, M. *et al.*, *Appl. Surf. Sci.* **197-198**, 710 (2002).
- [20] Kitajima, M. *et al.*, *Nucl. Instr. Meth. Phys. Res. B* **206**, 99 (2003).

- [21] Hase, M. *et al.*, *Physica B* **316-317**, 292 (2002).
- [22] Misochko, O.V., Sakai, K. and Nakashima, S., *Phys. Rev. B* **61**, 11225 (2000).
- [23] Misochko, O.V., Hase, M. and Kitajima, M., *JETP Lett.* **78**, 75 (2003).
- [24] Garrett, G.A. *et al.*, *Science* **275**, 1638 (1996).
- [25] Garrett, G.A. *et al.*, *Opt. Express* **1**, 385 (1997).
- [26] Dunn, T.J. *et al.*, *Phys. Rev. Lett.* **70**, 3388 (1993).
- [27] Garrett, G.A. *et al.*, *Phys. Rev. Lett.* **77**, 3661 (1996).
- [28] Misochko, O.V. *et al.*, *Appl. Phys. Lett.* **76**, 961 (2000).
- [29] Hunsche, S. *et al.*, *Phys. Rev. Lett.* **75**, 1815 (1995).
- [30] Hunsche, S., Weinecke, K. and Kurz, H., *Appl. Phys. A* **62**, 499 (1996).
- [31] Hunsche, S. and Kurz, H., *Appl. Phys. A* **65**, 221 (1997).
- [32] Tangney, P. and Fahy, S., *Phys. Rev. B* **65**, 054302 (2002).
- [33] Tangney, P. and Fahy, S., *Phys. Rev. Lett.* **82**, 4340 (1999).
- [34] Hase, M., Ishioka, K. and Kitajima, M., *Appl. Phys. Lett.* **82**, 3668 (2003).
- [35] Raty, J.Y. *et al.*, *Phys. Rev. B* **64**, 235209 (2001).
- [36] Ledgerwood, M.L. and van Driel, H.M., *Phys. Rev. B* **54**, 4926 (1996).
- [37] Pfeifer, T. *et al.*, *Phys. Rev. Lett.* **69**, 3248 (1992).
- [38] Du, D. *et al.*, *Appl. Phys. Lett.* **64**, 3071 (1994).
- [39] Stuart, B.C. *et al.*, *Phys. Rev. B* **53**, 1749 (1996).
- [40] Li, M. *et al.*, *Phys. Rev. Lett.* **82**, 2394 (1999).
- [41] Tien, A.-C. *et al.*, *Phys. Rev. Lett.* **82**, 3883 (1999).
- [42] Lenzner, M. *et al.*, *Phys. Rev. Lett.* **80**, 4076 (1998).
- [43] Hase, M. *et al.*, *Appl. Phys. Lett.* **83**, 4921 (2003).
- [44] Rabe, K.M. and Joannopoulos, J.D., *Phys. Rev. B* **36**, 6631 (1987).
- [45] Raty, J.Y. *et al.*, *Phys. Rev. B* **65**, 115205 (2002).
- [46] Raty, J.Y. *et al.*, *Phys. Rev. Lett.* **85**, 1950 (2000).
- [47] Forst, M. *et al.*, *Appl. Phys. Lett.* **77**, 1964 (2000).
- [48] Cockayne, E. and Rabe, K.M., *Phys. Rev. B* **56**, 7947 (1997).

- [49] Dougherty, T.P. *et al.*, *Science* **258**, 770 (1992).
- [50] Blinc, R. and Zeks, B., *Soft modes in ferroelectrics and antiferroelectrics* (Elsevier, New York, 1974).
- [51] Steigmeier, E.F. and Harbeke, G., *Solid State Commun.* **8**, 1275 (1970).
- [52] Eesley, G.L., *Phys. Rev. Lett.* **51**, 2140 (1983).
- [53] Schoenlein, R.W. *et al.*, *Phys. Rev. Lett.* **58**, 1680 (1987).
- [54] Brorson, S.D. *et al.*, *Phys. Rev. Lett.* **64**, 2172 (1990).
- [55] Kuznetsov, A.V. and Stanton, C.J., *Phys. Rev. Lett.* **73**, 3243 (1994).
- [56] Kuznetsov, A.V. and Stanton, C.J., *Phys. Rev. B* **51**, 7555 (1995).
- [57] Cho, G.C., Kutt, W. and Kurz, H., *Phys. Rev. Lett.* **65**, 764 (1990).
- [58] Kutt, W. *et al.*, *Semicond. Sci. Technol.* **7**, B77 (1992).
- [59] Pfeifer, T. *et al.*, *Appl. Phys. A* **55**, 482 (1992).
- [60] Scholz, R., Pfeifer, T. and Kurz, H., *Phys. Rev. B* **47**, 16229 (1993).
- [61] Kittel, C., *Quantum Theory of Solids* (John Wiley & Sons, New York, 1963).
- [62] Bailey, D.W., Stanton, C.J. and Hess, K., *Phys. Rev. B* **42**, 3423 (1990).
- [63] Kochelap, V.A., Sokolov, V.N. and Vengalis, B.Y., *Phase Transitions in Semiconductors with Deformational Electron-Phonon Interaction* (Naukova Dumka, Kiev, 1984).
- [64] Van Vechten, J.A., Tsu, R. and Saris, F.W., *Phys. Lett.* **74A**, 422 (1979).
- [65] Wood, R.F., White, C.W. and Young, R.T., "Pulsed Laser Processing of Semiconductors", *Semiconductors and Semimetals, Vol. 23* (Academic Press, Orlando, 1984).
- [66] Kurz, H. and Bloembergen, N., *Mat. Res. Soc. Symp. Proc.* **35**, 3 (1986).
- [67] Shank, C.V., Yen, R. and Hirliman, C., *Phys. Rev. Lett.* **50**, 454 (1983).
- [68] Shank, C.V., Yen, R. and Hirliman, C., *Phys. Rev. Lett.* **51**, 900 (1983).
- [69] Tom, H.W.K., Aumiller, G.D. and Brito-Cruz, C.H., *Phys. Rev. Lett.* **60**, 1438 (1988).
- [70] Sokolowski-Tinten, K. *et al.*, *Appl. Phys. A* **53**, 227 (1991).
- [71] Sokolowski-Tinten, K. *et al.*, *Phys. Rev. B* **58**, R11805 (1998).
- [72] Sokolowski-Tinten, K. *et al.*, *Phys. Rev. Lett.* **81**, 224 (1998).
- [73] Stampfli, P. and Bennemann, K.H., *Phys. Rev. B* **42**, 7163 (1990).
- [74] Stampfli, P. and Bennemann, K.H., *Phys. Rev. B* **46**, 10686 (1992).

- [75] Stampfli, P. and Bennemann, K.H., *Phys. Rev. B* **49**, 7299 (1994).
- [76] Huang, L. *et al.*, *Phys. Rev. Lett.* **80**, 185 (1998).
- [77] Fahy, S. and Merlin, R., *Phys. Rev. Lett.* **73**, 1122 (1994).
- [78] Silvestrelli, P.L. *et al.*, *Phys. Rev. Lett.* **77**, 3149 (1996).
- [79] Ziman, J.M., *Principles of the Theory of Solids* (Cambridge University Press, London, 1972).
- [80] Matin, R.M., *Phys. Rev.* **186**, 871 (1969).
- [81] Polatoglou, H.M., Theodorou, G. and Economou, N.A., *J. Phys. C* **16**, 817 (1983).
- [82] Katayama, S. and Murase, K., *Solid State Commun.* **36**, 707 (1980).
- [83] Islam, Q.T. and Bunker, B.A., *Phys. Rev. Lett.* **59**, 2701 (1987).
- [84] Seeger, K., *Semiconductor Physics: An Introduction* (Springer, New York, 2004).
- [85] Colinge, J.-P., *Physics of Semiconductor Devices* (Kluwer Academic Publishers, Boston, 2002).
- [86] Sze, S.M., *Semiconductor Devices, Physics and Technology* (John Wiley & Sons, New York, 2002).
- [87] Hase, M., Mizoguchi, K. and Nakashima, S., *J. Lumin.* 87-89, 836 (2000).
- [88] Mazur, E., "Interaction of Ultrashort Laser Pulses with Solids", *Spectroscopy and Dynamics of Collective Excitations in Solids* (Plenum Press, New York, 1997).
- [89] Van Driel, H.M., *Phys. Rev. B* **35**, 8166 (1987).
- [90] Kalt, H. and Rinker, M., *Phys. Rev. B* **45**, 1139 (1992).

Chapter 6

Ultrafast Triiodide Photochemistry in Solution

Among the most important examples of optical perturbations are those involving the breaking of chemical bonds between atoms, either in isolated molecules in the gas phase or in condensed phase systems. In this chapter, we investigate photodissociation events on an ultrafast time scale in solution, with particular attention to the manner in which the solvent environment mediates the dynamical response. The experiments are conducted initially on samples which are dissolved in solution and which do not preclude the use of multi-shot pump-probe methods. However, subsequent investigations are conducted under conditions which are closer to being truly irreversible, and the power of the single-shot method is apparent.

6.1 Introduction to the Triiodide System

The triiodide ion, I_3^- , is a 22-electron, three-atom ion which carries a single negative charge delocalized along the length of the principal axis. Isolated in the gas phase, the ion is linear and symmetric. However, in solution, the ion typically assumes a geometry which is slightly bent, although the included angle is rarely less than 170° . The bending angle is dependent upon the solvent and its ability to stabilize the distributed negative charge of triiodide[79,89-91].

The triiodide ion is the simplest member of the family of *polyhalide* ions, of which the polyiodides are the most prevalent. The existence of I_3^- in solution, typically in a solvent equilibrium with I_2 and I^- , has been known for decades. Literature reports of preparative schemes for triiodide species are found as early as 1923 [1]. The valence electrons of atomic iodine are localized in diffuse, extended orbitals – loosely bound relative to the other halogens. For this reason, iodine atoms are particularly amenable to the formation of polyatomic ions. The diffuse bonds which characterize such complex ions are covalent in character but generally much weaker than, say, the covalent carbon-carbon bonds in organic compounds. Nonetheless, a remarkable variety of polyiodide species can be prepared and crystallized from solution. The simplest ion, I_3^- , exists essentially as an isolated molecular unit, and systematic variation of the crystalline environment is achieved by introducing an appropriate cation. Triiodide is a large anion, and it is generally observed that the stability of crystalline triiodides is dependent upon the size and overall symmetry of the cation. Larger, symmetric cations yield crystals of higher quality and greater stability.

A tremendous amount of synthetic effort has been expended in preparing novel triiodides; references 1-18 provide numerous examples of such species, but by no means constitute a complete list. Polyiodides of higher order, including I_5^- , I_7^- , I_9^- , I_{11}^- , I_{13}^- , I_4^{2-} , I_8^{2-} , and I_{10}^{2-} have also been prepared [19-31], and when combined with intricate variations of counterions, the structural beauty of these compounds is striking. Although in most cases polyhalide species crystallize as ionic compounds, there are also certain instances where highly symmetric extended linear chains or two-dimensional networks of

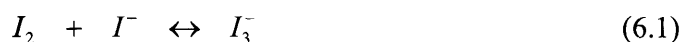
I_3^- anions exist [32-34]. Such systems have remarkable conductivity properties on account of their highly delocalized valence electron states.

The electronic spectra of triiodides have been the subject of experimental and theoretical work for some time [35-41], in spite of the fact that the complexity of the systems precludes exact all-electron calculations. The vibrational properties of these systems have also been studied by frequency-domain Raman and infrared methods [42-48], and the stability of triiodide crystals has been investigated from a thermodynamic point of view [49-50].

It is also important to note the existence of other polyhalide systems. The tribromide ion Br_3^- can be prepared with certain suitable counterions such that it exists in stable form as a crystalline solid, and there are reports of higher order polybromides as well [7,9,10]. The trichloride ion Cl_3^- is short-lived under ambient conditions, but can be prepared in gas-phase molecular beams. Finally, mixed polyhalides such as ClIBr^- and BrIBr^- have also been synthesized, although the stability of these species varies widely and multiple-domain crystals are often obtained.

It is clear that the polyhalide family of anions is a rich set of structural motifs, presenting remarkable opportunities for control of the crystalline environment through relatively straightforward manipulation of the chemical constituents of the system. In our studies, we have chosen to focus solely on triiodide species in order to simplify the analysis of our results. However, the extension of our methods to systems of greater complexity remains an attractive possibility. In this chapter our results on triiodide solutions are presented. Triiodide crystalline studies follow in the next chapter.

Preparation of the triiodide ion in solution is simple. Equimolar quantities of an ionic iodide salt (substituted ammonium and phosphonium cations are most stable) and iodine, with a slight excess of I_2 , are combined with gentle warming and stirring in ethanol. After about 15 minutes, the solution contains triiodide by virtue of the equilibrium



and aliquots are extracted and diluted with ethanol to a concentration of 2 mM. The absorption spectra of I_3^- and I_2^- in ethanol solution are shown in Figure 6-1. There are

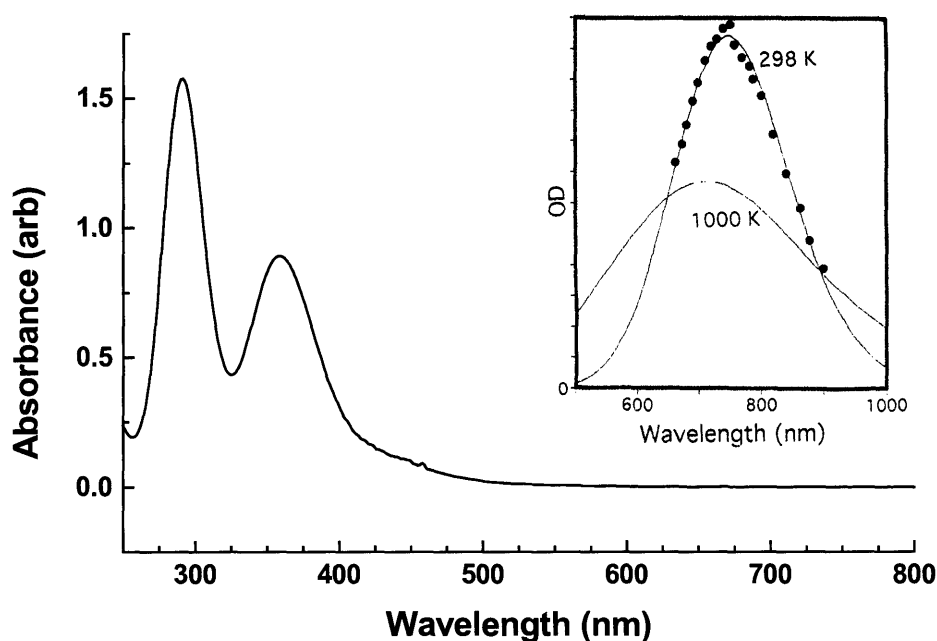


Figure 6-1. Absorption spectrum of triiodide ion in ethanol. Inset: Diiodide ion absorption spectrum in ethanol from reference 65.

two bands for I_3^- , and the assignment of these is an unresolved subject of discussion in the literature [37,41]. The most commonly held view is that excitation of I_3^- leads to one or more dissociative states which correlate with I_2^- ($^2\Sigma_u^+$) in its ground state, and atomic I

(²P) in one of its lowest two spin-orbit states [68]. Absorption experiments on crystalline I₃⁻ have demonstrated that optical transitions to either spin-orbit state are polarized along the molecular axis [41].

UV and resonance Raman scattering measurements in solution and in triiodide crystals show strong excitation of the symmetric stretch of I₃⁻ which implies that single-photon absorption leads to motion directed along this molecular coordinate [69-71]. However, the bent geometry of the ion in solution also suggests the possibility that motion along the asymmetric stretch coordinate also occurs. Further, in order for dissociation to take place, some asymmetry in the internal motion must be present.

The photoproduct which results from absorption in either the 300 nm or 370 nm bands of I₃⁻ is I₂⁻ in all known condensed phase systems. Current understanding of the electronic structure of triiodide is insufficient to provide a physically meaningful explanation for the absence of an alternate pathway involving I₂. The diiodide ion has been investigated both in solution [65,72] and in gas-phase clusters [73-74]. Its absorption spectrum consists of two bands, one which partially overlaps the triiodide spectrum in the near-UV and the other in the near-IR, centered at 740 nm in ethanol solution. The near-IR band is well isolated spectrally from the triiodide bands and provides a convenient means to interrogate diiodide species without interference from the parent ions.

The dissociation of triiodide also leads to the formation of iodine atoms which exhibit weak absorption near 400 nm in ethanol [75]. Decay kinetics of the iodine radical in solution proceed on time scales of picoseconds to nanoseconds [76,77] and as a result,

absorptive contributions due to iodine contribute negligibly to the results of our experiments.

The underlying aim of our photochemistry experiments is to investigate time-dependent bond cleavage in triiodide solution, focusing in particular on the manner in

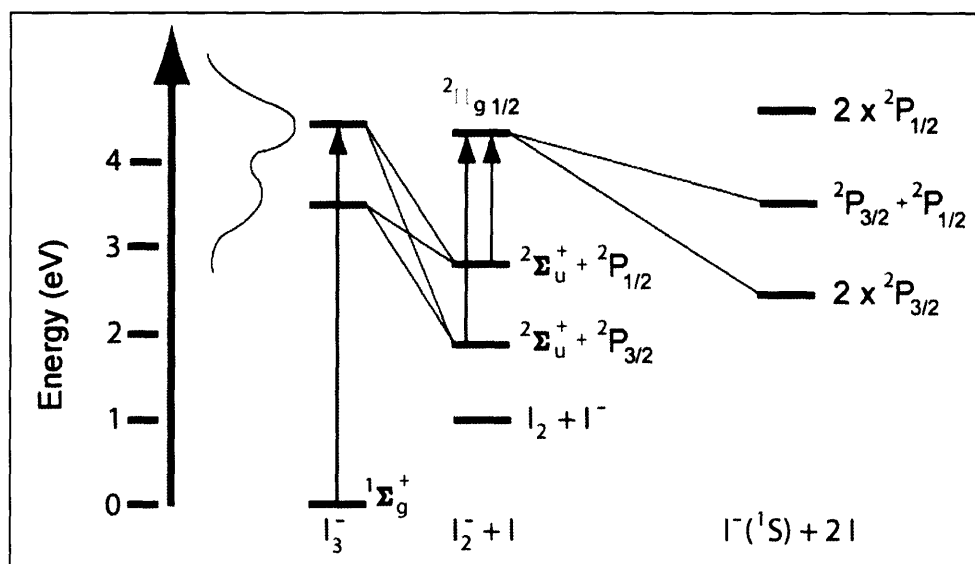


Figure 6-2. Gas-phase energy levels of triiodide, diiodide and iodine relevant to our experiments. Absorption from the ground state of triiodide into the high energy excited state band leads to photodissociation, yielding diiodide and atomic iodine in one of two spin states. Absorption by the nascent diiodide ion leads to further dissociation, giving iodide ion and an iodine atom.

which the environment affects the observed results. The spectrally isolated absorption bands of I_3^- and its photoproduct I_2^- provide the means to separately investigate the bond-breaking process as it is occurring in triiodide, and the nature of the product diiodide state. The relevant gas-phase energy levels for triiodide, diiodide and iodine atoms are shown in Figure 6-2 (note that not all levels appear, only those involved in the present experiments). Excitation from the ground state of I_3^- into the high energy band (300 nm)

yields an excited state of triiodide which is purely dissociative, yielding I_2^- in its ground state and an iodine atom in one of two spin states. A second absorption event to a repulsive excited state of I_2^- leads to further dissociation, yielding iodide ion in its ground (singlet) state and another iodine atom in one of two spin states. The overall energy landscape of the system is complex. Only those transitions which are believed to be strongest are shown.

The experiments described herein employ femtosecond transient absorption in a single laser shot. Although not strictly necessary for studies in flowable ethanol solutions, the utility of the single-shot technique will become apparent as the properties of the solution are altered in subsequent sections. Absorption in separate spectral regions allows us to investigate the evolving dynamics of both triiodide and diiodide on an ultrafast time scale.

Transient absorption of triiodide ions in solution has been examined in detail by Ruhman and co-workers [51-59] who have concentrated primarily on understanding the evolution of product diiodide fragments and remaining triiodide species as a consequence of the electronic energy levels involved in the photodissociation. A secondary focus of their work has been observing and modeling vibrational coherence transfer in solution, with particular regard to the influence of solvation-induced symmetry breaking. Vohringer and co-workers have also studied the reaction [60-64] using photolysis wavelengths of 400 nm and 266 nm in an effort to investigate alternate reaction pathways. Much of their work also involves the analysis of vibrational and rotational states of fragments in solution. Throughout the following discussion, reference will be made to the work of these research groups for comparative purposes.

6.2 Transient Absorption Experimental Setup

Transient absorption is a two-pulse experiment utilizing the variable wavelength capability of the NOPA introduced in Chapter 3. In order to generate the initial photolysis pulse, the center wavelength of one arm of the NOPA is adjusted to 600 nm. Following compression to the transform limit in the deformable-mirror pulse compressor, the 600 nm pulses pass through a second set of SF18 prisms which introduce negative group velocity dispersion. The pulses are subsequently frequency-doubled in a 250 μm BBO crystal. The negative GVD of the SF18 prism pair is adjusted such that the normal dispersion of the BBO crystal is counterbalanced, resulting in a 300 nm pulse which remains nearly unchirped. The 8 μJ , 600 nm pulses from the NOPA are converted to ultraviolet pulses of energy 1.0 μJ , and these are focused to a spot size of 150 μm and used for the photolysis of I_3^- .

The second arm of the NOPA is tuned such that transient absorption of either the I_3^- which remains after the photolysis pulse or the photogenerated I_2^- is interrogated. In order to probe ground state triiodide, the second NOPA output is tuned to 600 nm, precompressed, and then frequency-doubled, as for the photolysis pulses. To investigate transient absorption (TA) of diiodide, a two-step approach is utilized. For wavelengths on the high energy side of the absorption maximum (740 nm), the second NOPA output is tuned to the desired frequency and utilized directly. For wavelengths from 740 nm to 900 nm – a region not covered by the NOPA tuning range – continuum generation is employed by focusing a 1.5 μJ , 800 nm pulse to a spot size of 30 μm in a sapphire plate of thickness 1 mm. Subsequently, the bandwidth of the continuum pulses is reduced using 20 nm bandpass filters adjusted such that the center wavelength matches the probe

wavelength of interest. Finally, the pulses are compressed in a double-pass prism compressor and coupled into the single-shot experiment.

The probe pulses, whether derived from the NOPA or from continuum generation, pass through the same optical setup that was described in Chapter 2. All of our transient absorption experiments are performed in transmission mode. Probe pulse energies are maintained at 250 nJ, the lowest energy at which signal can be reasonably detected using our all-optical setup. Pump and probe pulse polarizations are oriented in a magic angle configuration to avoid signal contributions from molecular rotation in solution.

A solution of triiodide in a solvent such as ethanol is prepared, typically in a concentration of 2 mM, and placed in a quartz cuvette of path length 500 μm . The homogeneity of the solution avoids the difficulties with regard to sample quality which often arise in making single-shot measurements. Single-shot transient absorption spectra are recorded by gating individual pulses out of the amplified 10 Hz laser system. Pump (photolysis) and probe pulses are generated as described above from a single gated pulse and the transient absorption signal is captured on a CCD camera as a spatial modulation of transmitted probe light intensity. As before, the time-to-space mapping of the single-shot setup allows us to reconstruct the time-dependent absorption of the sample.

6.3 Transient Absorption of Triiodide and Diiodide in Ethanol

The results of transient absorption experiments on triiodide in ethanol solution are shown in Figure 6-3. The first panel illustrates transient absorption scans on the blue side of the diiodide absorption maximum, from 600-740 nm. Panel two contains the

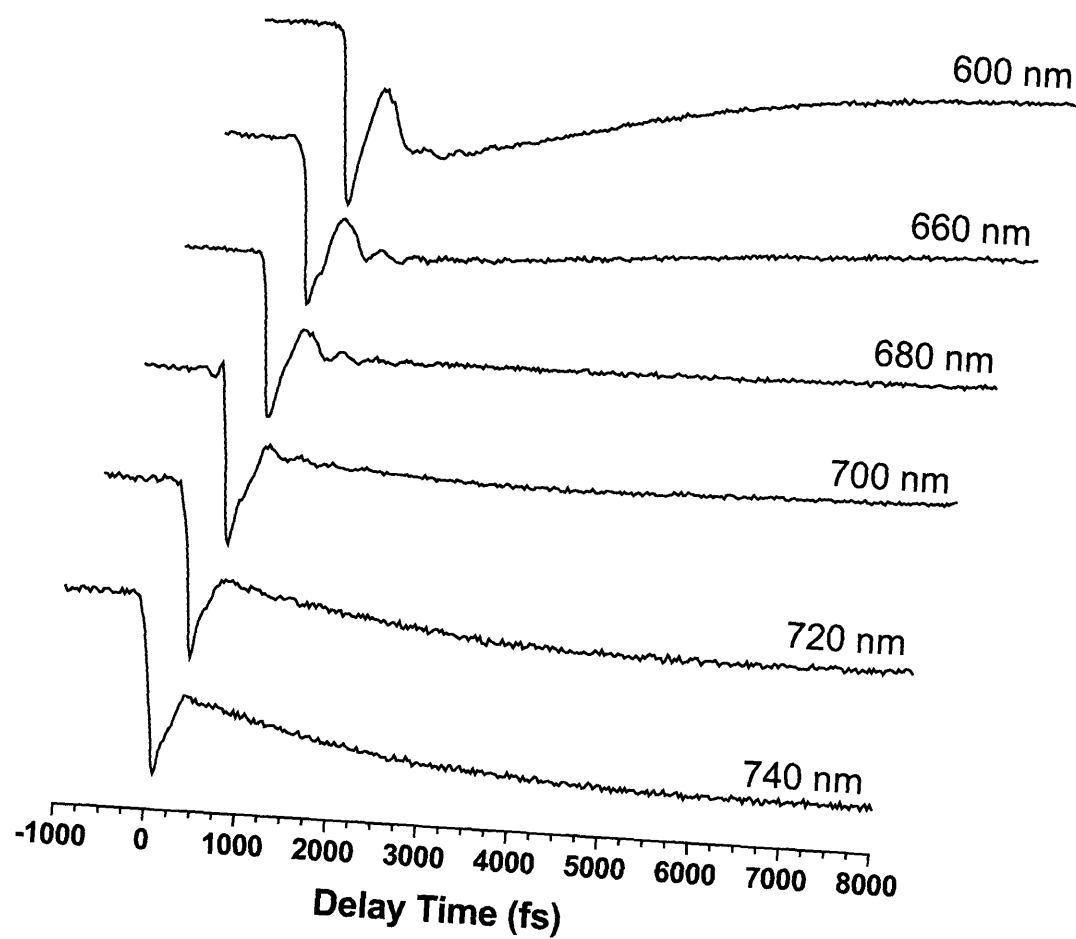


Figure 6-3. Single-shot transient absorption scans for triiodide in ethanol solution. The probe pulse wavelength is indicated on the right hand side of each trace. The wavelengths represented here probe the blue edge of the ground state diiodide absorption band, which is centered at 740 nm.

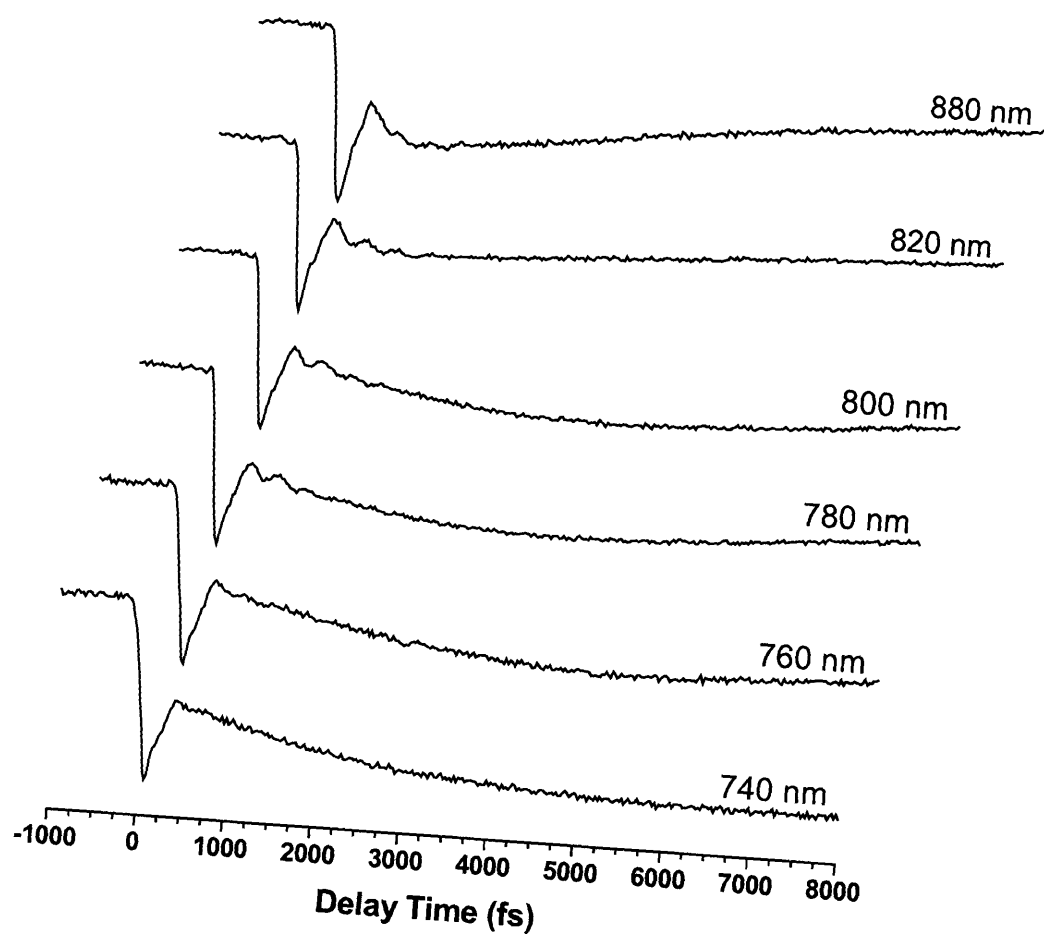


Figure 6-3 (cont'd). Single-shot transient absorption scans for triiodide in ethanol solution. The probe pulse wavelength is indicated on the right hand side of each trace. The wavelengths represented here probe the red edge of the ground state diiodide absorption band, which is centered at 740 nm.

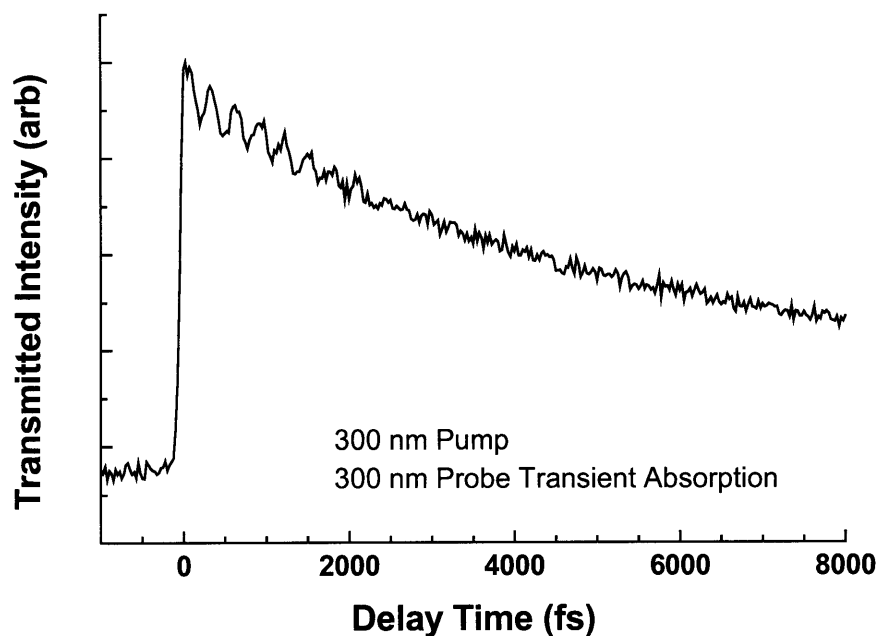


Figure 6-3 (cont'd). Transient absorption scan for triiodide in ethanol solution. The photolysis and probe pulses are both 300 nm, so the observed transient absorption dynamics are due to residual ground state triiodide ions.

absorption scans from the red side of the band, from 740-880 nm. Finally, the third panel illustrates a transient absorption scan at the photolysis wavelength, 300 nm.

Absorption features in the first two panels are largely due to diiodide ion, I_2^- . Absorption by I_3^- of the photolysis pump pulse at 300 nm creates triiodide in a fully dissociative excited state. The triiodide ion fragments, yielding I_2^- and atomic I. Probing with pulses of visible and near-IR wavelengths captures the dynamics of I_2^- since I_3^-

contains no absorption features in this spectral region. The transient absorption data offers ample insight into the photodissociation reaction. At all wavelengths, a fast initial absorption feature is observed (the sharp drop in transmitted intensity near $t = 0$). Absorption at these early times is likely due to the excited state of triiodide – that is, an absorptive transition to an even higher-lying excited state. This strong feature rapidly disappears, within about 300 fs, corresponding to the dissociation of I_3^- . The transient absorption signal then begins to strengthen again, as absorbing I_2^- fragments appear in solution. The intensity and duration of the TA signal due to I_2^- is strongly wavelength-dependent. On the wings of the absorption band (600 nm and 880 nm), the peak absorption is relatively weaker, reaches a maximum value in less than 1.5 ps, and then begins to decay. Near the center of the band at 740 nm, the absorption signal appears to grow throughout the time window of the experiment. At intermediate wavelengths, the absorption behavior falls between these extremes.

Close examination of the transients, particularly on the edge of the diiodide band (for example, 660 nm and 680 nm on the blue side, 800 nm and 820 nm on the red side) reveals the presence of oscillatory contributions to the TA signal. Fitting the signal to a damped sinusoid by LP-SVD gives a mean oscillation frequency of $99 \pm 5 \text{ cm}^{-1}$ and a damping time of $580 \pm 60 \text{ fs}$. These oscillations are due to coherently vibrating diiodide fragments produced in the (coherent) photodissociation. The rapid damping occurs because of facile energy exchange between the vibrationally hot fragment and the low-frequency bath modes of the ethanol solvent.

Data in the third panel correspond to TA of unreacted I_3^- in its electronic ground state. The initial photolysis pulse bleaches the ground state I_3^- absorption signal.

Triiodide ions absorb efficiently at 300 nm, with a molar extinction coefficient of $4.1 \times 10^4 \text{ M}^{-1} \text{ cm}^{-1}$ in ethanol. For an excitation pulse of 1.0 μJ focused to a spot size of 150 μm , virtually all of the I_3^- ions within the focal region are excited, and few remain immediately after the photolysis pulse to absorb at 300 nm. Gradually, however, the absorption signal becomes stronger as the population of ground state I_3^- re-grows,

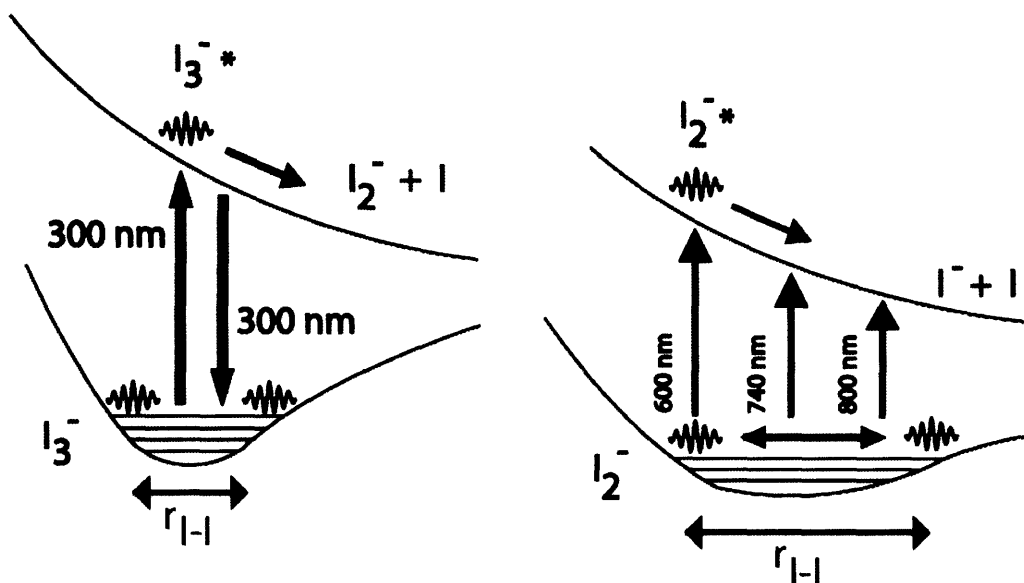


Figure 6-4. Wavepacket dynamics of triiodide and diiodide following interaction with a photolysis pulse at 300 nm. Wavelength-dependent probing in the visible and near-IR interrogates I_2^- at particular locations along the molecular coordinate. Due to the coherent nature of diiodide oscillations, opposite-phase behavior is observed on opposite sides of the absorption maximum.

although within the 10 ps window of our experiments, the initial equilibrium state prior to $t = 0$ has not been re-established. Strong oscillatory behavior in the TA scan is also observed. Fitting by LP-SVD techniques gives a frequency of $107 \pm 7 \text{ cm}^{-1}$ and a decay time of $1700 \pm 100 \text{ fs}$. These oscillations clearly correspond to coherent motion of triiodide ions in their electronic ground state. The coherence is the result of a second interaction with the photolysis pump field – resonance-enhanced impulsive stimulated

Raman scattering. Evidence for this is provided by the observation that the oscillations trace all the way back to $t = 0$ in the TA scan, suggesting the familiar sinusoidal phase dependence of the ISRS process. By contrast, the oscillatory motion in the diiodide scans does *not* trace back to $t = 0$ since it arises from a “coherent dissociation” which begins to occur after a few hundred femtoseconds.

The overall picture of the TA dynamics in the triiodide system is summarized in Figure 6-4. A second field interaction with the photolysis pulse creates a triiodide ground-state vibrational wave packet which evolves according to the shape of the ground state potential depicted in the figure. Oscillatory motion of the wave packet, which increases or reduces the distribution of absorbers at the 300 nm probe wavelength, is generally attributed to be responsible for the observed modulation in transient absorption signal [52,53,58,59]. However, it should be noted that spectral shifting due to ISRS, as was observed for BGO in Chapter 4, might also produce the oscillatory behavior observed when probing at 300 nm. In this case, the absorption spectrum would effectively function as the spectral filter. Wave packet motion is the dominant effect when displacements from the equilibrium geometry of the ion are large. ISRS spectral shifting would be the dominant effect when the vibrational velocity is large. In general it is difficult to ascertain which mechanism is dominant here, although the width of the 300 nm absorption band would seem to disfavor the argument for spectral shifts. Regardless of the mechanism, it is clear that the oscillatory behavior represents coherent vibrational motion of I_3^- ions on their ground state electronic surface.

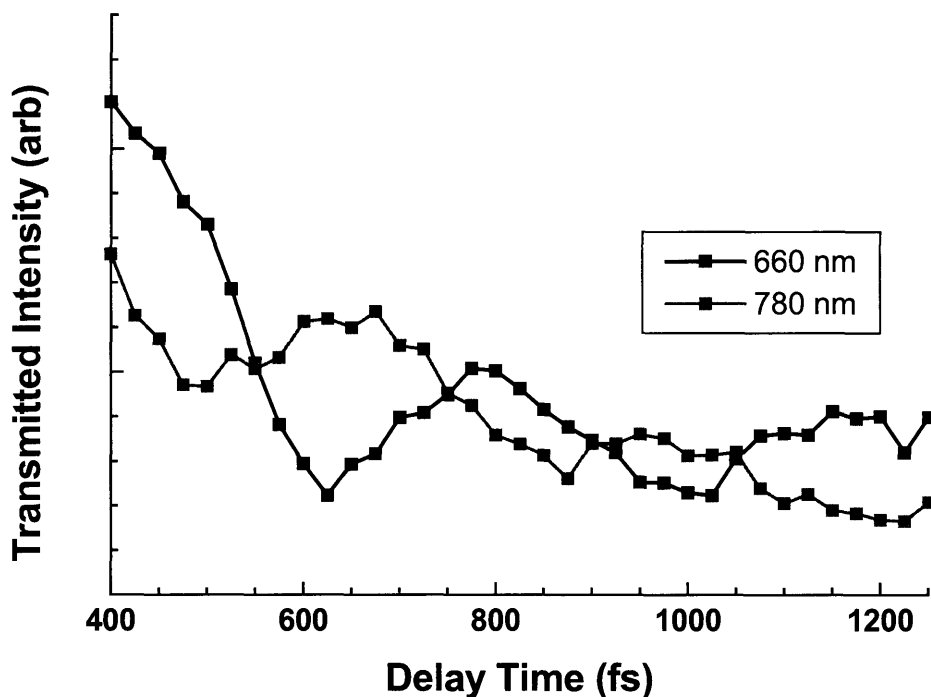


Figure 6-5. Comparison of the oscillatory component of transient absorption signals at 660 nm and 780 nm. The oscillations show opposite phases, reflecting the average location of the molecular wavepacket along the I-I vibrational coordinate.

Most of excited state triiodide dissociates and creates a vibrationally-excited I_2^- wave packet on the ground state electronic potential of I_2^- depicted on the right side of Figure 6-4. Absorption to an excited state of I_2^- is responsible for the TA signals in the visible and near-IR region. Probe pulses of different wavelengths interrogate different regions of the potential energy curves. Shorter wavelengths probe absorption in the region of the inner turning point, whereas longer wavelengths investigate wave packet dynamics near the outer turning point. The motion of diiodide wave packets on their electronic ground state is responsible for the modulations in the TA signal.

Figure 6-5 illustrates the influence of I_2^- wave packet motion. TA scans at 660 nm and 780 nm both show oscillatory behavior, but the phase relationship between the two is exactly opposite. When the wave packet maximum is located near the inner turning point of the ground-state diiodide potential, absorption at 660 nm will be strongest and absorption at 780 nm (near the opposite turning point) will be relatively weaker on account of the reduced wave packet density at that position along the I-I coordinate. As the wave packet propagates to the outer turning point, the situation is exactly reversed. As a consequence, absorption traces at both wavelengths yield oscillatory motion at the same frequency, but with opposite phase.

Our data are in close agreement with the multi-shot transient absorption measurements of Ruhman and co-workers [51-53,55] on the triiodide/ethanol system. Their experiments demonstrate coherent vibrational motion due to both triiodide and diiodide species with frequencies and dephasing rates which are similar ours (95 cm^{-1} and 450 fs for I_2^- , 111 cm^{-1} and 1500 fs for I_3^-). The work of Vohringer *et al.* also closely supports our results, particularly with regard to the shapes of the TA profiles at wavelengths in the visible region of the spectrum [63].

Consideration of the absorption profiles in Figure 6-3 reveals considerable time-dependent narrowing of the I_2^- absorption band. Lateral slices through the TA profiles at specific times are shown in Figure 6-6, together with fits which assume a Gaussian absorption profile. The widths of the diiodide band at times 1500, 3000, 5000 and 7000 fs are, respectively: 98 nm, 85 nm, 78 nm and 64 nm. Absorption narrowing is a process which should occur on two distinct time scales. The dynamics we observe are due to

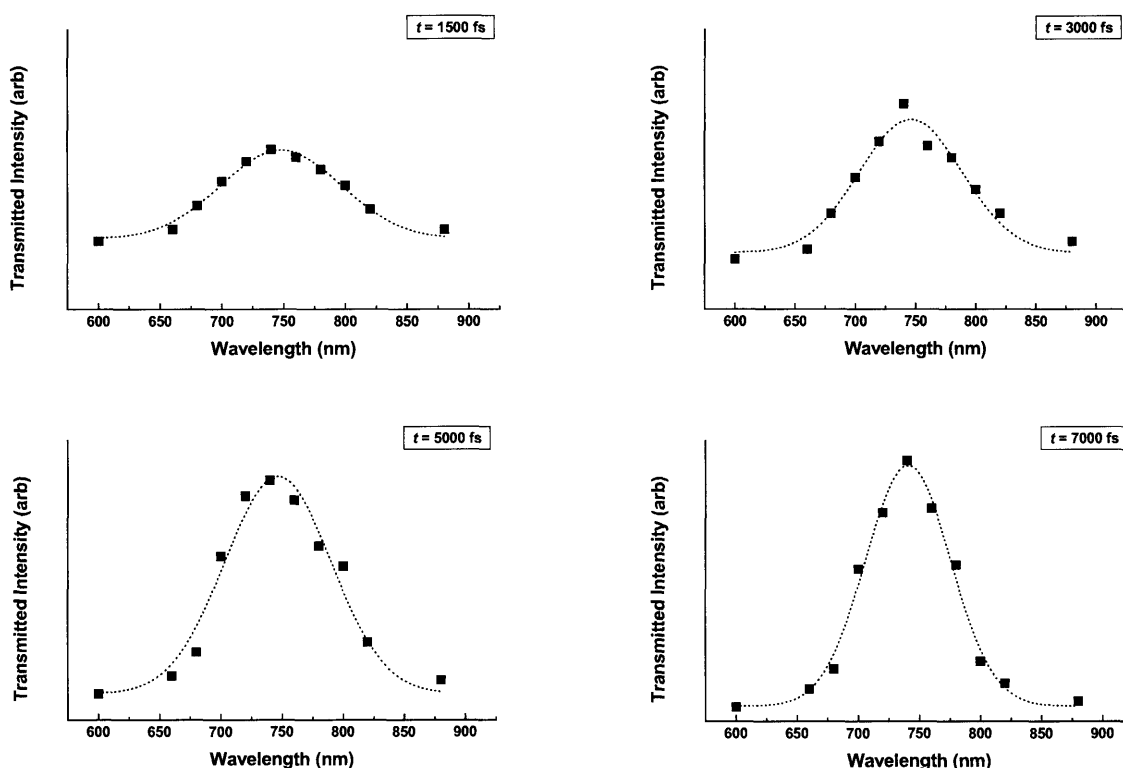


Figure 6-6. Diiodide absorption band narrowing in ethanol. Gaussian fits to transient absorption data at multiple wavelengths are shown at intervals of 1500, 3000, 5000 and 7000 fs following the initial photolysis pulse. The reduced width of the 740 nm absorption line at later times is clearly evident.

vibrational cooling in the hot I_2^- fragments. When diiodide is generated via photodissociation, the fragment ion contains considerable excess energy. Solvent modes act as acceptors for excess energy, reducing the overall vibrational energy of the fragment. This occurs for all diiodide ions which comprise the molecular wave packets responsible for the TA signal. As the mean vibrational energy of the wave packet is reduced, the amplitude of motion within the ground-state potential is reduced – the wave packet no longer samples regions of the I-I coordinate which are displaced as far from the minimum. As a result, absorption in the wings of the band decreases, relative to the

center wavelength (740 nm). Absorption at the band center does not decrease over the entire time window of the experiment, implying at later times that I_2^- fragments are still present, but most are located near the potential minimum. At very long delays of hundreds of nanoseconds or microseconds, the absorption intensity at all wavelengths should fall due to the loss of diiodide ions through recombination to form I_3^- again. Our data do not extend nearly far enough in time to observe such phenomena.

6.4 Solvent-Dependent Reaction Dynamics

As noted in the introduction, much experimental and theoretical work has focused on the dynamics of the photodissociation process in ethanol, to the point where the evolution of product states in terms of the topology of the potential energy surfaces rests on a firm foundation of both experimental observations and theoretical calculations. It is our intent to investigate the effect of solvent upon the reaction dynamics within the broader context of developing an understanding of the role of the environment in mediating the reactivity of chemical species. To this end, we have performed a further series of transient absorption experiments on triiodide ion dissolved in the solvents acetonitrile, acetone, *n*-butanol, *n*-octanol and tetrahydrofuran. Each of these solvents is polar, but as a group they exhibit variations in their ability to solvate negative charges, which suggests the possibility that the kinetics and efficacy of the photodissociation process might differ from one solvent to another.

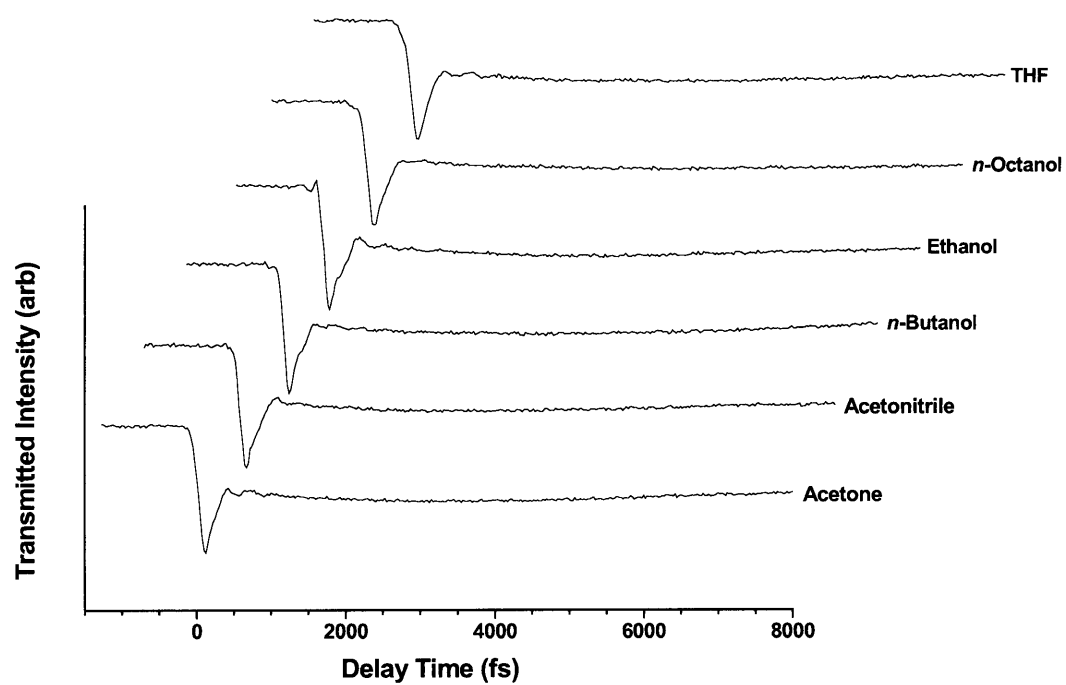
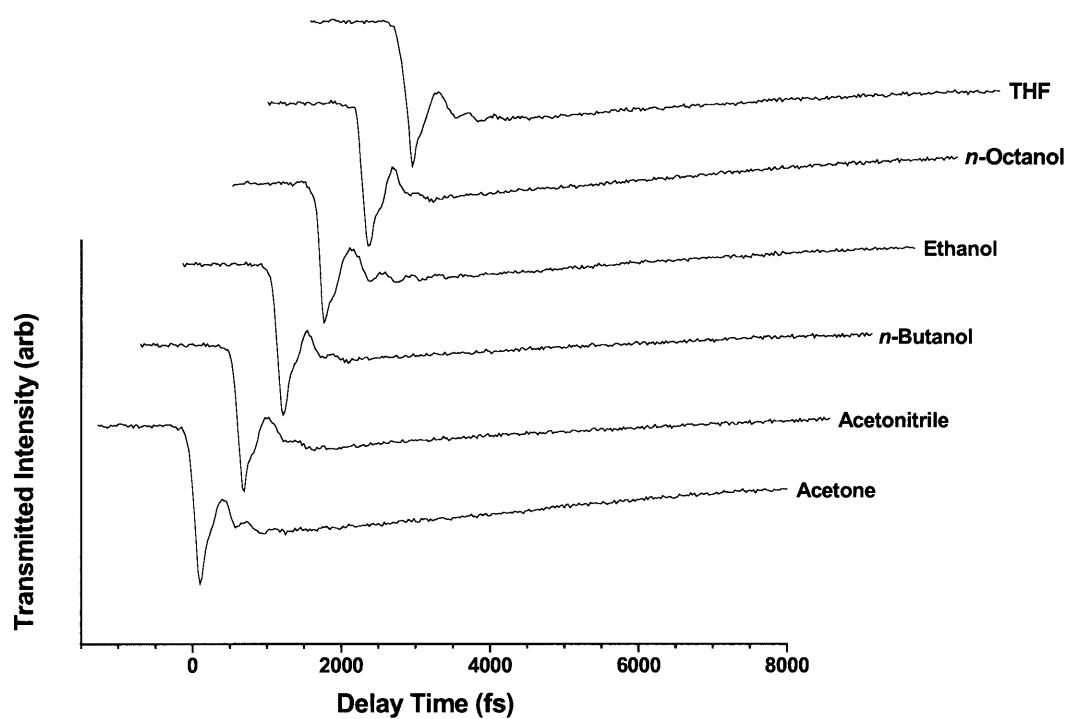


Figure 6-7. Transient absorption scans of photolyzed triiodide ion in a series of solvents (indicated at right). Probe wavelengths are 660 nm (top) and 700 nm (bottom).

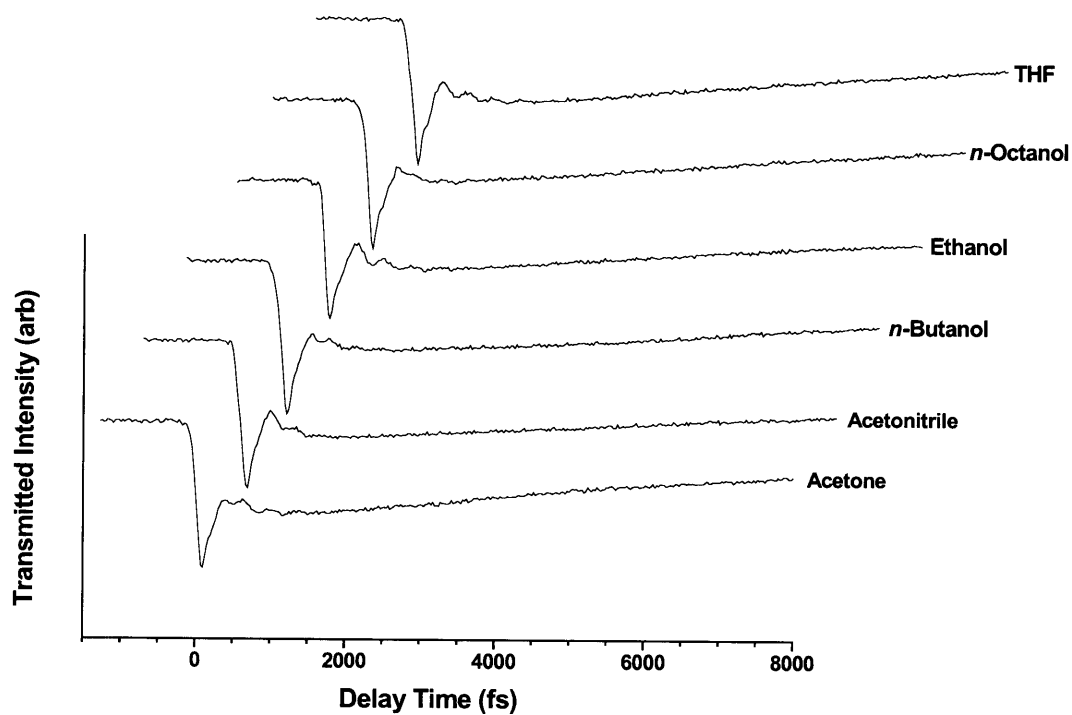
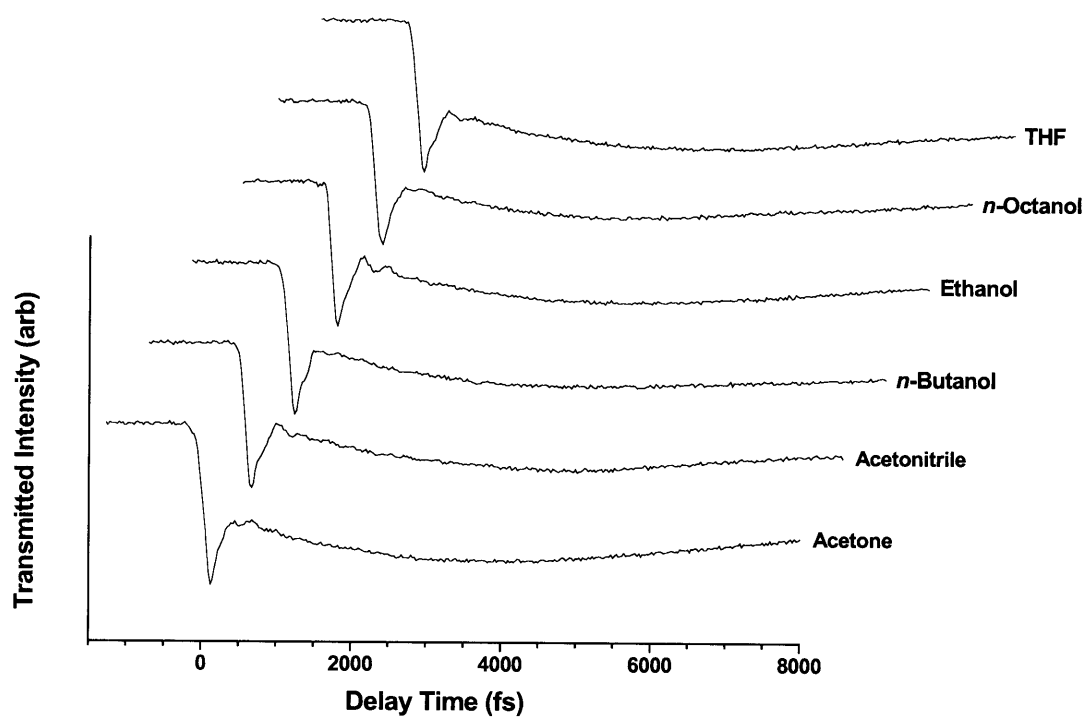


Figure 6-7 (cont'd). Transient absorption scans of photolyzed triiodide ion in a series of solvents (indicated at right). Probe wavelengths are 780 nm (top) and 820 nm (bottom).

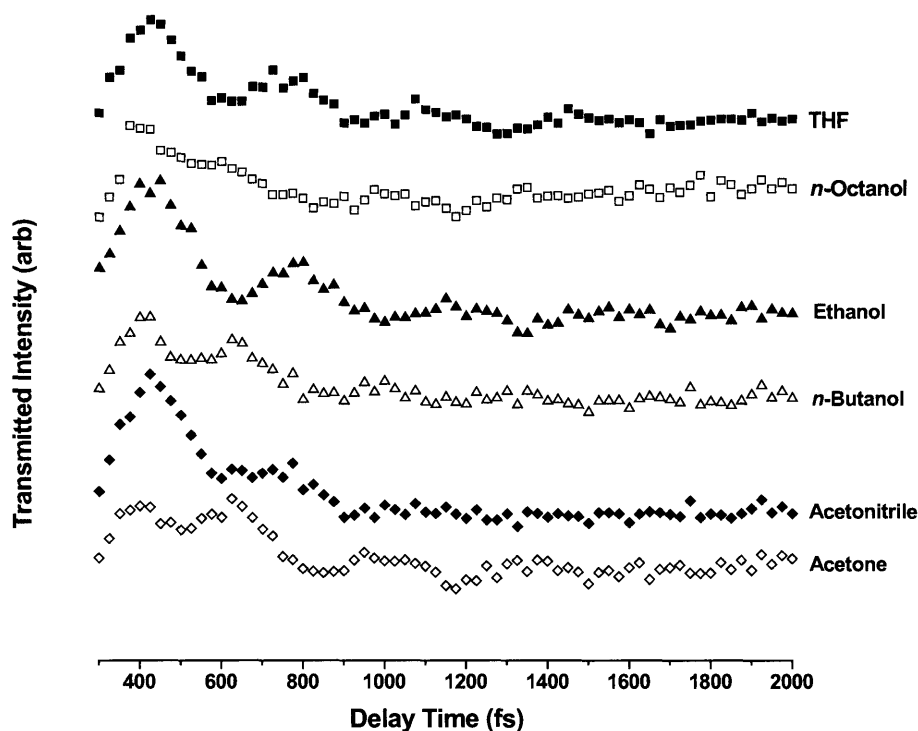


Figure 6-7 (cont'd). Expanded view of transient absorption of photolyzed triiodide ion at a probe wavelength of 660 nm. The solvent is indicated to the right of each data sweep.

Figure 6-7 shows the results of TA measurements of 2 mM solutions of triiodide in each of the five solvents mentioned. Scans for ethanol are also shown for the purposes of comparison. Four different probe wavelengths are used: 660 nm, 700 nm, 780 nm and 820 nm.

At wavelengths of 700 nm and 780 nm, only very weak oscillatory contributions to the TA signal are observed in any of the solvents. The previous data for ethanol at 11 different wavelengths supports this finding – as the probe wavelength approaches the center of the absorption band from either the red or blue side, the depth of modulation in

the oscillatory component of the signal decreases. Near the band center, almost no modulation is apparent. The reason behind this is the width of the I_2^- wave packet initially formed via photodissociation. A compact wave packet, such as that which might result from a Raman scattering process, is focused in position and momentum space so that the band of wavelengths over which absorption occurs is narrower. As the wave packet cycles back and forth along its electronic potential energy surface, the center frequency of the narrow band absorption shifts appropriately. The deepest oscillations are observed for wave packets with the narrowest widths. By contrast, the photodissociation process produces a broad I_2^- ground state wave packet due to a large excess of vibrational quanta and a distribution of bond-breaking times. As this defocused wave packet cycles molecular density back and forth along the ground state surface, the TA signal is again modulated. However, the depth of the oscillations will be severely reduced near the absorption band center since – due to the diffuse nature of the distribution of states – there is never a time when there is no appreciable wavepacket density near the minimum of the well. For this reason, oscillatory modulation of the TA signal is very weak in the vicinity of 740 nm for I_2^- absorption.

The TA signals show similar trends at 660 nm and 820 nm, and an expansion of the solvent dependent oscillations at 660 nm is shown in the fifth panel of Figure 6-7. The deepest modulations are observed in ethanol and tetrahydrofuran (THF) solvents. Weaker, but nonetheless apparent, are the oscillatory contributions to the signal in acetone, *n*-butanol and acetonitrile. There is almost no oscillation component visible in the TA data for *n*-octanol.

The different depths of modulation can be understood in terms of the solvation geometries of triiodide and diiodide in each case. A centrosymmetric, linear conformation of I_3^- in solution has two equivalent reaction channels along which dissociation can occur, each of which leads to the diiodide product. If the initial configuration is perfectly symmetric, quantum chemical calculations have shown [78] that a dispersive process of bifurcation occurs, with the reactive density occupying mostly the symmetric stretching mode. Absorption of the photolysis pulse strongly accelerates dissociative motion along both I-I stretching coordinates simultaneously, according to resonance Raman scattering results for the system [79]. Any asymmetry in the initial geometry of the triiodide ion, which corresponds to excitation of the anti-symmetric stretch, strongly favors one exit channel over the other. The reactive density, rather than remaining split between equivalent channels, is now preferentially directed toward one side. Photodissociation of triiodide under these circumstances is predicted to yield diiodide ions which are vibrationally cooler – more of the photon energy is converted to kinetic energy, particularly for atomic I – and an overall molecular wave packet which is more compact and localized, and therefore exhibits stronger modulation of the transient absorption signal. By contrast, if the triiodide ion is highly stretched along the symmetric coordinate before a choice of exit channel occurs, a diiodide fragment with large amounts of excess vibrational energy is the result. Such a wave packet is more diffuse and produces weaker overall modulations in the TA signal.

From CW Raman measurements, Johnson and Myers [66] have determined that I_3^- adopts a broken symmetry in ethanol, owing to the activity of the antisymmetric stretching fundamental in the spectrum of the ion. In acetonitrile, however, the

antisymmetric mode is absent, leading to the conclusion that triiodide ion is in a fully symmetric configuration. These observations are in agreement with the data of Figure 6-7. Qualitatively, the depth of modulation is much greater for I_3^- in ethanol than for acetonitrile, supporting the notion that pre-existing asymmetry prejudices the exit channel for the dissociation and produces a more focused I_2^- wave packet. Based upon the data for other solvents, we conclude that an asymmetric configuration is also adopted by I_3^- in tetrahydrofuran, although the modulations are clearly weaker and thus the initial asymmetry must not be as large. The modulation depth in acetone is quite comparable to that for acetonitrile, suggesting a very symmetric configuration for I_3^- , and out of all solvents, the weakest depth of modulation is observed for the long chain alcohols *n*-butanol and *n*-octanol, implying the most symmetric solvated configuration for triiodide ion.

The phase behavior of the transients in panel 5 of Figure 6-7 also differs according to the solvent. As a general trend, we observe that for ethanol and THF, the first maximum in TA occurs near $t = 470$ fs. Since the probe wavelength is fixed on the blue side of the absorption band, this maximum corresponds to a highly compressed I_2^- fragment near its inner turning point. By contrast, the first TA maxima for acetone and *n*-butanol occur roughly 130 fs later (the feature at 400 fs in each is due to decay of excited state absorption by triiodide ion, not due to diiodide). The timing of the maxima confirms our interpretation in terms of symmetry. For an asymmetric initial geometry, the dissociation reaction settles upon an exit channel earlier in time, and so the minimum-stretched configuration is reached sooner, upon recoil. When the initial geometry of I_3^- is nearly symmetric (as in acetone and *n*-butanol) the choice of exit channel is made later,

and so diiodide absorption near the inner turning point, which must await the compression of the stretched fragment from its outer turning point, occurs later. These findings are consistent with those of Gershgoren *et al.* who evaluated the effects of symmetry breaking by both the solvent (ethanol vs. acetonitrile) and chemical substitution (I_3^- vs. I_2Br^-) and found that selection of a reactive exit channel occurred earlier for symmetry-broken species in each case [53].

While our results in multiple solvents give important clues regarding the nature of triiodide in different environments, without accurate structural models for the solvation shells formed in each case, it is difficult to draw conclusions regarding the efficiency with which excess fragment vibrational energy is dissipated by solvent bath modes. Undoubtedly, the solute-solvent interactions are considerably different in each of the cases investigated above, as both the polarity (which affects the solvent's ability to stabilize the triiodide negative charge) and molecular shape (which influences the packing geometry of solvent molecules) vary dramatically. For instance, it is not too surprising that both of the long chain alcohols support a symmetric configuration for I_3^- . Due to their relatively non-polar nature, interactions between these solvent molecules and the negatively-charged triiodide ion are expected to be weaker, and therefore the symmetric, linear configuration of triiodide should be less-perturbed. A highly polar solvent such as ethanol will perturb the I_3^- geometry more strongly. Steric factors may also play a role here with regard to the efficiency of interaction between large numbers of solvent molecules and individual I_3^- ions. None of the solvents employed appear to impede the photodissociation in any way – the kinetics by which the diiodide absorption

band grows in are the same for each – it is only the vibrational energy content of the fragment which is influenced.

6.5 Viscosity-Dependent Reaction Dynamics

Triiodide ion, owing to the relatively delocalized character of its single negative charge, dissolves readily in most alcohols. We have already examined the transient absorption dynamics of I_3^- in ethanol, *n*-butanol and *n*-octanol, and on the basis of the observed depth of modulation of the TA signal, have formulated a consistent interpretation based upon the solvated symmetry of the ion. Unfortunately, the solute-solvent shell structure in solution is likely to be different for each of these solutions as the

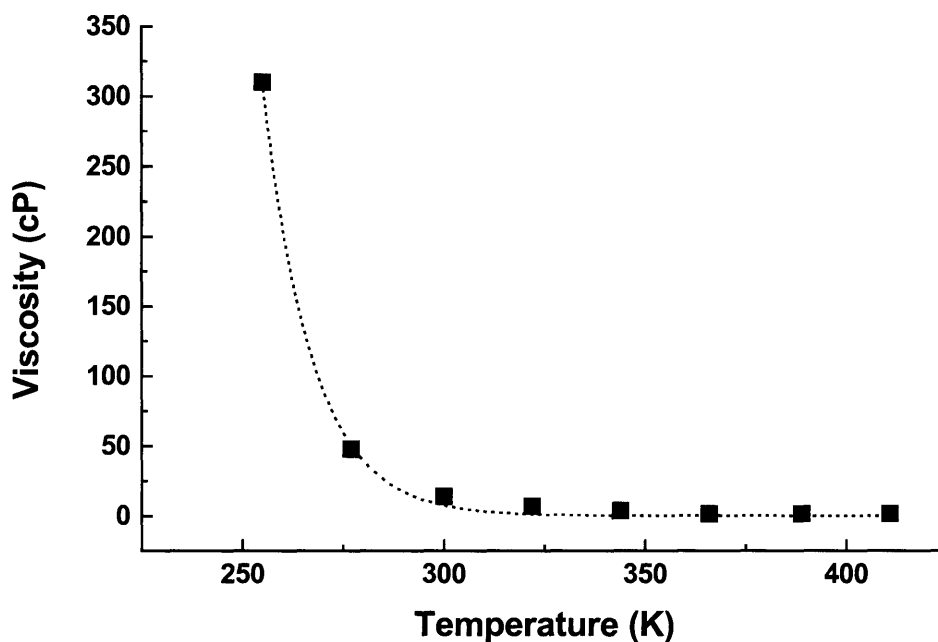


Figure 6-8. Temperature dependence of the viscosity of ethylene glycol.

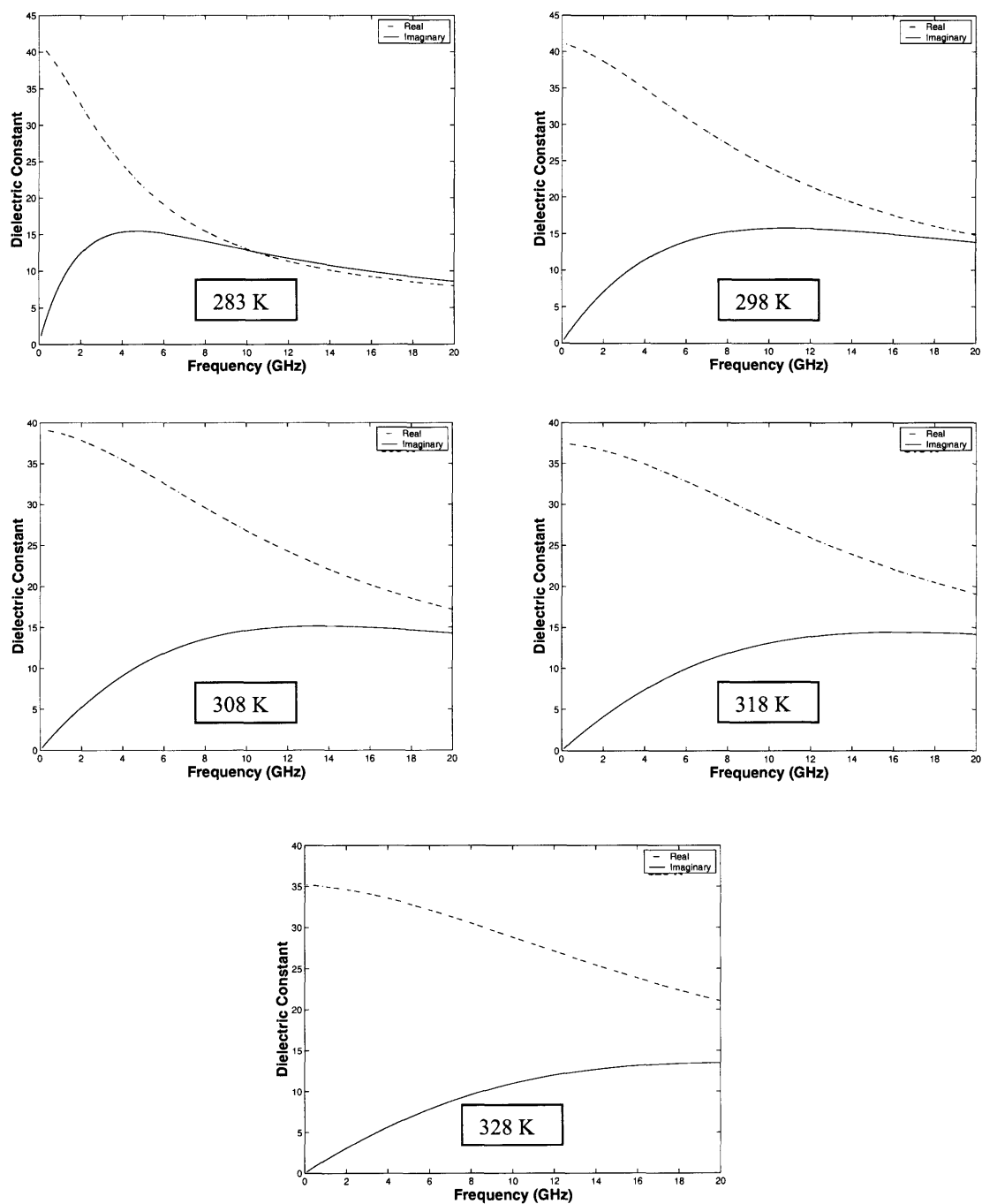


Figure 6-8 (cont'd). Dielectric spectra of ethylene glycol at various temperatures reproduced from data in references 92 and 93.

chain length of the alcohol increases. Triiodide is also soluble in ethylene glycol, which affords the opportunity to exert more exacting control over the properties of the solution without changing the fundamental solvation geometry. Specifically, the viscosity and dielectric properties of ethylene glycol are temperature-dependent, and thus we are afforded a means of adjusting the “stiffness” of the solvent environment. Ethylene glycol viscosity as a function of temperature is shown in the first panel of Figure 6-8. Dielectric spectra of ethylene glycol, reproduced from data in references 92 and 93, are shown in the subsequent panels of Figure 6-8 for the range of temperatures of interest in the current work.

A 1 mM solution of triiodide ion in ethylene glycol is prepared in the same fashion as for previous experiments. The reduced concentration used in these experiments is due to lower overall solubility of I_3^- in this solvent. The solution is placed in a quartz cuvette of 250 μm path length which is mounted in thermal contact with a large aluminum block. The block itself is thermally contacted to a resistive heating stage. A calibrated thermocouple (Omega Engineering) is attached to the side of the cuvette for accurate measurement of temperature. Unfortunately, the crowded geometry of the single-shot experiment does not permit incorporation of our cryostat, effectively limiting any temperature-dependent measurements to room temperature and above. For ethylene glycol, this means that the region of rapidly increasing viscosity below 290 K in Figure 6-8 cannot currently be accessed. In the region which is available, the temperature-dependent shifts in viscosity and dielectric response are considerably less dramatic. Nonetheless, TA measurements are conducted at a series of wavelengths in the visible and near-IR region in order to investigate the influence of temperature-dependent solvent

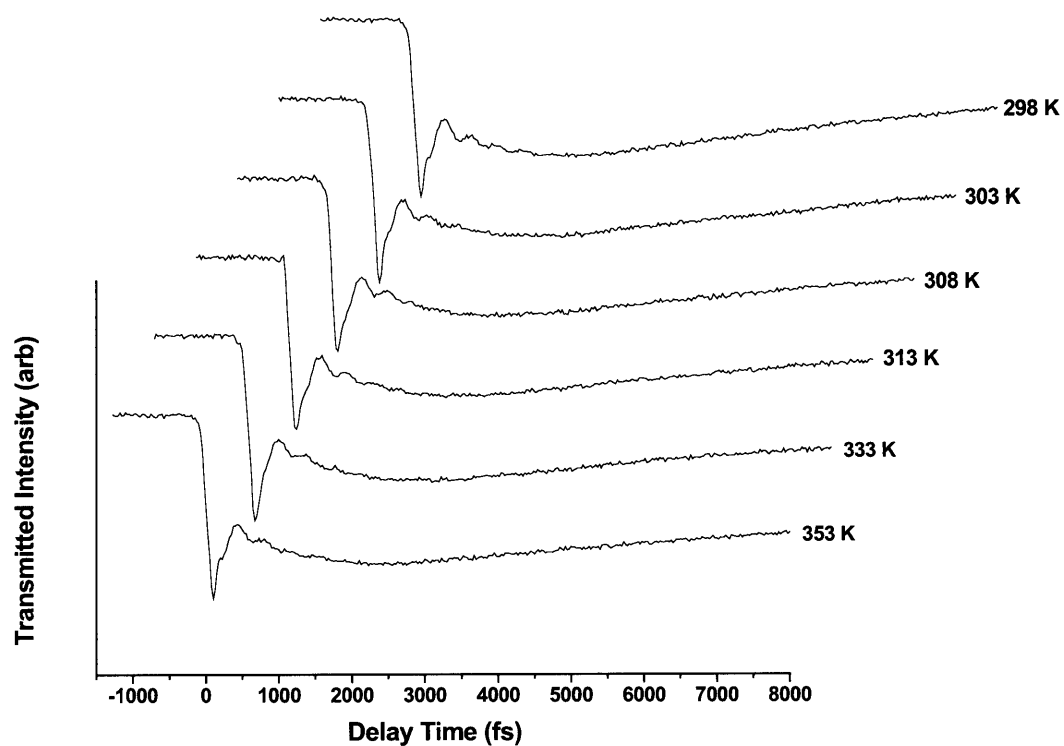
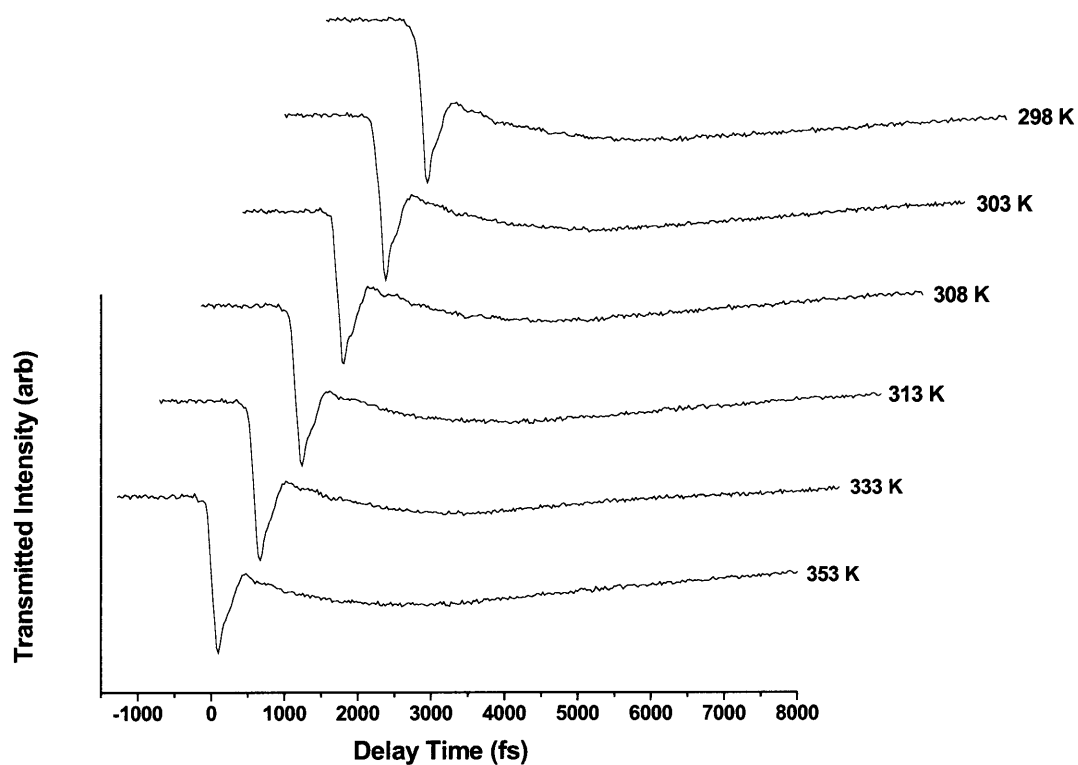


Figure 6-9. Temperature-dependent transient absorption measurements for triiodide in ethylene glycol. Probe wavelengths are 700 nm (top) and 800 nm (bottom).

response on the I_2^- dynamics. The results for 700 nm and 800 nm probing are shown in Figure 6-9. At 700 nm, almost no oscillatory component to the observed absorption signal is apparent. This is consistent with other TA observations near the 740 nm I_2^- band maximum. At 298 K, an extremely weak periodic modulation which is visible for only about two cycles is present; at the other temperatures, no such oscillation is strong enough to be detected. However, for probing at 800 nm (on the red edge of the absorption band, further out on the wing), periodic modulation of the TA signal is clearly observed at all temperatures. The depth of the modulations also follows a specific trend, although the differences from one temperature to the next are not dramatic. At the highest temperature (353 K), the depth of the oscillatory modulations is smallest. As the temperature is decreased, the depth of the modulations increases. Clear oscillations lasting for several cycles are observed in the scan at 298 K.

The increase in both oscillation amplitude and vibrational coherence time with decreasing temperature can be understood qualitatively in the context of the solvent response to interactions with a hot molecular fragment such as I_2^- . The temperature-dependent viscosity of Figure 6-8 essentially represents the zero-frequency limit of the dynamic response of ethylene glycol. A better measure of the ability of the solvent to exchange energy with I_2^- ions is given by the dielectric response. In particular, consider the real and imaginary components of the dielectric function of ethylene glycol in Figure 6-8. As the temperature is increased, the distribution shifts to higher frequencies, and the width of the response becomes much broader. Interactions with I_2^- (especially initially) will involve solvent modes with frequencies in the vicinity of 1 THz. Unfortunately, the available frequency-dependent dielectric data only extend to 20 GHz. However, the

trends can be extrapolated in a rough sense into the frequency range of hundreds of GHz to 1 THz. The dielectric response of ethylene glycol at high frequencies is stronger for increasing temperatures. Effectively, the solvent is better able to induce dephasing (real component) and exchange vibrational energy (imaginary component) with hot I_2^- fragments, leading to rapid loss of coherence in the molecular fragments. This is the reason for the weaker depth of modulation and more rapid dephasing observed at high- T for I_3^- dissociation in ethylene glycol. Note the high frequency tails of the dielectric spectra do not change drastically over the temperature range we have examined. The most obviously narrow spectrum is at 283 K; we were not able to reduce the temperature this low in our study. For this reason, the temperature-dependent changes we observe in the coherent components of the TA signals are modest. It is also for this reason that we do not observe dramatic temperature-dependent changes in the incoherent vibrational relaxation rate, which would manifest as strongly time-dependent absorption decay rates.

Thus, the results we observe for I_2^- absorption in ethylene glycol are consistent with a general picture incorporating energy exchange between the vibrationally excited fragment and the solvent environment. However, we are restricted in our ability to vary temperature-dependent solvent response for ethylene glycol. The limit reached when the temperature is further lowered is that of an amorphous, disordered solid or a glass. In the next section, we extend our measurements to this regime.

6.6 Triiodide in a Glass-Forming Liquid

It is clear from the previous section that solvent-dependent effects are manifest in the dynamics of triiodide photodissociation. In order to explore these properties in

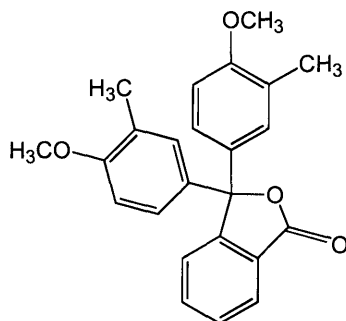


Figure 6-10. Structure of cresolphthalein dimethylether, a glass-forming liquid used as a solvent in the photodissociation reaction of triiodide ions.

greater detail, the glass-forming liquid cresolphthalein dimethylether (structure in Figure 6-10) was employed as the solvent for I_3^- in a series of photodissociation experiments. Cresolphthalein dimethylether (CDE) has a glass transition temperature of 310 K, which falls well within the available temperature range of our single-shot experiments. The methoxy substituents on the aromatic rings and the cyclic ester moiety in the five-membered ring structure are sufficiently polar to stabilize the negative I_3^- charge. Solutions of triiodide in CDE were readily prepared at 50°C by dissolution and stirring for about 30 mins. CDE was obtained in pure form from the group of Professor John Fourkas at Boston College.

The position of the (nominal) 300 nm absorption band was measured as a function of temperature in CDE solution. The results are shown in Figure 6-11. For a temperature window of 60 K, which includes the formation of a glassy solution, the shift of the absorption maximum is about 1.25 nm. The center wavelength of the photolysis pulse

therefore did not need to be adjusted at each temperature in order to ensure high photolysis yield.

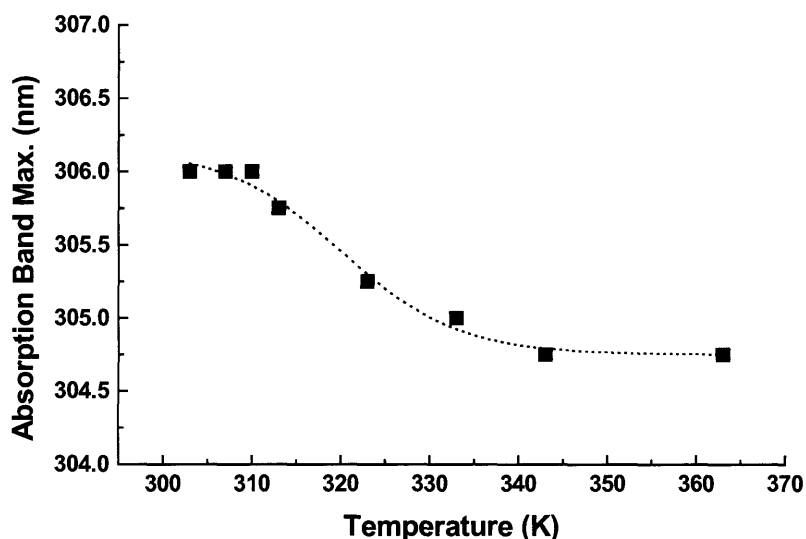


Figure 6-11. Position of the triiodide absorption maximum as a function of temperature.

Transient absorption measurements at probe wavelengths 660 nm, 700 nm and 300 nm are presented in Figure 6-12. As before, the 660 nm and 700 nm scans monitor I_2^- wavepacket dynamics, whereas the 300 nm scans interrogate residual (undissociated) I_3^- in solution. For data scans at temperatures of 323 K and under, long-lived bleaching of the sample is visible after 2-3 shots in the same spatial location, and some degree of bleaching likely occurs even after a single photolysis pulse. These experiments are necessarily one-shot scans (with sample translation in between shots) as a result. Photolysis pulses are of energy 1.0 μ J, and focused to a spot size of 150 μ m. Probe pulse wavelengths are controlled by adjustment of either the second arm of the NOPA, or by

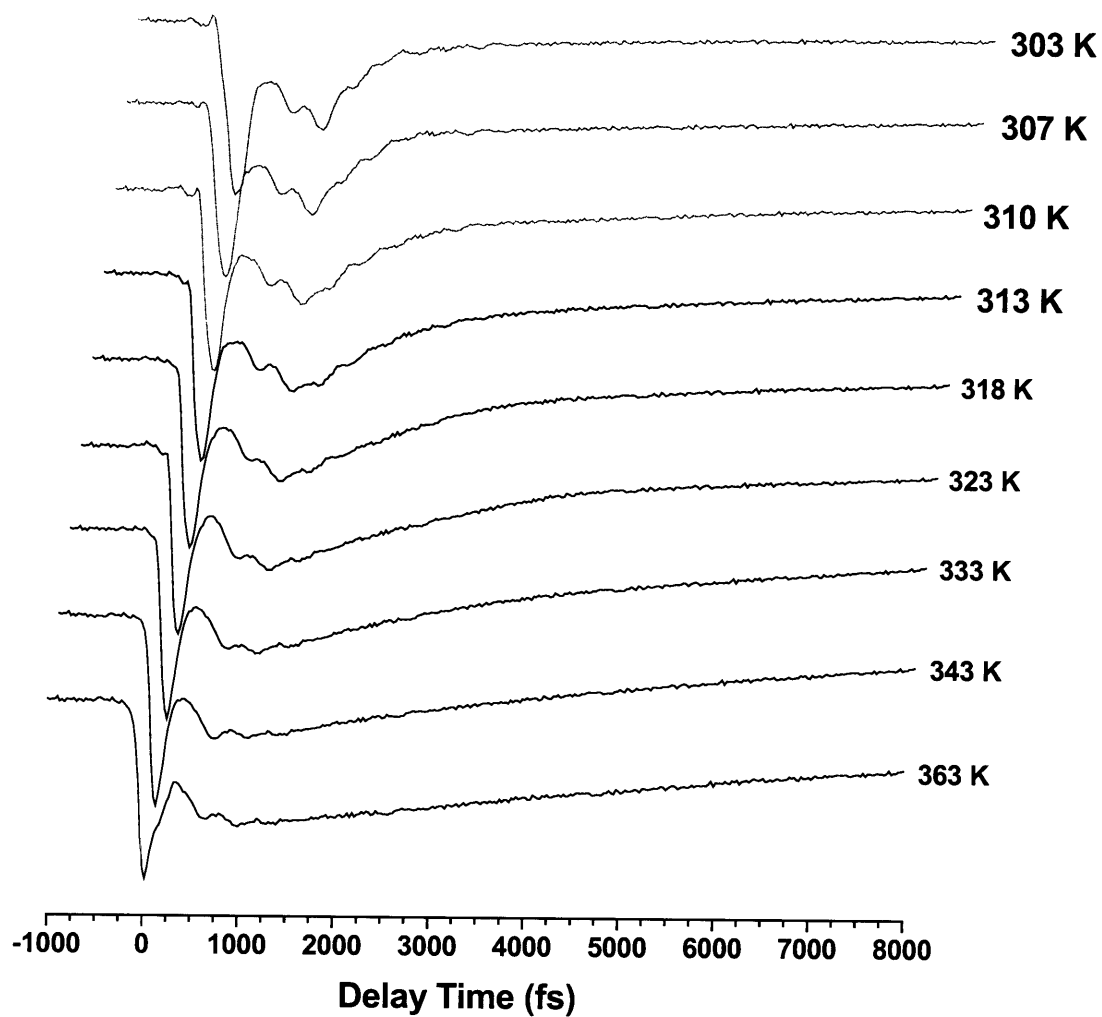


Figure 6-12. Single-shot transient absorption of diiodide ion at 660 nm in a solution of cresolphthalein dimethylether as a function of temperature (indicated to the right of each scan). Data sweeps which are shown in grey (310 K, 307 K and 303 K) correspond to solutions at or below the glass transition temperature for CDE.

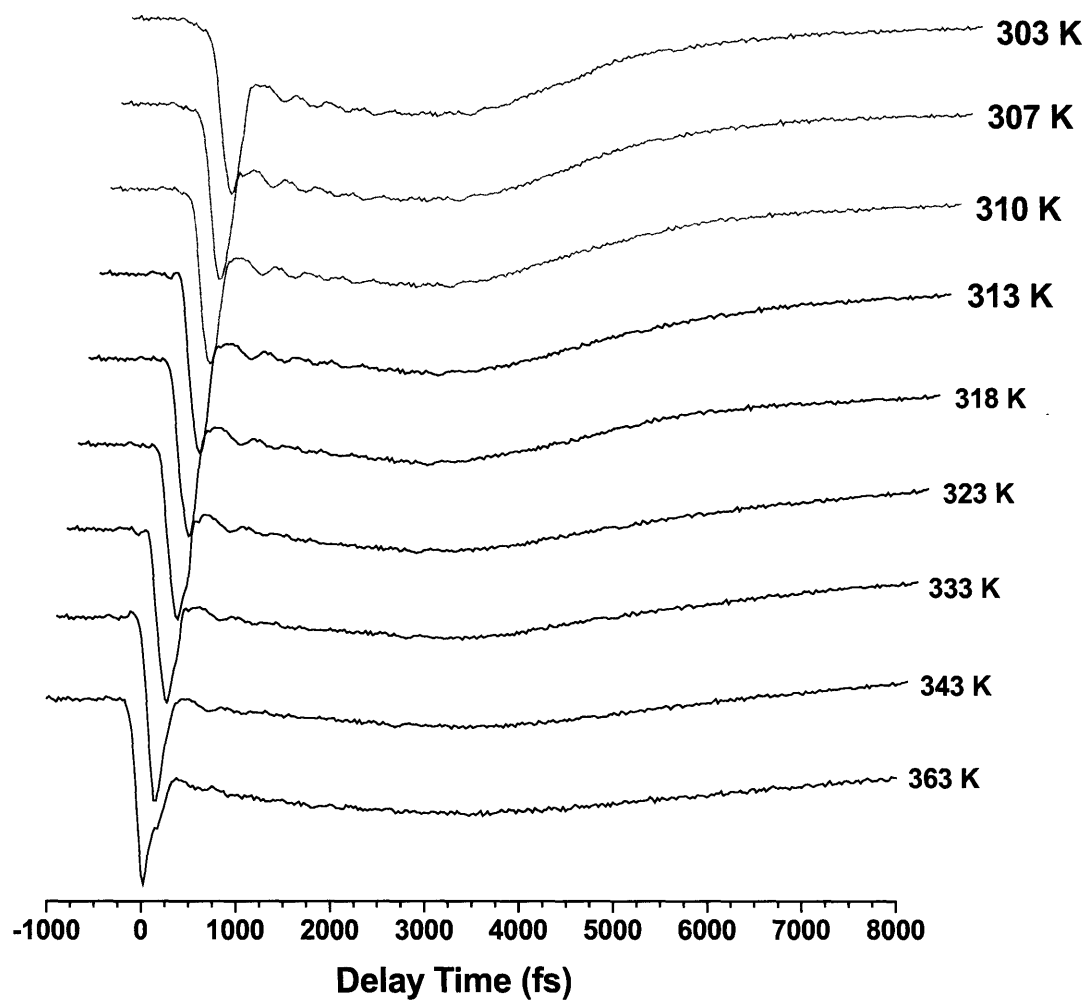


Figure 6-12 (cont'd). Single-shot transient absorption of diiodide ion at 700 nm in a solution of cresolphthalein dimethylether as a function of temperature (indicated to the right of each scan). Data sweeps which are shown in grey (310 K, 307 K and 303 K) correspond to solutions at or below the glass transition temperature for CDE.

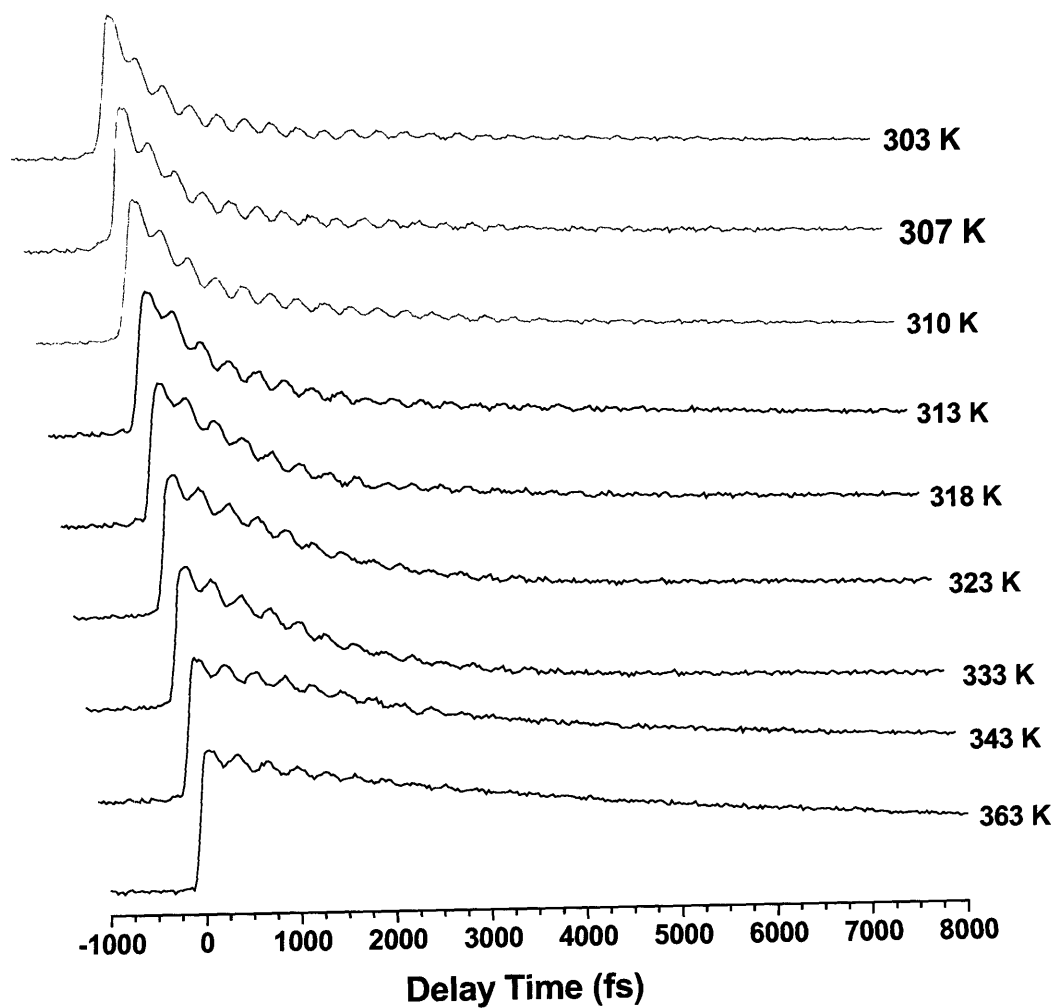


Figure 6-12 (cont'd). Single-shot transient absorption of triiodide ion at 300 nm in a solution of cresolphthalein dimethylether as a function of temperature (indicated to the right of each scan). Data sweeps which are shown in grey (310 K, 307 K and 303 K) correspond to solutions at or below the glass transition temperature for CDE.

continuum generation with spectral filtering. Probe pulse energies remain at 250 nJ in order to ensure that absorption is linear. Temperature control is achieved by adjustment of a variable-resistor heating block which is in thermal contact with the quartz cuvette containing the sample solution. Roughly one hour is allowed to elapse between adjustments of sample temperature to permit thermal equilibration prior to recording data.

The data of Figure 6-12 contain some familiar attributes. Transient absorption data at 660 nm and 363 K show a sharp initial absorption feature which persists for 300-400 fs, and which corresponds to excited state I_3^- following the photolysis pulse. Rapid absorption decay followed by a slower increase in the TA signal is indicative of the process of I_3^- dissociation to yield I_2^- which then provides the principal contribution to the absorption signal. Periodic modulation of the signal is observed and is presumably due to coherently oscillating I_2^- fragments, as we have previously noted. The I_2^- absorption band reaches maximum intensity at about 1200 fs, and then slowly decays throughout the rest of the experimental time window.

As the temperature is lowered and the glass transition temperature is approached, the solvent viscosity increases. While the temperature-dependent dielectric response of CDE has not been measured to our knowledge, we expect a trend similar to that observed for ethylene glycol, although the change in the width of the distribution should be much more dramatic at temperatures near T_g .

Three consistent trends emerge from the data. First, as the temperature is lowered, the maximum intensity of the I_2^- absorption decreases slightly, implying a marginally less facile dissociation pathway. The time scale upon which diiodide absorption grows in intensity remains roughly the same, however, indicating that the

reduced efficiency of dissociation is likely a caging effect from the solvent which prevents a small subset of excited I_3^- species from fully separating into I_2^- and I fragments.

Second, at low temperature, the rate at which diiodide absorption falls from its maximum intensity increases strongly, implying an enhanced rate of recombination to I_3^- . Thus, while the frozen solvent does not *prevent* the dissociation from occurring, it appears that the ability of the molecular fragments to escape the local cage environment is greatly reduced relative to a high- T solution. With a much smaller probability of local cage escape, the geminate recombination rate is much faster. The data at lower temperatures closely resemble the biexponential kinetics observed by Ruhman and co-workers [54,57] for solutions of I_3^- in glassy ethanol, although the time window of their measurements extended to over 400 ps.

Third, the depth of modulation of the coherent contribution to the signal is increased markedly at low temperature and the dephasing rate is reduced. A simple physical interpretation for this observation rests upon the fact that in order for rapid dephasing to occur, vibrationally hot I_2^- fragments must readily exchange energy with solvent modes over a broad range of frequencies. At high temperatures, the real and imaginary components of the dielectric spectrum of CDE are expected to be broader – and shifted to higher frequency – than at low temperatures near T_g . As a consequence, vibrational dephasing and absorption of excess vibrational energy in the 100 GHz – 1 THz region by solvent modes at low temperature are much less facile. Coherence dephasing therefore requires longer times, and the modulation depth of the observed oscillations is greater. This is the same mechanism which accounted for the temperature-

dependent effects in ethylene glycol. The only difference is that in the current set of experiments for CDE, we examine a larger range of solvent viscosities, and the temperature-dependent dielectric response varies much more significantly.

At 700 nm, similar trends as a function of temperature are observed. As the solution is cooled toward the glass transition, the periodic modulations in TA become more pronounced and the rate of disappearance of the I_2^- band increases. Closer to the I_2^- absorption band maximum, the 700 nm TA intensity is greater at all times for 700 nm probing than for 660 nm probing, and the decay rate of absorption is slower at equivalent temperatures, leading to the same time-dependent band-narrowing which was observed for ethanol solutions. No abrupt change in the absorption signals are apparent at any wavelength on passing through T_g .

The data which correspond to probe wavelengths near 300 nm follow the same pattern. The depth of modulation of the oscillatory component of the signal increases, and the dephasing rate decreases, with decreasing temperature. The reasons for this are similar to those above. The decay kinetics of the triiodide bleach signal also show a marked increase in the rate of bleach recovery – that is, recombination processes distinct from stimulated Raman scattering which lead to the formation of I_3^- on its ground state surface occur with greater probability in the glassy solution. This observation supports our earlier interpretation that while the glassy solvent does not appear to prevent photodissociation from occurring, the subsequent rate of geminate recombination is certainly enhanced, implying a lower probability of escape from the local coordination sphere.

In accordance with the generally accepted observation of exponential decay kinetics for triiodide and diiodide transient absorption in solution [51,55], the data at probe wavelengths of 660 nm and 300 nm in Figure 6-12 were fitted to the following functional form:

$$S(t) = \int_{-\infty}^{\infty} G(t-t) I_{probe}(t) dt \quad (6.2)$$

Following earlier work, the Green's functions employed to describe the molecular response were

$$G^{I_2^-}(t) = \begin{cases} 0 & t < t_0 \\ De^{-\Delta(t-t_0)} + C \cos(\omega(t-t_0) + \varphi) e^{-\gamma(t-t_0)} & t_0 < t \leq t_m \\ A + Be^{-\Gamma(t-t_m)} & t > t_m \end{cases} \quad (6.3)$$

$$G^{I_3^-}(t) = \begin{cases} 0 & t < t_0 \\ A + Be^{-\Gamma(t-t_0)} + C \cos(\omega(t-t_0) + \varphi) e^{-\gamma(t-t_0)} & t \geq t_0 \end{cases}$$

In order to fit the complicated form of the TA profiles, we have defined two times, t_0 and t_m . The time t_0 corresponds to the first appearance of absorption due to either I_3^- or I_2^- , depending upon which ion we are probing. For I_3^- scans, t_0 is zero since the oscillatory component at 300 nm in ethanol solutions was traceable to time zero. For I_2^- scans, t_0 was fixed at 350 fs, the approximate time at which diiodide absorption begins to grow in following the sharp feature due to excited state triiodide.

The second parameter is t_m , the inflection point in the transient absorption signal. For diiodide absorption, t_m is the time which corresponds to the maximum absorption signal. Naturally, this value of this parameter varies as a function of diiodide probe wavelength. The effect of this parameter in the fitting procedure for I_2^- is to change from the functional form on the second line of Equation (6.3) to the form on the third line of

Equation (6.3) on passing through t_m . For triiodide scans at 300 nm, there is no inflection point – the TA signal decays monotonically – and this parameter is not utilized.

Example fits for I_3^- absorption at 300 nm and I_2^- absorption at 660 nm are shown in Figure 6-13, along with the location of t_0 and t_m . Temperature-dependent fitting results

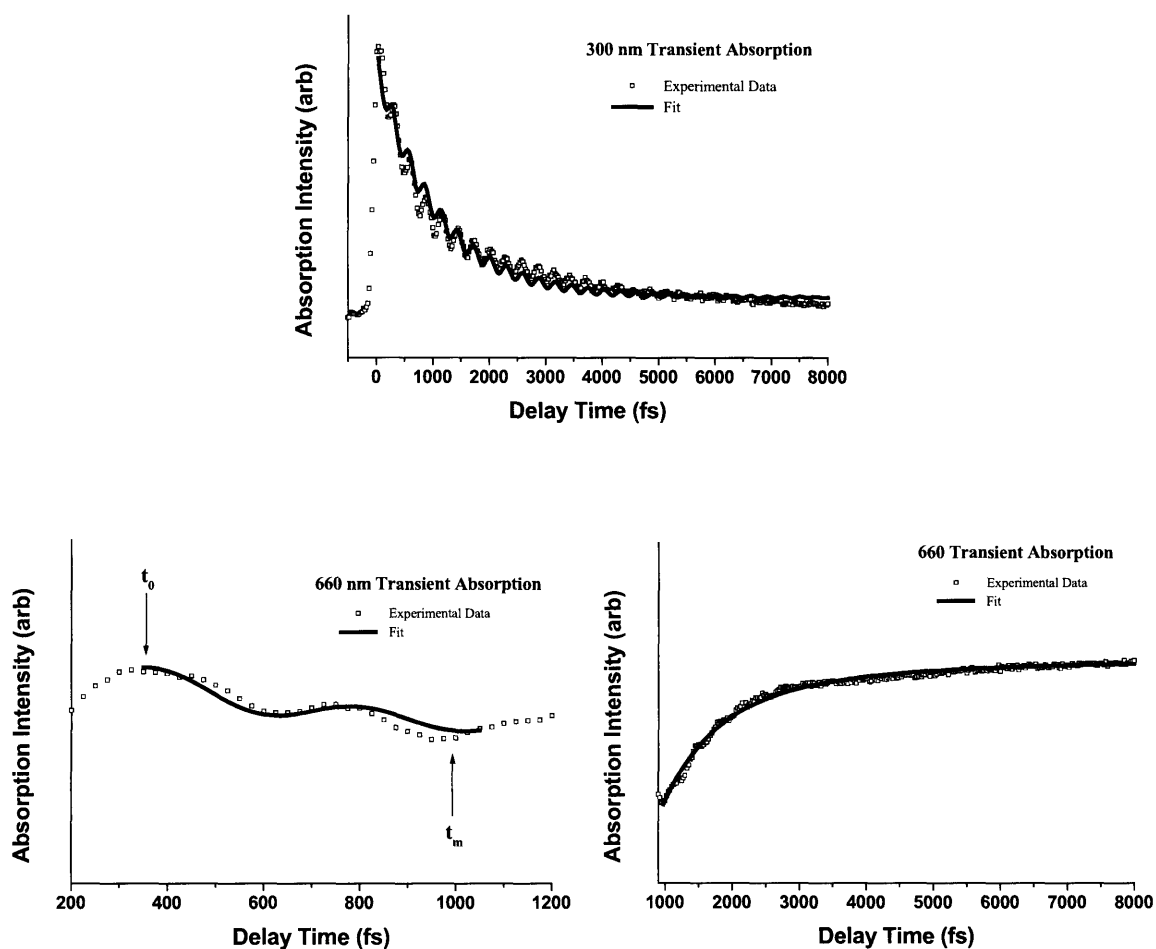


Figure 6-13. Fitting examples for transient absorption of triiodide and diiodide ions in CDE solution at 310 K.

at a probe wavelength of 660 nm are shown in Table 6-1. As noted previously, the dephasing rate decreases at lower temperatures due to the dielectric response of the CDE

Table 6-1. Fitting parameters for temperature-dependent transient absorption of diiodide ion in fluid and glassy CDE solution.

Temp. (K)	A	B	C	D	1/ Γ (ps)	1/ Δ (ps)	ω (cm ⁻¹)	ϕ (rad)	1/ γ (fs)
363	0.36	0.45	0.04	0.22	14 \pm 0.5	0.71	115 \pm 5	0.14 \pm 0.07	525 \pm 50
343	0.31	0.42	0.04	0.24	13 \pm 0.5	0.70	114 \pm 5	0.12 \pm 0.07	544 \pm 50
333	0.25	0.40	0.04	0.22	10 \pm 0.5	0.68	115 \pm 5	0.11 \pm 0.07	586 \pm 50
323	0.18	0.40	0.05	0.21	8.1 \pm 0.2	0.69	114 \pm 5	0.07 \pm 0.07	652 \pm 50
318	0.13	0.38	0.05	0.21	6.3 \pm 0.2	0.64	114 \pm 5	0.04 \pm 0.06	777 \pm 35
313	0.10	0.36	0.05	0.19	4.8 \pm 0.2	0.62	115 \pm 5	0.01 \pm 0.06	873 \pm 35
310	0.08	0.36	0.06	0.19	3.2 \pm 0.2	0.59	114 \pm 5	0.01 \pm 0.06	950 \pm 35
307	0.08	0.35	0.06	0.18	1.9 \pm 0.2	0.58	114 \pm 5	0.00 \pm 0.06	962 \pm 30
303	0.07	0.35	0.07	0.21	1.8 \pm 0.2	0.58	115 \pm 5	0.00 \pm 0.06	977 \pm 30

solution. The relative oscillation phase at 363 K is +0.14 rad, and it decreases to 0.00 as the solution becomes a glass. A possible explanation for this observation is that in the less viscous solution, a larger distribution of dissociation pathways are successful; the glassy solution may directly cage a small number of attempts to dissociate. However, we have previously observed that direct caging in CDE at any temperature does not occur with high probability, and given the very small range of phase angles, we remain very cautious regarding this interpretation.

The longer-time absorption decay rate Γ in effect describes temperature-dependent band narrowing. Given the faster rate of coherence dephasing at high temperature, it is reasonable to expect that incoherent vibrational cooling of I_2^- fragments would also be faster at elevated temperatures. In fact, we observe the opposite trend. The absorption at 660 nm decays much more rapidly at low temperature due to the dominant effect of geminate recombination. Following the initial period of internal bond stretching and dissociation, rigid solvent caging of the fragments ensures there is simply less I_2^- available to absorb, since a higher fraction recombines with atomic I to re-form ground state I_3^- .

Finally, the parameter A is observed to decrease with decreasing temperature. This parameter represents a constant offset to the decaying TA intensity, and has been interpreted in the literature as a measure of the probability of local cage escape by the dissociating fragments [54]. On the time scale of our experiment, A represents the loss of some fraction of the initial population of I_3^- molecules. This can result if the fragments from the photodissociation are able to escape their local solvent cage, and are therefore not available to recombine with other fragments and re-generate I_3^- . As one expects, the results of the fitting procedure indicate that for glassy solutions where deformational motions of solvent molecules are more difficult, the probability of local cage escape is greatly reduced.

Fitting parameters for probe data at 300 nm are shown in Table 6-2. Many of the same observations are relevant here. In particular, we note the decreasing probability of cage escape as the temperature is reduced, the large influence of geminate recombination at lower temperatures, and faster coherence dephasing at elevated temperatures.

Table 6-2. Fitting parameters for temperature-dependent transient absorption of triiodide in fluid and glassy CDE solution.

Temp (K)	A	B	C	1/ Γ (ps)	ω (cm ⁻¹)	ϕ (rad)	1/ γ (fs)
363	0.30	0.45	0.07	17 \pm 3	96 \pm 5	0.03 \pm 0.05	833 \pm 25
343	0.28	0.45	0.07	16 \pm 3	96 \pm 5	0.02 \pm 0.05	869 \pm 25
333	0.22	0.46	0.07	14 \pm 3	96 \pm 5	0.02 \pm 0.05	918 \pm 25
323	0.16	0.48	0.08	10 \pm 2	96 \pm 5	0.03 \pm 0.05	1060 \pm 25
318	0.10	0.48	0.09	6.5 \pm 1.2	97 \pm 5	0.03 \pm 0.05	1113 \pm 25
313	0.08	0.49	0.09	2.3 \pm 0.4	96 \pm 5	0.01 \pm 0.05	1222 \pm 25
310	0.04	0.49	0.10	1.9 \pm 0.3	97 \pm 5	0.00 \pm 0.05	1286 \pm 25
307	0.04	0.52	0.12	1.8 \pm 0.3	98 \pm 5	0.02 \pm 0.05	1324 \pm 25
303	0.04	0.50	0.12	1.8 \pm 0.3	97 \pm 5	0.00 \pm 0.05	1337 \pm 25

The one parameter which does not change significantly with temperature is the oscillation phase. The coherence in the TA signal at 300 nm is due to resonant impulsive stimulated Raman scattering. The interactions with the pump pulse electric field which are responsible for this effect are not influenced very much by the solvent environment, since the interaction occurs only when the pump pulse is present (for \sim 100 fs) and the amplitude of Raman oscillations is small.

6.7 Analysis of Vibrational Energy

An important aspect of condensed-phase reaction dynamics is the flow of excess energy from hot molecular fragments to acceptor modes of the solvent. In the dissociation reaction of triiodide, diiodide ions are created in a superposition of

vibrational eigenstates. The superposition state evolves coherently for a duration of roughly 500-1000 fs until the wave packet fully dephases via interactions with the solvent. Even after this occurs, the I_2^- fragments have substantial excess vibrational energy, and it is the transfer of this energy to the solvent which produces the band narrowing previously noted, for example, in ethanol solution. Band narrowing has been quantitatively examined by Vohringer and co-workers in ethanol [60], but so far no investigation of this process has occurred as a function of temperature, or in a viscoelastic liquid.

In order to investigate the distribution of vibrational states within the diiodide molecular wave packets, it is first necessary to obtain coarse-grained absorption profiles by taking slices through TA scans at various wavelengths, for particular time delays. As before, our pump-probe data for I_2^- covers the wavelength range 600 nm through 880 nm in CDE solution. Figure 6-14 shows the results for time delays of 1000 fs, 3000 fs, 5000 fs and 7000 fs at temperatures 363 K, 318 K and 310 K. In each case, band narrowing occurs as a function of time, but the absorption bandwidths at comparable times differ according to temperature.

The absorption profile can be calculated using the Frank-Condon reflection procedure under the assumption that the transition dipole moment which couples the ground and excited states of diiodide ion is coordinate independent. Potential energy surfaces for I_2^- have been derived by Chen and Wentworth [80]. The electronic ground state is represented by the Morse function

$$V_g^{I_2^-} = De^{-2a(r-r_0)} - 2De^{-a(r-r_0)} \quad (6.4)$$

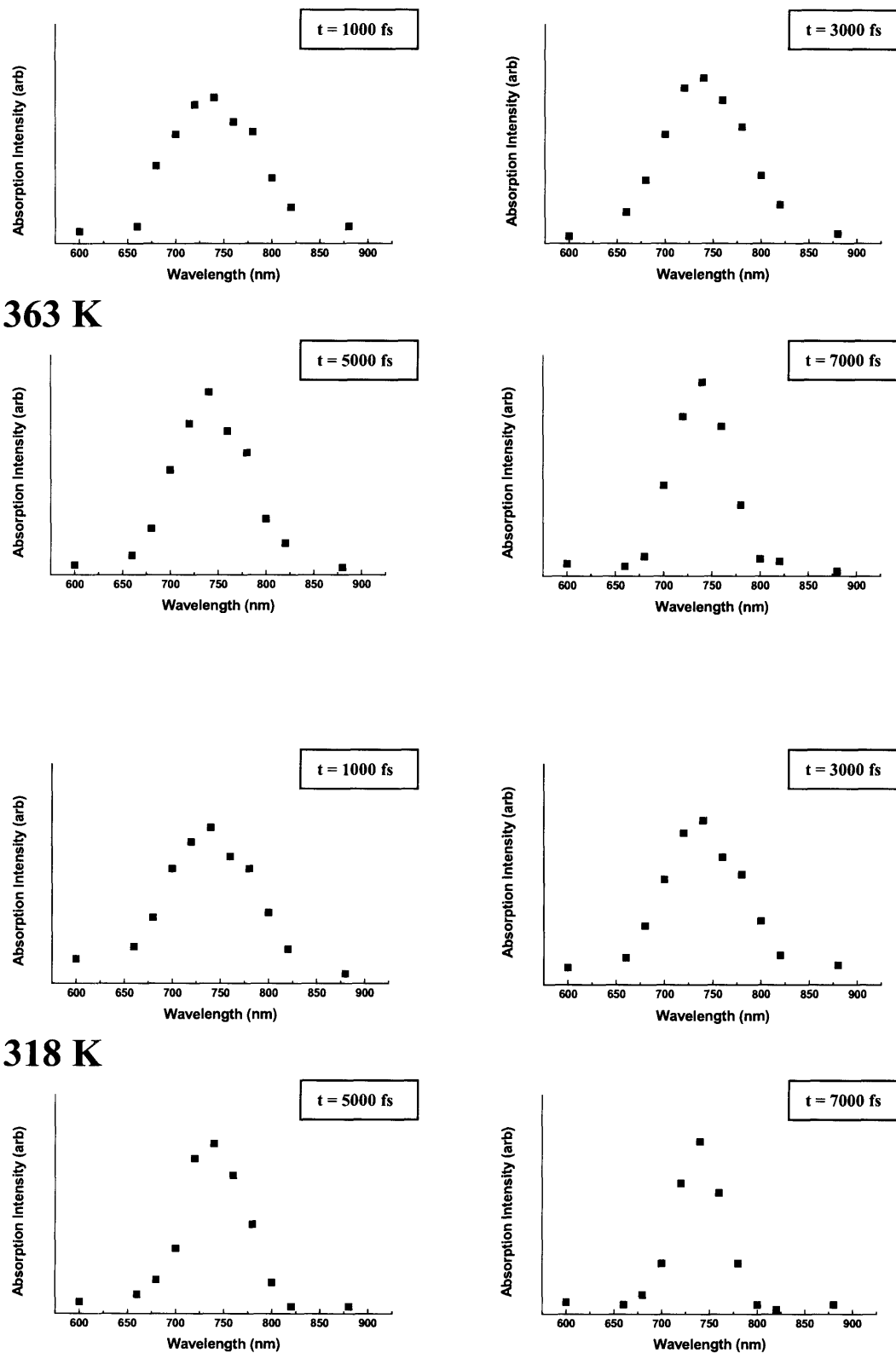


Figure 6-14. Time-dependent I_2^- absorption profiles at 363 K and 318 K in CDE solution.

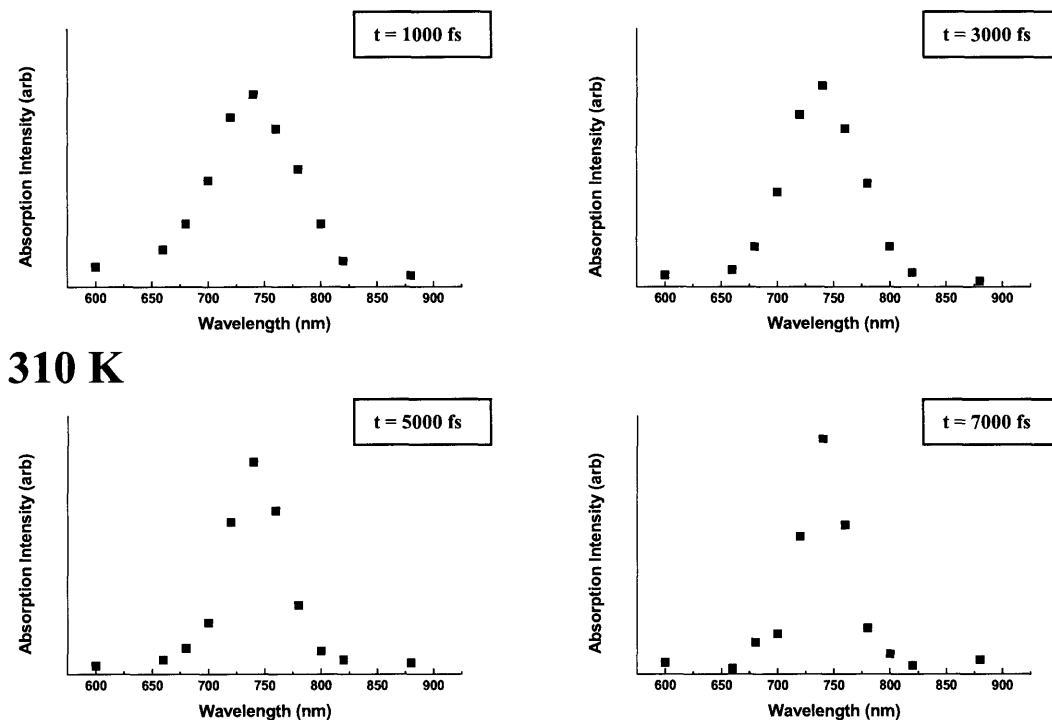


Figure 6-14 (cont'd). Time-dependent I_2^- absorption profiles at 310 K in CDE solution.

where the dissociation energy D is 0.9 eV, the equilibrium bond length is $r_0 = 3.1 \text{ \AA}$ and the scale factor $a = 1.31 \text{ \AA}^{-1}$. The dissociative excited state potential is conveniently described by the exponential function

$$V_e^{I_2^-} = be^{-\frac{r-r_0}{c}} \quad (6.5)$$

with parameters $b = 0.72 \text{ eV}$ and $c = 0.33 \text{ \AA}$. The implementation of the Franck-Condon procedure necessitates that a contribution to the absorption signal be included from each of the vibrational eigenstates of the ground electronic state for I_2^- . For a distribution of vibrational states $P(v)$, where v is the vibrational quantum number, the absorption spectrum has been approximated by several groups as [60,65]

$$I(\omega) \propto \omega \sum_{\nu} P(\nu) |\Psi(\nu, r)|^2 \quad (6.6)$$

For any particular value of the transition energy (which determines ω), the wavefunction $\Psi(\nu, r)$ must be calculated at an internuclear separation r which corresponds to the transition energy. Kuhne and Vohringer have introduced an analytic recursion expression for the wavefunction [60] which is based upon earlier work by Kobeissi [81]:

$$\Psi(\nu, r) = \Psi(\nu-1, r) \frac{k}{z(r)} \cdot \frac{k-2\nu+z(r)-(k-2\nu)R(\nu-1, r)}{2(k-\nu)-(k-2\nu)R(\nu-1)} \quad (6.7)$$

where the zero-th order wavefunction is defined as

$$\Psi(0, r) = \left[\frac{z(r)}{k} \right]^{\frac{k-1}{2}} e^{-\frac{z(r)-k}{2}} \quad (6.8)$$

The functions R and R' are defined as

$$R(\nu) = \frac{k-\nu}{\nu+1} \cdot \frac{-2\nu R(\nu-1) - (k-2\nu)}{(k-2\nu)R(\nu-1) - 2(k-\nu)} \quad (6.9)$$

$$R'(\nu) = \frac{k-\nu}{\nu+1} \cdot \frac{(k-2\nu-z(r))R(\nu-1, r) - (k-2\nu)}{(k-2\nu)R(\nu-1, r) - (k-2\nu+z(r))}$$

These functions are used to eliminate computationally-inefficient Laguerre polynomials which normally arise in the harmonic oscillator wavefunctions. When $\nu = 0$, $R(\nu) = 0$ and $R'(\nu) = k - z(r)$. The function $z(r)$ is given by

$$z(r) = ke^{-a(r-r_0)} \quad (6.10)$$

where a is the Morse potential parameter from Equation (6.4) and k is also related to the Morse function according to

$$k = \frac{4\pi}{ah} \sqrt{2\mu D} \quad (6.11)$$

In Equation (6.11), h is Planck's constant and μ is the reduced mass of the I_2^- ion.

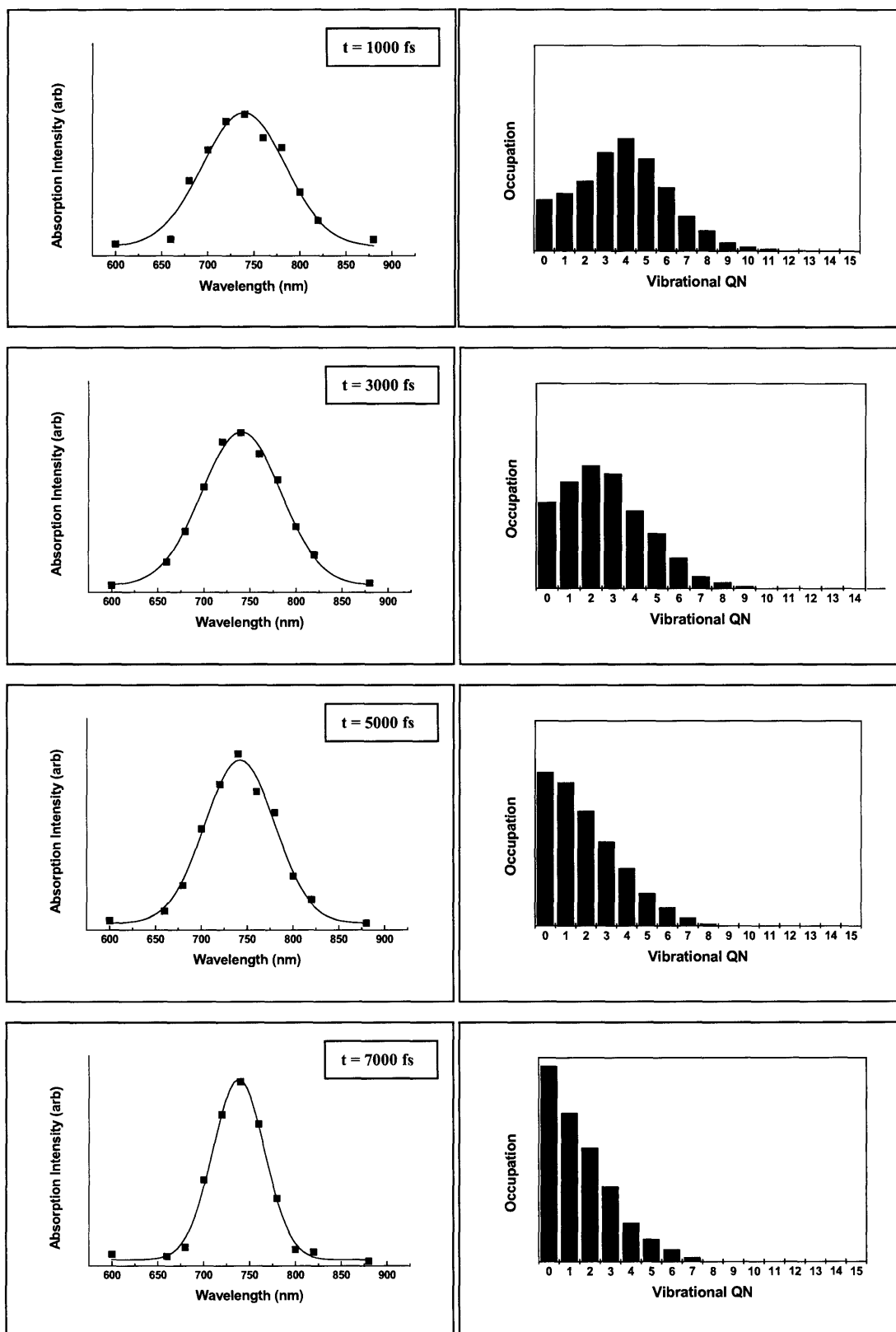


Figure 6-15. Calculated absorption profiles and vibrational distributions at four different time delays for I_2^- in CDE solution at 363 K.

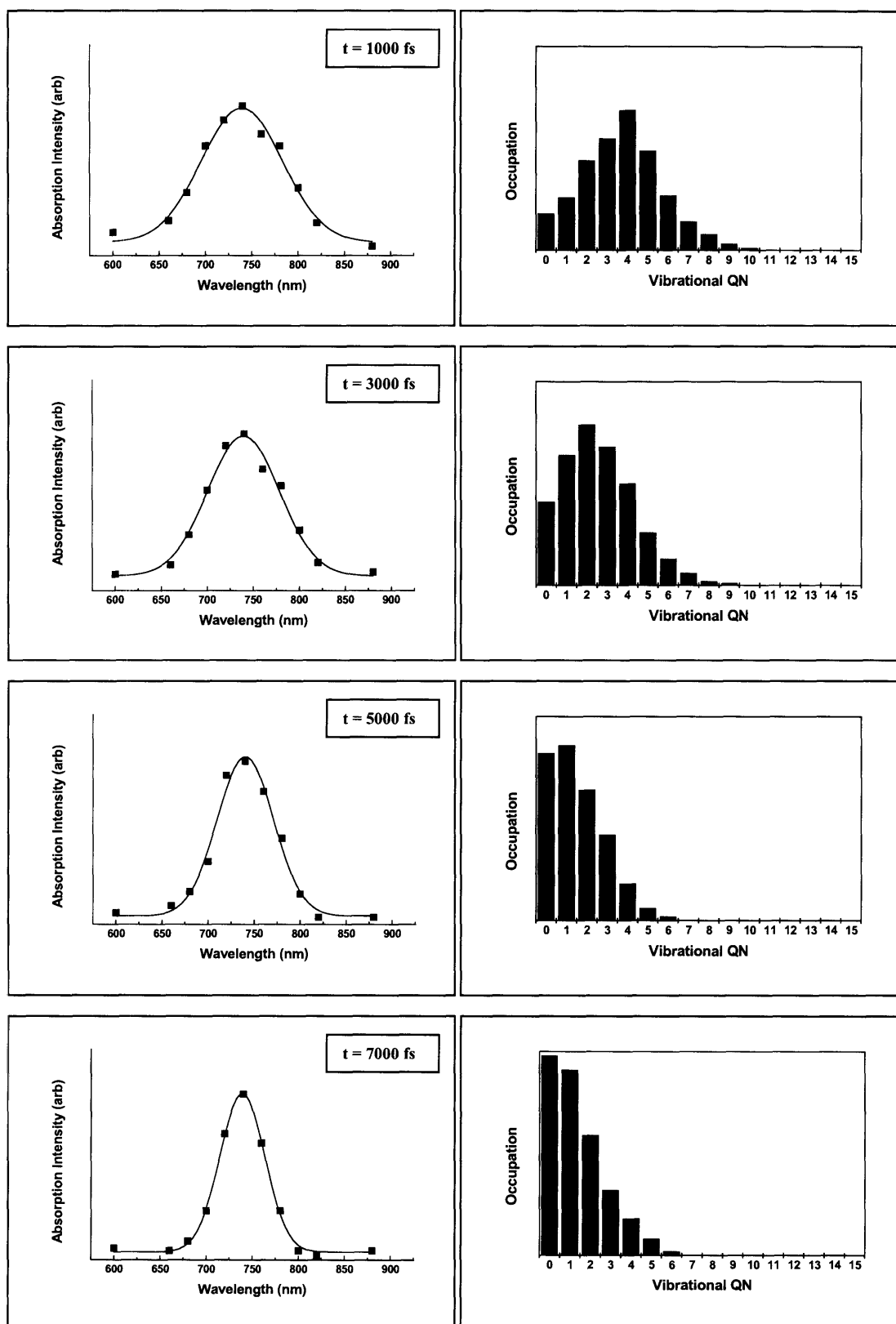


Figure 6-15 (cont'd). Calculated absorption profiles and vibrational distributions at four different time delays for I_2^* in CDE solution at 318 K.

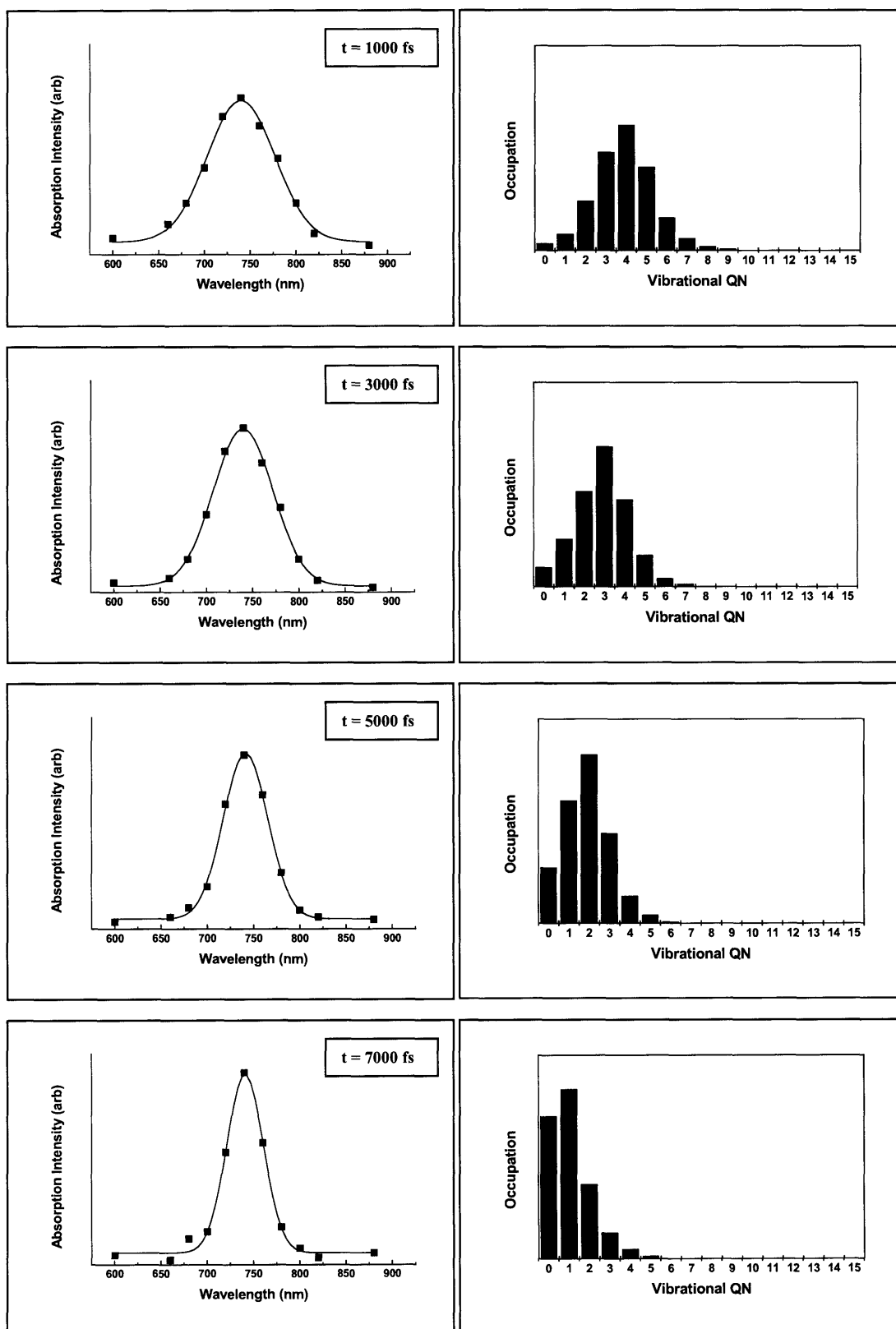


Figure 6-15 (cont'd). Calculated absorption profiles and vibrational distributions at four different time delays for I_2^- in CDE solution at 310 K.

This completes the prescription for reconstructing the instantaneous vibrational energy distributions from transient absorption measurements. For each of the absorption profiles in Figure 6-14, the vibrational distribution function $P(v)$ was determined by iterative fitting of the spectrum using the Franck-Condon procedure, as described in Equations (6.4)-(6.11), using a least-squares minimization routine. The available range of vibrational quantum numbers is confined to the interval [0,25]. Previous experiments have indicated that higher-lying vibrational levels are not populated in solution phase photodissociation of I_3^- [60], although in the gas phase, vibrational superposition states with contributions from higher levels have been measured. The results are shown in Figure 6-15 for each of four delay times at three different temperatures. The measured absorption profiles are indicated by solid squares (same as Figure 6-14) and the simulated profiles are indicated by solid lines. To the right of each absorption band is the best-fit vibrational distribution used to calculate the profile. At early delay times, the vibrational distribution function is peaked at values of $v > 0$. The center of the distribution is $v = 4$ at 1000 fs for each of the three temperatures. Solvent interactions appear to play little role in the direct caging of the photodissociation process at any temperature, as we have already observed. The most plausible explanation for this is that the solvation shell of I_3^- is large enough that in most cases, triiodide bond breakage occurs prior to interactions with surrounding solvent molecules. However, given that the distribution of solvation geometries is likely rather inhomogeneous, one would expect that in certain circumstances in a glassy environment, some direct caging might be possible, even if it occurs infrequently.

Even at the earliest delays, a subset of the I_2^- ions are in the ground vibrational eigenstate. This is significant because other authors have measured I_2^- vibration frequencies from 96 to 114 cm^{-1} in ethanol by instantaneous frequency analysis in the shortest times following dissociation [60]. Given the known anharmonicities of the diiodide potential, this implies an average vibrational quantum number of $v = 14$, only a few hundred femtoseconds prior to the 1000 fs results illustrated above. Since we have already determined that solvent effects (i.e. the caging of photodissociation) in CDE do not differ appreciably as a function of temperature at very early times, it is clear that loss of large quantities of initial excess vibrational energy must occur on a very fast time scale to solvent modes in a frequency regime which is not strongly affected by temperature.

The observed widths of the vibrational distributions at each of the three temperatures gives direct information regarding I_2^- relaxation dynamics. At 363 K, the distribution is wider (especially at the earliest times) on the *low-energy side* of the maximum vibrational quantum number, relative to the 310 K distribution. The same is true at 318 K, although the disparity is not quite as large. The effect of solvent-induced vibrational energy dissipation (which of course shifts the distribution toward lower vibrational levels) is already apparent. At later times, vibrational energy relaxation can be estimated by following the moment of the distribution (or even just the maximum position). Relaxation is most efficient at 363 K. As the temperature is decreased to 318 K and then to 310 K, relaxation proceeds more slowly. The 363 K distribution has collapsed at 7000 fs to a Boltzmann-like profile maximized at $v = 0$ with an extended high-energy tail, whereas at 310 K, the distribution remains peaked at $v = 1$.

Very rapid initial thermalization of vibrational energy has been observed by a number of authors [60,82-84] via transient absorption experiments on I_2^- in solution, and also through molecular dynamics simulations employing a Stokes-type hydrodynamic force as an additional source of anharmonicity in an equation of motion for the oscillator. Of particular note is the finding that much of the excess energy dissipation occurs in the first few hundred femtoseconds following photodissociation, and this rate is reasonably consistent for a number solvents. The implication of these findings is that at very early times, the vibrational thermalization rate is relatively independent of the details of the local solvation environment, in accordance with our findings for temperature-dependent measurements in CDE. Further calculations by Benjamin *et al.* [85] for I_2^- in acetonitrile solution which explicitly include a charge-shifting model for the ion have demonstrated that the additional force along the vibrational coordinate which arises from dynamic charge flow within the ion accelerates the vibrational relaxation rate. Since charge flow effects are strongest at the earliest times (when the range of motion sampled by the oscillator is greatest), this may provide a mechanistic interpretation for rapid energy thermalization at short time delays. The observed energy relaxation kinetics are highly non-exponential, reflecting the “turning-off” of the solvent-assisted charge flow effect as motion along the oscillator coordinate is reduced.

In oscillator systems, energy and phase relaxation are accounted for through the well-known relation

$$\frac{1}{T_2} = \frac{1}{2T_1} + \frac{1}{T_2^*} \quad (6.12)$$

where T_2 and T_2^* are the observed and pure dephasing times, and T_1 is the lifetime contribution, the inverse rate of population decay from vibrational eigenstates. An

investigation of both terms on the right hand side of Equation (6.12) is typically necessary in order to develop a clear picture of vibrational dephasing or equivalently, to understand the vibrational lineshape.

Pure dephasing often dominates the decay times in liquids. The description of pure dephasing is typically formulated as a stochastic model in which solvent-induced shifts of the vibrational frequency dephase a coherent ensemble of oscillators. The solvent itself is usually described as generating a Gaussian distribution of local instantaneous frequencies with rms width Δ . Solvent motions introduce a time-dependent spectral diffusion, which randomizes the frequencies of dissolved oscillators. The randomization occurs with mean characteristic time scale τ_c .

Vibrational coherence decay is described by the autocorrelation function of the oscillator's displacement coordinate, $Q(t)$. With Gaussian spectral modulation, the spectral diffusion may be imagined to occur on two limiting time scales. When the spectral diffusion time is much slower than $1/\Delta$, vibrational coherence decay is described by a Gaussian functional form

$$\langle Q(t)Q(0) \rangle \sim e^{-\frac{t^2 \Delta^2}{2}} \quad (6.13)$$

The other extreme is the so-called “fast modulation” or “motional-narrowing” limit, in which the spectral diffusion time is much faster than the inverse spread of frequencies. In this case, spectral diffusion occurs while the coherence evolves, i.e. while appreciable phase-structure exists. The coherence decay in this limit is exponential and is described by

$$\langle Q(t)Q(0) \rangle \sim e^{-\Delta^2 t \tau_c} \quad (6.14)$$

This results in a Lorentzian lineshape. The motional-narrowing limiting case was first formulated by Kubo [86] for magnetic systems and later modified by Oxtoby [87] to account for vibrational relaxation in solution.

For intermediate situations, hybrid dynamics are expected with Gaussian dephasing behavior initially and exponential damping at later times. When the frequency autocorrelation is assumed to decay exponentially, the dephasing behavior can be described conveniently [59] by

$$\langle Q(t)Q(0) \rangle = e^{-\Delta^2 \left[\tau_c^2 \left(e^{-t/\tau_c} - 1 \right) + t\tau_c \right]} \quad (6.15)$$

Some information regarding the contributions to the vibrational dephasing rate can be extracted from the time-resolved TA data of Figure 6-12. We will consider first the dephasing of I_2^- fragments by considering the TA data at visible and near-IR frequencies. From the vibrational eigenstate distributions $P(\nu)$ calculated at various temperatures, the average vibrational excess energy can be determined [65] as

$$\langle E(t) \rangle = \frac{\sum_{\nu} P(\nu, t) E(\nu)}{\sum_{\nu} P(\nu, t)} \quad (6.16)$$

We have shown eigenstate distributions for four different times in Figure 6-15. In order to characterize the relaxation dynamics for I_2^- in greater detail, the fitting procedure already described was repeated for successive absorption profiles every 100 fs, from an initial delay of 1000 fs to 7000 fs. The distributions $P(\nu, t)$ thus obtained were then used to calculate the vibrational excess energy according to Equation (6.16). The results are

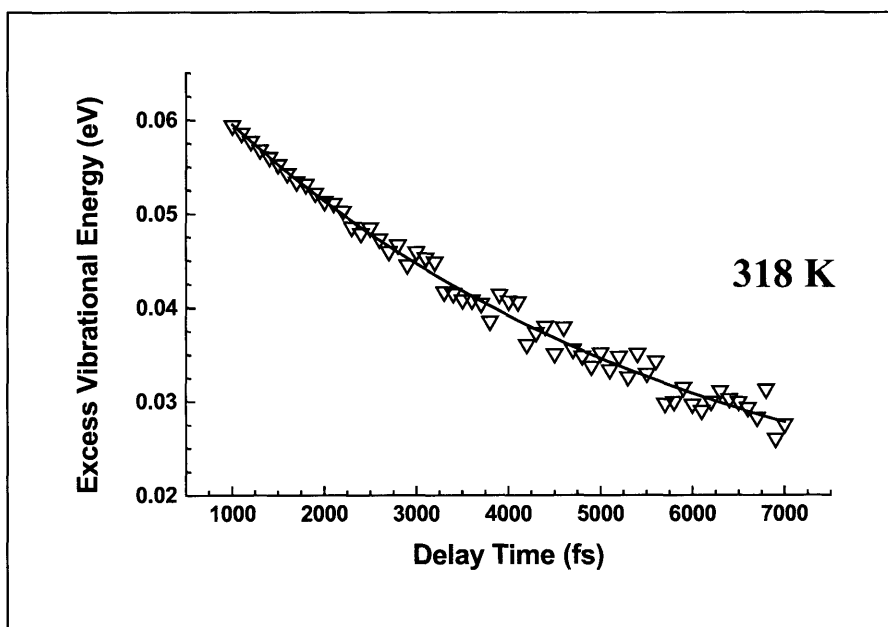
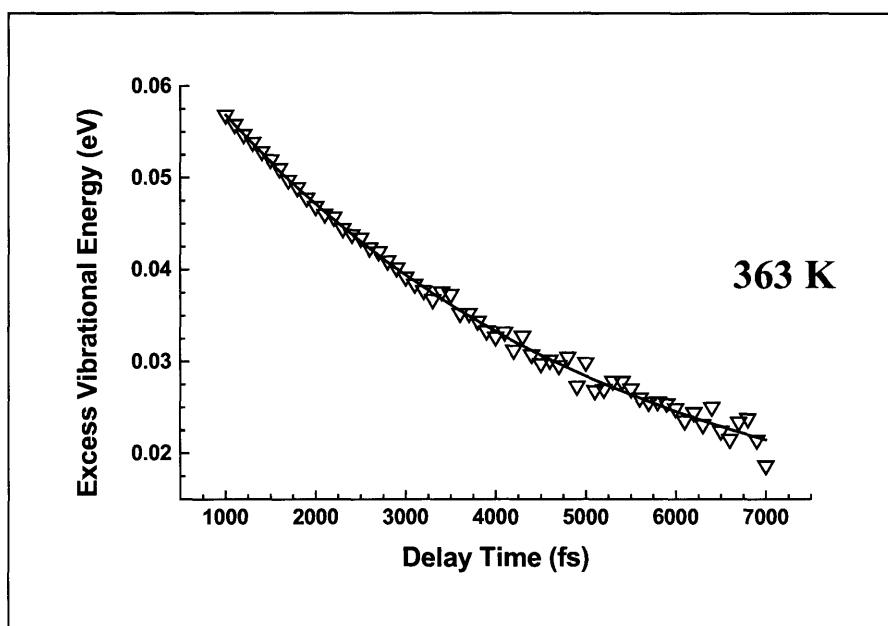


Figure 6-16. Diiodide excess vibrational energy as a function of time, calculated from instantaneous absorption spectra as demonstrated previously. Data are shown for 363 K and 318 K. In each case, the dissipation of excess energy follows single-exponential kinetics, with time constants of 3.6 ps and 4.1 ps, respectively.

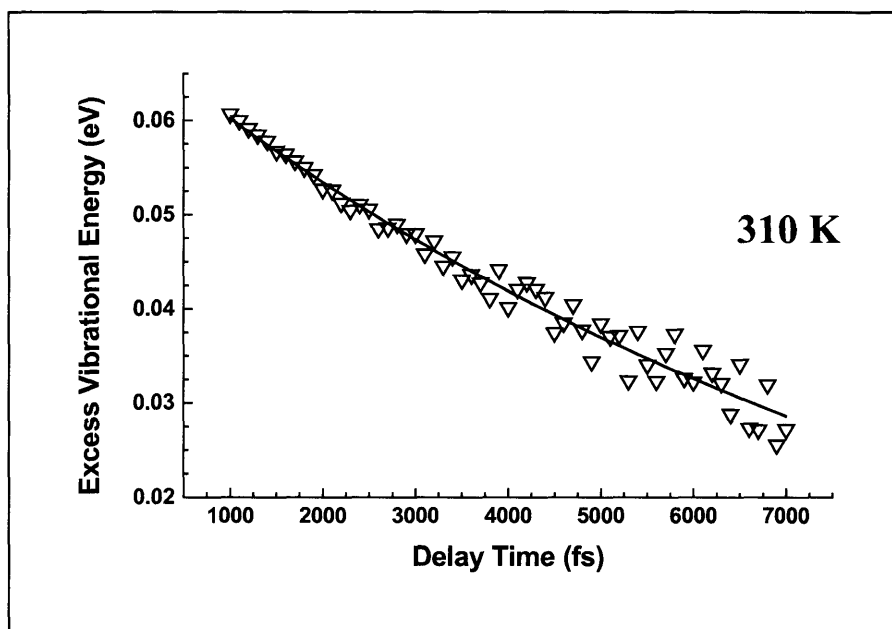


Figure 6-16 (cont'd). Diiodide excess vibrational energy as a function of time, calculated from instantaneous absorption spectra as demonstrated previously. Data are shown for 310 K. The dissipation of excess energy follows single-exponential kinetics, with a time constant of 4.4 ps.

displayed in Figure 6-16 as a function of the three temperatures 363 K, 318 K and 310 K. In each case, the energy dissipation dynamics follow single exponential kinetics. The decay constants are 3.6 ps, 4.1 ps and 4.4 ps, respectively, confirming that energy relaxation is slower in the glassy solution. The positive correlation between the observed coherence decay rates in Table 6-1 and the rate of excess energy dissipation as the temperature of the solution is lowered suggests that population relaxation plays a role in the dephasing dynamics of I_2^- coherences in CDE. Over the range of temperatures studied however, T_1 varies from 3.6 to 4.4 ps – and this encompasses a tremendous change in the solvent viscosity and dielectric response. In this same interval, the

observed dephasing time T_2 is 0.5-1 ps. Hence, we conclude that population relaxation plays a small but non-negligible role in both low- and high-viscosity CDE solutions.

Ruhman and co-workers have used resonant ISRS (RISRS) to examine the coherence dephasing dynamics of I_3^- in both cooled and room temperature ethanol solutions [54,57]. Calculations performed in their group have demonstrated that RISRS oscillations provide information regarding vibrational dephasing dynamics [88] and on the basis of this interpretation, they have examined the photobleaching signal of I_3^- in order to determine the relative contributions of population relaxation and pure dephasing to the coherence lifetime. Their measurements indicated a nearly constant lifetime contribution to the observed dynamics over the temperature range studied, implying that pure dephasing was the primary mechanism responsible for coherence loss, even in glassy solutions.

We have fitted transient absorption data at 300 nm for I_3^- in low- and high-viscosity CDE solutions (culminating in the glass transition at 310 K) to a single exponential decay function. The results of this procedure are shown in Figure 6-17 for three different temperatures: 310 K (top), 318 K (middle) and 363 K (bottom). The decay rates we recover are 2.9 ps, 3.4 ps and 3.8 ps respectively. According to the analysis of Ruhman *et al.*, the excellent fit of the exponential functions in each case provides experimental proof that the dephasing kinetics for the I_3^- mode are dominated by homogeneous mechanisms throughout the experimental temperature range.

The decay constant represents a measure of the population relaxation contribution T_1 to the dephasing rate. This contribution does not change drastically as a function of temperature, in agreement with Ruhman's observations for I_3^- in ethanol solution [88]

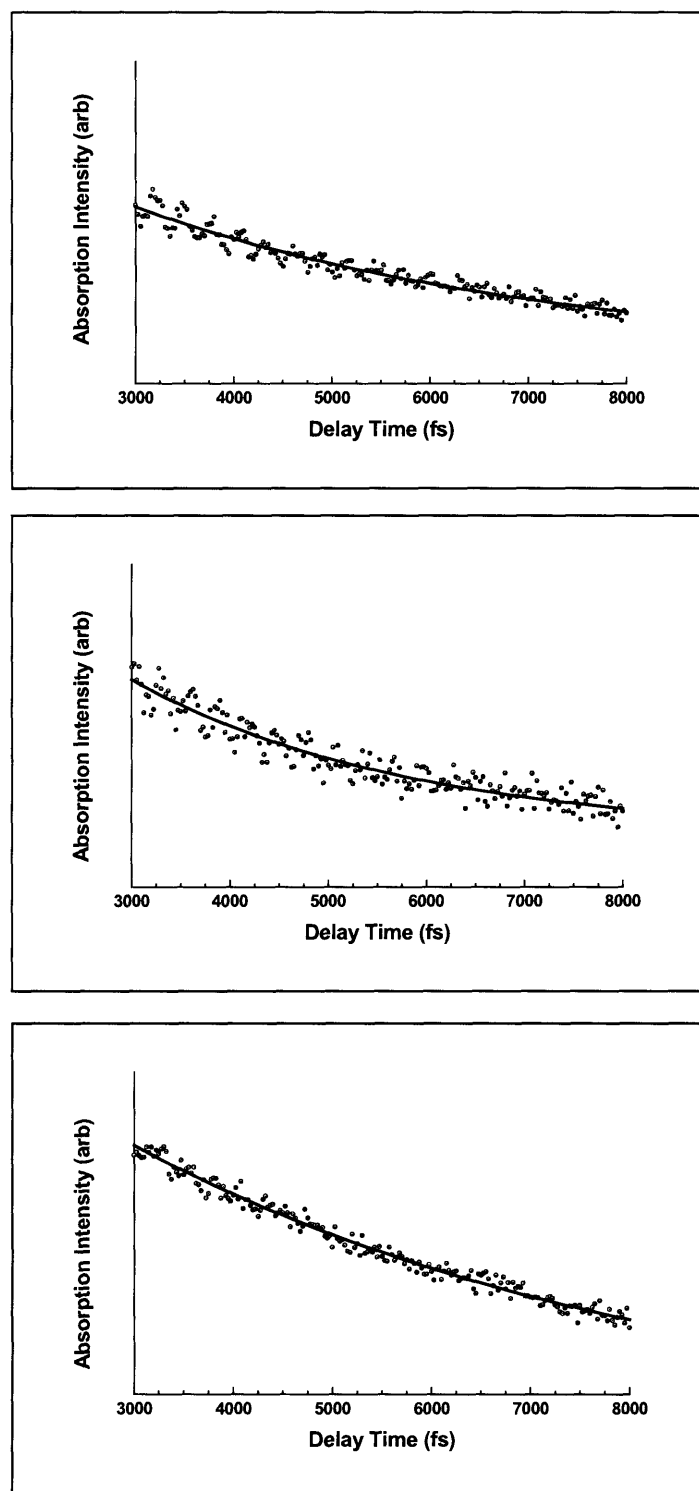


Figure 6-17. Single exponential fit of the fast decay component of I_3^- absorption in ethanol. The data corresponds to temperature 310 K (top), 318 K (middle) and 363 K (bottom).

and our own results for diiodide ions. Thus, for a given change in temperature, the observed changes in the dephasing rate are attributable largely to pure dephasing, rather than to relaxation. This poses an interesting problem: what mechanism is responsible for the temperature-dependent dephasing we observe in this system?

When the solvent is cooled through T_g , the dynamic inhomogeneities which are normally present as fluctuations along solvent coordinates are frozen into the local environment. Upon first consideration, this might suggest an additional dispersive contribution to solute-solvent interactions – in effect, a mechanism for inhomogeneous broadening. However, the degree to which local inhomogeneities dephase the distribution of coherent I_3^- oscillators depends not only on irregularity of the environment, but also on the specific, frequency-dependent interaction between solute and solvent. Little information is available regarding the structure of the CDE glass, so quantitative conclusions cannot be reached regarding the local ordering present in the glassy phase. We noted in our analysis of I_2^- vibrational relaxation that the efficiency of dissipation of excess vibrational energy is reduced on cooling. Clearly, this cannot be the case if inhomogeneous broadening due to static disorder in the glass is the dominant mechanism.

Based upon the results of our earlier examination of vibrational energy dissipation, we can only conclude that as the temperature of the CDE solution is reduced toward the glass transition, the dielectric response of the solvent in the spectral region which corresponds to acceptor modes for I_2^- vibrational energy decreases. As a result, energy flow from hot diiodide fragments into solvent bath modes is less efficient, and the energy relaxation proceeds on a slower time scale. A similar trend was observed in

viscous solutions of ethylene glycol, although the effect was not as dramatic since the dielectric response did not vary nearly as much (we assume) over the temperature range studied. In effect, cooling the solution “freezes out” certain frequency regimes in the bath density of states which correspond to interactions with I_2^- fragments. A similar mechanism may be responsible for the temperature dependence of the pure dephasing rate in I_3^- .

In viscous or glassy environments, the vibrational dephasing dynamics of solvated species are often dominated, to a very large extent, by inhomogeneous contributions to the linewidth [94]. This is not the case for the triiodide/diiodide system, where pure dephasing provides the major contribution even in a CDE glass. Gershgoren *et al.*, in a study of pure dephasing of the fundamental and first harmonic frequencies of I_3^- , found that the observed rates could only be explained in the context of a Poisson dephasing model of the type commonly used in describing hard collisions in the gas phase [59]. The fragments which result from triiodide photodissociation have substantial kinetic energy, and the viscous solvent employed in this study certainly may appear rigid on the time scale of molecular collisions. However, it remains unclear whether a hard-collision model is truly appropriate for describing the solute-solvent dynamics for this system.

6.8 Conclusion

In this chapter, we have explored in detail the photodissociation of triiodide ion via single-shot transient absorption measurements. The successful application of our methods illustrates that real-time measurements of photodissociation and subsequent relaxation dynamics can be conducted in many solvents, at different temperatures and

viscosities, including some conditions under which conventional measurements would not be possible due to build-up of reaction products.

The time-dependent features we observe in our transient absorption measurements – coherent vibrational motion of photoproducts, ISRS in parent ions and band narrowing due to vibrational energy relaxation – are explained within the context of a wave packet dynamical picture of the reaction.

We have also examined the nature of solvent interactions with molecular fragments, and the role this plays in determining product states. Temperature-dependent measurements in viscous solutions and glass forming liquids have shown that for the triiodide system, energy relaxation becomes relatively less efficient at lower temperatures. This suggests a mechanism whereby the dielectric response of the solvent in the vicinity of the absorption frequencies for I_3^- and I_2^- vibrational energy is reduced.

Finally, we have shown that coherence decay is due principally to pure dephasing, even in the glassy environment, which differs considerably from other work in glassy solutions where vibrational linewidths are strongly inhomogeneously broadened. Nonetheless, our results are in agreement with the work of other research groups on the triiodide system, and the mechanism for this unusual dephasing behavior remains under active investigation.

References

- [1] Chattaway, F.D. and Hoyle, G., *J. Chem. Soc.* **123**, 654 (1923).
- [2] Foote, H.W. and Fleischer, M., *J. Phys. Chem.* **57**, 122 (1953).
- [3] Babaeva, A.V. and Baranovskii, I.B., *Russ. J. Inorg. Chem.* **4**, 343 (1959).
- [4] Lobanov, N.I. and Konovalenko, O.S., *Russ. J. Inorg. Chem.* **5**, 407 (1960).
- [5] Wiebenga, E.H., Havinga, E.E. and Boswijk, K.H., "Structures of Interhalogen Compounds and Polyhalides", *Advances in Inorganic Chemistry and Radiochemistry, Vol. 3*, (Academic Press, New York, 1961).
- [6] Stepin, B.D., Plyushchev, V.E. and Fakeev, A.A., *Russ. Chem. Rev.* **34**, 811 (1965).
- [7] Popov, A.I., "Polyhalogen Complex Ions", *Halogen Chemistry, Vol. 1* (Academic Press, New York, 1967).
- [8] Konovalenko, O.S., Lobanov, N.I. and Vodinchar, L.S., *Russ. J. Inorg. Chem.* **15**, 1334 (1970).
- [9] Bailar, J. et al., *Comprehensive Inorganic Chemistry, Vol. 2* (Pergamon Press, New York, 1973).
- [10] Tebbe, K.-F., "Polyhalogen Cations and Polyhalide Anions", *Homoatomic Rings, Chains and Macromolecules of Main Group Elements* (Elsevier, New York, 1977).
- [11] Korte, H.-J. et al., *Inorg. Chim. Acta* **52**, 61 (1981).
- [12] Tebbe, K.-F. et al., *Acta Cryst. C* **41**, 660 (1985).
- [13] Sugano, T. et al., *Synth. Met.* **27**, B475 (1988).
- [14] Saito, K. et al., *Synth. Met.* **52**, 87 (1992).
- [15] Ohnuki, H. et al., *Synth. Met.* **71**, 2077 (1995).
- [16] Bakshi, P.K. et al., *Can. J. Chem.* **74**, 559 (1996).
- [17] Landrum, G.A., Goldberg, N. and Hoffmann, R., *J. Chem. Soc. Dalton Trans.*, 3605 (1997).
- [18] Wiczorrek, C., *Acta Cryst. C* **56**, 1079 (2000).
- [19] Filgueiras, C.A.L. et al., *Acta Cryst. E* **57**, 338 (2001).
- [20] Wiczorrek, C., *Acta Cryst. C* **56**, 1082 (2000).

- [21] Kloo, L., Svensson, P.H. and Taylor, M.J., *J. Chem. Soc. Dalton Trans.*, 1061 (2000).
- [22] Loukili, R. and Tebbe, K.-F., *Z. Anorg. Allg. Chem.* **625**, 650 (1999).
- [23] Tebbe, K.-F. and Loukili, R., *Z. Anorg. Allg. Chem.* **625**, 820 (1999).
- [24] Tebbe, K.-F. and Dombrowski, I., *Z. Anorg. Allg. Chem.* **625**, 167 (1999).
- [25] Richter, R., Seidelmann, O. and Beyer, L., *Z. Anorg. Allg. Chem.* **625**, 511 (1999).
- [26] Tebbe, K.-F. and Buchem, R., *Z. Anorg. Allg. Chem.* **624**, 679 (1998).
- [27] Tebbe, K.-F. and Loukili, R., *Z. Anorg. Allg. Chem.* **624**, 1175 (1998).
- [28] Tebbe, K.-F. and Buchem, R., *Z. Anorg. Allg. Chem.* **624**, 671 (1998).
- [29] Bailey, R.D. and Pennington, W.T., *Acta Cryst. B* **51**, 810 (1995).
- [30] Muller, V.U., *Acta Cryst. B* **35**, 2502 (1979).
- [31] Daly, J.J. and Sanz, F., *Acta Cryst. B* **31**, 620 (1975).
- [32] Wieczorrek, C., *Acta Cryst. C* **56**, 1085 (2000).
- [33] Svensson, P.H. and Kloo, L., *Inorg. Chem.* **38**, 3390 (1999).
- [34] Menon, S. and Rajasekharan, M.V., *Inorg. Chem.* **36**, 4983 (1997).
- [35] Gabes, W. and Nijman-Meester, M.A.M., *Inorg. Chem.* **12**, 589 (1973).
- [36] Konovalov, L.V., Konovalenko, O.S. and Lobanov, N.I., *Russ. J. Inorg. Chem.* **19**, 89, (1974).
- [37] Gabes, W. and Stuffkens, D.J., *Spectrochim. Acta* **30A**, 1835 (1974).
- [38] Tasker, P.W., Balint-Kurti, G.G. and Dixon, R.N., *Mol. Phys.* **32**, 1651 (1976).
- [39] Tasker, P.W., *Mol. Phys.* **33**, 511 (1977).
- [40] Sharp, S.B. and Gellene, G.I., *J. Phys. Chem. A* **101**, 2192 (1997).
- [41] Mizuno, M., Tanaka, J. and Harada, I., *J. Phys. Chem.* **85**, 1789 (1981).
- [42] Hayward, G.C. and Hendra, P.J., *Spectrochim. Acta* **23A**, 2309 (1967).
- [43] Maki, A.G. and Forneris, R., *Spectrochim. Acta* **23A**, 867 (1967).
- [44] Coignac, J.P. and Debeau, M., *Spectrochim. Acta* **30A**, 1551 (1974).
- [45] Sanyal, N.K., Verma, D.N. and Dixit, L., *Indian J. Pure Appl. Chem.* **12**, 393 (1974).
- [46] Gazquez, J.L., Ray, N.K. and Parr, R.G., *Theo. Chim. Acta* **49**, 1 (1978).
- [47] Ferraro, J.R. *et al.*, *J. Phys. Chem. Solids* **47**, 301 (1986).
- [48] Zambounis, J.S. *et al.*, *J. Raman Spect.* **23**, 81 (1992).

- [49] Rosztoczy, F.E. and Cubicciotti, D., *J. Phys. Chem.* **69**, 1687 (1965).
- [50] Topol, L.E., *Inorg. Chem.* **7**, 451 (1968).
- [51] Banin, U. and Ruhman, S., *J. Chem. Phys.* **99**, 9318 (1993).
- [52] Banin, U., Kosloff, R. and Ruhman, S., *Israel J. Chem.* **33**, 141 (1993).
- [53] Gershgoren, E., Gordon, E. and Ruhman, S., *J. Chem. Phys.* **106**, 4806 (1997).
- [54] Wang, Z. *et al.*, *Chem. Phys. Lett.* **313**, 155 (1999).
- [55] Gershgoren, E., Banin, U. and Ruhman, S., *J. Phys. Chem. A* **102**, 9 (1998).
- [56] Vala, J., Kosloff, R. and Harvey, J.N., *J. Chem. Phys.* **114**, 7413 (2001).
- [57] Wang, Z. *et al.*, *J. Mol. Liq.* **86**, 229 (2000).
- [58] Gershgoren, E. *et al.*, *J. Phys. Chem. A* **105**, 5081 (2001).
- [59] Gershgoren, E. *et al.*, *J. Phys. Chem.* **118**, 3660 (2003).
- [60] Kuhne, T. and Vohringer, P., *J. Chem. Phys.* **105**, 10788 (1996).
- [61] Bursing, H. *et al.*, *Appl. Phys. B* **71**, 411 (2000).
- [62] Kuhne, T. and Vohringer, P., *J. Phys. Chem. A* **102**, 4177 (1998).
- [63] Kuhne, T., Kuster, R. and Vohringer, P., *Chem. Phys.* **233**, 161 (1998).
- [64] Hess, S., Bursing, H. and Vohringer, P., *J. Chem. Phys.* **111**, 5461 (1999).
- [65] Kliner, D.A.V., Alfano, J.C. and Barbara, P.F., *J. Chem. Phys.* **98**, 5375 (1993).
- [66] Johnson, A.E. and Myers, A.B., *J. Chem. Phys.* **104**, 2497 (1996).
- [67] Lynden-Bell, R.M. *et al.*, *J. Chem. Phys.* **109**, 9928 (1998).
- [68] Isci, H. and Mason, W.R., *Inorg. Chem.* **24**, 271 (1985).
- [69] Kaya, K., Mikami, N. and Ito, M., *Chem. Phys. Lett.* **16**, 151 (1972).
- [70] Kiefer, W. and Bernstein, H.J., *Chem. Phys. Lett.* **16**, 5 (1972).
- [71] Mohammad, M.R. and Sherman, W.F.J., *Mol. Struct.* **27**, 115 (1984).
- [72] Johnson, A.E., Levinger, N.W. and Barbara, P.F., *J. Phys. Chem.* **96**, 77841 (1992).
- [73] Papanikolas, J.M. *et al.*, *J. Phys. Chem.* **95**, 8028 (1991).
- [74] Papanikolas, J.M. *et al.*, *J. Chem. Phys.* **97**, 7002 (1992).
- [75] De Violet, P., Bonneau, R. and Joussot-Dubien, J., *Chem. Phys. Lett.* **1**, 251 (1973).
- [76] De Violet, P., *Rev. of Chem. Inter.* **4**, 122 (1981).

- [77] Treinin, A. and Hayon, E., *Int. J. Radiat. Phys. Chem.* **7**, 387 (1975).
- [78] Ashkenazi, G. *et al.*, *J. Chem. Phys.* **103**, 5547 (1995).
- [79] Johnson, A.E. and Myers, A.B., *J. Chem. Phys.* **102**, 3519 (1995).
- [80] Chen, E.C.M. and Wentworth, W.E., *J. Phys. Chem.* **89**, 4099 (1985).
- [81] Kobeissi, H., *J. Comput. Phys.* **61**, 351 (1985).
- [82] Benjamin, I. and Whitnell, R.M., *Chem. Phys. Lett.* **204**, 45 (1993).
- [83] Alfano, J.C. *et al.*, *Chem. Phys.* **175**, 147 (1994).
- [84] Walhout, P.K. *et al.*, *J. Phys. Chem.* **99**, 7568 (1995).
- [85] Benjamin, I. *et al.*, *J. Phys. Chem.* **99**, 7557 (1995).
- [86] Kubo, R., "A Stochastic Theory of Line-Shape and Relaxation", *Fluctuation, Relaxation and Resonance in Magnetic Systems* (Oliver and Boyd, London, 1961).
- [87] Oxtoby, D.W., *J. Chem. Phys.* **70**, 2605 (1979).
- [88] Ashkenazi, G. *et al.*, *Adv. Chem. Phys.* **100**, 229 (1997).
- [89] Johnson, A.E. and Myers, A.B., *J. Phys. Chem.* **100**, 7778 (1996).
- [90] Johnson, A.E. and Myers, A.B., "Femtosecond Excited State Dynamics of Triiodide in Solution from Time- and Frequency-Domain Resonance Raman Spectroscopies", *Femtochemistry: Ultrafast Chemical and Physical Processes in Molecular Systems* (World Scientific, Singapore, 1996).
- [91] Johnson, A.E., Myers, A.B. and Ruhman, S., "A Comparison of Time and Frequency Domain Resonance Raman Spectroscopies in Triiodide", *Time Resolved Vibrational Spectroscopy VII* (LANL, Los Alamos, NM, 1997).
- [92] Kumbharkhane, A.C., Puranik, S.M. and Mehrotra, S.C., *J. Sol. Chem.* **21**, 201 (1992).
- [93] Sengwa, R.J., Kaur, K. and Chaudhary, R., *Polym. Int.* **49**, 599 (2000).
- [94] Tokmakoff, A. and Fayer, M.D., *J. Chem. Phys.* **103**, 2810 (1995).

Chapter 7

Solid State Triiodide Photochemistry

The dual-echelon single-shot technique is ideally suited to the study of materials which undergo irreversible structural change on ultrafast time scales, and which are available only in small quantity. This includes many laboratory-synthesized compounds which are grown as crystals from saturated solutions of reaction products. Solution-grown samples are often no more than 1 mm on each side, and may not be single-domain crystals, consisting instead of multiple intersecting growth zones and other local domains with relatively high defect densities. Undertaking spectroscopic measurements on such materials is challenging on account of the structural changes induced by the pump beam, and the very finite working area implies that raster-scanning across the surface of the crystal to interrogate an undamaged region with each successive shot is impractical. The single-shot method solves these problems and introduces the possibility of investigating broad new classes of materials under conditions of intense ultrafast optical excitation.

In this chapter, the work from Chapter 6 on triiodide photodissociation dynamics is extended to single-crystal solid-state triiodide samples. While solution phase experiments have yielded a wealth of information regarding the photodissociation kinetics, the dynamics of molecular coherences in photoproducts, the temporal evolution of the photoproduct absorption bands and the rate of dissipation of excess vibrational energy, theoretical modeling of dynamics in solution is difficult on account of the relative

disorder of the environment. Quite often, solvent-induced caging of photochemical reactions is described in terms of a hydrodynamic force exerted along a generalized “solvent coordinate”. While such a description improves the numeric agreement between simulation results and experimentally observed dynamical evolution of the reaction, it is difficult to extract any direct physical insight regarding the solvation geometries and specific interactions which restrict the available motion of the reactants and products since the solvent coordinate does not provide structural information, and the experimental data consists of ensemble averages over many different solute-solvent coordination shells.

In many respects, crystalline-phase photochemistry presents an opportunity to greatly enhance the deterministic aspects of the system under study. Single-crystal samples are ordered on an atomic scale and this ordering is known to very high precision from x-ray scattering measurements, ensuring that models of reaction dynamics can be constructed which are specifically dependent upon atomic coordinates. The potential exists for the interpretation of experimental measurements directly in terms of the time-dependent motions of the atoms involved, which provides direct insight into the nature of chemical bonding and structural rearrangement. In addition, the intramolecular repulsive forces that drive photodissociation in a reactive excited state potential energy surface might be more evenly balanced by the constraining forces in a crystalline solid than by those of a liquid. Thus the effects of the environment on reaction dynamics and yields might be more thoroughly explored in crystalline solids, especially if a family of crystals with similar reactive moieties but different crystalline structures can be examined.

Unfortunately, solid-state photochemistry has received comparatively little attention in ultrafast time-resolved spectroscopy, owing to the difficulties associated with obtaining suitable samples and the dearth of methods available for investigation. Attention has been focused on a small number of reversible reactions, such as those of excimers or of diatomic guests in rare gas matrix hosts. Such systems are interesting but only permit exploration of a subset of the responses involved in irreversible crystalline chemistry, in which significant alteration of the lattice surrounding the reacting species is generally required.

Herein we describe our efforts with three separate single-crystal molecular triiodides. Investigation of this family of organic crystals permits interpretation of the observed photochemical dynamics in terms of real-space structural models for each of the compounds and provides insight into the role of lattice structure in mediating or inhibiting reactivity.

7.1 Synthesis of Single Crystal Triiodide Samples

The synthesis of the triiodide molecular crystals utilized in our experiments was quite straightforward. All compounds synthesized were ionic in nature and consisted of negatively-charged triiodide ions and cationic, non-interacting counterions. The overall family of triiodide compounds is well suited for study owing to the efficacy with which the crystalline environment can be adjusted. By simply varying the nature of the counterion, a great variety of different crystal structures can be prepared, each with its own unique triiodide environment. Thus, systematic investigation of the effects of the local geometry upon the reaction dynamics is possible. Naturally, not all solid-state

triiodides yield crystals which are of suitable quality for study using the single-shot method. However, even a subset of possible compounds presents a tremendous opportunity for investigation.

The synthetic method we employed was adapted from the original report of Chattaway and Hoyle [1]. Roughly 2.5 mmol of the parent iodide compound RI was dissolved in 50 mL of warm (40° C) methanol. About 2.6 mmol (slight excess) of I₂ was dissolved in a separate 50 mL warm methanol solution. The two solutions were combined, covered, and stirred for 15 minutes with gentle warming.

Following this, the combined solutions were transferred to a second beaker and heated slowly to evaporate the solvent over a period of 3 hours. Crystals of the triiodide compound RI₃ precipitated in each case. The crystals were collected via filtration, washed with aliquots of warm methanol solution, and dried.

In order to prepare large crystals suitable for single-shot study, the RI₃ precipitate was transferred to a small beaker and dissolved in warm methanol. This beaker was placed inside a larger beaker containing warm methanol (not enough to spill over into the small beaker) and the opening to the large beaker was covered with wax film. Small perforations in the film permitted a tiny amount of solvent to escape. The dual beaker system was maintained at 30 °C on a heating plate for a period of 7-10 days, during which time the methanol solvent containing RI₃ slowly evaporated. Crystals of RI₃ were formed as the solvent evaporated. After the 7-10 day period elapsed, the crystals were collected by filtration and gentle washing with cold methanol, and dried.

7.1.1 Tetra-*n*-butylammonium Triiodide

Employing the parent compound tetra-*n*-butylammonium iodide (Aldrich) yielded deeply colored purple crystals of tetra-*n*-butylammonium triiodide. The crystals were very large, some as much as 7 mm on a side, and were longer in one dimension than the other two, a kind of columnar geometry. X-ray structural analysis of a single-crystal sample is shown in Figures 7-1 and 7-2. The triclinic P-1 structure has unit cell dimensions (in Angstroms) $a = 9.4658$, $b = 15.5659$ and $c = 15.8101$ with angles $\alpha = 83.5180^\circ$, $\beta = 74.1780^\circ$ and $\gamma = 78.4710^\circ$. As shown in Figure 7-1, the triiodide ions are arranged in two crystallographically independent, nearly linear chains oriented along the **a** axis, and the tetra-*n*-butylammonium cations form a network structure into which the triiodide ions are intercalated. There are four triiodide ions per unit cell. Dense packing of the anions accounts for the deep coloration of the crystals. The crystals are brittle and do not cleave or polish well, but the surface quality of solution-grown samples is good enough that suitably selected specimens can be examined under single-shot conditions. The structure determination is in very good agreement with a previously published report for this compound [2].

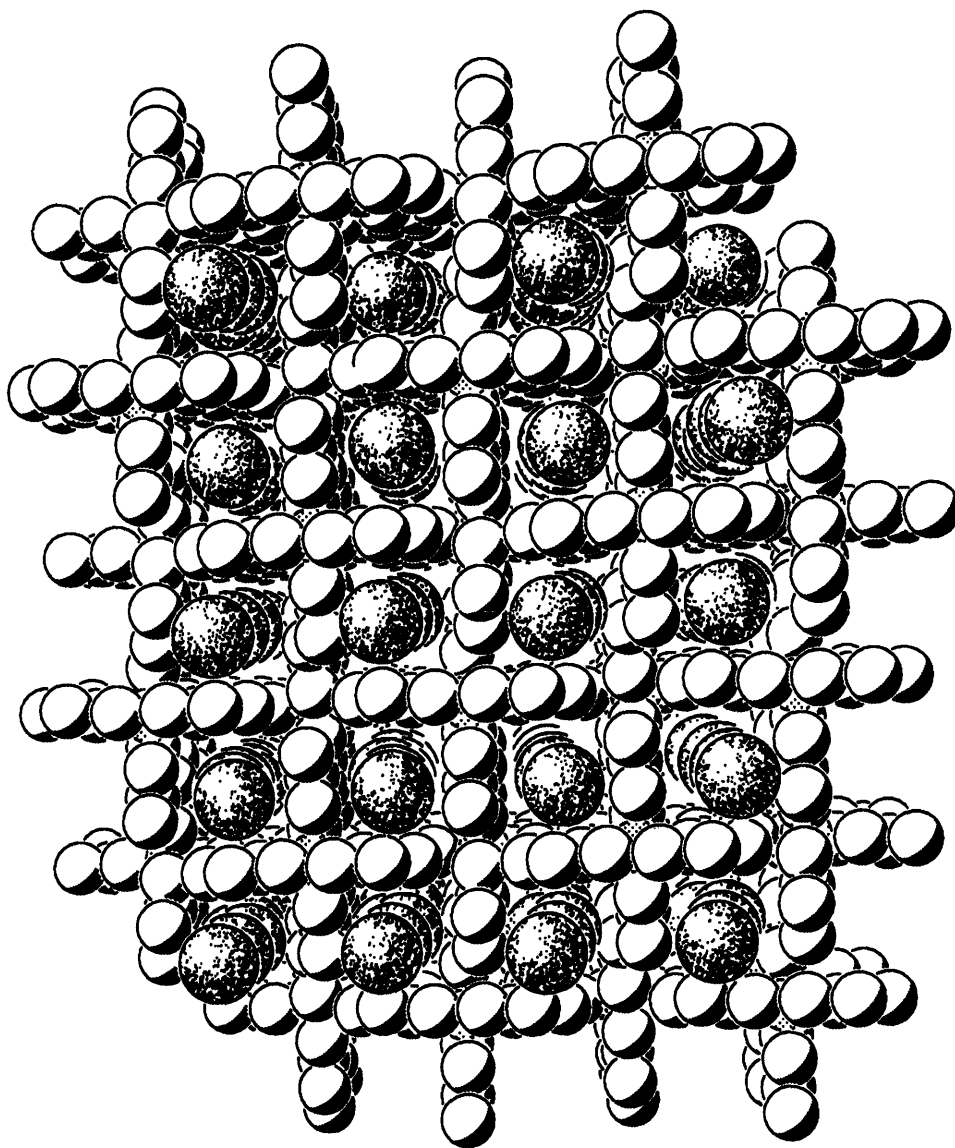


Figure 7-1. Crystal structure of tetra-*n*-butyl ammonium triiodide viewed along the *a* axis. The large, darkly shaded spheres are iodine atoms (as triiodide ions) arranged in two crystallographically independent, nearly linear chains. The smaller white spheres are the carbon and nitrogen atoms comprising the tetra-*n*-butylammonium counterions. The counterions are arranged in a network-like geometry, separating the triiodide chains.

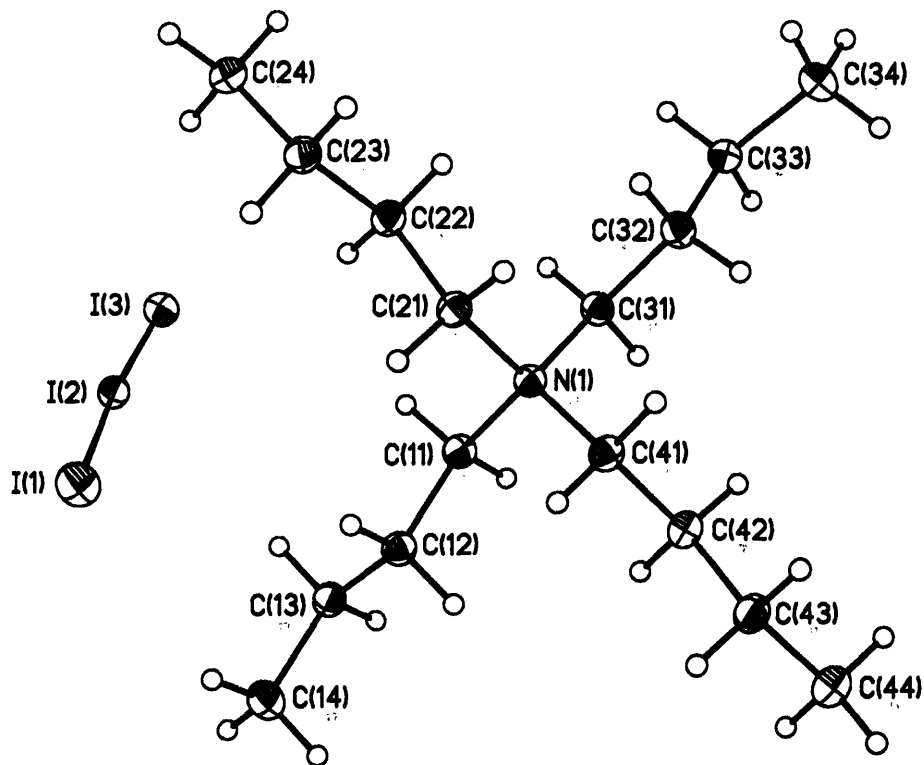


Figure 7-2. Expanded view of tetra-*n*-butylammonium cation and the triiodide ion, indicating the relative orientation of each within the triclinic crystal structure.

7.1.2 Tetraphenylphosphonium Triiodide

Crystals of tetraphenylphosphonium triiodide recovered from solution were deep reddish-purple in color, although not as strongly colored as tetra-*n*-butylammonium triiodide. The crystals were distinctively prismatic in shape with triangular faces measuring 2-3 mm per side. Successful cleavage of these crystals was not achieved,

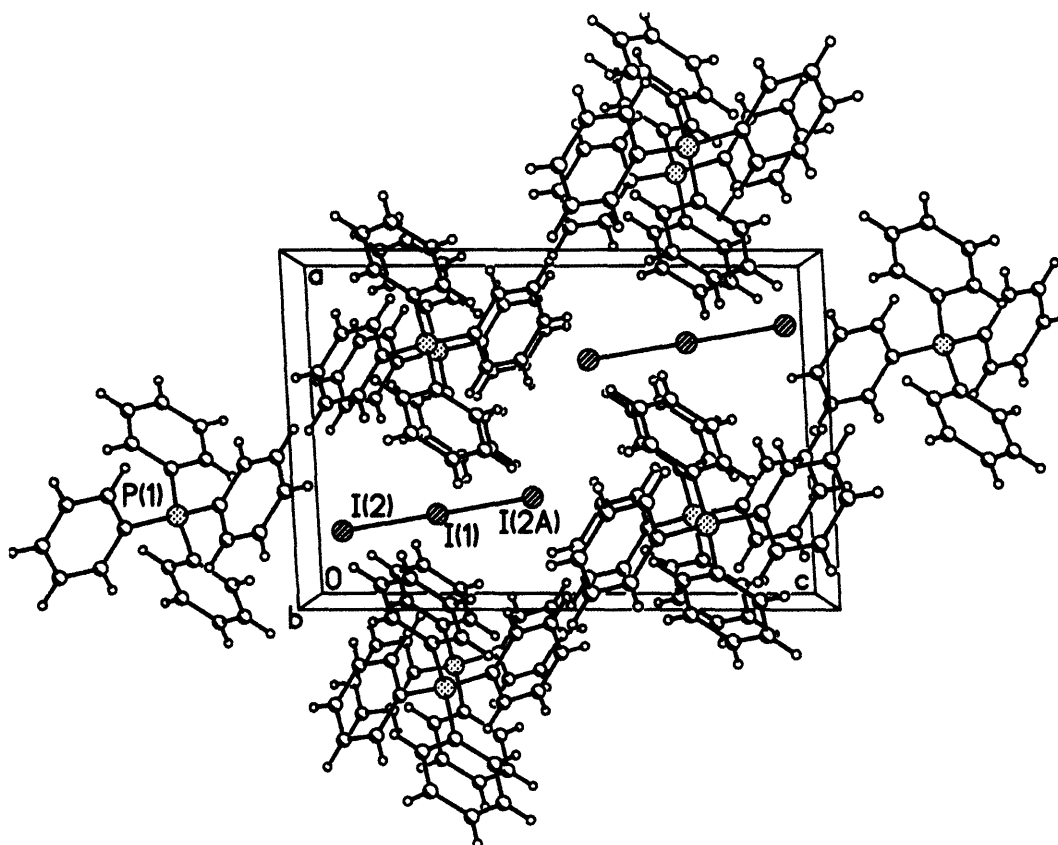


Figure 7-3. Unit cell for tetraphenylphosphonium triiodide. There are two triiodide ions per cell and each sits in a “pocket” formed by seven neighboring tetraphenylphosphonium cations. The overall structure is monoclinic.

although they were considerably less brittle than the crystals of the previous triiodide. Nonetheless, as before, the surface and internal quality of selected (smaller) specimens was sufficient for single-shot investigation. The crystal structure of this compound is depicted in Figures 7-3 and 7-4. The unit cell is monoclinic with space group $P2_1/n$ and dimensions (Angstroms): $a = 10.2102$, $b = 7.5555$, $c = 15.3253$. Cell angles are $\alpha = 90^\circ$, $\beta = 93.16^\circ$ and $\gamma = 90^\circ$. In this compound, the triiodide ions sit in “pockets” formed by seven neighboring tetraphenylphosphonium cations. It was originally anticipated that utilizing larger substituted phosphonium cations would result in larger lattice spacings

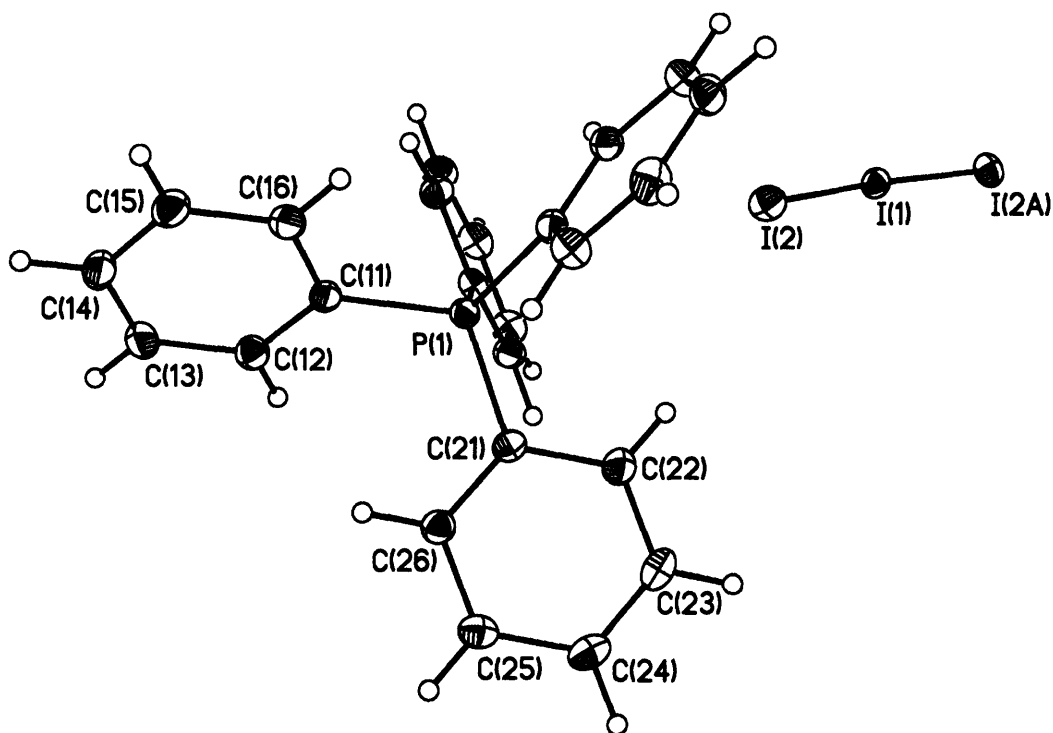


Figure 7-4. Enlarged view of tetraphenylphosphonium and triiodide ions within the crystal structure.

between the triiodide ions and their nearest neighbors, and this appears to be the case for tetraphenylphosphonium triiodide. This is, to our knowledge, the first report of this compound in the literature.

7.1.3 Tetraethylammonium Triiodide

Crystals of tetraethylammonium triiodide were deep purple in color and plate-like in appearance. Typical dimensions for these crystals were 1-2 mm on each of two (large) sides and considerably less on the third. The brittleness of these specimens precluded cleaving, but the relatively thin transverse dimension ensured that individual crystals of sufficient quality for use in experiments could be grown with careful attention to solvent

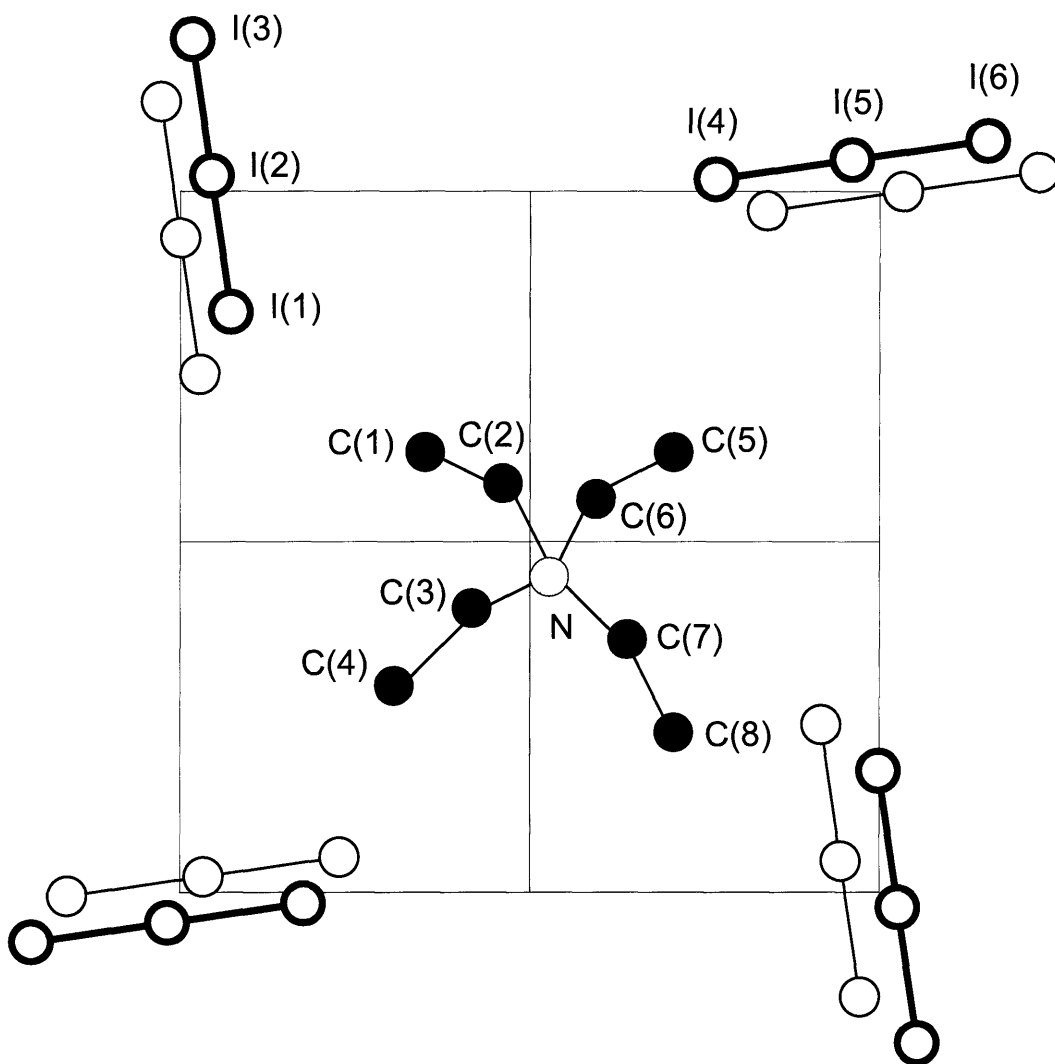


Figure 7-5. View of tetraethylammonium triiodide along the **b** axis, adapted from reference 3. Triiodide ions are located at the corners of the orthorhombic unit cell. Open circles are iodine atoms, with the heavy circles in the plane of the page and the lighter circles behind the plane. The triiodide ions form stacked arrays with columns of tetraethylammonium cations acting as spacers.

evaporation time. A depiction of the structure of the compound viewed along the **b** axis is shown in Figure 7-5. The structure is orthorhombic with *Pnma* symmetry and unit cell dimensions (in Angstroms) $a = 14.5582$, $b = 15.2269$ and $c = 15.1513$. Triiodide ions are

stacked in columns down the **b** axis, but perpendicular to the approximate axis of the ion, which lies in the **a-c** plane. This situation is similar to the structure of tetra-*n*-butylammonium triiodide except that in the latter compound, triiodide ions were arrayed longitudinally along the same direction as the axis of the ion. Two independent triiodide columns exist within the structure oriented nearly perpendicularly with respect to one another, and stacked arrays of tetraethylammonium cations act as spacers. The entire structure is densely packed, and the coloration of the crystals is intense. The x-ray determination reported here for tetraethylammonium triiodide is in close agreement with previously published data for the compound [3].

7.2 Transient Absorption of Solid-State Triiodides

In order to investigate the photodissociation dynamics of triiodide ions in crystalline environments, transient absorption experiments were performed on single-crystal samples of each of the three compounds described above. The experiments were similar in nature to those already discussed for triiodide ions in solution. An ultraviolet photolysis pulse (300 nm, 1.2 μ J) was generated by frequency-doubling the 600 nm output of NOPA beam 1, and was focused to a 150 μ m spot at the sample. Probe pulses were generated either by utilizing the second NOPA beam, or by continuum generation in sapphire (to reach the near-IR region). The number density of absorbers in a crystalline triiodide is significantly larger than in solution and as a result, in all but two fortuitously thin samples, it was impossible to measure transient absorption at a 300 nm probe wavelength because all the probe light was absorbed – none was detected at the rear of crystal. For this reason, we elected to focus on the absorption of photogenerated diiodide

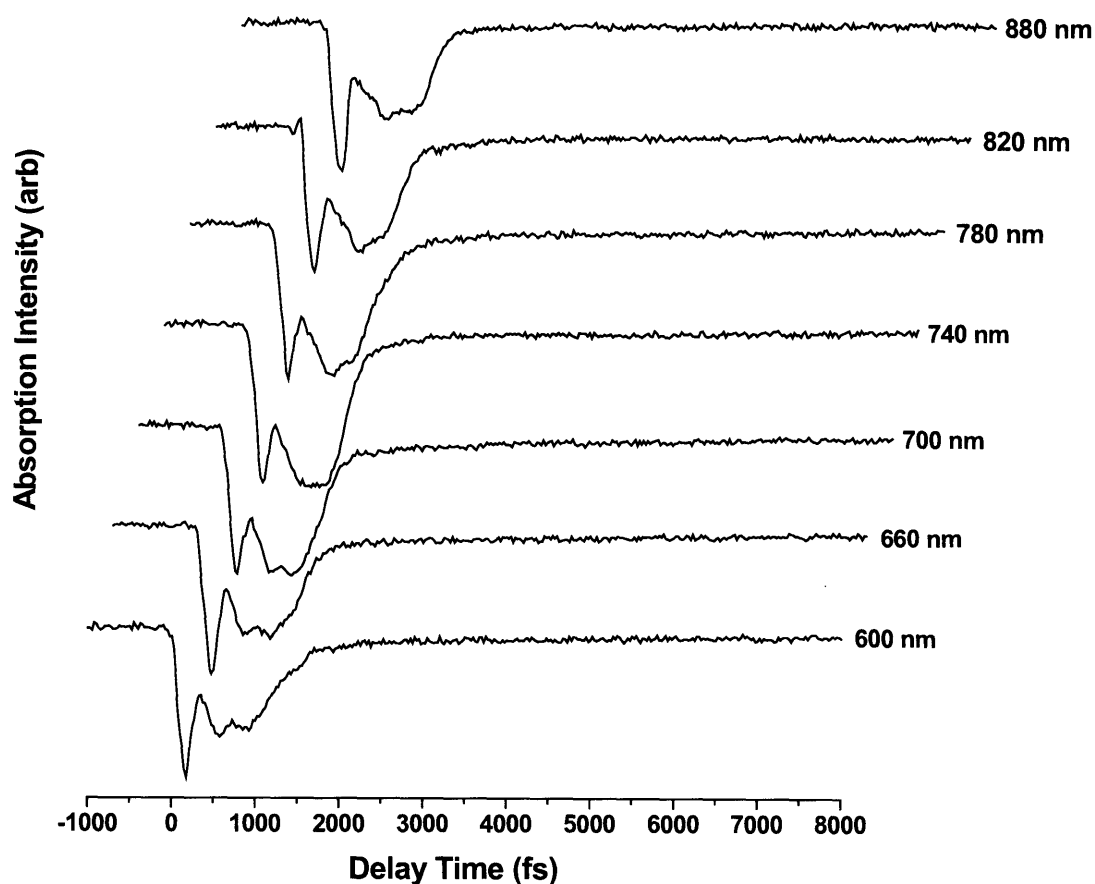


Figure 7-6. Single-shot transient absorption of photogenerated diiodide ions in the photodissociation of tetra-*n*-butylammonium triiodide. The photolysis wavelength is 300 nm and the probe wavelength, indicated to the right of each data sweep, is adjusted to monitor wave packet dynamics of the diiodide ions in various geometries. Single-shot damage in the crystal is observed by visual inspection, so each scan is recorded after translating and optimizing the orientation of the sample under very low illumination intensity.

ions as the signatures of reaction dynamics. Probe wavelengths of 600, 660, 700, 740, 780, 820 and 880 nm were used to interrogate nascent diiodide ions at various times after excitation. The experimental arrangement for transient absorption in crystalline samples was the same as that employed in solution phase work, and detection was once again achieved in a single laser shot through time-to-space mapping of the probe pulse delay. Subsequent processing of the data images by our automated algorithms yielded wavelength- and time-dependent diiodide absorption intensity for the crystalline samples.

Transient absorption data is shown for tetra-*n*-butylammonium triiodide in Figure 7-6. Damage is observed in the crystal by visual inspection after single excitation pulses in many cases, so each data sweep is recorded after translating and re-optimizing the alignment of the crystal using helium-neon laser illumination, where the He-Ne is oriented to follow the same beam path as the probe pulse. Damage spots typically appear as small regions of slightly less intense color, and range in size from 20-50 μm diameter.

Unlike the data from diiodide absorption in ethanol, the transient absorption scans in Figure 7-6 are similar, even for a large range of wavelengths on either side of the absorption maximum (roughly 740 nm). The 300 nm photolysis pulse is absorbed by I_3^- ions, and the initial sharp absorption feature in each trace which persists for about 300 fs is due to visible and near-IR absorption by excited state triiodide. As the triiodide dissociates, the sharp feature rapidly disappears but the transient absorption signal then grows in again. The second broad absorption feature is due to absorption by diiodide ions which are produced in the dissociation reaction. In the sweeps shown, diiodide absorption increases at each wavelength until between 1000-1100 fs, when the absorption signal rapidly decays to near zero over a time period of about 300 fs on average. This

behavior is distinctly different from the results for TA of I_2^- in ethanol solution, where the TA signal persisted for considerably longer times at every wavelength. In addition, the solution phase TA measurements showed a clear band-narrowing as a function of time which was attributed to contributions from the dissipation of excess diiodide vibrational energy, and to fragment recombination to re-form I_3^- on its electronic ground state.

The situation is clearly much different here, as absorption at all wavelengths decreases rapidly only about 750 fs after generating the I_2^- photoproduct. Coherent contributions to the TA signal are apparent, particularly in the TA scans which

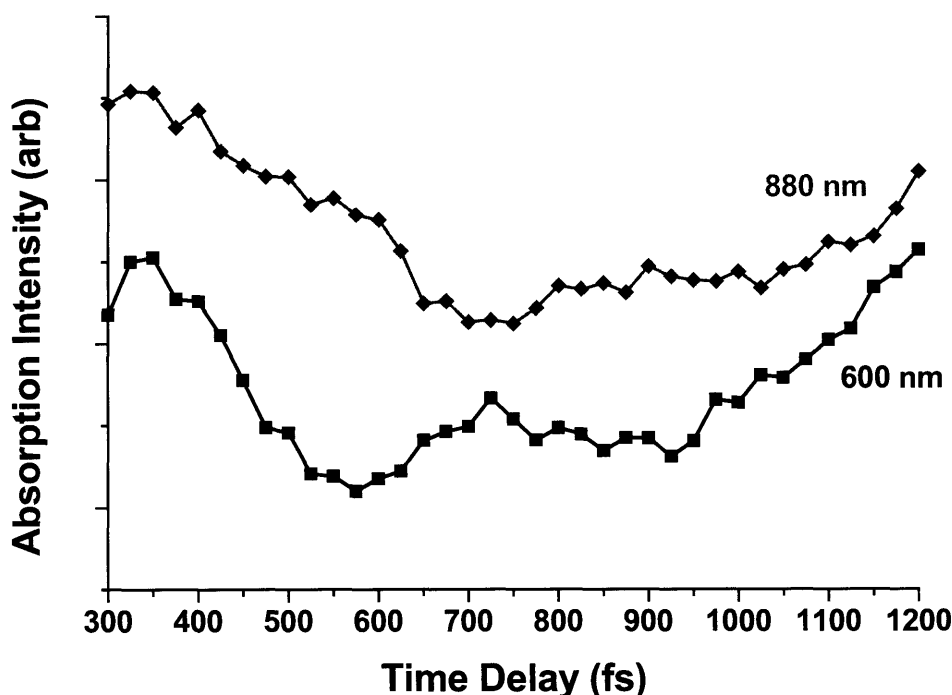


Figure 7-7. Comparison of single-shot transient absorption signals for photogenerated diiodide ion in tetra-*n*-butylammonium triiodide single crystals. Sweeps at 600 and 880 nm each display contributions from coherent motion of the I_2^- fragment, although these are almost exactly out of phase since the two wavelengths probe opposite sides of the diiodide ground state potential energy surface. The oscillation frequency is roughly 105 cm^{-1} which corresponds well with the gas phase value for diiodide ion.

correspond to wavelengths that are absorbed most strongly by highly stretched and compressed I_2^- ions on the ground state potential. Comparison of data sweeps at 600 nm and 880 nm is shown in Figure 7-7. The oscillatory signals are clearly out of phase with respect to one another on account of the coherent motion of the diiodide vibrational wave packet as it propagates back and forth along the bond stretching coordinate. The oscillation frequency, determined by LP-SVD analysis, is about 105 cm^{-1} , in close agreement with previous solution phase measurements and also gas phase results for the I_2^- vibrational frequency.

Most of the features of the absorption profiles in Figure 7-6 are consistent with solution phase observations for this system except for the rapid decrease in absorption intensity at all wavelengths in the vicinity of $t = 1000\text{ fs}$. Without a basis of comparison for solid-state absorption, however, it is difficult to correlate the observed profiles to the microscopic structure of the tetra-*n*-butylammonium triiodide crystal. In view of this, we measured transient absorption profiles at the same wavelengths for tetraphenylphosphonium triiodide single crystals. As for the tetra-*n*-butylammonium derivative, the tetraphenylphosphonium crystals frequently showed visual evidence of single-shot damage extending inward into the bulk of the crystal from the surface. Crystal samples were re-optimized to a new spot following each individual data scan.

The wavelength-dependent TA data are shown in Figure 7-8, and are strikingly different from the results for the previous compound. The same initial sharp absorption feature due to excited state I_3^- appears and persists for the same duration, roughly 300 fs. This is expected of course – each of the structures in section 7.1 contains relatively well-isolated triiodide ions which would be expected to interact only with the photolysis pulse

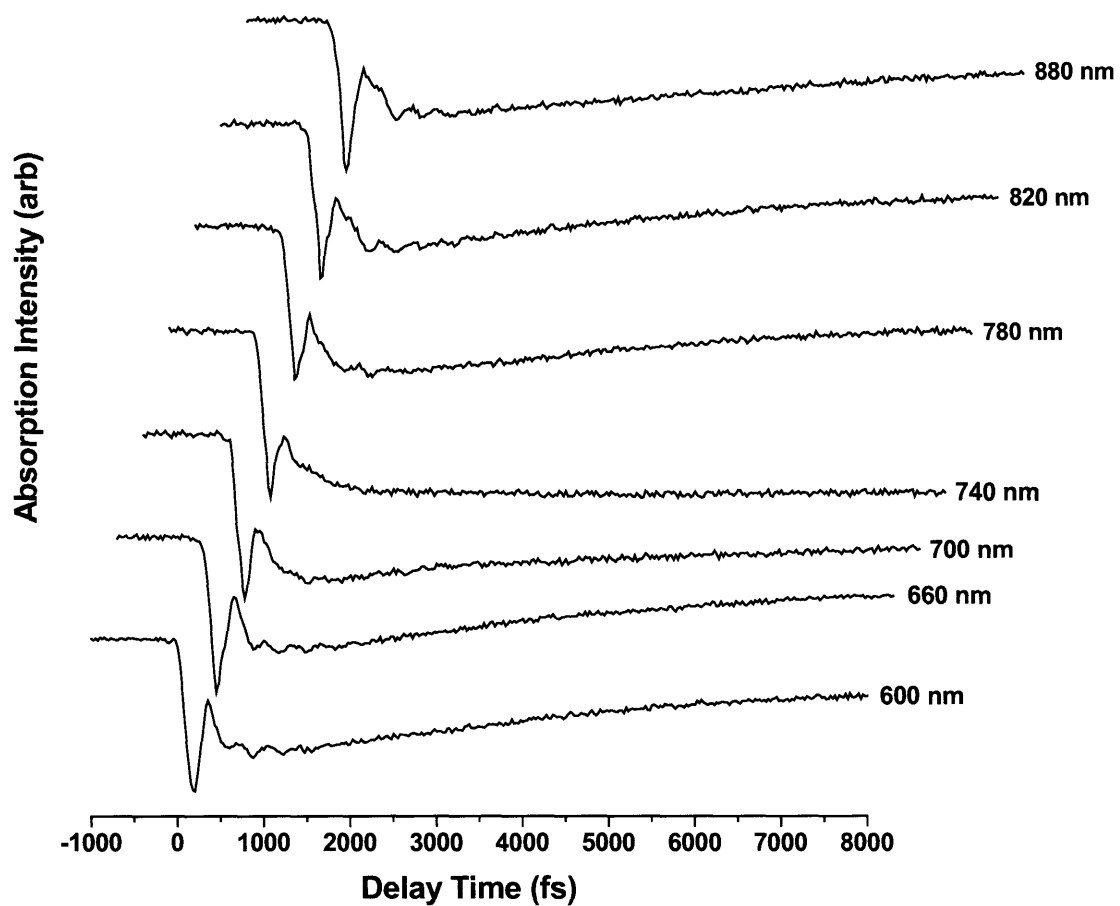


Figure 7-8. Single-shot transient absorption of diiodide ions following photolysis at 300 nm of tetraphenylphosphonium triiodide single crystals. The probe wavelength is indicated to the right of each data sweep. Coherent contributions to the TA signal are observed when probing near the edges of the diiodide absorption band, and reflect time-dependent motion of the diiodide wave packet.

initially, not strongly with neighboring triiodide ions or the counterions.

At each wavelength, the absorption signal due to I_2^- grows in following the dissociation of I_3^- . However, the dynamical evolution of the absorption signal at each wavelength differs. Near the edges of the band, initial absorption is strong and then decays as a function of time. As the probe wavelength is adjusted closer to the center of

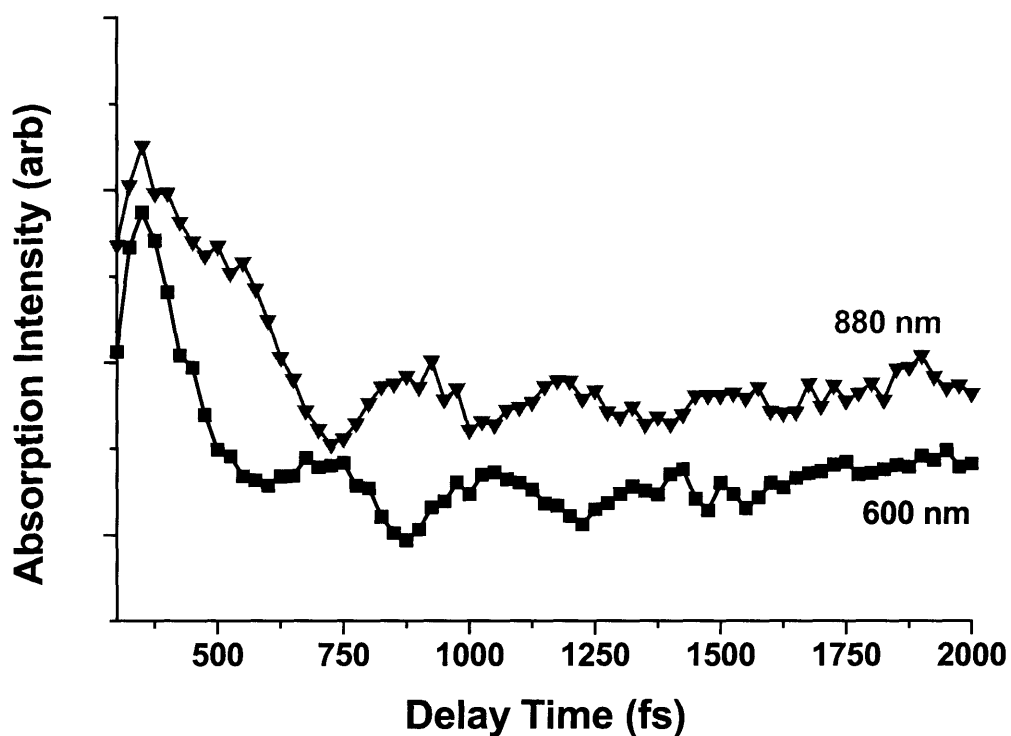


Figure 7-9. Short-time evolution of transient absorption signals at probe wavelengths of 600 and 880 nm for photogenerated diiodide ions in tetraphenylphosphonium triiodide. Coherent oscillations due to diiodide vibrational motion are clearly observed and are anti-phased when measured on opposite sides of the absorption band center.

the absorption band, the transient absorption signal persists for longer durations. At 740 nm, almost no absorption decay is observed over the time window of the experiment.

These results are more consistent with previous observations for the triiodide/diiodide system in solution. The time-dependent narrowing of the absorption band is attributable principally to collapse of the initial superposition of I_2^- vibrational states into the lowest lying levels. Oscillatory contributions due to coherent motion of I_2^- are apparent, especially near the band edges. Figure 7-9 illustrates this for 600 and 880 nm TA traces. The oscillatory component appears to be considerably stronger for this compound than for the previous triiodide crystal. Overall, the data for tetraphenylphosphonium triiodide correspond well with previous results and thus raise the question: what is unique about tetra-*n*-butylammonium triiodide that should produce such markedly different TA results?

We investigated single crystal samples of tetraethylammonium triiodide via transient absorption in the same manner. Data sweeps at the same selection of probe wavelengths are shown in Figure 7-10. Certain features are once again consistent with the previous crystals: a rapid initial absorption peak of duration ~ 300 fs, followed by growth of the diiodide band. Coherent I_2^- oscillations are apparent for the tetraethylammonium crystal as well.

However, the most significant feature in comparison to the observations above is the rapid disappearance of absorption signal over an interval of 350-500 fs for all wavelengths starting near $t = 1400$ fs. The observed TA traces for tetraethylammonium triiodide are qualitatively similar to the profiles for tetra-*n*-butylammonium triiodide except that the onset of decay of the absorption band appears later in time, and occurs over a slightly longer time window. In addition, the absorption intensity following this

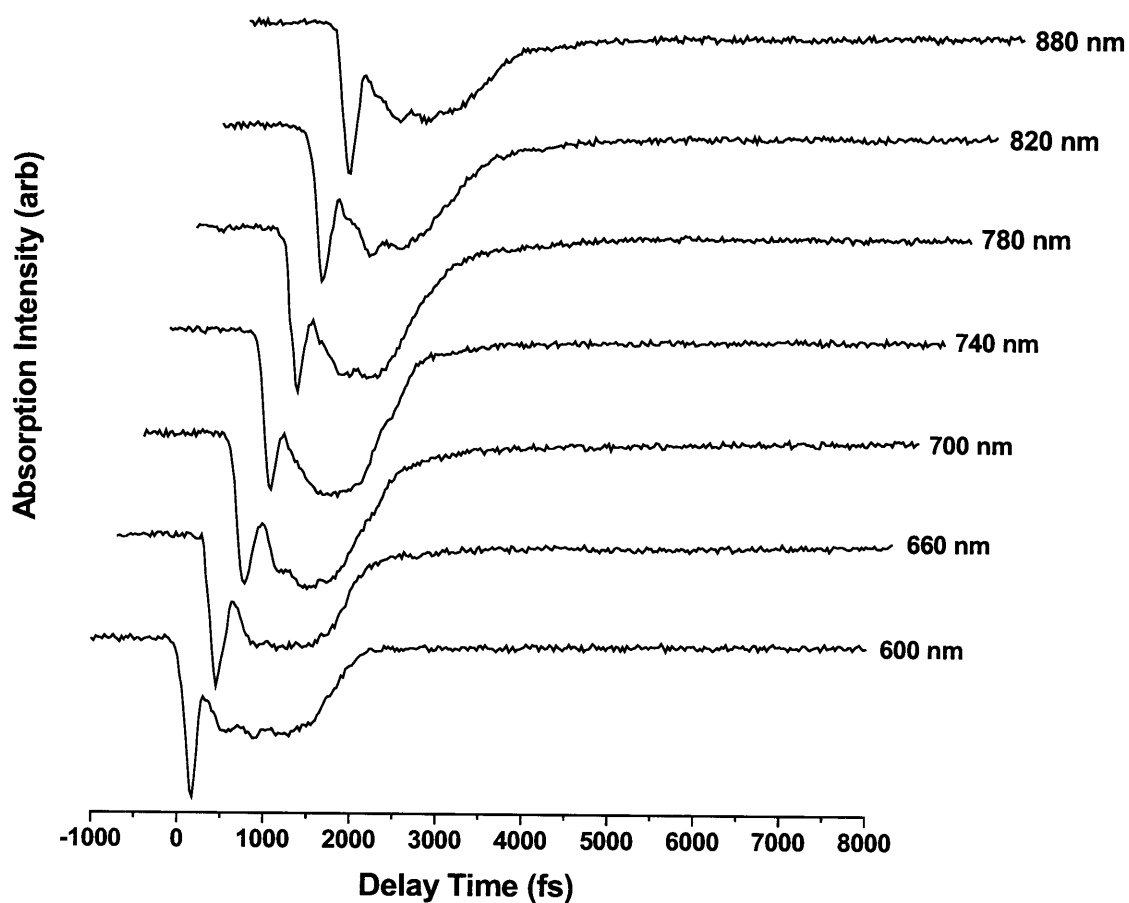


Figure 7-10. Single-shot transient absorption of diiodide ions generated in the photolysis of tetraethylammonium triiodide single crystals. The probe wavelength is indicated to the right of each data sweep. As in the TA profiles for the other crystals employed in these experiments, an oscillatory contribution to the absorption signal is visible at wavelengths near the diiodide absorption band edge.

rapid decay appears to stabilize at a steady-state value which is small but somewhat larger at most wavelengths than that observed earlier.

The fact that the dynamics of transient absorption by the diiodide photoproducts in each crystal differ so markedly suggests a structural correlation. Since the nature of the diiodide fragment should be unchanged among these samples, the dynamical evolution must be dependent upon the crystalline environment, and particularly the local environment surrounding the diiodide absorbers. On the basis of these measurements, we therefore infer that the evolution and ultimate fate of the products from photodissociation of triiodide single crystals is strongly coupled to the specific geometry of the crystal lattice.

7.3 Molecular Dynamics Simulation of I_3^- Photodissociation

Although crystalline photochemistry is a relatively unexplored field, a considerable body of work has emerged which centers upon the investigation of photoinduced reaction dynamics in rare gas matrices [4-8] (also see [9] and references therein). In such experiments, individual molecules of a photochemically active species such as iodine are crystallized together with a rare gas such as argon or krypton. The I_2 molecules occupy substitutional sites within the rare gas lattice. Although randomly oriented with respect to the bulk crystal's cubic axes, individual iodine molecules experience a reasonably uniform environment. These experiments can be conducted in a conventional manner since the photofragments are unable to escape their immediate environment and undergo geminate recombination, thereby averting a build-up of reaction product over many laser shots.

The photodynamics of such isolated species have been investigated on an ultrashort time scale, enabling much insight into the caging and energy dissipation effects of the surrounding lattice. The experiments are typically complemented by molecular dynamics simulations which connect explicitly the structural environment to the equations of motion describing the evolution of the photodissociated fragments.

In the spirit of this prior work, and in order to acquire more insight regarding the contributions of the microscopic lattice geometry to the unusual features observed in our transient absorption data, we constructed straightforward simulations of the triiodide photodissociation reaction by means of a molecular dynamics approach. The method is as follows: from x-ray data, an equilibrium model of the crystal under study is constructed in Cartesian coordinate space. The model crystal typically consists of 27 unit cells arranged in a $3 \times 3 \times 3$ array, and the overall data set contains several hundred atoms.

In order to mimic the uncertainty inherent in quantum systems, a Gaussian thermal distribution of 30,000 trajectories is constructed and propagated in each simulation. The initial momenta and displacements from equilibrium for each atom in the model crystal are adjusted such that the overall collection of initial trajectories represents a minimum uncertainty distribution at temperature T (taken to be 298 K).

The molecular dynamics simulation is then launched by solving the classical equations of motion for each atom in the model crystal. The well-known Verlet algorithm is used to compute new atomic positions from the first and second time-derivatives after each 1 fs time increment. As noted above, the dynamics for any given trajectory are completely deterministic; it is only by virtue of the initial Gaussian distribution of trajectories that we approximate the uncertainty in a quantum system,

since each initial set of conditions will propagate to a different result. The most significant aspect of the calculation is the choice of potential energy functions to describe the interactions among individual atoms. Fortunately, theoretical work on triiodide and diiodide ions (primarily in the gas phase) has provided simple expressions which describe well the potential surfaces for these ions when they are in the vicinity of their equilibrium geometries. The ground and excited state triiodide potentials are taken from work by Benjamin, Banin and Ruhman [10] on photodissociation of I_3^- in ethanol solution. The ground state potential is given by

$$V_{ground}^{I_3^-} = \frac{1}{2}k_{II}(r_{12}-r_{II}^{eq})^2 + \frac{1}{2}k_{II}(r_{23}-r_{II}^{eq})^2 + k_{tb}(r_{12}-r_{II}^{eq})(r_{23}-r_{II}^{eq}) + \frac{1}{2}k_{\theta}(\theta-\pi)^2 \quad (7.1)$$

where r_{12} and r_{23} are the triiodide bond lengths and θ is the bond angle. The first two terms are harmonic stretching terms involving extension or compression of each bond (by itself) and the third term is a pseudo-three-body deformation contribution. The fourth term represents a bending contribution to the potential, independent of bond lengths. The parameters and force constants for this potential, determined from fitting to the fundamental vibrational frequency of the (linear) triiodide ion, are

$$\begin{aligned} r_{II}^{eq} &= 2.90 \text{ \AA} \\ k_{II} &= 433 \text{ kJ mol}^{-1} \text{ \AA}^{-2} \\ k_{tb} &= 124 \text{ kJ mol}^{-1} \text{ \AA}^{-2} \\ k_{\theta} &= 301 \text{ kJ mol}^{-1} \text{ rad}^{-2} \end{aligned} \quad (7.2)$$

The excited state potential for I_3^- is considered purely dissociative in either displacement coordinate, but must maintain a symmetric dependence on each. In order to

model this dependence, the adaptable London-Eyring-Polanyi-Sato (LEPS) potential is employed:

$$V_{excited}^{I_3^-} = \Delta E_0 + Q_1 + Q_2 + Q_3 - \sqrt{J_1^2 + J_2^2 + J_3^2 - J_1 J_2 - J_2 J_3 - J_3 J_1} \quad (7.3)$$

The following quantities are defined in Equation (7.3):

$$\begin{aligned} {}^1E(r_i) &= {}^1D_i \left[1 - e^{-{}^1\beta_i(r_i - {}^1r_i^{eq})} \right]^2 - {}^1D_i \\ {}^3E(r_i) &= {}^3D_i \left[1 + e^{-{}^3\beta_i(r_i - {}^3r_i^{eq})} \right]^2 - {}^3D_i \\ Q_i &= \frac{1}{2} [{}^1E(r_i) + {}^3E(r_i)] \\ J_i &= \frac{1}{2} [{}^1E(r_i) - {}^3E(r_i)] \end{aligned} \quad (7.4)$$

In Equations (7.3) and (7.4), the values Q_i represent Coulomb contributions and the J_i parameters are exchange contributions. Indices “1” and “3” refer to singlet and triplet states, respectively. Parameters for Equations (7.3) and (7.4) are determined from fitting to the absorption spectrum for I_3^- in ethanol solution:

$$\begin{aligned} {}^1r^{eq} &= 3.23 \text{ \AA} \\ {}^3r^{eq} &= 2.98 \text{ \AA} \\ {}^1\beta &= 1.16 \text{ \AA}^{-1} \\ {}^3\beta &= 1.0 \text{ \AA}^{-1} \\ {}^1D &= 1.1 \text{ eV} \\ {}^3D &= 1.009 \text{ eV} \\ \Delta E_0 &= 3.4 \text{ eV} \end{aligned} \quad (7.5)$$

Equations (7.3) and (7.5) have been employed quite successfully to model the dissociative dynamics of excited state triiodide ions.

The potentials for diiodide ion are adapted from the work of Kuhne and Vohringer [11], who utilized the previous results of Chen and Wentworth [12]. The ground state I_2^- form is a parametrized Morse potential

$$V_{ground}^{I_2^-} = De^{-2a(r-r_{eq})} - 2De^{-a(r-r_{eq})} \quad (7.6)$$

where the parameters, chosen to reproduce the I_2^- stretching frequency in ethanol solution, are $D = 0.9$ eV, $a = 1.31 \text{ \AA}^{-1}$ and $r_{eq} = 3.04 \text{ \AA}$. The excited state surface is represented by a simple exponential form

$$V_{excited}^{I_2^-} = Be^{\frac{r-r_{eq}}{A}} \quad (7.7)$$

with $A = 0.33 \text{ \AA}$ and $B = 0.72$ eV.

In studies of matrix-isolated I_2 , classical simulations were able to reproduce the observed dissociation dynamics reasonably well for several picoseconds of simulation time, for two reasons. First, very accurate gas phase iodine potentials have been calculated theoretically and in particular, such potentials remain accurate for large displacements from the I-I equilibrium separation. Second, the I-I bond can be treated as unbroken throughout the entire simulation. As such, switching between sets of surfaces to account for dissociation need never occur – all of the molecular dynamics takes place on the separate ground and excited state I_2 potentials. In contrast, a difficult aspect of the triiodide/diiodide system is choosing when to “dissociate” the I_3^- ion. We noted previously in the discussion of solution phase absorption measurements that breaking of either of the I-I bonds in I_3^- follows a period of bond extension and bifurcation in response to the promotion of the triiodide ion to its fully dissociative excited state. In the actual molecular species, the process of dissociation which leads to diiodide ion and

atomic iodine is a continuous one, and the excited state potential of I_3^- is smoothly connected to the ground state I_2^- surface. However, we have no information regarding the shapes of these potentials in this intermediate region. This has two implications. First, it is necessary to introduce a cutoff displacement distance in the MD simulation which represents dissociation. Whichever iodine atom exceeds this displacement distance first is the one which dissociates. It is at this instant that I_2^- is “born”, rather than occurring gradually over an extended period of bond stretching. The displacement distance is somewhat arbitrarily set at 15% of the equilibrium bond length in our simulations in order to reproduce the time of initial appearance of diiodide absorption in transient absorption measurements. Second, it is impossible to correctly model the component of transient absorption at very short times which is due to excited state I_3^- since we have no information regarding either higher-lying states of the ion or the shape of the dissociative first excited surface far from the Franck-Condon region. On account of this, in our simulations visible and near-IR absorption begins suddenly when the I_2^- ions are born.

The other potentials in the system fall into one of two classes. The first involves direct covalent bonds between atoms other than iodine. These include, for example, all of the C-C and C-N bonds in the tetra-*n*-butylammonium ion. Interactions of this type are modeled using the well-known reactive bond-order potentials originally introduced by Brenner [13] and subsequently modified for use in systems containing hydrocarbons and heteroatoms [14, and references therein]. The functional form of the reactive bond-order potential characterizes the strength of a given bond (i.e. the force constant) in terms of the number of bonds the involved nuclei form with other atoms, the nature of those bonds,

and the known thermodynamic properties (such as atomization energy and zero-point energy) of the atoms involved.

The second family of potentials involves interactions between non-bonded atoms. These include both long- and short-range forces between closed- and open-shell species which may or may not bear charges. Clearly, this aspect of the characterization of interatomic potentials is the most difficult to describe analytically. Fortunately, the initial reaction dynamics principally involve interactions between directly bonded atoms and optical pump and probe pulses. In constrained environments such as crystals, non-bonded collisional interactions will clearly arise, particularly as photodissociation liberates molecular fragments. However, from the point of view of the reaction coordinate, such contributions only become significant at later times. In order to model these terms, we employ a standard Lennard-Jones model with widely available parameters for any given pair of atomic interactions. Dipole interactions and the overall electronic structure of the species involved are not explicitly included. Given the charges on I_2^- and the counterions in each lattice, this is necessarily a crude approximation to the intermolecular interactions. However, while our observations of I_2^- dynamics are certainly sensitive to the time scales and consequences of collisions among crystalline constituents, they do not permit detailed examination of the collisions themselves. Therefore we hope to obtain results that can be compared usefully to the observations at hand.

With these interatomic potentials, each individual trajectory consisting of a complete set of atomic coordinates describing a model crystal is propagated forward in time according to classical dynamics. The photolysis pulse is introduced at an arbitrary

time following the zero-time start of the simulation. The quantum yield of triiodide photolysis at 300 nm is assumed to be unity, so the time-dependent absorption process is modeled in straightforward fashion as a convolution between the distribution of absorbing I_3^- ions in the crystal and a Gaussian pulse of duration 30 fs centered at 300 nm. The ground state I_3^- ions which absorb are promoted to the excited state surface and begin to dissociate. When one of the outer atoms in a given I_3^- ion reaches the dissociation threshold, the ion is considered to have dissociated and the character of the fragments is switched to atomic I and ground state I_2^- . The first 20 time steps for the new diiodide fragment are evaluated on a potential surface which is interpolated to connect the excited state of triiodide to the ground state of diiodide in a smooth, continuous fashion. In this way, we avoid discontinuities in the fragment's potential energy. Recombination dynamics are treated in an analogous manner. When a free I atom and I_2^- ion approach within an arbitrary bond formation distance (12% of the equilibrium bond length) and also within the limits of a collision angle cone of 30° , recombination occurs by joining the fragments and transferring the three atoms to the ground state surface of triiodide via cubic spline interpolation between the potentials for 20 time steps.

Propagation of each trajectory continues for 10 ps. In order to calculate the transient absorption signal due to I_2^- at a given frequency ν and time t , we must first determine the classical probability density $\rho(R,t)$ of I_2^- molecules at internuclear separation R for time t . For our simulations, the distribution is discretized in both the time variable (step size 1 fs) and spatial separation (0.001 Å grid size), $H(R_0+\Delta R, t_0+\Delta t)$. For each time slice $t_i = t_0 + (i-1)\Delta t$, a Gaussian probability distribution function $\rho(R, t_i)$ is fitted to the discretized probability density $H(R_0+\Delta R, t_i)$. The signal intensity $S(t_i)$ at a

frequency ν is proportional to the population density of I_2^- absorbers at internuclear separations which correspond to a transition frequency of ν . Mathematically, this is expressed as a convolution between $\rho(R, t_i)$ and a delta function at frequency ν :

$$S(\nu, t_i) \propto \int \mu^2(R) \rho(R, t_i) \delta(\Delta V(R) - h\nu) dR \quad (7.8)$$

where the term $\Delta V(R)$ is the energy difference between the ground and excited I_2^- states at an internuclear separation R . For simplicity, we neglect the distance dependence of the transition dipole moment μ and set its value to unity. In practice, the frequency spectrum is discretized in units corresponding to 0.5 nm about the center wavelength of the transition and the instantaneous signal intensity is calculated in discrete steps.

The probe pulses employed in our simulations are centered at frequency ν_p and time t_p and are assumed Gaussian in both frequency and time with a frequency FWHM bandwidth of 20 nm and a temporal FWHM duration of 30 fs. The observed TA signal is the convolution of the instantaneous signal intensity $S(\nu, t)$ in both time- and frequency-space with the probe pulse:

$$\sigma(\nu_p, t_p) = S(\nu - \nu_p, t - t_p) \otimes P(\nu - \nu_p, t - t_p) \quad (7.9)$$

As described previously, rather than computing the integral in Equation (7.9), the Gaussian probe pulse is discretized in terms of both frequency and time, and the calculation of the TA intensity is given by a direct summation as

$$\sigma(\nu_p, t_p) = \sum_{i=-n}^n \sum_{j=-m}^m S(\nu_p + i\Delta\nu, t_p + j\Delta t) \cdot P(\nu_p + i\Delta\nu, t_p + j\Delta t) \quad (7.10)$$

where $\Delta\nu$ and Δt are the sampling intervals and the functions S and P are the discrete representations of the instantaneous signal and the probe pulse.

An important feature of the simulations is the inclusion of transient absorption signal only from diiodide ions which originate from the center unit cell. Since our model crystals consist of a $3\times3\times3$ array of cells, only contributions from diiodides in cell (2,2,2) are permitted. This restriction ensures that no effects due to the artificial edges of the crystal are included in the simulation. Atoms in other cells are permitted to move about, and all triiodide ions can absorb probe light, dissociate to I_2^- and the products recombine, but the contributions to the absorption signal from all but the center cell are neglected. This has the added advantage of greatly reducing the computational time involved in calculating the instantaneous signal S .

There are two absorption processes which occur in our simulation of the experiments. The first is absorption of the photolysis pulse by triiodide ions within the bulk of the crystal. The unit cell sizes for each of the three crystals employed in our experiments differs, but for an average cell of size 13 Å on each side, the cell volume is about 2.2×10^{-21} cm³. There are also different numbers of triiodide ions per unit cell from one crystal to the next and the orientations matter, since the transition dipole lies along the ion's axis. Assuming two ions per cell properly aligned with the laser pulse polarization such that absorption occurs, the number density of absorbers is about 10^{21} cm⁻³. The pump pulses each contain about 1.8×10^{12} photons, and so the total volume of the region in which absorption occurs is 2×10^{-9} cm³. The pump spot covers a transverse area of 1.8×10^{-4} cm², and so the penetration depth of the pump pulses is about 100 nm. Thus, all of the signal we observe experimentally is generated in about the first 100 nm of the crystal. Our simulation therefore corresponds to a collection of 27 unit cells in this region.

The second process is absorption at the probe wavelength by diiodide ions. In our simulations, we have treated this process in simple fashion. If a diiodide ion has been generated via photodissociation, we calculate the absorption probability as the normalized projection of the pulse polarization in the direction of the I_2^- bond axis. If the polarization and molecular axis are perfectly aligned, the absorption probability is unity. If they are orthogonal, the diiodide fragment does not absorb. The actual fraction of diiodide ions which absorbs in a given simulation at a particular time is dependent upon the arrangement of parent triiodide ions in the crystal and orientational dynamics of the diiodide fragments following photolysis.

The instantaneous signal calculated for tetra-*n*-butylammonium triiodide is shown in Figure 7-11. The simulation time is displayed on the horizontal axis and the probe frequency is shown on the vertical axis. The intensity of the signal is plotted as a function of each, with increasing intensity appearing whiter. The plot is effectively a transient absorption spectrogram for the diiodide absorption in this compound.

There is no absorption prior to about 340 fs – this is the region in which the sharp TA spike appears in the data, and is attributed to absorption by excited state I_3^- . Our simulations only calculate I_2^- absorption, not I_3^- absorption, so no TA signal is apparent. Near 340 fs, the diiodide ions are “born” suddenly when the dissociation threshold is reached (this region is not infinitely sharp due to the fact that we started with a thermal distribution of initial states). Absorption signal grows quickly, first in the near-IR region since the I_2^- ions are generated in a stretched configuration, and then later oscillating back and forth as the diiodide wave packet propagates along the I_2^- ground state electronic

potential. After a little more than two cycles, the TA signal vanishes abruptly near 1000-1100 fs. No further I_2^- absorption is observed throughout the duration of the simulation.

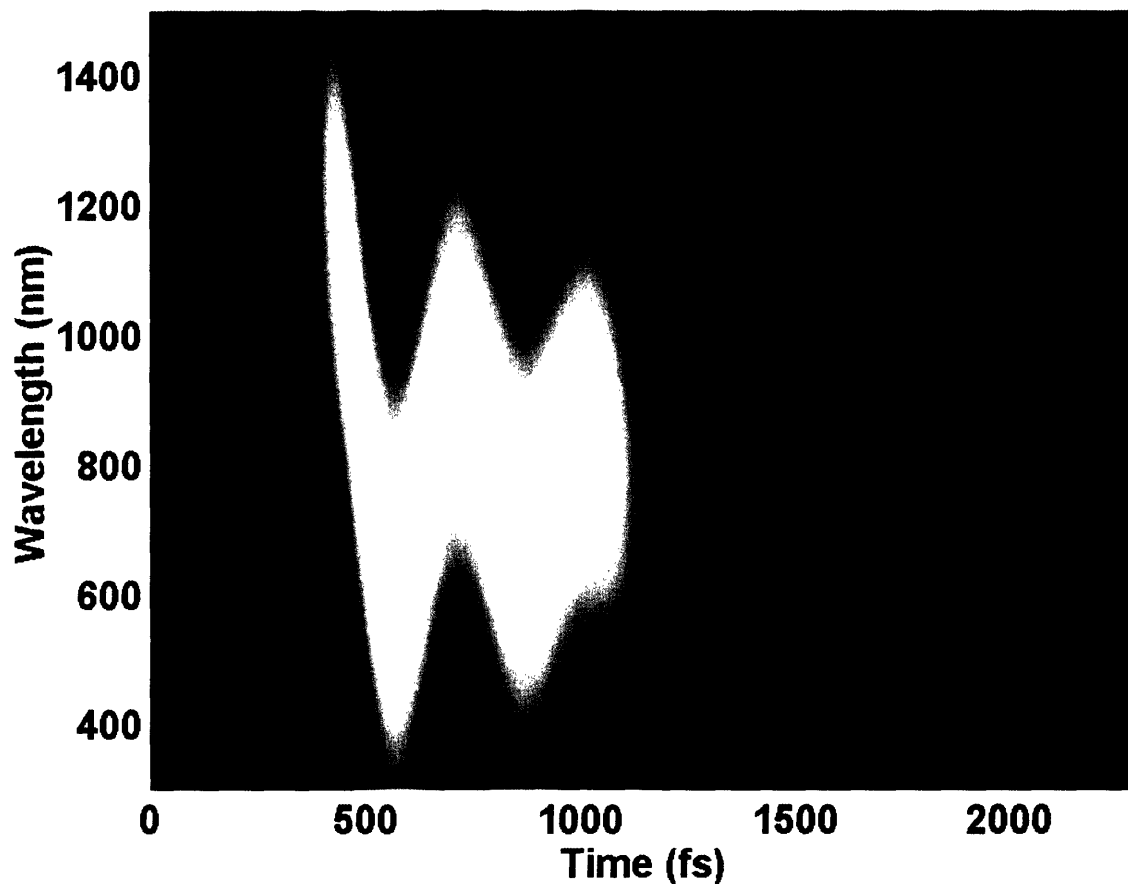


Figure 7-11. Simulated transient absorption spectrogram for the diiodide ions in the photodissociation of crystalline tetra-*n*-butylammonium triiodide. The signal shows oscillatory behavior as the diiodide wave packet propagates along its ground state electronic surface.

In the simulated photodissociation of tetra-*n*-butylammonium triiodide, the birth of I_2^- also corresponds to the birth of free I atoms at 340 fs. The I atoms propagate along trajectories which at short times are approximately defined by the I_3^- symmetric

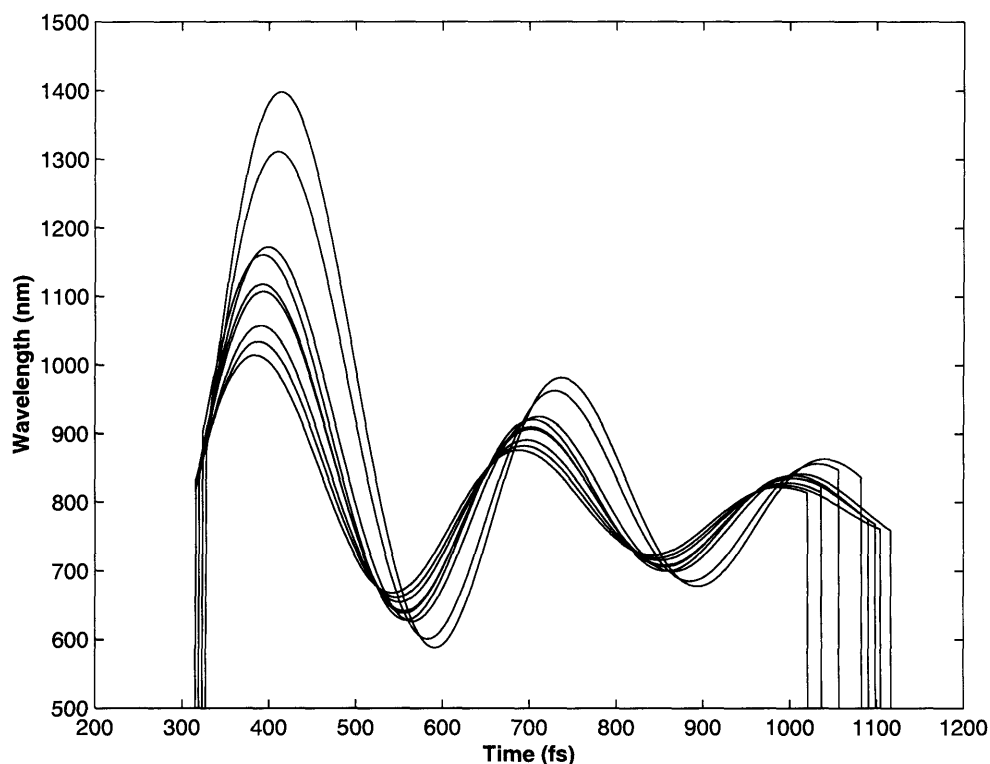


Figure 7-12. Nine randomly selected classical diiodide trajectories from the photodissociation simulation for tetra-*n*-butylammonium triiodide, illustrating varied contributions to the overall transient absorption signal which result from different initial states.

stretching mode. The first encounter with the lattice cage occurs at about 720 fs. Because of the highly congested nature of the lattice geometry of tetra-*n*-butylammonium triiodide, free I atoms collide with other I atoms (either free or as diiodide ions) and appear to immediately recoil backwards along a similar trajectory. Depending upon the initial configuration of the lattice, glancing collisions with the tetra-*n*-butylammonium ions may occur but motion is strongly directed back toward the initial position and corresponding I₂⁻ fragment. Recombination occurs in the interval 1000-1100 fs, at which point the diiodide is converted to triiodide and the TA signal rapidly disappears. As

before, the thermal distribution of initial conditions ensures that this signal disappearance is not instantaneous, but instead occurs over a temporal range of about 300 fs. The influence of individual trajectories is seen in Figure 7-12, in which nine randomly chosen trajectories from the initial distribution of 30,000 are plotted.

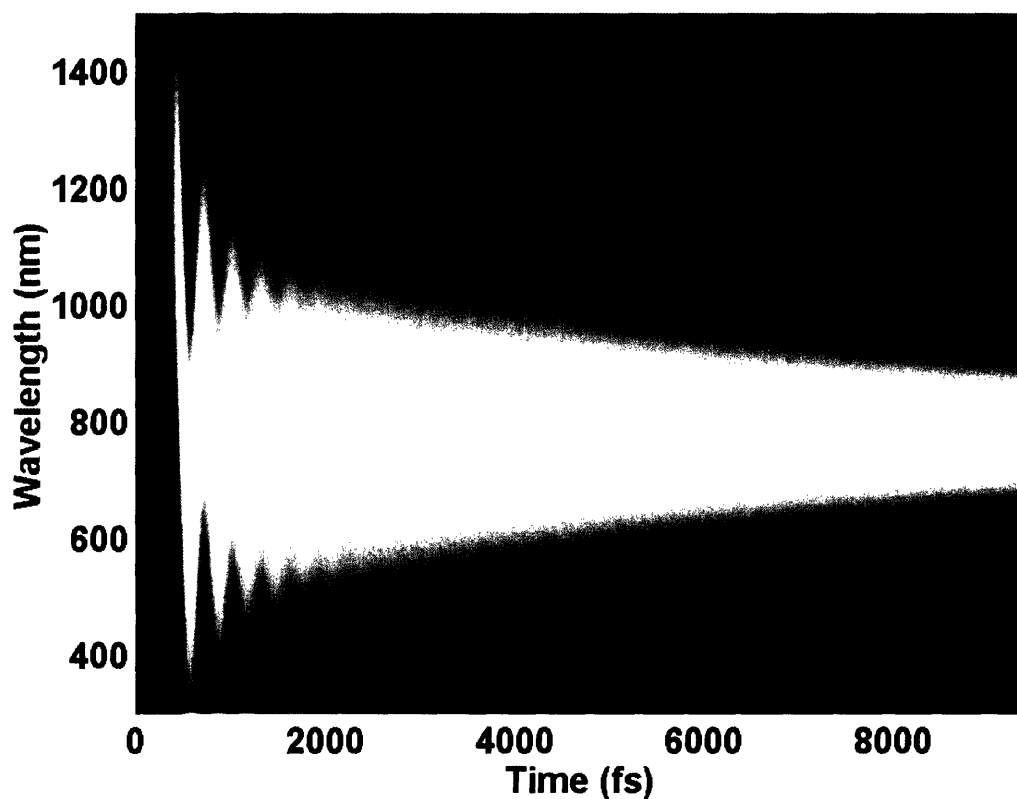


Figure 7-13. Simulated transient absorption spectrogram for crystalline tetraphenylphosphonium triiodide. Several coherent oscillation cycles are visible after the diiodide ions are born between 300-350 fs, and these gradually dephase, accompanied by incoherent relaxation of excess vibrational energy which produces the absorption band narrowing at later times.

The molecular dynamics photodissociation simulation for tetraphenylphosphonium triiodide was conducted in exactly the same fashion, and the

instantaneous transient absorption spectrogram is shown in Figure 7-13. Short-time dynamics of I_2^- are similar, with triiodide dissociation occurring during the 300-350 fs interval, followed by subsequent wave packet oscillations of the coherently vibrating I_2^- fragments. Many oscillations are visible, followed by vibrational dephasing and a long period of incoherent vibrational relaxation. The narrowing of the transient absorption band is clearly observed after several picoseconds.

The principal difference between the results of this simulation and the results for tetra-*n*-butylammonium triiodide is that in tetraphenylphosphonium triiodide, no sudden decrease in the TA signal is observed. On an atomic scale, free I atoms are ejected along the symmetric stretching direction following dissociation of triiodide ions. However, because of the larger “pocket” in which the I_3^- ions rest, cage collision only occurs after a longer interval. Even then, the shape of the lattice cage is such that the majority of free iodine atoms do not recoil along their initial trajectories, but instead follow a variety of meandering excursions. Rotational motion of I_2^- fragments is greater for this compound as well owing to the relatively more spacious local lattice geometry. Recombination is less favorable on account of this randomization of initial atomic positions after short times, and indeed most free I atoms do not recombine with diiodide ions within the 10 ps window of the simulation. Hence, the I_2^- transient absorption signal is not quenched.

Finally, in Figure 7-14 we present the calculated spectrogram for tetraethylammonium triiodide, along with fifteen randomly chosen trajectories in Figure 7-15 to indicate various contributions to the overall calculation. The initial dynamics of I_2^- photogeneration in this compound are very similar to those in the previous two cases. However, we note the disappearance of diiodide absorption at all wavelengths beginning

at about 1400 fs, over a period of about 400-500 fs. The simulation result is qualitatively similar to the results for tetra-*n*-butylammonium triiodide, except that TA signal loss occurs at a later time. On an atomic scale, dissociation of triiodide ions produces free I

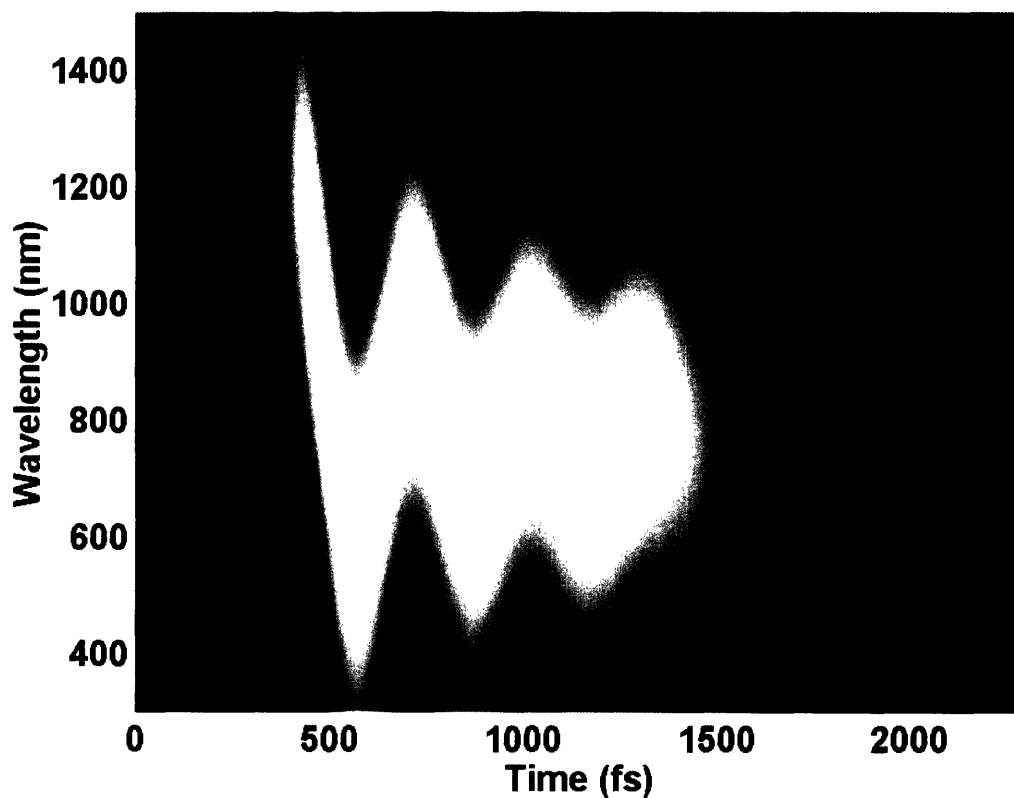


Figure 7-14. Simulated transient absorption spectrogram for the dissociation of crystalline tetraethylammonium triiodide. The initial signal is similar to the results for other solid-state triiodides, with coherent wave packet motion observed for about three cycles. The absorption signal decays rapidly starting at about 1400 fs.

atoms which interact initially with triiodide ions oriented in nearly perpendicular chains. Recoil of the free I atoms along their original trajectory occurs in many cases, although diffusive motion is more common than in tetra-*n*-butylammonium triiodide since the

lattice environment is less constrained. The cage encounter occurs on average at approximately $t = 950$ fs, and geminate recombination occurs near 1450 fs. Recoil trajectories are not as confined in this compound as in tetra-*n*-butylammonium triiodide

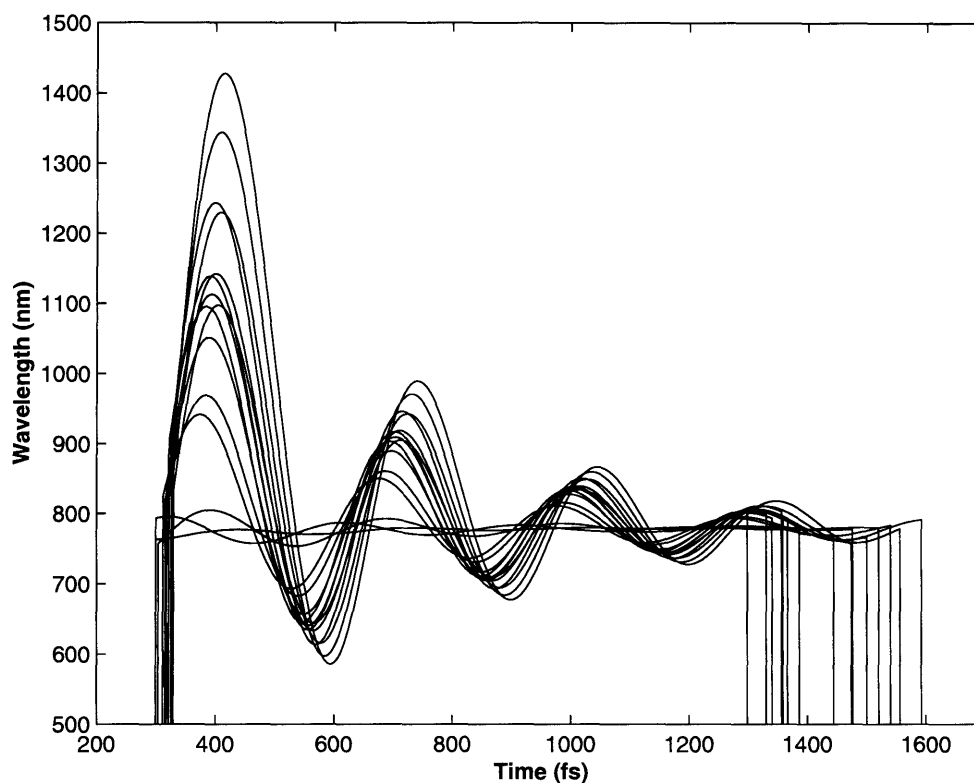


Figure 7-15. Fifteen randomly-selected trajectories from the Gaussian swarm used to simulate the tetraethylammonium triiodide transient absorption spectrogram.

so the distribution of recombination times is a little wider, resulting in a slightly broader absorption tail.

Thus, on the basis of our simulation results, we conclude that the rapid loss of transient absorption signal in the photodissociation of crystalline tetra-*n*-butylammonium triiodide and tetraethylammonium triiodide is due primarily to lattice caging of the

primary fragments, recoil along (approximately) their initial dissociation trajectories, and subsequent geminate recombination. The time scales of these events differ due to the unique local lattice environment which the triiodide ions experience in each compound. In tetraphenylphosphonium triiodide, the lattice “pocket” is large enough that excursions of the dissociated fragments – especially free I atoms – leads to long-lived diiodide atoms which do not, on average, recombine within the time window of our simulation. For this reason, the transient absorption spectrogram shows strong signal due to I_2^- even 10 ps after the initial photolysis pulse.

7.4 Discussion of Results

We are now in a position to compare our simulation results to the experimental transient absorption data for the three crystalline triiodides under study. Absorption profiles are calculated at specific probe wavelengths according to Equation (7.10). Figure 7-16 shows the measured and calculated absorption profiles for tetra-*n*-butylammonium triiodide at three different wavelengths: 600 nm, 740 nm and 880 nm. The measured absorption profile in each case is shown in black, and the calculated data are shown in grey. At each of the three wavelengths, the molecular dynamics simulations approximately reproduce all of the important aspects of the observed data. Consider for example the sweep at 600 nm. The simulation results faithfully reproduce the onset of absorption due to diiodide ions which occurs near $t = 325$ fs. Both the experimental and calculated data show rapid growth of the diiodide band in the region labelled “A” on the figure. In the “B” region, coherent oscillations due to I_2^- wave packet motion are observed experimentally and reproduced numerically, including the proper phase

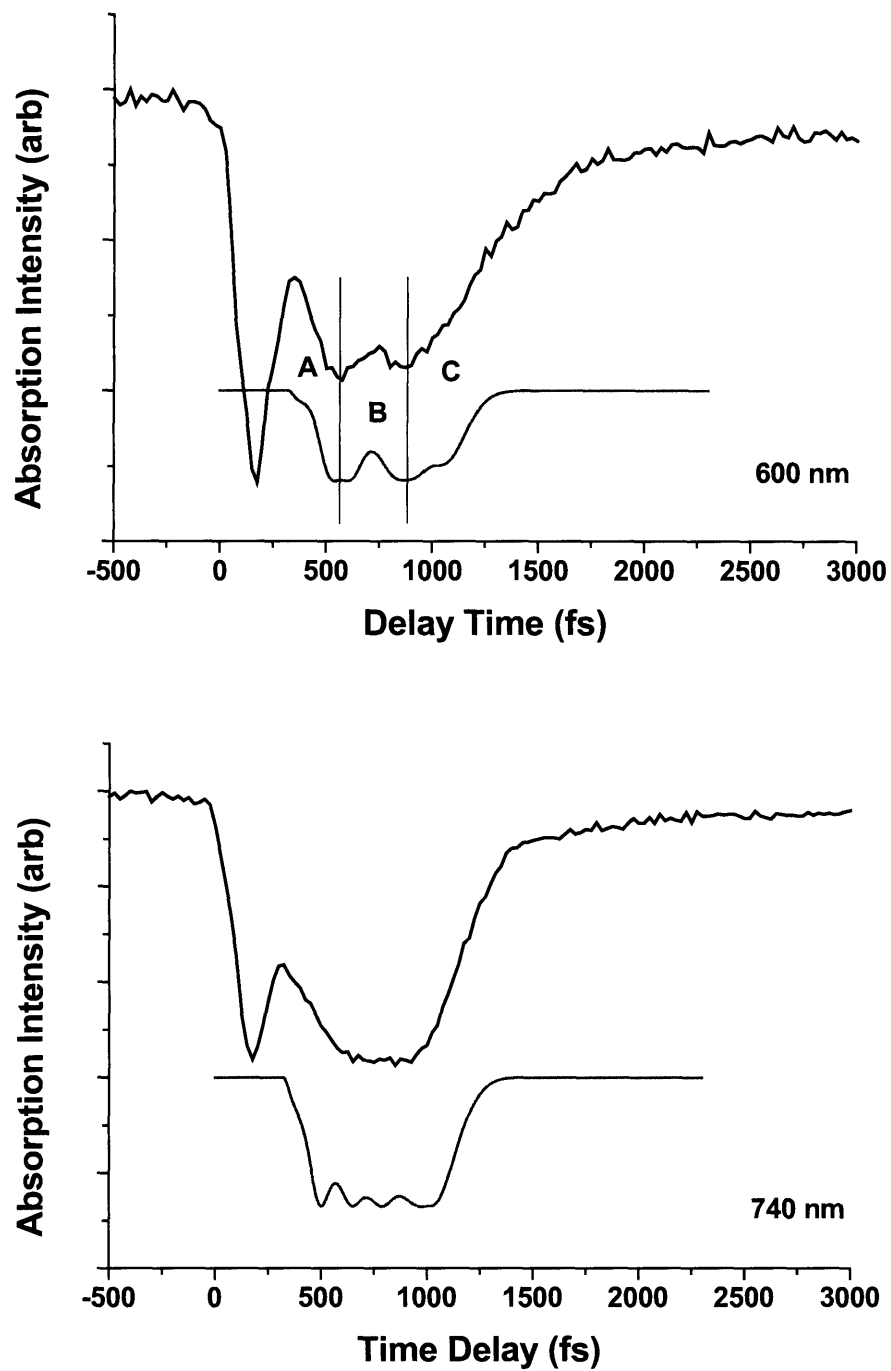


Figure 7-16. Measured (black) and calculated (grey) transient absorption profiles for diiodide ions generated in the photodissociation of crystalline tetra-*n*-butylammonium triiodide. Probe wavelengths are 600 nm (top) and 740 nm (bottom).

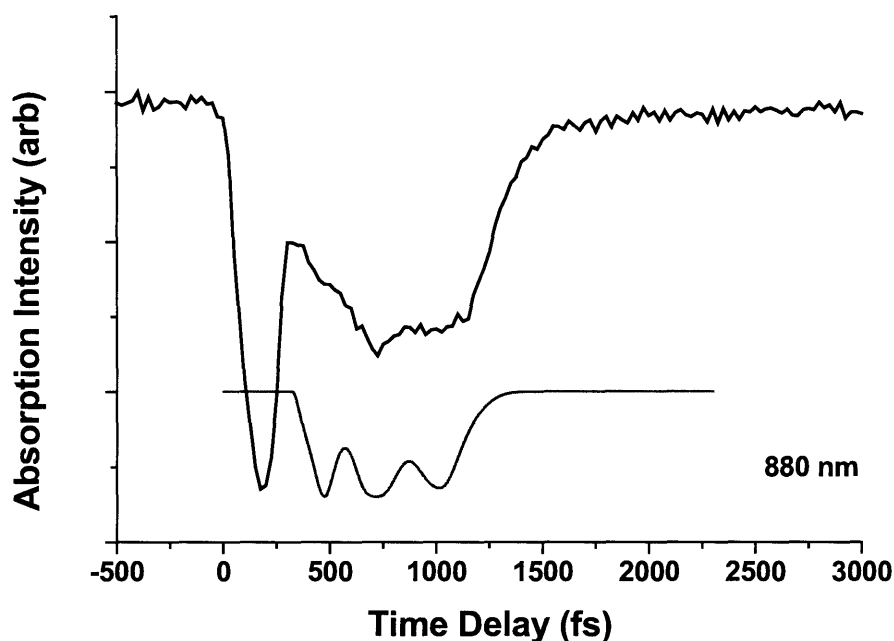


Figure 7-16 (cont'd). Measured (black) and calculated (grey) transient absorption profiles for diiodide ions generated in the photodissociation of crystalline tetra-*n*-butylammonium triiodide. The probe wavelength is 880 nm.

behavior. Finally, in region “C”, the onset of absorption decay near $t = 1000$ fs is accurately modeled. It should be noted that not all features of the TA data can be properly reproduced. For instance, the time scale over which the TA band disappears is faster in the simulated data than in the experimental measurements. This is undoubtedly due to collisions within the lattice which are approximately, but not perfectly, treated by the approximate potentials of our simulation. These result in a slightly greater diffusional contribution to the atomic motion than we have obtained numerically. Also, our simulation predicts virtually 100% geminate recombination, while based upon our experimental data, a very small fraction of the dissociated triiodide ions do not recombine

within 10 ps. Again, this discrepancy is due to the difficulty associated with accurately treating the energetics and dynamics of atomic collisions within the lattice. Contributions may also arise that depend upon the fraction of triiodide ions that are excited by the excitation pulse in a more complicated fashion than we have treated the process. Nonetheless, we are confident based upon these data that we are able to accurately reproduce the main features of photodissociation dynamics in crystalline tetra-*n*-butylammonium triiodide during the first few picoseconds following photolysis.

Simulated and measured absorption profiles for tetraphenylphosphonium triiodide are illustrated in Figure 7-17 for the same three wavelengths. Once again, all of the salient features of the experimental data are approximately reproduced numerically. Vertical lines are superimposed over the 600 nm traces to illustrate the agreement between the phases of the coherent portion of the signal. The slow decay dynamics are reproduced qualitatively at all wavelengths – the decay rate on either side of the absorption maximum is faster than at the band center – but the rates are not quantitatively correct. Improved numerical accuracy can be achieved by introducing larger phenomenological vibrational energy dissipation rates, but this offers no additional insight into the molecular dynamics. It is also possible that the geminate recombination rate is slightly underestimated by our MD simulation. Improvements in these features would require more careful consideration of the non-bonding interatomic potentials employed.

Finally, Figure 7-18 presents a comparison between the observed and calculated absorption profiles for tetraethylammonium triiodide at wavelengths of 660 nm, 740 nm and 820 nm. As for the other solid-state triiodides, all of the salient features found in the

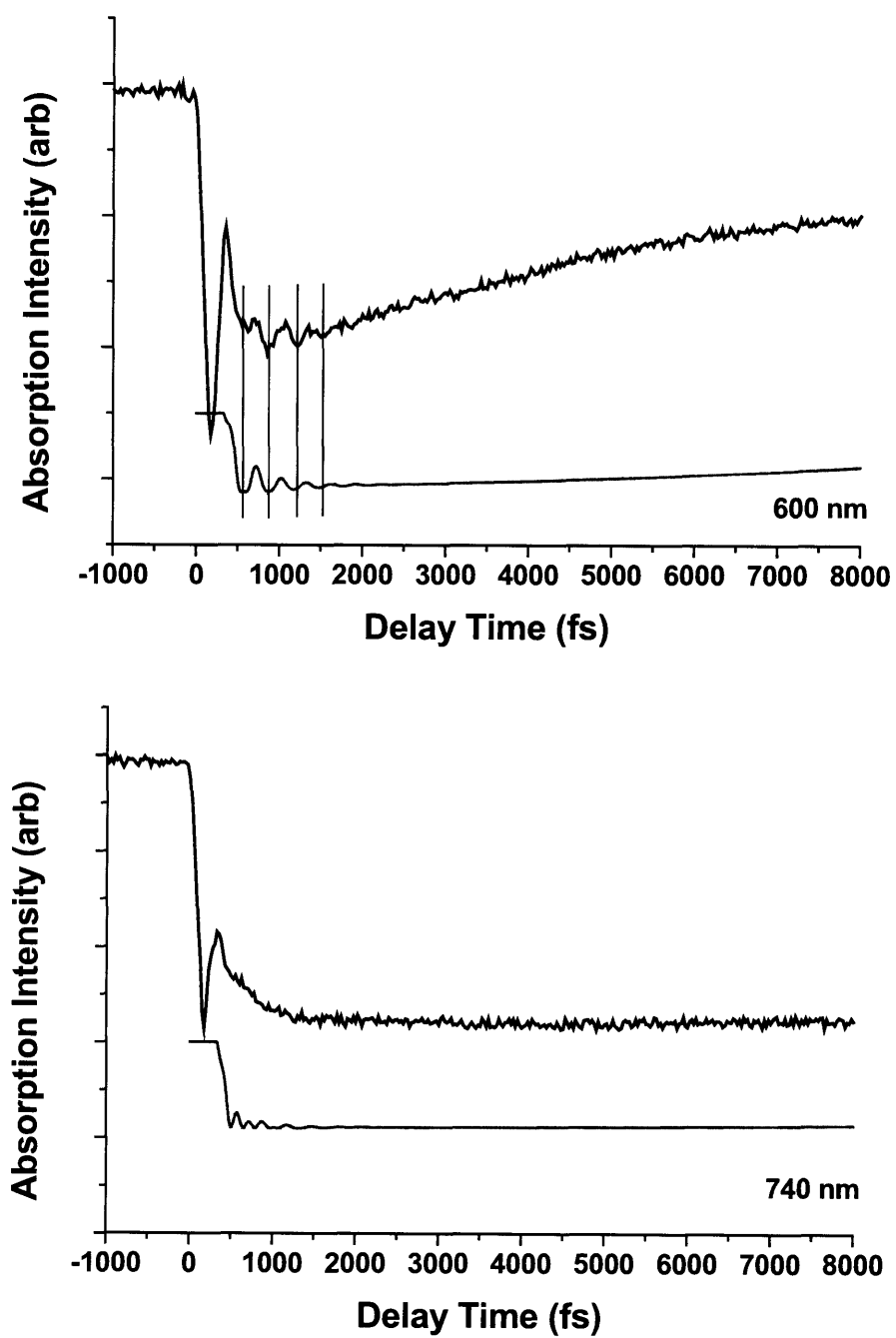


Figure 7-17. Simulated (grey) and measured (black) transient absorption profiles at a probe wavelengths of 600 nm and 740 nm for the photodissociation of crystalline tetraphenylphosphonium triiodide.

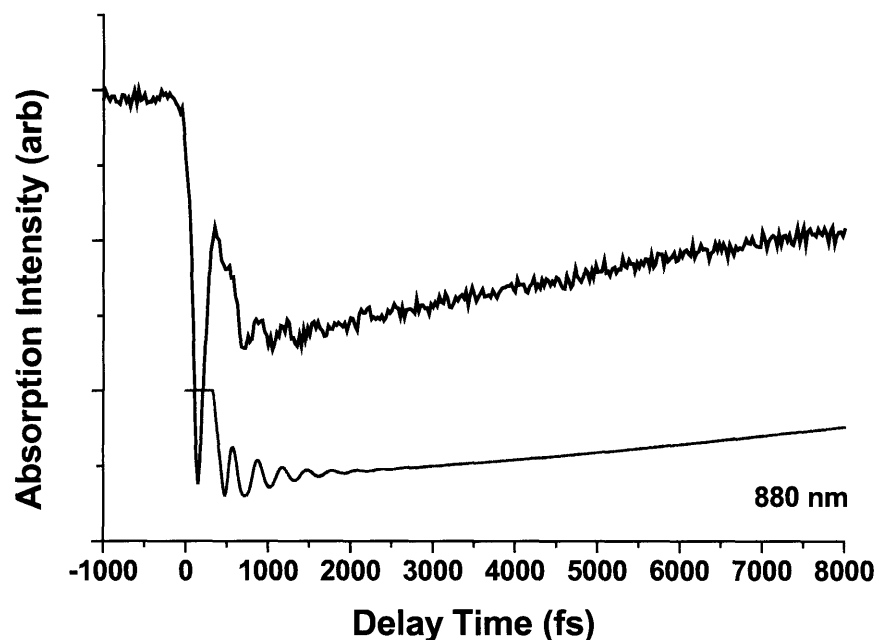


Figure 7-17 (cont'd). Simulated (grey) and measured (black) transient absorption profiles at a probe wavelength of 880 nm for the photodissociation of crystalline tetraphenylphosphonium triiodide.

experimental data at short times can be approximately reproduced via simulation. The phases of oscillations on either side of the absorption maximum are properly recovered, and the absence of oscillatory behavior near the center of the band is also properly treated (although there is a very small oscillatory signal in the simulated data at 740 nm, the contribution is much smaller than at either 660 nm or 820 nm). The time scale over which the transient absorption decays rather abruptly at all wavelengths is also recovered, although as observed before for tetra-*n*-butylammonium triiodide, we calculate nearly complete geminate recombination whereas the data appear to indicate that a small fraction of the diiodide fragments remain throughout our 10 ps window. It is very likely that the fragments from these dissociation reactions escape their local lattice cage and

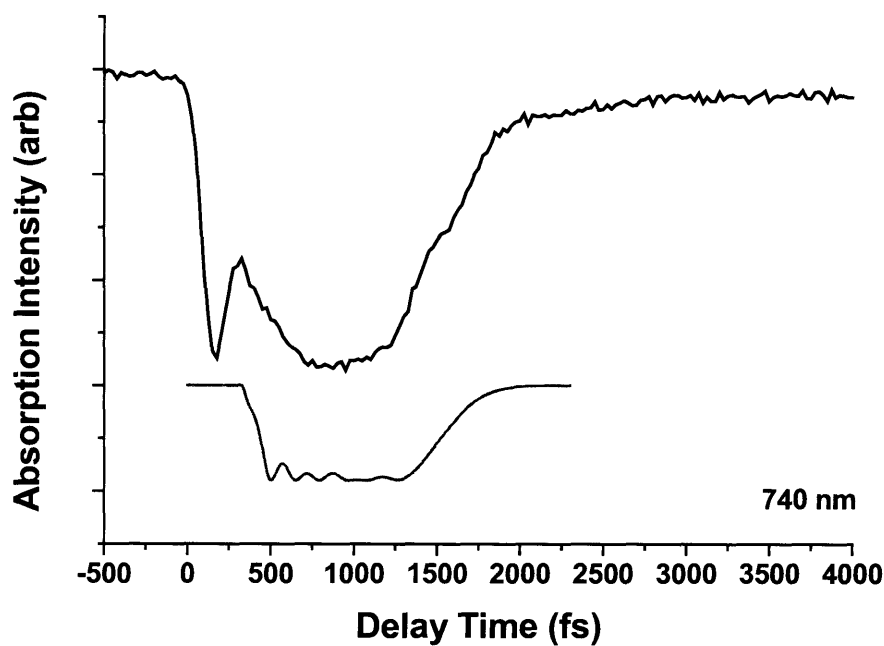
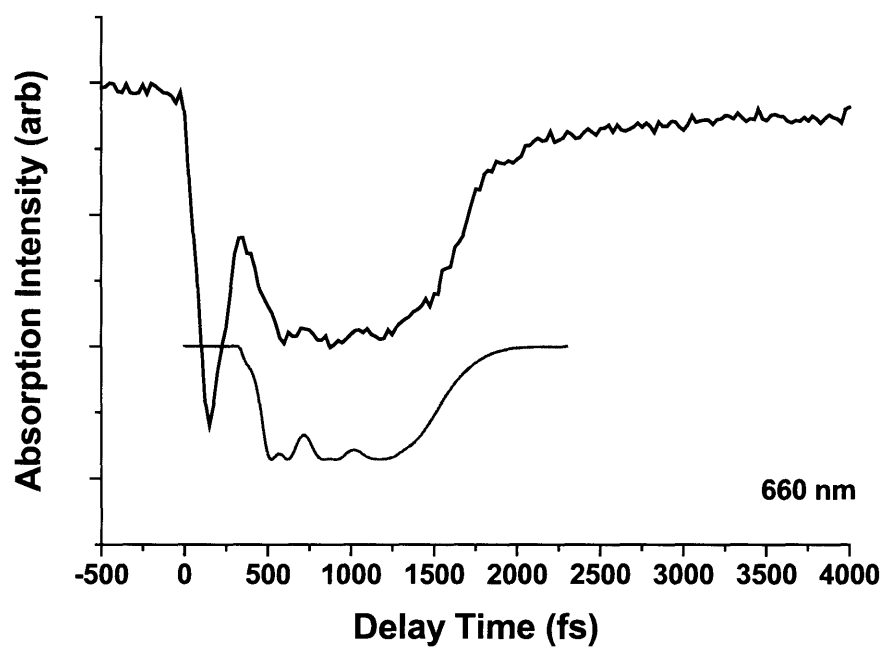


Figure 7-18. Calculated (grey) and measured (black) transient absorption profiles for diiodide ion generated in the photodissociation of crystalline tetraethylammonium triiodide. The probe wavelengths are 660 nm and 740 nm.

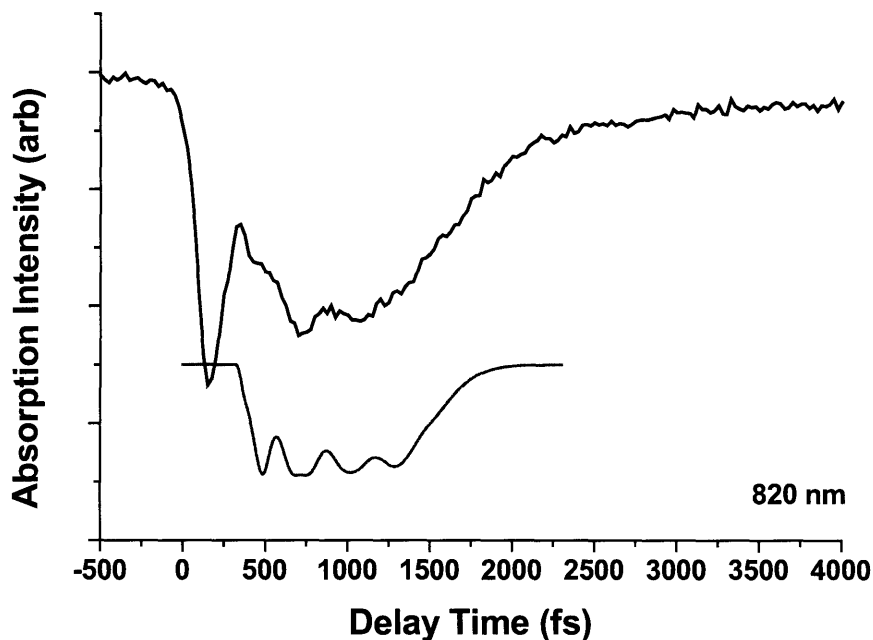


Figure 7-18 (cont'd). Calculated (grey) and measured (black) transient absorption profiles for diiodide ion generated in the photodissociation of crystalline tetraethylammonium triiodide. The probe wavelength is 820 nm.

undergo extended diffusional motion. Although we have no direct information about what gives rise to permanent visible damage to the crystals after a single laser shot, it is possible that long-lived photoproducts and local structural rearrangements around them are responsible. Another possibility is that the iodine radicals and diiodide ions react chemically with other lattice constituents, generating unusual species locally within the structure.

The data and simulations we have presented strongly support the following picture of the dissociation dynamics in triiodide molecular crystals. In both tetra-*n*-butylammonium triiodide and tetraethylammonium triiodide, dissociation of triiodide ions due to the action of the photolysis pulse occurs on an ultrafast time scale. Diiodide

reaction products are first discernable after only 325 fs. Both the iodine atoms and the diiodide ions undergo rapid collisions with the surrounding lattice cage. Because of the structural environment of tetra-*n*-butylammonium triiodide, the recoil dynamics are strongly directed backwards along the original motion coordinate, and geminate recombination occurs with high efficiency in about 1000-1100 fs. In tetraethylammonium triiodide, the lattice environment is marginally less constrained, providing an opportunity for slightly more prolonged motions of separated fragments. However, geminate recombination occurs here too with high efficiency after about 1400-1600 fs. For crystalline tetraphenylphosphonium triiodide, the situation appears to be completely different. The relatively large “pocket” in which the triiodide ion sits creates ample opportunity for the photodissociated fragments to interact multiple times with the lattice cage. Although some geminate recombination does occur within the window of the experiment, it is clear that after 10 ps, a substantial fraction of the original I_3^- ions remain dissociated, and they are responsible for the strong transient absorption signal for this compound for $t > 2000$ fs, which neither of the other crystalline triiodides exhibits.

7.5 Conclusion

In this chapter, we have presented the first measurements of the photodissociation dynamics of crystalline triiodides. The single-shot transient absorption technique we have developed provides a sensitive structural probe for I_2^- ions, and gives an accurate picture of the time scale for their formation, their coherent vibrational motion, and their disappearance due to geminate recombination processes. Through molecular dynamics simulations, we have been able to interpret our data in terms of the atomic scale motions

of photofragments and their interactions with the surrounding lattice atoms. Very strong correlations were observed between the specific lattice structure and the transient absorption behavior of each of the triiodides, due mainly to the range of translational motion afforded to reaction products within the constraints of their local environments. This unique lattice-based “caging” of the dissociation reaction in constrained geometries is analogous to the phenomenon observed in solution-based photochemical processes. However, the highly ordered crystalline environment affords us the opportunity to describe the dynamical nature of these interactions on a molecular scale.

References

- [1] Chattaway, F.D. and Hoyle, G., *J. Chem. Soc.* **123**, 654 (1923).
- [2] Ferraro, J.R. *et al.*, *J. Phys. Chem. Solids* **47**, 301 (1986).
- [3] Migchelsen, T. and Vos, A., *Acta Cryst.* **23**, 796 (1967).
- [4] Zadoyan, R. *et al.*, *J. Chem. Phys.* **101**, 6648 (1994).
- [5] Li, Z. *et al.*, *J. Phys. Chem.* **99**, 7453 (1995).
- [6] Zadoyan, R., Sterling, M. and Apkarian, V.A., *J. Chem. Soc. Faraday Trans.* **92**, 1821 (1996).
- [7] Sterling, M., Zadoyan, R. and Apkarian, V.A., *J. Chem. Phys.* **104**, 6497 (1996).
- [8] Bargheer, M. *et al.*, *J. Chem. Phys.* **111**, 8556 (1999).
- [9] Apkarian, V.A. and Schwentner, N., *Chem. Rev.* **99**, 1481 (1999).
- [10] Benjamin, I., Banin, U. and Ruhman, S., *J. Chem. Phys.* **98**, 8337 (1993).
- [11] Kuhne, T. and Vohringer, P., *J. Chem. Phys.* **105**, 10788 (1996).
- [12] Chen, E.C.M. and Wentworth, W.E., *J. Phys. Chem.* **89**, 4099 (1985).
- [13] Brenner, D.W., *Phys. Rev. B* **42**, 9458 (1990).
- [14] Brenner, D.W. *et al.*, *J. Phys. Condens. Mat.* **14**, 783 (2002).

Chapter 8

Conclusions and Future Work

This thesis has discussed the development and application of dual echelon single-shot femtosecond spectroscopy to the study of several classes of materials which undergo structural and chemical transformations on ultrafast time scales. The single-shot technique has been described in terms of its execution from the point of view of both data collection and automated analysis. We are now in a position in our laboratory to sensitively detect very rapid changes in material structure and recover time dependent responses automatically from our analysis algorithms.

We have also extended the utility of the single-shot setup greatly through the construction of a synchronized two-beam noncollinear optical parametric amplifier. This device provides two independent output pulses, each of sub-20 fs duration, which can be individually tuned to any wavelength from 500-720 nm. Frequency conversion in nonlinear crystals extends the effective range of the instrument even further. Wavelength tunability opens many new avenues for study by single-shot methods, since we can take advantage of resonance enhancement of stimulated Raman scattering, as well as (resonant) transient absorption, to probe material responses which were previously inaccessible – the stronger sample responses in these probing schemes relative to methods such as nonresonant stimulated Raman scattering are useful when data averaging is not employed.

We have used the single-shot setup to examine ISRS in both ionic crystals and molecular liquids, and have recovered material responses which are fully consistent both with established theory and the results of similar multi-shot measurements.

Intense femtosecond excitation of the semimetals bismuth, antimony and tellurium has revealed coherent oscillatory motion in the crystal lattice which is electronic in origin. Relatively weaker screening of ionic charges following promotion of valence electrons to the conduction band launches nuclear motion along fully-symmetric lattice coordinates. At the highest pump pulse intensities, coherent responses dephase very rapidly and only return after delays of several tens of picoseconds, suggesting the possibility of non-thermal melting of the lattice.

Similarly intense excitation of germanium telluride has led to rapid loss of lattice coherence commensurate with a solid-solid phase transition. Crystal bonds are weakened sufficiently by the generation of hot carriers that the energy barrier separating the low- and high-temperature phases can be overcome. Since the structural phase transition occurs along the A_1 mode coordinate, substantial softening of this mode is observed in the time-resolved reflectivity of the material.

The photochemistry of the triiodide/diiodide system has been investigated in detail in a number of solvents, allowing us to examine the effect of the local environment in mediating chemical reactivity. We have also extended our measurements to glassy environments in an attempt to exert some temperature-dependent control over the chemical dynamics. The roles of population relaxation and pure dephasing have been examined in the context of hot diiodide fragments which are generated in the reaction.

Finally, we have been able to correlate transient absorption measurements in solid-state molecular crystals of triiodide compounds with the results of molecular dynamics simulations, and in so doing develop a real-time picture of molecular photodissociation in ordered, highly-constrained environments. These measurements, along with the high intensity investigation of the semimetals, are true one-shot experiments since sample damage is commonly observed. Our single-shot methods give insight into the underlying mechanisms which would be difficult to acquire by other means.

Condensed phase photochemistry is particularly amenable to study using the single-shot method, and our results thus far on triiodide photodissociation suggest a number of interesting avenues to explore. Triiodide molecular crystals are easily prepared with a variety of counterions, each of which strongly influences the lattice structure and hence, the environment of the triiodide ion. Systematic variation of these environments should permit very detailed examination and simulation of the evolving molecular dynamics of photofragments. The loss of phase coherence in diiodide ions, in addition to vibrational cooling and rotational diffusion, reveal important details regarding the manner in which the lattice constrains a chemical reaction through strong interaction with the products. It may even be possible to detect phonon modes in the surrounding lattice which are excited via nuclear collisions.

Many other polyiodide species exist as well, including for example pentaiodide (I_5^-), heptaiodide (I_7^-), and decaiodide (I_{10}^{2-}). It would be extremely interesting to explore the photochemical behavior of these species, all of which assume different geometries: pentaiodide is V-shaped, heptaiodide is Z-shaped, and decaiodide is ring-shaped. In our

studies, we have focused on molecular triiodide crystals; that is, crystals which consist of more-or-less isolated triiodide ions surrounded by a matrix of non-interacting, inert cations. However, crystal morphologies within this family vary widely, and there are known compounds where the triiodide (or polyiodide) ions form one-dimensional chains or two-dimensional network structures. Often, these compounds have high conductivity on account of the orbital overlap between neighboring ions. Correlation of electronic charge-transfer dynamics with coherent nuclear motion might reveal interesting electron-phonon coupling behavior. The ordered geometry of such crystals (and their low dimensionality) would provide an appealing target for simulation.

In addition, mixed trihalides such as I_2Br^- and higher polyhalides can be prepared in a manner similar to the triiodides. The study of such compounds might be used to investigate the role of symmetry-breaking on the coherent dynamics of molecular fragments. With a carefully designed experiment on a suitable solid-state asymmetric trihalide, it might be possible through judicious choice of pulse frequency and phase to exert control over the reaction products; in other words, to force dissociation to one side or the other under the influence of the photolysis pulse.

Finally, there are countless other experiments, in addition to photochemistry, which would benefit from the application of single-shot methods. Stimulated Raman scattering or transient absorption experiments in energetic materials under shock-loading (either laser-induced or via a compressed-gas gun) have traditionally been difficult to conduct since the sample is destroyed under these highly nonequilibrium conditions. Probing with single-shot methods is naturally advantageous in these systems. Investigation of the dynamics of laser-generated plasmas in dielectric materials, structural

phase transitions in ferroelectrics, and non-thermal melting in semiconductors would also be of great interest, and would benefit from our single-shot measurement technique.